Gas flow measurements in shales: laboratory, field and numerical investigations

Konstantin Rybalcenko

Submitted in accordance with the requirements for the degree of
Doctor of Philosophy

The University of Leeds

School of Earth and Environment

January 2017

Declaration of authorship

The candidate confirms that the work submitted is his own and that appropriate credit has been given where reference has been made to the work of others.

Publications

Fisher, Q., Grattoni, C., **Rybalcenko, K**., Lorinczi, P., Leeftink, T. (2016). Laboratory Measurements of Porosity and Permeability of Shale. Fifth EAGE Shale Workshop, DOI: 10.3997/2214-4609.201600389.

Lorinczi, P., Burns, A. D., Lesnic, D., Fisher, Q. J., Crook, A. J., Grattoni, C., **Rybalcenko, K.** (2014). Direct and inverse methods for determining gas flow properties of shale, *Society of Petroleum Engineers*, pp.1-26. doi: 10.2118/167750-MS.

Lorinczi, P., Burns, A. D., Lesnic, D., Fisher, Q. J., Crook, A. J., Grattoni, C., **Rybalcenko, K.** (2014) Finite volume method for modelling gas flow in shale. In: *ECMOR XIV - 14th European conference on the mathematics of oil recovery*. 14th European conference on the mathematics of oil recovery, 8-11 September 2014, Catania, Italy. EAGE , 1 – 13, doi.org/10.3997/2214-4609.20141795.

Acknowledgments

Abstract

A multi-disciplinary research project including experimental and modelling studies was carried out on shale samples to characterise their porosity and permeability. Pressure expansion techniques were used, including current industry-standard methods as well as new methods developed and modified throughout this research. The derived porosity and permeability values were cross-checked with the results from commercial laboratories. Finally, the results obtained were applied to a shale resource play currently being appraised to understand its commercial viability.

Precise grain density results were achieved using the crushed shale method as helium is able to rapidly intrude small sample pores and is not significantly adsorbed onto the constituents of the shale. Precise bulk volume measurements were obtain using mercury immersion but these are ambient stress measurements and need correcting for *in-situ* conditions. Mercury probably does not enter the pore-space of shale at low pressures during MICP tests and instead closes artificial microfractures. So the results may provide a method to estimate bulk density at the reservoir stresses.

The porosity measured using the crushed shale method is more accurate compared to core plug methods. It is important to dry crushed samples to standardise porosity measurements. Other laboratories produced comparable results except for one laboratory which most likely did not conduct sample cleaning procedures properly.

Permeability values obtained using the crushed shale method were orders of magnitudes different between the measurements conducted during this study and commercial laboratories. Overall, this test appears to provide no useful information regarding the flow properties of shales. Measurements made on core plugs are often dominated by the presence of microfractures but it is possible to obtain reasonably reliable permeability estimates by inverting the experimental data using a dual porosity-permeability model.

To assess the applicability of porosity and permeability methods on commercial shale play, a significant amount of *in-situ* field data (i.e. well tests, core data etc.) were gathered and tested during the collaborative project in Sweden with a local gas exploration company. Gas-In-Place (GIP) and Estimated Ultimate Recovery (EUR) values were produced and based on these the project was approved by the company for the next stage of development. However the model constructed lacked the ability to reproduce the well flow production rates.

Contents

x

List of figures

List of tables

1 Chapter
Introduction

1.1 Overview

Natural gas is an important source of cheap, safe and reliable energy for both industrial and domestic users. Gas extraction in the USA has made a considerable contribution to the economy, allowing local producers to lower their costs and stay competitive in the global markets. Natural gas generates around 30% of total electricity in the USA (EIA, 2016) and around 15% of total electricity in European Union (Eurostat, 2014). In 2000 shale gas, which is classified as an unconventional gas resource because of its production method, accounted for only about 1% of overall gas production in the USA, whereas in 2010 its contribution rose to 20% (EIA, 2012; Stevens, 2012). In fact, increased local production from the shale gas resources over the past decade allowed the USA to end reliance on imported natural gas and to become one of the largest gas producers (CIA, 2011). It is also estimated that shale gas will account for over 40% of the overall gas production in the USA by 2035 (Stevens, 2012; EIA, 2016). The latest U.S. Energy Information Administration update on the shale gas estimates proven reserves of shale gas in USA to be >2 TCF (EIA, 2015).

Shale production rise has particularly benefited from innovations made by independent oil and gas companies who have managed to refine drilling and completion strategies. On the other hand, core analysis seems not to have played a significant role in this success possibly because it produces unacceptable errors even in standard techniques such as porosity and permeability measurements. Various commercial laboratories show differences in porosity results of up to 100% and permeability of up to 4 orders of magnitude for the same shale samples (Figure 1.1). Identifying the reason for these inconsistencies was a key aim of this research.
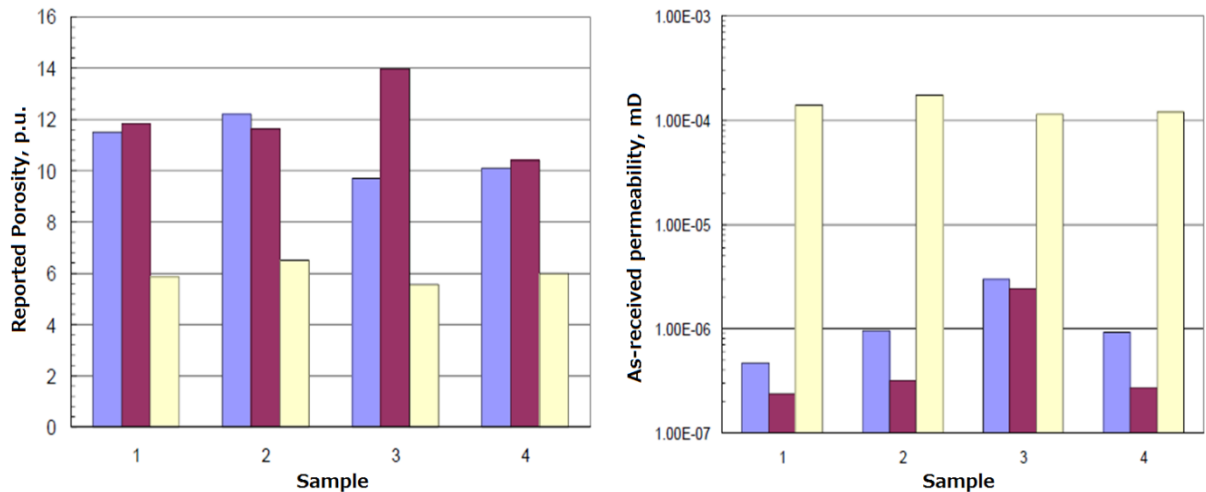
Figure 1.1. Porosity and permeability results for the same shale samples from three different laboratories – the number on the x - axis represent the sample and the colour different laboratory (Passey et al., 2010).

1.2   Shale gas development

Shales have been exploited for the gas production since the 1820's (Drake, 2007). Well stimulation procedure by hydraulic fracturing was introduced by Stanolind, an exploration and production branch owned by Amoco, in 1947 and has been applied in millions of well treatments since then (Jones and Britt, 2009). The technological developments that focus on shale production started in the 1970's with the joint efforts of the US Department of Energy (DOE), Gas Research Institute (GIP) and several independent companies in the Devonian shale formation (King, 2010). Many technological innovations were developed at that time, including improvements in horizontal well drilling and hydraulic fracturing. Later the independent companies started to apply hydraulic fracturing on a larger scale in the Barnet shale and consequently the whole shale gas industry started to expand between 1990 and 2010 (Jones and Britt, 2009). The new techniques are briefly described below.

- **Hydraulic fracturing** has become the primary technological driver that has allowed the economic production of gas from shale resource plays. It involves pumping high pressure fluids to create fractures followed by proppant injection (sand similar material designed to keep fractures open) (King, 2010).   The procedure can include up to twenty stages and is performed to increase the contact area between the well bore and the shale formation (Figure 1.2). Microseismic data have been interpreted to suggest that sophisticated multi-stage hydraulic fracturing procedure can create a complex fracture network

reaching up to 9,000,000 m^2 of contact area between the fracture and the matrix (Warpinski et al., 2008).
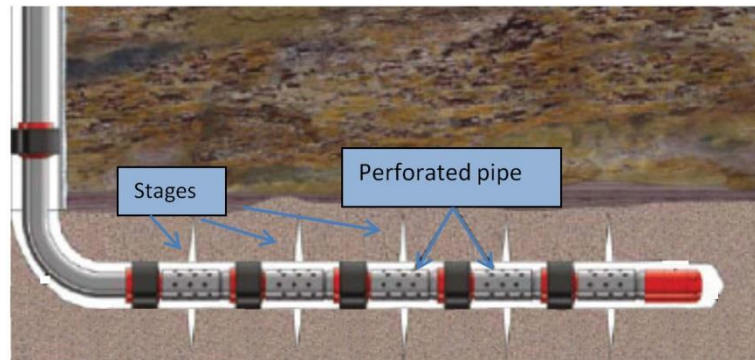
Figure 1.2. Multi-stage horizontal well stimulation representation. Packers are used to isolate the stages to be simulated. Water is pumped into each zone creating fractures within the shale layer (Halliburton, 2015).

- **Horizontal wells** have a major advantage over the vertical wells in terms of the contact area with the shale formation. The horizontal section is isolated using packers or degradable frac-balls to enable multistage fracturing (Britt and Schoeffler, 2009; Cipolla et al., 2009; Aviles et al., 2013).

- **Slick-water fracturing** (SWF) was an improvement that considerably increased the effectiveness of hydraulic fracturing operations. The technique makes use of lower viscosity water with a lower concentration of small proppant. This distributes proppant deeper within the fracture network and allows a more complex fractures to develop (Britt and Schoeffler, 2009; King, 2010).

1.3   Origin of shale gas

Natural gas is liberated from organic matter as it is heated up during burial and is then stored in the shale. The gas is stored as "free gas" in pores and natural fractures present in the shale matrix. Clays and organic matter within the shale may also adsorbed gas increasing the overall storage capacity of the shale (Lu et al., 1995; Kang et al., 2010). In other words, gas is released from a number of storage systems during the production.

Shale formations are characterised by their ultra-low permeability caused by the small pore sizes, which results in a huge restriction to the gas flow through the matrix. In laboratories, shale core plugs may take weeks to achieve the steady-state gas flow during permeability analysis. In addition, narrow pore throats create non-Darcy flow conditions, which can differ in conductivity compared to surrounding microfractures and high

conductivity pathways by several orders of magnitude, making the overall behaviour of gas in shale difficult to predict.

1.4 Challenges

In the past, the ultra-low conductivity of the fine grained rocks such as shale were mostly analysed for their sealing abilities for the nuclear waste repositories and as seals for conventional petroleum reservoirs (Brace, 1980; Davies et al., 1991; Coyner et al., 1993; Osborne and Swarbrick, 1997; Dewhurst et al., 1998; Katsube, 2000; Yang and Aplin, 2007; Boulin et al., 2011). In such cases, low permeability is considered as a vital feature for the whole system. In contrast, for the development of shale plays and in particular for the petrophysical analysis of shale samples, low permeability is the main challenge to overcome.

1.4.1 Core handling and preparation

There are many challenges making the analysis of shale a complex task. The fragile shale samples may be damaged during coring and particularly during core extraction as the low permeability of the shale prevents the gas reaching pressure equilibrium and may result in the formation of fractures (Blackbourn, 2012). Even after a successful coring trip and transportation to the laboratory, obtaining undamaged core plugs is problematic because shale is often laminated so it is prone to split easily during analysis.

Another challenge related to the core handling is the preparation of the sample for the experiment. Although there is an industry standard for conventional core preparation (Brunton et al., 1985; Blackbourn, 2012), there is no standard method for dealing with shale samples from the well to the experimental apparatus, which is crucial given the sensitivity of the shale core analysis. Also, water often cannot be used for drilling core plugs as it reacts with the shale resulting in shale splitting along the bedding. Instead, core plugs often need to be drilled using either diesel or air as the lubricant.

After the core sample is prepared, it undergoes routine core analysis (RCA) and special core analysis (SCAL) during which various petrophysical parameters are measured (API, 1998; Andersen et al., 2013). Porosity and permeability are the most important parameters that laboratories attempt to measure. However, there is no agreed standard method for measuring the porosity and permeability of shale. Instead, most methods used by service companies are proprietary and the methods used are not even disclosed to customers.

1.4.2 Heterogeneity of the cores

Shale formations often have a complex geology and potentially several gas storage systems exist, which may be difficult to distinguish in experiments (Figure 1.3). For this reason, many researchers have suggested that double and triple porosity models used to simulate the gas storage in coals should be applied to shales (Brunauer et al., 1938; Dubinin, 1975; Arri et al., 1992; Bae et al., 2009; Cui et al., 2009). However, heterogeneity analysis on higher scale is also important as shale is often strongly laminated and the results of the experiments are affected by the orientation at which the core plugs are drilled.
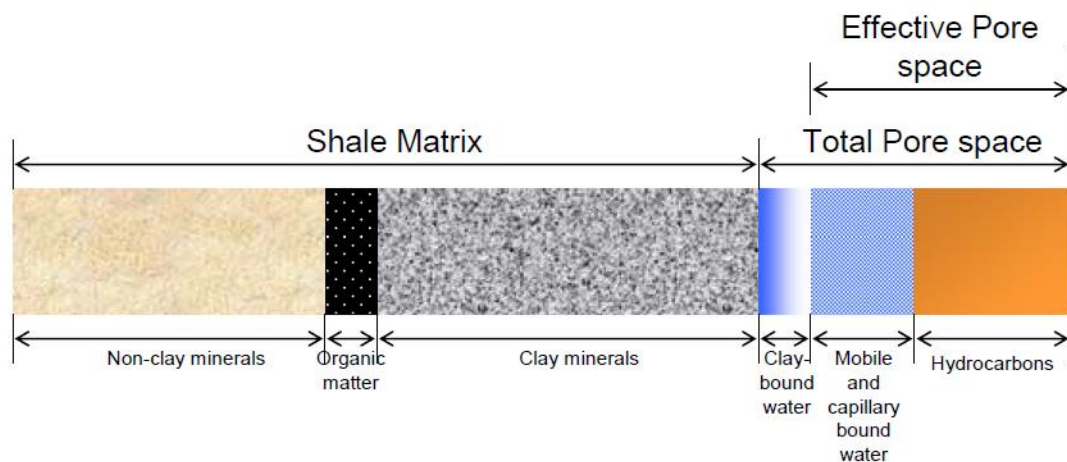
Figure 1.3. Complex porous system of the shale samples (Passey et al., 2010).

1.4.3 Computational challenges

Most experiments conducted during this research involved recording a pressure transient as gas was expanded into or out of the shale samples. The pressure transient was then inverted to estimate permeability and other parameters that are needed to model gas flow in shale. There exist several models to invert pressure transients for these parameters (Civan et al., 2011; Lorinczi et al., 2014), however most include terms that are challenging to obtain experimentally (e.g. tortuosity).

Inverting pressure transients often results in non-unique solutions, especially when deriving strongly coupled parameters. This means that inversion might produce several sets of completely different permeability values that all match the experimental data. There are many other computational limitations when modelling full-scale shale resource plays. The difficulties arise because of the high complexity of the shale formations and requirements for high definition fracture representation. For example, industry-standard methods for modelling shale gas resource plays, such as the Volumetric Fracture

Modelling Approach (VFMA), requires huge computational resources (Harikesavanallur et al., 2010; Kalantari-Dahaghi and Mohaghegh, 2011).

1.5 Objectives

This Thesis was structured to solve the challenges outlined in the previous section. Essentially, all objectives can be grouped into two tasks: understanding gas behaviour in a shale matrix and development of improved methods for measuring gas flow in shale; specific objectives include:

- Conducting a wide variety of experiments under different conditions, compare the results and propose a standardised most optimum methods for porosity and permeability determination of shales. That includes analysing and comparing the results of other laboratories.

- Understanding gas storage mechanisms within shale matrix and how to define it using porosity.

- Understanding the impact of sample heterogeneity on porosity and permeability results; this includes heterogeneity on both micro and macro levels.

- Improving the measurement and inversion of porosity and permeability of fractured shale samples (both core plugs and crushed particles).

- Simplifying the shale parameter inversion process, especially when considering complex flow equations including terms for gas flow mechanisms other than simply Darcy flow.

- Implementing the simplified permeability and porosity solution process into industry-standard software package.

1.6 Organization of the Thesis

This thesis contains four broad topics, divided into eight chapters including this introduction. The four topics are: a general overview of the shale gas, an industry and shale analysis; literature review critically assessing current shale permeability measurement techniques; methodologies; results and discussion of the research conducted. The details of the following chapters are:

Chapter 2 provides a literature review and critical assessment on the subject.

Chapter 3 describes the shale samples used, experimental techniques and methodologies.

Chapter 4 presents results and discussion on shale structure characterisation. Origin of the samples, petrophysical properties, matrix imaging results and analysis are presented.

Chapter 5 presents a discussion on porosity results using pressure expansion experiments. Results from various experimental and simulation methods are discussed and cross-compared.

Chapter 6 presents a discussion on permeability results using pressure expansion experiments. Improvements for the more accurate shale permeability measurements are suggested.

Chapter 7 presents field study results. Work on the shallow shale gas field characterisation is provided and the estimations of the possible reserves are given.

Chapter 8 provides the summary of the research.

2 Chapter
Gas flow in shales

This chapter provides a review of the current knowledge on gas flow in shales and methods used to characterize the porosity and permeability of shale. The chapter starts by describing porosity of shale matrix (Section 2.1). Gas flow mechanisms in shales are then described, including an overview of the main flow parameters (Sections 2.2 – 2.5).

The theory is followed by a description of the techniques currently used for porosity and permeability determination (Sections 2.6 and 2.7 respectively). Adsorption models are then described, including critical assessment of currently used methods (Section 2.8). Finally, numerical and analytical models are presented that are used for determining the permeability of shale from experimental results (Section 2.9).

2.1 Porosity

Porosity (Φ) is the proportion of pore volume (V_p) within a rock that can contain water or hydrocarbons. It is an intrinsic property of the rock and is a primary parameter for the Gas-in-Place (GIP) estimations. Porosity is derived from measurements of bulk volume (V_B) and grain volume (V_G) as described in the Recommended Practices for Core Analysis (API, 1998):

$$V_P = (V_B - V_G) \qquad \text{(Equation 2-1)}$$

$$\Phi = (V_B - V_G)/V_B \qquad \text{(Equation 2-2)}$$

Two types of porosity are defined depending on the connectivity of the pores: effective and total. Effective porosity represents the pores that are interconnected excluding isolated pores. In contrast, total porosity accounts for the overall void space within the rock. It becomes challenging to distinguish between the total and effective porosities in shale because of the tight pore spaces. Furthermore, sample preparation and cleaning might alter the matrix structure. Therefore different petrophysical laboratories can provide porosity results that vary by up to 100%.

Shales have large surface area due to their fine grain size whereas the presence of kerogen and clays give them a high adsorption potential for the gasses like methane (Schettler et al., 1991). Consequently, adsorption has to be determined and taken into account when calculating GIP. The effective porosity due to gas adsorption is given in terms of the Langmuir-type gas adsorption (Cui et al., 2009) (Equation 2-3). According to

the Langmuir-type gas adsorption, porosity contribution by gas adsorption onto the rock sample increases with decreasing experimental pressure. The amount of gas that a rock sample can adsorb is determined by the Langmuir volume of that rock. Cui et al. (2009) showed that 10 $cm^3 g^{-1}$ of Langmuir volume can create as much as 50% of adsorption porosity at pressures below 1 MPa (145 psig).

$$\Phi_a = \frac{\rho_s}{V_{std}} \frac{(1-\Phi)}{c_g \rho} \frac{q_L p_L}{(p_L + p)^2}$$
(Equation 2-3)

where Φ_a is the effective adsorption porosity (dimensionless), ρ_s is the density of the sample (g/cm^3), V_{std} is the molar volume of gas at standard pressure and temperature (m^3/mol), Φ is porosity (dimensionless), c_g is gas compressibility (Pa^{-1}), ρ is the density of gas (mol/m^3), q_L and p_L are Langmuir volume (cm^3/g) and pressure (Pa) respectively, which are specific for the rock, and p is the experimental pressure (Pa).

Adsorbed molecules can move along the pore surface depending on the concentration gradient of the gas (Mason and Malinauskas, 1983); this phenomenon is called surface flow. Unfortunately, little research has been done on surface flow and it is not taken into account by standard simulation models. Therefore, surface flow was neglected in this study and the main focus was put on simulating viscous flow and slip flow, which are described below.

2.2 Viscous flow

Viscous (or convective) flow is the most important gas flow mechanism in conventional reservoirs. It results from potential energy within the gas phase (Mason and Malinauskas, 1983). The basic equation describing viscous flow was derived by Henry Darcy (Dake, 1978):

$$Q = \frac{kA}{\mu} \frac{\Delta P}{L}$$
(Equation 2-4)

where Q is flow rate (cm^3/sec), k is the permeability (m^2), μ is viscosity (cP), ΔP is the pressure drop across a sample (atmos) and L is the length of the sample (cm). In traditional (i.e. non-SI) units, a rock with a permeability of 1 Darcy will allow a fluid with a viscosity of 1 cp to flow through a cross sectional area of 1 cm^2, at a pressure gradient of 1 atmos/cm at a rate of 1 cm^3/sec.

Darcy's equation links the flow rate with the permeability constant, which is an important characteristic describing the movement of fluid through porous media and depends on the connectivity of pores, sorting, mineralogy and rock electrical properties (Ogilvie et al., 2002). It is an indicator of hydrocarbon recovery and overall performance of a reservoir, which makes permeability a vital parameter in shale gas plays. Acompressibility term is added to the Darcy's equation for the gas flow calculation (Dake, 1978):

$$Q = \frac{kA}{\mu B}\frac{\Delta P}{L}$$

(Equation 2-5)

where *B* is gas formation volume factor, expressed as:

$$B = \frac{V_R}{V_{SC}} = \frac{znRT}{p} = \frac{p_{sc}Tz}{pT_{sc}}$$

(Equation 2-6)

where V_R is volume of gas at reservoir temperature and pressure (m^3), V_{SC} is volume of gas at standard conditions (m^3), *n* is number of moles (mol), *R* is ideal gas-law constant (J mol^{-1} K^{-1}), P_{sc} is pressure at standard conditions (Pa), *T* is absolute temperature (K), *z* is compressibility factor (dimensionless), *p* is absolute pressure (Pa) and T_{sc} is temperature at standard conditions (K).

Darcy equation was derived from the Hagen – Poiseuille flow (Equation 2-7), where it was suggested that the flow rate within a capillary is directly proportional to the radius of the tube (Sutera and Skalak, 1993).

$$Q = -\frac{\pi r_0^4}{8\mu}\frac{\Delta P}{L}$$

(Equation 2-7)

where *r* is the radius of the capillary (cm). According to this equation, the flow is directly proportional to the radius of the capillary by the fourth power. In the porous medium consisting of a cluster of identical tubes with the effective radius r_{eff}, the effect of reduction of the pore radius by a factor of 2 would reduce the flow through each tube by a factor of 16. However, in this case, the number of tubes would be increased by 4 to compensate for the overall area, therefore the flow rate is proportional to the effective pore radius squared (Clennell, 1997) (Equation 2-8). Permeability is directly proportional to the flow rate, hence it should also scale with the grain radius in the same way as shown in Equation 2-9. Following the relation from Equation 2-9, many empirical permeability equations were derived based on pore radius knowledge. Kozeny (1927) introduced his

semi-empirical equation of permeability based on relation in Equation 2-9 (Equation 2-10) (Clennell, 1997).

$$Q \propto r_{eff}^2 \qquad \text{(Equation 2-8)}$$

$$k \propto r_{eff}^2 \qquad \text{(Equation 2-9)}$$

$$k = \frac{\Phi r_h^2}{C_k} \qquad \text{(Equation 2-10)}$$

where r_{eff} is effective radius of the capillary (cm), r_h is the hydraulic radius defined as the ratio of the cross-sectional area normal to flow and wetted perimeter of the flow channels (dimensionless), C_k is the Kozeny constant (dimensionless), Φ is porosity (fractional), Q is flow rate (cm^3/sec) and k is permeability (m^2).

By assuming pore space as a bundle of parallel capillary tubes with a common hydraulic radius and cross section of r_h/C_k - Kozeny (1927) stated that the flow path could be tortuous and have an effective hydraulic length, l_{eh}. In this case the permeability is reduced by l_{eh} divided by the minimum length between the flow paths, l_{min}, deriving hydraulic tortuosity (Equation 2-11).

$$\tau_{hK} = \frac{l_{eh}}{l_{min}} \qquad \text{(Equation 2-11)}$$

Several models were derived based on the Hagen – Poiseuille equation, accommodating many flow mechanisms described in the sections below. However, most of these models used for modelling gas flow in shales are unsatisfactory because of the inadequate representation of other flow regimes. The permeability derived using these theoretical methods might deviate from true permeability and needs various corrections before it becomes representative of the shale formation.

Mason and Malinauskas (1983) assessed errors in flow calculations caused by different porosity systems. They assumed a system of parallel pores, having their own lengths and cross sections, positioned in the parallel arrays. The base case of this system being a heteroporous arrangement (different arrays having their own porosities) was compared to the case of homoporosity (averaging porosities into single effective porosity value). The lower and higher error boundaries were derived for these cases. The result was that the maximum error boundary was achieved by the system composed of the large pores surrounded by the small pores, so that the small pores would add up to the majority of

the porosity (>90%), but most of flow would happen through the large pores (Mason and Malinauskas, 1983) (Figure 2.1). Conversely, the minimum error was shown by the homoporous system with equal pores. They calculated that most pore distributions caused small to moderate errors, with largest deviations being caused only by exceptional circumstances.

	Highest error	Lowest error
Large pores	Volume: <10% Flow: >90%	Homoporous system
Small pores	Volume: >90% Flow: <10%	
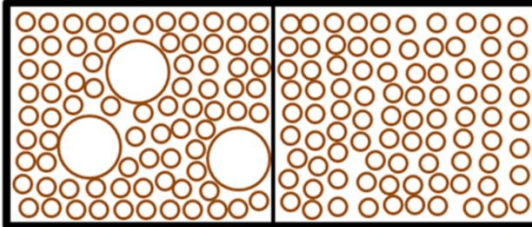
Figure 2.1. Schematic representation of the Mason and Malinauskas (1983) porosity system analysis.

2.3 Gas slippage

Thye narrow pore throats within shale mean that gas flow may occur by several mechanisms (Javadpour, 2009; Freeman et al., 2011). A parameter called the Knudsen number provides a measure of which gas flow mechanism operates within narrow pore throats (Equation 2-12).

$$K_n = \frac{\bar{\lambda}}{r_{pore}}$$
(Equation 2-12)

where K_n is the Knudsen number (dimensionless), $\bar{\lambda}$ is the mean free path of the molecules (m) and r_{pore} is the pore throat radius (m). A Knudsen number of 0.01 is the highest limit of viscous flow. At Knudsen numbers greater than 0.01, gas behaviour starts to deviate from the Darcy flow. Transitional and slip flow (occurring at $0.1 < K_n < 10$ and $0.01 < K_n < 0.1$, respectively) are considered to be dominant for shale reservoirs (Figure 2.2).

It is usually the case that the mean free path of the gas molecules becomes similar in length to the pore throat radius of the shale (Javadpour, 2009). In which case, the

Knudsen number starts to increase and is no longer negligible. Molecules collide less frequently with each other and more often with the surfaces of the pores.

Physically this results in a non-zero velocity of the gas molecules at the surface of the pores, as the absence of the inter-molecular collisions cause inviscid flow. Consequently, gas flow starts to deviate from that described by Poiseuille's equation and by Darcy's Law. Therefore a correction term is required. The Knudsen number defines the extent to which flow deviates from Darcy flow. It has to be noted however that mean free path of the molecules is also influenced by the temperature therefore flow mechanisms might be different in subsurface conditions than in laboratory.
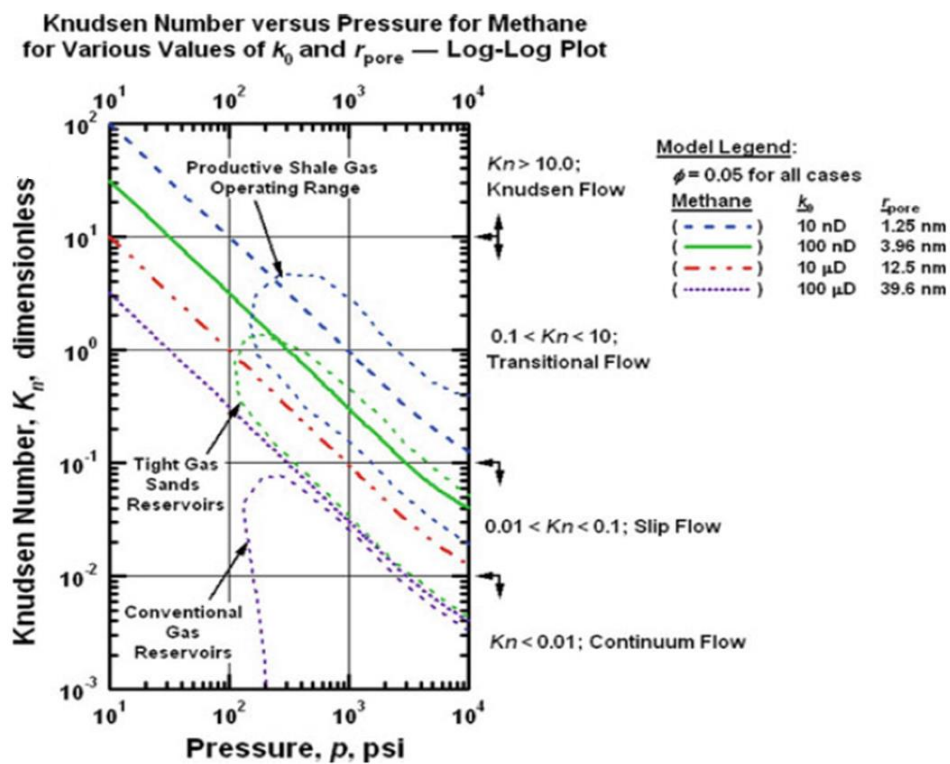
Figure 2.2 Gas flow type depending on Knudsen number (Freeman et al., 2011).

Klinkenberg (1941) considered the implication of the narrow pore throats on the flow. He pointed out that measurement of the gas permeability through such system overestimates permeability due to slip flow. Klinkenberg derived an equation to correct gas permeability measurements for slip flow (Klinkenberg, 1941):

$$k_a = k_0 \left[1 + \frac{b_K}{p} \right] \qquad \text{(Equation 2-13)}$$

where k_a is the apparent permeability (m^2), k_0 is the true or intrinsic permeability (m^2), p is the pressure (Pa) and b_K is the Klinkenberg constant (Pa). In the transitional region,

variable b_K should be used for more accurate permeability calculation (Freeman et al., 2010).

According to Equation 2-13, the Klinkenberg correction becomes more important as pressure is decreased as would occur as gas is produced from a reservoir. To avoid pressure dependence, Klinkenberg suggested measuring permeability at several pressures and extrapolating the results to infinite pressure; in practise this is achieved by plotting measured permeability against 1/P and then extrapolating the best fit line to 1/P = 0 (Figure 2.3). Mason and Malinauskas (1983) pointed out that extrapolated lower value of permeability is the first approximation for the Knudsen permeability (or Knudsen diffusion coefficient) $(K_0)_1$ rather than exact permeability value (Mason and Malinauskas, 1983). So although higher order approximations can be used, practically the difference between first and second order estimations is insignificant.
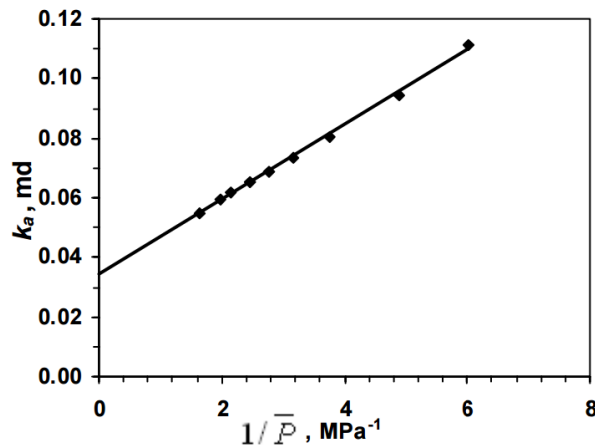
Figure 2.3. Apparent gas permeability vs. reciprocal mean pressure (Li et al., 2004). Extrapolation to the 0 x value is done to obtain first approximation of Knudsen permeability (intrinsic permeability).

2.4 Molecular diffusion

An alternative way of dealing with gas flow in shale is by considering that gas is composed of various components. Gas mixtures tend to separate due to the narrow pores in shale, hence a concentration gradient is created between the molecules of different gasses, which create molecular diffusion. Gas diffusion is described using Fick's law (Fick, 1995):

$$N_i = \frac{-D_e}{RT} \nabla(x_i p)$$

(Equation 2-14)

where N_i is the molar flux of component i (mole/ m^2 sec), D_e is the effective gas diffusivity (m^2/sec) and x_i is the mole fraction of component i. The disadvantage of Fick's law is that there are no parameters representing the matrix.

Two models that are usually used for the combined gas-phase diffusion and advection modelling are Advective Diffusive Model (or ADM) and Dusty Gas Model (or DGM) (Webb and Pruess, 2002). The ADM solves matrix representation problem by simple linear addition of Fick's and Darcy's equations and introduction of saturation, porosity and tortuosity multipliers to represent the porous media. In contrast, the DGM is a more elaborate method where porous medium is treated as a motionless and uniformly distributed one component gas mixture (Mason and Malinauskas, 1983). Particular parameters in the DGM compensate for the effect of forces on this gas mixture, therefore neither pressure gradient, nor any other kind of force affects this porous medium.

The difference between the two models increases with decreasing permeability (Webb and Pruess, 2002). In fact, when derived using both ADM and DGM methods, samples with permeabilities in the range of microDarcies, result in 2 orders of magnitude difference between permeability values at atmospheric pressure (Webb and Pruess, 2002). These models were not attempted in this study due to their complexity.

2.5   Tortuosity

There are several types of tortuosity including geometrical, electrical, diffusional and hydraulic. Each is employed in a different field, but essentially they all describe the resistive effect of the structure on a range of conduction, advection and diffusion processes (Clennell, 1997). In fluid flow, tortuosity is the ratio of the length of the tortuous flow path, l_e, to the straight line along the flow l, as was shown in Equation 2-11 (see Section 2.2) by Kozeny (1927) and also later by other authors (Carman, 1956). Current technology does not allow individual flow paths to be resolved and measured. Instead, the flow is homogenised and represented as population of tortuosities.

Most authors (Golin et al., 1992; Clennell, 1997) describe tortuosity as a structural characteristic of the medium. However, it correlates with permeability to such an extent that some studies indicate that it is practically impossible to simultaneously derive tortuosity and permeability (Clennell, 1997; Lorinczi et al., 2014). Mason and Malinauskas (1983) attempted to write the relationship for the tortuosity by defining a viscous flow parameter B_0. They assumed that a porous medium with porosity Φ, area A and length L

consists of a structure of non-interconnected circular capillaries with radius r, lengths L_{eff} and an area of πr^2. For one capillary, B_0 equals $r^2/8$. The general equation for the viscous flow flux is Equation 2-15, and per unit area of assumed surface it becomes Equation 2-16 or Equation 2-17. Mason and Malinauskas (1983) then substitute the porosity parameter to derive effective value for B_0 as Equation 2-18.

$$J_{visc} = Flow/Area = -(nB_O/\eta)\nabla p \qquad \text{(Equation 2-15)}$$

$$J_{visc} = -\frac{\pi r^2}{A}\left(\frac{n}{\eta}\right)\left(\frac{r^2}{8}\right)\frac{\partial p}{\partial z_{eff}} \qquad \text{(Equation 2-16)}$$

$$J_{visc} = -\frac{\pi r^2}{A}\left(\frac{n}{\eta}\right)\left(\frac{r^2}{8}\right)\left(\frac{L}{L_{eff}}\right)\frac{\partial p}{\partial z} \qquad \text{(Equation 2-17)}$$

$$B_0 = \frac{\varepsilon}{\left(L/L_{eff}\right)^2}\left(\frac{r^2}{8}\right) = \frac{\varepsilon}{q}\left(\frac{r^2}{8}\right) \qquad \text{(Equation 2-18)}$$

where distance parameter z_{eff} is measured along the path of the pore. To convert this distance z_{eff} to distance measured straight throughout the medium z, z_{eff} is multiplied by L/L_{eff} as in Equation 2-17.

2.6 Experimental methods for porosity derivation

2.6.1 Conventional methods

Porosity is defined as a fraction between the pore volume and the bulk volume. There are several ways to obtain bulk volume: Archimedes mercury immersion, mercury displacement and calliper (API, 1998), these methods are described in the Methodology Section 3.3. Pore volume is normally derived by subtracting the grain volume from bulk volume; the former is obtained by using either mercury injection or pressure expansion methods (Equation 2-19). Porosity is then calculated using:

$$\Phi = \frac{V_b - V_g}{V_b} = \frac{V_p}{V_b} \qquad \text{(Equation 2-19)}$$

where Φ is porosity (fraction), V_b is the bulk volume (cm³), V_g is the grain volume (cm³) and V_p is the pore volume (cm³).

Pressure expansion for grain volume measurement is performed using pycnometer. This device consists of two known volume chambers – one for the sample and the other is used for the volume expansion. The detailed description of the equipment and

methodology is described in the Methodology Chapter 3.5. Boyle's law (Equation 2-20) is used for the determination of porosity as shown in Equation 2-22.

$$P_1 V_1 = P_2 V_2 \qquad \text{(Equation 2-20)}$$

$$P_1 V_1 = P_2 (V_1 + V_2 + \Phi - V_b \qquad \text{(Equation 2-21)}$$

$$\Phi = \frac{P_1 V_1 - P_2 (V_1 + V_2 - V_b)}{P_2} \qquad \text{(Equation 2-22)}$$

Where V_1 is the reference cell volume (cm^3), V_2 is the sample cell volume (cm^3), P_1 is the initial reference cell pressure (psig) and P_2 is the final stabilized pressure (psig).

2.6.2 Scanning Electron Microscope for porosity analysis

Scanning Electron Microscope (SEM) images can be used to derive the fraction of porous volume within the given image scale (Rine et al., 2013). The pores are outlined using image analysis methods and their area is calculated. This porous area is then divided by the overall given sample area. A detailed description of the method is provided in the Chapter 3.3.

2.6.3 Nuclear Magnetic Resonance for porosity analysis

Nuclear Magnetic Resonance (NMR) is a non-intrusive method that provides a range of data including formation porosity, distribution of pore sizes and types of fluids occupying the pores. The tool provides a breakdown of relaxation times that correlate to formation properties. In conventional rocks, relaxation time (T_2) cut-off of 33 ms is normally used to determine effective porosity, however this value was proven to be inaccurate for the interpretation of tight formations such as shales (Lewis et al., 2013; Zhang et al., 2013). Lewis et al. (2013) conducted a research on Eagle Ford shale and identified the T_2 values to be around 4.2 μm/s.

2.7 Experimental methods for permeability derivation

2.7.1 Conventional gas flow methods

Steady state gas permeametry is the most commonly used method for measuring the permeability of reservoir rocks (Yortsos and Chang, 1990; Virnovsky et al., 1995; Rushig et al., 2004). A core sample is placed into a core holder and a confining pressure is applied. Gas is then flowed through the sample with the flow rate and pressure difference across

the sample recorded once steady state is achieved. Darcy's Law (see Equation 2-4 in Section 2.2) is then used to calculate permeability.

However, this technique has several issues for samples with very low permeability, mainly due to the length of time that it takes for the flow to reach steady-state. In addition, samples might contain artificially induced microfractures, which create high conductivity pathways, which cannot be identified using the steady-state method.

Pulse decay permeametry (PDP) is a transient technique commonly used to measure permeability of tight rocks (Brace et al., 1968). The equipment consists of a core holder as well as upstream and downstream volumes. Gas is expanded into the upstream and downstream chambers as well as the shale sample and left to equilibrate. A pressure pulse is then applied to the upstream volume and the pressure transient created. As the gas flows through the shale into the downstream chamber, its volume is measured and used to calculate permeability (Cui et al., 2009). The experiment can be repeated for a number of different upstream pressures so that a slip correction can be made.

It is often argued that PDP is superior to the steady state technique for measuring the permeability of tight rocks because it is faster and easier to use (Haskett et al., 1986; Gilicz, 1991). The PDP system can be used to measured permeabilities in the range of 10 nD up to 0.1 mD (Jones, 1997). The steady state method is better for higher permeability samples. Furthermore, considerable improvement of the PDP method was made by Haskett et al. (1986), where both permeability and porosity could be derived simultaneously.

2.7.2 GRI method on crushed shale and core plugs

Another technique used for permeability derivation is the Gas Research Institute (GRI) method, which conducts measurements on crushed shale. A specific size fraction of crushed shale is placed into a sample chamber into which gas is expanded from a reference chamber (Luffel et al., 1993). Permeability is then calculated from the pressure transient created as gas flows into the shale matrix. The experiment is much faster than core plug sample methods as crushed shale particles have higher surface area into which the gas can flow. The range of the permeability values that can be obtained with this method depends on the experimental volumes and the type of pressure transducers used, but is generally within the nanoDarcy range for the crushed shale samples (Civan and

Devegowda, 2014; Heller et al., 2014) and up to miliDarcy range for the core plug methods such as PDP.

Permeability can be calculated numerically or using analytical equations. The latter use the slope of pressure decay, which depends upon the ratio of the void space in the sample cell and the void space in the sample itself, as well as the ratio of mass fraction of the gas which is able to go into the sample pores, and the mass fraction of the gas that will actually go into the sample pores (Cui et al., 2009).

GRI experimental results allow Boyle's Law (see Equation 2-20 in Section 2.6.1) to be applied to derive grain density, which together with bulk volume can be used to obtain porosity value using Equation 2-22 (see Section 2.6.1). This in turn means that both permeability and porosity values can be derived simultaneously from one GRI experiment. However Profice et al. (2011) analysed the sensitivity of such simultaneous derivations and showed high sensitivity of GRI tests to the porosity of the medium concluding that simultaneous porosity and permeability determination is highly biased.

Since the publication of the GRI method (Luffel et al., 1993) several improvements and recommendations have been suggested (Handwerger et al., 2011; Tinni et al., 2012; Civan et al., 2013). Luffel et al. (1993) applied the GRI method to measure the permeability of 23 Devonian shale samples. It was argued that the technique avoids misinterpretations caused by the presence of microfractures induced by coring and/or present naturally. Luffel et al. (1993) argued that crushed particles are unlikely to contain microfractures that would give misleading results because shale is likely to crack along microfractures and bedding planes during crushing.

GRI (1992) also showed that a similar technique could be applied to measure the permeability of intact core plugs. The core plug GRI method has the advantage of better shale matrix representation due to the presence of intact shale matrix (Heller et al., 2014). In addition, damaged or split cores can be used for porosity and in some cases permeability derivation, as the gas flow front develops by surrounding the sample, hence high conductivity pathways and heterogeneities do not make such a large impact on the results as compared to steady-state permeability analysis.

Tinni et al. (2012) contradicted the assumption that crushed particles do not contain microfractures, by injecting mercury into the particles and then imaging them with a micro-CT. Images showed the presence of microfractures of 10 to 20 µm. Although Tinni et al. (2012) showed that it is possible to close microfractures in shale particles to obtain

more representative values, they concluded that crushed core technique cannot be used for the matrix permeability determination and favoured measurements conducted on core plugs over crushed samples.

Luffel et al. (1993) described the lack of overburden stress as the main disadvantage of the crushed technique. Presence of overburden stress during the experiment creates conditions that are more representative of the subsurface (Casse, 1974; Brighenti, 1989; Chenevert and Sharma, 1993; Sakhaee-Pour and Bryant, 2012). Indeed, several studies have shown that shale permeability may decrease by several orders of magnitude as confining pressure is increased from ambient to *in-situ* values (Zhengwen et al., 2003). In other words, conducting measurements at ambient conditions can result in an overestimation of shale permeability by several orders of magnitude.

2.7.3 Modified Pressure Decay

A modified pressure decay (MPD) experiment, proposed in this research, is a combination of the GRI and PDP experiments. It can measure permeabilities from <0.1 nD up to 100 µD as suggested by this study. MPD system consists of a core holder and upstream/downstream volumes. Shale core sample is placed into the core holder and a confining pressure is applied. Gas is then expanded into the upstream volume and then allowed to flow into the shale. The pressure transient is recorded and inverted to calculate permeability using a flow simulation. The flow simulation allows the inclusion of the high-conductivity layer/fracture to take into account the presence of high permeability pathways such as fractures. Laminar flow is assumed throughout the sample, as that is the condition of the Darcy flow (Perry, 2007). In this research several samples were measured with three types of gasses: helium, methane and xenon.

The method is described in detail in Section 3.5; the main advantages over the standard pulse decay method are:

- It is not necessary to wait until gas pressures have equilibrated and the transient data collected over the first minutes/hours may be sufficient to allow permeability to be estimated.

- Controlled upstream and downstream volumes, which can be considerably minimised for more accurate measurements. Also the calibration of the volumes is more accurate.

- Permeability inversions can be done on the fluid flow of different geometry, i.e. samples with/without drilled holes.

- A higher resolution pressure transducer is installed.

- It has the potential to be used at the well side.

2.7.4 Indirect methods

2.7.4.1 Mercury Injection

Mercury injection porosimetry is used to obtain information on the pore throat size distribution in a sample, which is then used to calculate permeability. The instrument estimates pore throat size distributions from intrusion volumes and pressure data using the Washburn equation (Washburn, 1921). Permeability can be estimated from Hg-injection data using a range of methods (Purcell, 1947; Swanson, 1981; Wells and Amaefule, 1985; Huet et al., 2005). All of the methods use a relationship between Hg-air capillary pressure and pore throat entry radius (Washburn, 1921; Comisky et al., 2007) (Equation 2-23).

$$R = 2(0.417)\sigma_{Hg-air}cos_{(\theta_{Hg-ari})}\frac{1}{p_c} \qquad \text{(Equation 2-23)}$$

where R is pore throat radius (µm), σ_{Hg-air} is interfacial tension between mercury and air, typically around 480 dynes/cm (dynes/cm), θ_{Hg-air} is the contact angle between mercury and air, typically around 140 degrees (degrees) and p_c is the capillary pressure between the Hg and air phases (psia). Although the experiment is relatively fast (hours to days) samples are tested at non-reservoir conditions (i.e. absence of confining stress and reservoir fluids) (Huet, 2005). A lot of research is currently being carried out on this topic and improved correlations are being developed for very low permeability reservoirs (Comisky et al., 2007).

2.7.4.2 Nuclear Magnetic Resonance

Nuclear magnetic resonance (NMR) spectrometry can be used both in the laboratory and in the bore hole. Unlike methods involving gas flow, it is often argued that NMR is insensitive to sample damage such as stress-release microfractures (Prince et al., 2010). The principle of this technique is that fluids inside the pore space of the sample core respond to the tool creating a distribution of the relaxation times T_2, where bigger times correspond to larger pores (Prince et al., 2010). A particular cut-off value of T_2 is chosen to

separate porosity into two parts: bound volume index and free fluid index; the ratio of these numbers is thought to correlate to permeability. The disadvantage of this technique is that various models result in permeabilites that are orders of magnitude different, so particular coefficients that are specific to the rock and fluid type are required to improve the accuracy of this method (Dastidar et al., 2004).

2.8   Adsorption representation in numerical models

The simplest adsorption model is the Langmuir monolayer (Langmuir, 1918) (Figure 2.4a). This model assumes that the gas molecules are adsorbed by a fixed amount of well-defined localised sites, each of which can only adsorb one gas molecule. Currently, all the complex gas flow models that include adsorption are based on the Langmuir equation (Cui et al., 2009; Civan et al., 2011; Crook, 2012; Lorinczi et al., 2014).

The Brunauer, Emmet and Teller (BET) model (Figure 2.4b) complements the Langmuir model by considering a system where gas is adsorbed onto a surface as a series of multilayers, i.e. a third dimension is introduced. The advantage of this model is that it is relatively easily implemented, fits all types of Langmuir isotherms and can be applied to a wider range of different surfaces compared to single Langmuir model.

The disadvantage of both Langmuir and BET models is that they are not valid for micropores with similar sizes to the gas molecules, which is usually the case for the shales. This is because the adsorption fields arising from the opposing walls of such a micropore and affect the gas molecule. Polayni (1932) explained this phenomenon by the existence of a potential adsorptive field around the surface of the solid into which the gas molecules fall. The adsorption potential is then defined as the work done per mole of adsorbate to transfer molecules from gaseous state to adsorbed state and that can be represented by the sorbed volume (Polayni, 1932).

Dubinin (1967; 1975) complemented the Polayni (1932) model and introduced the theory of volume filling, where instead of monolayer surface adsorption, the adsorbate occupies the micropore volume by filling the "adsorption pore space" within the micropores (Figure 2.4c). Equation 2-24 describes this behaviour (Dubinin and Astakhov, 1971):

$$V = V_0 Exp[-K\{ln(P_0/P)\}^n] \qquad \text{(Equation 2-24)}$$

where V is adsorbed pore space, V_0 is the volume of micropores (m^3), K is a constant for a particular adsorbate-adsorbent system (dimensional), n is a constant parameter = 2, p is the saturation vapour pressure (Pa) and p is the experimental pressure (Pa).

Although most of authors use basic Langmuir model in their numerical derivations (Civan et al., 2013; Civan and Devegowda, 2014) the model of Dubinin (1966) was found to produce the most accurate adsorption results by several authors (Clarkson et al., 1997; Clarkson and Bustin, 2000; Bhowmik, 2012). Jianchao et al. (2015) has compared Langmuir, BET and Dubinin models and concluded that Langmuir model can be used to fit the data, however both BET and Dubinin models indeed provide more accurate results. Furthermore, by combining BET or Dubinin models with pure-mineral adsorption data, full potential adsorption capability of shale can be calculated (Jianchao et al., 2015).
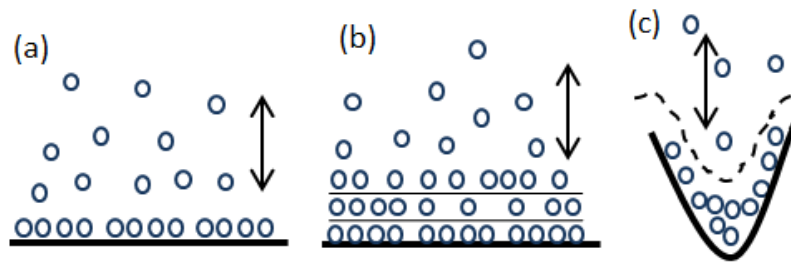
Figure 2.4. Representation of adsorption/desorption models. Langmuir model (a), BET model (b) and Dubinin and Astakhov's (D-A) model (c).

2.9 Numerical and analytical methods for parameter inversion

Analytical methods are available to allow the interpretation of transient tests but assumptions are often required to simplify the mathematics. As an alternative, numerical models were used in the current study to interpret transient pressure experiments. Below a description is provided of the current analytical methods used for the permeability derivation followed by the description of a numerical method used in this study.

2.9.1 Cui's method

Cui et al. (2009) presented a model to account for adsorption of gas in shales and methodology for permeability derivation from crushed and canister desorption methods. According to Cui et al. (2009), analytical equations describing the flow of gas into the crushed particles can be divided into early time and late time solutions. Permeability is calculated using the ratio of the mass fraction (F_R) of gas that is able to get into the sample to the gas which is actually getting into the sample, which can be calculated as Equation 2-25.

$$F_R = 1 - \frac{(K_c + 1)(\rho_{c0} - \rho)}{\rho_{c0} - \rho_0}$$

(Equation 2-25)

$$K_c = \frac{\rho_b V_c}{M[\Phi + (1 - \Phi)K_a]} \qquad \text{(Equation 2-26)}$$

$$\rho_{c0} = \frac{\rho_{r0} V_r + \rho_0 (V_s - V_b)}{V_r + V_s - V_b} \qquad \text{(Equation 2-27)}$$

$$F_R = 6K_C(K_C + 1) \sum_{n=1}^{\infty} e^{-K\alpha_n^2 t/R_a^2} \frac{1}{K_C^2 \alpha_n^2 + 9(K_C + 1)} \qquad \text{(Equation 2-28)}$$

$$\tan \alpha = \frac{3\alpha}{3 + K_C \alpha^2} \qquad \text{(Equation 2-29)}$$

$$F_R = \frac{6}{\pi} \sum_{n=1}^{\infty} e^{-\pi^2 n^2 Kt/R_a^2} \frac{1}{n^2} \qquad \text{(Equation 2-30)}$$

where K_c is the ratio of the gas storage capacity of the total void volume of the expansion and sample cells to the total volume of the sample particles (dimensionless) and is given by Equation 2-26, V_c is the total volume of open space in reference and sample cells (cm^3), ρ_b is bulk density of the samples (g/cm^3), ρ_0 is initial gas density of the sample (mol/m^3), ρ_{r0} is initial gas density (mol/m^3), M is the sample mass (g), Φ is porosity (frac), K_a partial derivative of adsorbate density (dimensionless) and ρ_{c0} is the average initial gas density in the sample and reference cell, given as Equation 2-27, V_r is reference cell volume (cm^3), V_s is the sample cell volume (cm^3), V_b is bulk volume of the sample (cm^3), R_a is the radius of crushed particles, F_R is the residual gas fraction in Equation 2-28 and 2-30, K is the apparent transport coefficient, t is time (s), and α_n is the nth root of Equation 2-29.

2.9.1.1 Cui's late time solution

Analytical solutions using several K_c values given by Cui et al. (2009) show that logarithmical value of F_R becomes a linear function of time when dimensionless time is larger than 0.1. The exact F_R solutions become similar and nearly identical to the end analytical solution (Equation 2-31) when K_c is equal or larger than 50. The permeability can be calculation used the following equations:

$$\ln(F_R) = f_0 - s_1 t \qquad \text{(Equation 2-31)}$$

$$s_1 = \frac{K\alpha_1}{R_a^2} \qquad \text{(Equation 2-32)}$$

$$f_0 = \ln\left(\frac{6K_C(K_C+1)}{K_C^2\alpha_1^2 + 9(K_C+1)}\right)$$ (Equation 2-33)

$$k = \frac{R_a^2[\Phi + (1-\Phi)K_a]\mu c_g s_1}{\alpha_1^2}$$ (Equation 2-34)

where t is time (s), f_0 is y-intercept and s_1 is the slope of the straight line in Equation 2-32, α_1 is the first solution of Equation 2-29, μ is gas viscosity (Pa s^{-1}), c_g is gas compressibility (Pa^{-1}) and the y-intercept of the straight line is Equation 2-33. The rest of the terms are the same as for Equations 2-26 to 2-30.

2.9.1.2   Cui's early time solution

According to Carslaw and Jaeger (1947) and Do (1988), analytical early time solution can be approximated as Equation 2-35. Cui et al. (2009) noted that several problems exist with the early time data, especially adiabatic temperature change. Cui et al. (2009) also argued that gas enters into the pores too rapidly for the early time pressure data to be recorded. Their solution was to rely more on the late time data. Profice et al. (2011) agreed that initial pressure response of the crushed GRI experiment, which lasts only a few seconds, is insufficient for proper characterization. Instead, they are suggesting using the late time technique. However it was found that late time data are very sensitive to the leakages, which can significantly affect the permeability results (Fisher et al., 2016). Fisher et al. (2016) argued that it is the very early (<10-15 sec) data which are the most important, as will be explained in this report.

$$F_U = 1 - F_R = \frac{6\sqrt{K}}{\sqrt{\pi R_a^2}}\sqrt{t}$$ (Equation 2-35)

where F_U is the cumulative gas uptake, the ratio of the gas that has entered the sample particles to the total gas that eventually will be taken up by the sample. The early-time data versus the square-root of time then becomes a straight line, the slope (s_0) can be obtained through curve-fitting, and the effective permeability can be determined as Equation 2-36.

$$k = \frac{\pi s_0^2 R_a^2[\Phi + (1-\Phi)]\mu c_g}{36}$$ (Equation 2-36)

Cui et al. (2009) obtained smaller errors using late time technique than early time technique, however they used very large pressure changes from 200 Pa to 100000 Pa,

that is 500-fold increase, which could distort the data. Although Cui et al. (2009) argued that it does not have a large affect, it was found in this research that such pressure changes create permeability values that vary several orders of magnitude.

Cui et al. (2009) also conducted an extensive testing on employing different experimental gasses, in particular methane. Cui et al. (2009) obtained smaller errors in the late time technique when using methane compared to helium. They also argue in their work that the usage of methane as an experimental gas is more representative of the reservoir conditions.

To represent adsorption of gas onto the shale matrix, Cui et al. (2009) use Langmuir equation. To distinguish between adsorptive and true porosities, they derived the ratio of true effective porosity over effective porosity contributed by adsorption f_a (Equation 2-37), where Φ_a is defined as the effective adsorption porosity, derived as Equation 2-38. The resulting factor indicates by how much porosity is increased due to adsorption.

$$f_a = \frac{\Phi_a}{\Phi}$$
(Equation 2-37)

$$\Phi_a = (1 - \Phi)K_a$$
(Equation 2-38)

where K_a is partial derivative of adsorbate density with respect to gas density (fraction).

2.9.2 Civan's method

Civan et al. (2011) recognized the limitations of conventional methods used to simulate gas flow in shales using only Darcy flow, and presented an improved method to model the behaviour of gas in shales. The model presented by Civan et al. (2011) is based on the Hagen-Poiseuille type of mass balance equation representing adsorption/desorption and incorporates various flow regimes such as continuum, slip, transition and free molecular flow by use of various pressure dependent parameters. Following Cui et al. (2009), Civan et al. (2011) included an adsorption parameter K_a (m^3 gas/m^3 solid) into their model (Equation 2-39).

$$K_a \equiv \frac{\partial q}{\partial \rho} = \frac{\rho_s M_g}{\rho \beta_\rho(p) V_{std}} \frac{q_L p_L}{(p_L + p)^2} = \frac{q}{\rho \beta_\rho(p)(p_L + p)}$$
(Equation 2-39)

where ρ is gas density (kg/m^3), q is the mass of gas adsorbed per solid volume (kg/m^3), ρ_s is the material density of the porous sample (kg/m^3), M_g is the molecular weight of gas

(kg/kmol), β_ρ is isothermal coefficient of compressibility for fluid density (Pa^{-1}), p is absolute gas pressure (Pa), V_{std} is the molar volume of gas at standard temperature (273.15 K) and pressure (101,325 Pa) (stdm^3/kmol), q_L is the Langmuir gas volume (std m^3/kg) and p_L is the Langmuir gas pressure (Pa). In these new improved models gas flow is calculated using an equation which takes into account the gas already present in the sample, the new intake of Darcy flow and adsorbed gas, namely (Civan et al., 2013):

$$\frac{\partial(\rho\Phi)}{\partial t} + \frac{\partial}{\partial t}[(1-\Phi)q] = \frac{\partial}{\partial x}\left[\frac{\rho}{\mu}k\left(\frac{\partial p}{\partial x}\right)\right] \qquad \text{(Equation 2-40)}$$

where ρ is the gas density (kg/m^3), Φ is the porosity of the rock sample (dimensionless), t is time (sec), q is the mass of adsorbed gas per unit volume (kg/m^3), μ is the viscosity (Pa s), p is the pressure (Pa), k is the intrinsic permeability (m^2) and x is the Cartesian distance in the flow direction (m). Gas adsorption parameter can be either removed or calculated according to Langmuir isotherm (Civan et al., 2011):

$$q_a = \frac{q_L p}{p_L + p} \qquad \text{(Equation 2-41)}$$

In Equation 2-41, q_a is the standard volume of gas adsorbed per solid mass (m^3/kg), q_L and p_L are Langmuir volume (cm^3/g) and pressure (Pa) respectively, which are specific for rock, and p is the gas pressure (Pa). Civan et al. (2011) concluded that the improved model resulted in more accurate representation of the gas flow in the shale medium than the standard Darcy method.

2.9.3 Numerical Inversion

Civan et al. (2011) used the finite difference method with discretized grid points to model gas flow in shales. The average values of pressures at each grid point are calculated based on the current iteration step and are assigned as the initial pressures for the next step. Several iterations are used to generate the numerical solutions for all time steps until convergence is obtained (Civan et al., 2013). However the models proposed by Civan (see Equation 2-39 in Section 2.9.2) have a large number of unknown parameters.

Lorinczi et al. (2014) used a finite volume method (FVM) based on Civan et al. (2010; 2011) work to model the gas flow through shale. The model accommodates a wide range of flow mechanisms including continuum, Knudsen and free molecular flow. Adsorption can be included using Langmuir equation. The model can be applied to either steady or

unsteady state flow regimes and also allows for the inversion of several unknown parameters.

Profice et al. (2012) argued that determination of several parameters at once is more representative of the sample and therefore is more desirable. Profice et al. (2012) tried to determine three parameters (b, k_i and porosity) using one experiment – pulse decay on crushed samples. Their model was constructed and validated with approximated analytical solution. The conclusion was that porosity can be accurately determined if experimental volumes are calibrated correctly, however the identification of both b and k_i is seriously compromised (Profice et al., 2011). On the other hand, the accurate calibration of the experimental volumes at the required accuracy that Profice et al. (2012) discussed is practically very difficult to obtain due to the temperature and kinetic errors.

One of the objectives of this research was to develop a working inversion method and generate enough simulation results for comprehensive analysis. The production simulation software Eclipse incorporating transient solution algorithm and variable time steps was used to model the single phase gas flow. Simulations were based on viscous flow gas transport regime, governed only by Darcy's equation (see Equation 2-4 in Section 2.2). Some of the models used include Klinkenberg correction and heterogeneities.

3 Chapter
Equipment and Methodology

3.1 Introduction

This chapter presents the samples and methodology used in this research. Firstly, the samples are presented including their origin, dimensions and preparation (Section 3.2). Secondly, sample characterisation methods are described (Section 3.3). Thirdly, pressure expansion experiments are presented, including crushed and core plug methods (Sections 3.4 and 3.5). Simulation modelling methods are then described (Section 3.6). Finally, experiments conducted in the field are presented (Section 3.7).

3.2 Shale samples

3.2.1 Origin of the samples

Overall 89 different shale samples were analysed in this research. The sample locations are either currently being explored for shale gas, or are already under development and production including North America (Canada, USA), Europe (UK, Netherlands, Romania, Sweden) and Africa (South Africa). The amount of core material varied with a lot of samples from Sweden and only one sample from South Africa. A summary of all samples is provided in Appendix A.

Samples from Netherlands (28 in total, see Appendix A) were taken from two potential onshore shale gas plays: the Lower Jurassic Altena Group, which contains the Posidonia and Aalburg shale formations and the older Lower Namurian Geverik formation (Bouw & Lutgert, 2012). Extensive research has been done on these shale plays and is described by Leeftink (2015), Mezger (2014) and Kee (2010).

The samples from Sweden were cored from the shallow north and east dipping Alum Shale formation in Östergötland during the shale play exploration operations. A total of 42 Alum Shale samples retrieved from a depth of 30 - 110 m were analysed in this thesis (Appendix A). Alum Shale formation with its surrounding geology was studied by Nielsen and Schovsbo (2007).

The sample from South Africa was brought from the Whitehill formation in Karoo. Although it is regarded as an outcrop sample, it was taken from the quarry from about 10 - 20 m depth, and was not exposed to weathering. There was enough sample material to test in both core plug and crushed forms.

A total of 11 Devonian shale samples were obtained from the Horn River play in British Columbia, Canada; 2 Carboniferous samples from USA, 1 Carboniferous sample from Romania and 2 Carboniferous samples from Netherlands. These samples have no full description provided due to confidentiality. There are also 2 samples from UK, brought from the Carboniferous shale outcrop in Whitby.

This research focused on 6 samples (NEX7, NEX15, NEX33, EBN20, CHE2 and CHE3), which were analysed in Leeds and sent off to three leading commercial laboratories for bulk density, grain density, porosity and permeability analysis. The results of these measurements were considered to be the reference point in this research. These 6 samples from this point onwards are referred to as Control-Test samples, and the companies as Control-Test companies.

3.2.2   Preparation of the samples

Shale material for the study was received in the form of well cores. CT-scanning was conducted on these cores to locate representative regions to drill 1.5 inch core plugs. Air is preferred instead of water during the sample coring due to the possible damage of the shale with water (Kulander et al., 1990; Blackbourn, 2012). The drilled core plug samples were then trimmed using an electric saw and placed in the desiccator to prevent from the atmospheric moisture.

The offcut cutting material was used to prepare sub-samples of around 1 cm^3 for the mercury injection experiments, 1 mm^2 samples for the SEM (Scanning Electron Microscope) analysis, crushed samples of various sizes for the crushed GRI (Gas Research Institute) and powder for the tests requiring samples in the powder form. Table 3.1 summarizes sample cleaning methods conducted by Leeds and Control-Test laboratories for the cruished shale analysis. The low permeability of the shale meant that it was not possible to clean core plugs so these were treated as "as received". Details of further sample preparation for each particular experiment are described in the corresponding sections.

Table 3.1. Comparison of cleaning methods for crushed shale analysis.

Laboratory	Cleaning method	Sample storage
Leeds	Oven drying at 110˚C for 7 days, reweighed to determine amount of lost water; For comparative reasons several shale samples were left in as-received conditions.	Placed in desiccator immediately after drying
Lab A	Dean Stark method, refluxed in toluene for 7 days; Oven drying at 110˚C for 7 days.	Placed in desiccator
Lab B	Retort method; Oven drying at unspecified temperature and unspecified amount of time; For comparative reasons one shale sample left in as-received conditions.	No details
Lab C	Drying at 100˚C for unspecified amount of time; For comparative reasons one shale sample left in as-received conditions.	No details

3.2.3   Configuration of the samples

Core plug samples both parallel and perpendicular laminated were analysed in this research; these are referred to as linear parallel and linear perpendicular respectively. After measurements, a small hole (∼3 mm diameter) was drilled into the centre of core plugs to test samples perpendicular to the direction in which the core plugs were drilled (Figure 3.1b & d). This new experimental technique is referred to as thick walled cylinder pressure decay test (TWC or radial pressure decay). Attempts were made to drill in the middle of all Control-Test samples to obtain such samples. However due to lack of material, not every configuration of the core plug could be made for every sample. Table 3.2 presents an overview of the main core plug samples including their dimensions and weights.

Table 3.2. General characteristics of the main core plug shale samples. Bolded are Control-Test samples.

Sample	Weight, g	Length, cm	Diameter, cm	Hole length, cm	Hole diameter, cm
EBN9 parallel	75.06	2.62	3.38		
EBN5 parallel	153.13	5.06	3.79	2.00	0.32
CHE2 perpendicular	117.19	4.25	3.60		
NEX7 parallel	76.51	2.82	3.75	2.82	0.38
NEX7 perpendicular	90.57	2.8	3.74		
NEX33 parallel	75.43	2.25	3.73	2.25	0.46
CHE3 perpendicular	81.59	3.06	3.75		
CHE3 parallel	60.40	2.25	3.73	2.25	0.47
EBN20 perpendicular	59.06	2.23	3.74	2.23	0.37
EBN20 parallel	80.13	3.01	3.74	3.01	0.37
EBN20 parallel long	203.29	7.22	3.81		
EBN33 parallel	71.48	3.11	3.83	3.11	0.46

The reason samples are called parallel and perpendicular is the behaviour of the gas flow front that is assumed to develop through them during the MPD (modified pressure decay) experiment as shown in Figure 3.1. The goal is to simulate these different gas flows and compare the derived properties of the shale matrix. Drilled hole allows additional type of flow to be measured, which could be considered as a mix between perpendicular and parallel.
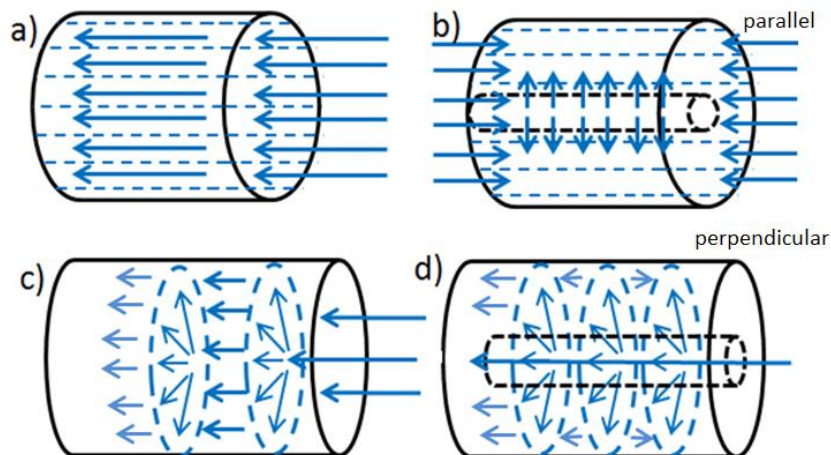
Figure 3.1. Schematic representation of the gas flow fronts in the samples cored parallel and perpendicular to the bedding.

3.3 Sample characterisation

This section describes the core analysis experiments conducted on the samples. The experiments were performed in a specific order to maximise the number of measurements conducted and amount of data collected on limited shale material (Figure 3.2). However, not all samples have undergone full analysis procedure due to the lack of shale material. The names of the samples measured by each experiment are provided in each chapter accordingly.
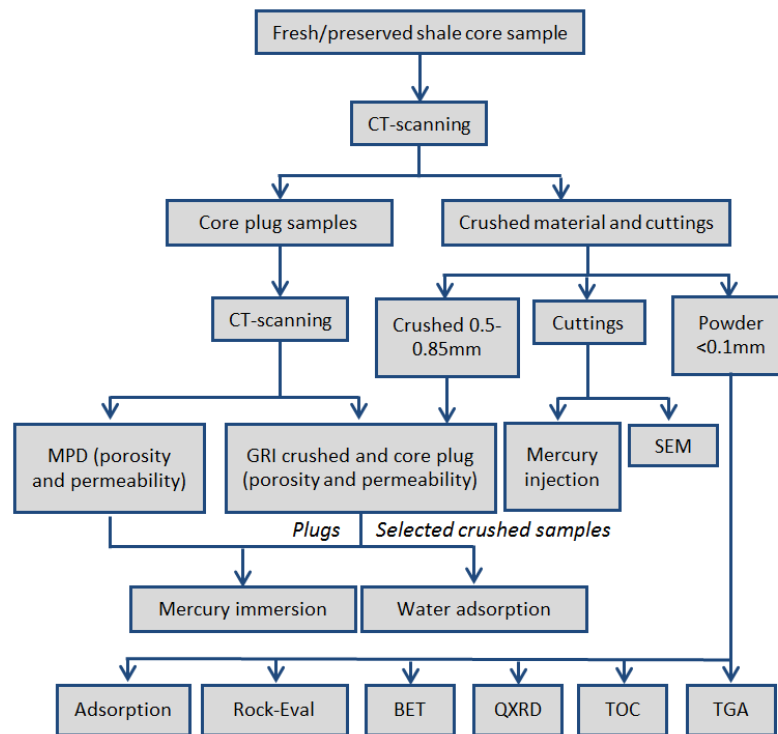
Figure 3.2. General workflow scheme of the conducted experiments.

3.3.1 Computer-Tomography (CT)

Medical-type Picker PQ2000 dual energy CT-scanner was used in this research to produce CT images of the shale samples. This type of scanner has a round X-ray source/detector configuration able to fully rotate around the specimen and capture tens of thousands of images (Rodriguez et al., 2014). The samples may be also imaged while under the confining pressure within the metal pressure flow set-up. The range of scanned samples varied from 5x3 cm core plugs to 50x5 cm well cores obtained from the field. In addition, some CT scans were conducted on samples that have been flooded with xenon as part of the flow development imaging experiment.

Helical and axial scans of the samples were made. The number and location of the scans depends on the predefined parameters: in this research scans were made each 5 mm

along the core plugs. The resolution of the scanner used in this research is around 1 mm. Overall there are various types of CT scanners which have different resolutions depending on their design. Generally, the faster the scanning process and wider the focus area, the lower the resolution of the obtained images (Rodriguez et al., 2014).

3.3.2 Bulk Volume and Density

Sample bulk volume can be measured using mercury immersion and calliper methods. Detailed methodology for both methods is provided by Recommended Practice for Core Analysis 40 (API, 1998). The calliper method assumes core plug samples to be perfect cylinders and uses the volume (Equation 3-1) to determine the bulk volume. The length and diameter are obtained by measuring the sample using Vernier or digital callipers. It is recommended to take measurements at several positions along the length and diameter of the sample to define any irregularities.

$$BV = \pi \times L \times r^2 \qquad \text{(Equation 3-1)}$$

where L is the length of the sample (cm) and r is the radius of the sample (cm).

For the mercury immersion test, the sample is weighed and then submerged into the mercury where the amount of fluid displaced is measured. The bulk volume is derived by dividing the mass of the displaced mercury by its density (Equation 3-2). Toxicity of the mercury is the main drawback of this method.

$$BV = \frac{m_{Hg}}{q_{Hg} \ (13.5377 \frac{g}{mm^3})} \qquad \text{(Equation 3-2)}$$

where m_{Hg} is the mass of mercury displaced (g) and q_{Hg} is the density of the mercury at measurement temperature (g/mm^3). Bulk density is then calculated by dividing the sample weight by the bulk volume:

$$BD = \frac{m}{BV} \qquad \text{(Equation 3-3)}$$

where BV is bulk volume of the sample (cm^3) and m is the weight (g). Sample weight is obtained using electronic weights where 3 significant figures were noted.

3.3.3 Grain Density

Grain density values were obtained using a number of various methods, including mercury injection capillary pressure (MICP); helium pycnometry on crushed samples (GRI), water

pycnometry (WP) and QXRD-TOC derivation. Grain density estimation using QXRD-TOC and pressure expansion methods is described in Sections 3.3.4 and 3.4 respectively. This sub-section provides details of grain density measurement using mercury and water pycnometry methods.

MICP analysis was undertaken on ~1 cm^3 sub-samples cut from each sample and oven dried at 105°C for 48 hours. The measurements were carried out using a Micromeretics Series V Hg-injection porosimeter. The sample is placed into a glass penetrometer, which is then evacuated and flooded with mercury. The pressure is then applied and the mercury starts to intrude the sample pore. The pressure was increased from 1.5 to 59000 psig where 10 seconds was allowed for pressure equilibrium. After reaching equilibrium at each pressure increment the volume of mercury intruded is recorded. Grain density can then be calculated assuming that all the pore space is occupied by the mercury (Equation 3-4). However the assumption that mercury intrudes all of the pores could be wrong due to small pore sizes within shale. Chapter 5 dicusses this problem further.

$$GD = \frac{m_s}{(V_s - V_i * m_s)} \qquad \text{(Equation 3-4)}$$

where m_s is sample mass (g), V_s is sample volume (cm^3) and V_i is intrusive volume (cm^3).

Water pycnometry for the shale grain density is measured on finely crushed (<100 μm) samples using a simple glass pycnometer. Around 10 g of the sample powder is added to the pycnometer and weighed. Distilled water is then added and the sample is allowed to saturate. The weight of the intruded water within the sample can be calculated and as the density of the water is known the grain density can be determined. It has to be noted that the experiment has to be done under stable temperature conditions.

3.3.4 Quantitative X-ray diffraction (QXRD)

QXRD analysis requires preparation of samples with random orientation (Brindley, 1984). A spray dry technique has now been developed that appears to produce such samples for QXRD even when they contain significant proportions of clays (Hillier, 1999; 2000). The technique involves mixing around 5 g of powdered shale sample with a standard 20 wt.% corundum. Then the sample is ground with ethanol for 12 minutes. The mixture is sprayed through an air brush into a tube furnace to form ~30 μm wide spherical aggregates.

The spheres are top loaded into a specimen holder and then analysed using Philips PW1050/1730 Diffractometer. The diffraction results obtained are analysed by either

reference intensity ratio (RIP) or a Rietvold method to produce mineralogical analyses that are accurate at 95% confidence level to $\pm X^{0.35}$, where X is the concentration in wt.%. A detailed methodology can be found in Hillier (2000).

The results of QXRD test were grouped into three categories: total phyllosilicates, total carbonates and quartz + others. The phyllosilicates group included the percentage sum of mica, illite/smectite, kaolin and chlorite. Carbonates involved the minerals with the carbonate group CO_3^{2-}, in this case calcite and dolomite. Finally, the quartz + others group included silica dioxide based minerals (quartz, albite and microcline), together with several other identified minerals, such as pyrite. This mineral grouping was later used to construct a ternary diagram and overall is an easy and convenient method for the cross-sample comparison.

QXRD data can be used for the estimation of grain density, if TOC and Rock-Eval information for hydrogen and oxygen indexes is known. The minerals and organic matter are multiplied by their respective densities and added together. Obviously, this method is sensitive to the assumed density values. Although densities of minerals such as quartz are well known, care must be taken when assigning density values for clays and organic matter. The example for calculation of grain density in excel using this data is provided in Appendix H.

3.3.5   Scanning Electron Microscope (SEM)

In this research SEM was used to produce shale surface images ranging from 75 μm to 300 μm with the resolution of 1 μm. Sample preparation is vital for obtaining good quality SEM images of shale. Initially, SEM images of broken or mechanically polished samples provided only limited observations about the shale matrix (Driskill et al., 2013). However, recent applications of ion beam polishing have greatly improved the capability of SEM method to produce high quality images.

In this study, 2 mm disks were cut from shale thin sections and then polished using a broad ion beam (BIB) miller. All samples were carbon coated to prevent them from charging. The samples were then analysed using a FEI Quanta 650 FEGESEM environmental SEM with an Oxford Instruments INCA 350 EDX system/80 mm X-Max SDD detector. Secondary electron (SE) microscopy was used to give information on the topography of the surface of shale samples (up to 50 nm of electron beam penetration into the shale sample surface, according to Rodriguez et al., 2014) whereas back scattered

electron (BSE) microscopy was used to assess the distribution of minerals and pore space. The voltage settings were set at 20kv, spot size was set at 5 and aperture at 4.

3.3.6 Image post-processing

Image post-processing for analysis purposes was undertaken using ImageJ v.1.48i analysis and processing software (NIH, 2016). Using this software, the SEM images were converted into binary images and then the pore parameters listed below were calculated and categorised according to the methodology proposed by Rine et al. (2013). The images were calibrated according to their scale bars using ImageJ set scale function.

Pore type parameters:

- Area of the pores;

- Fraction of each pore area relative to the overall pore area;

- Percentage of overall pore area relative to overall sample area (porosity);

- Maximum and minimum diameters of the pores (longest and shortest distances between the two points within the area of interest i.e. pore (termed Feret by ImageJ);

- Circularity parameter (ranges from 0 for infinitely elongated polygon to 1 for perfect circle);

- Aspect ratio (or AR), defined as the ratio between major and minor axis of the pore.

For CT images, ImageJ was employed to manipulate the colours of the images using pseudocolour conversion, as described by Camp and Wawak (2013). The aim was to enhance the contrast of structural features and help to distinguish between natural and artificial fractures. Pseudocolour images are created by assigning a specific colour to each grayscale value to enhance it, thus improving the capability of the observer to interpret the subtle variations in density.

3.3.7 Water pycnometry

Water pycnometry (water adsorption) experiment was not a standard experiment carried on every shale sample. It was done primarily to test the potential for the shale samples to imbibe the moisture from the atmosphere and demonstrate the need to keep the samples in the desiccator at all times. The experiment was done by weighing crushed shale samples (0.5 mm - 0.85 mm size) and then placing them into the humidity chamber. The weight of the samples was recorded constantly for several days.

3.3.8   Thermogravimetric Analysis (TGA)

TGA measures the weight change of a powdered sample as it is slowly heated. The results provide information that can be related to the evaporation of water and hydrocarbons from various structural positions as well as the degradation of carbonates and the oxidation of pyrite. However in this research it was primarily used to learn at what temperature the crushed samples have to be baked to remove the free water from the pores to prepare them for the porosity and permeability experiments.

About 50 mg of sample was crushed to <100 μm and then loaded into a Mettler Toledo TGA/DSC1 analyser in which it was heated at a constant rate of 10˚C /min over the temperature range 30˚C to 1000˚C. All experiments were conducted at atmospheric pressure using nitrogen as the purge gas with a flow rate of 50 ml/min. The mass and temperature measurements of the instrument were calibrated beforehand using calcium oxalate as the standard material. The weights of the samples are measured as function of temperature and recorded by the TGA device. Weight loss (TG) and differential loss (DTG) measurements were taken and corresponding curves were constructed.

3.3.9   Total Organic Carbon (TOC)

Total carbon within samples was measured on around 5 g of powdered samples using a LECO SC-144DR carbon analyser. Samples were analysed before and after acid treatment to provide data on the total carbon and total inorganic carbon present. Diluted hydrochloric acid (10%) was used to dissolve the carbonate (Rather, 1917). Inorganic carbon is then subtracted from the total carbon to obtain the amount of total organic carbon. The final result is displayed as a weight percentage.

3.3.10 Brunauer-Emmet-Teller surface area (BET)

The BET experiment provides information on the surface area of the grains within the shale sample. For the experiment 5 g of shale crushed to <100 um was placed into a sample chamber of a Quantachrome version 10.01 Instrument and degassed, the degassing took 2 hours. The sample was cooled to -195.8C and nitrogen gas of 0.808 g/cm^3 was passed through the sample. During the experiment detectors measured the changes in gas volume as it was adsorbed onto the surfaces of the shale. The amount of gas adsorbed at a given pressure allows to derive the surface area using BET equation (Brunauer et al., 1938; Fagerlund, 1973). The BET value is expressed as an adsorptive area per mass of the sample (m^2g^{-1}).

3.3.11 Rock-Eval pyrolysis

Rock-Eval provides quantity, type and thermal maturity of the samples (Nunez-Betelu and Baceta, 1994). The experiment was performed by heating around 100 g of crushed sample in the pyrolysis oven at around 500˚C - 600˚C. The temperature in the oven is increased stepwise allowing different types of organic compounds to be released at different temperatures, depending on the maturity of the samples. The data are recorded and pyrolysis graphs are produced.

3.3.12 Methane Adsorption

Methane adsorption isotherms were measured by research partners at the Bengal Engineering and Science University in West Bengal, India. The shale samples selected for the test were NEX7, NEX33, NEX15, EBN2a0, CHE2, CHE3, BC9, BC7, F1, E3 and E16. Samples were crushed to below mesh size 44 (i.e. <0.44 mm). Matrix void volume was calibrated for the derivation of adsorption values using helium gas. The samples were kept afterwards in the environmental chamber for 48 hours to prepare them for the ASTM (American Society for Testing and Materials) moisture equilibration of coal procedure, and when the test was ready the samples were transferred to the sample cell.

Isotherm tests were conducted at 30˚C (±0.1˚C) and up to ~8500 kPa (~1232.8 psig) pressure of methane. The tests were performed in 8 pressure steps with a uniform interval between successive steps. Experimental adsorption values were first calculated as "excess" sorption and then converted to the corresponding "absolute" values after considering a sorbed phase density of methane of 421 kg/m^3 for each pressure step.

3.4 GRI crushed and core plug GRI methods

The principle of GRI technique is that gas is applied into a chamber containing crushed or core plug shale sample. The pressure in the chamber is recorded as gas flows into the shale. The resulting pressure decay curve (pressure transient) is then inverted to obtain permeability and, in the crushed sample case, grain volume.

3.4.1 Apparatus

The GRI experiment was carried out using a gas expansion system (Figure 3.3). The device consists of two stainless steel vessels – upstream (V1), where initial gas pressure is set, and downstream (V2), where the sample is placed and where the gas is expanded. The system accommodates three sets of valves to regulate the experiment. Three

experimental vessels are shown in Figure 3.3: G1, G2 and G3. Vessels G1 and G2 have fixed experimental volumes, whereas vessel G3 can be set to have several different set-ups of experimental volumes. The vessels are designed to withstand maximum pressures of around 700 psig. The sample vessel accommodates a removable plactic infill, which holds the crushed sample.

The standard GRI device has a simple seal method, where the lid of the downstream vessels is tied using bolts. This system allows the vessels to be exhibited to pressures of up to 1000 psig. A different type of sealing mechanism consisting of hydraulic ram was developed for the GRI devices shown in Figure 3.3 a. This sealing method decreases the amount of leakages and also reduces the amount of time needed to load the sample. However the hydraulic ram limits the maximum pressure that can be applied to 240 psig.
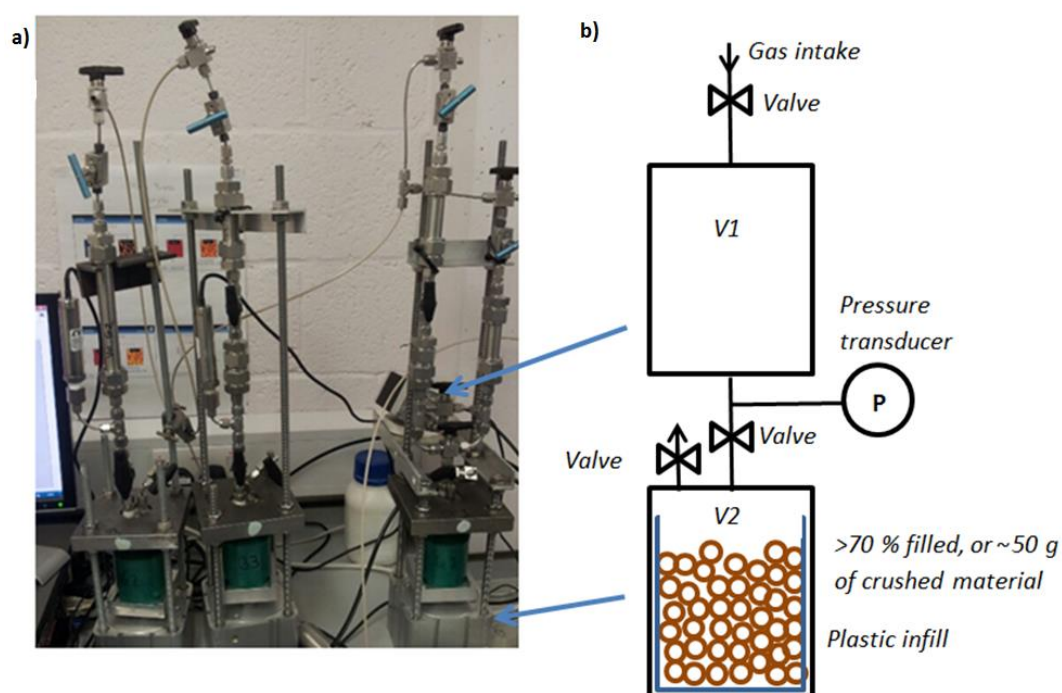
Figure 3.3 Equipment used for the GRI experiment (a) and a schematic representation of this (b). Experimental vessels from left to right in Figure a: G2, G1, G3.

Omega Engineering electronic pressure transducers were fitted to the system. The transducers have a specific maximum pressure range of 0.1% of the maximum system pressure, and a corresponding level of errors (i.e. pressure transducer with the pre-defined maximum pressure of 100 psig has an error of 100 psig x 0.1% = ±0.1 psig. The transducers used have a maximum pressure readings of 250 psig, hence an error margin in the pressure readings of ±0.25 psig. Full specifications of the transducers are given by the Omega Engineering (Omega, 2015).

Experiments were also done using a high precision Mensor pressure transducer, which can take millisecond readings and has the error margin of ±0.0005 psig (Mensor, 2015). These high-tech specifications enable better resolution of the initial pressure response during the experiments, which, as shown in this thesis, is of high importance in the shale permeability determination.

3.4.2 Experimental procedure

Tinni et al. (2012) conducted a range of experiments and concluded that at least 75% of the sample vessel has to be filled for crushed GRI experiments. For the experimental volumes used in this research, 75% of the sample vessel means there has to be at least 50 g of crushed shale material. Therefore around 80-100 g of each sample was crushed using an agate pestle and mortar. The crushed shale sample was then sieved to obtain the 500 < d < 850 μm size (20/40 US mesh size) (Figure 3.4), which is then placed in an oven for drying. The temperature of the oven is set according to the TGA test, as explained in Section 3.3.8. The weight of the sample is monitored and once it stabilizes, the sample can be moved to a desiccator until the experiment is ready to be performed.
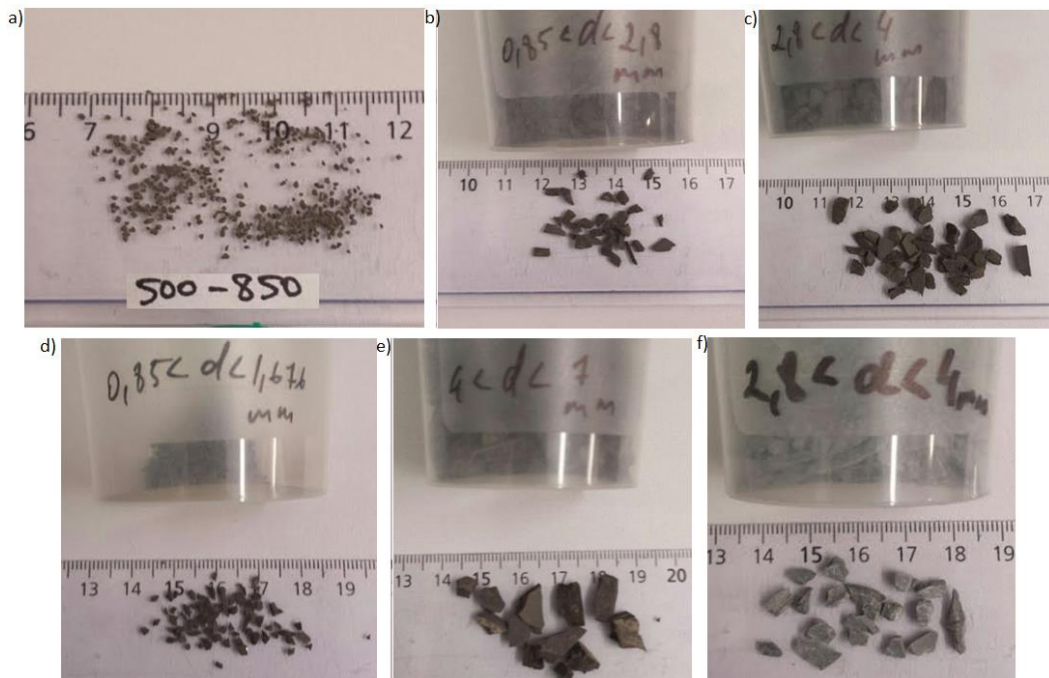
Figure 3.4 Crushed samples for the GRI experiment. The crushed particle size is presented within each image.

It has been suggested that the sample chamber should be placed under vacuum before the experiment (this is known as flushing). However the experiments can be conducted either way – with or without flushing. In this research, the system was not placed under a

vacuum before the experiment. Tinni et al. (2012) found no difference in placing the sample under vacuum when using nitrogen gas for the test, however when using helium there was a difference between flushed and not flushed experiments. The difference was reported to decrease with increasing experimental pressure. However there is no clear consensus on this subject.

Sample chips have to be weighed before placing into the sample vessel for the crushed GRI experiment so that their bulk volume can be estimated. Once ready, the known volume of gas is expanded onto the crushed sample and the pressure is logged until it reaches stability, at this point the experiment is complete. The pressure might not reach the equilibration when the experiment is run on a core plug, in which case the experiment is run just for 2-3 hours to obtain enough of the pressure decay curve for the inversion process. It is useful to perform multiple pressure steps test (referred as pressure series test), where the gas is expanded onto the sample several times to obtain results at different pressures. Similarly, reverse pressure decay experiment can be run, where the gas from the already saturated sample is expanded into an empty vessel, and the pressure build-up is recorded. Gas pressures used in the experiments varied from around 100 psig to 240 psig for crushed and 100 psig to 1000 psig for core plugs.

3.4.3 Analysis of results

It has been argued that crushed GRI can provide shale bulk and grain density values in addition to porosity and permeability (Luffel et al., 1993). The problem is that the high resolution pressure transducer is not able to record the initial pressure points correctly (Figure 3.5). In fact, any transducer would not be able to pick up these initial pressure points due to the chaotic behaviour of gas the moment after expansion, as was demonstrated during the callibration process (Figure 3.6).

To overcome this issue, the pressure curve versus square root of time is extrapolated to $t^{0.5} = 0$ (Figure 3.5a & b). This extrapolation is not intended to represented the actual behaviour of gas during this initial time, as it goes into the matrix too quickly. It is rather made to obtain the very initial pressure value of the gas before it enters the shale (t=0) (Figure 3.6). The time when gas starts to intrude pores is denoted by t1, wheras the equilibrium time by teq.
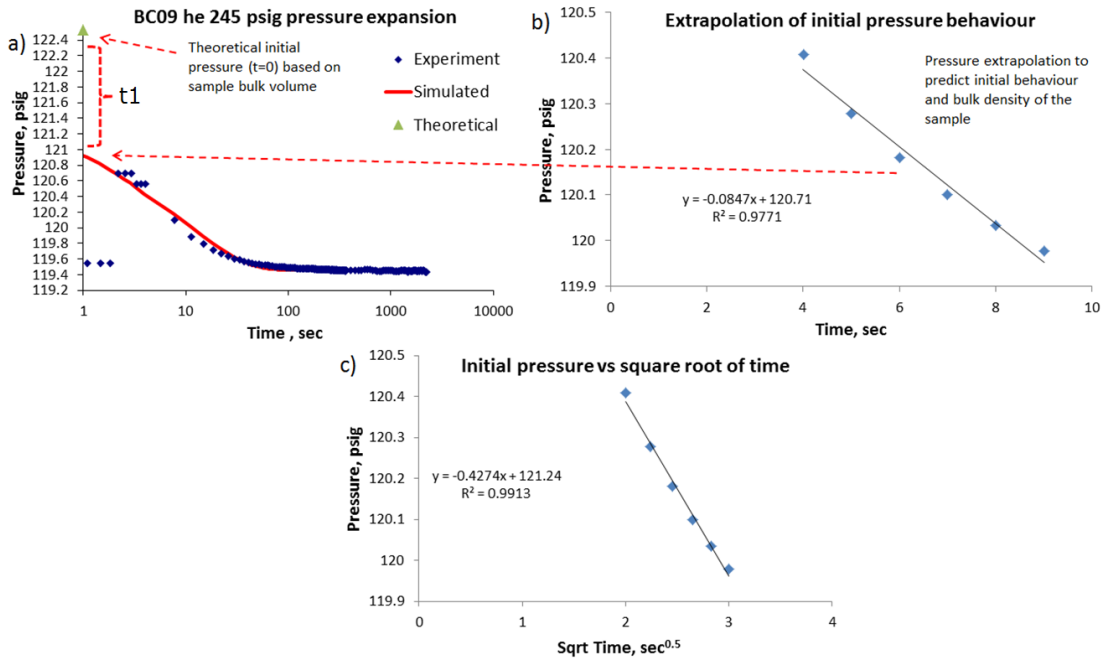
Figure 3.5. Initial pressure behaviour is extrapolated (Figure b) to estimate the unaccounted gas decay t1 shown in Figure 1. Some authors plot initial pressure values against square root of time as shown in Figure c to obtain higher pressure values.
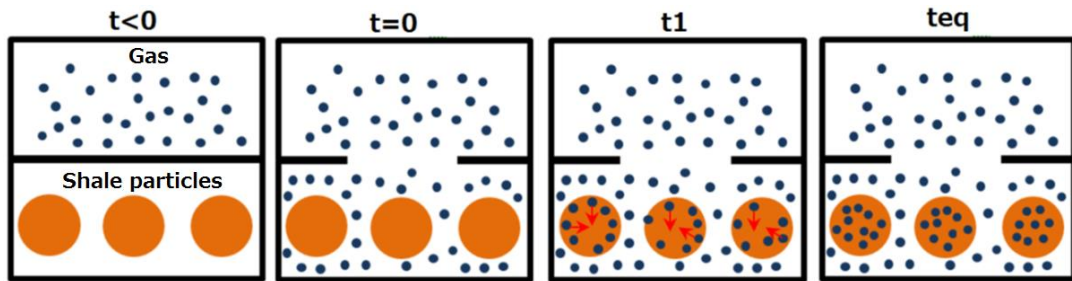
Figure 3.6. Schematic of the gas behaviour during pressure expansion. Once the valve is opened the gas at time t=0 surrounds the pores, then at time t=1 the gas starts entering the pores and at teq the gas has fully saturated the pores.

3.4.3.1   Porosity

Porosity was obtained directly from the bulk volumes and pressure differences (see Equation 2-2 in Section 2.1 and Equation 2-22 in Section 2.6.1) and set as a known parameter in the history matching procedure. Porosity can also be inverted during the history matching procedure together with permeability, as explained in Section 3.6.5.

3.4.3.2   Permeability

In this thesis permeability values were obtained by history matching the pressure decay curves. "Tempest" and "Eclipse" reservoir simulation software were used for the single phase isothermal gas flow modelling. Construction of the simulation models is explained in Appendix B.

3.4.3.3 Crushed sample volume

Modelling of the crushed core experiment requires the free volume of the sample vessel, unoccupied by chips volume. To obtain this volume, the bulk volume of the crushed sample chips must be known, which is obtained by dividing the mass of the chips placed in the vessel by the bulk density. In theory, bulk volume can also be calculated using the pressure data collected during the experimentby rearranging Boyle's law (see Equation 2-20 in Section 2.6.1):

$$V_b = V_2 - (V_1 \times [P_1 - P_3]/[P_3 - P_2]) \qquad \text{(Equation 3-5)}$$

where V_b is the bulk volume obtained from the experimental pressures (cm^3), V_2 is the volume of the sample vessel (cm^3), V_1 is the volume of the sample vessel (cm^3), P_1 is the initial expansion pressure (psig), P_3 is the initial theoretical maximum pressure just after the expansion of the upstream vessel, obtained by extrapolation (psig) and P_2 is the initial pressure at the sample vessel (psig).The experimental bulk density can now be calculated by dividing the bulk volume by the weight of the crushed sample. However it has to be pointed out that the bulk density calculated from pressure data represents dried samples (see Table 3.1 in Section 3.3.2), whereas bulk density used from Hg-immersion experiment was obtained on the as-received samples. Therefore there is a mismatch between these two values and a correction might need to be applied. Further discussion on this issue is provided in Chapter 5.4.1.

Grain volume of the sample is calculated using experimental pressure data:

$$V_g = V_2 - (V_1 \times [P_1 - P_4]/[P_4 - P_2]) \qquad \text{(Equation 3-6)}$$

where V_g is the sample grain density obtained from the experimental pressures (g/cm^3), V_2 is the volume of the sample vessel (cm^3), V_1 is the volume of the sample vessel (cm^3), P_1 is the initial expansion pressure (psig), P_4 is the final equilibrium pressure the upstream vessel and P_2 is the initial pressure at the sample vessel (psig).

$$\Phi = 1 - \rho_b/\rho_g \qquad \text{(Equation 3-7)}$$

where Φ is the porosity (fractional), ρ_b bulk density of the sample (g/cm^3) and ρ_g is the grain density of the sample (g/cm^3).

3.4.4 Calibration and Leakage of the system

3.4.4.1 Calibration

Determination of the experimental volumes is achieved by calibrating the equipment using a gas expansion procedure and Boyle's Law (see Equation 2-20 in Section 2.6.1). Gas expansion procedure is performed several times under different conditions, so that a system of equations can be set up, from which the unknown parameters (i.e. volume values) of the device are derived. A set of reference plugs is used in the process.

Tables of the results of the gas expansions are provided in Appendix C. The calculated volumes of the experimental vessels G1, G2 and G3 are presented in Figure 3.7. The obtained volumes were averaged and are presented in Table 3.3. It has to be noted that a plastic infill (Figure 3.3b) used in the crushed GRI experiments was calibrated separately to reduce any uncertainty. The volumes of the vessels considering these plastic infills are also provided in Table 3.3. To assess the quality of the calibration, the pressure ratios are plotted versus the calibration grain volumes used (Figure 3.8). The coefficient R^2 of each produced curve indicates the repeatability and quality of the pressure ratios.
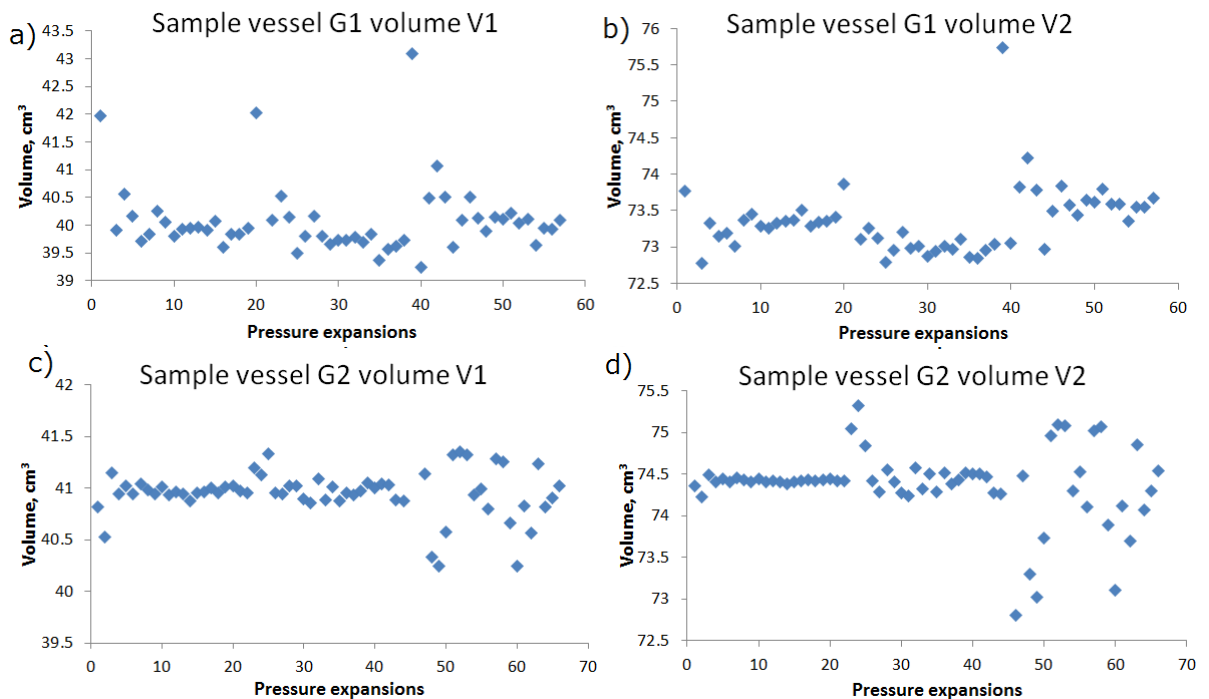
Figure 3.7. Derived volumes of the GRI equipment. Calibration was done to obtain the volumes.
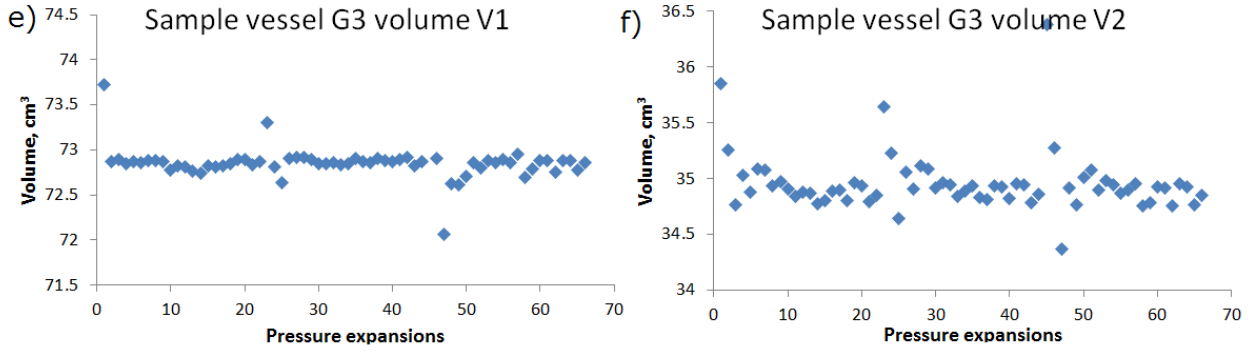
Figure 3.7 continued. Derived volumes of the GRI equipment.

Table 3.3.Averaged values of the GRI volumes that were used in the simulations. Note plastic infill was not used for the vessel G1.

Vessel	Upstream vol V1, cm^3	St. dev, dimension less	Downstream vol V2, cm^3	St. dev, dimension less	V2 with plastic infill, cm^3	St. dev, dimension less
G1	40.10	0.46	73.37	0.46	N/A	
G2	40.95	0.22	74.37	0.40	65.96	0.35
G3	34.95	0.67	72.88	0.29	64.24	0.32
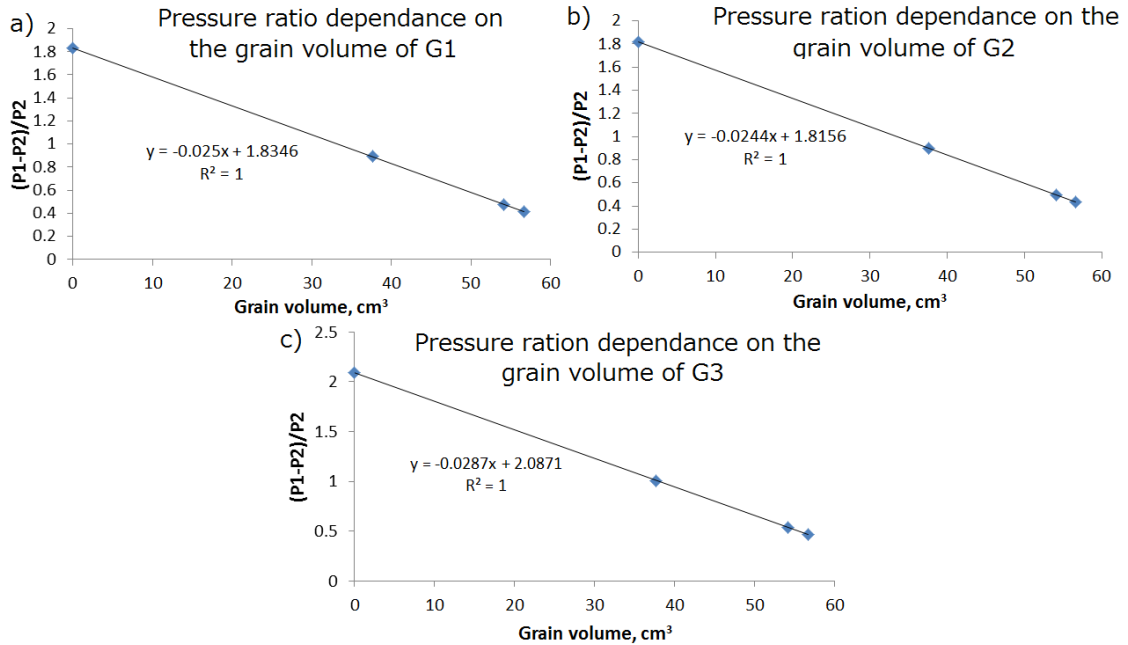
Figure 3.8 Calibration ratios plotted against the used grain volume.

3.4.4.2 Pressure response testing

Reference runs were carried out to gain an understanding of the standard pressure behaviour within the system. Pressure equilibrates within the system with different speeds depending on the surface area of the sample loaded because of the adiabatic

temperature response. Therefore a series of gas expansion tests were conducted on glass beads to obtain a control-pressure response behaviour (Figure 3.9). Figure 3.10 shows the initial pressure expansion response for the vessel G1.

The empty vessel (Figure 3.10a) creates the largest pressure response. Noticeable distortions are seen up to 1 second after opening *V1*, whereas it takes up to 10 seconds for the pressure to equilibrate. Although there are still some pressure distortions that can be seen in the expansion to the vessel containing a glass cylinder (Figure 3.10b), the equilibration is much faster and takes just over 2 seconds. The pressure response to the vessel filled with glass beads (Figure 3.10c & d) is much smoother than with the glass cylinder; there are no pressure distortions and equilibrations happens faster than 1 second. This fast equilibration without any noticeable pressure distortion is crucial in the crushed shale tests. Essentially, the pressure response results indicate that the experiment becomes more accurate as the volume between the crushed shale fragments is reduced.
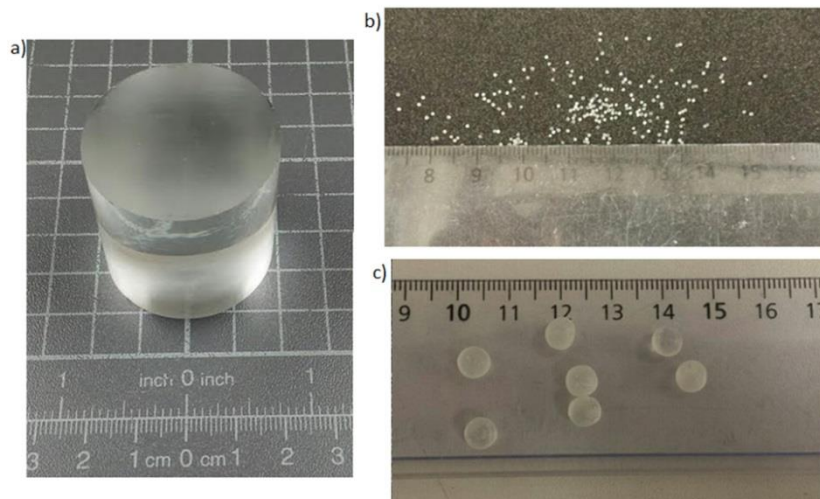
Figure 3.9 Reference glass plugs used for the behavioural analysis of the gas pressure expansion experiments.
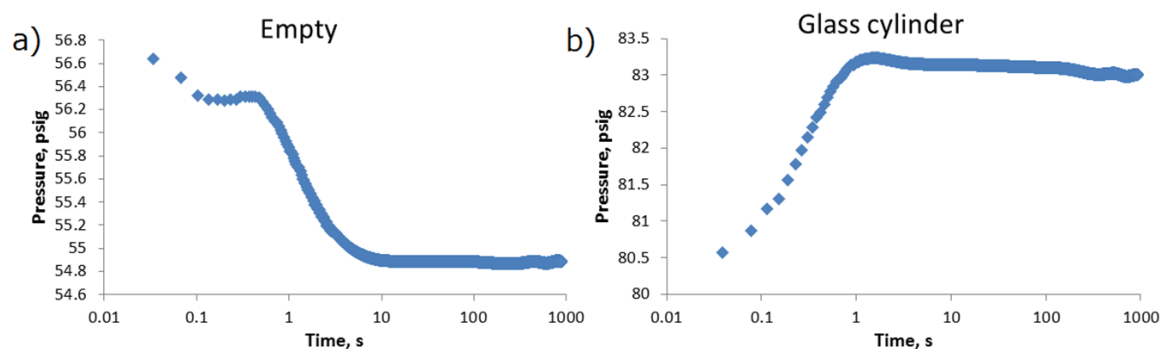
Figure 3.10.Gas expansion behavioural experiments conducted in the GRI equipment.
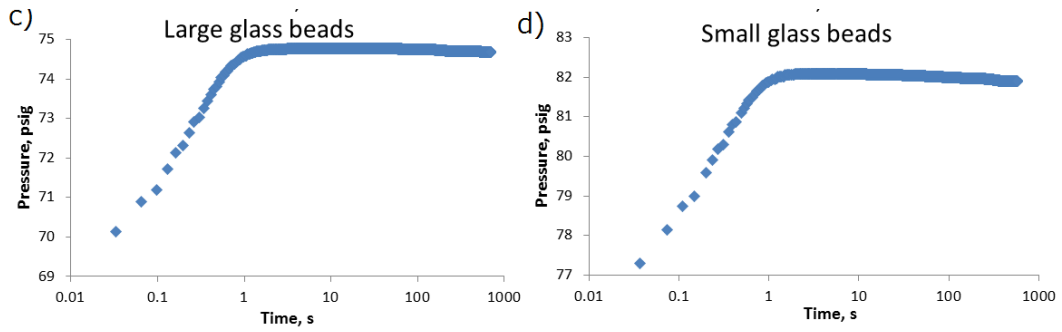
Figure 3.10 Continued. Gas expansion behavioural experiments conducted in the GRI equipment.

3.4.4.3 Pressure expansion errors

To determine the error of the equipment in determining the grain volume, a set of reference balls of known volume was tested using calibrated volumes. The results are provided in Appendix D. On average, the errors in grain volume varied between 2.6% and 3.2%. The errors increased with an increase in pressure. The sensitivity analysis was performed to determine the effect of the pressure uncertainty on the results based on the calibration error results provided in Appendix D. The obtained results are provided in Figure 3.11; a full table of the sensitivity analysis is provided in Appendix E. Essentially, uncertainty in the pressure creates most errors in the lower pressure experiment, with errors decreasing as pressures increase (Figure 3.11).
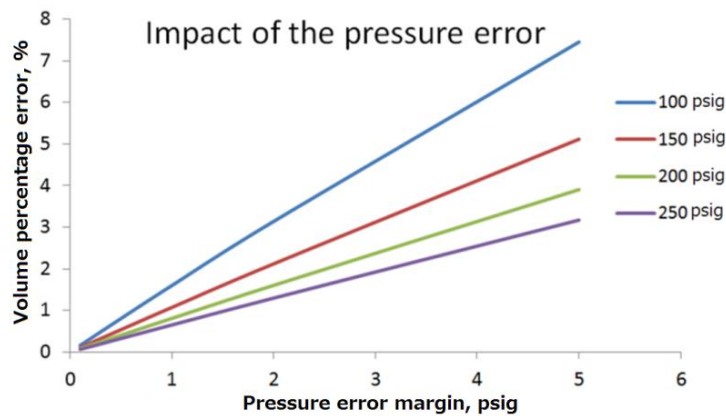
Figure 3.11 Extrapolation of pressure uncertainty on the equipment volume. The error range of the graphs is up to 3.2%.

Another source of error is the irregularity of the sample surfaces, which are difficult to eliminate given the issues in obtaining core plugs from shales. Irregular sample surfaces might create extra volume that would add to the V2 volume. This is an issue for the core

plug type of experiments (core plug GRI and modified pressure decay), whereas crushed GRI tests avoid surface irregularity errors.

Overall all samples were evenly shaped close to ideal cylinder and without any noticeable irregularities. The outlier was sample EBN9, which had noticeable surface irregularity of maximum 1 mm (Figure 3.12). The sample was not shaped as much as the others in an attempt to keep it safe from any damage as it was the only sample from the particular well received from the sponsor company. Therefore, although most samples had much smaller surface irregularity, the error is counted on maximum possible surface irregularity of around 1 mm as for sample EBN9.

The impact of the irregularity effects on the overall volume of the sample could make up to around 1.1 cm^3. This in turn would create around 2.5% -3% of uncertainty compared to the overall volume of the samples in this research (Figure 3.13). In addition, it creates up to 1.6% of uncertainty in volume compared to the downstream GRI vessel volumes. All the volumetric errors described in this chapter for the GRI method sum up to around 5.9% of the overall volume of the system. This in turn transmits into around 30-50% of possible porosity errors according to Figure 3.13. The porosity uncertainty is shown to increase with an increase in experimental pressure.
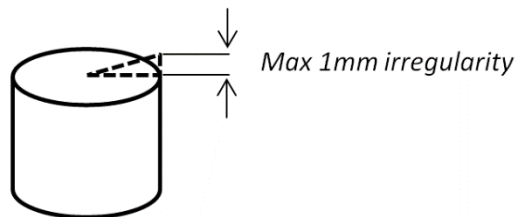
Figure 3.12 Representation of the surface irregularity on the sample.
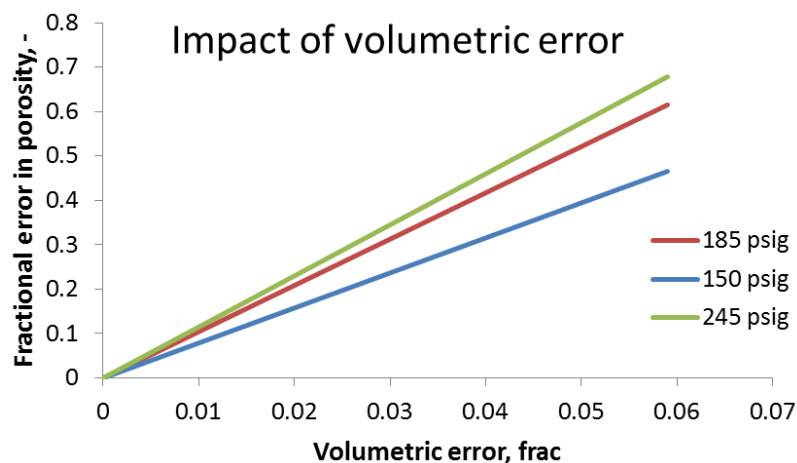
Figure 3.13. Extrapolation of uncertainty in experimental volume on fractional porosity. The error range of the graph is 3%.

3.4.4.4   Leakage

Gas leakage from the equipment can occur through the seal, piping connections or the valves and is identified on the pressure decay curve (Figure 3.14). Attempts were made to include leakage in the numerical models used to invert the experiments, however it was soon realised that prevention of the leakage is a better option. To minimise leakage, equipment was redesigned to include less piping connections and more effective seals. In particular, a pneumatic ram sealing mechanism reduced the leakage significantly (Figure 3.3). Essentially, every modification that reduced human involvement in the system helped to reduce the leakage.

The leakage rate was tested on the improved equipment at three different pressures (low, medium and high); the results are shown in Figure 3.14 and summarised in Table 3.4. It is evident that leakage is increasing with an increase in pressure, however in general the leakage was kept low over the longer term. Therefore the modifications made on the equipment to prevent the leakage were successful and the uncertainty caused by the leakage was drastically reduced (Table 3.4).
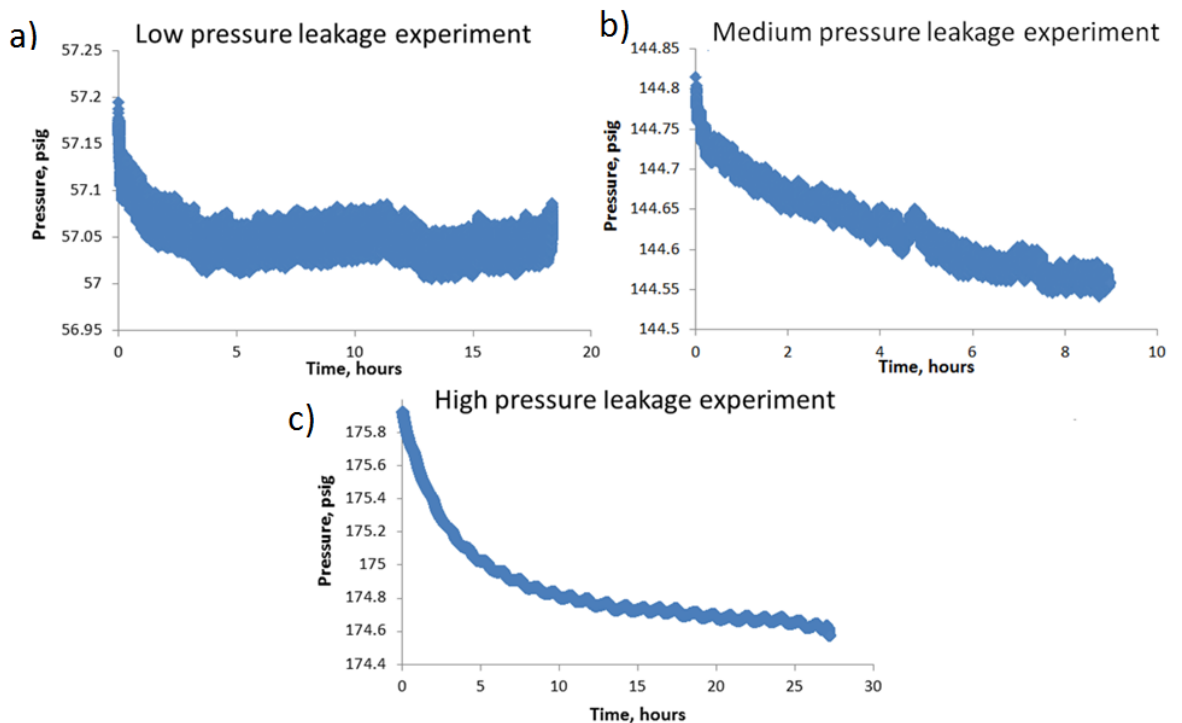
Figure 3.14 Leakage tests conducted on the GRI equipment over the various pressure ranges. The error range of the graphs is 3%.

Table 3.4. Leakage rates calculated from the leakage tests in Figure 3.14 and the error it creates for the volume of the system.

Parameter	Low	Medium	High
ΔP, psig	0.064	0.247	1.323
Δt, hours	18.0	8.9	27.0
$\Delta P/\Delta t$	0.004	0.028	0.049
Leakage error,%	0.002	0.017	0.029

3.5   Modified pressure decay measurement

The principle of this technique is that gas in a reference volume under a particular pressure is applied to the sample and the pressure response is monitored at both ends. The gas enters the sample from the upstream chamber and then flows through the sample to the downstream reference volume. The recorded pressure decay curve is used for the permeability inversion.

3.5.1   Apparatus

Modified pressure decay experiments were carried out using a gas expansion type of device presented in Figure 3.15. The device was designed in the laboratory and manufactured by a local engineering company. This device was also used for the simulations by Lorinczi et al. (2014). The system includes an upstream vessel (V_u) from which the gas is expanded towards the downstream vessel (V_d). The cylinder where the sample is placed (V_{us}) and locked contains an oil filled volume separated from the sample by the rubber sleeve. This enables a confining pressure to be applied to the sample; the core holder is designed for a maximum pressure of 5000 psig.

Upstream and downstream vessels are connected to the pressure transducers. The upstream pressure is monitored using a high precision electronic Mensor pressure transducer (P_u) with a maximum pressure of 5000 psig, and the downstream pressure is monitored using Omega Engineering electronic pressure transducer (P_d), with a maximum pressure 500 psig). There are another two pressure transducers: one monitors the pressure at the upstream vessel (P_{u1}) with a maximum pressure 1000 psig and the other monitoring the confining oil pressure (P_c) with a maximum pressure 5000 psig. The error ranges of the transducers were provided in Section 3.4.1.
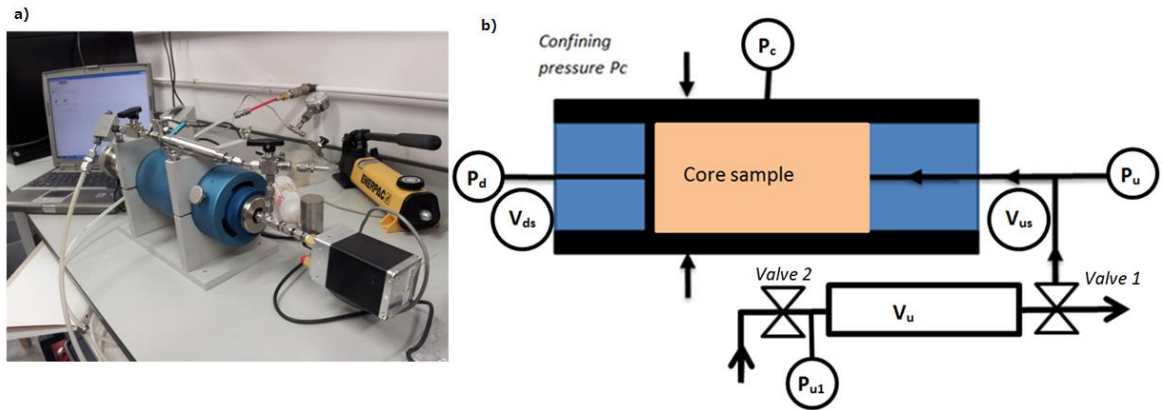
Figure 3.15. Schematic representation of the pressure decay experiment.

Cylinder-shaped core plugs were prepared for the experiment. The dimensions of the prepared samples were given in Table 3.2 in Section 3.2.3. The sample is placed into the core holder and a confining pressure is applied. In this study several confining pressures were tested from 1000 psig to 2500 psig. Gas is introduced at the upstream vessel and the pressure drops as the helium moves through the sample, where it is also recorded by another pressure transducer. Pressure equilibration is usually slow, therefore after a couple of hours the experiment is either stopped or, in case of a pressure series test, a consecutive pressure step is applied. Once the experiment is finished, the reverse pressure expansion experiment (pressure build-up) may be run, by expanding the gas from the sample into the emptied upstream (or downstream) vessel.

3.5.2   Analysis of results

3.5.2.1   Porosity

Theoretically grain density and hence porosity can be calculated from the MPD test by using the difference between initial and final pressures; bulk volume is known (see Equation 2-22 in Section 2.6.1). However, that is assuming full pressure equilibration is achieved, which is unlikely for the ultra-tight shale sample plugs. For this reason, it is recommended to obtain the porosity using the crushed GRI technique, and use it as an input parameter to derive permeability from the MPD technique. Nevertheless, some porosity values were calculated from the measurements for comparative reasons.

3.5.2.2   Permeability and *b*-factor

Permeability was derived using a history matching procedure where the modelled pressures were matched with the experimental decay curves. "Tempest", "Eclipse" and "ParaGeo" software were used for the single phase isothermal gas flow modelling,

governed by Darcy's equation (see Equation 2-4 in Section 2.2). Klinkenberg correction (see Equation 2-13 in Section 2.3) was used to correct for the slip flow. This enabled the *b*-factor to be derived. A code was written to implement this correction and obtain the *b*-factor (Appendix F). Construction of the simulation models themselves is explained in Appendix B.

3.5.3   Validation of the method

Gas leakage from the system can cause significant errors. Therefore it is important to verify that the pressure decay during the experiment happened because the gas actually entered into the sample, rather than leaked out of the system. A reverse pressure expansion experiment was therefore carried out after each GRI experiment. The derived porosities of the samples agreed with the forward pressure expansion tests and validated the GRI experiments undertaken in this research.

Another important assumption of this method is that the gas actually flows through the matrix of the sample to the downstream volume. However, the presence of fractures within the sample may dominate the results from the flow experiment. Similarly, any conductive pathway between the sample and the surrounding rubber sleeve resulting from any irregularities of the core plug can alter the results. For this reason, an experiment was conducted to validate that gas was flowing through the sample matrix instead of between the sample and the core sleeve. Xenon is particularly effective at attenuating X-rays (Diffen, 2015; Healthcare, 2015) so it was used as the test gas during experiments in which gas invasion was monitored using a medical CT scanner. The results are presented and discussed in Chapters 4 and 6.

3.5.4   Calibration and leakage of the system

The procedure of the calibration for the MPD is the same as described for the GRI – a series of pressure expansions are performed under different pressures and volumes using several reference plugs. As a result, a series of equations are made and the required volumes can be derived. The volume values obtained are presented in Figure 3.16, where relatively wide range of errors can be seen. This is mostly the result of the relatively small volumes of the system, as more precise equipment is needed to calibrate small volumes. The highest error range of 11.5% was obtained for the volume V_3. The averaged results used in simulations are presented in Table 3.5.
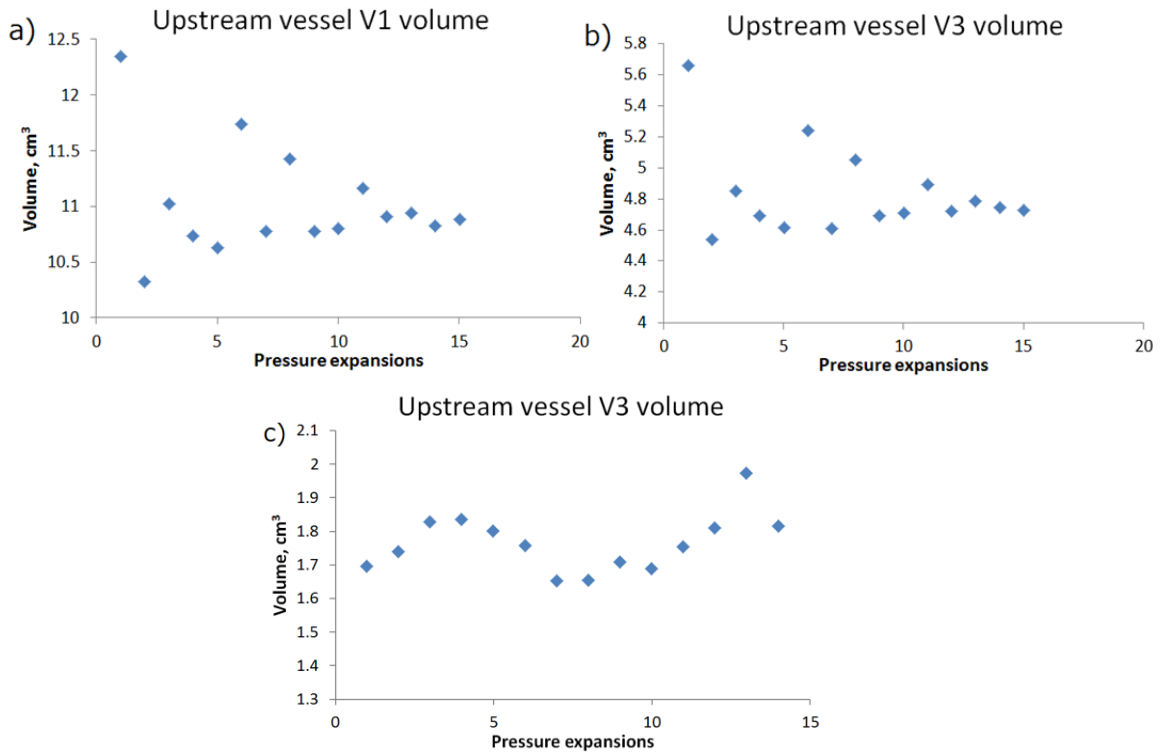
Figure 3.16. Derived volumes of the modified pressure decay experiment. The error margin is 3%.

Table 3.5 Averaged results used for the simulations.

Volume	Volume, cm^3	St. dev, dimensionless
Upstream V1	10.90	0.48
Sample upstream V2	4.75	0.28
Downstream V3	1.83	0.28
Reference plug	4.62	

3.5.4.1 Validation of the calibration

The accuracy of the permeability measurement was tested using a special reference plug constructed according to Sinha et al. (2012). The theoretical permeability of the constructed reference plug was 11 µD. The MPD experiment also gave a value of 11 µD for this reference plug; therefore the ability of the method to derive permeability values was verified.

3.5.4.2 Pressure expansion errors

Pressure sensitivity analysis was done to determine the effect of the pressure uncertainty on the system volume. The obtained values are provided in Figure 3.17; a full table of sensitivity analysis values is provided in Appendix E. The uncertainty in pressure creates

most of errors in the lower pressure ranges, with errors decreasing as pressures increase (Figure 3.17).
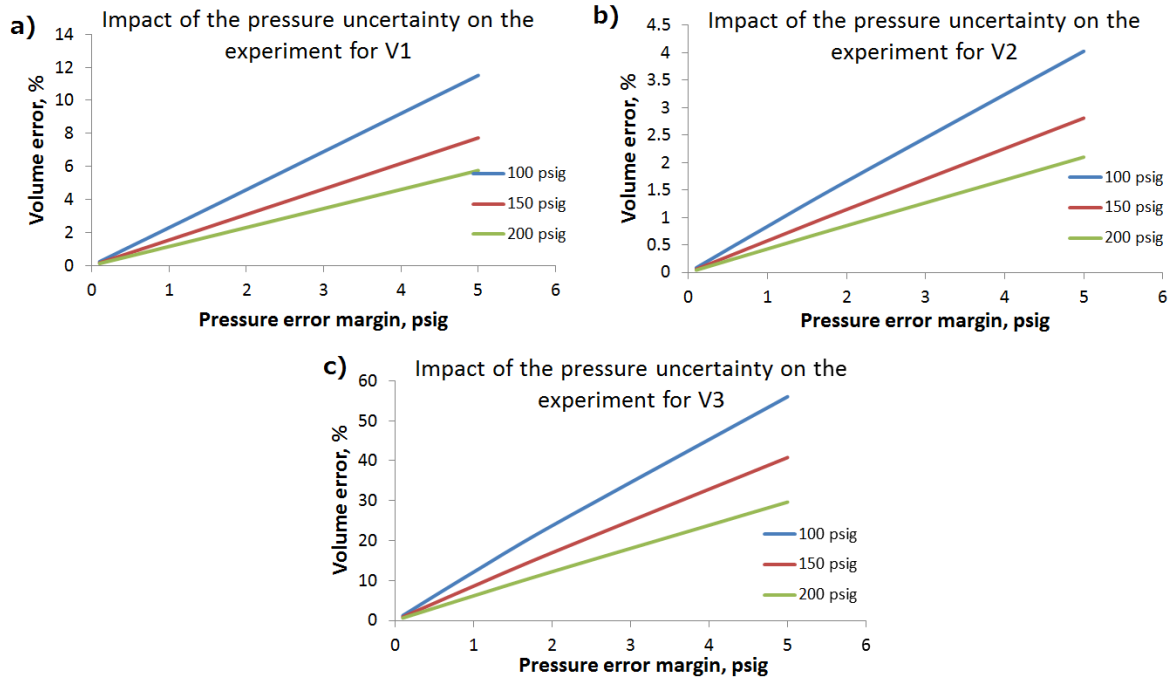
Figure 3.17. Extrapolation of pressure uncertainty on the experimental volumes. The error range of the graphs is 3%.

The irregularity of the sample creates more errors in MPD experiment due to relatively smaller overall volumes compared to the GRI vessels. The sample with 1.13 cm^3 of possible additional volume due to irregularity as described earlier (see Figure 3.12 in Section 3.4) could create up to 24% of volumetric error at the V_{us} part of the system and up to 11% in the overall upstream volume. Overall volume errors in the MPD experiment sum up to around 55%, with the highest errors created by the calibration of volumes (up to 24%), followed by the irregularity of the sample (up to 11.5%), derivation (9%), leakage (up to 6%) and pressure uncertainty (up to 5%). Nevertheless, this would only result in porosity errors of around 9% as shown in Figure 3.18. The porosity errors increase with pressure, however they overall remain relatively low due to low experimental volumes. It has to be noted that MPD tests are not practical for the porosity estimation due to long experimental times.
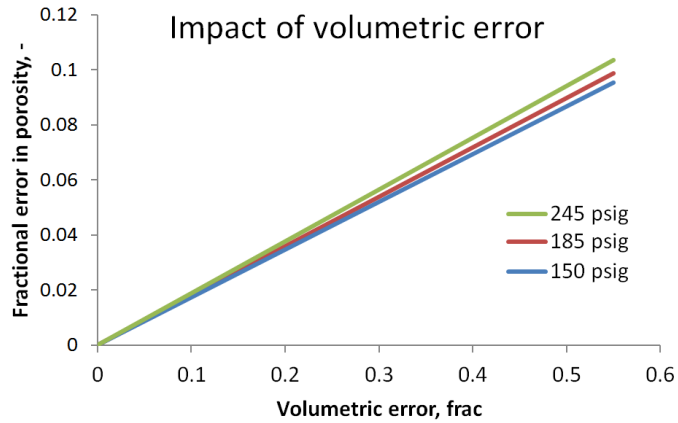
Figure 3.18. Extrapolation if experimental volume uncertainty on the fractional error in porosity. The error range of the graph is 3%.

3.5.4.3   Leakage

Leakage in the device might occur through the piping connections and the valves. The MPD experiment is conducted without waiting for the pressure equilibration (due to time experimental constraints), which makes it difficult to assess whether any leakage took place. Similarly to GRI, the goal was to minimise the leakage rather than to model it. Leakage as low as 0.1 psig/hour was achieved (Figure 3.19) during the long-term experiment, which meant uncertainties in the system up to 6% (Table 3.6). This level of leakage was treated as acceptable.
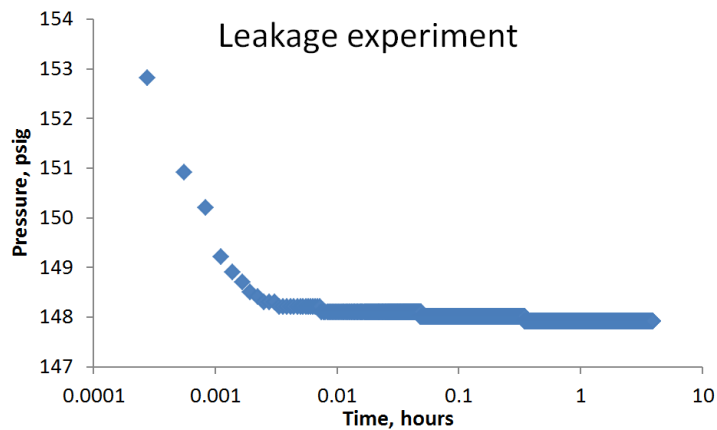
Figure 3.19. Leakage of the modified pressure decay test. The error range of the graph is 3%.

Table 3.6. Leakage rates derived from the leakage tests from the Figure 3.19.

hours	3.89
Δp, psig	0.40
Δp/hour, psig/hour	0.10
V1 error,%	1.14
V2 error,%	0.42
V3 error,%	6.10

3.6 Simulation

History matching-type modelling using industry standard simulators was undertaken to invert pressure decay data from experiments to estimate permeability. This type of derivation method was chosen due to its simplicity, ability to adapt to various experimental configurations and its potential to integrate numerous third party applications to improve the process. Different models were prepared for each simulation type: core plug GRI, MPD (modified pressure decay) and crushed GRI experiments; the description of the models is provided in this section.

The principle behind this procedure is to correctly represent the sample and experimental volumes. Pressure is set at the upstream part of the model and the gas flows across the sample. The flow across the cells is computed using Darcy's equation corrected for the slip using Klinkenberg Equation 2-13 (see Section 2.3). The method solves the experimental data by generating an inverse numerical formulation: several runs are made, pressure outputs of which are compared with the experimental pressures. The derived results are then selected from the closest fit simulation runs.

3.6.1 Core plug GRI (CPGRI) simulation model

Simulation models are shown in Figure 3.20. Model cells have to represent the core and the surrounding free external volume. For the core plug GRI, radial *23 * 2 * 100+X* Eclipse (version 2013.7) models were generated with 21 * 2 * 100 cells acting as a core plug and the remainder *2 * 2 * X* cells acting as the external volume, depending on the size of the core plug. The *X* term is used to account for the differences in core lengths. The porosity of the external volume was adjusted so that the ratio of the external pore volume and that of the bulk volume of the core plug was the same as that within the actual pressure cylinder. The permeability of the cells representing the external volume has to be very high compared to that of the sample, in this case it was set to 100 mD.
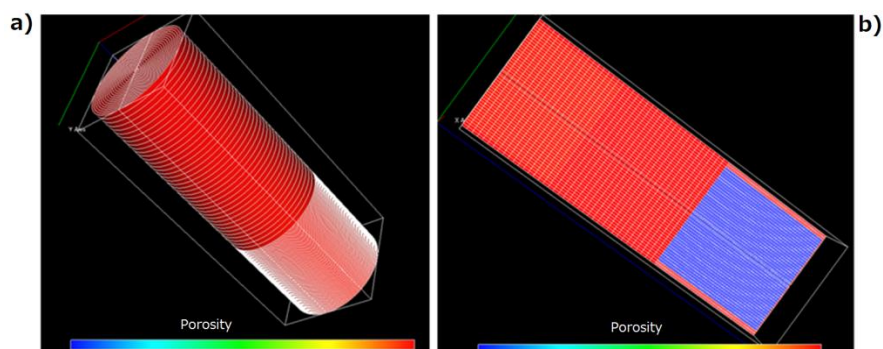
Figure 3.20. Core scale GPGRI model (a) and a cross section of it (b). The sample is denoted by the blue, the free space by the red and the expansion volume by the lighter shade of red.

3.6.2 Modified pressure decay simulation model

For the MPD, rectangular prism shaped models were constructed (Figure 3.21). A rectangular model was chosen as, unlike in GRI, during MPD experiment the flow occurs linearly from the upstream towards the downstream. The cross sectional area of the core plug has to be represented correctly when simulating cylindrical core plug as a rectangular prism (Figure 3.22).

The number of cells in the *X* direction depends on the length of the core plug. The upstream and downstream volumes were represented by several layers of cells. Although the values are constant, the cell volumes had to be adjusted according to the varying length of the samples. First and last rows of the models were used for the upstream/downstream volume representations. The middle layer of each model core represented the fracture. The fracture was composed of one layer of cells along the entire length of the model in the *Z* direction. The fracture was selected to be in the middle of each model for simplicity.
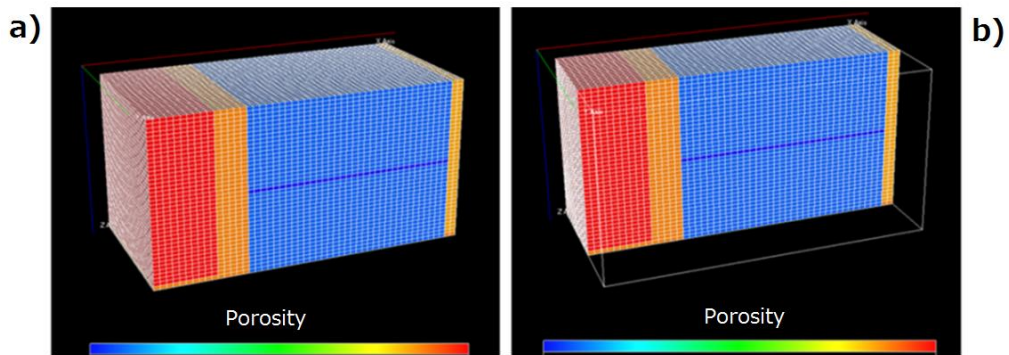
Figure 3.21. Core scale model of the MPD experiment (a) with its cross section (b). The sample is represented by the blue colour, the fracture within the sample by the darker shade of blue, the upstream and downstream volumes by orange and the expansion volume by the red colour.
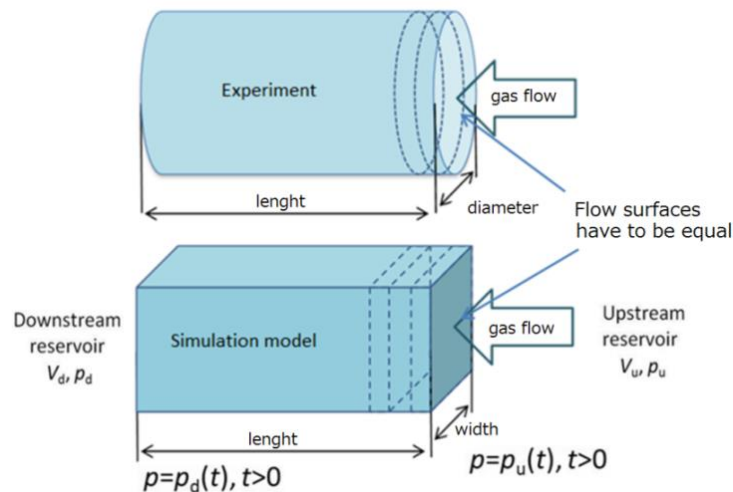
Figure 3.22. Geometrical simplification assumptions of the flow in the model.

3.6.3 Crushed GRI simulation model

To model crushed experiments, each particle of crushed shale material was assumed to be a shard of 600 μm x 600 μm x 1800 μm. The particle is surrounded by a high permeability zone (100 mD) which represents the surrounding space in the vessel. Extra 6 x 6 x 18 100 μm^3 cells at the top of the model were included to represent the expansion volume. Luffel et al. (1993) in his original model assumed similar cylindrical particles with diameter equal to the average mesh size and length twice the height.

Simulation models attempting to represent double and triple porosities were also constructed and applied to the experimental results. In those models, the shale particle was divided into two and three equal parts respectively (Figure 3.23c & d). Permeability and porosity of those parts were set to represent the high and low conductivity regions of the shale. The details of the models are presented in the following sections.

Variable time step is needed for better representation of the pressures just after the experiment starts, as the majority of pressure decrease occurs at the beginning of the measurement. During the later stages larger time steps are therefore used. Time integration is performed using an implicit unconditionally-stable backward Euler algorithm.
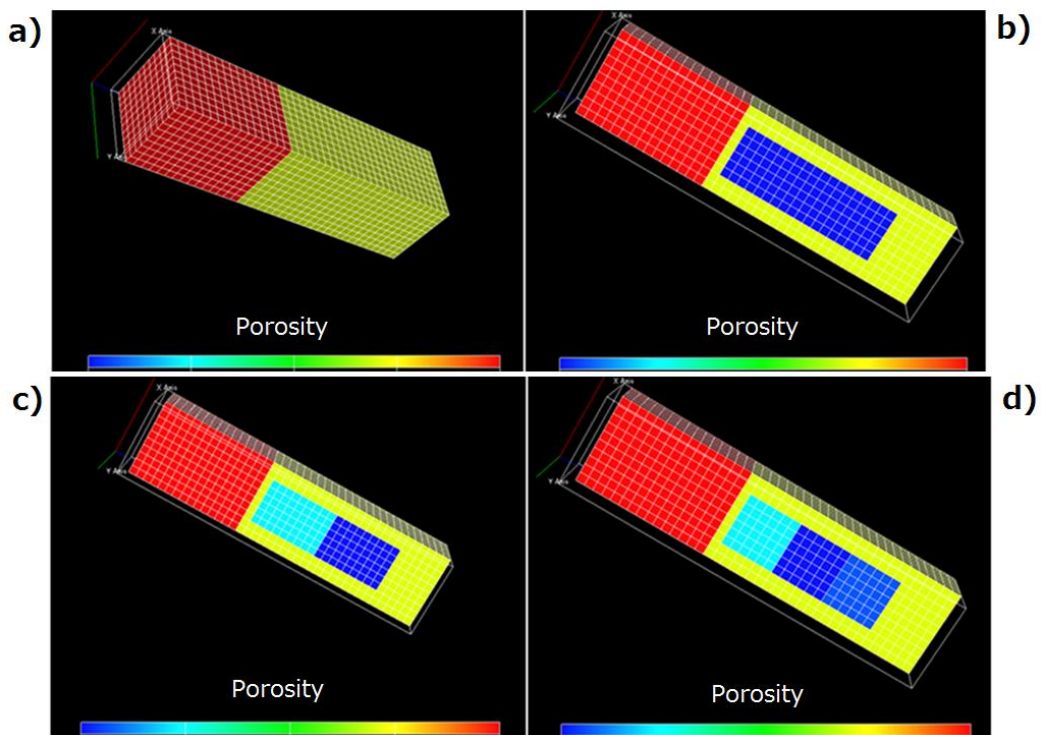
Figure 3.23. Diagrams showing cross sections through a particle scale crushed GRI model. Red represents the reference chamber, blue the shale and yellow the void volume around the shale. Figure b shows the single porous system model (matrix only), c - double model (matrix and fractures) and d - triple model (two types of matrix and fractures).

3.6.4 Modelling assumptions

Deriving results from the gas expansion experiments using simulation models described in this section requires several conditions to be assumed:

- The first assumption is that the gas behaves according to the ideal gas law. This assumption is applied in each model in this research.

- Homogeneity of the sample is another assumption made in the core plug experiments, although a high conductivity layer is included to represent the fracture, the matrix of the model has uniform parameters throughout the sample model.

- The gas is assumed not to leak from the system.

- Single phase single species gas flow is assumed in the simulation models. The laboratory gas used for the experiments is specified by the manufacturer to be 99.8% pure.

- Thermodynamic effects are neglected in the model, however it was attempted to reduce temperature effects both during the experiment and the calculations.

- The simulator errors are extremely small - Eclipse is a fully implicit simulator meaning its equations are stable over long time steps. Most of the residual sum errors are negligible (Schlumberger, 2011).

3.6.5 Inversion procedure

Once the model is constructed, the history matching is performed using Tempest Enable software. Tempest Enable runs many simulations of the model using a predefined range of parameters which are then used to derive a response surface. The software then compares the outcome of each simulation to the experimental data of the model. Based on the quality of the fit between the simulated and the experimental data, the software generates a new series of parameters and identifies the ones that produce the best fit. This ability of Tempest Enable to automatically create a wide breakdown of results using a pre-defined range of parameters was also used in GIP calculations using Monte Carlo method described in Chapter 7.

3.7 Field experiments

Gripen Oil & Gas collaborated with the University of Leeds on an exploration and appraisal programme in 2012 to 2014 aimed at assessing the possibility of commercial natural gas extraction in shallow shale gas play in the Östergötland county, located in the southern

part of Sweden. The main objective of this programme was to estimate potential gas reserves of the field, given by the Estimated Ultimate Recovery (EUR) as well as gas flow rates. The secondary objective was to better understand the reservoir and attempt to simulate the future production. The findings of the study would help the company to decide on the next steps in the exploration campaign; whereas the shale research at the University of Leeds would obtain field testing data and selected shale cores agreed between the research participants and the company. In addition, the equipment for the shale measurements at field conditions designed at the University of Leeds would be tested.

The study included collection of field data using equipment designed in the laboratory and built locally. Among the collected field data is the core desorption, well pressure build-up, gas flow rate measurements and the shale cores brought back to the laboratory. These cores were then cored into smaller samples and crushed following the procedures applied on other shale samples in this research (see Figure 3.2 in Section 3.3). The samples were used in the pressure decay experiments to obtain permeability, porosity and various other results including SEM and CT data. Several samples were sent to the research partners at Bengal University of Science and Technology for the adsorption tests.

3.7.1   Canister desorption

Gas desorption is routinely conducted at the well side to determine the volume of gas within shale samples. It has also been suggested that the results can be used to estimate shale permeability (Cui et al., 2009). In this study 10 stainless steel cylinders (Figure 3.24a) were designed and constructed to enable gas desorption tests to be conducted as soon as core was brought to the surface. All cylinders are identical – they are 50 cm in length and 5.2 cm in internal diameter. Each cylinder has a volume of 1128 cm^3 plus an additional 10 cm^3 volume of the piping connecting the transducer.

Figure 3.24 Desorption cylinders (a) and bourdon gauge (b).

For the desorption test, the recovered cores are placed into the cylinders filled with water. Normally, one core sample of about 40-50 cm length and 5 cm diameter can fit into one cylinder. After the core is placed into the cylinder, the displaced water is collected for the bulk volume measurement whereas the cylinder with the core is sealed. The pressure build-up within the cylinder is monitored using either manual or electronic pressure transducer. Normally, the desorption graphs are extrapolated to account for the lost gas while the core is retrieved. However, in this study it was assumed that the cores do not lose significant amount of gas due to relatively quick retrieval process (less than 30 minutes due to short depths) and also for simplicity reasons. Desorption cylinders are kept in the water tank during the experiment to keep their temperature constant and this allows leaks to be identified.

After the pressure equilibration, the amount of gas at surface conditions is measured by displacing the water from the measurement tube (Figure 3.25). The cylinder is then opened and the core is removed. Most of cores were held in the cylinders for a couple of hours before removing them and placing into core storage box, whereas the cylinders were filled with new cores. This allowed measurements to be made on up to 30 cores per day, using all 10 cylinders. Some of the cores were left for longer time pressure build-ups: overnight, weekend and six months.

Figure 3.25 Water displacement measurement method.

The amount of gas at the surface conditions was derived using the canister desorption pressure values. It shows the corrected volume of gas desorbed from the core relative to the atmospheric pressure. It is calculated using Boyle' law (see Equation 2-20 in Section 2.6.1), by deriving the value *V2*. In Equation 2-32, *P1* is the accumulated core pressure, *P2* is the atmospheric pressure and *V1* is the free pressure within the desorption canister.

Water saturations were derived for some cores using the amount of gas generated by the core, the bulk volume of the core (obtained from the amount of displaced water) and the porosity of that core derived in the laboratory (provided the core sample was delivered to the laboratory). The desorbed gas content indicates the gas-filled volume within the shale cores, whereas porosity derived in the laboratory provides the overall matrix accessible volume. The difference between the two shows the volume un-occupied by the gas, i.e. water-filled volume (Figure 3.26). Water saturation can then be obtained by dividing water volume by the pore volume of the core.
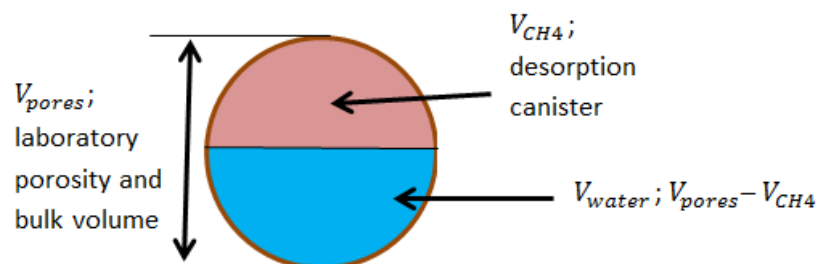
Figure 3.26. Schematic representation of the shale volumes derived.

3.7.2   Well pressure build-up

Well pressure build-up is conducted to characterize the dynamic behaviour of a formation; the obtained data can be analysed for the depletion identification, possible flow rate and also assessment of the well completion (Dake, 1978). The test is carried out after setting the packer at the limestone/shale contact (Figure 3.27). Pressures were recorded with a laptop (using electronic pressure transducer) with time steps of 1 to 5 seconds or logged manually each minute (using the mechanical type bourdon gauge). The collected data can be used for the analysis of the gas behaviour and the construction of the reservoir model.
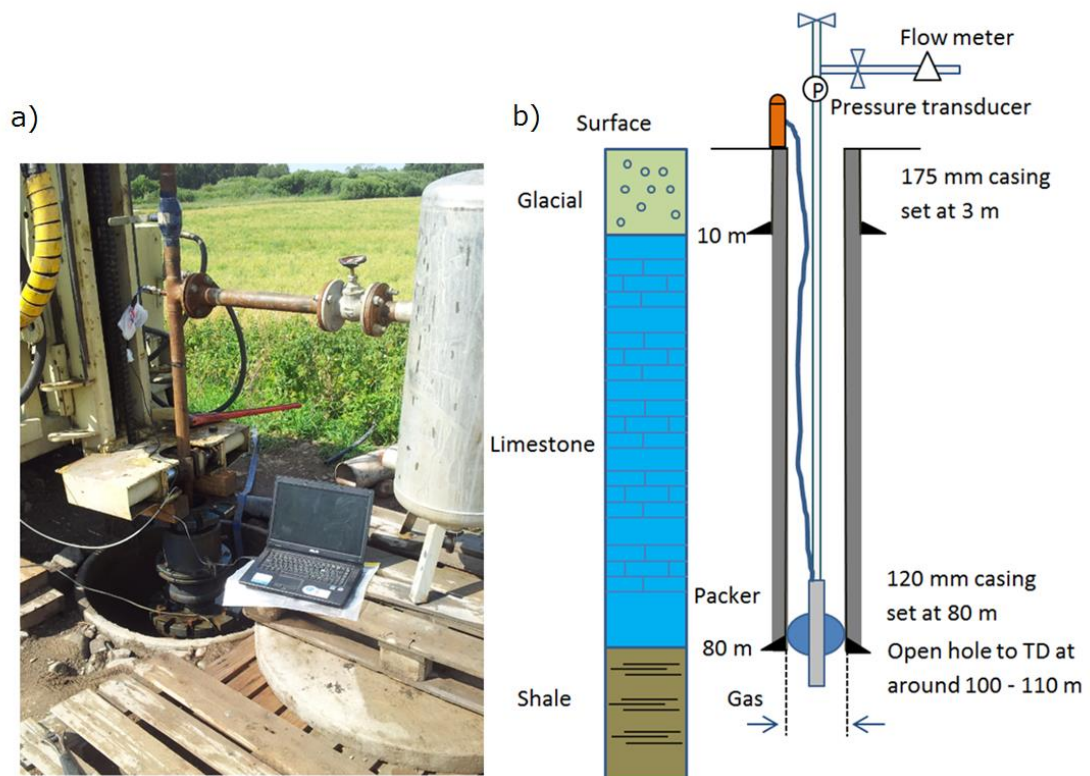
Figure 3.27 Well pressure build-up setup (a) and its schematic representation (b).

Pressure build-up testing was carried out under different conditions:

- Several build-ups were performed to compare the consistency of the results of repeated measurements. The pressure of the well is set to build-up, then after equilibration is reached, it is released and set up again.

- The pressure build-up while the neighbouring well is producing.

- Pressure build-up during the water stimulation of the neighbouring well. The pressure response due to the injection at the neighbouring well was recorded.

- Pressure build-up of the well after water stimulation. The change of the pressure build-up due to the stimulation of the formation.

It has to be noted that water flush-out procedure is carried out by displacing formation water within the well by pumping in the nitrogen gas (Figure 3.27), therefore it is likely that some of the gas might intrude into the formation. This might result in the increased well pressure build-up reading as some of the produced gas is not natural methane but rather nitrogen, which was injected to flush-out the water. This pressure overestimation was avoided by making several pressure build-ups.

3.7.3 Well flow measurements

Gas flow rate is the primary indicator of the potential of a well to deliver gas. It was done to assess the capability of formation to supply the gas and to obtain the data for the production simulation model. A hand-held gas flow meter was used for checking the short-term flow. The device had limitations for the minimum continuous gas flow rate of at least 25 scf/h necessary for the flow to be recorded. Therefore only the continuous flow of 25 scf/h or higher was recorded with anything lower regarded as a no-flow. The measurement was carried out after the well pressure build-up; the valve was opened and the gas flow rate was recorded.

For the long-term measurement, the remote gas flow measurement equipment able to feed data online was set up on three wells (Figure 3.28). Production estimations were achieved by combining flow rate with pressure build-up data. Similarly to well pressure build-up, various cases for well production were tested, including before/after water flush-out; before/after well stimulation; with/without twin wells under production.

Figure 3.28. Well flow rate measurement system with the SIM card to monitor data remotely.

3.7.4   Well stimulation

3.7.4.1   Nitrogen packer method

Nitrogen fracturing is the cheapest and quickest method at such small-scale field operations. It is done by setting up the packer at the shale-limestone boundary: the productive shale layer is then isolated by inflating the packer. Nitrogen gas was then expanded into the shale formation, at a pressure of around 500 psig (30 - 40 bar) for about 5 - 10 min, to open microfractures and sweep out the free methane gas. The pressure of the nitrogen was monitored using a manual pressure transducer.

Gas flow rates measured after this operation may be unrealistically high because they will contain the injected nitrogen. Indeed, this was proved by sampling the gas into special plastic bags and sending it for compositional testing. It was found that in some cases the nitrogen comprised up to 80% of overall gas collected just after nitrogen stimulation due to the nitrogen flow back.

3.7.4.2   Acid treatment

Acid treatment of the well was implemented by filling the bore hole with hydrochloric acid. The treatment was intended to clean up the surface of the formation from the mud cake and reduce the pore blockage (Figure 3.29). About 30 litres of 17% concentration hydrochloric acid was used. The procedure was performed several times, each time the acid was left in the wellbore for different amounts of time varying from 30 minutes to 6 hours. After that acid was flushed out and collected into tanks.
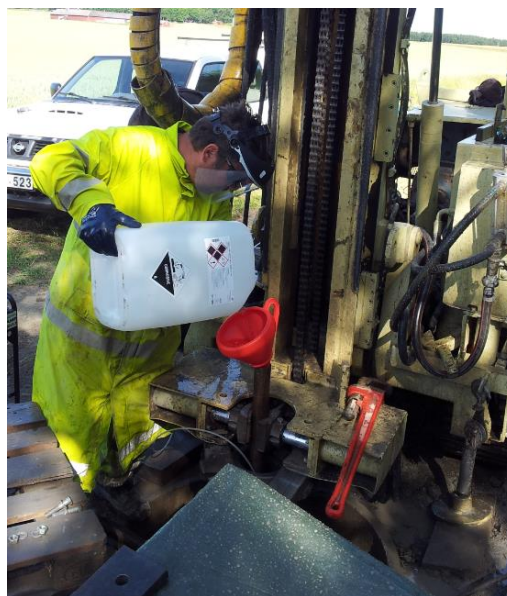
Figure 3.29 Acid treatment procedure.

3.7.4.3 Hydraulic fracturing

To hydraulically fracture the formation, water was pumped into the formation at around 550 psig pressure for around 15 minutes time period using the injection truck (Figure 3.30 a). To improve the transport of sand within the fractures and stability of the wellbore, polymers were used for the suspension enhancement and shale stability. The amount of sand used in the liquid was around 3.5 kg/m^3. Several different sand concentrations were tested. The best results were achieved using larger concentrations of sand in the liquid. Coarser sand of the mesh size 20/40 (0.5 mm - 0.8 mm) was chosen for the operation for it being standard size used in most U.S. fracturing jobs (King, 2010). The pressure was recorded using Omega Engineering pressure transducers directly to the laptop (Figure 3.30 b). Furthermore, pressure response in the twin wells was also monitored.
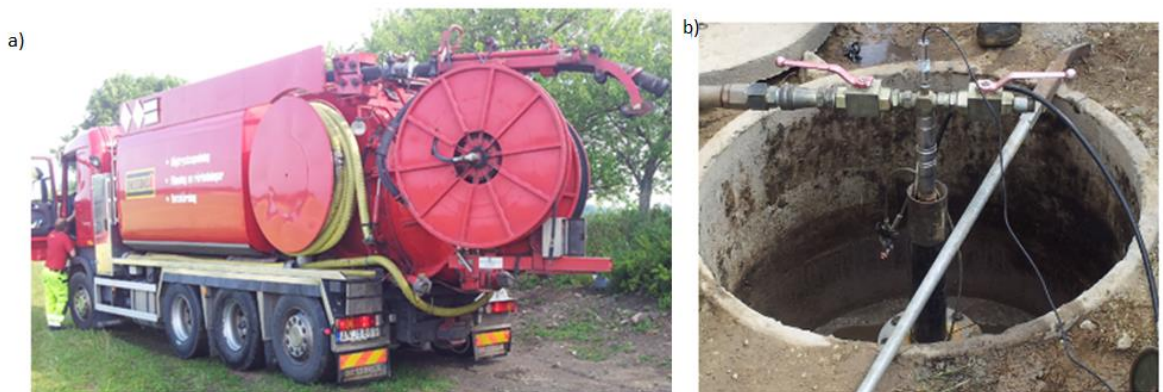
Figure 3.30 Hydraulic fracturing procedure. Shown is water injection truck (a) and the pressure transducer (b) logging injection pressures.

4 Chapter
Shale characterisation

4.1 Introduction

The complex structure of shale matrix is a major control on gas storage and flow potential. On the micro-scale, pores are often extremely small (<10 nm) and may be poorly connected. On the larger scale, shale may be inter-bedded with siltstone or sandstones that provide high permeability flow paths. In addition, there may be many other structural features such as faults or fractures that can act as conduits for flow. Therefore to successfully describe shale porosity and permeability, this internal structure has to be understood.

Measurements undertaken to understand the controls on porosity and permeability include mineralogical analysis such as quantitative X-ray diffraction (QXRD) and microstructural analysis such as scanning electron microscopy (SEM), and computer tomography (CT). These tests produce compositional data or images visualising the structural framework of the shale matrix. Various techniques can be utilised (e.g. ion-polishing or image post-processing) to improve the quality of the obtained images.

Unfortunately, the heterogeneous nature of shale means that even a few micrometres of shale matrix might exhibit significant heterogeneity. Similarly, a square centimetre of shale may contain several lithologies with varying microstructure. This complicates the identification and description of the porosity and makes it practically impossible to obtain any quantitative estimate for permeability from SEM or CT images. These challenges call for a multi-scale analysis approach to successfully characterise the shale matrix.

In this chapter a compositional analysis together with imaging of shale matrix at different scales is presented. The objective is to characterise the principal structural controls of matrix on the pore space and fluid flow potential by utilising a systematic approach of data upscaling from micro to macro structure (QXRD → SEM → CT). Additional data including Rock-Eval maturity, total organic carbon (TOC) and surface area (BET) are also presented and discussed to complement the results.

The chapter begins by describing the use of the experimental methods outlined in Section 3.3 (Section 4.2). The results are then presented in Section 4.3 and discussed in Section 4.4. The chapter ends with the summary of the findings on this topic (Section 4.5).

4.2 Methods

Table 4.1 presents the samples and corresponding experiments conducted. Overall, 12 samples were analysed for QXRD, BET, TOC, Rock-Eval, SEM and CT. Limited time resources meant not all experiments could be performed on all samples; therefore the samples were prioritised according to the research objectives and sponsor requirements. The most complete analysis was conducted on Control-Test samples (see Section 3.2.1).

Table 4.1. Overview of the sample characterisation experiments analysed in this chapter. Grey cells denote that the experiments were not performed.

Sample	Test						
	TOC	BET	Rock-Eval	QXRD	SEM	CT	CT-xenon
EBN20	✓	✓	✓	✓	✓	✓	✓
EBN5							✓
NEX7	✓	✓	✓	✓	✓	✓	
NEX15	✓	✓	✓	✓	✓	✓	
NEX33	✓	✓	✓	✓	✓	✓	
CHE2	✓	✓	✓	✓	✓	✓	
CHE3	✓	✓	✓	✓	✓	✓	✓
Grpn7	✓	✓	✓	✓	✓	✓	
F3	✓	✓		✓	✓	✓	
E9	✓	✓		✓	✓	✓	
OA-1						✓	
Karoo							✓

4.3 Results

4.3.1 Composition of shale samples

QXRD results of the samples are given in Table 4.2. Samples EBN20 and NEX33 reveal strong carbonate presence (54.6% and 62.5% respectively). NEX33 sample stands out as being composed mostly of calcite (59.4%), whilst EBN20 is composed mostly of dolomite (46.2%). All other samples exhibit quartz-clay dominance, with some of the samples (NEX7, NEX15 and Gripen group) containing up to 37.2% of clay. Despite containing a lot of clay, samples NEX7 and NEX15 also show the largest percentage of quartz among all samples, i.e. 44.5% and 44.8% respectively. Gripen group of samples show the largest presence of pyrite, notably in the range of 19.1% - 25.3%. CHE group of samples exhibits considerable mica presence of 38% for CHE2 and 33.3% for CHE3. Data for the rest of the samples are provided in Appendix G.

Table 4.2. QXRD results for the Control-Test and Gripen group of samples.

Sample	EBN20	NEX7	NEX15	NEX33	CHE2	CHE3	Grpn7	F3	E9
Quartz,%	10.1	44.5	44.8	7.8	26.2	32	29.1	25.9	24.8
Albite,%	1.9	1.7	1.8	2.9	8.9	6.2	3.7	3.5	4.2
Microcline,%	0	1.9	0	0.6	0	0	9.4	13.6	10.7
Calcite,%	8.4	7.6	9.9	59.4	12	3.1	1.1	0	0
Dolomite,%	46.2	1.6	3.2	3.1	0	2.1	1.3	0	0
Mica,%	16.4	3.1	2.7	2.6	38	33.3	10.9	12.8	21.9
Illite/smec,%	5.1	32.5	26.7	20.2	4.8	14.1	22.6	21.4	15.6
Kaolin,%	5	3.9	4.9	0	0	0	2.7	3.6	3.5
Chlorite,%	0	0.8	0.8	1.2	13.1	4.2	0	0	0
Pyrite,%	4.4	2.2	4.9	2.2	0	5.4	16	16.9	16.4
Siderite,%	0	0.2	0.2	0	0	0	0.7	0	0

Ternary plot made to display results visually (Figure 4.1) illustrates the quartz-clay dominance in all but two samples. The main phyllosilicates identified by XRD were mica and illite (Table 4.2) although in reality it is difficult to separate these minerals using QXRD. Figure 4.2 presents all distributions of different clay minerals: samples EBN20, NEX7, NEX15 and the Gripen group also included significant amount of kaolin, whereas CHE group of samples together with NEX33 contained chlorite as the third most abundant clay mineral.
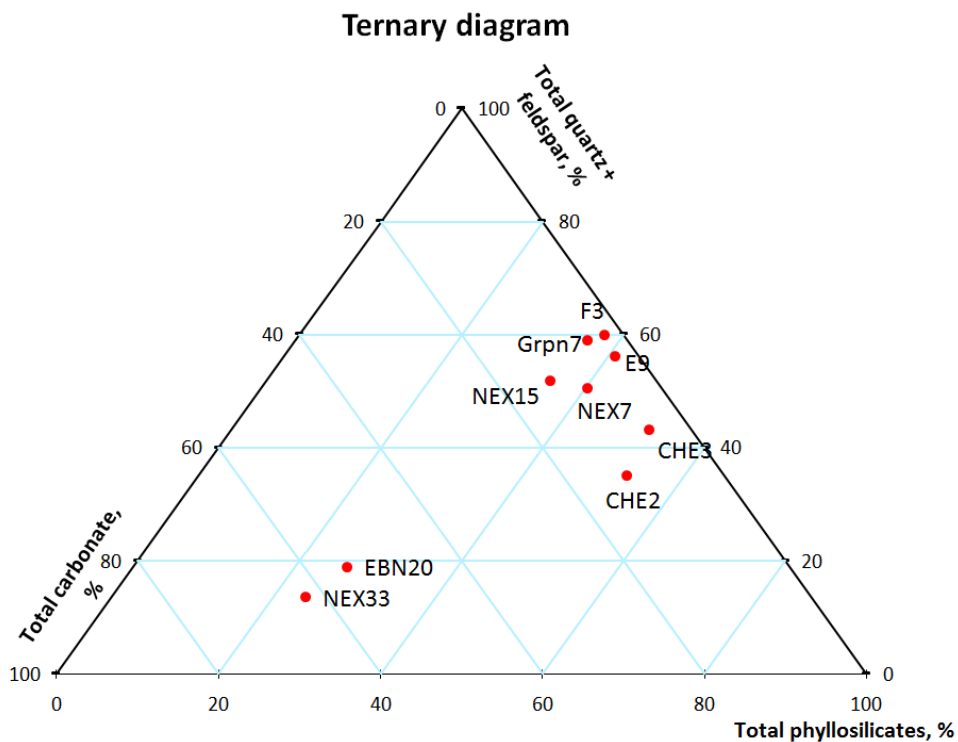
Figure 4.1.Compositional analysis results on the Control-Test samples plotted on a ternary plot. Minerals were grouped into three groups: Carbonates, Phyllosillicates and Quartz + feldspar.
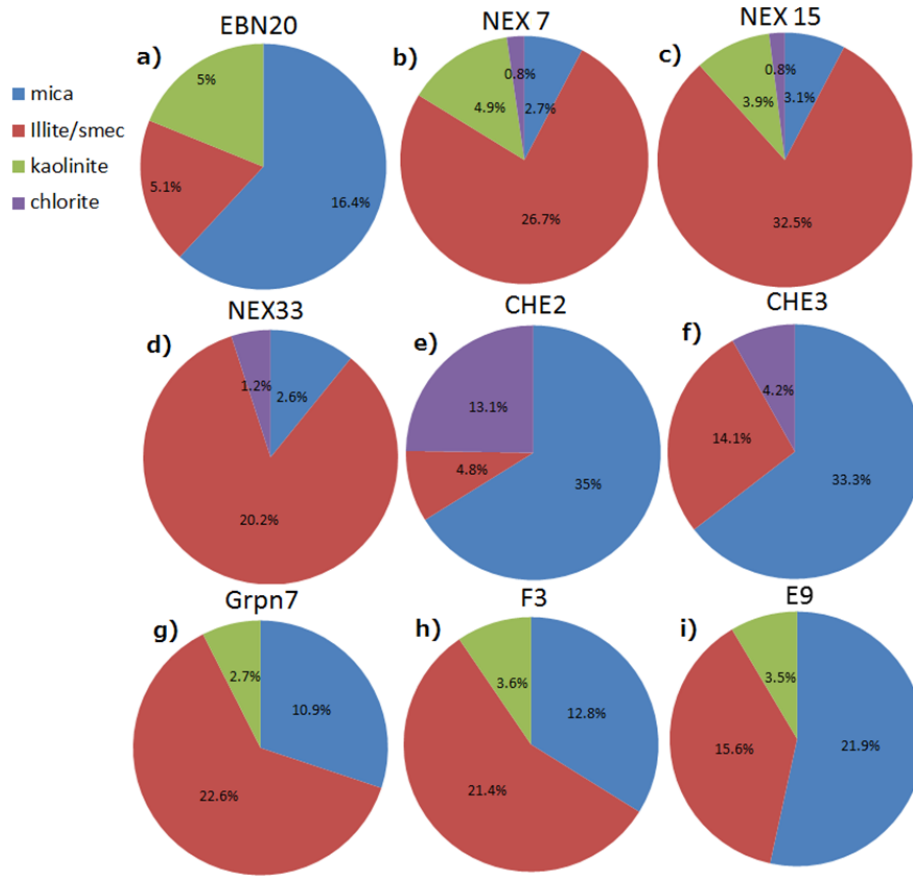
Figure 4.2. Analysis of the clay type. Four main clay groups were identified: mica, illite/smectite, kaolin and chlorite.

Table 4.3 presents the results of BET and TOC analysis for the samples listed in Table 4.1 (see Section 4.2); the results for the remaining samples are provided in Appendix G. The Control-Test samples exhibit larger BET values than the Gripen samples (Grpn7, F3 and E9), with the results ranging from 4.8 m^2g^{-1} (NEX7) to 11.8 m^2g^{-1} (CHE2) compared to 1.2 m^2g^{-1} (Grpn7) to 2.3 m^2g^{-1} (E9). However, Gripen samples contain a large amount of TOC, with sample F3 reaching 20.2%. Control-Test samples show TOC values from 2.0% (NEX33) up to 5.7% (EBN20).

Table 4.3. BET and TOC results of the samples.

Sample	BET, m^2g^{-1}	TOC, wt%		Sample	BET, m^2g^{-1}	TOC, wt%
EBN20	6.03	5.67		NEX33	7.17	2.01
CHE2	11.78	2.54		Grpn7	1.23	15.87
CHE3	5.18	4.43		F3	1.94	20.18
NEX7	4.79	3.27		E9	2.32	14.30
NEX15	5.77	3.21				

4.3.2   Rock-Eval

The results of the Rock-Eval experiment for the Control-Test and Gripen group of samples are provided in Table 4.4. The S1, S2 and S3 values as well as Tmax values are presented. S1 values show the amount of free hydrocarbons; S2 represent the hydrocarbons generated through thermal cracking during the pyrolysis experiment; whereas S3 shows the amount of CO_2 produced from the thermal breakdown of the kerogen within the sample. Finally, T_{max} indicates the temperature at which the largest release of hydrocarbons during the pyrolysis experiment occurs (Nordeng, 2012).

T_{max} allows the level of maturation to be determined. Normally, T_{max} between 435-450˚C indicates the intense level of oil/gas generation, whereas the zone between 400-435˚C is associated with immature organic content (Nordeng, 2012). The NEX samples clearly contain mature organic content, whereas Grpn7 and CHE samples appear immature (Table 4.4). EBN20 is on the edge between immature and mature levels with T_{max} of 433˚C. However, better interpretations are achieved when combining T_{max} with the kerogen type to understand the likely product of the petroleum generation within the given formation (Nordeng, 2012).

Hydrogen and oxygen indices were derived from the S2 and S3 respectively to construct a Van Krevelen diagram and interpret the Kerogen types of the samples (Figure 4.3). It can be seen from Figure 4.3 that EBN20 and Grpn7 samples contain Type I kerogen, unsuitable for the gas generation. In contrast CHE3 contains Type III kerogen, able to generate gas. All other samples include a mix of Type I and Type II kerogens.

Table 4.4. Rock-Eval experimental results.

Sample	S1,mg/g	S2,mg/g	S3,mg/g	T max, C˚
EBN20	2.77	36.47	0.69	433
CHE2	0.33	0.61	0.46	413
CHE3	0.33	0.61	0.46	413
Gripn7	1.70	69.79	0.46	419
NEX7	1.29	6.40	0.26	438
NEX15	0.85	5.47	0.24	441
NEX33	0.43	4.70	0.29	441
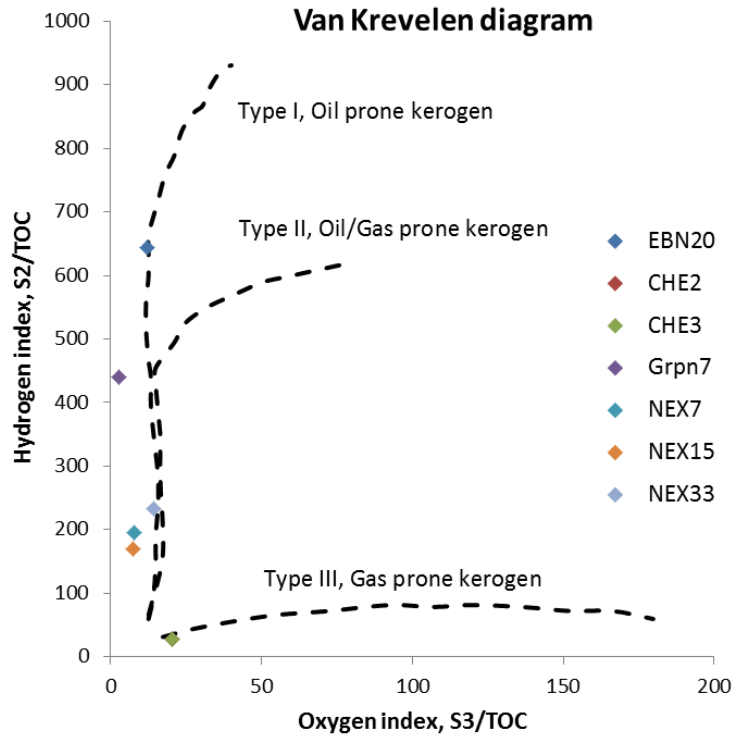
Figure 4.3. Van Krevelen diagram showing the hydrogen index as a function of the oxygen index for distinguishing between the kerogen types.

4.3.3 SEM analysis

A key aim of SEM analysis is to visualise pores within the shale matrix and understand the major structural features associated with them. QXRD and TOC results were utilised to aid the interpretation of the pores (see Table 4.2 and Table 4.3 in Section 4.3.1).

SEM images of the CHE2 sample (Figure 4.4) show heterogeneous matrix with considerable amount of pyrite. The elongate clays are mostly orientated along one direction. The dark areas between the grains are organic matter. No fractures can be observed. Smaller scale field view (Figure 4.4 c, d, e & f) reveals a clay-rich matrix. Quartz and calcite can also be seen surrounded by clays and organic matter.

Porosity is observed in the SE images as dark spots with a black centre (Figure 4.4d). Sometimes pores can be brightly highlighted (Figure 4.4b), which is caused by the electrons reflecting from the pore edges (Rine et al., 2013). Some pores might be present within larger minerals, hence would belong to the intraparticle class. Indeed several micro pores can be identified within the chlorite as shown in Figure 4.4 d.

The pores observed in sample CHE2 are mostly round, ellipsoidal and limited to the micrometer scale. No clear interconnected pathways between the pores can be identified.

However, most of the pores are filled with bitumen indicating that they were once sufficiently interconnected for bitumen to migrate (Bernard et al., 2013).
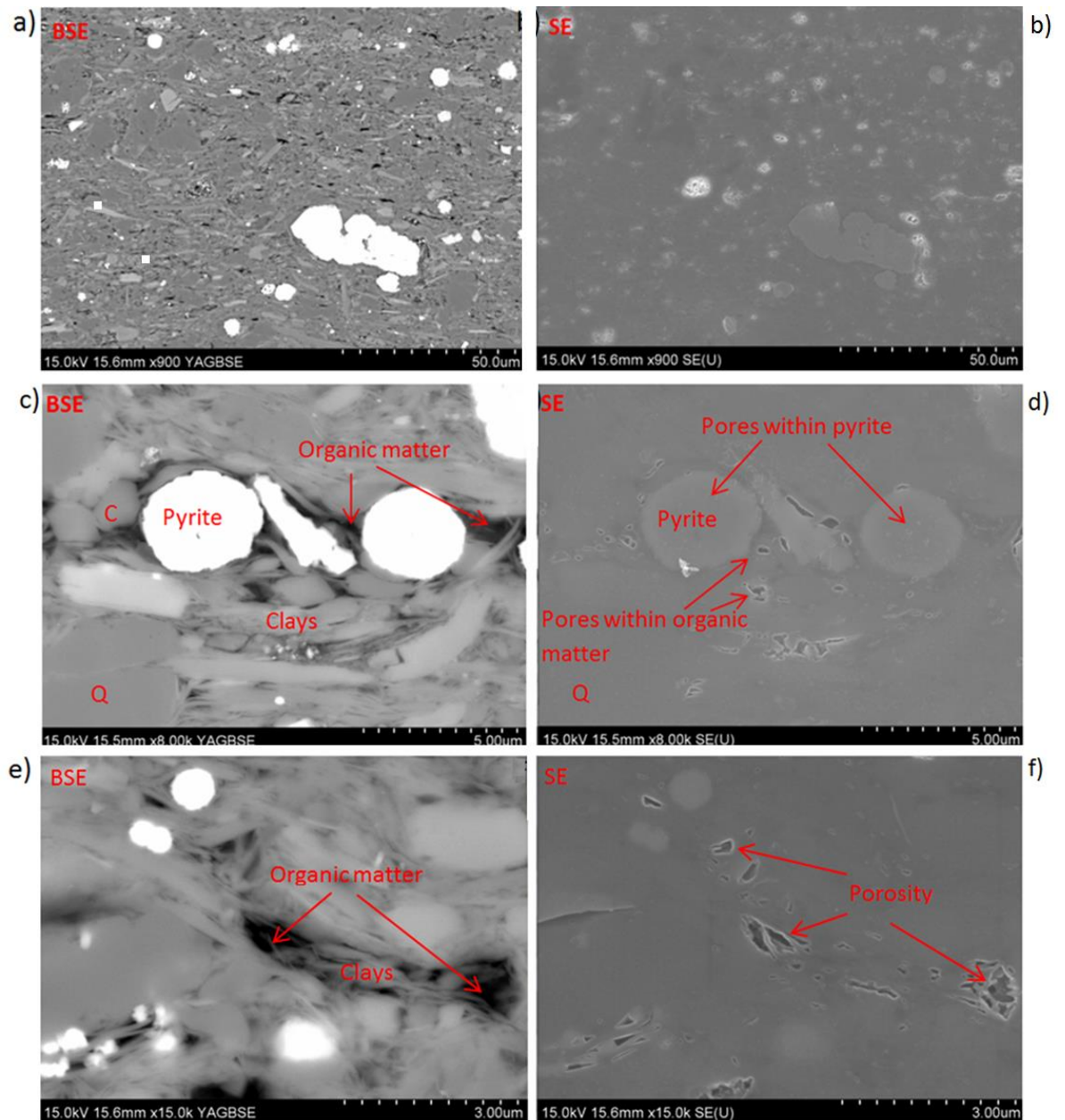
Figure 4.4. CHE2 SEM images. Note the contrast between carbonate and silica grains is much higher in SE than in BSE. However the pores are more visible in SE than in BSE. Highlighted minerals include: Pyrite (P); Calcite (C) and Quartz (Q).

CHE3 SEM images (Figure 4.5) reveal quartz-dominated matrix with considerable presence of organic matter and clays, surrounding the quartz grains. Dolomite can also be identified, together with the elongated mica particles, which are dispersed all across the matrix. Similarly to CHE2, most clay particles are orientated in one primary direction. However, unlike CHE2, the pyrite content of CHE3 is considerably lower.

Porosity is clearly visible in the SE images of CHE3 (Figure 4.5b & d) as the dark spots with bright edges along the organic matter. In fact, organic matter is associated with relatively large round/ellipsoidal pores of around 10 μm, which appear to be better interconnected compared to CHE2. Many of those are filled with organic matter, which has possibly migrated between the pores at some point. This in turn suggests that the matrix at some time was sufficiently permeable for the oil to migrate. These textures are typical of a mature shale (Loucks et al., 2010).
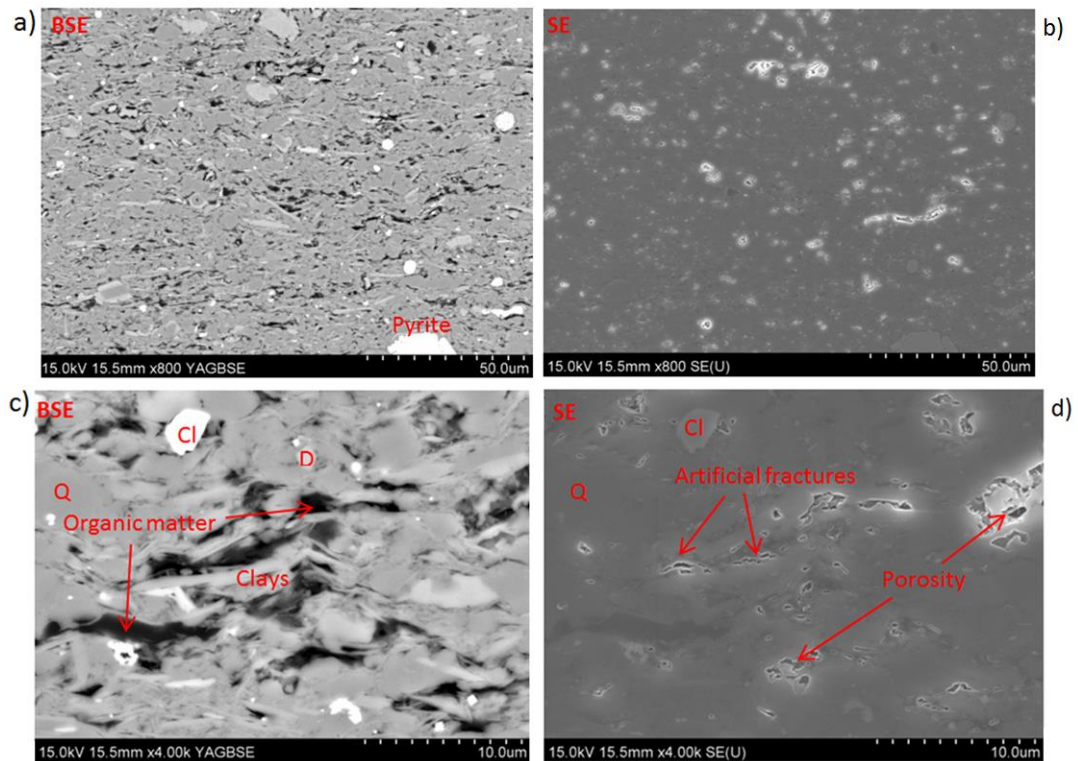
Figure 4.5. CHE3 SEM images. Note how clearly porosity can be seen within the matrix in the BSE but not in the SE. Presence of pores within the organic matter indicate good maturation level of shale. Highlighted minerals include: Chlorite (Cl); Dolomite (D) and Qu.

SEM images of the sample EBN20 (Figure 4.6) show dolomite-dominated matrix, with coarse grained dolomite rhombs comprising more than 50% of the sample (see QXRD analysis results in Table 4.2). The grains have no preferential orientation unlike in the CHE2 and CHE3 cases. Also, smaller amounts of clay and organic matter are present in comparison to the previous CHE group of samples.

The sharply-elongated shape of the fractures surrounding the organic matter indicates that these fractures could not have existed in subsurface conditions. These fractures might create considerable amount of pore volume, which might be wrongly mistaken for the actual porosity during the pressure expansion experiments. The relative amount of

volume created by these fractures compared to the original pores is evaluated and analysed in the discussion section.

Cluster of pores concentrated within the inter-particle space can be seen in Figure 4.6f. The pores appear to be filled with organic matter, which may have migrated into these pores. These mostly irregular shaped pores are around 2-4 µm in size and are reasonably well interconnected on the short range within that pore cluster. However, it is difficult to assess the inter-connectivity on the larger scale. Artificial fractures could considerably increase the interconnectivity, thus altering the permeability readings. Further analysis on fracture effect on permeability is presented in Chapter 6.
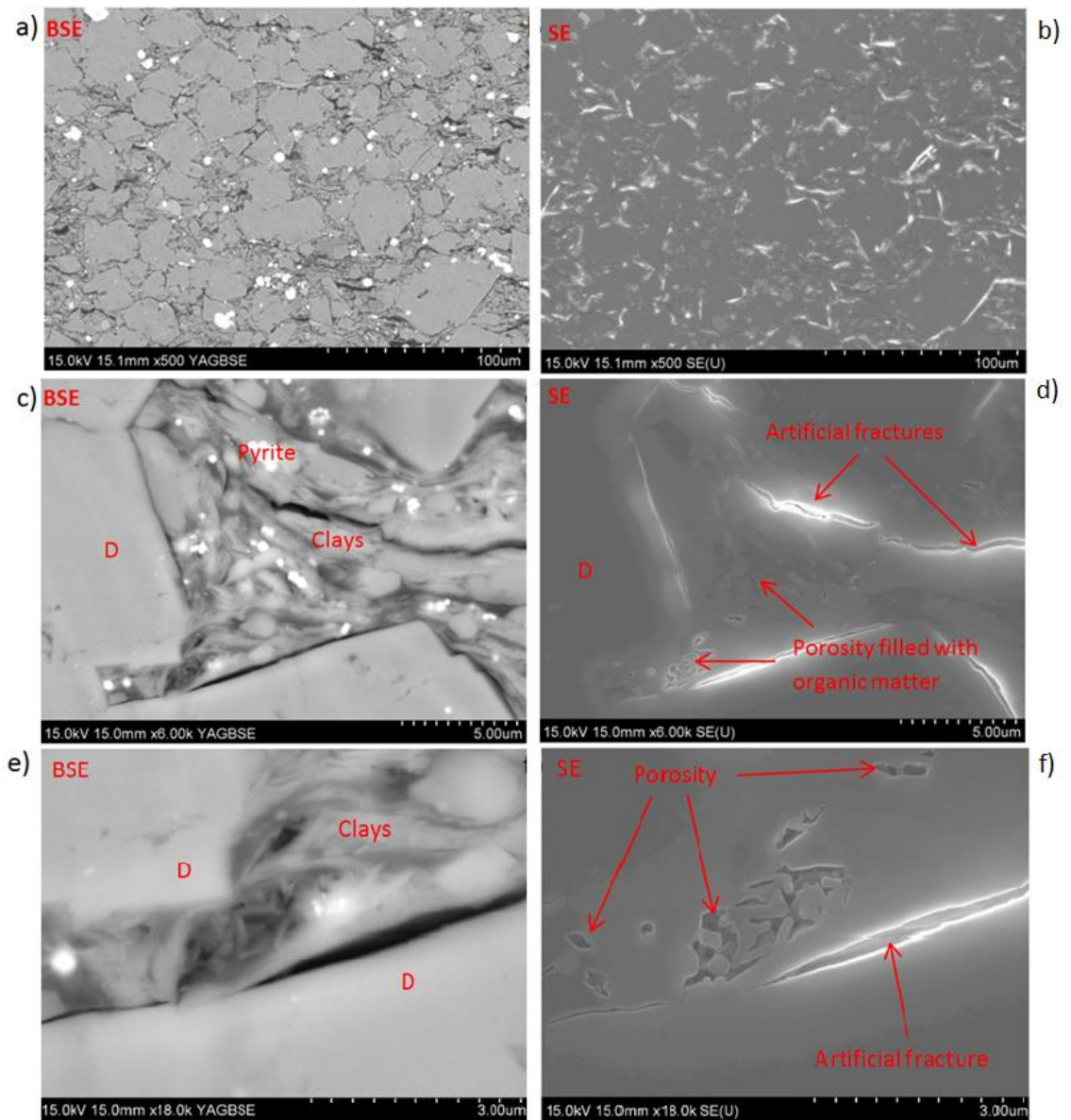
Figure 4.6. EBN20 SEM images. Note the different pattern of pores compared to CHE group of samples. Highlighted minerals include Dolomite (D).

NEX7 SEM images (Figure 4.7) reveal a heterogeneous sample with complex structural elements. Poorly sorted quartz grains dominate the matrix along with pyrite framboids, illite clays and dolomite. The SEM images confirm the presence of artificial fractures, which appear to be fractured along one primary direction.

Important feature in Figure 4.7c is 200 μm x 30 μm wide natural fracture filled with organic matter. Such features provide pathways for the kerogen comprising organic matter to migrate within the shale formation. TOC analysis indicates that sample NEX7 contains relatively high TOC levels (3.3%). Figure 4.7d indicates presence of round pores within the organic matter, formed during the creation of gas during the shale maturation. However these pores appear to be poorly interconnected.
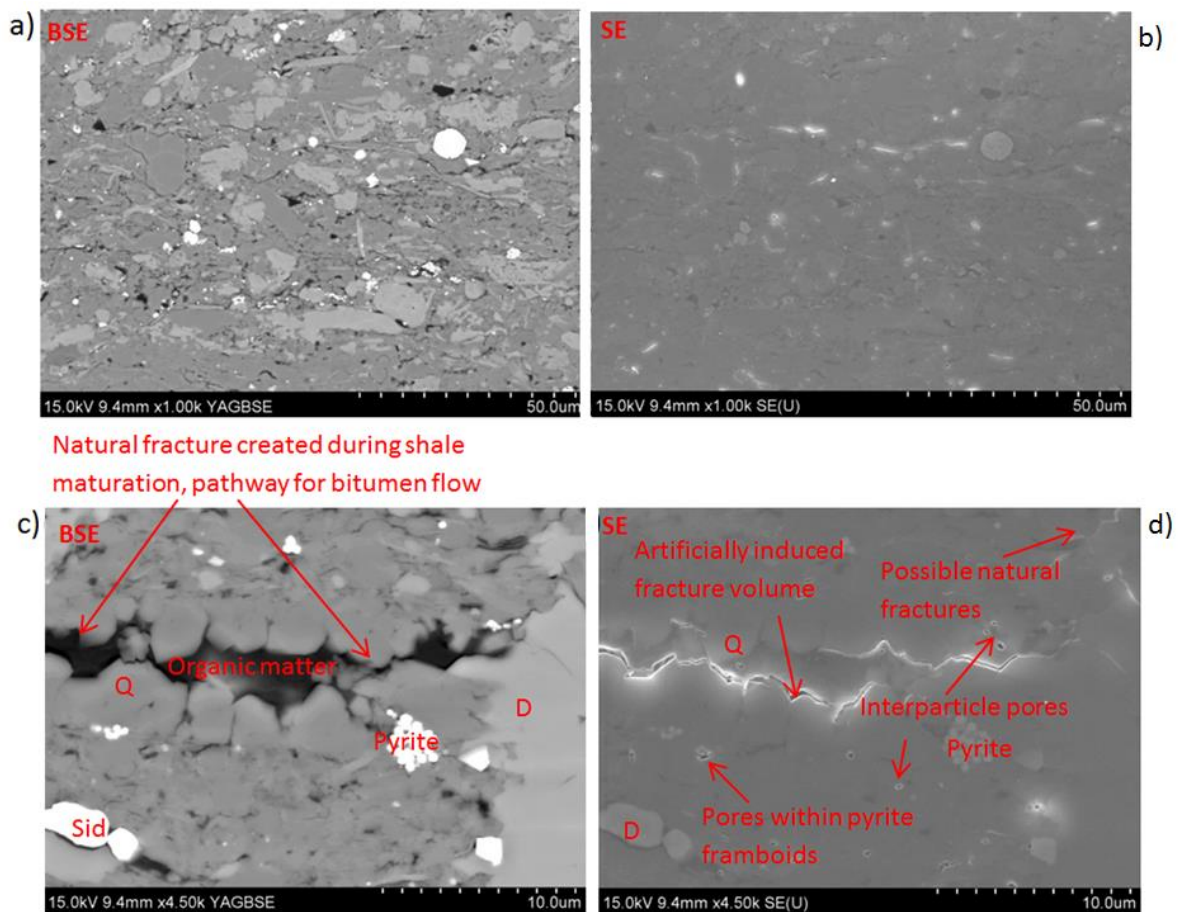
Figure 4.7. NEX7 SEM images. Note the empty space within the elongated fracture-like features, indicating artificial origin. Highlighted minerals include: Dolomite (D); Quartz (Q) and Siderite (Sid).

NEX15 SEM images (Figure 4.8) reveal highly heterogeneous and poorly sorted matrix, composed mainly of quartz and illite clays. Pyrite framboids up to 50 μm are present within the sample, together with prominently dolomite and calcite. No preferential

78

orientation of the grains can be identified. Most of intergranular areas are filled with organic matter, which is likely to have migrated during diagenesis.

Porosity seen in the BSE image mainly consists of isolated round pores of around 5-10 µm. Most of pores appear to be present within the organic matter indicating mature shale, however a few interparticle pores can still be identified. In addition pyrite is filled with organic matter and may contain secondary porosity. Important aspect observed in Figure 4.8c & e is the wide natural fracture filled with organic matter. It indicates the shale matrix had good interconnectivity for the kerogen to saturate. The large content of organic matter observed in the images is also reflected in the TOC test, indicating 3.2% TOC for NEX15.
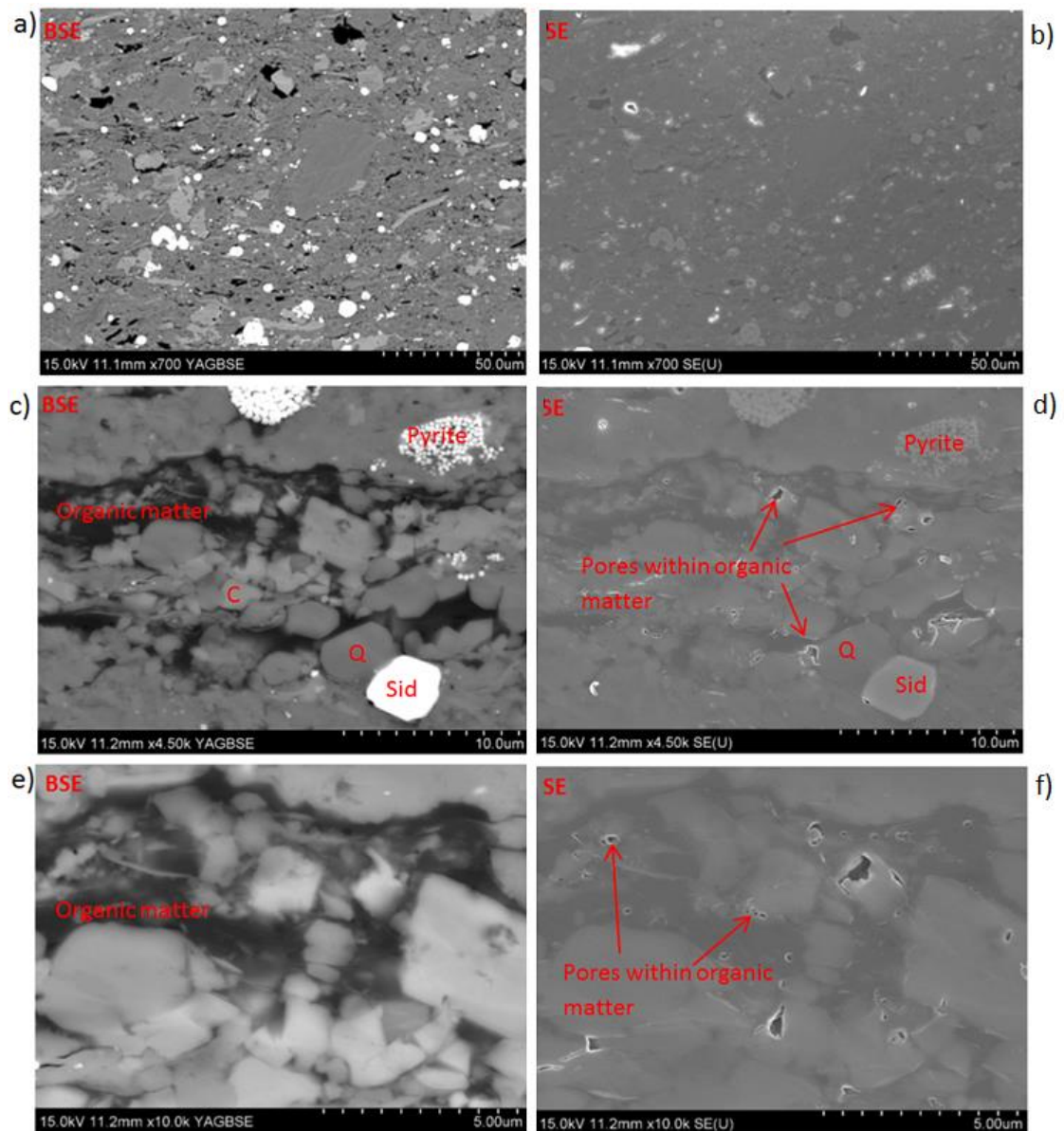
Figure 4.8. NEX15 SEM images. Note the large pyrite framboids, which might contain pores within their crystals. Highlighted minerals include: Calcite (C); Quartz (Q) and Siderite (Sid).

Similarly to other NEX samples, NEX33 (Figure 4.9) is largely heterogeneous and composed of poorly sorted grains, which are slightly elongated and orientated in one dominant direction. Calcite is a major component, alongside illite clays and some quartz. Unlike other NEX samples, NEX33 has relatively small amount of organic matter.

The fractures clearly seen in the images could not have existed in the subsurface conditions due to their shape, therefore they are most likely to be artificial. These fractures compose the majority of the pore space in the given sample area, which in turn might be mistakenly measured as porosity by the gas expansion test. Nevertheless some isolated natural pores of around 2 μm can be found across the matrix. Both SEM images and TOC analysis (2.0%) suggest little organic matter present. Furthermore, it appears to have little porosity associated with it, suggesting immature shale.
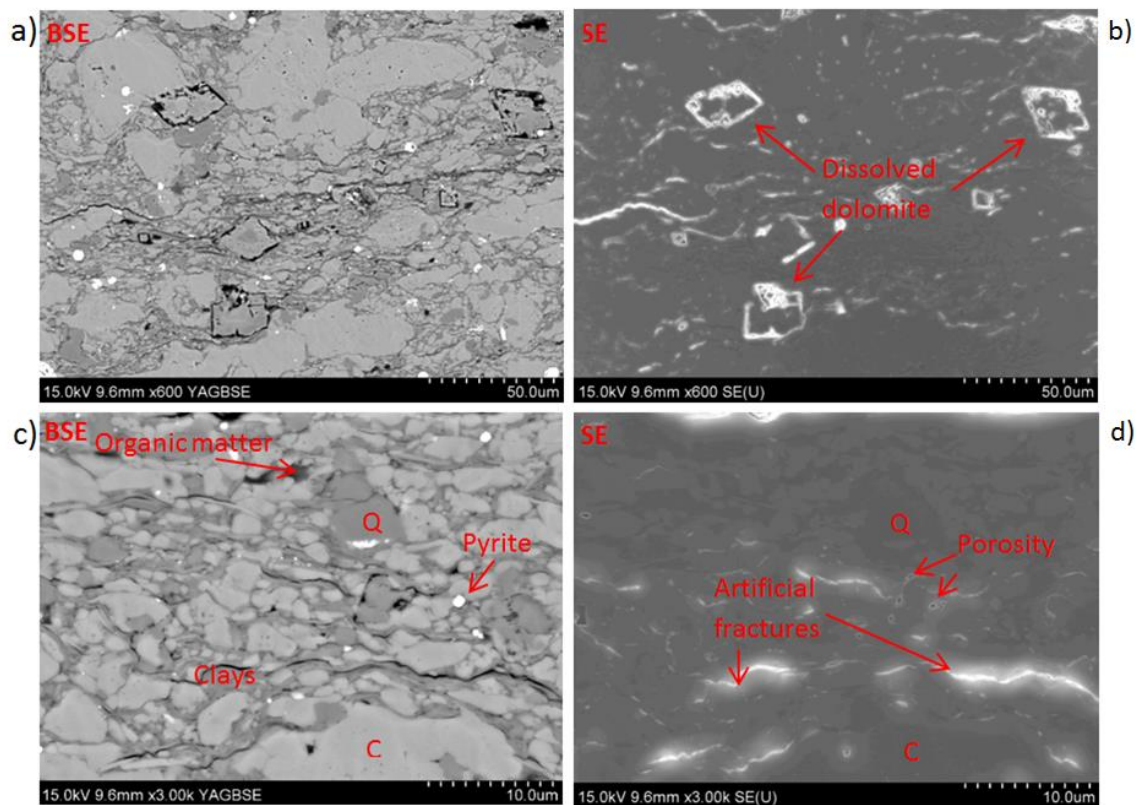
Figure 4.9. NEX33 SEM images. Note the dissolution around the calcite particles. Highlighted minerals include: Calcite (C) and Quartz (Q).

Gripen samples E-9 and F-3 (Figure 4.10) have undergone a different type of analysis, and although ion beam technique was applied for better quality, only BSE images were obtained. Nevertheless, interesting data can be seen from Gripen samples as they showed very different matrix structure, especially the absence of clear porosity indicators, compared to Control-Test samples. Essentially, it all adds to the overall understanding of the diversity of shale structure.

E9 and F3 (Alum shale) are highly laminated, which is reflected by the elongated nature of the fabric (Figure 4.10a). The samples are clay to fine silt in grain size, moderately sorted and contain dolomite rhombs and framboidal pyrite grains dispersed all along the matrix (Figure 4.10c & d). Although quartz is the single most dominant mineral, the most prominent feature in the SEM images is the large amount of clays and organic matter. Porosity cannot be resolved from neither of the images of two Gripen samples.
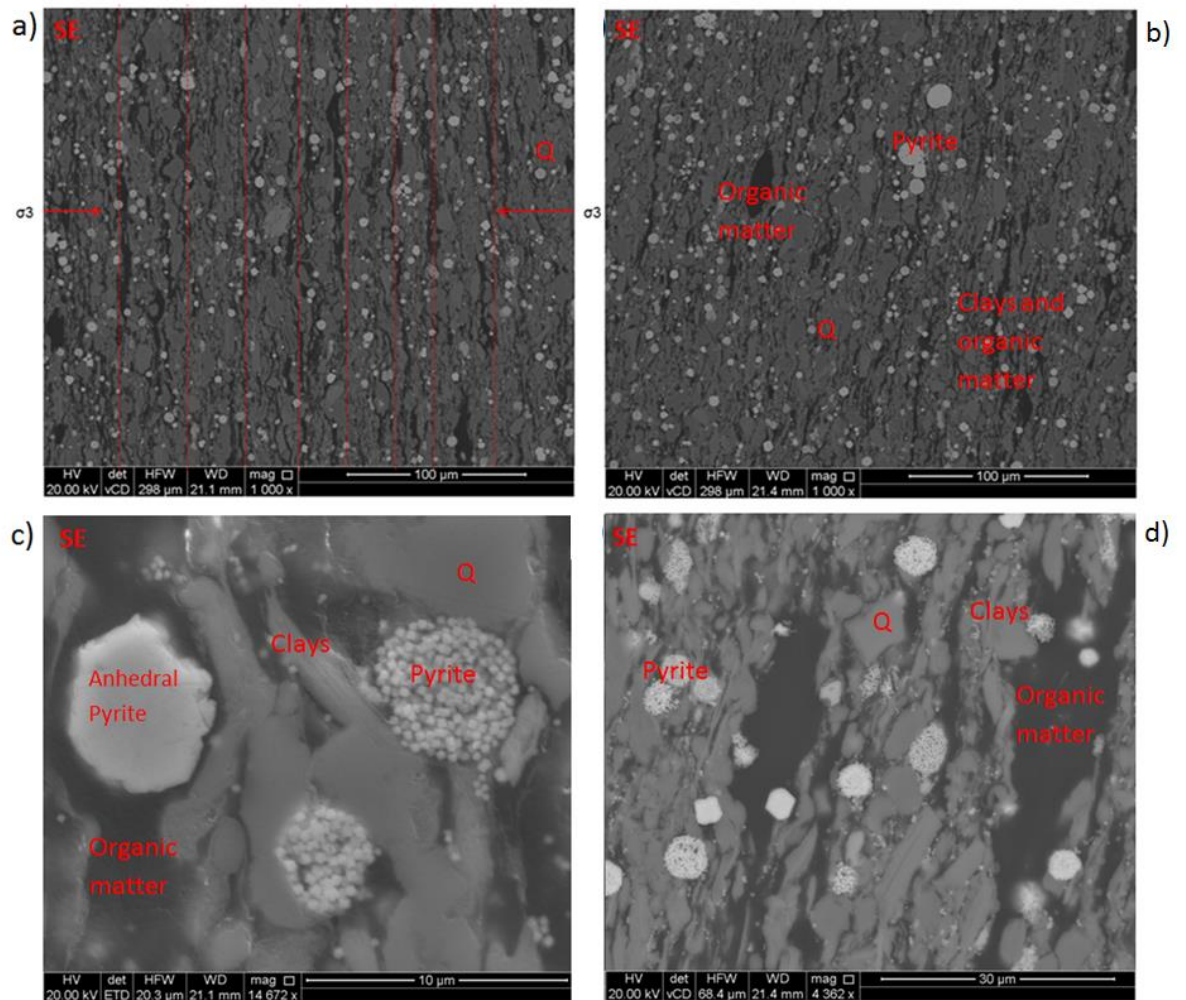
Figure 4.10. F3 (a and c) and E9 (b and d) SEM images. Note the laminated fabric of the shale (red lines) and abundance of pyrite (Table 4.2). Highlighted minerals include Quartz (Q).

Similarly to F3 and E9, Grpn7 sample (Figure 4.11) is highly laminated and exhibits elongated structure of the fabric. The matrix consists of poorly sorted quartz grains, dolomite and abundant organic matter and clays between the grains. Pyrite framboids of various sizes are clearly seen all across the matrix.

Round and isolated pores of around 3-6 μm can be identified in the BSE images of Grpn7 (Figure 4.11b & d). The pores appear to be located mostly within particle boundaries,

though a couple can be found within the organic matter and also along the grain particles. The lack of pore space within the organic matter means the shale is immature.
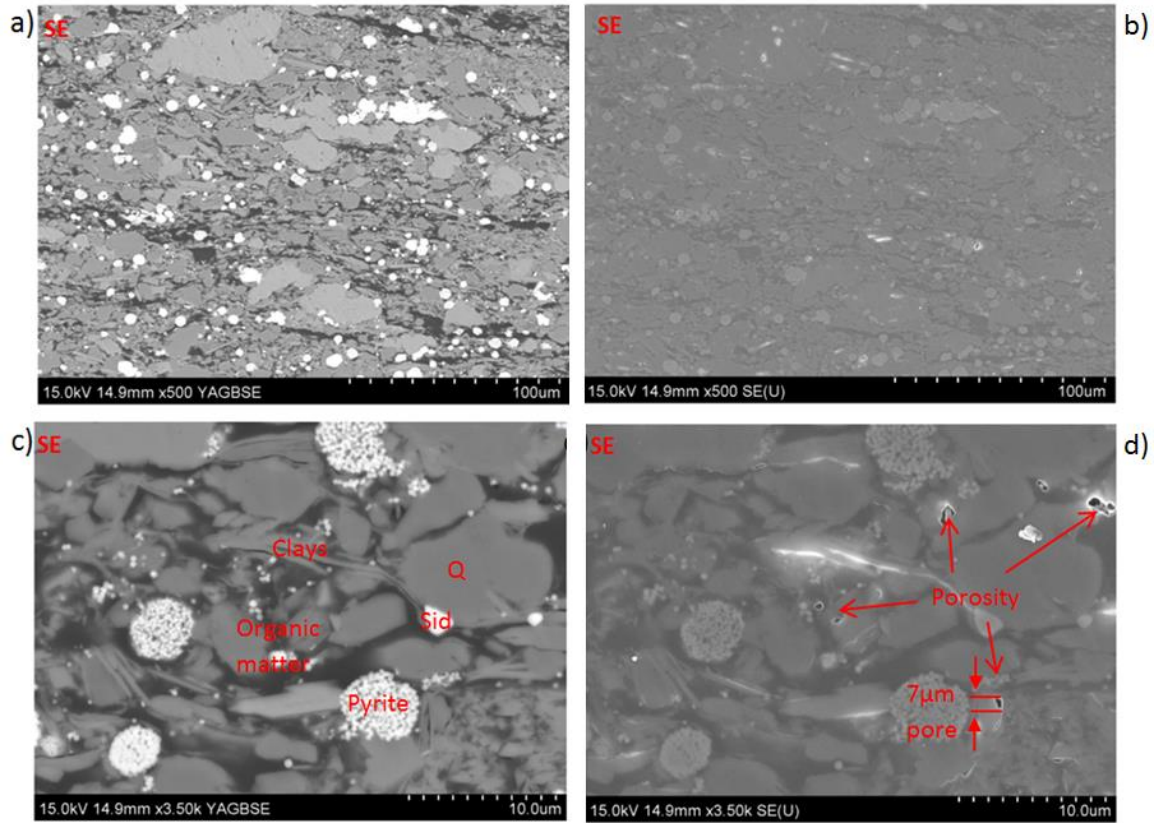
Figure 4.11. Grpn7 SEM images. Highlighted minerals include: Quartz (Q) and Siderite (Sid).

4.3.4 Computer Tomography and xenon injection test

This section presents the CT images of the samples. Figure 4.12 shows the relative locations across the samples where the CT scans were taken. The images are displayed in Figure 4.13 and Figure 4.14. Dimensions of each sample and the number of CT scans are provided in Table 3.2 in Section 3.2.3. Low density materials appear darker in CT images (higher transmittance hence less energy reflected back) and high density materials appear brighter (lower transmittance hence more energy reflected back).

CT scan slices across the sample
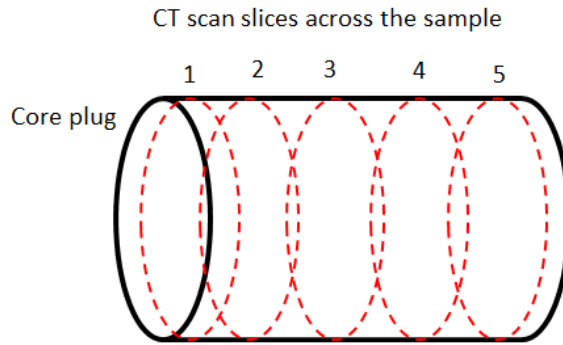
Figure 4.12. CT scan locations for Figure 4.13 and Figure 4.14.
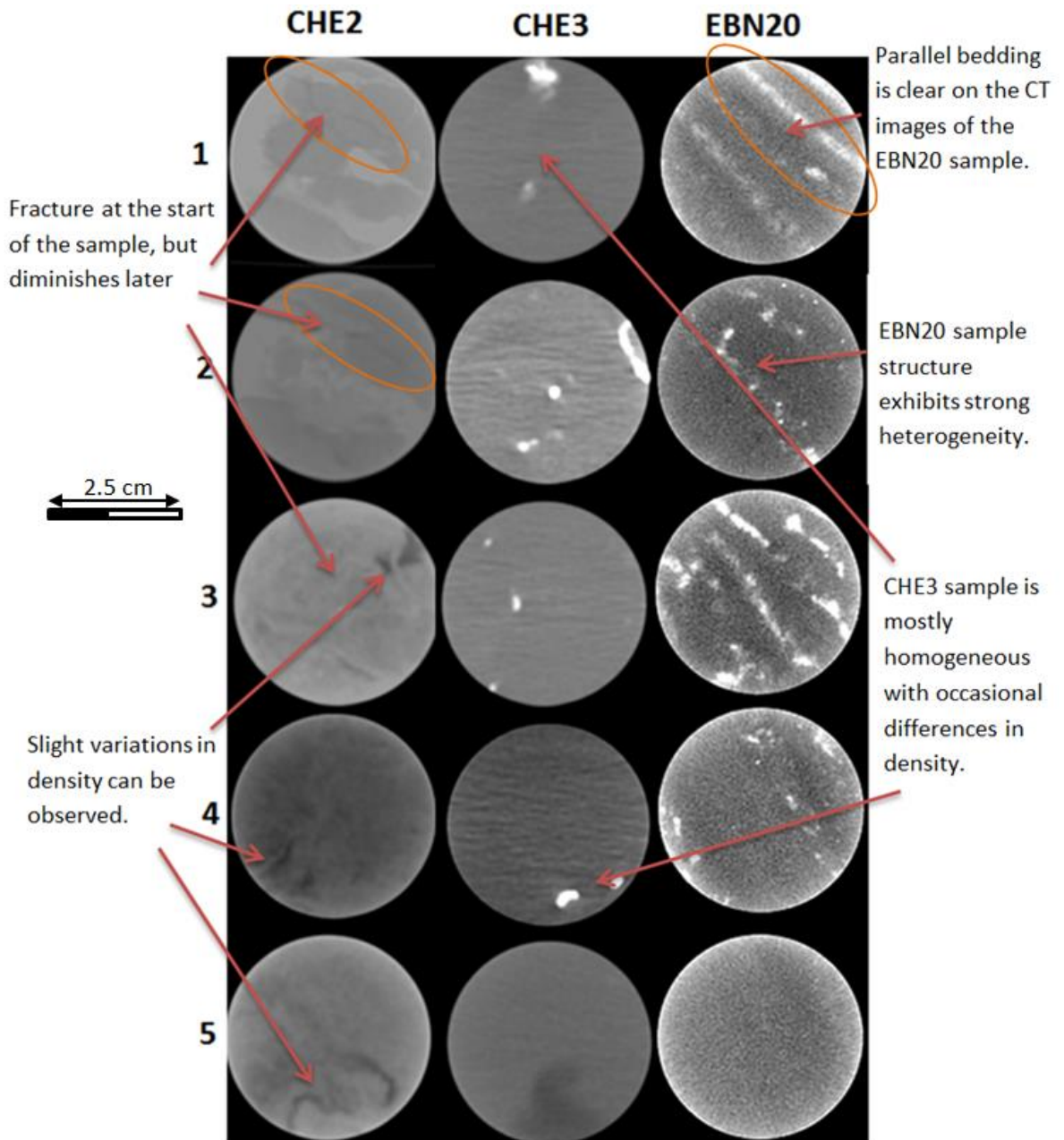
Figure 4.13. CT scans of the Control-Test samples. Variations in contrast represent different structural features.
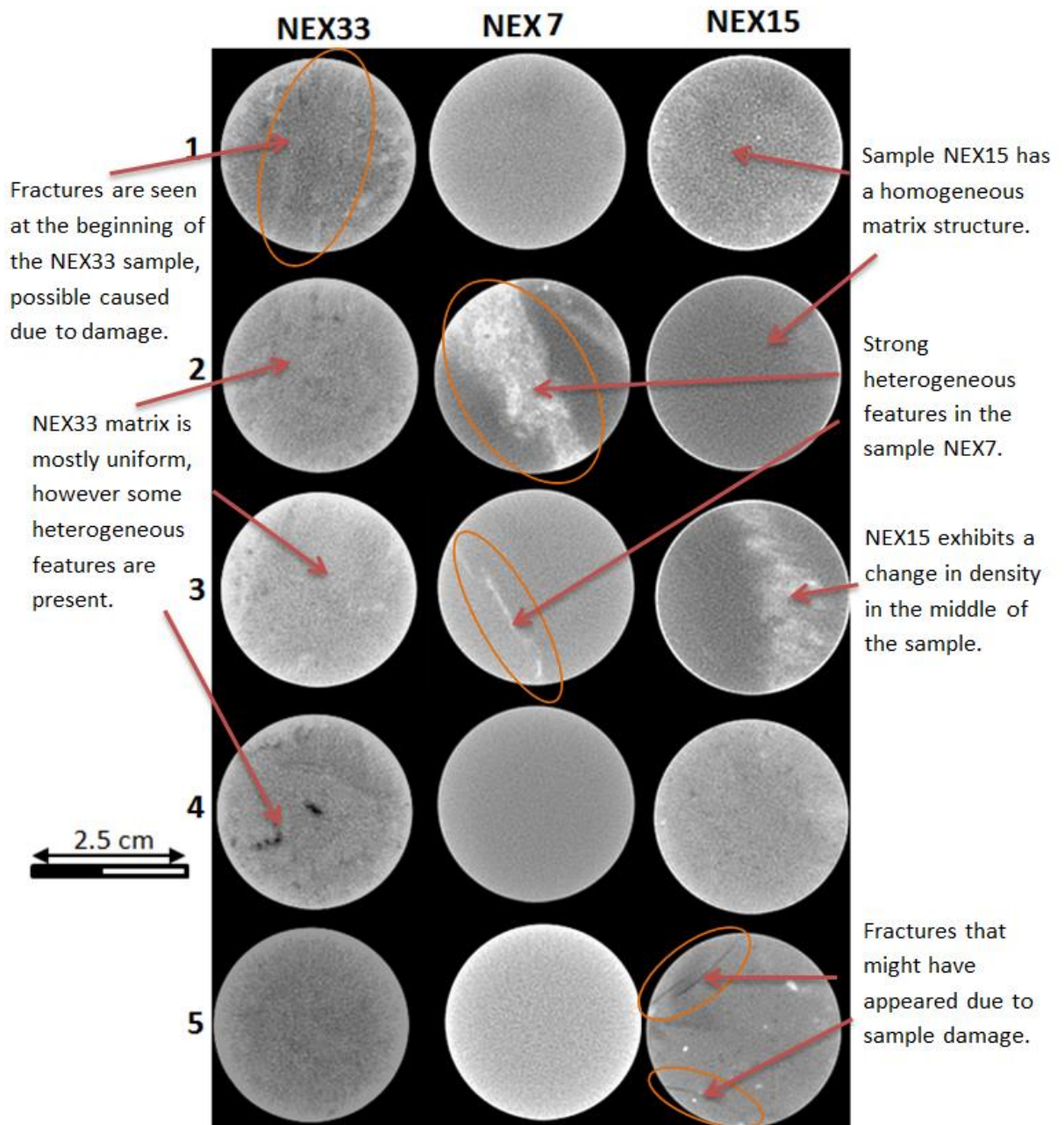
Figure 4.14. CT scans of the Control-Test samples.

CT images clearly show the shale samples are heterogeneous, however the resolution of the images does not allow anything smaller than 1 mm to be identified. Fracture can be seen at the first two scans of the sample CHE2, with various other structural features noticeable throughout all of the sample (for example likely matrix damage). Images of the sample CHE3 clearly show pyrite occurring throughout the core plug, however no fractures can be identified. The CT images from sample EBN20 show the presence of layers with different densities that are most likely inter-bedded siltstone along with pyrite. NEX33 and NEX15 exhibits signs of core damage (Figure 4.14). In contrast, NEX7 looks relatively homogeneous with three scans showing no noticeable changes in the

matrix structure. The second scan of NEX7 indicates a change in lithology (possible pyrite), however it decreases in the third scan.

4.3.4.1 Xenon visualisation

CT scans on the samples injected with xenon gas were performed to investigate the distribution of gas within the shale matrix and eventually to better understand the effect of matrix structural features, such as highly conductive inter-bedded layers or fractures. The main challenge during xenon experiments was that it was difficult to notice the xenon gas within the shale matrix in the CT images. As a result it was challenging to develop systematic comparative methods between the empty samples, and the ones filled with xenon. Therefore the conclusions made during these experiments have to be taken with care. Figure 4.15 shows the CT images of the sample confined in the MPD (modified pressur decay) equipment and filled with xenon gas.
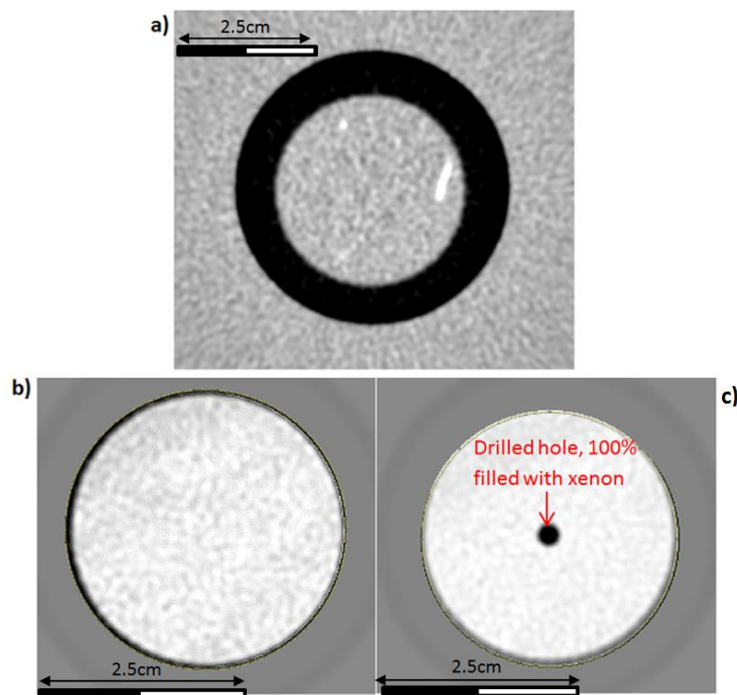
Figure 4.15. a) EBN20 core after xenon flooding; b) and c) shows EBN5 xenon flooded sample without and with the drilled hole visible.

In Figure 4.15a, the pattern within the rubber ring of the MPD and surroundings, which is everything outside the thick black belt, looks very similar, with only a few larger minerals standing out. Figure 4.15b and c shows the CT results of xenon injected sample EBN5, which has a hole drilled halfway. Clear indications of xenon can neither be seen within the matrix, nor the hole, supposedly filled with this highly CT-luminous gas.

The attempted approach was to edit the images using ImageJ software according to their CT unit values. Figure 4.16 presents the CT images edited using this software: Figure 4.16a shows the empty CHE3 sample whereas Figure 4.16b shows the same sample filled with xenon gas and left for a day to equilibrate. With the help of CT in Hounsfield Units (HU) values and shading option in the software, slight differences can be seen between the images in Figure 4.16. Further analysis of the results using simulation modelling is provided in the discussion section.
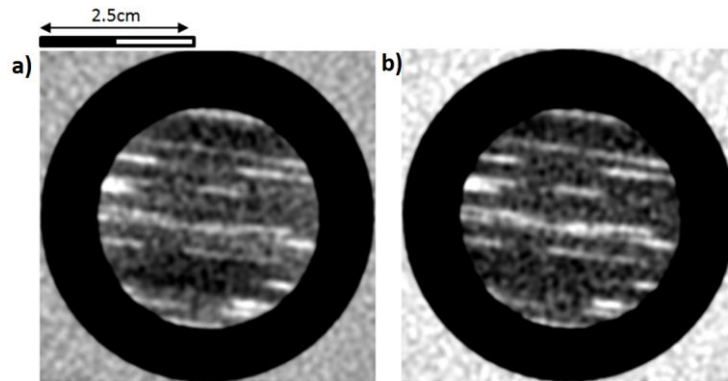
Figure 4.16. CHE3 before (a) and after (b) xenon flooding. Images taken from the same location.

4.4 Discussion on shale structure

This section analyses the presented results to understand the implications of the shale matrix structure on gas storage (Section 4.4.1), gas flow (Section 4.4.2) and the use of a CT scanner to characterise structural heterogeneity (Section 4.4.3). The findings of this chapter also provide framework for further research in Chapters 5, 6 and 7.

4.4.1 Gas storage types

4.4.1.1 Pore types

Firstly, to determine different storage systems within shale the pores were categorised into groups according to their origin. Loucks et al. (2010) classified pores into three main categories: organic-matter-related intraparticle pores, non-organic interparticle pores and non-organic intraparticle pores. If one pore type constitutes 75% or more of the overall pore volume then that pore type is classified as dominant. If no pore type is greater than 75%, the pore network is classified as mixed (Loucks et al., 2010). However, Wust et al. (2013) remarked that Loucks et al. (2010) ignored the larger micro and sub-millimetre-scale pores present in some of the shale reservoirs.

Rine et al. (2013) stated that the classification of Loucks et al. (2010), which divided pores into "interparticle" and "intraparticle" is too interpretive. In particular, the classification

method is based on simple delineation of pore boundaries, whereas Rine et al. (2013) preferred to rely on BSE intensity values in the SEM images and additional data such as TOC. Rine et al. (2013) used a simplified pore classification and subdivided the pores into organic, matrix and artificial fractures. The cut-off for dominant pore type was also selected as 75%.

The rational of Rine et al. (2013) for distinguishing between the matrix and organic pore is that the latter was formed together with the original kerogen surrounded by the matrix, whereas the matrix pore is not contiguous with organic material and was formed as part of the original inter-particle porosity. A matrix pore might contain hydrocarbons; however they are only related to the secondary migrated hydrocarbons. In this work, pores were analysed based on the method of Rine et al. (2013) as it is more simple compared to the method proposed by Loucks et al. (2010), and it can be better applied to the tested samples.

The SEM images were analysed using ImageJ as described in Section 3.3.6. Figure 4.17 to Figure 4.23 present the processed SEM images. Green colour denotes organic pores; yellow colour denotes matrix pores and the red colour denotes artificial microfractures. Table 4.5 presents the processing output. TOC and maturity analysis provided a better overview of the organic matter content within each sample, thus they helped to distinguish between the organic and matrix pores.
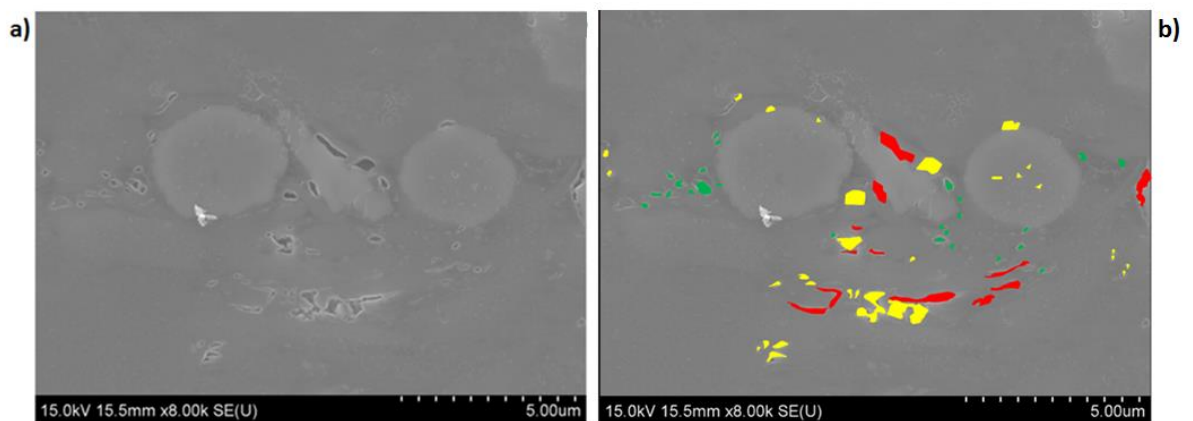
Figure 4.17. CHE2 SEM image analysis. Pores were selected based on the interpretation of their origin: organic (green) were generated within the organic matter, matrix (yellow) were generated within the matrix and artificial microfractures (red) do not exist in subsurface conditions.
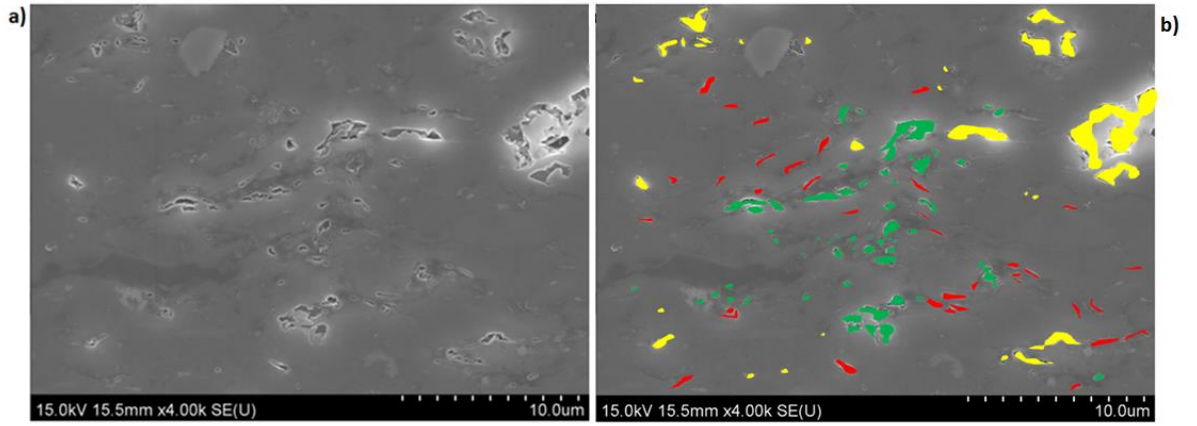
Figure 4.18. CHE3 SEM image analysis. Complex pore structure can be seen.
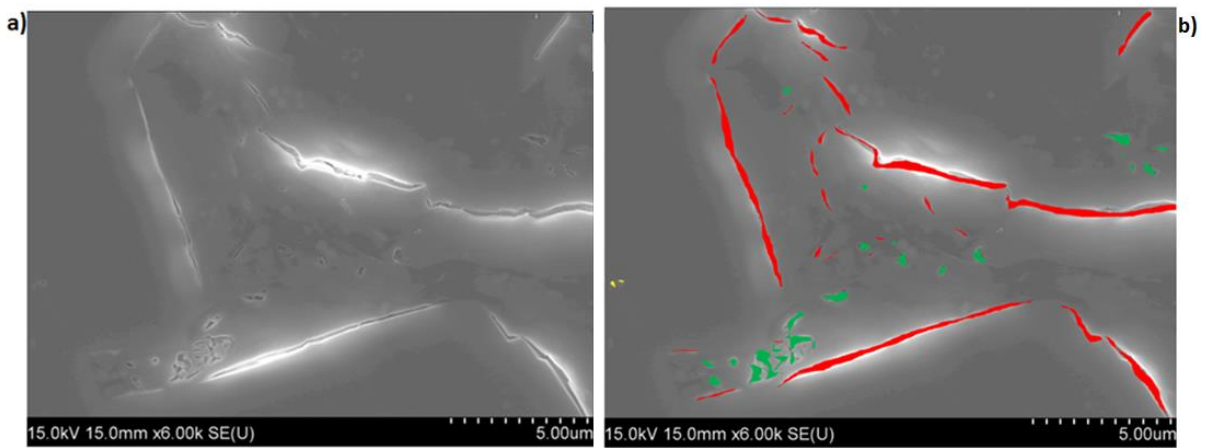
Figure 4.19. EBN20 SEM image analysis. Artificial microfractures dominate pore volume.
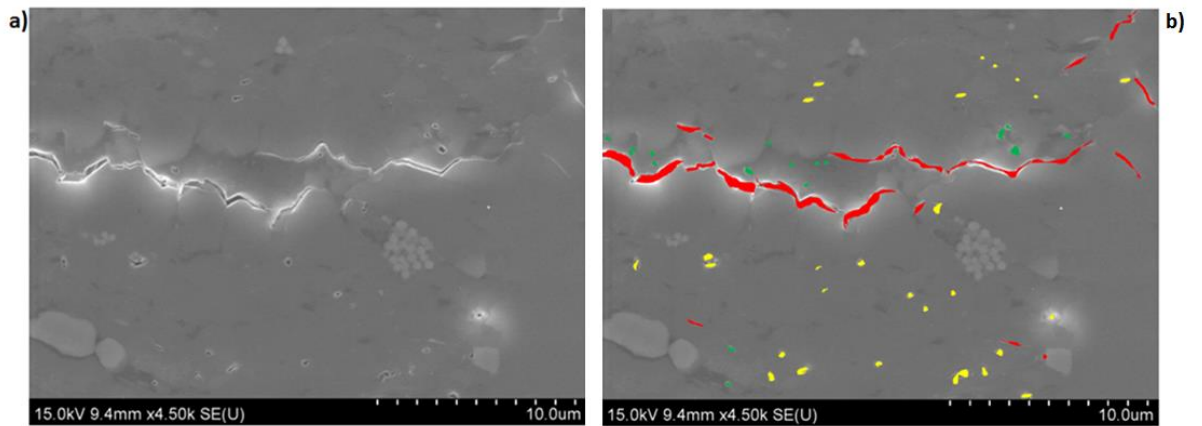
Figure 4.20. NEX7 SEM image analysis. Large concentration of organic matter between the grains can be seen.
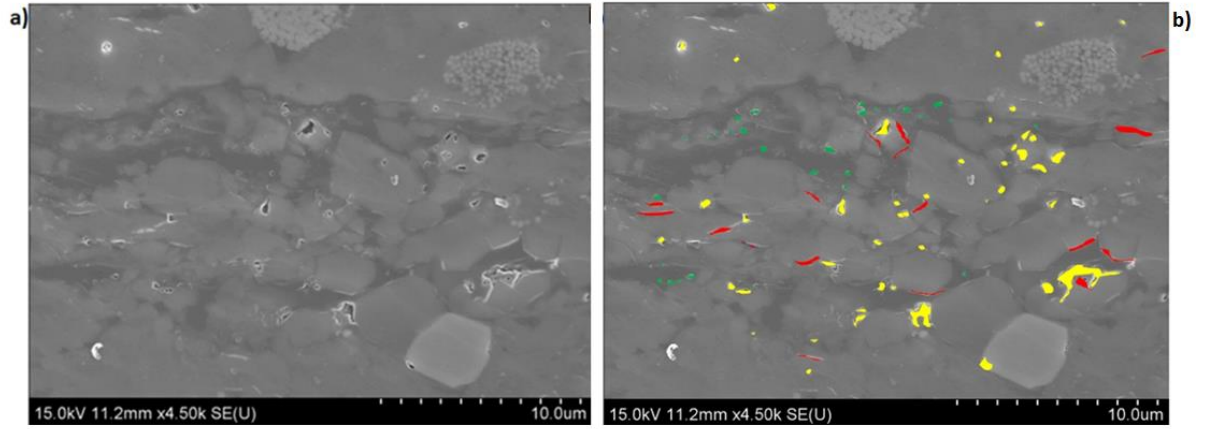
Figure 4.21. NEX15 SEM image analysis. Large concentration of organic matter between the grains can be seen.
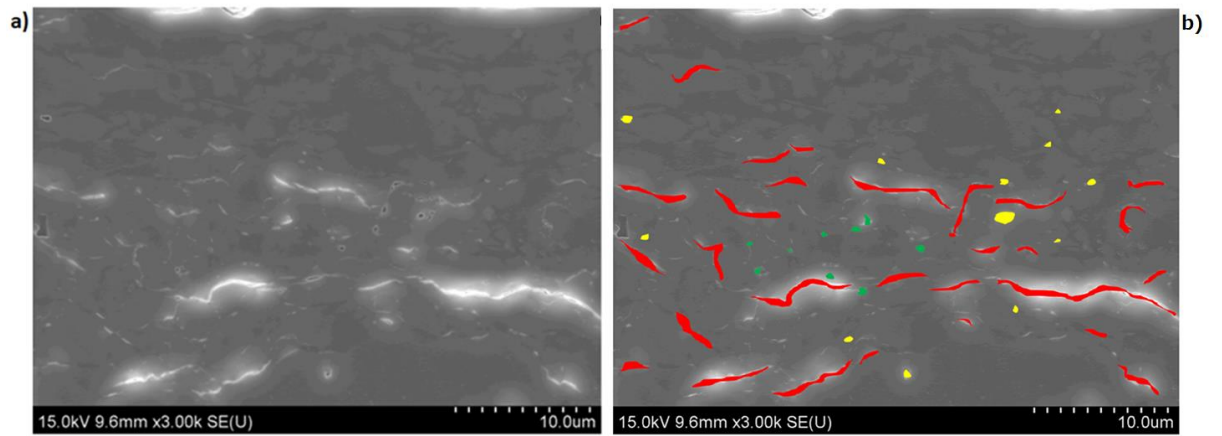
Figure 4.22. NEX33 SEM image analysis. Artificial microfractures dominate pore volume.
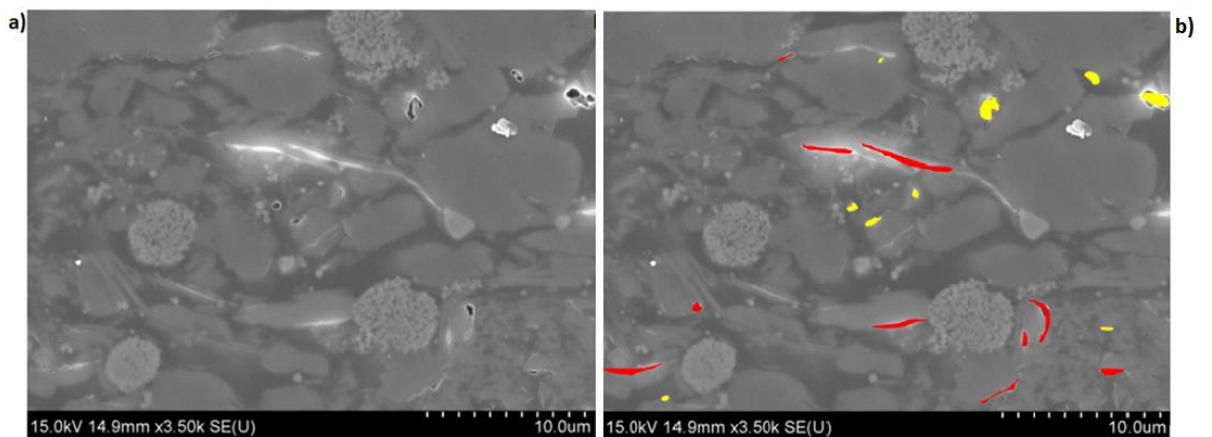
Figure 4.23. Grpn7 SEM image analysis. Absence of organic porosity indicates immature organic matter.

Table 4.5. Pore typing results for the Control-Test and Gripen samples. The pores were divided into three groups and various parameters were derived for them.

Sample	Pore type	Pore type area, μm	Total pore area, μm	Total given sample area, μm	Frac of pore area, frac	Porosity,%	Circularity, dimensionless	Feret, μm	MinFeret, μm	AR, dimensionless
CHE2	organic	74	932	54165	0.08	1.72	0.014	309	133	2.48
	matrix	631			0.68		0.086	157	84	4.18
	artificial fracture	228			0.24		0.029	253	108	1.34
CHE3	organic	7880	26708	638957	0.30	4.18	0.004	77326	54757	1.52
	matrix	15234			0.57		0.017	71306	30853	2.77
	artificial fracture	3594			0.13		0.026	63269	44466	1.20
EBN20	organic	266	1121	25424	0.24	4.41	0.028	193	54	9.50
	matrix	28			0.03		0.113	227	19	10.36
	artificial fracture	826			0.74		0.007	211	165	1.59
NEX7	organic	1652	14416	716729	0.11	2.01	0.032	928	453	2.96
	matrix	2089			0.14		0.016	915	581	1.21
	artificial fracture	10675			0.74		0.013	957	509	3.88
NEX15	organic	100	960	60460	0.10	1.60	0.014	307	134	2.23
	matrix	594			0.62		0.037	277	211	1.33
	artificial fracture	267			0.28		0.012	299	191	2.05
NEX33	organic	140	2474	105127	0.06	2.35	0.032	310	100	2.85
	matrix	560			0.23		0.011	425	213	2.42
	artificial fracture	1775			0.72		0.005	423	289	1.78
Grpn7	organic	0	156	15933	0.00	0.98				
	matrix	79			0.51		0.016	126	96	1.70
	artificial fracture	77			0.49		0.038	161	107	1.37

Analysis disclosed the coexistence of different pore types within the shale matrix; however neither pore type could be treated as dominant according to Loucks et al. (2010) 75% cut-off value (Figure 4.24). Nevertheless it is clear that the porosity in many samples is heavily influenced by the artificial fractures, in particular EBN20, NEX7, NEX15 and

Grpn7 (Figure 4.24, also see SEM images in Figure 4.19, Figure 4.20, Figure 4.22 and Figure 4.23 respectively). If artificial fractures would be discounted, matrix pores would be clearly dominant in samples CHE2, NEX15, NEX33, Grpn7 and CHE3, whereas organic pores would be dominant in EBN20 (Figure 4.25). NEX7 would have no dominant pore type. Despite showing the highest TOC values, Grpn7 contain no pores within the organic matter. This is because the organic matter within Grpn7 is immature (see Table 4.4 in Section 4.3.2) and is made out of Type I kerogen, unsuitable for gas generation (see Figure 4.3 in Section 4.3.2).

Apart from Grpn7, there is a good correlation between the TOC content and interpreted amount of organic porosity (Figure 4.24). Sample EBN20 was interpreted to have the most of organic pores among the Control-Test samples, which corresponds to its large TOC content. Sample CHE3 was also found to contain a lot of organic pores, which are explained by high TOC content and matured organic matter.
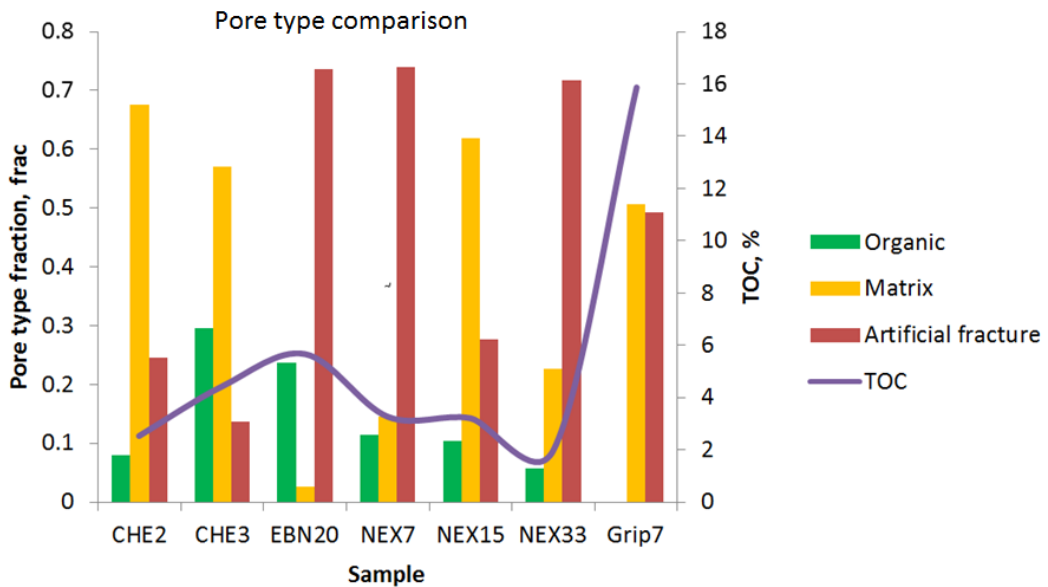
Figure 4.24. Comparison of the pore types for the samples together with TOC values.
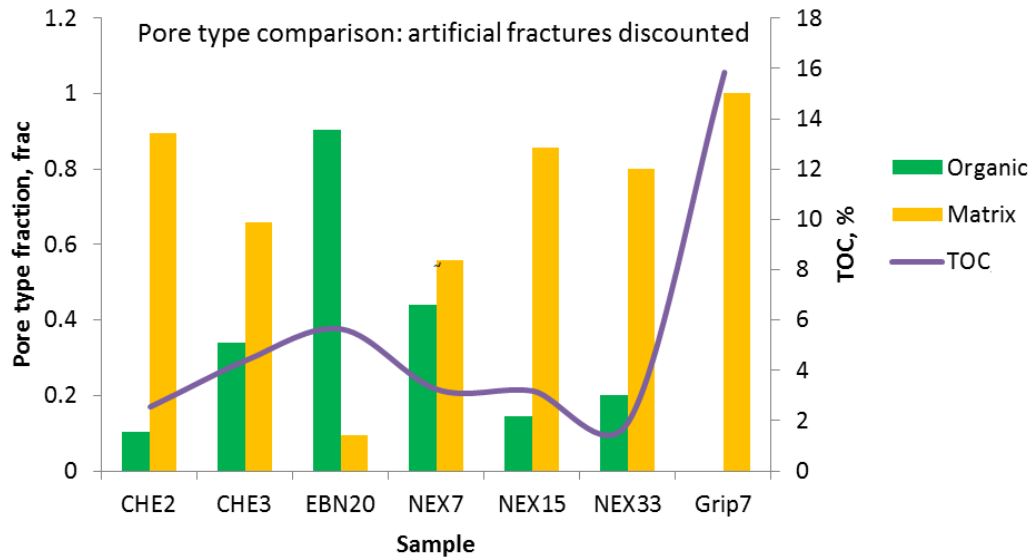
Figure 4.25. Organic and matric pore type comparison together with TOC values.

Organic pores are commonly observed in thermally mature shales within oil and gas windows and are interpreted to be the result of solid organic matter conversion to hydrocarbons (Loucks et al., 2010; Driskill et al., 2013). The nature of these organic pores depends on the diagenesis, composition and the type of organic matter. The current assumption is that after deposition the non-mineral shale volume was filled with the organic matter, and once the rock matures, pendular or bubble pores start developing within the oil window (Driskill et al., 2013).

Significant amount of shale pores may not be identified during the SEM analysis due to the resolution limitations of around 0.5 µm. According to the IUPAC (1994) pore classification system, pores are classified into macro-pores (>50 nm), meso-pores (2 nm – 50 nm) and micro-pores (< 2 nm) (Verba et al., 2016). This in turn means that significant part of macro-pores may not be visualised at the current resolution. Different shale formations might have different distribution of pores sizes, with some shale formations such as Pierre composed almost entirely of macro-pores and others such as Bakken dominated by micro-pores (Verba et al., 2016). In this research this type of porosity can only be revealed with the pressure intrusion experiment, therefore is analysed in the following Chapter 5.

Pore space within the minerals might sometimes form due to the corrosion of the pyrite framboids and chlorite. Organic matter might then infill this pore space, which is typical for the Devonian black shales (Schieber, 2013). In this research, pores along the edges of the pyrite framboids were identified to contain organic matter; however it was

challenging to interpret any pore space between the crystallites. Overall, the pore space associated with pyrite framboids was negligible in Control-Test group of samples. In contrast, Gripen samples contained significant amount of pyrite, which might play an important role in gas storage.

4.4.1.2   Adsorptive porosity types

SEM images presented in Section 4.3.3 show that the space between the grains is mostly filled by clay and organic matter. Organic matter is known for its strong adsorptive properties (Zhang et al., 2013). On the other hand, clay minerals also show the ability to adsorb methane molecules, due to the presence of the nano-pores and relatively large surface area exhibited by the clay minerals (Zhang et al., 2013). Methane-sorption capacity of clays depends on the type of the clay minerals present; in terms of the relative adsorption potential: montmorillonite >> mixed illite/smectite > kaolin > chlorite > illite (Zhang et al., 2013). Therefore, considering the abundance of highly sorptive clays in the tested shale samples (see Table 4.2 and Figure 4.1 in Section 4.3.1), clay adsorption could contribute to the overall gas storage capacity.

Sorptive capacity values of the sample are linearly correlated with BET results (Zhang et al., 2013; Kumar et al., 2015). However, the BET values obtained during this study do not appear to produce any clear correlation with sorptive illite/smectite, which is abundant in most of the samples. In fact, the highest BET surface area of 11.8 m^2g^{-1} was produced by sample CHE2, which had the lowest amount of illite/smectite present of just under 5% (see Table 4.3 and Table 4.2 in Section 4.3.1).

Good correlation was obtained between the amount of kaolin from the samples containing this clay group (NEX7, NEX15, EBN20, Grpn7, E3 and F9) and BET values of these samples (Figure 4.26). BET results usually reflect the adsorption potential of the matrix, consequently BET-kaolin dependence indicates kaolin group is likely to affect adsorption as well. On the other hand, NEX33 and both CHE samples do not contain kaolin, instead show higher chlorite. According to Zhang et al. (2013), sorptive properties of the chlorite are weak, so it would not add substantially to adsorption porosity.
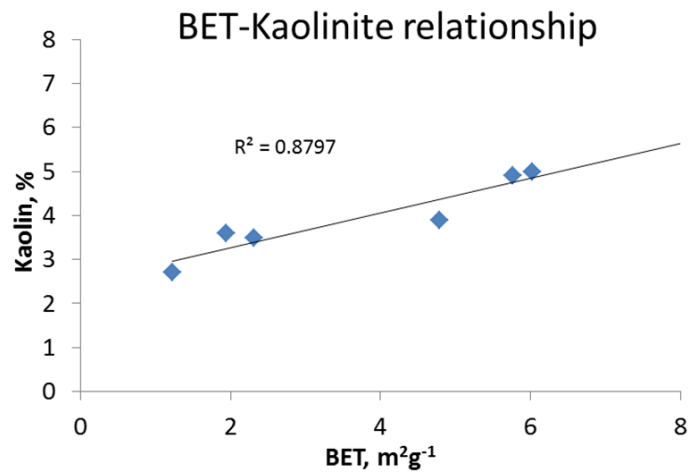
Figure 4.26. BET values of the Control-Test samples correlated against kaolin content of those samples, showing possible adsorptive relationship.

Overall, shales contain various groups of clays, which in turn might result in different adsorption porosity types. Gas results of the samples together with adsorption values can provide further information on the storage properties and type of porosities. These results are presented and analysed in Chapter 5.

4.4.2 Flow path characterisation

4.4.2.1 Natural fractures

Control-Test samples, in particular NEX group of samples (see Figures 4.7; 4.8 and 4.9 in Section 4.3.3) have microfractures filled with organic matter which also contains porosity. These microfractures most likely formed during the oil migration but now could act as flow paths for gas. Considerable amount of organic pores was identified within the organic material in these microfractures (see Table 4.5 and Figure 4.25 in Section 4.4.1.1).

Several authors argue that organic pores are usually well interconnected. Driskill et al. (2013) used 3D DRP (three-dimensional digital rock physics) FIB-SEM models to show how well organic pores are connected outside the plane of the 2D SEM images. In addition, they applied the lattice Boltzman computational algorithm described by Tolke et al. (2010) and derived permeability values. Driskill et al. (2013) obtained higher permeability values for the oil-window samples compared to gas/condensate-window (90 – 2640 nD compared to 9 – 1000 nD respectively). Oil-window samples were described to have small intragranular and grain side contact pores, with open pore space in the larger voids (Driskill et al., 2013). On the other hand, gas/condensate-window samples had "spongy" pores. 3D SEM was not done in this research, therefore quantitative permeability values could not be obtained from this method.

The amount and type of clays present may also affect the ability of shale to transport the gas. Fibrous clays such as illite block the gas flow path, which in turn reduces the permeability significantly. In fact, SEM images showed that clay minerals often formed fibrous aggregates surrounded by the organic matter (see Figure 4.4 in Section 4.3.3). However, it is difficult to quantitatively asses the mineralogy effect on shale permeability using only static data such as QXRD and SEM images, therefore it is analysed utilising gas flow measurements in Chapter 6.

4.4.2.2 Artificial microfractures

Artificial microfractures appeared to be important feature in the SEM images of the NEX7, NEX33 and EBN20 samples (see Figure 4.24 in Section 4.4.1.1). The exact origin of these microfractures is still under investigation, however it is widely accepted that the stress release in the cores during the core retrieval procedures might be the main reason (Ramos and Rathmell, 1989; Santarelli and Dusseault, 1991; Rune and Cor, 1992). Handwerger et al. (2011) explain that complex rock fabric and weak organic/inorganic contacts within shale matrix are one of the main reasons why stress release tends to result in a much higher number of microfractures in shales compared to conventional rocks.

The single orientation of fractures in the sample NEX33 supports the theory of microfractures appearing as a result of the stress release. Also, there are no cements or organic matter filling material within those microfractures, which would otherwise confirm their natural origin. So the fractures identified would not be present at the subsurface conditions so corrections have to be made for their impact on the permeability and porosity results.

Structural results suggest that even after the shale sample is crushed, the microfractures might still remain within the particles. SEM examination of the crushed shale fragments revealed that the fragments contain a high density of microfractures (Figure 4.27). Similar results were obtained by Tinni et al. (2012), who injected resin into the shale particles, imaged it under the SEM and note that microfractures were present throughout the shale particles.
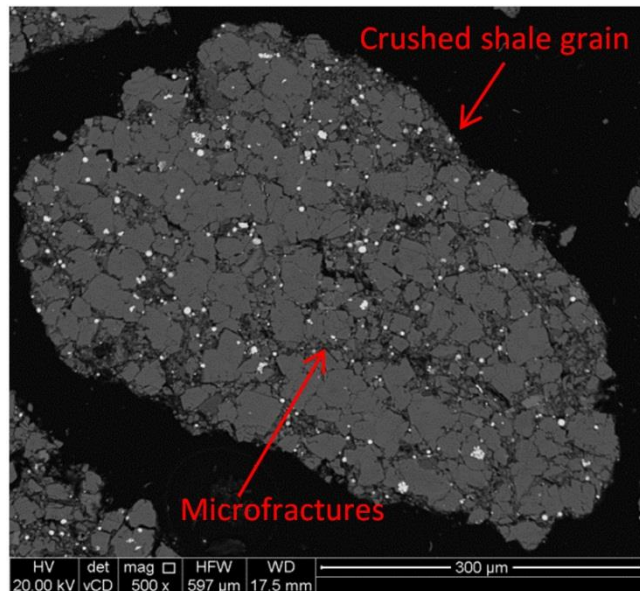
Figure 4.27. BSE SEM micrograph of a crushed shale fragment. Note the large number of microfractures is present within the shale.

4.4.2.3 Scale implications

Although microfractures can be seen on the SEM scale in the tested samples, it is difficult to judge on the extent of these fractures on the higher scale. For a 1.5 inch diameter core plug, standard SEM image means that less than 0.0001% of the sample surface is actually imaged. Essentially, to get some qualitative indication of the gas flow through the matrix, higher scale shale matrix imaging has to be done.

Tiling and stitching the SEM images together enables larger scale high resolution SEM images to be created for more representative analysis (Lemmens and Richards, 2013). However, for this thesis, the objective for pore characterisation was already achieved by the simple SEM images, while for the gas flow qualitative analysis core plug scale is required. Furthermore, fractures were not identified on the SEM images of other samples. Therefore CT scanning was chosen for this purpose, as it is able to image macro-scale core images at the expense of poorer resolution images at the millimetre scale.

4.4.3 CT scan and xenon injection to characterise shale structure

4.4.3.1 Microfracture conductivity

Microfractures outlined in SEM analysis are not evident in the CT images at a given millimetre scale resolution (see Figure 4.13 and Figure 4.14 in Section 4.3.4). In fact, only one sample, CHE2, showed a large visible fracture along the entire width of the sample. Nevertheless, even if the microfracture is well below the CT resolution, it might still

dominate the flow throughout the matrix: a 10 X 0.1 mm microfracture with permeability of 1 mD and pressure difference of 6.8 atmos (100 psig) according to Darcy's Equation 2-4 (see Section 2.2) could conduct 0.36 cm^3/sec gas flow rate, i.e. causing MPD experiment to equilibrate in around half a minute (10.9 cm^3 upstream volume / 0.36 cm^3/sec fracture flow rate = 30.5 sec).

Xenon injection was used to test for the influence of high conductivity regions within the matrix. The idea behind this experiment is that xenon is highly CT luminous – medical research showed it to enhance the grey matter by 19 ± 4 HU and white matter by 24 ± 4 HU in the CT images (Segawa et al., 1983). Therefore by scanning the sample before and after the xenon injection, the distribution of xenon could be traced and mapped.

Unfortunately, the CT resolution did not allow a visual representation of the flow paths within the shale samples. Extreme pixelation was encountered in the derivative images representing the difference between initial and xenon flooded states of the sample cores (Figure 4.28). The error margin of these 2D images was therefore too high to map the gas distribution along the slices.

However, the ImageJ v.1. 48i image analysis software possesses a function to plot the averaged CT units across each of the 2D images and create a cross section. A good trend representing the gas distribution along the sample was obtained using this method. Figure 4.29a and b shows a cross section of averaged CT values of the EBN20 core plug.
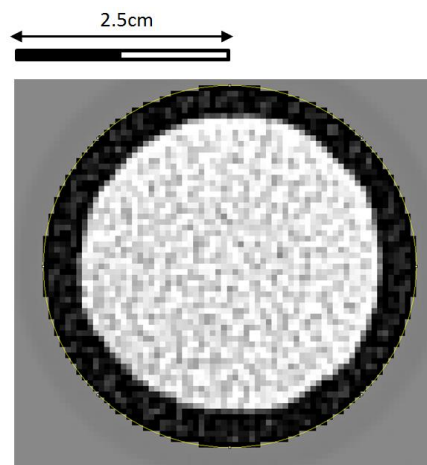
Figure 4.28. Processed SEM image of the Karoo sample, obtained by subtracting the CT units from the before and after CT images.
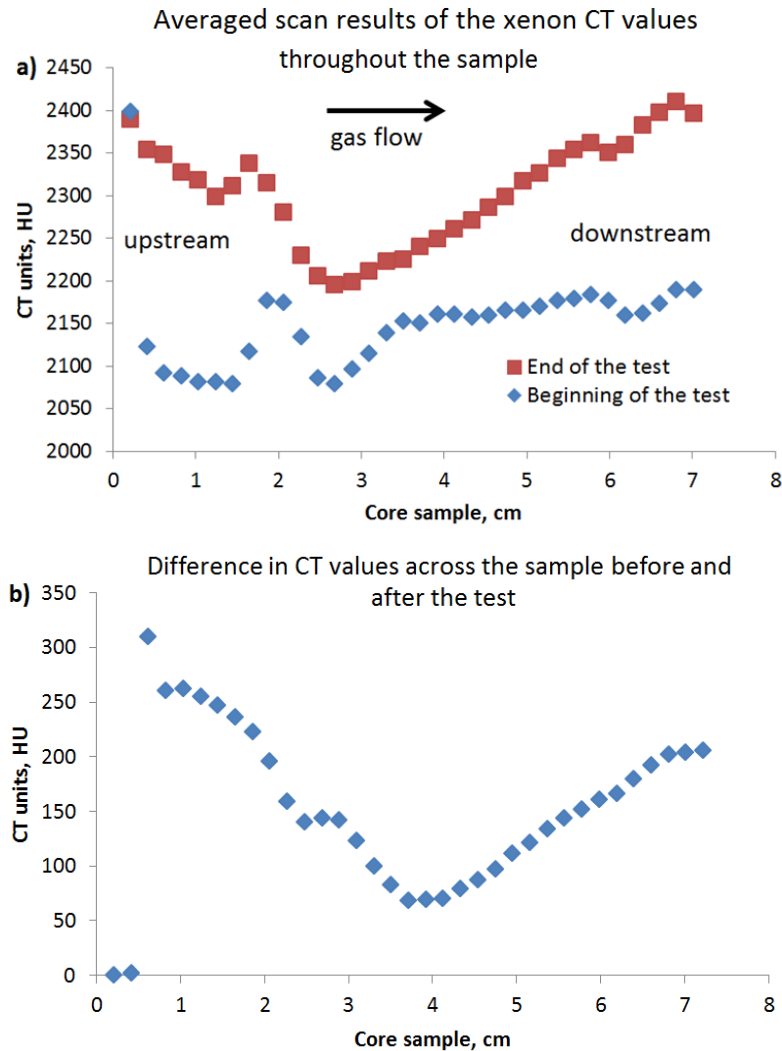
Figure 4.29. Plots of the CT measurements of EBN20 radial, showing: a) the results before and after flooding and (b) the difference between values of before and after flooding. Both are displayed over the length of the core with the injected xenon entering the upstream part of the sample and flowing downstream.

According to Figure 4.29, after the experiment the gas is present at the upstream and downstream ends of the sample with the decreasing amount of gas in the middle of the sample. This type of gas distribution would result if the microfracture or relatively high permeable inter-bedded layer is present within the core matrix - the gas travels through the microfracture towards the downstream first equalising the pressures at the both sides of the sample, and after that the gas would be absorbed by the matrix. An attempt was made to reproduce this type of behaviour using simulation models of fractured cores, with the results analysed in Chapter 6 (see Figure 6.21 in Section 6.4.2.1).

Although gas flow was not imaged in this sample using CT test several other authors have managed to enhance the CT results and obtain such images. Fogden et al. (2014) has demonstrated the use of the staining agents to highlight the sub-resolution regions of gas

saturation within the shale samples. He scanned the samples before and after the saturation with the highly X-ray attenuating liquid diiodomethane (CH_2I_2). Fogden et al. (2014) argued that the technique is useful for highlighting the areas where most of gas is concentrated within the sample, thus showing the areas of effective porosity. The graphs they presented in Figure 4.30 reveal that gas is mostly concentrated around the fractures. This observation supports the argument that gas flow is dominated by fractures and therefore the validity of the constructed model in Figure 6.21 in Section 6.4.2.1. However, there are very few successful recent attempts to image gas within the unconventional samples (Fogden et al., 2014; Saraji and Piri, 2014), as most of work on visualizing fluid flow within the porous media has been conducted on conventional rocks (Cuthiell et al., 1993; London et al., 2014).
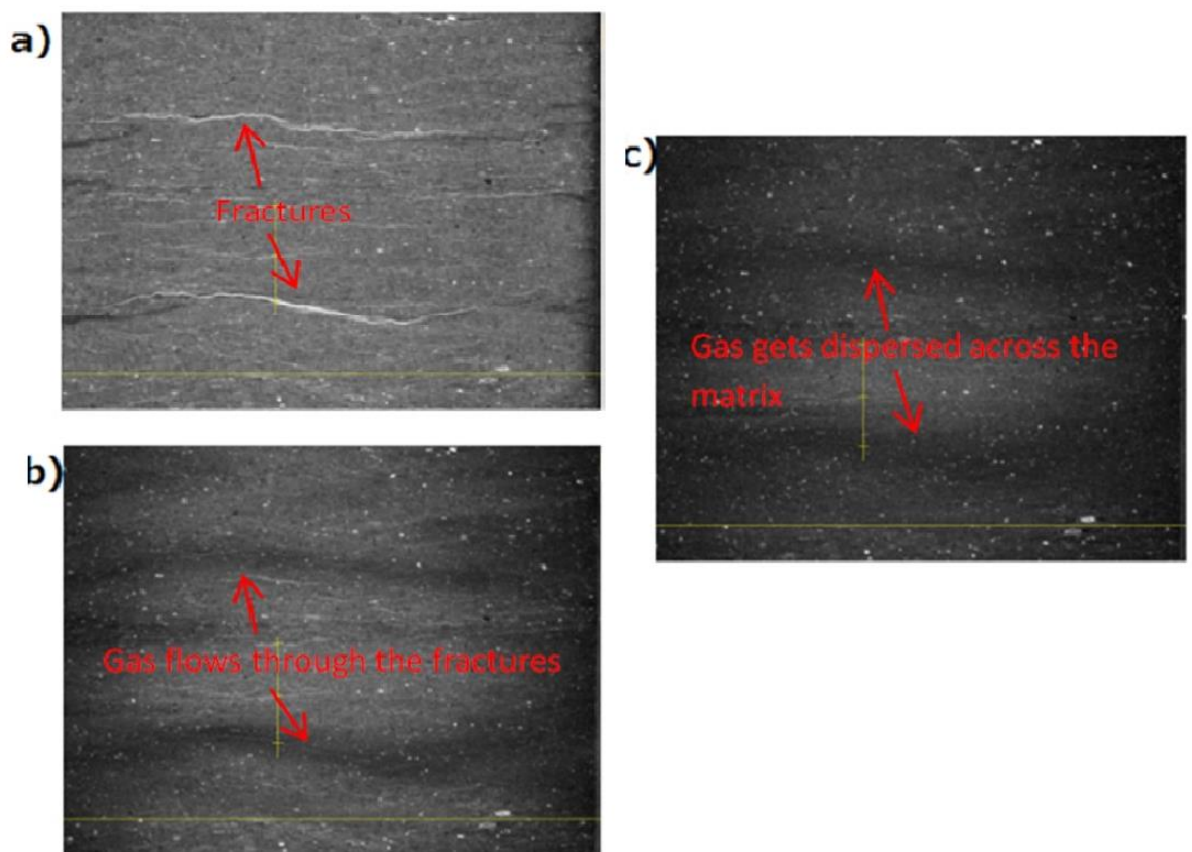
Figure 4.30. Fogden's et al. (2014) diiodomethane visualisation experiment on tight sandstones, showing a) dry sample before experiment; b) injection of diiodomethane; and c) movement of gas from fracture into the matrix.

4.4.3.2 Microfracture visualisation

To determine whether the visible microfractures within samples are artificial or natural, the nature of the fill was analysed. Microfractures are natural if they are filled with

minerals, clays or organic matter, and potentially artificial if they are void (Camp and Wawak, 2013). The issue here is that in the digital CT images the subtle variations in grey may be difficult to interpret for the human eye, especially within such delicate features as microfractures. Therefore images were attempted to be processed for pseudocolour conversion to distinguish between natural and artificial microfractures as shown in Figure 4.31.

A large microfracture in sample CHE2 was better defined with the help of the colour reprocessing (microfracture #1 in Figure 4.31d). Another microfracture was also identified, which was previously not noticed in the original image (fracture #2 in Figure 4.31d). The low density of the fractures suggests probable artificial origin. Re-processing of NEX15 CT images revealed a number of low density streaks (Figure 4.31e), which could be interpreted to be different lithology or microfractures within the matrix. For the NEX33 (Figure 4.31c and f) and other samples, processed SEM images did not reveal or improve any new structural information about the matrix. So the benefit of the technique is arbitrary; however higher scale image reprocessing study with more labour and time resources could potentially help to map out the larger scale microfractures within the sample.
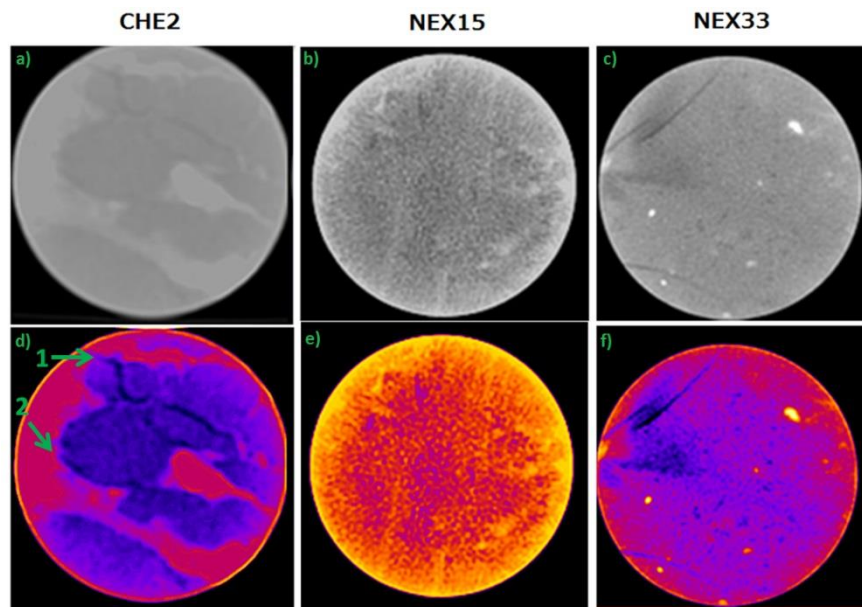
Figure 4.31. Comparison of contrast enhancement of greyscale (a; b and c) and pseudocolour (d; e and f) CT scans. Colour processing is done to improve the interpretation of the features withing the samples.

4.4.3.3 Large-scale image description

Many samples are layered, so in case the layer exhibits higher permeability than the surrounding matrix, it will also act similarly to the microfracture. Layered structur clearly visible on the higher core scale in Figure 4.32b, with the space between the layers filled with pyrite.

Generally, on the macro-scale shale matrix is continuous and similar in appearance across all of the samples (see Figure 4.13 and Figure 4.14 in Section 4.3.4). It does not contain any structurally complex features such as faults or stark differences in lithology. Nevertheless, there are gentle variations in density across the samples, indicating inter-bedded layers of mudstones and siltstones.

The scale of CT images in Figure 4.13 and Figure 4.14 (see Section 4.3.4) is too small to represent this type of shale structure, though some indications of layered shale nature were shown by CT slices of sample EBN20 (see Figure 4.13 in Section 4.3.4). However, the CT image obtained on the Gripen core on the larger scale (Figure 4.32) visualises layered share structure very clearly - beds of silt, clay and tight sandstone, manifested by the slight density changes are clearly visible within the shale. These layers may have varying grain sizes and clay content, so are likely to exhibit different conductivity properties towards the gas flow.
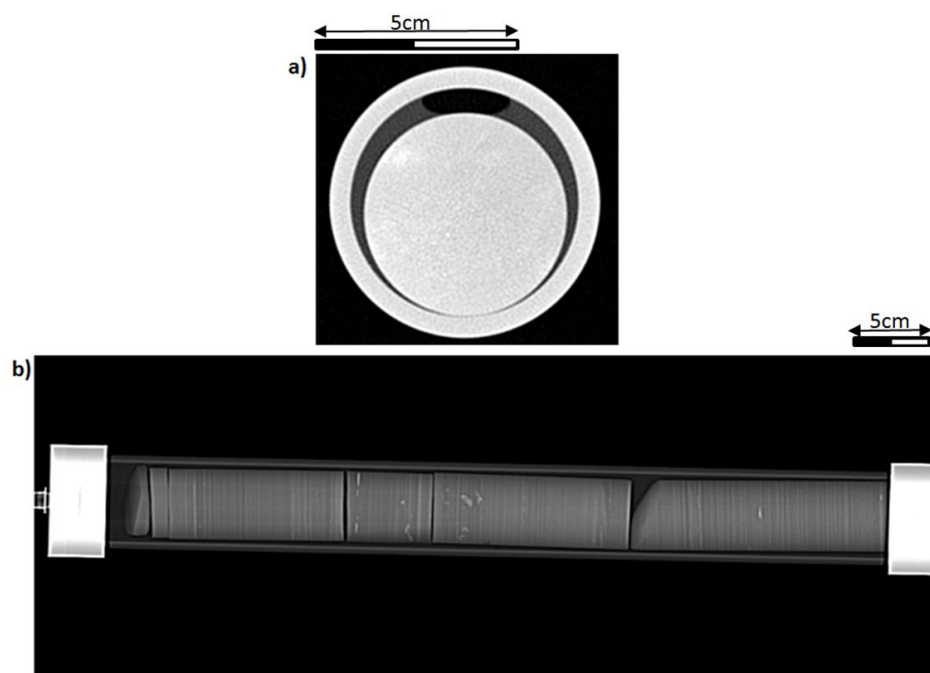
Figure 4.32. OA-1 shale core sample preserved in the field just after coring trip. Figure a shows the CT scan slice where the sample is seen submerged in the water (air bubble is seen on the top). Figure b shows the entire cross-section of the sample.

4.4.3.4 Effect of pyrite

Bright pyrite framboids is the most obvious feature from the Gripen CT images is (see Figure 4.10 and Figure 4.11 in Section 4.3.3); they appear in the form of clusters of crystals and tend to be concentrated in planar bands parallel to the bedding (Clavier et al., 1976). Pyrite forms under reducing conditions as a result of microbially mediated sulphate reduction being the dominant organic matter mineralizaion process. Pyrite is therefore particularly common in organic-rich shales deposited in a marine environment and in some cases can be used as an indicator for TOC (Witkowsky et al., 2012).

Pyrite might contain interparticle pore space, whereas clusters of pyrite framboids might form a network creating paths for the gas to flow. Control-Test group of samples contain relatively small amount of pyrite. In contrast the Gripen group of samples, containing on average 16.4% of pyrite, may need further research regarding the effect of pyrite on gas storage and transport. In this work, neither density corrections, nor the effect of pyrite on the gas flow and gas storage were studied.

Pyrite has a considerable impact on shale density estimation due to its distinctively high density value (5 gm/cc compared to around 2.5 gm/cc of shale). In Haynesville kerogen-bearing shale, 7% of pyrite was shown to affect shale grain density (Witkowsky et al., 2012). In comparison, some of the samples studied in this research contained up to 17% of pyrite (see Table 4.2 in Section 4.3.1).

4.5 Conclusions

Analysis of the SEM images revealed three types of the pore volume: organic pores, matrix pores and artificial fracture volume. Matrix pores were the largest among identified pores, however, they appeared not to be connected. Some of the matrix pores were identified within the mineral grains or pyrite framboids, which also appeared not to be connected to other porosity. However, it must be noted that the connectivity of the pores cannot be objectively evaluated using two-dimensional SEM images.

The organic pores were sometimes present within natural fractures filled with the organic matter. Good correlation of organic pores with the TOC values and maturity of the samples indicated that the pores were formed during the maturation of organic matter and its conversion into natural gas. In addition, different potential adsorption sources were identified, including organic matter and clays, which might create adsorptive volume. The adsorption values for the samples are provided in the Chapter 5.

Artificial microfracture-related pore space identified on the SEM scale was found to considerably influence the overall pore volume: in some samples the microfracture-related volume constituted up to 74% of overall pore volume. Microfractures and inter-bedded layers identified in CT scans were recognised to be most influential structural features in terms of the gas transport, effectively splitting the matrix into two conductivity regions: high and low. This was supported experimentally by injecting the xenon and interpreting within the sample and imaging low permeability matrix and highly permeable conductive region.

Considerable further improvements in terms of the structural shale characterisation could be done in CT gas flow imaging. When using luminous gasses such as xenon, it is recommended to allow full saturation of the sample followed by the introduction of another non-luminous gas to create a contrast. The non-luminous gas in this case could be methane – in this way the flow and distribution of this reservoir gas within the shale matrix could be understood better. The experimental set-up could stay the same as was proposed in this research as it proved to work.

The key point summary of the main structural implications found in Chapter 4:

- Clay mineral composition varies from 20 to 30%.
- Samples EBN20 and NEX33 have large carbonate contents of around 50%.
- Control-Test samples show TOC values up to 6%, whereas Gripen TOC up to 21%.
- Control-Test samples are mature, whereas Gripen samples are immature.
- Microfractures impact pore volumes and also gas distribution within the sample.
- Microfractures can be seen in crushed shale particles, despite many authors claiming crushing removes microfractures.

5 Chapter
Shale porosity and gas storage

5.1 Introduction

Shale porosity is a key parameter for the assessment of gas storage potential in shale plays. However, the fine-grained, multicomponent, nature of shale makes it challenging to both define and measure porosity. Normally, laboratory measurements of shale porosity are used as the most reliable and accurate value as oppose to log-derived values. Furthermore, laboratories use porosity themselves to cross-correlate against other petrophysical parameters both for research and QC purposes. Therefore, accurate and representative porosity values are crucial, otherwise many other errors would follow.

Porosity can be calculated from two of the following three measurements: bulk volume, grain volume, and pore volume. These measurements can be made on either core plugs/pieces using mercury methods (see Methodology Section 3.3), or crushed shale using Gas Research Institute pressure expansion method (Luffel et al., 1993). Derived porosity is usually assumed as a single value representing single volume system within the shale matrix. However, this is a common misconception, as several authors have already argued that fluids are stored in the different porous volumes within the shale (Figure 5.1). This in turn creates large inaccuracies in porosity values provided by various vendors with little information on experimental specifications. In fact, studies have shown that the porosity results for the same shale sample provided by different service companies can vary up to 30%.

Figure 5.1. Storage volume systems within the shale matrix (East, 2011).

The aim of this chapter is to analyse the reasons behind these porosity discrepancies and essentially understand the gas storage mechanism in shales. Pressure expansion method was employed to generate the data (see Section 3.4). The measurements were conducted at various conditions using different gasses. In addition, adsorption values for the tested shale samples were obtained. The information collected was analysed and the keys factors affecting various porosity measurements were described. Consequently, suggestions for increasing the accuracy of shale porosity measurements are suggested.

The chapter begins with the outline of the experimental methods described in Section 3.4. The results are then presented, including the values provided by the Control-Test laboratories. The discussion section then attempts to draw these results together to meet the objectives of the chapter. Finally, the findings are summarised in the conclusions section.

5.2 Methods

5.2.1 Overview of the methods

Porosity of 47 samples was measured using the crushed shale method described by Luffell et al. (1992). Core plug porosity measurements were conducted on 7 samples. Overall 659 measurements were conducted on crushed and core plug samples combined (485 and 174 respectively). Most of those measurements were performed on the Control-Test and Gripen samples, i.e. 494 (or 75%) of all measurements. Adsorption experiments were conducted on 11 shale samples. The basic description of all samples is provided in Section 3.2.1. Table 5.1, Table 5.2 and Table 5.3 provide an overview of the experiments discussed in this chapter.

Table 5.1. Breakdown of crushed porosity experiments. The names of the samples and corresponding tests that were made on them are presented.

Name	AR or Dry	Size, mm								Gas			Pressure Series	Reverse	Double model	No. of test
		0.25<d<0.5	0.5<d<0.85	0.85<d<1.676	1<d<2	0.85<d<2.8	1.676<d<2.8	2.8<d<4	4<d<7	He	CH$_4$	N$_2$				
EBN20	Dry	✓	✓		✓					✓	✓	✓	✓	✓	✓	21
CHE2	Dry		✓							✓	✓	✓	✓	✓	✓	22
CHE3	Dry		✓							✓	✓	✓	✓	✓	✓	31

NEX7	Dry		✓							✓	✓	✓	✓	✓	✓	24
NEX15	Dry		✓							✓	✓	✓	✓	✓	✓	31
NEX33	Dry		✓							✓	✓	✓	✓	✓	✓	24
N2	Dry+AR						✓	✓	✓	✓			✓	✓	✓	22
NG2	Dry+AR					✓		✓	✓	✓			✓	✓	✓	29
NG3	Dry+AR					✓		✓	✓	✓			✓	✓	✓	37
NG3#2	Dry+AR					✓	✓	✓	✓	✓			✓	✓	✓	26
NG8	Dry+AR			✓		✓	✓		✓			✓	✓	✓		25
NG10	Dry+AR			✓		✓			✓			✓	✓	✓		19
NG12	Dry+AR			✓		✓		✓	✓			✓	✓	✓		39
NA-6	Dry					✓		✓								6
NA-2	Ar			✓						✓			✓	✓	✓	4
BC01	Dry+AR		✓							✓			✓	✓	✓	3
BC02	Dry+AR		✓							✓			✓	✓	✓	3
BC03	Dry+AR		✓							✓			✓	✓	✓	3
BC04	Dry+AR		✓							✓			✓	✓	✓	3
BC05	Dry+AR		✓							✓			✓	✓	✓	3
BC06	Dry+AR		✓							✓			✓	✓	✓	4
BC07	Dry+AR		✓							✓			✓	✓	✓	4
BC08	Dry+AR		✓							✓			✓	✓	✓	3
BC09	Dry+AR		✓							✓			✓	✓	✓	4
BC10	Dry		✓							✓			✓	✓	✓	2
BC10	Dry+AR		✓							✓			✓	✓	✓	5
EBN1	AR		✓							✓						1
EBN16	Dry		✓							✓			✓	✓	✓	2
EBN19	Dry+AR		✓							✓			✓	✓	✓	4
EBN21	Dry+AR		✓							✓			✓		✓	6
EBN22	AR		✓							✓			✓		✓	3
EBN23	Dry+AR		✓							✓			✓		✓	10
EBN24	Dry+AR		✓							✓			✓		✓	10
EBN25	Dry+AR		✓							✓			✓		✓	6
EBN26	Dry+AR		✓							✓			✓	✓		5
EBN27	Dry+AR		✓							✓			✓		✓	6
EBN28	AR		✓							✓			✓		✓	3
EBN29	Dry+AR		✓							✓			✓		✓	4
EBN30	AR		✓							✓			✓		✓	2
EBN31	Dry		✓							✓					✓	1
EBN32	Dry		✓							✓			✓	✓	✓	3
EBN33	AR		✓							✓			✓		✓	2

EBN35	Dry+AR		✓						✓			✓		✓	7
EBN36	Dry+AR		✓						✓			✓	✓	✓	6
EBN7	Dry		✓						✓			✓	✓	✓	3
EBN8	AR		✓						✓					✓	1
NEX205	Dry		✓						✓			✓		✓	3

Table 5.2. Breakdown of core plug GRI (Gas Research Institute) porosity experiments. Note core plug gas invasion porosity was not obtained for NEX group of samples.

Name	Gas			Pressure series	Reverse	Double model	No. of tests
	He	CH$_4$	N$_2$				
EBN20	✓	✓	✓	✓	✓	✓	41
CHE2	✓	✓		✓	✓	✓	29
CHE3	✓	✓		✓	✓	✓	47
EBN5	✓						1
EBN9	✓	✓	✓	✓	✓	✓	16
EBN33	✓	✓		✓	✓	✓	20
Karoo	✓	✓		✓	✓	✓	20

Table 5.3. Outline of density and adsorption results.

Sample	Grain density			Bulk density			Adsorption	
	MICP	Water pycnometry	GRI	Hg immersion	MICP	GRI	Helium calibration	Krypton calibration
EBN20	✓	✓	✓	✓	✓	✓	✓	
CHE2 and CHE3	✓	✓	✓	✓	✓	✓	✓	
NEX7 and NEX33	✓	✓	✓	✓	✓	✓	✓	✓
NEX15	✓	✓	✓	✓	✓	✓	✓	
E-3; F-1 and E-16	✓			✓			✓	
N2 and NG2			✓	✓		✓		
NG3 and NG4			✓			✓		
NG8; NG10 and NG12			✓	✓		✓		
EBN1		✓	✓					
EBN3	✓	✓		✓				

EBN4		✓	✓	✓				
EBN5		✓		✓				
EBN7		✓	✓	✓				
EBN9		✓		✓				
EBN13		✓						
EBN14	✓			✓				
EBN18		✓	✓	✓				
EBN19		✓	✓					
Casp; Toup, ABE and Pyrn	✓	✓	✓	✓				
EBN21 and EBN22	✓	✓		✓				
EBN23 and EBN24	✓	✓	✓	✓				
EBN25 and EBN26	✓	✓		✓				
EBN27		✓						
EBN28	✓	✓	✓	✓				
EBN29	✓	✓		✓				
EBN30 to EBN32	✓	✓	✓	✓				
EBN33	✓	✓		✓				
EBN34 and EBN35	✓	✓	✓	✓				
EBN36	✓	✓		✓				
CHE1	✓	✓		✓				
Gripn7		✓	✓					
BC1 to BC8	✓	✓	✓	✓				
BC9	✓	✓		✓				
BC10		✓						
BC11	✓	✓	✓	✓				
NEX205	✓	✓	✓	✓				
NEXH1	✓		✓	✓				

5.2.2 Quality control

The primary objective of this chapter was to understand the reasons why different service companies provide different porosity values when analysing the same sample. So quality control of the results obtained in this research was crucial. The two biggest error sources in the pressure decay experiment are leakage and temperature fluctuations (see Section 3.4.4). Pressure curves with continuous and constant decline rate were discarded, as well as the ones affected by temperature (Figure 5.2). The simulation results were also compared with the experimental results and visually classified as good, moderate and

poor fits. Examples of these are provided in Figure 5.3. All results with poor fits were discarded.
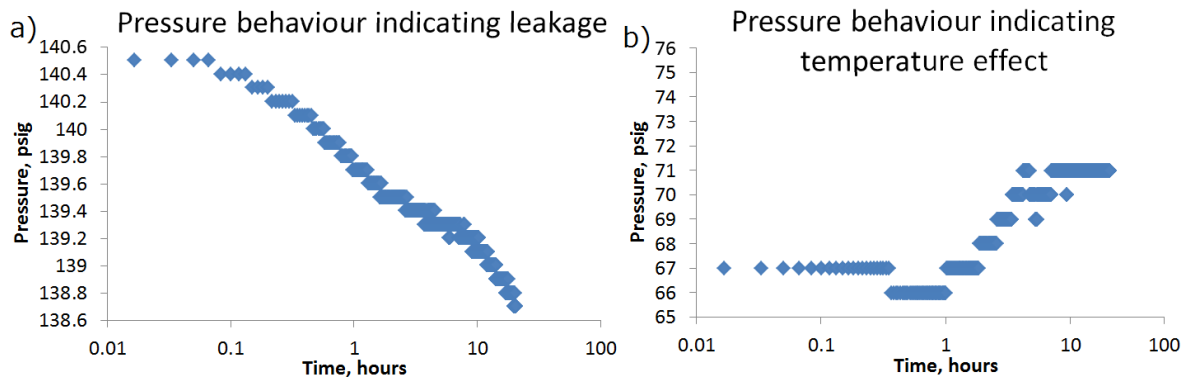
Figure 5.2. Leakage (a) and temperature (b) effects on the pressure decay behaviour.
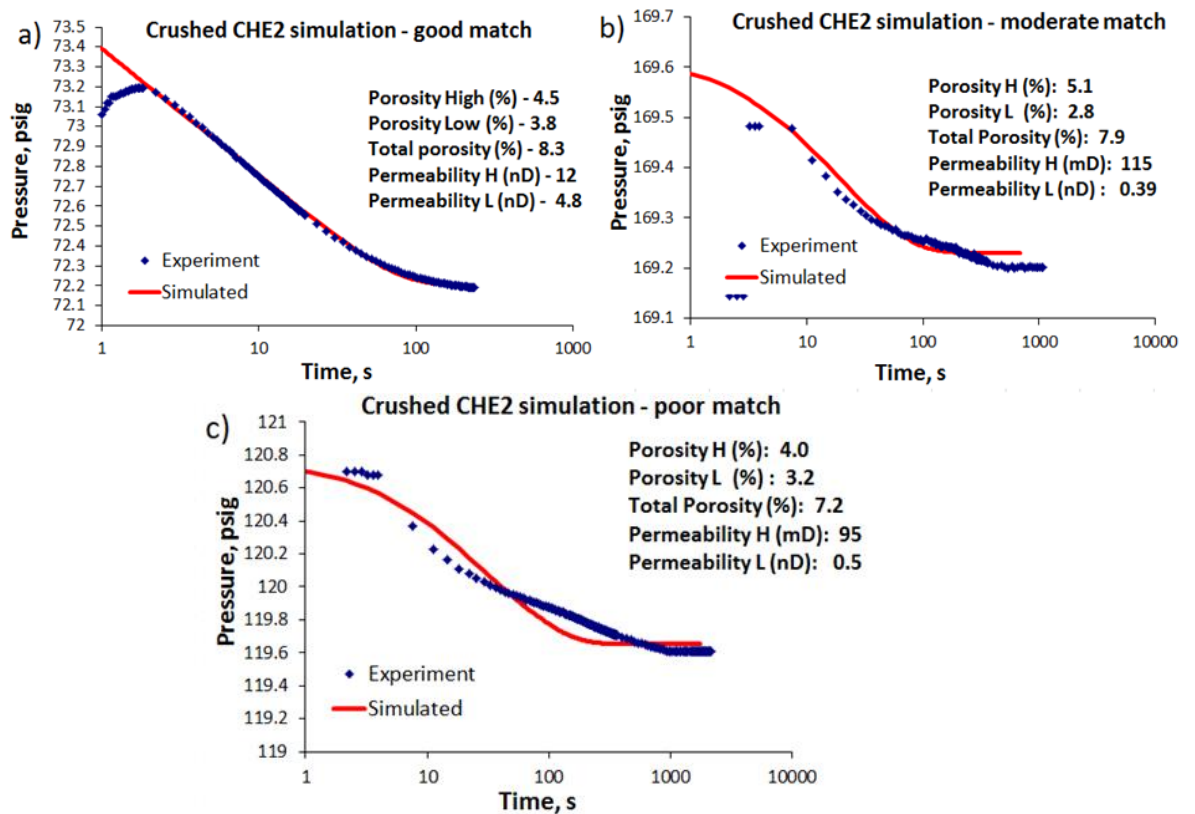
Figure 5.3. Comparison of the quality of the history match for crushed sample; a) shows good fit, b) shows moderate fit and c) shows a poor fit.

Pressure series experiment (see Section 3.4.2) generates a number of porosity/permeability values for the sample from the single experiment, therefore allows any outlier values to be identified. Pressure series tests also include a reverse test, where the gas leaving the sample is recorded (see Section 3.4.2). This enables a cross-check of the mass balance of the gas entering and leaving the sample to be made. In most cases

shale core plugs do not reach experimental equilibrium, making mass balance comparison not applicable for QC purposes. However in the case of the crushed samples, mass balance can provide clear and fast evaluation of experimental data.

5.3 Results

In this section, porosity, adsorption and density experimental results are presented with the focus on Control-Test samples, with the results for the remaining samples provided in Appendix I. Results from the other samples are still discussed and analysed. This section also presents the Control-Test porosity and grain density values cross-compared with the results obtained in this research.

5.3.1 Crushed results

Porosity values of the crushed samples are presented in Table 5.4, together with the grain sizes, sample weight, sample set up (X; G1; G2 and G3, see Section 3.4.1), sample conditions and applied experimental pressure. Analogue tables of crushed porosity results but different utilised experimental gas are provided in the follow up Table 5.5 and Table 5.6.

Table 5.4. Crushed Control-Test and Gripen experimental porosity results using GRI test with helium gas.

Sample	Size, mm	Setup	Sample conditions	P1 (V1), psig	Total porosity, %	High porosity, %	Low porosity, %
CHE2	500-d-850	X	AR	237.70	5.27	2.68	2.59
CHE2	500-d-850	G3	AR	149.90	9.32	5.14	4.18
CHE2	500-d-850	G3	AR	180.67	7.12	4.43	2.69
CHE2	500-d-850	G3	AR	209.35	7.63	4.28	3.35
CHE2	500-d-850	G3	AR	0.00	7.05	2.50	4.54
CHE2	500-d-850	G2	Dry	243.51	9.04	5.34	3.71
CHE2	500-d-850	G2	Dry	154.54	8.67	4.38	4.30
CHE2	500-d-850	G2	Dry	182.22	7.90	4.38	3.52
CHE2	500-d-850	G2	Dry	211.30	8.36	4.97	3.39
CHE2	500-d-850	G2	Dry	0.00	6.67	3.01	3.66
CHE2	500-d-850	G3	Dry	235.81	10.89	0.25	10.65
CHE2	500-d-850	G3	Dry	0.00	8.79	2.79	6.00
CHE2	500-d-850	G1	Dry	150.68	8.81	4.49	4.32
CHE2	500-d-850	G1	Dry	179.30	8.38	4.80	3.58

CHE3	500-d-850	G3	AR	150.10	10.42	8.19	2.23
CHE3	500-d-850	G3	AR	179.57	11.41	8.02	3.38
CHE3	500-d-850	G3	AR	210.16	8.88	7.65	1.23
CHE3	500-d-850	G3	AR	240.29	14.25	8.29	5.96
CHE3	500-d-850	G3	Dry	149.20	13.12	10.49	2.63
CHE3	500-d-850	G3	Dry	179.77	11.86	9.64	2.22
CHE3	500-d-850	G3	Dry	209.66	11.25	10.34	0.91
CHE3	500-d-850	G3	Dry	240.37	12.14	10.40	1.74
CHE3	500-d-850	G3	Dry	0.00	10.94	8.95	1.99
CHE3	500-d-850	G3	AR	0.00	8.83	6.79	2.05
CHE3	500-d-850	G3	Dry	238.93	12.86	7.80	5.06
CHE3	500-d-850	G3	Dry	0.00	10.88	6.25	4.63
CHE3	500-d-850	G1	Dry	150.39	10.87	10.87	0.00
EBN20	500-d-850	G3	AR	243.79	4.15	0.75	3.39
EBN20	500-d-850	G3	AR	239.33	3.53	0.00	5.51
EBN20	500-d-850	G3	AR	240.97	4.85	0.80	4.05
EBN20	500-d-850	G2	Dry	243.68	7.70	6.29	1.41
EBN20	500-d-850	G2	Dry	238.87	7.95	0.00	9.38
EBN20	500-d-850	G2	Dry	247.10	7.66	6.23	1.43
EBN20	500-d-850	G2	AR	229.32	4.35	2.97	1.38
EBN20	500-d-850	G2	AR	247.51	4.04	3.63	0.41
EBN20	500-d-850	G2	AR	220.60	5.75	4.39	1.36
EBN20	500-d-850	X	AR	232.30	3.77	3.77	0.00
EBN20	500-d-850	G1	Dry	178.90	7.17	6.86	0.31
NEX7	500-d-850	G3	Dry	0.00	4.89	3.51	1.38
NEX7	500-d-850	G3	Dry	213.05	5.83	4.93	0.91
NEX7	500-d-850	G3	Dry	0.00	6.23	4.12	2.11
NEX7	500-d-850	G3	Dry	184.53	6.46	5.77	0.69
NEX7	500-d-850	G3	Dry	274.93	6.52	5.51	1.01
NEX7	500-d-850	G3	Dry	221.46	6.53	5.34	1.19
NEX7	500-d-850	G3	Dry	167.40	6.99	5.55	1.44
NEX7	500-d-850	X	AR	243.70	2.11	1.04	1.07
NEX7	500-d-850	G2	Dry	238.17	8.67	4.82	3.85
NEX7	500-d-850	G2	Dry	0.00	5.41	2.38	3.03
NEX7	500-d-850	G1	Dry	145.26	5.09	5.09	0.00
NEX15	500-d-850	X	AR	225.80	3.84	2.08	208.38
NEX15	500-d-850	G3	Dry	146.30	8.70	1.14	114.05
NEX15	500-d-850	G3	Dry	161.10	7.51	0.61	60.87
NEX15	500-d-850	G3	Dry	186.82	7.30	0.34	34.21

NEX15	500-d-850	G3	Dry	206.61	7.24	0.54	53.61
NEX15	500-d-850	G3	Dry	226.80	7.87	1.14	113.78
NEX15	500-d-850	G3	Dry	241.69	7.46	0.65	64.86
NEX15	500-d-850	G3	Dry	265.30	7.37	0.71	70.62
NEX15	500-d-850	G3	Dry	175.14	7.89	0.54	53.61
NEX15	500-d-850	G3	Dry	206.58	7.56	0.74	74.16
NEX15	500-d-850	G3	Dry	227.34	7.46	0.80	80.17
NEX15	500-d-850	G3	Dry	152.28	8.02	0.55	54.55
NEX15	500-d-850	G3	Dry	180.70	7.44	0.61	60.94
NEX15	500-d-850	G3	Dry	211.70	7.39	0.62	61.80
NEX15	500-d-850	G3	Dry	240.65	7.37	0.54	53.78
NEX15	500-d-850	G3	Dry	0.00	5.94	-0.91	-91.36
NEX15	500-d-850	G3	Dry	0.00	6.45	1.31	130.99
NEX15	500-d-850	G3	Dry	0.00	6.37	1.00	100.22
NEX15	500-d-850	G3	Dry	0.00	6.91	1.31	131.06
NEX15	500-d-850	G3	Dry	0.00	6.23	0.86	85.65
NEX15	500-d-850	G3	Dry	0.00	6.79	1.21	120.95
NEX15	500-d-850	G3	Dry	235.86	10.77	14.70	1470.09
NEX15	500-d-850	G3	Dry	0.00	7.07	2.64	263.75
NEX15	500-d-850	G1	Dry	150.50	6.96	0.79	79.42
NEX33	500-d-850	G2	Dry	180.19	7.06	6.63	0.43
NEX33	500-d-850	G2	Dry	192.04	7.10	6.87	0.23
NEX33	500-d-850	G2	Dry	240.11	7.34	6.72	0.63
NEX33	500-d-850	G2	Dry	274.72	7.86	6.88	0.97
NEX33	500-d-850	G2	Dry	190.90	7.08	6.40	0.68
NEX33	500-d-850	G2	Dry	247.91	7.30	6.54	0.76
NEX33	500-d-850	G2	Dry	271.19	7.90	6.63	1.27
NEX33	500-d-850	G2	Dry	0.00	5.56	4.88	0.68
NEX33	500-d-850	X	AR	234.80	5.36	5.36	0.00
NEX33	500-d-850	G2	Dry	233.08	10.99	3.93	7.06
NEX33	500-d-850	G2	Dry	0.00	6.88	6.25	0.64
NEX33	500-d-850	G1	Dry	179.04	7.06	6.63	0.43
N-2	1.676-d-2.8	G2	Dry	149.72	6.00	2.90	3.60
N-2	1.676-d-2.8	G2	Dry	178.99	8.00	3.70	4.50
N-2	1.676-d-2.8	G2	Dry	0.00	7.00	0.00	7.30
N-2	2.8-d-4	G3	Dry	152.38	7.00	2.90	4.20
N-2	2.8-d-4	G3	Dry	176.21	6.00	2.50	3.80
N-2	2.8-d-4	G3	Dry	0.00	7.00	1.10	6.10
N-2	4-d-7	G3	Dry	149.88	6.00	2.60	3.30

N-2	4-d-7	G3	Dry	176.09	8.00	2.60	5.20
N-2	4-d-7	G3	Dry	0.00	6.00	0.20	6.20
NG-2	0.85-d-2.8	G3	Dry	147.67	14.00	9.10	4.60
NG-2	0.85-d-2.8	G3	Dry	181.67	10.00	8.90	0.70
NG-2	0.85-d-2.8	G3	Dry	0.00	11.00	5.90	5.20
NG-2	2.8-d-4	G3	Dry	150.62	14.00	8.10	5.70
NG-2	2.8-d-4	G3	Dry	180.06	12.00	7.50	4.50
NG-2	2.8-d-4	G3	Dry	0.00	12.00	6.00	6.40
NG-2	4-d-7	G2	Dry	151.56	11.00	6.10	4.60
NG-2	4-d-7	G2	Dry	182.28	10.00	5.00	5.40
NG-2	4-d-7	G2	Dry	0.00	9.00	3.30	5.70
NG-3	0.85-d-1.676	G2	Dry	149.21	12.00	7.60	4.70
NG-3	0.85-d-1.676	G2	Dry	182.64	10.00	6.40	3.80
NG-3	0.85-d-1.676	G2	Dry	0.00	10.00	4.20	6.10
NG-3	1.676-d-2.8	G1	Dry	152.31	9.00	6.60	2.50
NG-3	1.676-d-2.8	G1	Dry	181.71	11.00	7.50	3.50
NG-3	1.676-d-2.8	G1	Dry	0.00	10.00	5.50	5.00
NG-3	2.8-d-4	G2	Dry	150.05	11.00	6.20	4.90
NG-3	2.8-d-4	G2	Dry	181.25	10.00	5.00	5.40
NG-3	4-d-7	G1	Dry	151.79	9.00	5.60	3.70
NG-3	4-d-7	G1	Dry	180.15	10.00	5.90	3.80
NG-3	4-d-7	G1	Dry	0.00	10.00	4.60	4.90
NG-4	0.85-d-2.8	G2	Dry	150.56	13.00	6.90	5.70
NG-4	0.85-d-2.8	G2	Dry	181.91	10.00	6.00	4.10
NG-4	0.85-d-2.8	G2	Dry	0.00	11.00	3.90	6.80
NG-4	2.8-d-4	G2	Dry	150.48	10.00	5.50	4.60
NG-4	2.8-d-4	G2	Dry	183.83	7.00	4.40	3.10
NG-4	2.8-d-4	G2	Dry	0.00	0.00	-4.20	4.20
NG-4	4-d-7	G3	Dry	152.34	12.00	7.30	4.40
NG-4	4-d-7	G3	Dry	181.96	11.00	6.50	4.30
NG-4	4-d-7	G3	Dry	0.00	10.00	5.00	5.10
NG-8	0.85-d-1.676	G2	Dry	153.44	16.00	11.50	4.10
NG-8	0.85-d-1.676	G2	Dry	179.42	14.00	9.50	4.80
NG-8	0.85-d-1.676	G2	Dry	0.00	8.00	32.60	0.00
NG-8	1.676-d-2.8	G3	Dry	152.53	16.00	13.00	3.00
NG-8	1.676-d-2.8	G3	Dry	182.65	15.00	11.70	3.60
NG-8	1.676-d-2.8	G3	Dry	0.00	14.00	10.40	3.10
NG-8	2.8-d-4	G1	Dry	151.47	15.00	10.60	4.40
NG-8	2.8-d-4	G1	Dry	180.90	16.00	11.40	4.30

NG-8	2.8-d-4	G1	Dry	0.00	0.00	-4.00	4.00
NG-10	0.85-d-1.676	G2	Dry	150.48	10.00	6.10	3.50
NG-10	0.85-d-1.676	G2	Dry	181.52	10.00	5.90	4.60
NG-10	0.85-d-1.676	G2	Dry	0.00	8.00	4.10	4.40
NG-10	1.676-d-2.8	G1	Dry	149.31	0.00	0.00	3.79
NG-10	1.676-d-2.8	G1	Dry	181.24	11.00	0.00	4.26
NG-10	1.676-d-2.8	G1	Dry	0.00	9.00	0.00	3.89
NG-12	0.85-d-1.676	G3	Dry	148.03	19.00	19.20	-0.60
NG-12	0.85-d-1.676	G3	Dry	182.35	18.00	17.90	0.10
NG-12	0.85-d-1.676	G3	Dry	0.00	17.00	16.40	0.80
Ng-12	1.676-d-2.8	G3	Dry	146.65	19.00	18.50	0.10
Ng-12	1.676-d-2.8	G3	Dry	178.97	18.00	18.00	0.40
Ng-12	1.676-d-2.8	G3	Dry	0.00	18.00	16.00	1.70
NG12	4-d-7	G3	Dry	150.94	19.00	16.30	2.70
NG12	4-d-7	G3	Dry	182.45	18.00	15.40	2.90
NG12	4-d-7	G3	Dry	209.16	19.00	15.30	3.30
NG12	4-d-7	G3	Dry	0.00	18.00	12.70	5.50

Table 5.5. Crushed Control-Test and Gripen experimental porosity results using GRI test with methane gas.

Sample	Size, mm	Setup	Sample conditions	P1 (V1), psig	Total porosity,%	High porosity,%	Low porosity,%
CHE2	500-d-850	G2	Dry	149.93	24.00	6.40	17.80
CHE2	500-d-850	G2	Dry	181.40	17.00	5.90	10.80
CHE2	500-d-850	G2	Dry	196.87	17.00	6.60	10.10
CHE2	500-d-850	G2	Dry	0.00	18.00	8.60	9.30
NEX15	500-d-850	G2	Dry	150.16	17.00	9.60	7.60
NEX15	500-d-850	G2	Dry	168.94	13.00	8.30	5.20
NEX15	500-d-850	G2	Dry	0.00	16.00	11.20	4.40
NEX33	500-d-850	G3	Dry	150.25	15.00	12.30	2.60
NEX33	500-d-850	G3	Dry	167.76	13.00	10.50	2.30
NEX33	500-d-850	G3	Dry	0.00	15.00	13.90	1.40
NEX7	250-d-500	G1	Dry	151.64	12.00	2.70	9.50
NEX7	250-d-500	G1	Dry	167.65	11.00	2.60	8.30
NEX7	250-d-500	G1	Dry	0.00	18.00	2.30	16.00
NEX7	500-d-850	G1	Dry	150.93	19.00	8.30	10.30
NEX7	500-d-850	G1	Dry	180.79	15.00	8.70	6.20
NEX7	500-d-850	G1	Dry	195.07	14.00	9.30	4.70
NEX7	500-d-850	G1	Dry	0.00	18.00	12.00	5.70

EBN20	1-2 mm	G1	Dry	148.56	13.00	10.20	2.50
EBN20	1-2 mm	G1	Dry	178.35	10.00	8.80	1.40
EBN20	1-2 mm	G1	Dry	0.00	14.00	13.20	0.80
EBN20	250-d-500	G2	Dry	150.98	23.00	19.50	3.30
EBN20	250-d-500	G2	Dry	179.61	20.00	17.70	2.40
EBN20	250-d-500	G2	Dry	0.00	24.00	23.20	0.90
CHE3	500-d-850	G3	Dry	151.33	24.00	10.70	13.70
CHE3	500-d-850	G3	Dry	181.66	19.00	11.10	8.40
CHE3	500-d-850	G3	Dry	195.96	20.00	11.50	8.40
CHE3	500-d-850	G3	Dry	0.00	20.00	13.20	7.10
EBN20	500-d-850	G3	AR	155.57	11.00	8.40	2.40
EBN20	500-d-850	G3	AR	0.00	11.00	10.10	0.70

Table 5.6. Crushed Control-Test and Gripen experimental porosity results using GRI test with nitrogen gas.

Sample	Size, mm	Setup	Sample conditions	P1 (V1), psig	Total porosity,%	High porosity,%	Low porosity,%
NEX7	500-d-850	G2	Dry	148.49	10.00	7.10	2.80
NEX7	500-d-850	G2	Dry	179.04	10.00	7.00	2.70
NEX7	500-d-850	G2	Dry	210.93	10.00	7.20	2.50
NEX7	500-d-850	G2	Dry	0.00	10.00	6.50	3.10
NEX33	500-d-850	G3	Dry	150.69	9.00	3.50	5.50
NEX33	500-d-850	G3	Dry	180.53	9.00	0.70	8.50
NEX33	500-d-850	G3	Dry	208.52	10.00	-3.20	13.50
NEX33	500-d-850	G3	Dry	0.00	7.00	-8.00	14.90
NEX33	500-d-850	G2	Dry	148.10	9.00	8.40	0.80
NEX33	500-d-850	G2	Dry	181.22	8.00	7.10	0.90
NEX33	500-d-850	G2	Dry	211.15	8.00	6.90	1.20
NEX33	500-d-850	G2	Dry	0.00	8.00	7.50	0.10
CHE3	500-d-850	G3	Dry	146.93	16.00	9.90	5.60
CHE3	500-d-850	G3	Dry	181.29	14.00	10.20	4.20
CHE3	500-d-850	G3	Dry	210.53	14.00	10.50	3.80
CHE3	500-d-850	G3	Dry	0.00	14.00	9.30	4.50
EBN20	500-d-850	G1	Dry	148.45	8.00	7.30	0.50
EBN20	500-d-850	G1	Dry	181.06	8.00	7.50	0.40
EBN20	500-d-850	G1	Dry	210.56	8.00	7.40	0.50
EBN20	500-d-850	G1	Dry	0.00	8.00	7.60	0.30
NEX15	500-d-850	G1	Dry	150.34	10.00	7.30	2.80

NEX15	500-d-850	G1	Dry	177.51	10.00	8.10	2.10
NEX15	500-d-850	G1	Dry	211.67	9.00	8.20	0.60
NEX15	500-d-850	G1	Dry	0.00	10.00	7.90	2.30
CHE2	500-d-850	G1	Dry	151.02	10.00	0.80	9.20
CHE2	500-d-850	G1	Dry	180.57	8.00	1.40	7.00
CHE2	500-d-850	G1	Dry	210.66	9.00	1.70	7.00
CHE2	500-d-850	G1	Dry	0.00	8.00	0.40	7.80
CHE3	500-d-850	G3	AR	150.16	13.00	9.30	3.90
CHE3	500-d-850	G3	AR	180.73	14.00	9.20	5.10
CHE3	500-d-850	G3	AR	210.45	14.00	9.60	4.00
CHE3	500-d-850	G3	AR	240.38	14.00	10.30	3.50
CHE3	500-d-850	G3	Dry	150.52	17.00	10.00	6.70
CHE3	500-d-850	G3	Dry	180.20	16.00	10.30	5.90
CHE3	500-d-850	G3	Dry	209.93	16.00	10.70	5.10
CHE3	500-d-850	G3	Dry	250.74	15.00	10.80	4.40
CHE3	500-d-850	G3	AR	0.00	13.00	9.10	4.10
CHE3	500-d-850	G3	Dry	0.00	15.00	10.30	4.40

5.3.2 Core plug results

Core plug porosity values are given in Table 5.7; Table 5.8 and Table 5.9 (note grain size does not apply for core plugs, core volume is given instead). Porosity values for both matrix and high conductivity layer (fracture) were obtained (high and low porosity respectively, see Sections 3.6.1; 3.6.2 and 3.6.3). Total porosity value shows the sum of low and high porosities.

Table 5.7. Control-Test core plug experimental porosity results using GRI test with helium gas. All experiments were done using G1 experimental setup.

Sample	Condition	P1 (V1), psig	Matrix poro,%	Frac poro,%
EBN20	Dry	144.19	9.01	
EBN20	Dry	196.71	4.95	
EBN20	Dry	246.74	3.75	
EBN20	Dry	297.51	5.09	
EBN20	Dry	401.04	5.03	
EBN20	Dry	0.00	4.54	
EBN20	Dry	144.19	10.08	9.34
EBN20	Dry	196.71	8.67	9.40
EBN20	Dry	246.74	7.08	9.37
EBN20	Dry	297.51	5.12	6.40
EBN20	Dry	401.04	6.43	8.06

EBN20	Dry	0.00	12.12	8.61
EBN20	Dry	68.00	5.14	12.46
EBN20	Dry	0.00	10.27	11.75
EBN20	Dry	132.20	4.03	11.24
EBN20	Dry	623.00	5.15	10.61
EBN20	Dry	0.00	4.71	8.03
EBN20	Dry	665.00	4.43	5.54
EBN20	Dry	668.00	4.23	12.42
EBN20	Dry	0.00	4.57	5.20
EBN20	Dry	68.00	4.90	
EBN20	Dry	0.00	4.99	
EBN20	Dry	132.20	4.03	
EBN20	Dry	623.00	4.77	
EBN20	Dry	0.00	4.83	
EBN20	Dry	665.00	4.91	
EBN20	Dry	0.00	5.15	
EBN20	Dry	668.00	4.38	
EBN20	Dry	0.00	4.82	
CHE2	Dry	489.19	5.64	
CHE2	Dry	692.24	5.32	
CHE2	Dry	899.79	5.62	
CHE2	Dry	1196.03	5.61	
CHE2	Dry	1326.61	17.52	0.00
CHE2	Dry	0.00	4.03	0.00
CHE2	Dry	489.19	9.34	9.34
CHE2	Dry	692.24	9.44	21.76
CHE2	Dry	899.79	9.42	21.79
CHE2	Dry	1196.03	4.67	21.46
CHE2	Dry	1326.61	14.21	6.42
CHE2	Dry	0.00	4.00	9.20
CHE2	Dry	490.19	7.00	
CHE2	Dry	693.24	5.80	
CHE2	Dry	900.79	6.55	
CHE2	Dry	1197.03	7.10	
CHE2	Dry	1327.61	15.00	
CHE2	Dry	0.00	4.60	
CHE2	Dry	490.19	6.64	2.53
CHE2	Dry	693.24	6.06	4.14
CHE2	Dry	900.79	6.60	5.14

CHE2	Dry	1197.03	7.40	2.73
CHE2	Dry	1327.61	13.80	2.65
CHE2	Dry	0.00	4.10	13.80
CHE2	Dry	489.19	5.64	0.00
CHE3	Dry	150.30	8.39	
CHE3	Dry	180.43	7.70	
CHE3	Dry	210.39	7.91	
CHE3	Dry	240.83	7.15	
CHE3	Dry	150.30	8.40	10.74
CHE3	Dry	180.43	7.07	11.38
CHE3	Dry	210.39	7.12	8.92
CHE3	Dry	240.83	8.42	8.42
CHE3	Dry	0.00	9.21	8.52
CHE3	Dry	150.30	8.30	
CHE3	Dry	180.43	8.80	
CHE3	Dry	210.39	7.90	
CHE3	Dry	240.83	7.15	
CHE3	Dry	150.30	8.40	10.70
CHE3	Dry	180.43	7.07	11.38
CHE3	Dry	210.39	7.12	8.90
CHE3	Dry	240.83	6.80	8.40
CHE3	Dry	496.63	8.11	
CHE3	Dry	697.17	7.44	
CHE3	Dry	930.74	10.10	
CHE3	Dry	1106.83	10.50	
CHE3	Dry	1323.92	9.90	
CHE3	Dry	496.63	8.28	2.99
CHE3	Dry	697.17	8.68	1.20
CHE3	Dry	930.74	11.00	8.70
CHE3	Dry	1106.83	11.70	8.66
CHE3	Dry	1323.92	8.80	1.19

Table 5.8. Core plug Control-Test and Gripen experimental porosity results using GRI test with methane gas. All experiments were done using G1 experimental setup.

Sample	Condition	P1 (V1), psig	Matrix poro,%	Frac poro,%
EBN20	Dry	165.86	11.12	0.00
EBN20	Dry	185.89	12.40	0.00
EBN20	Dry	208.10	7.05	0.00
EBN20	Dry	0.00	8.54	0.00
EBN20	Dry	0.00	8.14	0.00
EBN20	Dry	165.86	9.34	10.75
EBN20	Dry	185.89	12.70	12.02
EBN20	Dry	208.10	12.25	13.16
EBN20	Dry	0.00	15.19	8.09
EBN20	Dry	0.00	11.03	8.98
CHE2	Dry	149.29	19.85	0.00
CHE2	Dry	0.00	14.30	0.00
CHE2	Dry	149.29	18.08	16.39
CHE2	Dry	0.00	12.53	9.23
CHE3	Dry	151.16	14.15	
CHE3	Dry	180.45	11.99	
CHE3	Dry	211.37	12.49	
CHE3	Dry	0.00	10.07	
CHE3	Dry	0.00	11.98	
CHE3	Dry	151.16	13.35	16.74
CHE3	Dry	180.45	11.58	21.12
CHE3	Dry	211.37	11.32	18.47
CHE3	Dry	0.00	11.28	23.56
CHE3	Dry	0.00	13.43	11.47
CHE3	Dry	149.47	7.95	
CHE3	Dry	180.94	6.13	
CHE3	Dry	209.03	5.14	
CHE3	Dry	0.00	8.78	
CHE3	Dry	0.00	9.60	
CHE3	Dry	149.47	7.29	11.03
CHE3	Dry	180.94	5.79	6.30
CHE3	Dry	209.03	6.00	12.87
CHE3	Dry	0.00	8.18	18.75
CHE3	Dry	0.00	10.97	20.83

Table 5.9. Core plug Control-Test experimental porosity results using GRI test with nitrogen gas. All experiments were done using G1 experimental setup.

Sample	Condition	P1 (V1), psig	Matrix poro,%	Frac poro,%
EBN20	Dry	124.50	8.00	
EBN20	Dry	0.00	5.00	

5.3.3 Density results

Grain and bulk density values are given in Table 5.10 derived using different methods (see Sections 3.3.2 and 3.3.3). The most complete analysis was done on the Control-Test and Gripen group of samples. Results for the remaining samples are provided in Appendix G.

Table 5.10. Bulk and grain density results using various methods.

Sample	Bulk density (Hg), g/cm^3	Bulk density (GRI), g/cm^3	Grain density (Hg), g/cm^3	Grain density (WP), g/cm^3	Grain density (GRI), g/cm^3	Grain density (QXRD), g/cm^3
EBN20	2.53	2.59	2.74	2.61	2.65	2.56
CHE2	2.40	2.62	2.68		2.74	2.65
CHE3	2.45	2.64	2.66		2.74	2.68
NEX7	2.52	2.55	2.59	2.94	2.59	2.52
NEX15	2.48	2.60	2.64	2.81	2.64	2.56
NEX33	2.49	2.65	2.68	3.04	2.68	2.62
E-3	2.41		2.24			
F-1	2.25		2.14			
E-16	2.51		2.40			
N2	2.13	2.18			2.29	
NG2	2.03	2.18			2.29	
NG3		2.16			2.26	
NG4		2.15			2.25	
NG8	1.91	2.21			2.23	
NG10	2.27	2.04			2.12	
NG12	2.30	2.76			2.81	

5.3.4 Control-Test results

All Control-Test laboratories provided very close bulk density values, with the most noticeable outlier being Lab B with 5.6% diference for the sample NEX7 (Figure 5.4). The most accurate results were delivered for the sample CHE2, with each laboratory results

falling within 2% difference. All other values fall within a 4% difference between the laboratories.

Results for grain density were exceptionally close, with the largest uncertainty coming again from the Lab B for the sample NEX7 (2.7% difference) compared to all laboratories (Figure 5.5). In contrast, the difference between the results for the sample NEX33 was just 1.1% between all laboratories. The rest samples fell within 1.9% uncertainty. Overall bulk and grain density results revealed Lab B to provide consistently lower results compared to Leeds and all other laboratories (on average by 1.5% lower for bulk and 1.4% lower for grain density) for all samples except EBN20, for which Lab B provided higher values (by 2.1% for bulk and 1% for grain densities).

Porosity results showed higher variation between the laboratories (Figure 5.6). Lab B was systematically different to Leeds and other laboratories with the 15% lower results for all the samples except NEX7 with a 21% higher result compared to Leeds and other laboratories. The results from the other laboratories were far more consistent with a 18% difference for the sample EBN20 and up to 5% difference in all other results.

	Leeds, %	Lab A, %	Lab B, %	Lab C, %
CHE2	2.53	2.51	2.50	2.51
CHE3	2.40	2.39	2.37	2.40
EBN20	2.45	2.53	2.55	2.50
NEX7	2.52	2.48	2.38	2.51
NEX15	2.44	2.48	2.46	2.49
NEX33	2.46	2.51	2.50	2.51
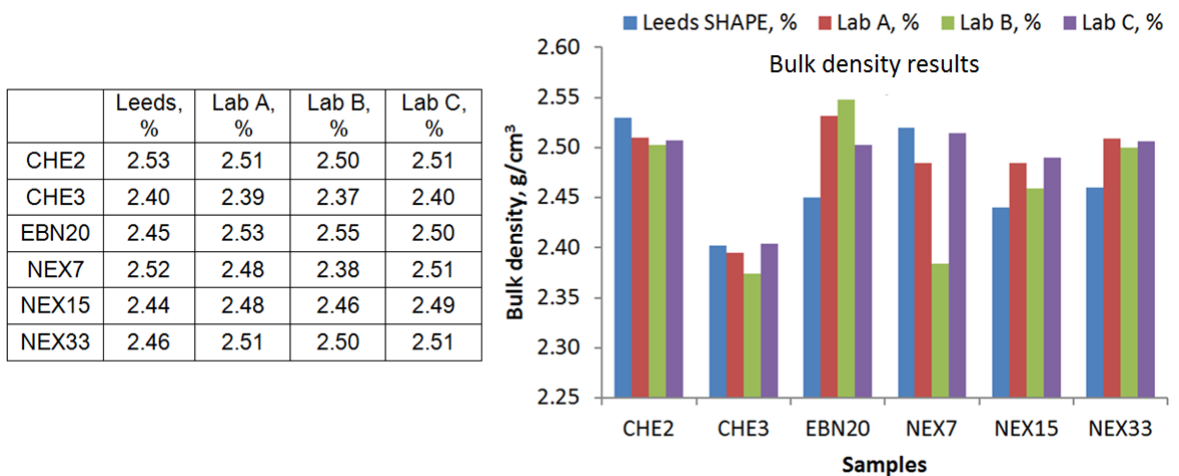
Figure 5.4. Bulk density results provided by different laboratories for Control-Test samples.

	Leeds, %	Lab A, %	Lab B, %	Lab C, %
CHE2	2.74	2.73	2.70	2.71
CHE3	2.68	2.67	2.63	2.68
EBN20	2.66	2.69	2.71	2.68
NEX7	2.59	2.63	2.57	2.64
NEX15	2.64	2.65	2.61	2.64
NEX33	2.68	2.69	2.66	2.67
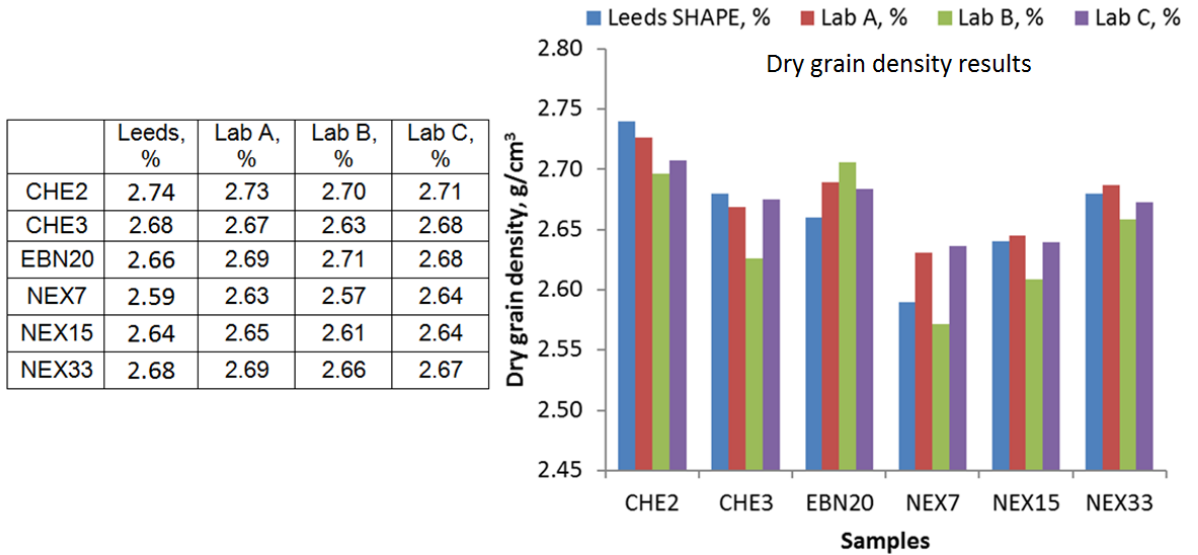
Figure 5.5. Dry grain density results provided by different laboratories for 6 samples analysed.

	Leeds, %	Lab A, %	Lab B, %	Lab C, %
CHE2	8.10	8.65	7.35	8.27
CHE3	11.10	11.09	9.99	11.23
EBN20	7.80	6.85	6.43	8.29
NEX7	6.40	6.89	8.29	6.36
NEX15	7.30	7.38	6.00	7.48
NEX33	7.10	7.46	6.50	7.53
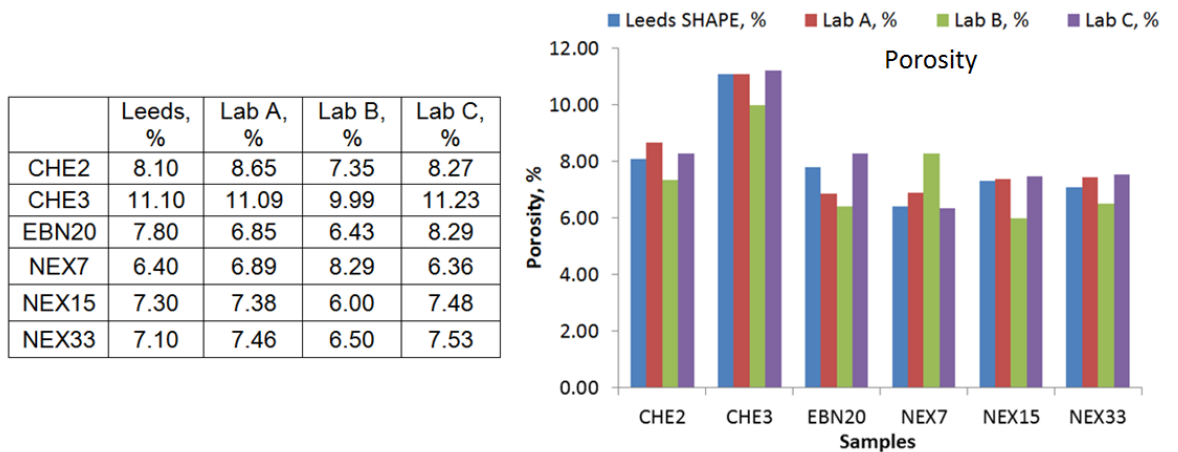
Figure 5.6. Porosity results provided by different laboratories for 6 samples analysed.

5.3.5   Density correlation comparison

The following diagrams (Figure 5.7 to Figure 5.11) were plotted to compare the bulk and grain density values obtained by various methods and different laboratories. The objective was to identify any systematic bias in the values that laboratories might be producing. It was found that crushed GRI method produces higher bulk density values than MICP and all other laboratories. On the other hand, bulk densities measured using Hg immersion were lower than other laboratories but similar to the values produced by MICP.

The crushed GRI method produced slightly higher values of grain density compared to MICP, however it gave a good match with other laboratories. MICP itself did not show a

clear bias to grain density values compared to Lab A and Lab C, however MICP produced a slightly lower value than Lab B. Grain density calculated from QXRD results was also lower compared to all laboratories and also MICP. Finally, water pycnometry produced lower grain density measurements than all other methods and laboratories except crushed GRI. The reason for this behaviour is discussed in the discussion Section 5.4.
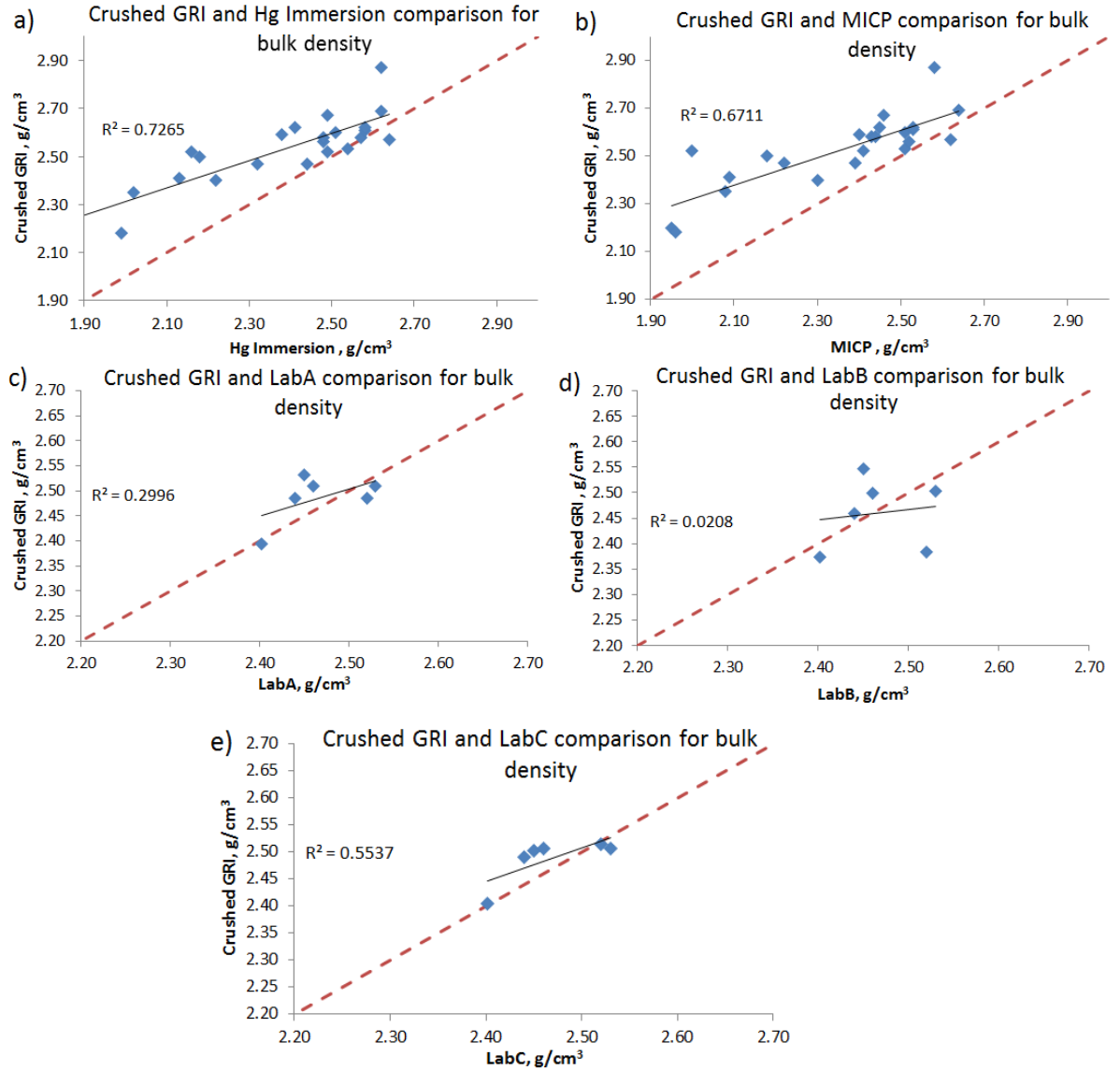
Figure 5.7. Crushed GRI bulk density comparison with Hg Immersion and MICP methods. Also provided are the correlations between control-Test companies.
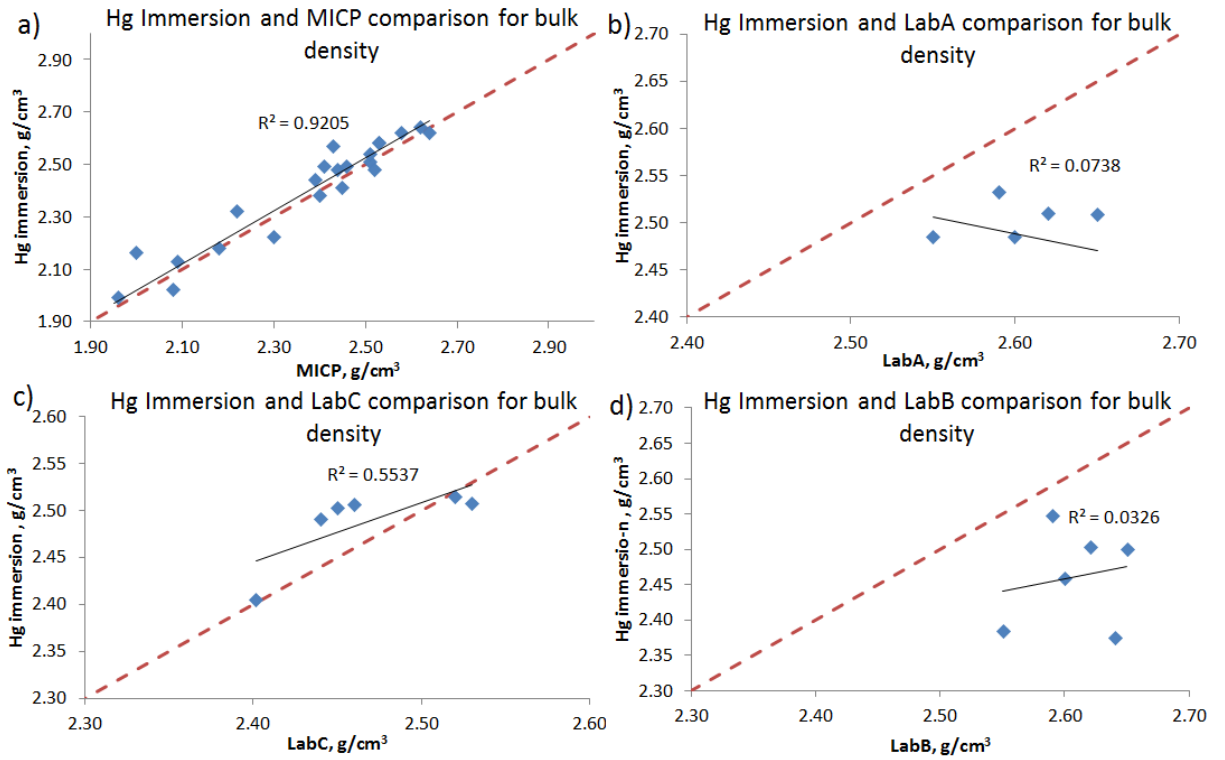
Figure 5.8. Hg immersion bulk density comparison with MICP method. Also provided are the correlations between Control-Test companies.
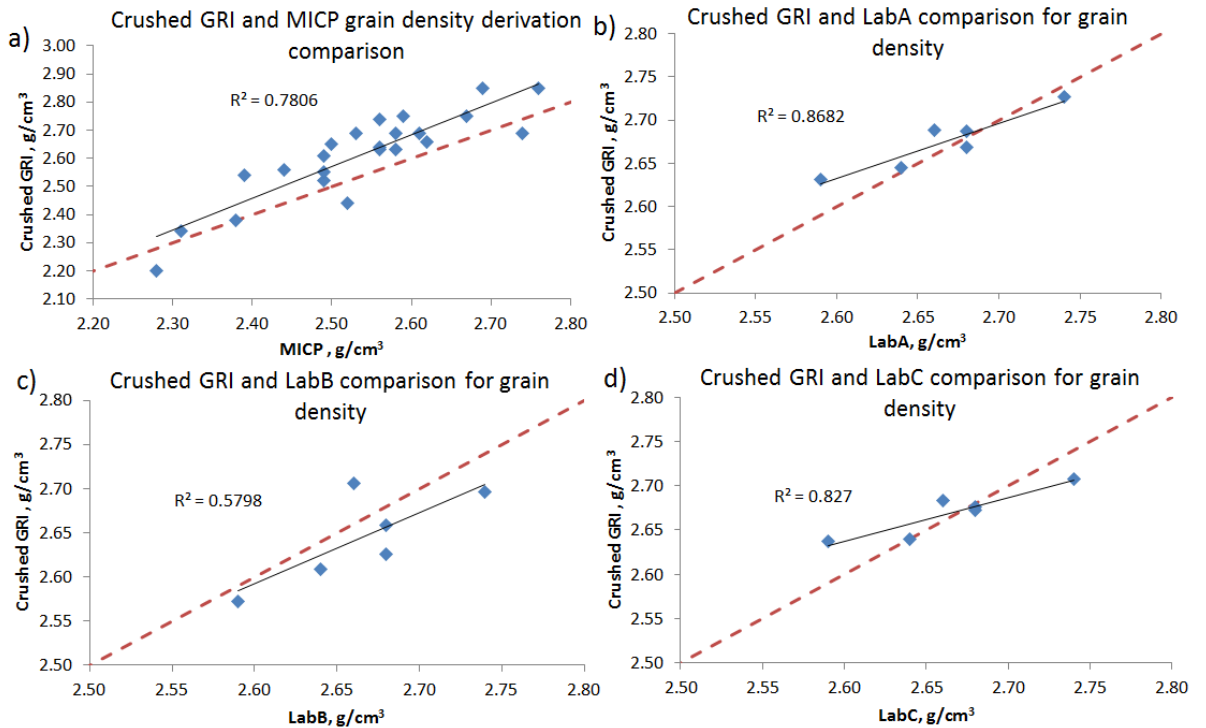
Figure 5.9. Crushed GRI grain density comparison with MICP method. Also provided are the correlations between Control-Test companies.
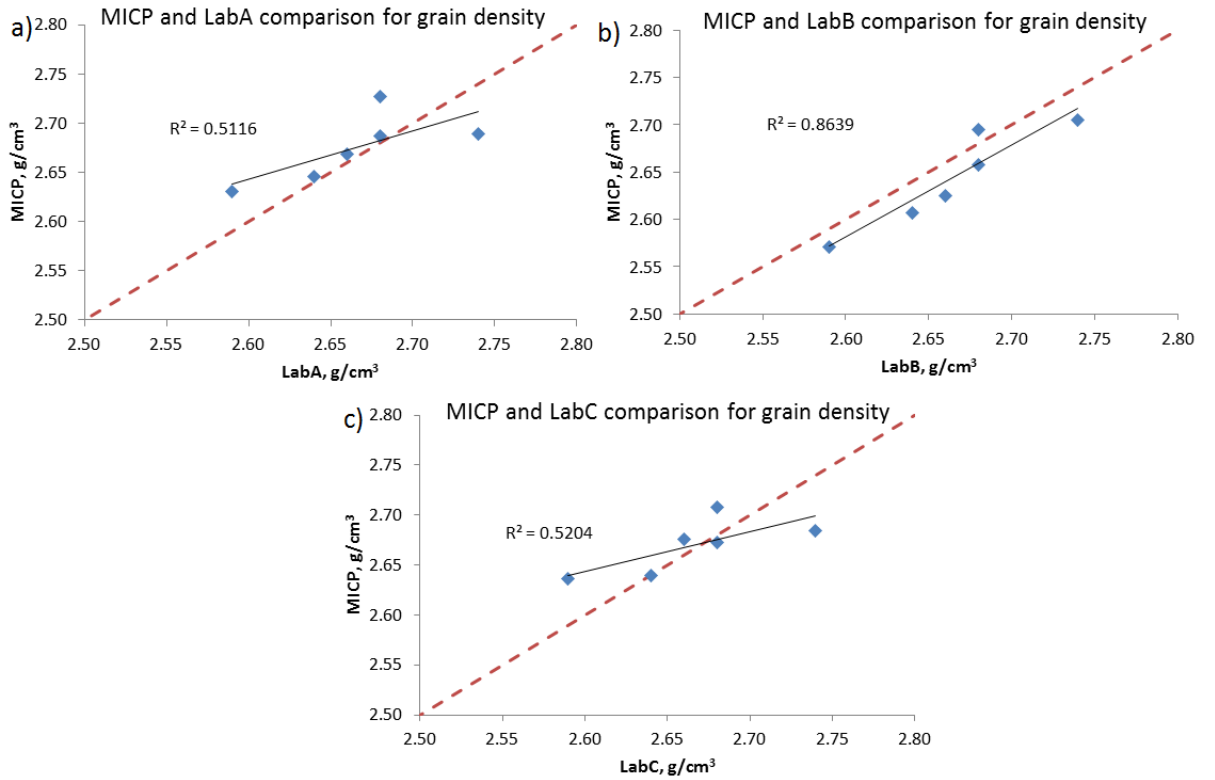
Figure 5.10. MICP grain density correlations with Control-Test results.
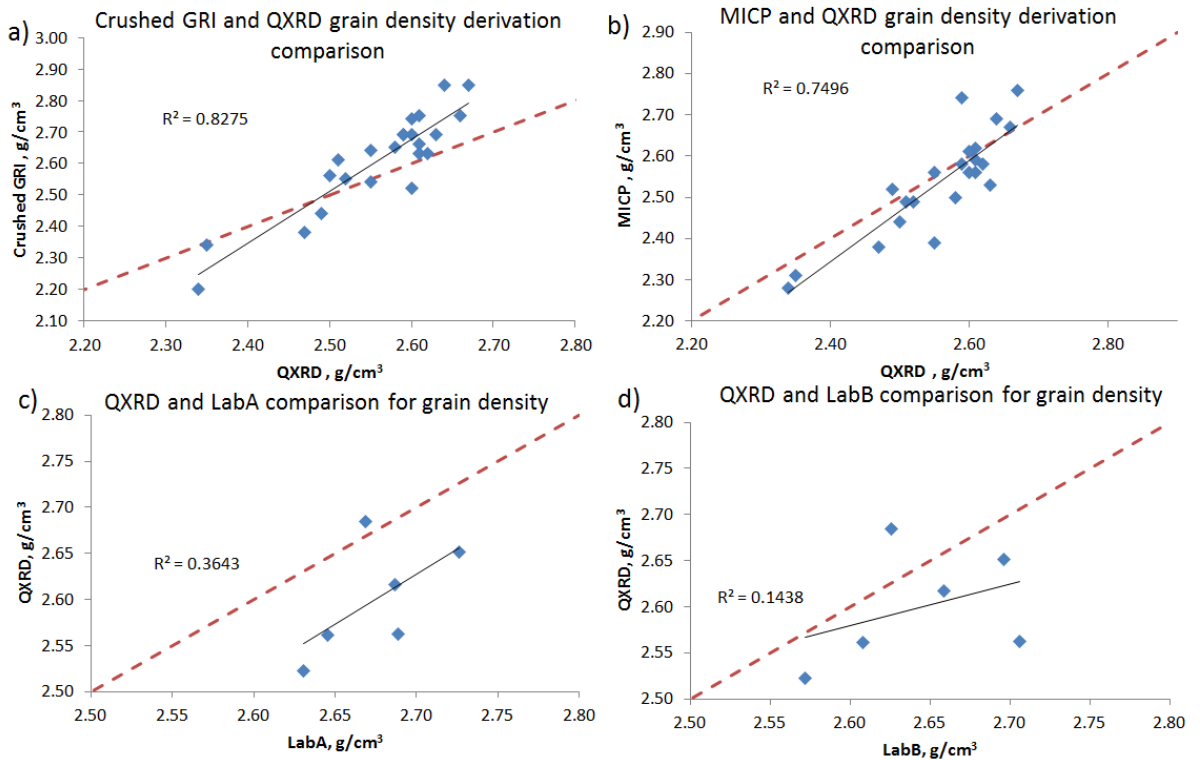
Figure 5.11. QXRD grain density correlations with crushed GRI and MICP methods. Also provided are the correlations between Control-Test companies.
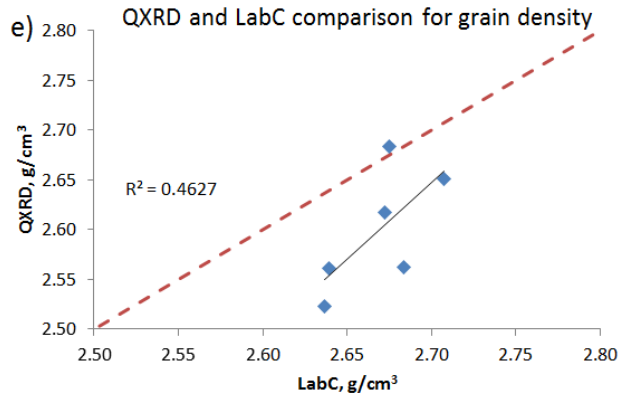
Figure 5.11.Continued. QXRD grain density correlations with crushed GRI and MICP methods. Also provided are the correlations between Control-Test companies.
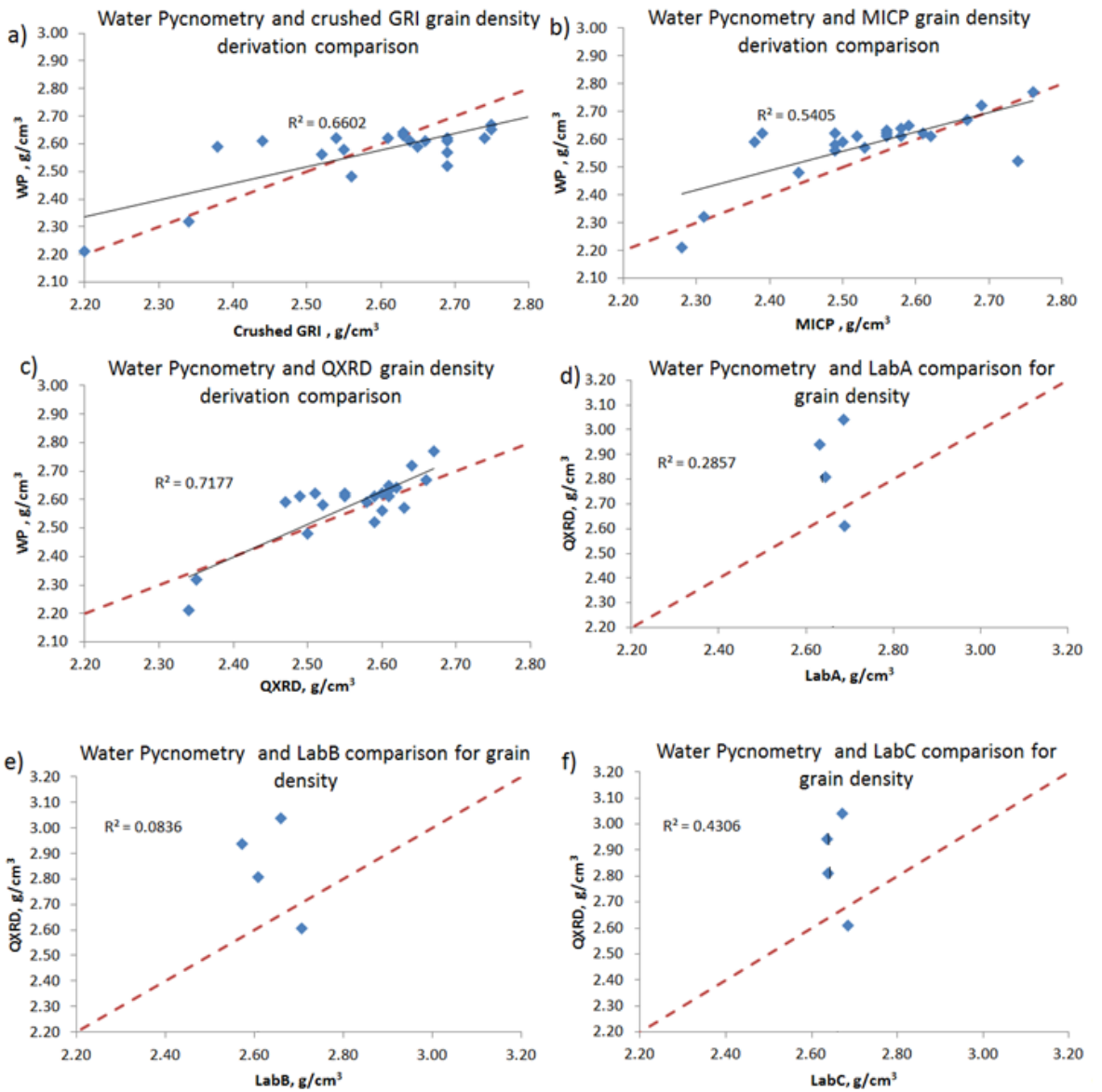
Figure 5.12. Grain density comparisons.

5.3.6 Adsorption results

Results of the adsorption experiments are presented in Figure 5.13a & b for samples whose pore volume was measured with helium and krypton respectively. Figure 5.13c shows helium calibrated results for the Gripen samples. Table 5.11 provides a summary of experimental results and also calculated Langmuir parameters. The results of desorption experiments are provided in Figure 5.14.

All samples represent Langmuir Type 1 sorption behaviour (Langmuir, 1918). Sample EBN20A, whose pore volume was measured using helium, showed continuously increasing adsorption behaviour with pressure, attaining maximum of 3.67 cm^3/g at 1200 psig. On the other hand, the NEX15 sample reached 0.14 cm^3/g at 1200 psig. It can be seen that some of the graphs are showing reduced adsorption with increasing pressure; these points are neglected from the calculations. Sample EBN20B, whose pore volume was measured using krypton, adsorbed the most methane with a value of 1.26 cm^3/g at the pressure of 1200 psig whereas NEX7b adsorbed the least methane with a value of 0.22 cm^3/g at the same pressure. E-9 and F-1 produce the highest adsorption curves among the Gripen group of samples compared to the E-16. The Gripen group of samples overall exhibits the highest adsorption values compared to all other samples.

The impact of the gas used for the calibration process on the obtained adsorption values can also be seen in Figure 5.13a & b. It can be seen that calibration with helium results in higher adsorption values than the calibration with krypton. The explanation for this phenomenon is difference in the molecular size of the gasses, as helium (molecular diameter 28 nm) being smaller can penetrate deeper in the sample where krypton (molecular diameter 40 nm) is blocked.

It can be observed that samples EBN20, CHE2, CHE3 and NEX15 showed little or almost no hysteresis (mismatch in the forward and reverse experimental behaviour) between the adsorption and desorption experiments, whereas NEX7 and NEX33 showed strong hysteresis (Figure 5.14a & e). Krypton calibrated sample EBN20B showed no hysteresis. This might indicate either complex matrix structure or experimental inaccuracies (Lancaster et al., 1993).
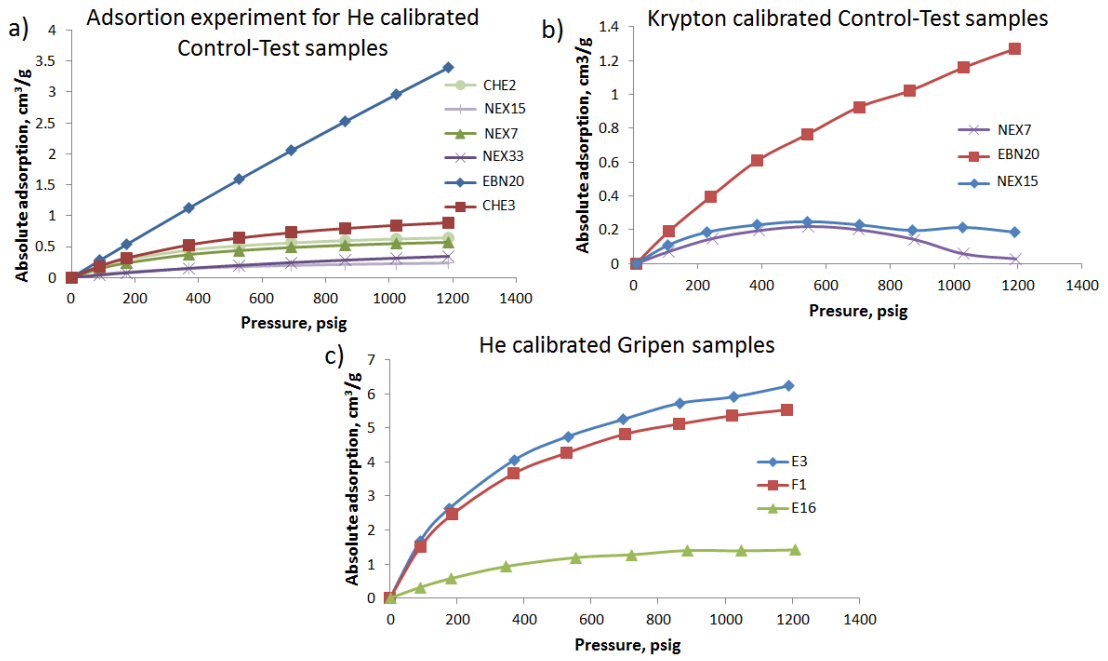
Figure 5.13. Adsorption parameters for the samples calibrated with helium (a) and krypton(b). Also adsorption results for Gripen samples are provided (c). Sample EBN20 is clear outlier, the sample showed high dolomite content of 46%, TOC of 5.67% and BET of 6.03 m^2g^{-1}. Also pore analysis showed EBN20 to contain mostly organic type of pores.

Table 5.11. Summary of adsorption experiments.

Sample	Exp. Cal. He Density, g/cm3	Exp. Cal. Kr Density, g/cm3	Max. Exp. Pressure, psig	Max. Abs Ads, cm3/g	V_L, cm3/g	PL, kPa
EBN20	2.67		1256.2	3.67	39.56	87226.0
CHE2	2.69		1194.1	0.56	0.81	2100.7
CHE3	2.72		1196.0	0.78	1.29	3654.7
NEX7	2.72	2.64	1242.7	0.59	0.75	2609.0
NEX15	2.61		1063.0	0.18	0.33	3106.0
NEX33	2.75	2.63	1189.7	0.34	0.82	11315.0
E-3	2.24		1187.2	6.23	8.01	2446.0
F-1	2.14		1184.5	5.53	7.15	2391.5
E-16	2.40		1205.4	1.42	2.00	2683.1
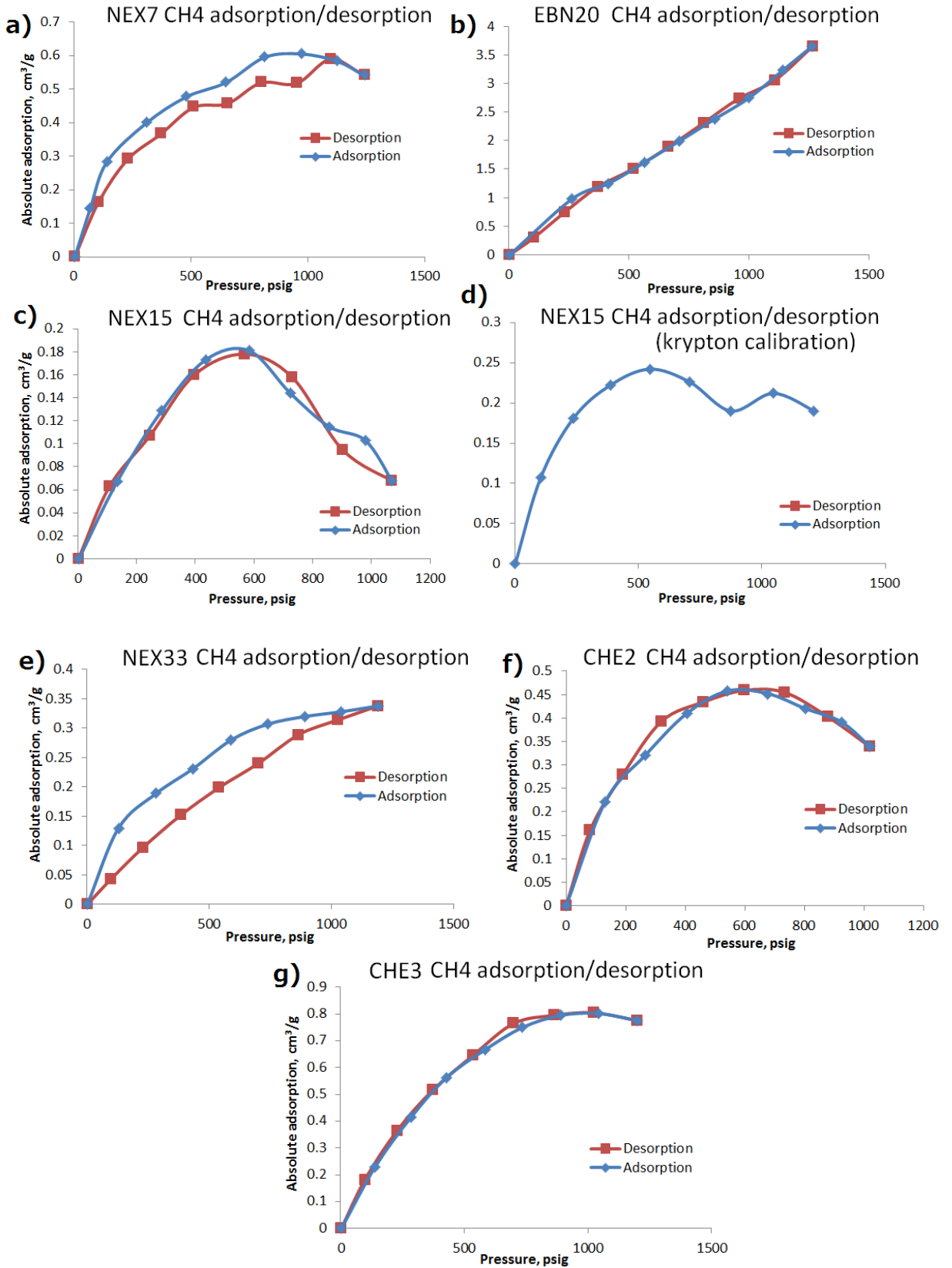
Figure 5.14. Adsorption results of the Control-Test samples measured with methane gas. All samples were calibrated with helium gas, NEX15 was additionally calibrated with krypton gas.

5.3.7 Desorption results

Table 5.12 and Table 5.13 present the desorbed core pressure values (see Section 3.7.1) at a range of different depths for samples from wells KN-1 and FA-2. Well KN-1 has 17 pressure values over the depth range of 85 - 104 m, whereas well FA-2 has 10 pressure values over the range of 72 - 84 m. These values were used to derive the volumes of gas stored in both pore space and adsorbed volume by using Langmuir parameters and porosity values.

The long-term desorption tests were also conducted on cores from other wells and are presented in Figure 5.15 and Figure 5.16. One desorption experiment lasted about 6 months, during which more than 330 psig of methane had accumulated (Figure 5.15). The gas was then vented out from the canister and the second desorption experiment produced 50 psig of gas (Figure 5.16). Finally, the gas was vented out again and the adsorption experiment was attempted: 104 psig pressure was applied on the core and the pressure reduction was monitored (Figure 5.17).

Table 5.12. KN-1 gas desorption results.

Depth, m	Pressure, psig	Depth, m	Pressure, psig
85	5.0	97	1.4
89	1.0	98	13.4
90	5.0	99	6.1
91	2.5	100	15.0
92	31.7	101	2.0
93	70.0	102	2.5
94	2.6	103	2.0
95	7.7	104	1.0
96	22.6		

Table 5.13. FA-2 gas desorption results.

Depth, m	Pressure, psig
72	1.6
73	48.0
75	14.2
76	11.4
77	0.6
79	25.0
80	0.3
81	19.1
82	3.2
84	13.1

130

Desorption experiment
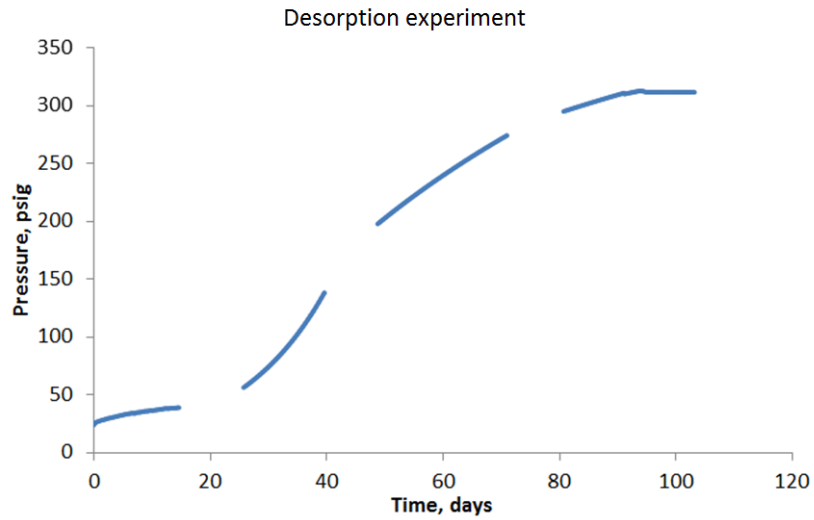
Figure 5.15. Long-term core desorption experiment. The gaps in the curve denote missing data as the pressure was recorded periodically due to extended measurement time.

Desorption experiment
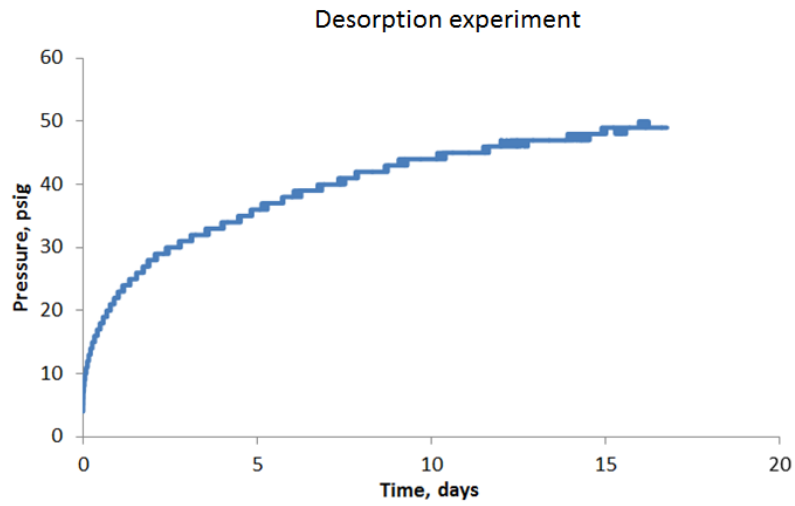
Figure 5.16. Second long-term desorption experiment. Note fundamentally different gas accumulate rate from the first accumulation.

Long term core pressure decay
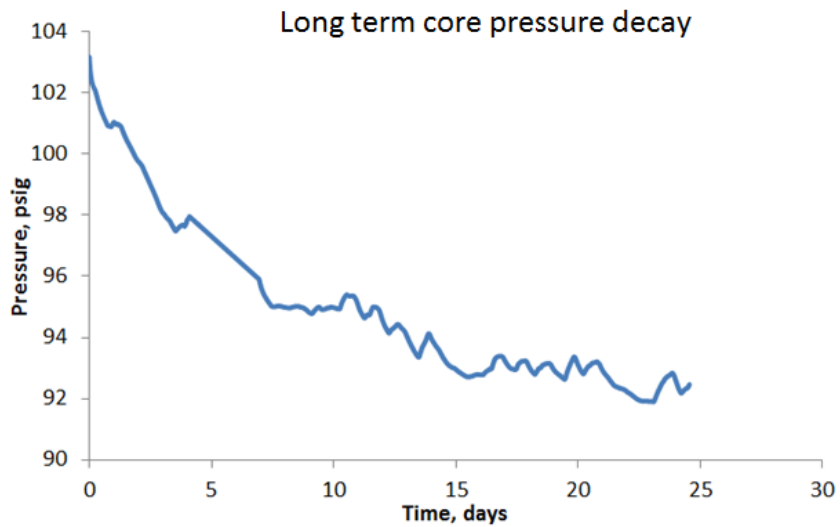
Figure 5.17. Long-term adsorption experiment done on the core sealed in the canister.

5.4 Discussion

Two major observations can be made from the obtained results, which in turn can lay the framework for the discussion. The first observation is that the results showed that 3 out of 4 laboratories (including Leeds) produced very similar values for grain density, bulk density and porosity (see Figure 5.4; Figure 5.5 and Figure 5.6 in Section 5.3.4). The comparison of standard deviations of each laboratory from the average of the other laboratories is provided in Figure 5.18. The level of precision obtained shown in Figure 5.18 is comparable to the API standards for sandstones (orange bar in Figure 5.18) (API, 1998).
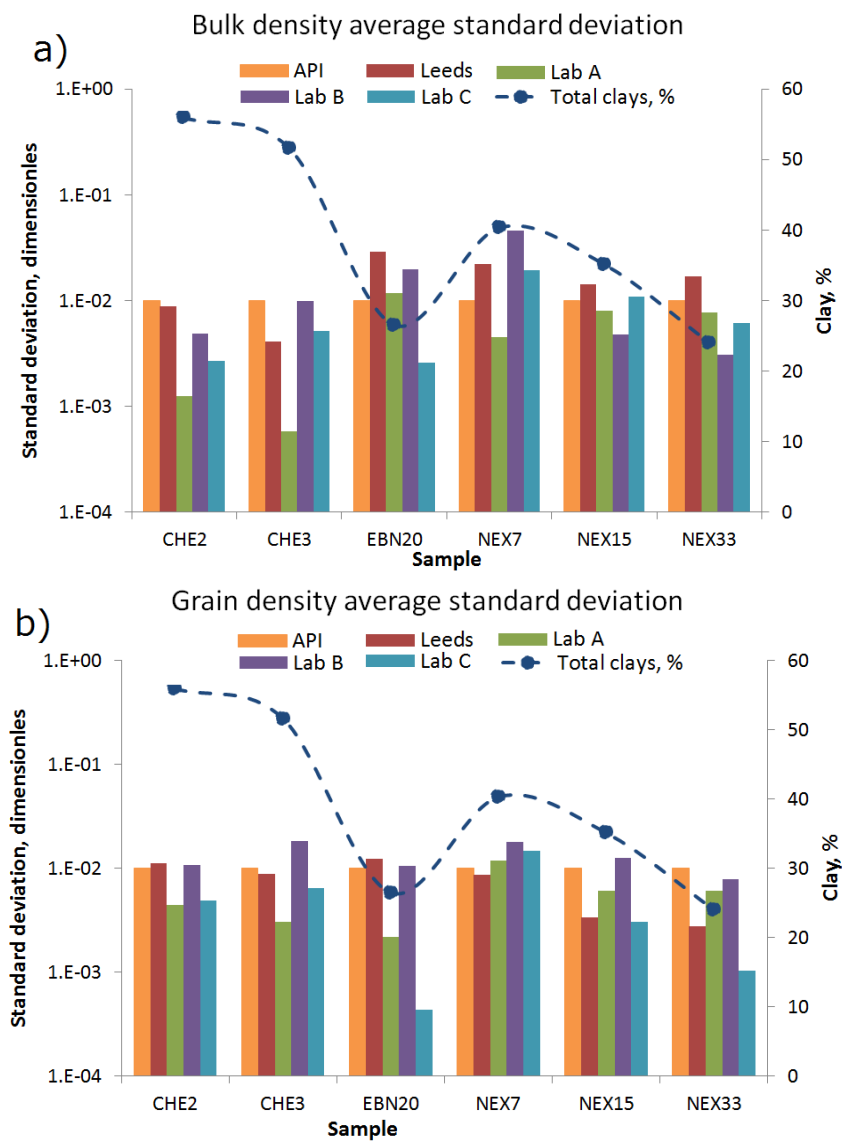
Figure 5.18. Comparison of average standard deviations between laboratory measurements. Amount of clays is overlain for comparison.
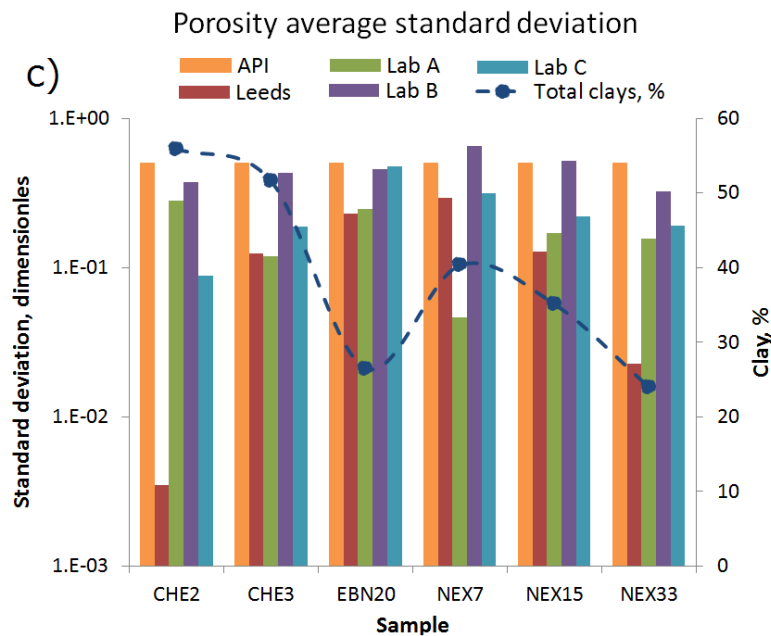
Figure 5.18. Continued. Comparison of average standard deviations between laboratory measurements.

The second observation is that Lab B values (both density and porosity) show repeatedly different results from the other laboratories and from Leeds values. Numerous studies have shown that systematic inconsistencies in porosity measurements may occur due to different sample cleaning techniques - more specifically the use of solvent extraction may remove clay bound water (Handwerger et al., 2011; Lalanne et al., 2014).

Lab B was the only laboratory to apply retort method on the samples, which according to the literature might be the reason for systematic inaccuracies shown by this laboratoty. However clay-bound water is not the reason for the inaccuracies between the cleaning methods, despite the clays being abundant in all tested samples. There is no noticeable correlation between the amount of clays and average standard deviations between the Control-Test results as shown in Figure 5.18. Instead, it is likely, that the retort method used by the Lab B did not remove sufficient amount of water because it was not run for the sufficient amount of time.

5.4.1 Density

The presented density correlations between various methods (see Section 5.3.5) imply these differences to be systematic, i.e. grain and bulk density values vary depending on the measurement method. For instance, bulk volume measurements are not made under the stress, therefore much of the artificial porosity (microfractures, as discussed in Chapter 4) are included into the measured porosity, therefore bulk volume is

overestimated. The section below analyses each method and suggests the most optimum solution for the density and porosity measurements.

5.4.1.1 Bulk density

All bulk density measurements contained some level of errors as showed by the standard deviations between Leeds and Control-Test values (Table 5.14). Hg immersion is measured on the as-received core plugs, whereas crushed GRI – derived bulk density values were obtained using dried samples (see Section 3.2.2). Therefore the difference in sample mass due to lost water should reduce crushed GRI bulk density values compared to Hg immersion. However Figure 5.7a (see Section 5.3.5) reveals that crushed GRI produced higher bulk density values compared to Hg immersion.

Table 5.14. Average standard deviations for bulk density.

Test	Hg-immersion	MICP	GRI
Average standard deviation	0.03	0.03	0.06

Both Hg immersion and crushed GRI are conducted at ambient conditions so artificial fractures are likely to affect the bulk volume. In fact, presence of microfractures would underestimate bulk volume (overestimate bulk density) as gas intrudes the microfractures unnocited, whereas in the case of Hg-immersion mercury does not intrude microfractures and overestimates sample bulk volume (underestimate bulk density). In this case microfractures explain the higher crushed GRI values compared to Hg-immersion in Figure 5.7a (see Section 5.3.5).

Comparison of Hg-immersion bulk volume values used to estimate experimental pressures P2 (applying Boyle's law) with the same pressures obtained by GRI extrapolation method (see Section 3.4.3) is shown in Table 5.15. The difference in unnacounted pressure by the GRI method is provided in the last column. NEX13, NEX33 and CHE3 samples show the largest unnacounted pressure differences between the Hg immersion and GRI methods, possibly caused by the microfractures. However the cross-comparison of this pressure difference with the fraction of artifical porosity, derived from SEM analysis (see Table 4.5 in Section 4.4.1.1), does not reveal any noticeable correlations. In fact, it may be the presence of different lithologies within the shale matrix (observed in the CT scans Figures 4.12 and 4.13 in Section 4.3.4) that are affecting the GRI method and causing faster decay into the sample matrix. Chapter 6 further explores highly conductive regions in terms of modelling and permeability.

Table 5.15. Comparison of Hg immersion and GRI derived pressures. P2 from Hg immersion were obtained from the weight and bulk density of the sample, whereas P2 extrapolated were estimated using the extrapolation method showed in Figure 3.5.

Sample	Pressure, psig			
	P1	P2 (Boyle's + Hg Immersion)	P2 GRI extrapolated squared time	Missed GRI vs Hg Immersion
CHE2	149.90	72.13	71.10	1.03
	154.54	77.99	77.26	0.73
	150.68	74.27	73.51	0.76
CHE3	150.10	72.21	70.25	1.96
	149.20	71.62	69.30	2.32
	150.39	69.38	68.11	1.27
EBN20	243.79	114.06	113.34	0.72
	238.87	117.28	118.01	-0.73
	229.32	116.08	114.57	1.51
NEX7	184.53	90.66	90.00	0.66
	167.40	82.24	81.82	0.42
	145.26	71.20	70.70	0.50
NEX15	146.30	70.52	68.62	1.90
	175.14	84.42	82.10	2.32
	152.28	73.40	71.40	2.00
	150.50	75.61	73.60	2.01
NEX33	192.04	101.76	98.75	3.01
	190.90	101.15	98.33	2.82
	233.08	121.17	121.10	0.07
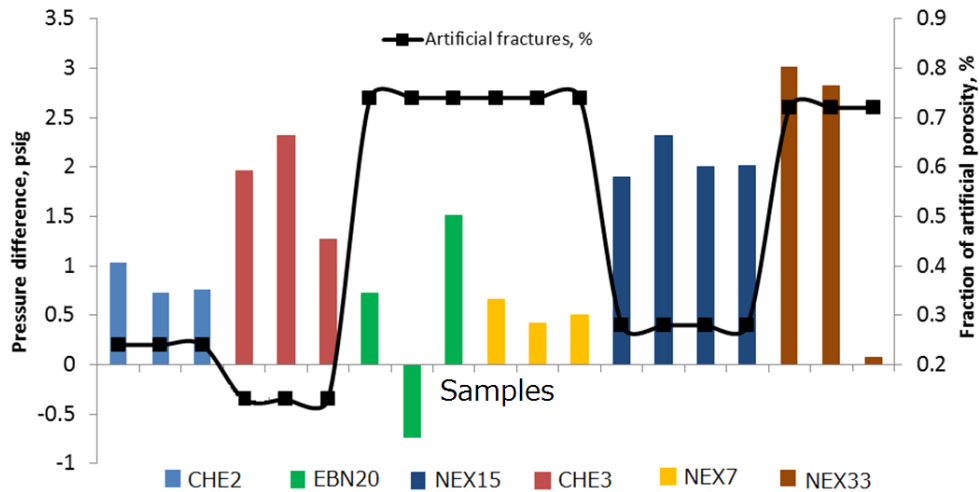
Figure 5.19. Comparison of pressure differences obtained by using Hg-immersion and GRI bulk volumes with the amount of identified microfractures. Crushed GRI pressure P2 was higher than P2 estimated by Hg-immersion. Probable reason for that was the extrapolation method used for crushed GRI estimations, which might have overestimated the pressure.

MICP (Mercury Injection Capillary Pressure) bulk density results were lower than both Hg-immersion and GRI (see Figure 5.7b and Figure 5.8a in Section 5.3.5). It has to be noted that MICP may be equally affected by the microfractures increasing bulk volume thus reducing bulk density. However some properties of the shale matrix, such as ultra-small pores, can be exploited in favour of shale characterisation when using MICP. If the pores are small enough, mercury will not be able to intrude the sample at the initial stages of injection. Instead, the mercury will compress the sample, which in turn might close cracks and provide shale bulk density at elevated confining pressure (i.e. reservoir conditions). Amann-Hildenbrand et al. (2016) indeed showed that shale samples are likely to be compressed during the MICP test and not intrude the pores. This means that MICP results for the shale samples could be interpreted as compaction instead of intrusion, therefore the obtained results could be interpreted as bulk volume and bulk density values of the shale at the *in-situ* stress.

5.4.1.2 Grain density

Crushed GRI can be successfully applied for the calculation of the grain density values of shale samples. Comparison of grain density values from other methods and Control-Test laboratories reveal GRI method to be among the most consistent and show the best

correlation coefficients (see Figures 5.9; 5.10 and 5.11 in Section 5.3.5) and to have the lowest average standard deviation (Table 5.16).

Table 5.16. Comparison of standard deviation of grain density for different experiments.

Test	QXRD	MICP	GRI	WP
Average standard deviation, dimensionless	0.03	0.03	0.02	0.08

Table 5.16 reveals GRI standard deviation to be comparable to QXRD, which is important as QXRD provides an independent grain density measure, which, unlike gas expansion measurements, is not affected by small or isolated pores. The biggest uncertainty with QXRD method arises from the assumption of the density values for clays, organic matter and minerals with complex solid solution ranges such as dolomite (see Table 4.2 in Section 4.3.1). It has to be noted that majority of the crushed GRI pressure curves showed equilibrium at the end of the tests (Appendix J). This all indicates that crushed GRI is most likely not affected by the ineffective saturation when measuring helium uptake by shale.

Grain density determined using the GRI method is higher by around 0.09 g/cm^3 (or about 4%, see Figure 5.9a in Section 5.3.5) than measured by MICP. MICP has a tendency to underestimate grain density values, which might be caused by mercury not entering all the pore spaces within shale as discussed in the previous section. Indeed, many isolated pores were identified in the SEM images of the samples, which may not be accessible by gas or mercury (see Figure 4.17 to Figure 4.23 in Section 4.3). Small nano-scale pores are most probably present but were not identified with the SEM given the resolution restrictions of the obtained images. This is proven by the porosity differences between SEM-derived porosity values (see Table 4.5 in Section 4.4.1.1) and GRI-derived porosity values (see Section 5.4.2). The presence of small pores might be exploited in favour of the bulk volume measurement using mercury injection (MICP) method.

MICP method requires pore throats larger than 3 nm for the mercury to intrude (Aboujafar, 2009; Kuila, 2013). In case shale matrix is dominated by smaller pores such that mercury is not able to intrude and the theory of sample compaction becomes viable (Amann-Hildenbrand et al., 2016). Many authors have indeed suggested that smaller than 3 nm pores do occur in shales (Javadpour, 2009; Kuila, 2013).

5.4.1.3 Water pycnometry for grain density

The grain density results obtained from water pycnometry experiment showed the widest spread of values when plotted against pressure expansion, MICP and Control-Test results

(see Figure 5.12 in Section 5.3.5). Nevertheless, there is no clear trend for this method thereby producing higher to lower grain densies compared to the other tests. However, this method is likely to suffer from the same pore size and pore connectivity issues as the other two methods because it also depends on the effective saturation of the. Furthermore, it was noticed that the ambient temperature has a great impact on the results, and a 1°C change in temperature might cause the density measurement to be in error by 0.1 g/cm^3. On the other hand, the experiment has a potential for greater accuracy when a better temperature regulatory system is installed. Nevertheless, the obtained correlations are reasonable considering the simplicity of the method. Essentially, water pycnometry is a cheap and easy method for generating grain density values.

5.4.2   Porosity and gas storage mechanisms

This section discusses and suggests that shale porosity can be well characterised using the crushed GRI method. The main arguments for this statement are that crushed GRI is faster, more precise and the results obtained can be easily quality controlled when compared to the core plug pressure expansion methods. However, there are still several issues with crushed particles, such as the assumptions regarding the matrix integrity and microfractures, which in turn cause errors for the bulk volume measured at the no-stress conditions. Nevertheless, it is argued in this section that the crushed GRI method provides repeatable and logical results and is able to produce good shale porosity estimation for the improved understanding of the gas storage in shales.

5.4.2.1   Crushed and core plug methods

A total of 485 crushed GRI and 174 core plug GRI experiments conducted during this research indicate that both methods can produce highly variable results (see Sections 5.3.1 and 5.3.2). An attempt was made to identify any trends within this data by sorting the porosity results by the applied pressure, fracture presence, type of sample etc., however the data remained very scattered without obvious correlations. The average crushed porosity values differed by around 20% from the Control-Test values (Table 5.17), whereas core plugs differed by around 30%, with some of the core plug methods resulting in more than 60% higher or lower porosity values. Passey et al. (2010) also presented very similar porosity uncertainty of 30% between the measurements from different laboratories.

Several other authors agree that crushed GRI analysis provided more consistent porosity values than other methods (Karastathis, 2007; Sondergeld et al., 2010). Karastathis (2007)

conducted similar experiments on the crushed samples using helium gas and stated that crushed shale samples of size around 40 µm produce reasonable and consistent porosity values. However, in this research it was found that particle size between 500-850 µm is the most optimum: lower sized particles produce pressure decay, which is difficult to record whereas samples with larger size shale fragments take longer to equilibrate, which in turn increases the risk of leakage issues.

Table 5.17. Uncertainty comparison of different methods relative to the Control-Test results.

Sample	Control-Test			Leeds crushed				Leeds core plug GRI		
	Lab A	Lab B	Lab C	Average	stdev	Uncertainty from Control-Test,%	Best fit	Average	stdev	Uncertainty from Control-Test,%
CHE2	8.65	7.35	8.27	8.31	1.33	11.55	8.25	8.97	4.51	18.06
CHE3	11.09	9.99	11.23	11.71	1.51	14.69	9.90	8.75	1.14	22.08
EBN20	6.85	6.43	8.29	5.54	1.68	33.17	6.20	6.43	2.22	22.44
NEX7	6.89	8.29	6.36	5.96	1.59	28.11	7.10			
NEX15	7.38	6.00	7.48	7.55	1.11	20.53	6.30			
NEX33	7.46	6.50	7.53	7.46	1.16	12.87	7.70	17.44	3.34	62.73

These inaccuracy problems are reflected in the experimental pressure decay graphs in Appendix J – in some cases the best fit model misses the final equilibrium point, in others leakage occurred. The porosity data get much closer to the Control-Test results if only the very best fit graphs are selected (Figure 5.20). This indicates that for accurate porosity values, only the very best fitting pressure decay curves have to be used, instead of performing several experiments and averaging the values.
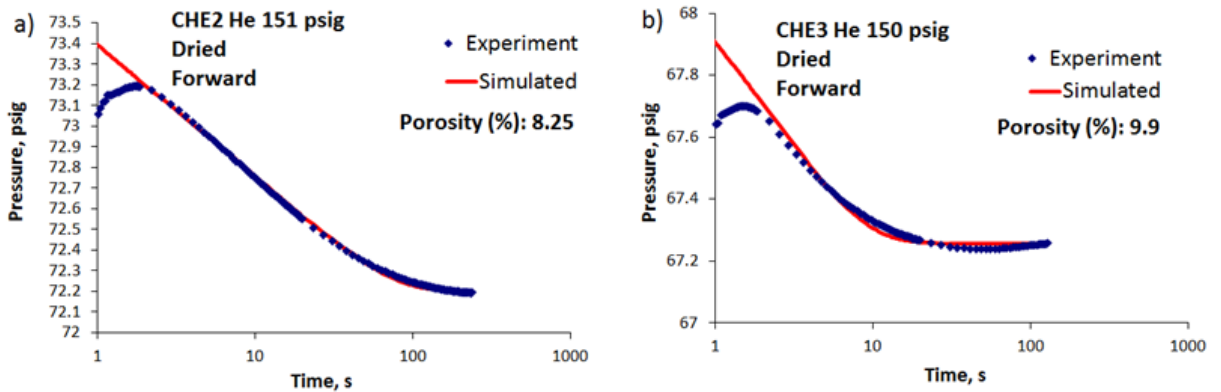
Figure 5.20. Selected best fit pressure decay curves for each Control-Test sample.
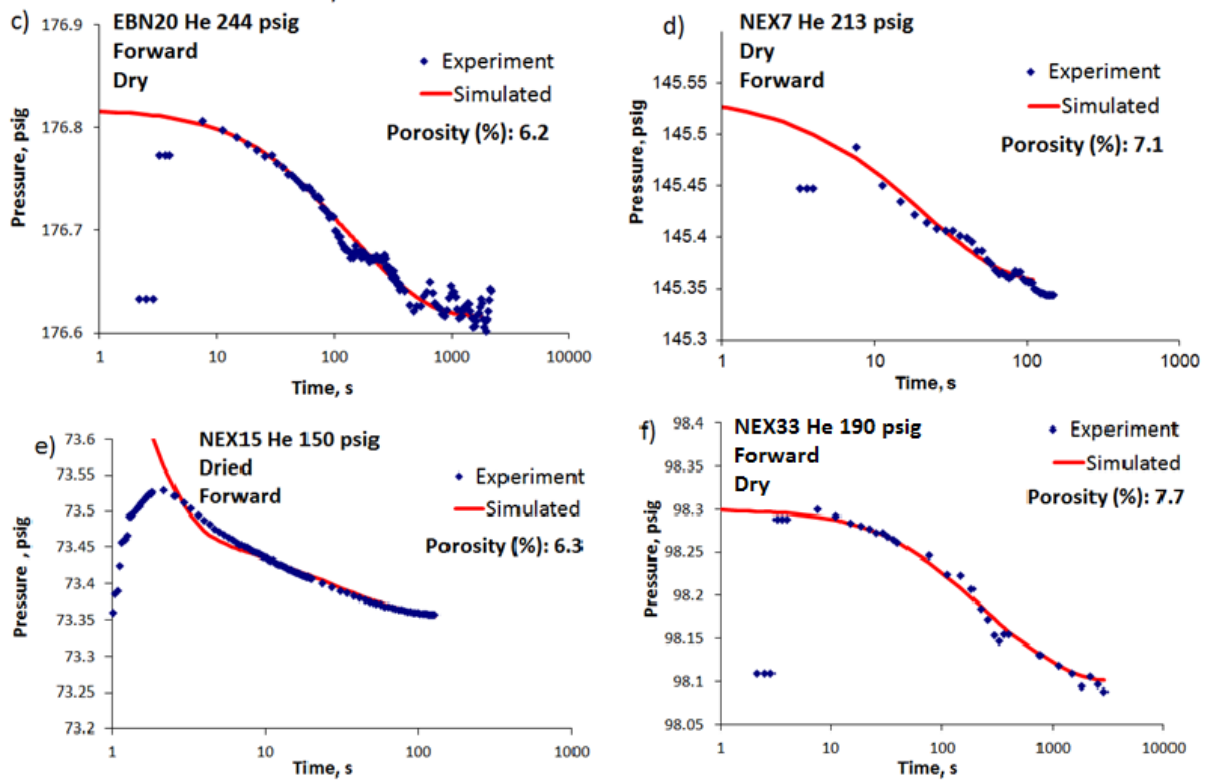
Figure 5.20 Continued. Selected best fit pressure decay curves for each Control-Test sample.

5.4.2.2 Pressure curve analysis

Pressure transients from crushed samples (Appendix J) suggest that pressure equilibration occurs within the first 1000 seconds (around 15 min). In comparison, it takes several hours to days for the core plug tests to show this type of equilibration (Appendix O and Appendix P). Essentially, it becomes challenging to distinguish between the pressure decay into the core matrix and the leakage out of the system over this extended period of time. In contrast, there is a sufficient amount of certainty that during the first 15 minutes of the crushed GRI experiment the leakage is not considerably affecting the system (see leakage tests in Section 3.4.4.4).

Figure 5.21 demonstrates the ability of the reverse experiment to verify the mass balance by comparing forward and reverse pressure build-ups. Figure 5.21a & b show the experiment where the porosity obtained from the reverse test matched the one derived from the forward test. This indicates a high level of confidence for this porosity value as the gas movement in and out of the sample matrix can be proved. In comparison Figure 5.21c & d demonstrates the case when the amount of gas intruding the shale matrix was overestimated, as the forward test provides a higher porosity value than the one obtained by the reverse test. This type of result might be caused either by the leakage from the

system, or insufficient experiment time given for the reverse test, as not all the gas that penetrated the sample during the pressure decay might have desorbed from the sample. The latter option is more likely as good pressure equilibrium was achieved during the forward test, indicating no leakage from the system. Reverse experiments are taking longer to equilibrate due to the experimental set-up: during pressure series experiment, a number of forward tests are conducted one after the other, followed by the reverse test. Therefore there is more of the gas in the compressible storage to be relesead during the reverse test compared to any of the forwards tests, which consequently takes more time to equilibrate.

Finally, Figure 5.21e & f shows the case when the forward experiment underestimated the amount of gas penetrating the matrix, as it produced lower porosity value than the reverse test. This might be caused by gas entering high conductivity region within the shale matrix faster than the pressure transducer could record it. However the unaccounted gas is disclosed during the reverse test, producing corrected porosity values.
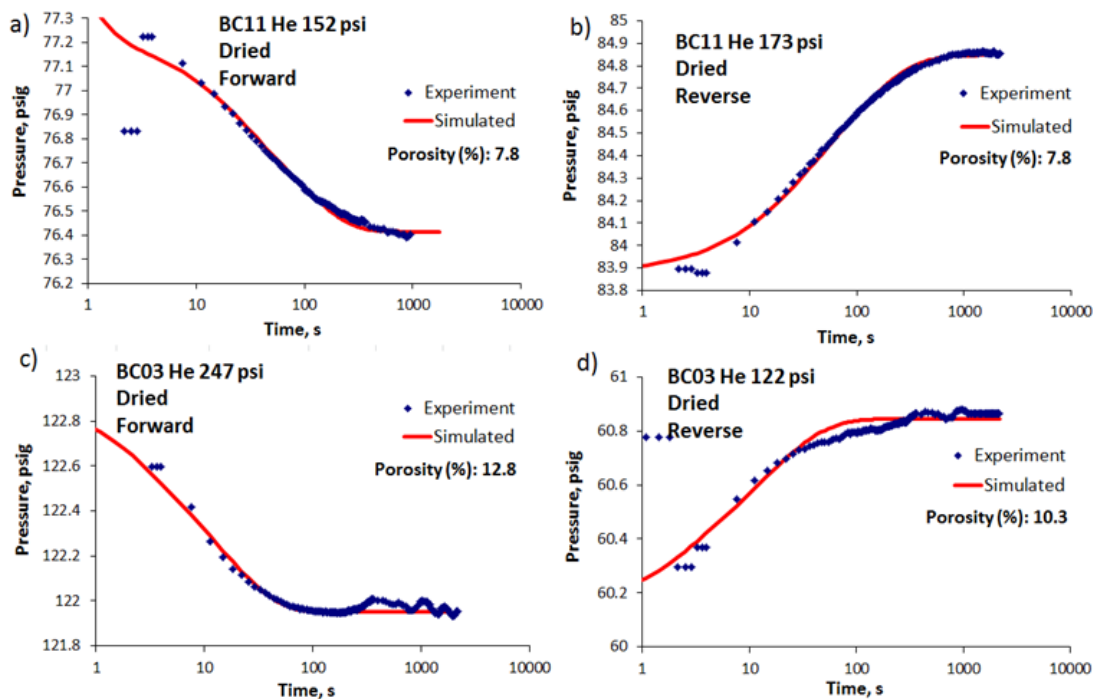
Figure 5.21. Quality check of the crushed porosity values.
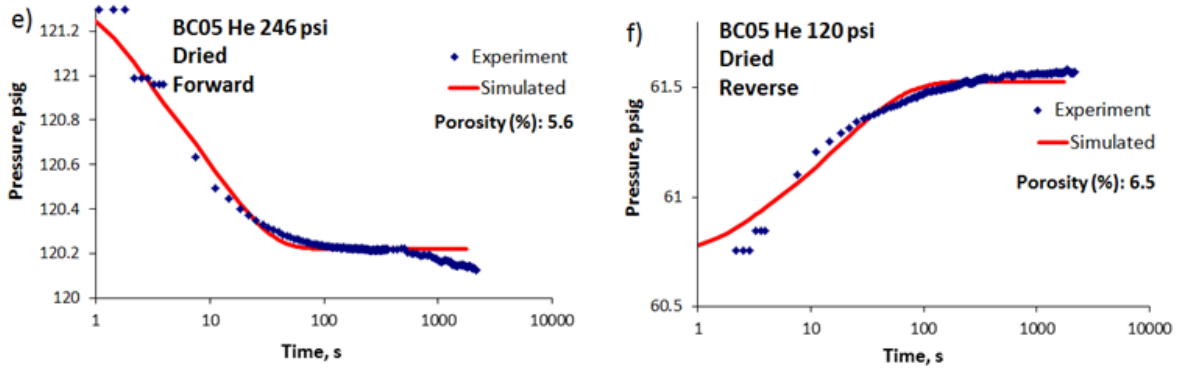
Figure 5.21. Continued. Quality check of the crushed porosity values.

The confidence level of QC using the reverse method is high. This is proved by the statistical analysis of crushed GRI forward and reverse methods in Table 5.18, where reverse results show good repeatability (low deviation from the average value) and close similarity to the values obtained from samples subjected to the Control-Test (lower percentage difference). Therefore the combination of forward and reverse tests have the potential to provide consistent shale porosity values with low uncertainty margin.

Table 5.18. Porosity comparison of crushed GRI forward (for) and reverse (rev) methods. All results are provided in Appendix K.

Sample	Control-Test,%			Leeds					
	Lab A	Lab B	Lab C	Crushed for,%	For stdev	Differenc from control-test, %	Crushed rev, %	Rev stdev	Difference from control-test,%
CHE2	8.70	7.30	8.30	8.35	1.35	12.68	7.00	0.26	6.45
CHE3	11.10	10.00	11.20	11.01	1.42	9.98	10.90	0.04	9.84
NEX7	6.90	8.30	6.40	6.58	1.10	28.11	6.20	0.67	7.59
NEX15	7.40	6.00	7.50	7.76	0.89	13.74	7.10	0.40	8.22
NEX33	7.50	6.50	7.50	7.72	1.27	15.84	5.60	0.93	5.7

5.4.2.3 Impact of sample drying on crushed shale GRI results

Water in various states (free, adsorbed, capillary etc.) may occupy a considerable amount of the shale porosity. The affinity of this porosity for water may vary greatly due to the compositional heterogeneity of shale (Kumar et al., 2015). This in turn complicates the core analysis and consequently pore space calculations as it becomes unclear what is the natural connate water saturation within the shale matrix.

To standardise the measurements, shale samples are usually oven dried to remove water and avoid errors (Kumar et al., 2015). This ensures that the same pore volume is

142

measured and compared by different laboratories. The obvious drawback of using dried samples for porosity estimation is that it is unclear how much water needs to be removed if at all to correctly measure the pore volume storing gas.

Shale samples are very susceptible for the water imbibition from the moisture within the atmosphere. Their susceptiblitity to imbibition stems from the narrow pore sizes which leads to higher capilary pressures. Water adsorption experiments were carried out on several shale samples to test the rate of moisture absorption. The amount of adsorbed water increases sharply during the first hours (Figure 5.22). Therefore drying the sample restores the reference point of the moisture and pore space within the matrix that can be measured and compared by different laboratories.
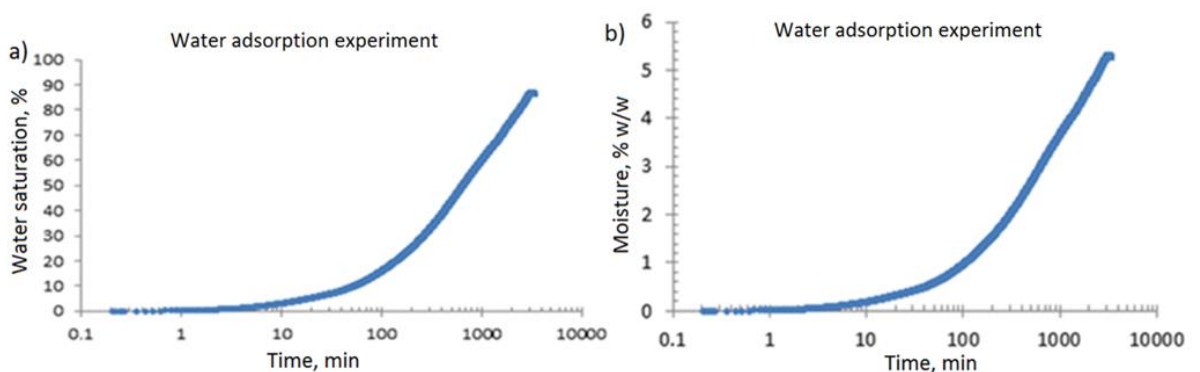
Figure 5.22. Water adsorption experimental graphs for the crushed sample EBN20. Significant moisture absorption by the shale samples can be observed.

The procedure for sample drying is faster for crushed samples than core plugs because of the larger surface area available. However, the surface area also affects crushed samples as different sized-particles impact the gas penetration into the matrix. Figure 5.23 provides a comparison of the porosity results of differently sized dry and wet (i.e. non-dried or in as-received conditions) shale particles.
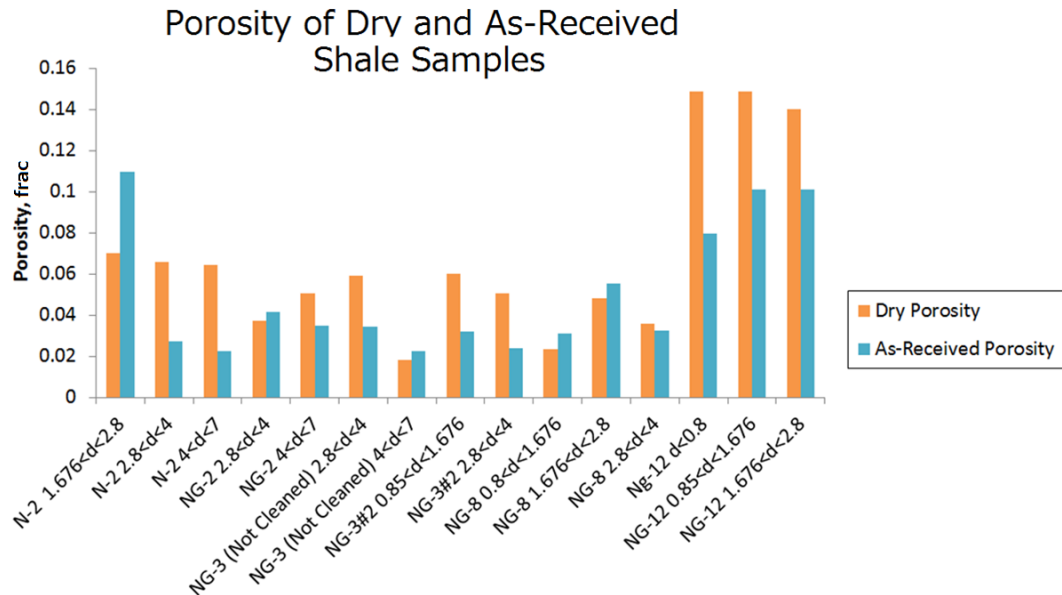
Figure 5.23. Porosity comparison for As-Received (wet) and dry samples. Dried samples showed 1.5 stdev while AR samples showed 2.5 stdev.

Dry shale particles produce higher porosity results than the As-Received shale particles (Figure 5.23). Furthermore, the dry porosity values mostly stayed consistent and did not vary between the different sized grains as much as the As-Received particles. In comparison, As-Received samples showed the highest variation and produced the lowest porosity values: N-2 (2.4 <d< 7) with the porosity value of 2.1% compared to the dried 6.2% and NG-3 (not cleaned 4 <d< 7) with the value of 2.1% compared to the average dried value of 5.8%. Low porosities were mostly obtained for the bigger particles as gas is less able to penetrate the matrix. There is however one porosity outlier: sample N-2 1.676 <d< 2.8 produced higher As-Received porosity value than dry (Figure 5.23). This must be either human error or experimental inaccuracy as all other N-2 sample measurements (2.8 <d< 4 and 4 <d< 7) showed constant dry porosity value, yet varying As-Received porosity value.

Generally, the results obtained using dried shale samples are more consistent than the results using non-dried (As-Received) samples. This is shown by the statistical comparison of the dried vs As-Received shale samples provided in the Table 5.19. The difference is most evident where the comparison with the results from other laboratories indicate uncertainties up to 72% for As-Received samples. The particle size appears not to influence porosity results, with particles with varying diameters producing same porosity results.

Table 5.19. Statistical analysis of dried and non-dried (wet- as received) crushed samples.

Sample	Control-Test,%			Leeds crushed GRI						
	Lab A	Lab B	Lab C	Dried, %	Dried stdev	Difference from control-test, %	AR (non-dried), %	AR stdev	Difference from control-test, %	Dry-AR difference, %
CHE2	8.70	7.30	8.30	8.31	1.33	11.55	7.33	1.66	26.78	0.98
CHE3	11.10	10.00	11.20	11.71	1.51	14.69	11.23	2.26	26.37	0.48
EBN20	6.85	6.43	8.29	7.62	0.33	15.59	4.44	1.79	51.75	3.27
NEX7	6.90	8.30	6.40	5.54	1.68	33.17	2.11	2.67	71.57	3.43
NEX15	7.40	6.00	7.50	5.96	1.59	28.11	3.83	1.88	49.89	2.13
NEX33	7.50	6.50	7.50	7.55	1.11	20.53	5.3	1.10	29.06	2.25

Difference between As-Received and dry derived porosity values shows the NEX group of samples containing more water than the CHE group of samples (Table 5.19). The different water saturations may possibly reflect the contrasting affinities to water of the constituents of these shales. Indeed, Borysenko et al. (2009) found that shales with high illite and smectite content tend to be hydrophilic, whereas kaolinitic shales tend to be hydrophobic. QXRD analysis of samples (see Table 4.2 in Section 4.3.1), reveals that NEX samples are dominated by illite/smectite, whereas CHE samples contain only small amounts of these minerals. EBN20 appears to be an outlier in this case, with low illite/smectite content yet high amount of water.

In addition, water tends to occupy smaller pores and also pores with less organic content, as it is hydrophobic (Borysenko et al., 2009; Kumar et al., 2015), which would result in those pores containing more water than gas. In contrast, samples with hydrophobic pores would have more small pores available for gas. This would result in CHE group of samples potentially having more gas stored within small pores than the NEX samples.

Water occupying small pores can be identified by comparing porosity values obtained by SEM (see Table 4.5 in Section 4.4.1) with the gas expansion derived As-Received and dry porosities (Table 5.19). The comparison should correlate to the amount of the micro-pores unseen by the SEM, as it is based on the visual delineation of the pores down to a certain resolution limit (see Section 4.4.1.1). Comparison of porosities is provided by the Table 5.20 and Figure 5.24: dried porosity values are the highest, whereas SEM are the lowest, indicating that dried shale matrix includes a lot of micro-porosity, which is beyond the resolution of the SEM images (<1 μm).

SEM porosity values closely match As-Received porosity values, especially for the EBN20 and NEX samples (Table 5.20 and Figure 5.24). As-Received porosities for the CHE samples are more similar to the dry porosity values, while they differ significantly from the SEM porosity value. This is consistent with water being present in the micropores of the EBN and NEX samples, which are blocked during the porosity measurement, whereas the water in the CHE samples is not present in the micropores.

Table 5.20. Comparison of porosities obtained by different methods: visual (SEM) and gas expansion (both dry and As-Received).

Sample	Porosity,%			Ratio	
	SEM	Dried	AR	SEM/dried	SEM/AR
CHE2	1.72	8.31	7.33	0.21	0.23
CHE3	4.18	11.71	11.23	0.36	0.37
EBN20	4.41	7.62	4.44	0.58	0.99
NEX7	2.01	5.54	2.11	0.36	0.95
NEX15	1.6	5.96	3.83	0.27	0.42
NEX33	2.35	7.55	5.3	0.31	0.44
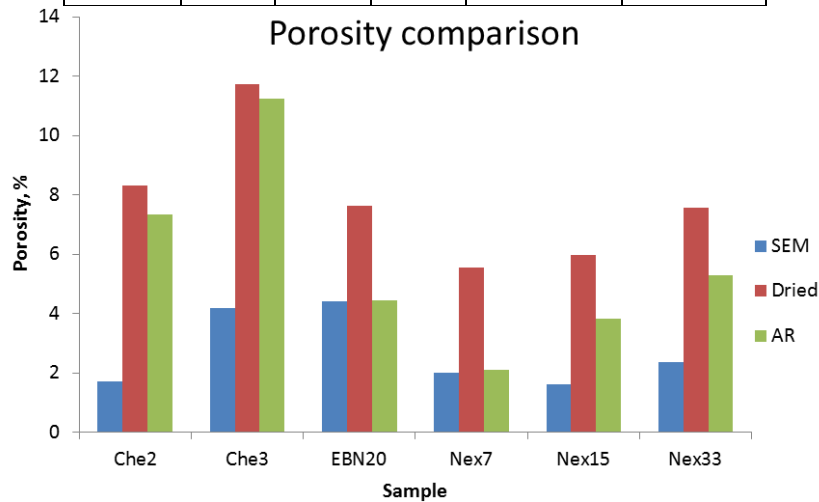
Figure 5.24. Comparison of porosity values obtained by different methods. Dried samples showed 1.5 stdev while AR samples showed 2.5 stdev.

5.4.2.4   Impact of highly permeable region

The highly permeable region manifests itself in terms of fast pressure decline into the matrix (see Figure 3.5 in Section 3.4.3). The pressure transducers are not able to record such a fast decline. However the use of dual permeability/dual porosity model enables porosity of this region to be estimated (see Section 3.6 and Chapter 6). Tthe porosity values become the sum of two separate porosities modelled within the shale particles. The first type of porosity represents the high conducting volume of the shale matrix, where the gas flows within the first seconds of the experiment. The second type of

porosity represents the low conducting part of the shale in which gas enters at lower rate (Figure 5.25).

The breakdown for the Control-Test samples, and its constituting low and high porosity values are shown in Figure 5.26. All double porosity results are provided in Appendix K and Appendix L. It can be seen in Figure 5.26 that only two samples: CHE2 and EBN20 have balance between low and high porosities. All other samples are dominated by high porosity. However there seems to be no correlation with the fraction of identified artificial pores from SEM analysis (see Table 4.5 in Section 4.4.1.1).

High porosities appear to correlate with the estimated P2 pressure differences between Hg-immersion bulk volume and GRI bulk volume as shown in Figure 5.27, which as noted before should represent artificial fractures due to Hg-immersion and GRI experimental differences (see Table 5.15 in Section 5.4.1.1). It can be observed that the highest high-porosity values are produced by the samples with largest Hg-GRI pressure difference (CHE3, NEX15 and NEX33). This means that the fractures affecting bulk volume measurements using Hg-immersion method are affecting GRI porosity measurements as well. This in turn would suggest that the highly permeable region highlighted in Figure 5.25 is not an area of different lithology, but in fact microfractures.
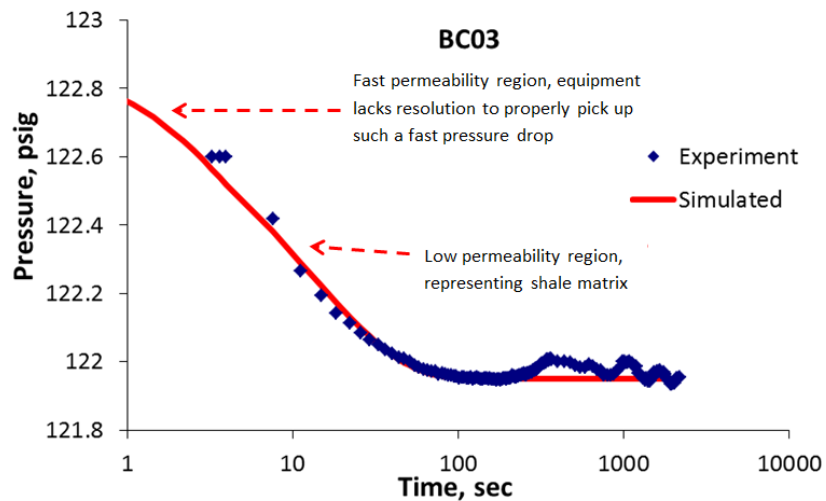
Figure 5.25. Analysis of the pressure decay curve.
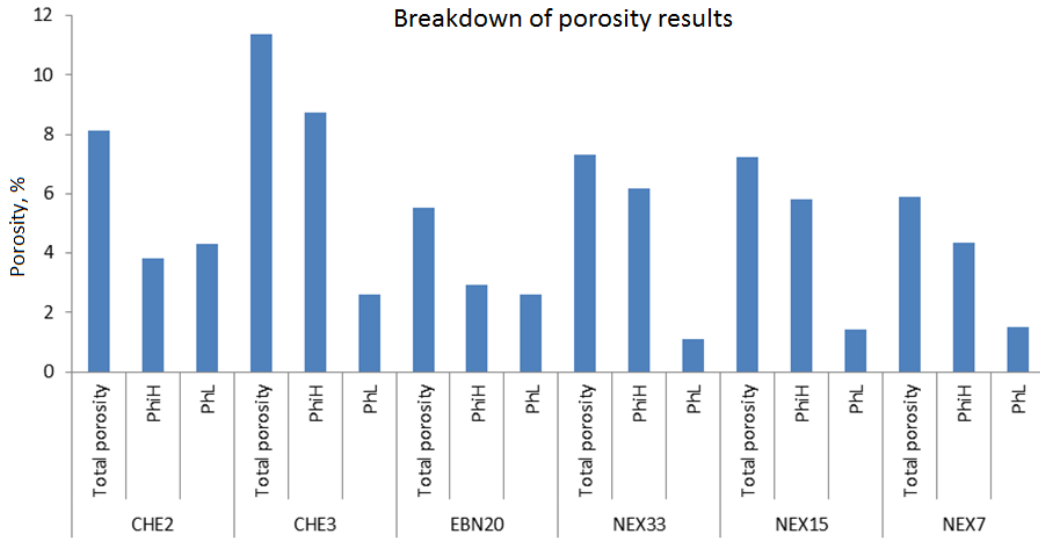
Figure 5.26. Porosity breakdown of high (fracture) and low (matrix) derived porosities.
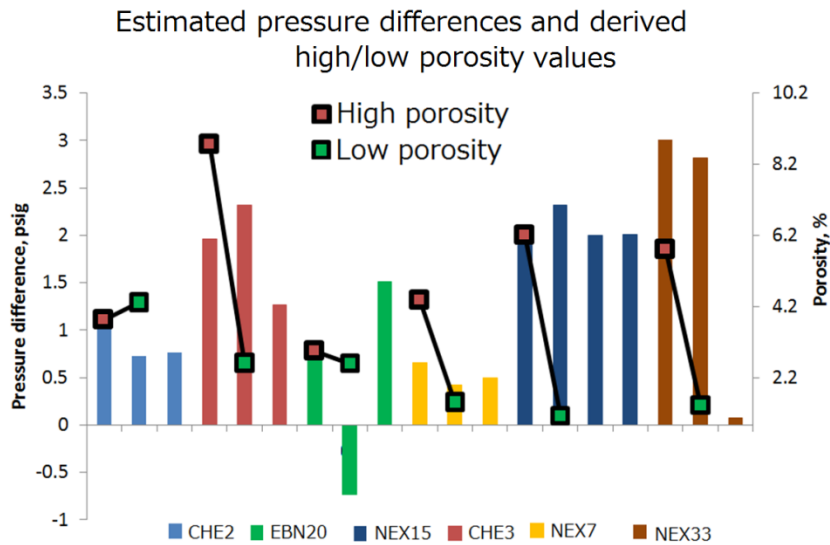
Figure 5.27. Comparison of high (fracture) and low (matrix) porosities with pressure differences.

5.4.2.5 Impact of confining pressure on porosity results

Shale porosity values obtained under three different confining stress conditions during the MPD (modified pressure decay) test showed no correlation with increase in stress (Table 5.21). The value drops with an increase in stress from 1500 psig to 2000 psig, however porosity then increases again under the stress of 2500 psig. The only consistent observation is that all confined pressure-derived porosity values are lower than those derived using crushed method (i.e. without confined pressure). However, the level of uncertainty of the MPD method has to be taken into account, which is reflected by high standard deviation values, especially for the confining pressure of 2500 psig (Table 5.21).

Table 5.21. Main results at each confining pressure for sample NEX15.

MPD of NEX15	Confining pressure, psig			Crushed	Control-Test
	1500	**2000**	**2500**	**N/A**	**N/A**
Average porosity,%	4.11	2.96	4.12	7.55	6.96
Standard deviation	1.75	1.64	2.83	1.11	0.82

5.4.3 Adsorption-desorption experiments and comparison of different gasses

Organic matter within shale has strongly adsorptive properties towards methane. This results in some methane being stored in an adsorbed state in subsurface conditions. Adsorbed gas may account for at least 50% of overall GIP in shale formations (Lane et al., 1990). In this study, it was shown that the contribution of the adsorbed gas is a function of time: initially it accounts for around 30% of all gas released, but in time it might be found that over 60% of overall gas could be stored in the adsorbed state.

Helium normally used in experiments has smaller molecular radius than methane, hence they have different abilities to enter small pore spaces (Figure 5.28). Consequently, porosity measurements made using helium could overestimate the pore space available to methane. However, methane is strongly adsorbed to organic matter within shale so using methane to measure grain volume could result in an overestimation of porosity. At the same time swelling of clays and organic matter could reduce the pore space and outweigh any adsorption increase.

This section starts with an analysis of the gas stored in an adsorbed state: amount of gas released over the short term is compared to the long term desorption. After that the use of methane gas for the porosity measurements is discussed. The degree of uncertainty between the methane and helium gasses is provided and the correction of that uncertainty is described.
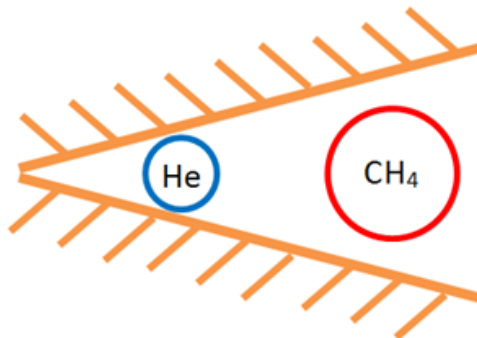
Figure 5.28. Helium and methane molecular size implications on tight pore space in shale.

5.4.3.1 Adsorption gas storage monitored over the short-term

Matrix porosity was found to be the dominant gas storage type over the short-term for all Control-Test and Gripen samples. Specific adsorption volumes for 9 samples are presented in Table 5.11 (see Section 5.3.6). Generally high adsorption values exhibited by the shale samples can be explained by their high TOC value (especially for Gripen samples, Figure 5.29).
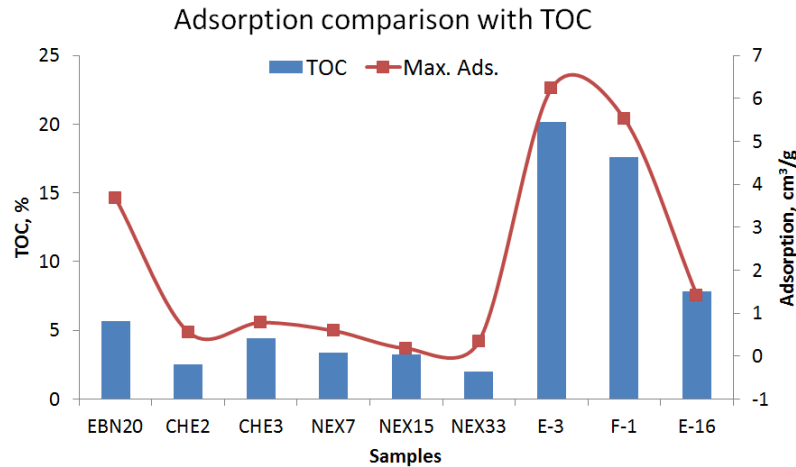
Figure 5.29. Comparison of TOC and adsorption values, strong positive trend can be observed.

To compare the gas volumes stored in matrix porosity and adsorbed state, these volumes were calculated using adsorption parameters (see Table 5.11 in Section 5.3.6) and porosity values (see Table 5.4 in Section 5.3.1). The obtained values were then compared with the actual *in-situ* desorbed gas volumes over the entire shale region for the E and F Gripen wells (see Table 5.12 and Table 5.13 in Section 5.3.7). Desorption measurements were conducted in the field during the shale gas exploration campaign in Sweden, and are further described in Chapter 7. They are regarded as short-term desorption results as they were recorded within the first several hours after being cored (Appendix Q). This allowed the actual distribution of *in-situ* gas in each volume (matrix porosity and adsorption) to be assessed.

Using the porosity and bulk density values of the samples (see Table 5.4 in Section 5.3.1 and Table 5.10 in Section 5.3.3), the theoretical amount of gas stored per 1 cm^3 of porous space was calculated by first deriving bulk volume (V_b) of 1 gram of the sample (Equation 5-1) and then multiplying it by the corresponding porosity values (Equation 5-1). These volumes were then adjusted to the surface conditions according to the ideal gas law to obtain the amount of gas stored at each pressure value, $V_{por\,cor}$ (Equation 5-2). The

resulting gas storage values per gram of shale for both adsorbed and matrix pores are provided in Table 5.22 and Table 5.23.

$$V_b = \frac{m}{\rho_b} = \frac{1}{\rho_b} \qquad \text{(Equation 5-1)}$$

$$V_{por\ cor} = \frac{V_{por} \cdot P}{P_{atm}} \qquad \text{(Equation 5-2)}$$

The adsorbed volume was calculated employing Langmuir adsorption isotherm (see Equation 2-41 in Section 2.9.2), which describes the amount of adsorbed gas as a function of pressure at a fixed temperature (Cui et al., 2009; Civan et al., 2011). To compare both adsorbed and porous volumes, the ratio of the gas stored in the adsorbed state to the one stored between the pores was derived by dividing the adsorption storage by the porosity storage. A similar parameter was defined by Cui et al. (2009), f_a, called the ratio of true effective porosity over effective porosity contributed by adsorption (Equation 5-3). This is a measure of the amount by which the gas volume in the adsorbed state is different from the one stored between the pores. Instead of deriving the gas volumes, Cui et al. (2009) expressed the ratio in terms of porosities as:

$$f_a = \frac{\Phi_a}{\Phi} \qquad \text{(Equation 5-3)}$$

It is clear that for Gripen samples, the majority of gas released during the initial time was stored in the matrix pore space (Table 5.22, Table 5.23 and Figure 5.30). Adsorbed gas accounted for about 30% - 40% of overall gas recorded. Control-Test samples were not examined for this comparison, however they showed much lower TOC and Langmuir volume values than Gripen samples (Figure 5.29), therefore would most likely produce even higher contrast between porous volume and adsorption. This indicates matrix porosity to be the main source of gas production in the shale reservoirs during the initial time.

Table 5.22. Well E gas storage potential.

Depth, m	Pressure, psig	$V_{por\ cor}$, cm³/g	V adsorbed, cm³/g	V total, cm³/g	f_a ratio, dimens
85	5.0	0.06	0.02	0.07	0.29
89	1.0	0.01	0.01	0.01	0.29
90	5.0	0.06	0.02	0.07	0.29
91	2.5	0.03	0.01	0.04	0.29
92	31.7	0.36	0.10	0.47	0.28
93	70.0	0.80	0.22	1.02	0.28
94	2.6	0.03	0.01	0.04	0.29
95	7.7	0.09	0.03	0.11	0.29

96	22.6	0.26	0.07	0.33	0.28
97	1.4	0.02	>0.01	0.02	0.29
98	13.4	0.15	0.04	0.20	0.28
99	6.1	0.07	0.01	0.09	0.29
100	15.0	0.17	0.05	0.22	0.28
101	2.0	0.02	>0.01	0.02	0.10
102	2.5	0.02	>0.01	0.02	0.10
103	2.0	0.02	>0.01	0.02	0.10
104	1.0	0.01	>0.01	0.01	0.10

Table 5.23. Well F gas storage potential.

Depth, m	Pressure, psig	$V_{por\,cor}$, cm^3/g	V adsorbed, cm^3/g	V total, cm^3/g	f_a ratio, dimens
72	1.6	0.01	>0.01	0.02	0.39
73	48.0	0.37	0.14	0.51	0.38
75	14.2	0.11	0.04	0.15	0.39
76	11.4	0.09	0.03	0.12	0.39
77	0.6	>0.01	>0.01	0.01	0.39
79	25.0	0.19	0.07	0.27	0.39
80	0.3	>0.01	>0.01	>0.01	0.39
81	19.1	0.15	0.06	0.20	0.39
82	3.2	0.02	0.01	0.03	0.39
84	13.1	0.10	0.04	0.14	0.39
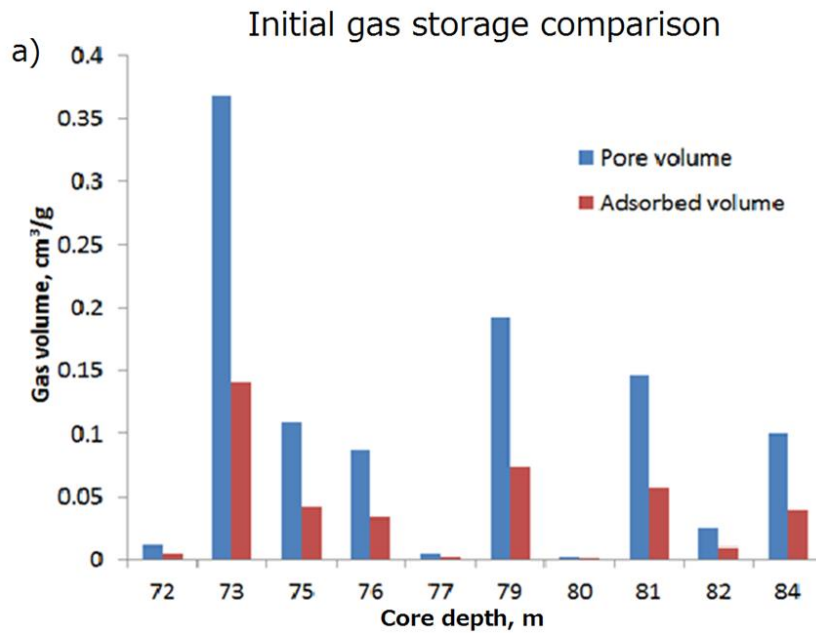
Figure 5.30. Comparison of early time gas storage. Values obtained from the field cores using desorption canisters.
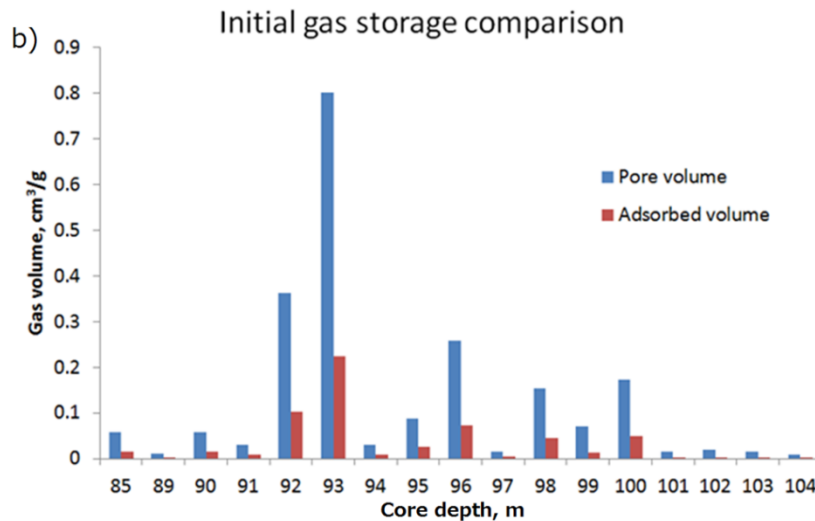
Figure 5.30 Continued. Comparison of early time gas storage. Values obtained from the field cores using desorption canisters.

5.4.3.2 Full adsorption potential on gas storage

It was found in this study that over 60% more gas may be stored in the adsorbed state rather than in the matrix porosity and the full potential of the adsorbed gas manifests itself over the long-term. In fact, according to the Langmuir equation, more gas is being freed from the adsorbed state as the pressure decreases. However, it has to be noted that the measurements in this study were done at the surface temperature conditions. The Van del Waal's forces acting between the adsorbate (matrix) and adsorbent (methane gas) get weaker with the increase in temperature, which is the case with subsurface (Walls et al., 1982). Therefore the amount of gas stored in the subsurface temperature conditions might be lower than that calculated at the surface temperature conditions.

The Langmuir equation might not be sufficient for the correct estimation of the released gas volume and more advanced equation such as Dubinin's (see Figure 2.4 in Section 2.8) might need to be used. An experiment was done in this study demonstrating that the application of Langmuir pressure indeed might massively under-predict the amount of gas held in an adsorbed state (long-term desorption test, see Figure 5.15 in Section 5.3.7).

The core was retrieved from the 32 m depth, however it accumulated over 330 psig of methane pressure (see Figure 5.15 in Section 5.3.7). The formation testing and short-term core desorption (see Table 5.12, Table 5.13 in Section 5.3.7) indicated bottom-hole-pressure of just 15 psig. Langmuir states that there has to be a dynamic equilibrium between the adsorbed and free gasses (Langmuir, 1918). However, a huge disparity between the gas pressures at adsorbed and free state (330 psig and 15 psig) indicated

that there possibly have to be more complex terms included to support the dynamic equilibrium between the adsorbed gas at such a high pressure and the free gas at a much lower pressure.

The gas accumulated during this first desorption test was released and a second desorption test was conducted on the same core; the results are shown in (see Figure 5.16 in Section 5.3.7). The gas accumulation behaviour during secondary desorption test is fundamentally different. In particular, almost all gas accumulated during the first 5-10 days, with almost no increase in pressure afterwards. This implies that most of the gas stored in an adsorbed state must have been released from this state during the first build up, whereas during the second build-up, gas must have been provided by the matrix porosity and microfractures. The latter is supported by the fast accumulation of pressure. Therefore Figure 5.13 (see Section 5.3.7) should show the maximum possible desorption potential of the given shale sample.

According to the ideal gas law, the amount of gas accumulated during the first desorption experiment is 134.7 cm^3. As the volume of both canisters (1,128 cm^3), the core (795 cm^3) and the free space within the canister (6 cm^3) are known, porosity was calculated as 16.94% of the whole core. The actual porosity of this sample was obtained from the crushed GRI experiment, and was estimated to be 5%. The difference between these values (16.94%- 5% = 11.94%) should be the adsorptive porosity, which corresponds to 79 cm^3 out of 134.7 cm^3 being stored in adsorptive state. Langmuir adsorption value was not obtained for this OA-1 well sample, however the absorptive volume ratio to the porous volume f_a is much higher (11.94/5 = 2.39) than the ones obtained in Table 5.22 and Table 5.23 (see Section 5.4.3.1) indicating clear dominance of the adsorptive volume over the porosity in the long-term.

Therefore the analysis indicates clear differences between the short- and long-term pressure desorption results. The relative equilibration noticed during the short-term was attributed to the matrix porosity and microfractures. However the cores appeared to continue to desorb gas, with the OA-1 core reaching equilibrium only after 6 months, compared to the short-term desorption of 2-3 hours. Ultra-low matrix permeability is the main reason it takes a long time for the desorbed gas to flow through the matrix and find high conductive paths.

An important observation is the mismatch between the accumulated pressure and the recorded bottom-hole pressure in the field, which is around 15 psig (see Table Q. 5 in

Appendix Q). Furthermore, short- vs long-term desorption measurement comparison suggests that potentially the formation should also be able to release similar amount of gas produced by the tested core and accumulate over 330 psig of pressure. However, given that the tested formation is situated at around 30 m from the surface, it is unclear with what mechanism it is able to store this amount of gas. The field study is discussed in Chapter 7, however the mentioned storage mechanism needs further study.

The secondary desorption test produced much less, namely 20.4 cm^3 or 2.56% in terms of porosity. The test was conducted after the initial pressure build-up (see Figure 5.16 in Section 5.3.7) was released to the atmosphere and the cylinder was sealed immediately after that. Apart from the lower pressure, the main difference is the gradient of the pressure curve – it is logarithmic-type curve throughout the entire build-up period. In contrast, the first accumulation showed more gradual exponential-type curve at the initial time, turning into exponential only later, before equilibration. The steepness of the curve means fast gas accumulation supposedly from the matrix porosity and microfractures. This accumulation considerably diminished after around 10 days, indicating a very small amount of gas remained in the adsorbed state.

After the desorption tests, the core was left in the atmosphere for some time to completely desorb before the pressure was applied for the long-term methane adsorption experiment. The adsorption test resulted in a pressure drop from the maximum of 103 psig to around 93 psig in around 600 hours (25 days) (see Figure 5.17 in Section 7.4.1). The initial pressure decay within the first 250 hours (10 days) follows the standard decline gradient demonstrated by crushed samples and core plugs, but over a more extended period of time. After that, during the late time (from 250 hours onwards), signs of equilibration could be identified, however it is difficult to define the actual pressure decline due to the obvious temperature effects. Therefore it was demonstrated that gas behaves in a similar way over the large scale shale specimen to the smaller samples, with only the time as a principal difference.

Similarly to the desorption tests, the volume of gas was derived from the pressure transient, and was calculated to be 40.59 cm^3. This corresponds to 5.1% of the porous volume, which interestingly is very close to the porosity estimated from the crushed GRI (5%) (Table 5.24). The assumption that could be drawn is that it was the matrix porosity that caused all this pressure decay, whereas for the adsorption to take place the right conditions were not created. As stated before, the temperature of the reservoir was not

monitored therefore the *in-situ* adsorption condition could not be derived. Table 5.24 presents the summary of adsorption-desorption analysis results.

Table 5.24. Desorption values analysed in terms of gas volume.

	Amount of gas produced/adsorbed, cm^3	% of overall core volume	Actual core porosity,%	Adsorptive porosity,%
Primary desorption	134.70	16.94	5.00	11.94
Secondary desorption	20.40	2.56	5.00	0.00
Adsorption	40.59	5.10	5.00	0.10

Neither ground nor air temperatures were monitored during the tests, therefore proper temperature dependence assessment cannot be made. It was assumed that the temperature would have no significant effect as the given shale play is very shallow (30 - 110 m), therefore there should be no large temperature variations. Normally prospective shale plays occur at depths of around 2-3 km, where the effect of temperature is strong.

Overall, it was shown that shale formations present at shallow depths are able to contain considerable amount of gas in the adsorbed state. Desorption tests indicated the ability of the shale formation to contain a majority of the gas in an adsorbed state rather than matrix porosity, despite formation exhibiting low bottom hole pressures. The time it takes for the desorbed gas to travel through the matrix was also found to be a considerable issue, mostly depending on the permeability of the matrix, discussed in Chapter 6. Overall, it is important to obtain the desorption parameters of the prospective shale plays to properly asses the gas storage.

5.4.3.3   Impact of methane in porosity measurements

Pressure expansion results indicate that porosity measurements made using methane are higher than those made using helium (Figure 5.31). The reason for that is the sorption effect, which increases the gas storage volume of the shale matrix. An attempt was therefore made to subtract the adsorptive volume from the porosity results and obtain the corrected porosity value.
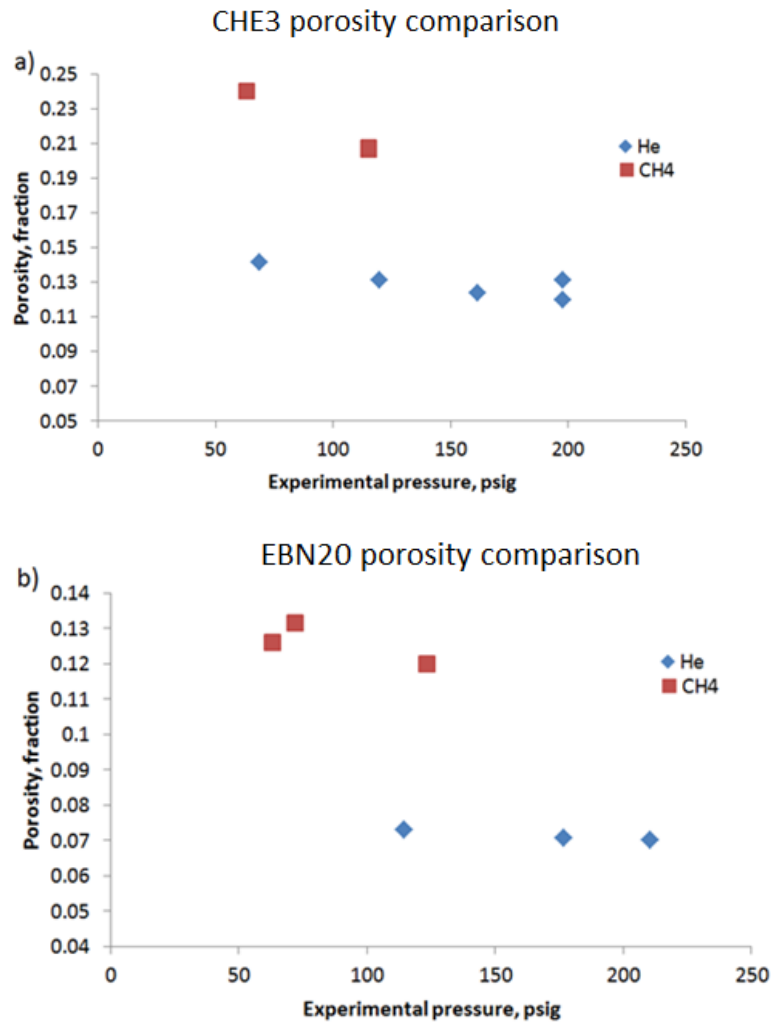
Figure 5.31. Porosity difference using helium and methane as experimental gass for the samples CHE3 (a) and EBN20 (b).

The methane porosity was corrected by deriving the total volume of gas contained within the matrix and subtracting from it the volume of gas that was supposedly adsorbed. Two cases were compared: full adsorption and 30% adsorption, based on results obtained by the short-term *in-situ* shale gas desorption tests (see Table 5.22 and Table 5.23 in Section 5.4.3.1). The aim is to observe how close the results can be corrected to the values obtained by helium.

The mass balance principle was utilised for calculations. First the porosity values obtained were converted into porous volume per gram of the sample. The total amount of gas contained within that porous volume was then derived using ideal gas law. Finally, the absorbed gas volume per gram of shale was subtracted from the total gas pore volume and the result was converted back into the porosity value. The results of the corrections together with the porosity comparison are given in Tables 5.24 to 5.29.

Table 5.25. EBN20 comparison of adsorption-corrected methane porosity estimations with the helium porosity results.

EBN20 methane porosity				Helium
Pressure step, psig	Porosity from test,%	Complete adsorption correction,%	30% adsorption correction,%	Mean porosity,%
72.21	13.12	3.63	10.27	
123.74	11.97	1.80	8.92	5.54
63.69	12.57	3.28	9.78	

Table 5.26. CHE3 comparison of adsorption-corrected methane porosity estimations with the helium porosity results.

CHE3 methane porosity				Helium
Pressure step, psig	Porosity from test,%	Complete adsorption correction,%	30% adsorption correction,%	Mean porosity,%
63.62	24.00	18.74	22.42	
115.55	20.63	14.80	18.88	11.71
115.55	20.71	14.87	18.95	

Table 5.27. CHE2 comparison of adsorption-corrected methane porosity estimations with the helium porosity results.

CHE2 methane porosity				Helium
Pressure step, psig	Porosity from test,%	Complete adsorption correction,%	30% adsorption correction,%	Mean porosity,%
74.68	24.00	19.39	21.15	
125.31	17.00	11.57	15.71	8.31
159.63	17.00	12.64	15.96	
79.13	18.00	13.49	15.96	

Table 5.28. NEX7 comparison of adsorption-corrected methane porosity estimations with the helium porosity results.

NEX7 methane porosity				Helium
Pressure step, psig	Porosity from test,%	Complete adsorption correction,%	30% adsorption correction,%	Mean porosity,%
151.64	12.00	7.20	5.75	
167.65	11.00	6.30	4.88	
150.93	19.00	14.19	12.75	5.96
180.79	15.00	10.38	8.99	
195.07	14.00	9.47	8.11	

Table 5.29. NEX15 comparison of adsorption-corrected methane porosity estimations with the helium porosity results.

NEX15 methane porosity				Helium
Pressure step, psig	Porosity from test,%	Complete adsorption correction,%	30% adsorption correction,%	Mean porosity,%
150.16	17.00	15.16	16.45	7.55
168.94	13.00	11.20	12.46	

Table 5.30. NEX33 comparison of adsorption-corrected methane porosity estimations with the helium porosity results.

NEX33 methane porosity				Helium
Pressure step, psig	Porosity from test,%	Complete adsorption correction,%	30% adsorption correction,%	Mean porosity,%
150.25	15.00	13.47	14.54	
167.76	13.00	11.47	12.54	7.46
115.55	15.00	13.48	14.54	

Normally, the behaviour of ideal gasses matches that of the real gasses; however at high pressures considerable deviations might occur (Dzyaloshinskii et al., 1961). The reason for this is the ideal gas assumption that gas molecules occupy negligible fraction of the total gas volume. Once pressure is applied, the volume of gas reduces, and therefore the volume of the molecules become no longer negligible in comparison to the total gas volume (Figure 5.32). Van der Waals proposed a correction factor *nb* to the ideal gas law (Equation 5-4), which is negligible when the pressure is small (hence the volume is large), but it corrects the ideal gas equation at higher pressures when the volume is relatively small.

$$P(V - nb) = nRT \qquad \text{(Equation 5-4)}$$
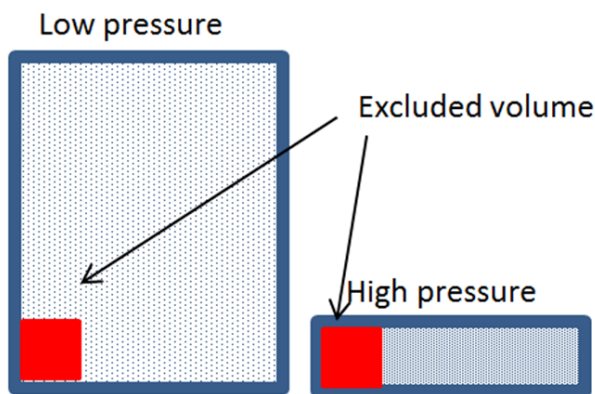
Figure 5.32. The impact of higher pressure on the control volume of the ideal gas.

Another inaccuracy noted by Van der Waals was the assumption that no forces exist between the ideal gas molecules (Dzyaloshinskii et al., 1961). Van der Walls noted that this assumption is fundamentally wrong, as if there would be no forces between the molecules, the gasses could not form liquids. This assumption also affects the accuracy of the ideal gas behaviour at high pressures – the pressure of real gas might be smaller than the ideal gas at relatively high pressures due to this effect. To correct it, Van der Walls added a correction constant *a* in the form of an^2/V^2 to the pressure parameter in the Equation 5-4, therefore turning it into Equation 5-5:

$$\left(P + \frac{an^2}{V^2}\right)(V - nb) = nRT \qquad \text{(Equation 5-5)}$$

The constants for Van der Waals corrections are different for various gasses, including helium and methane (Table 5.31). Therefore when interchanging helium and methane in the high pressure experiments while assuming the same equation for the ideal gas law, errors might occur. The amount of errors was not studied in this research.

Table 5.31. Van der Waals constants for various gasses (Kaye and Laby, 1986).

Gas	a (L^2-atm/mol^2)	b (L/mol)
He	0.03412	0.02370
Ne	0.2107	0.01709
H_2	0.2444	0.02661
Ar	1.345	0.03219
O_2	1.360	0.03803
N_2	1.390	0.03913
CO	1.485	0.03985
CH_4	2.253	0.04278
CO_2	3.592	0.04267
NH_3	4.170	0.03707

Almost no improvement was achieved by the complete adsorption correction: the porosity was either massively overcorrected (EBN20), or the correction was not sufficient to bring the original methane porosity down to that measured using helium. The partial 30% adsorption correction also produced mixed results with most samples still hugely over predicting the porosity values. However, very close values for the NEX7 sample were obtained to the helium porosity results. Overall, there is a potential for further

improvement of the methane porosity estimations using the adsorption corrections. The challenge for the adsorption corrections is a lack of information on the amount of gas actually adsorbed during the experiment.

In addition, the particle size of the sample may be too large. It has to be noted that for the adsorption experiment shale samples were crushed to smaller sizes (<0.4 mm) than for the GRI experiment (0.5 mm <d< 0.85 mm). The solution would be to conduct further adsorption-desorption experiments on the samples to understand the sorption process better. In particular to understand which of the volumes – matrix porosity or adsorption acts as a main gas storage mechanism within the timescale of the experiment.

Another widely discussed effect of methane for the porosity measurements is molecular size. The effect of this was assessed by utilizing nitrogen as the experimental gas, because it has similar molecular diameter but different adsorptive properties than methane. In contrast to the notion that porosity would be lower when measured using nitrogen than helium due to the difference in molecular size (see Figure 5.28 in Section 5.4.3), porosity values obtain using nitrogen appear to be slightly higher than those measured using helium (see Figure 5.31 in Section 5.4.3). In fact, porosities obtained using nitrogen appear to be mid-way between helium and methane porosities, with some values closely matching adsorption corrected methane porosities.

Higher porosities obtained when using nitrogen gas are possibly the result of nitrogen exhibiting sorption towards the shale samples. Some degree of positive relationship can be identified between BET values and porosity in Figure 5.33, as CHE2 and NEX33 show high BET values and highest porosities, whereas other samples show lower BE and porosity values. However methane and helium porosities appear to differ more than nitrogen with the change in BET values.
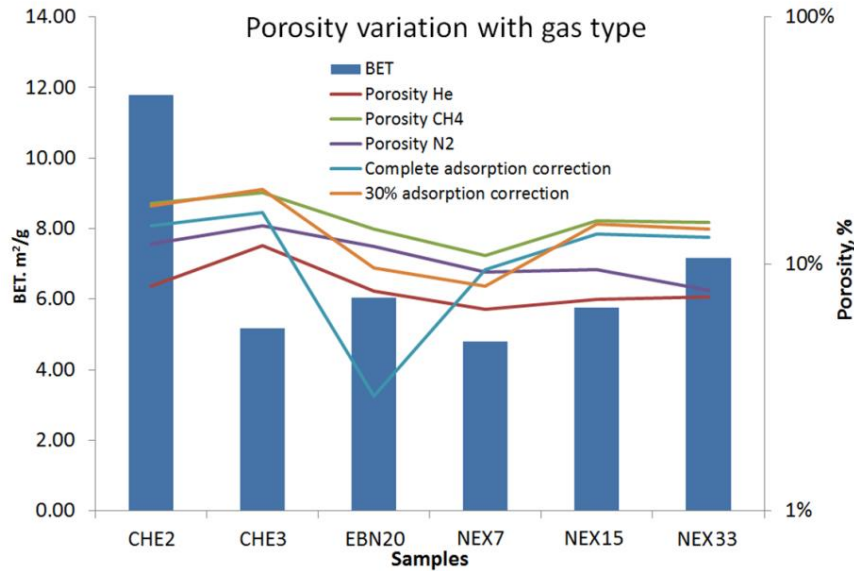
Figure 5.33. Comparison of porosity results for control-Test samples obtained using different experimental gases. BET values are also given for comparison.

5.5 Conclusion

The crushed GRI method for grain density measurement was found to be the most consistent in comparison with other methods. MICP and water pycnometry provided lower grain density values compared to crushed GRI, most likely due to ineffective saturation. In fact, it is unclear whether mercury during MICP test actually intrudes the sample pores or compresses the sample. QXRD grain density results are sensitive to inaccuracies when assigning the density values for each mineral.

The conducted Control-Test comparison showed that the largest uncertainty among the Control-Test results was produced by the laboratory which applied a different sample cleaning method using solvent extraction than compared to other laboratories. This produced a systematic error observed in all results categories of that laboratory. However the reason of the error was not the removal of clay bound water using solvent extraction, but rather the cleaning procedure was not completed.

Microfractures present within the shale produce high uncertainties for Hg immersion and GRI methods regarding bulk density estimations. To solve the microfracture problem stress conditions need to be applied. MICP might be an answer to this issue: due to the small pore throats within the shale matrix, the mercury might be compressing the sample instead of intruding the pores.

Porosity tests confirmed crushed GRI method to be faster and produce more comparable to Control-Test porosity results than analogue core plug tests. The main reason for

crushed method being more accurate than core plug is that gas fully enters the matrix within reasonable amount of time. This in turn also enables reverse pressure build-up test to be performed, which allows the porosity results to be quality checked. The study confirmed the need to account for highly-permeable and low-permeable regions when deriving porosity: it allows to separate between the matrix porosity and microfracture-affected porous space. Furthermore, it is recommended to oven dry crushed shale particles before porosity measurements to remove the water occupying the pores and therefore standardise the measurements and improve comparability between different service companies.

The desorption analysis of *in-situ* methane showed that during the initial production around 30% of gas from shale matrix was produced from the adsorbed state while the rest was produced from the matrix porosity. However, at the later stages the desorption began to dominate the gas production. In fact, it was found that massive amount (over 60%) of gas was stored in an adsorbed form, which in turn is a considerable economic factor. It is suggested to conduct research on improving the adsorption model, possibly by considering multi-layering desorption described by Dubinin & Astakhov (1971).

6 Chapter
Measurement of shale permeability

6.1 Introduction

Since the start of the "shale gas revolution" it has become routine practise to attempt to measure the gas permeability of cores recovered from shale gas resource plays. Undertaking such measurements using the steady-state technique, which is used in the analysis of cores from conventional reservoirs, would be time-consuming. Consequently, it has become industry practise to measure permeability of shale samples using various pressure transient techniques.

These measurements can be made on either crushed shale or on core plugs. Analysis of core plugs is often undertaken using a pulse decay technique similar to that described in Jones (1997), whereas measurements on crushed shale are made using the method developed by the Gas Research Institute (Luffel et al., 1992). Both methods require inversion of experimental data using analytical or numerical models to obtain the permeability.

The crushed experiments are undertaken without the application of a confining pressure. In contrast, a confining pressure is usually applied to core plugs during the modified pressure decay (MPD) permeability analysis, which is an advantage as it enables subsurface conditions to be replicated better. However, it is often argued that core plugs contain microfractures resulting from core damage, which distort the permeability results (Luffel et al., 1992). Those in favour of the crushed shale method argue that crushing the shale removes these fractures and therefore the results from these experiments provide a better measure of *in-situ* matrix permeability of shale (Luffel et al., 1992).

Unfortunately, several studies have compared results from the main service companies and have found that permeabilities obtained using the crushed shale method can vary by several orders of magnitude for the same sample (Clarkson et al., 2012; Rushing et al., 2004; Sinha et al., 2012; Ghanizadeh et al., 2015; Moghadam and Chalaturnyk, 2015). Furthermore, the parameter derivation process is complex and simulation models often require a myriad of properties (e.g. tortuosity) that cannot be directly measured in the laboratory (Lorinczi et al., 2014; Moghadam and Chalaturnyk, 2015). Service companies tend not to reveal details of how experiments were conducted or how permeability values are obtained from pressure transient data. Overall, there appears to be no consensus regarding the reasons on why results between the laboratories vary so much.

It is the aim of the current chapter to explore the reasons for these discrepancies and to assess whether alternative pressure decay methods for measuring gas permeability provide more consistent results. To meet this aim, industry standard numerical modelling and experiments were employed (see Sections 3.4; 3.5 and 3.6). The chapter begins by outlining the conducted experiments, the samples used and the number of measurements. The results are then presented and modelled using the inversion techniques described in Chapter 3.6. To help understand the causes of the differences between methods, the measurements conducted in Leeds during this research have been compared with the measurements made during the Control-Test exercise described in Section 3.1. The discussion provided further in Section 6.4 attempts to draw together these results with references to published work and with the aid of further numerical modelling to provide both advantages and disadvantages of each method and recommendations for further work.

6.2 Methods

6.2.1 Overview of methods used

Permeability of 59 samples was measured using the crushed GRI (Gas Research Institute) method described by Luffel et al. (1992). An overview of the samples described in this chapter is provided in Appendix A. Details of the grain sizes and pressure used for the crushed shale analysis are provided in Table 6.1. Overall 294 crushed GRI experiments using helium gas were conducted. The core plug method was applied to 9 samples. Details of the core plug measurements for gas and confining pressures are described in Tables 6.2 to 6.9. Overall 163 measurements were done for the Modified pressure decay (MPD), 238 for the Core Plug GRI (CPGRI), and 60 for Radial Pressure Decay (RPD) experiments.

Six of the samples were sent to three major service companies for the Control-Test where attempts were made to measure their permeability using the crushed shale method and pulse decay permeametry. Unfortunately, the service companies did not provide the raw pressure data that they acquired and used to estimate permeability. They also did not provide details of the size fraction used during the experiments, details of the experimental setups (e.g. volumes) or the method used to invert the results. However, one of the laboratories is thought to have made the PDP measurements using the method of Jones (1997) and the crushed shale measurements using the method of Luffel et al. (1992).

Table 6.1. Overview of the crushed GRI experiments. Presented are the samples, particle size fraction and the conducted experiments.

Samples	Size fraction	Gas Pressures Class, psig				
		150	180	210	240	REV
BC01 - BC11	0.5<d<0.85	✓	✓	✓	✓	✓
CHE2 and CHE3	0.5<d<0.85	✓	✓	✓	✓	✓
EBN1	0.5<d<0.85	✓			✓	
EBN7 and EBN8	0.5<d<0.85	✓	✓			✓
EBN16 - EBN36	0.5<d<0.85	✓	✓	✓	✓	✓
EBN20	0.5<d<0.85	✓	✓	✓	✓	✓
EBN20	0.25<d<0.5	✓				✓
EBN20	1<d<2	✓				✓
NEX7	0.5<d<0.85	✓	✓	✓	✓	✓
NEX7	0.25<d<0.5	✓				✓
NEX15 and NEX33	0.5<d<0.85	✓	✓	✓	✓	✓
NEX205	0.5<d<0.85	✓	✓	✓		✓
N-2	1.676<d<2.8	✓	✓	✓	✓	✓
N-2	2.8<d<4	✓	✓	✓	✓	✓
N-2	4<d<7	✓	✓	✓	✓	✓
NG-2	0.85<d<2.8	✓	✓	✓	✓	✓
NG-2	2.8<d<4	✓	✓	✓	✓	✓
NG-2	4<d<7	✓	✓	✓	✓	✓
NG-3#2	0.85<d<1.676	✓	✓	✓	✓	✓
NG-3#2	1.676<d<2.8	✓	✓	✓	✓	✓
NG-3#2	2.8<d<4	✓	✓	✓	✓	✓
NG-3#2	4<d<7	✓	✓	✓	✓	✓
NG-8	0.8<d<1.676	✓	✓	✓	✓	✓
NG-8	1.676<d<2.8	✓	✓	✓	✓	✓
NG-8	2.8<d<4	✓	✓	✓	✓	✓
NG-10	0.85<d<1.676	✓	✓	✓	✓	✓
NG-10	1.676<d<2.8	✓	✓	✓	✓	✓
NG-12	0.85<d<1.676	✓	✓	✓	✓	✓
NG-12	1.676<d<2.8	✓	✓	✓	✓	✓
NG-12	4<d<7	✓	✓	✓	✓	✓

Table 6.2. Overview of the MPD experiments.

Samples	Number of samples	Number of experiments		
		Parallel	Perpendicular	Total
EBN9	1	12	0	12
EBN20	3	39	36	75
EBN33	2	20	0	20
NEX7	2	0	14	14
NEX15	2	0	41	41
Total	10	71	91	162

Table 6.3. Break-down of the MPD experiments.

Sample	Pressure class, psig						Confining pressure, psig			
	Low (<100)	100	150	200	high (>200)	REV	1000	1500	2000	2500
EBN9			✓	✓	✓	✓	✓			
EBN20	✓	✓	✓	✓	✓	✓	✓			
EBN33			✓	✓	✓	✓	✓			
NEX7	✓	✓	✓	✓	✓	✓	✓	✓	✓	✓
NEX15	✓	✓	✓	✓	✓	✓	✓	✓	✓	✓

Table 6.4. Overview of the MPD-RPD experiments.

Samples	Number of samples	Number of experiments		
		Radial parallel	Radial perpendicular	Total
EBN5	1	10	0	10
EBN20	2	23	4	27
CHE2	1	2	0	2
CHE3	2	2	0	2
NEX7	1	2	0	2
NEX15	1	2	0	2
NEX33	1	2	0	2
Total	9	43	4	56

Table 6.5. Break-down of the MPD-RPD experiments.

Samples	Pressure class, psig						Confining pressure
	Low (<100)	100	150	200	high (>200)	REV	1000
EBN5	✓	✓	✓	✓	✓	✓	✓
EBN20	✓	✓	✓			✓	✓
CHE2 and CHE3			✓			✓	✓
NEX7; NEX15 and NEX33			✓			✓	✓

Table 6.6. Overview of the CGPRI experiments. Number of samples and experiments is presented.

Samples	Number of Samples	Perpendicular	Parallel	Total
EBN20	3	35	34	69
EBN5	1	0	1	1
EBN9	1	0	15	15
EBN33	2	0	20	20
CHE2	2	2	40	42
CHE3	2	42	5	47
NEX7	2	1	0	1
NEX15	2	1	0	1
NEX33	2	1	0	1
Karoo	2	10	10	20
Gripen	16	0	21	21
Total	35	92	146	238

Table 6.7.Break-down of the CPGRI experiments.

Sample	Pressure class, psig					
	Low (<100)	100	150	200	high (>200)	REV
EBN20	✓	✓	✓	✓	✓	✓
EBN5		✓				
EBN9		✓	✓	✓	✓	✓
EBN33			✓	✓	✓	✓
CHE2 and CHE3			✓	✓	✓	✓
NEX7; NEX15 and NEX33			✓	✓	✓	✓
Karoo				✓		✓
Gripen				✓		✓

Table 6.8. Overview of the CPGRI – RPD experiments.

Samples	Number of samples	Number of experiments		
		Radial parallel	Radial perpendicular	Total
EBN5	1	2	0	3
EBN20	2	5	3	10
CHE3	2	3	0	5
NEX33	1	2	0	3
Karoo	1	2	0	3
Total	7	14	3	24

Table 6.9. Break-down of the CPGRI – RPD experiments.

Sample	Pressure class, psig					
	Low (<100)	100	150	200	high (>200)	REV
EBN5	✓					
EBN20	✓	✓	✓	✓	✓	✓
CHE2 and CHE3		✓	✓			✓
NEX33			✓			✓
Karoo			✓			✓

6.3 Permeability Results

In this section permeability results obtained by various methods are presented with the focus on Control-Test samples. A massive number of analyses were conducted during this study, so most of the results are provided in Appendix K, Appendix M and Appendix N. Nevertheless each results category, including experimental method, particle size (for crushed samples) and bedding direction (for core plug samples) is provided within the main text.

6.3.1 Crushed shale

Results from the crushed shale analysis are presented in Table 6.10 and Table 6.11. The information provided in the tables describes the condition of the sample (dry or as-received), applied pore pressure (P_0) and two permeability values - K_h representing high permeability region (highly-conductive area of the sample or the fracture) and K_l representing low permeability region (or the matrix). All samples are crushed to standard 0.5 mm <d< 0.85 mm unless stated otherwise.

Table 6.10. Crushed GRI results of control-test group of samples.

			Dual system	
Sample	AR or Dry	P0, psig	Kh, mD	Kl, mD
CHE2	Dry	122.97	95.48	5.02E-07
CHE2	Dry	129.70	87.53	9.24E-07
CHE2	Dry	170.28	115.52	3.85E-07
CHE2	Dry	83.45	179.81	6.86E-07
CHE2	Dry	114.10	10.40	4.41E-07
CHE2	Dry	56.46	118.37	1.59E-06
CHE3	Dry	71.84	124.59	1.31E-06
CHE3	Dry	122.10	191.90	2.27E-06
CHE3	Dry	163.10	112.26	3.12E-06

CHE3	Dry	199.42	7.40	1.06E-07
CHE3	Dry	102.48	104.69	1.34E-06
CHE3	Dry	118.79	197.74	1.19E-06
CHE3	Dry	56.60	53.69	5.93E-07
EBN20	Dry	177.96	72.15	2.36E-08
EBN20	Dry	211.20	59.14	5.13E-08
NEX7	Dry	146.90	10.07	1.13E-07
NEX7	Dry	83.60	63.93	2.02E-07
NEX7	Dry	121.47	157.99	4.04E-07
NEX7	Dry	57.66	148.73	6.97E-07
NEX15	Dry	70.41	10.96	2.35E-08
NEX15	Dry	73.29	5.62	4.67E-07
NEX15	Dry	123.90	5.43	2.78E-08
NEX15	Dry	165.43	10.96	2.35E-08
NEX15	Dry	56.44	143.00	7.61E-07
NEX33	Dry	95.04	0.08	1.04E-08
NEX33	Dry	100.69	2.16	1.97E-08
NEX33	Dry	177.09	1.15	1.07E-08
NEX33	Dry	225.69	9.60	6.43E-09
NEX33	Dry	121.00	72.72	9.47E-08
NEX33	Dry	55.81	50.84	2.68E-06

Table 6.11. Crushed GRI results of non-control-test samples in as received and dried conditions.

Sample	AR or Dry	Po	Kh, mD	Kl, nD
BC02	Dry	127.86	4.20E-02	1.22E-07
BC02	Dry	59.40	6.51E+01	1.19E-07
BC02	AR	133.02	6.39E+01	1.36E-07
BC03	Dry	127.96	1.39E+02	8.79E-07
BC03	Dry	58.54	9.58E+01	1.55E-06
BC03	AR	137.27	2.64E+02	1.47E-07
EBN21	Dry	112.33	4.51E+01	8.50E-08
EBN21	AR	110.60	7.21E+01	6.73E-09
EBN22	AR	107.79	3.23E+01	1.92E-08
EBN23	Dry	116.24	1.36E+01	1.44E-07
EBN23	AR	205.48	3.94E+01	2.76E-08
EBN24	Dry	173.61	9.03E+01	4.40E-08
EBN24	AR	180.84	6.69E+01	3.05E-08
EBN25	Dry	189.70	1.64E+02	8.80E-08
EBN25	AR	157.79	6.33E+01	6.94E-08
EBN27	Dry	70.18	5.93E-01	5.44E-08

EBN27	Dry	64.89	1.73E+01	1.17E-08
EBN27	AR	116.77	1.00E+02	4.87E-08
EBN27	AR	168.75	5.55E+00	3.29E-08
EBN27	AR	197.72	1.49E+02	5.14E-08
EBN28	AR	171.74	2.23E+01	1.39E-08
EBN28	AR	203.40	5.42E+01	3.80E-08
EBN29	Dry	106.54	1.43E+01	1.14E-07
EBN29	Dry	166.25	1.05E+02	5.73E-06
EBN29	Dry	193.49	3.85E+01	5.19E-07
EBN29	AR	83.22	1.71E+02	9.66E-08
EBN30	AR	116.30	1.46E+02	1.20E-08
EBN35	Dry	111.09	1.82E+02	1.98E-06
EBN35	AR	117.24	2.77E+00	1.22E-08
EBN35	AR	173.72	1.23E+02	9.24E-05
EBN36	Dry	71.14	1.50E+01	3.39E-08
EBN36	Dry	64.94	3.79E+01	1.38E-07
EBN36	AR	92.12	6.43E+01	3.15E-08

Graphs containing experimental and simulated pressures are presented in Figure 6.1. Inverted results such as porosity and permeability values are also shown. Only Control-Test samples are presented, while the graphs of other samples are provided in Appendix J. The first 2-3 sec give no match, however in Section 3.4.4.2 it was demonstrated that this initial region corresponds to where temperature equilibrium has not been achieved and therefore should be ignored. Good to moderate history matches pressure data was achieved after 2-3 s for most samples. Some samples showed a slight mismatch between the experimental data and simulation in particular regions of the curve, which could be explained by complex microfracture gas flow behaviour shown in Figure 6.1b, d and h. Fluctuations caused by the temperature effects can also be observed in Figure 6.1e, f, I and j.
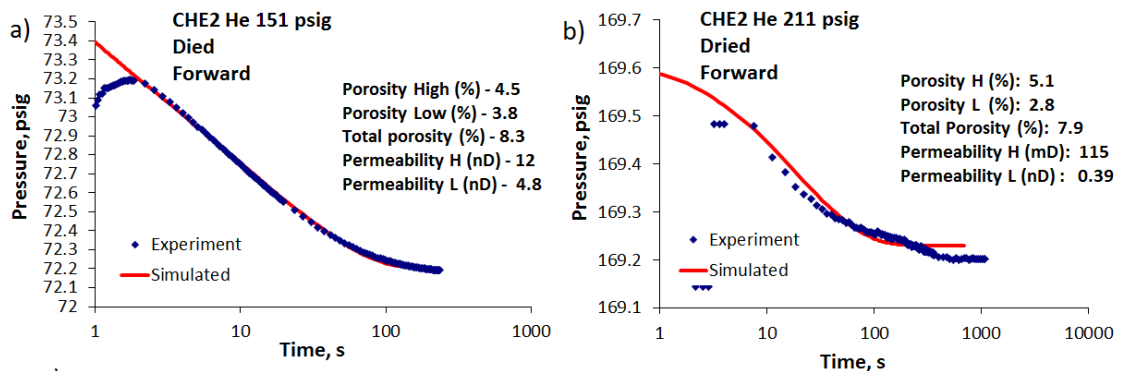
Figure 6.1. Simulations of crushed GRI experimental data for Control-Test samples.
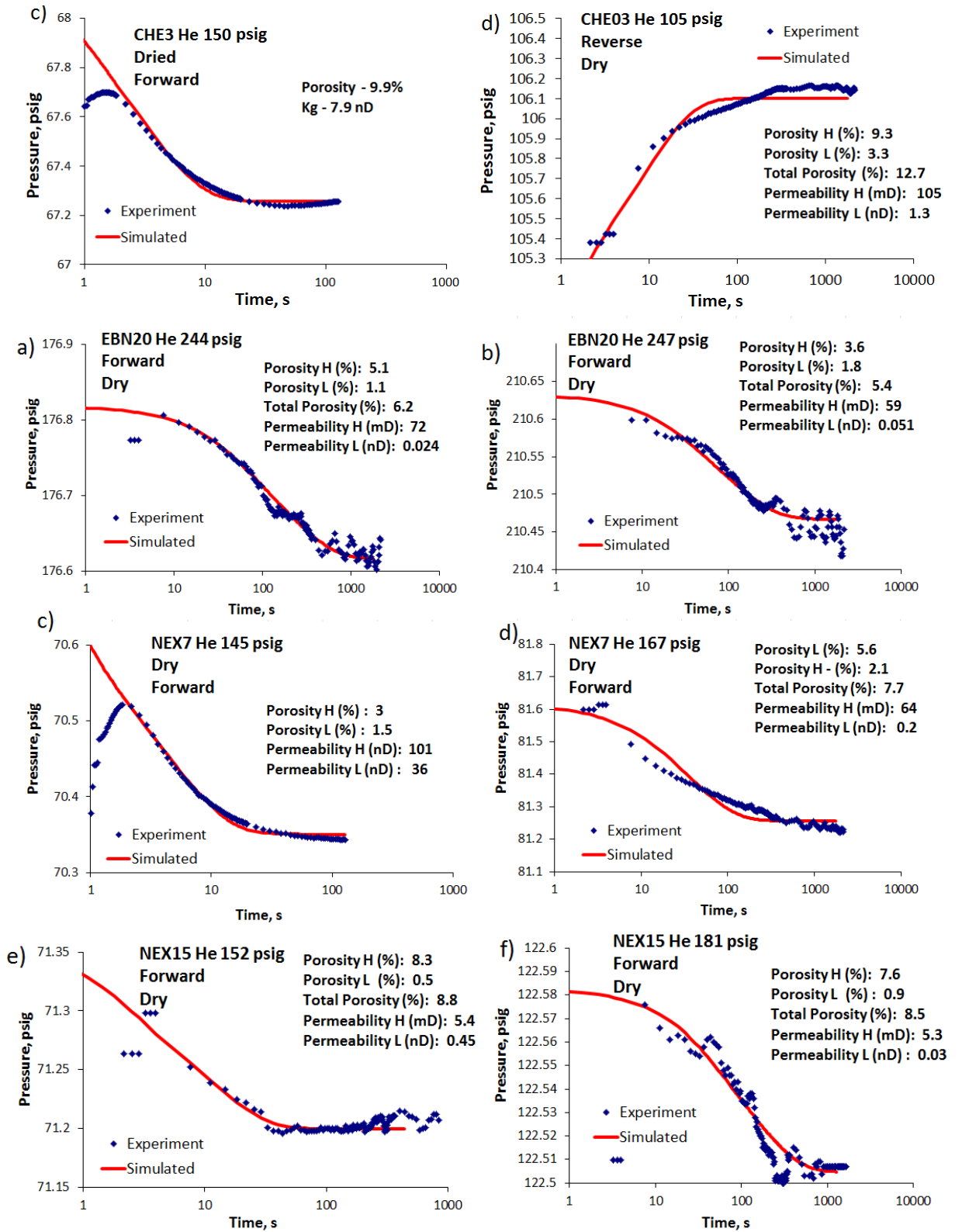
Figure 6.1. Continued. Simulations of crushed GRI experimental data for Control-Test samples.
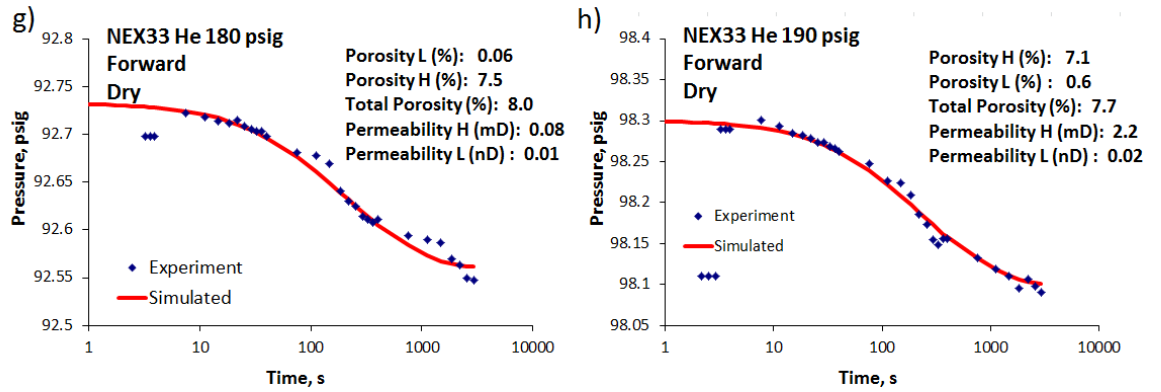
Figure 6.1 Continued. Simulations of crushed GRI experimental data for Control-Test samples.

6.3.2   Core Plug GRI (CPGRI) and Radial Pressure Decay GRI (CPGRI-RPD)

CPGRI permeability results are presented in Table 6.12 and Table 6.13 obtained from dual and single porosity models respectively. CPGRI-RPD permeability results are given in Table 6.14. The information provided in the tables shows the direction of the lamination (parallel or perpendicular, see Figure 3.1 in Section 3.2.3), applied pore pressure (P_0), permeability values – K_h for double porosity model, representing high permeability region (or the fracture) and K_l representing low permeability region (or the matrix). In addition, b-factor values for the Klinkenberg corrected results are provided. Other permeability results are provided in Appendix M.

Table 6.12. Core plug gas invasion results using fractures in the simulation. REV in the gas column indicates desorption experiment (reverse).

Sample	Lamination	Po, psig	Kh, mD	Kl, nD	b factor, psig^{-1}
CHE2	perp	146.64	3.91E-04	1.43E-05	
CHE3	parallel	122.7	4.18E+00	6.87E-04	
NEX7	perp	74.87	4.37E-03	1.06E-04	
NEX15	perp	75.73	5.68E-04	4.73E-04	
NEX33	parallel	69.04	5.68E-04	4.91E-04	
EBN20	perp	111.83	7.33E-04	8.37E-05	
CHE2	perp	REV	2.70E-03	3.53E-07	8997
CHE3	parallel	122.7	3.76E-05	2.70E-05	2792
EBN20	perp	REV	2.75E+00	6.75E-05	4

Table 6.13. Core plug gas invasion results without fracture in the simulation. REV in the pressure column indicates reverse pressure build-up test.

Sample	Lamination	Po, psig	Kl, nD	b factor, psig^{-1}
CHE2	perp	490.19	2.30E-06	
CHE3	parallel	697.17	6.89E-04	
NEX7	perp	REV	4.37E-03	
NEX15	perp	150	3.34E-03	
NEX33	parallel	210	5.68E-04	
EBN20	perp	REV	2.33E-04	
CHE2	perp	692.24	1.07E-06	2664
CHE3	parallel	697.17	3.26E-05	27048
EBN20	perp	193.87	1.14E-05	608
NEX7	perp	524	2.60E-05	27850
NEX15	perp	620	1.23E-05	2476
NEX33	parallel	REV	6.80E-03	148

Table 6.14. Core plug gas invasion results for the samples with a hole.

Sample	Lamination	Po, psig	Kl, nD	b factor, psig^{-1}
EBN20	parallel	153.42	7.22E-04	
EBN20	parallel	153.42	1.05E-05	29920

Graphs showing experimental and simulated pressures are provided in Figure 6.2. Only Control-Test samples are presented, while the graphs of other samples are provided in Appendix O. Overall moderate history matches were obtained for the pressure transient data obtained from most samples. However, history matches for some samples produced good fits while for others the history matches were poor. An important factor when inverting data obtained from transient tests on core plugs is that some of the pressure curves continued to decline, partly due to them not reaching equilibrium and partly due to gas leakage. The curves that indicated obvious leakage were discarded, however, in some cases it is difficult to distinguish between slight leakage and matrix absorption. Pressure oscillations seen in some of the simulations (Figure 6.2f and h) are due to the wider time-steps in the simulation model, and have no effect on the derived results.
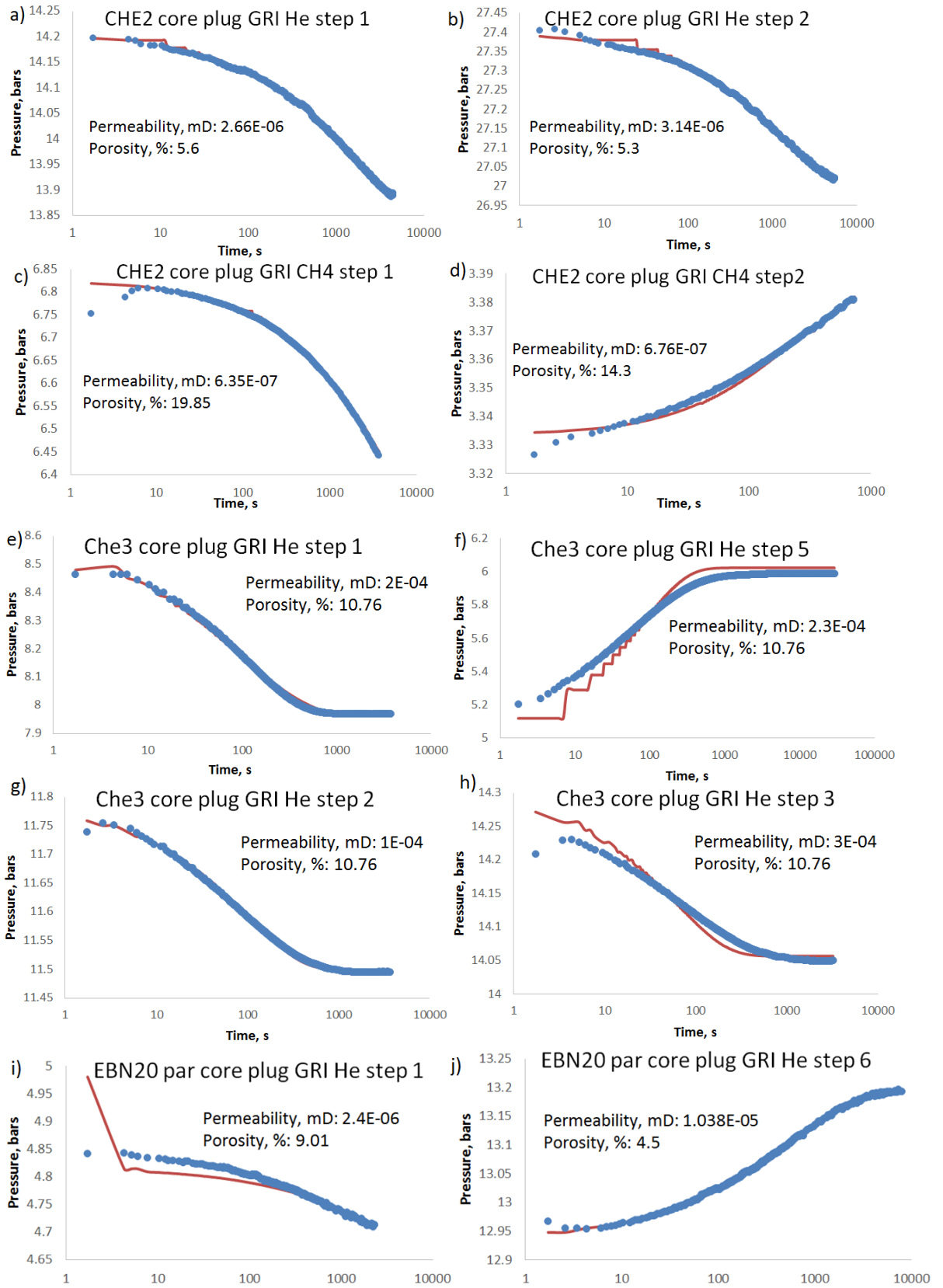
Figure 6.2. Simulations of the core plug GRI experimental results for Control-Test samples.
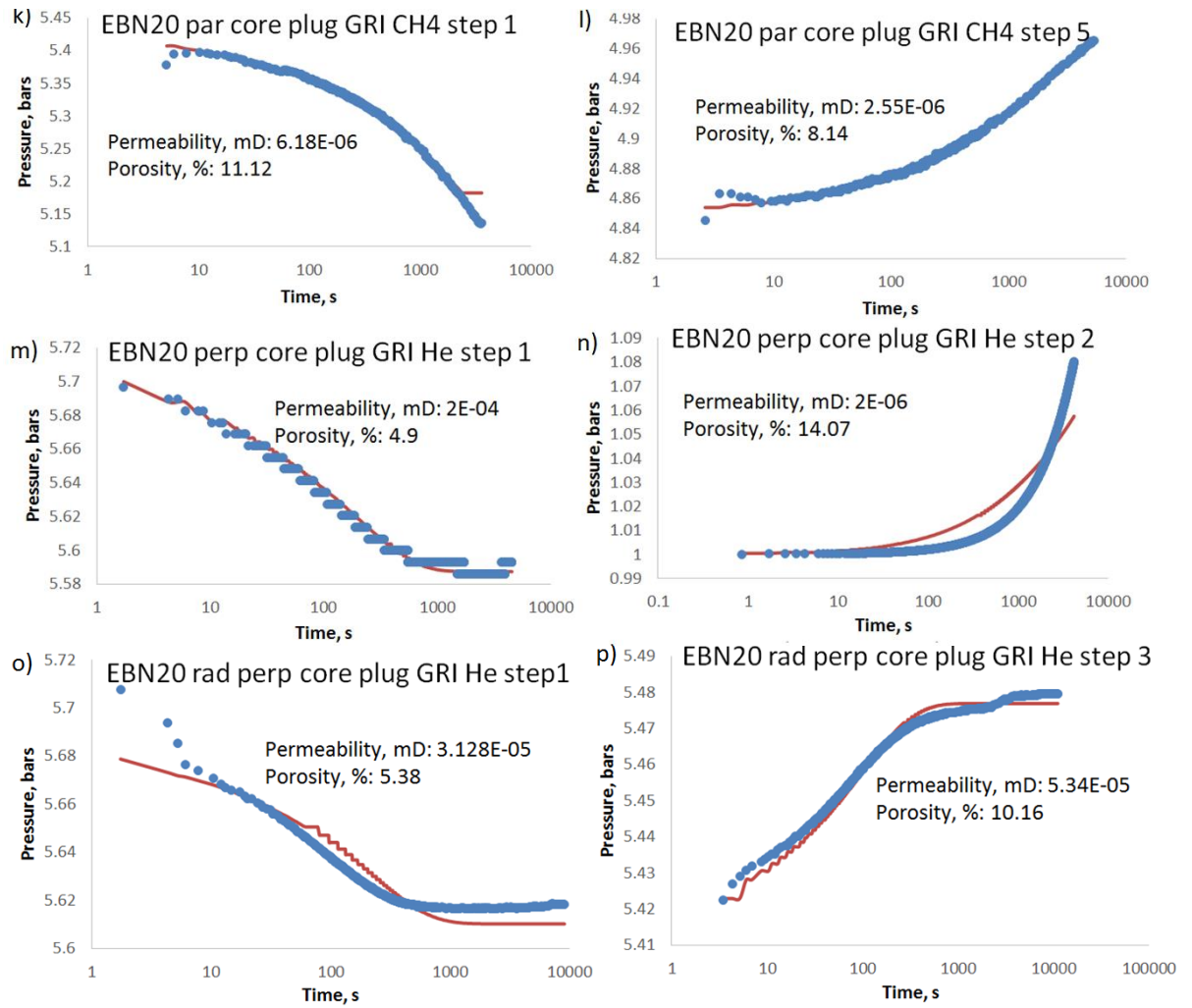
Figure 6.2 continued. Simulations of the core plug gas invasion experimental results for Control-Test samples.

6.3.3 Modified Pressure Decay (MPD) and Radial Pressure Decay (MPD-RPD)

Permeability results from the MPD experiment are presented in Table 6.15 (for single porosity model), Table 6.16 (for double porosity mode) and Table 6.17 (for radial pressure decay). The information provided in these tables is similar to those provided in other results tables presented in this chapter. All the rest of the permeability results are provided in Appendix N.

Table 6.15. MPD results using single model.

Sample	Lamination	Po, psig	Kl, nD	b factor, psig^{-1}
CHE2	parallel	514	1.26E-04	
CHE3	parallel	150	2.87E-04	
EBN20	perp	71.55	3.31E-05	
NEX7	perp	748	3.54E-03	
NEX15	perp	509	3.25E-05	
NEX33	parallel	150	4.73E-04	
CHE2	parallel	218	5.50E-06	5241
CHE3	parallel	REV	3.12E-06	753
EBN20	perp	REV	7.19E-06	415
NEX7	perp	641	1.13E-04	12655
NEX15	perp	532	8.90E-07	18709
NEX33	parallel	206	5.30E-04	290

Table 6.16. MPD results using dual model.

Sample	Lamination	Po, psig	Kh, mD	Kl, nD	b factor, psig^{-1}
CHE2	parallel	620	2.90E-03	5.00E-05	
CHE3	parallel	150	1.30E-03	5.62E-04	
EBN20	perp	108	1.02E-01	7.56E-04	
NEX7	perp	748	1.62E-03	2.67E-07	
NEX15	perp	735	1.14E-04	1.18E-05	
NEX33	parallel	210	2.30E-04	3.88E-05	
CHE2	parallel	218	4.00E-05	5.93E-07	14616
CHE3	parallel	206	1.48E-04	1.16E-04	2333
EBN20	parallel	157	3.00E-05	2.01E-07	541
NEX7	perp	524	3.82E-03	1.16E-10	67516
NEX15	perp	509	6.36E-05	1.08E-07	14781

Table 6.17. MPD-RPD results.

Sample	Lamination	P0	Kh	Kl	b	Hole drilled
EBN20	Parallel	158	1.99E-03	4.14E-04	1376.33	All the way
EBN20	Parallel	281	1.05E-03	8.14E-04		All the way
EBN20	Parallel	158		9.84E-04		All the way
EBN20	Perpendicular	71		7.31E-06	3364.91	All the way
EBN20	Perpendicular	71		3.31E-05		All the way
EBN5	Parallel	158	8.00E-04	4.00E-03		Upstream
EBN5	Parallel	190		2.50E-05		Downstream

Graphs showing experimental and simulated pressures are provided in Figure 6.3. Unlike in previous experiments (crushed shale and CPGRI), there are two pressure curves to match in this case – upstream and downstream. Overall moderate history matches was obtained. The difficulty in some of the cases was that pressures would not equilibrate even after long experimental time as shown on Figure 6.3b, e and f.
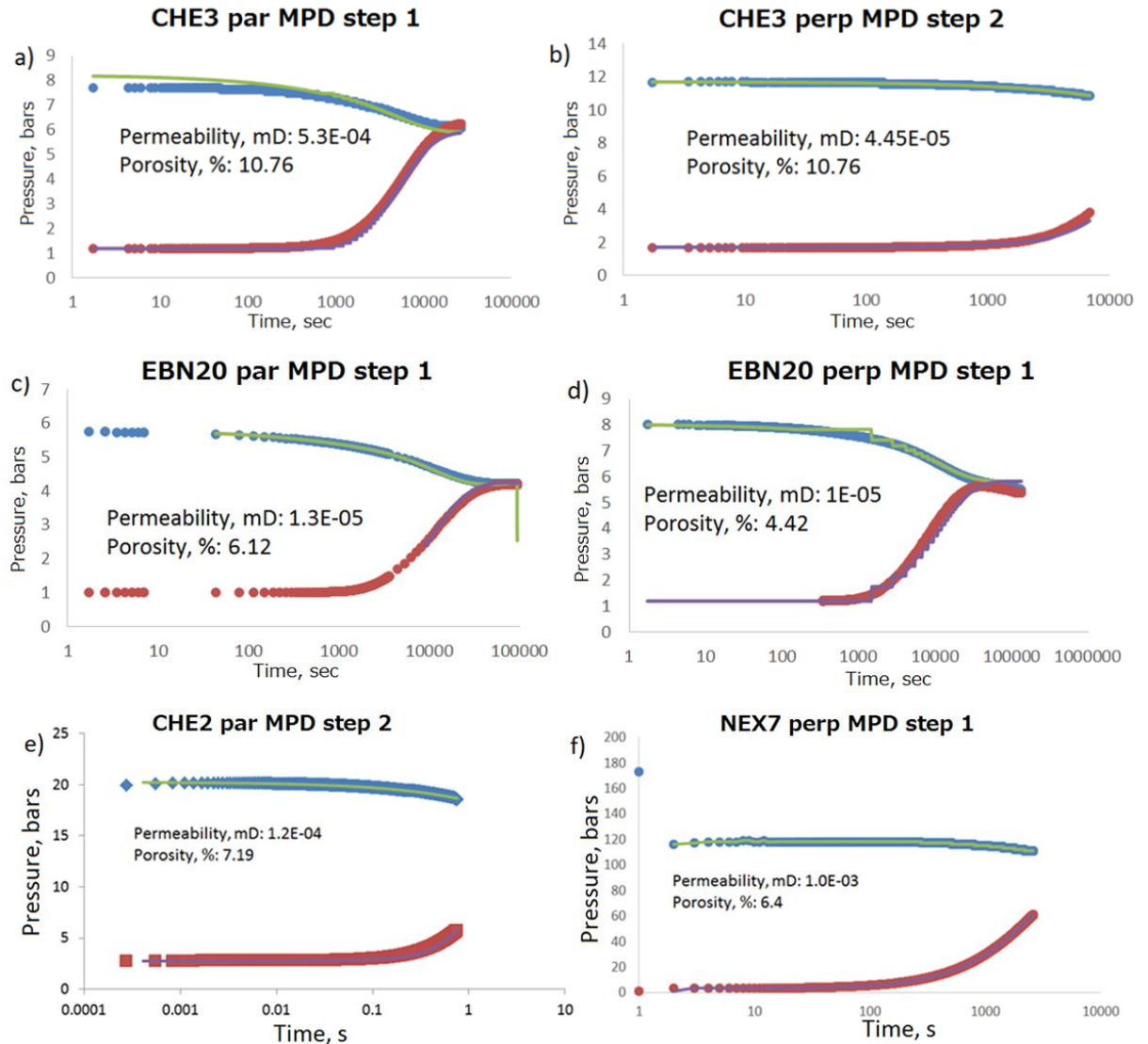
Figure 6.3. Simulations of MPD experimental data.

6.3.4   Control-Test results

6.3.4.1   Control-Test crushed shale permeability results

Each of the three laboratories provided single crushed shale permeability value for every Control-Test sample. These values were compared to the best-fit double porosity model permeability values obtained from this research; the results are presented in Figure 6.4.

	Leeds	Lab A	Lab B	Lab C
CHE2	7.55E-07	1.07E-05	5.33E-04	3.41E-05
CHE3	1.42E-06	9.39E-05	1.56E-04	2.47E-04
EBN20	3.75E-08	2.73E-06	4.56E-05	1.56E-03
NEX 7	3.54E-07	1.50E-06	1.59E-04	6.04E-06
NEX15	2.61E-07	2.15E-06	3.03E-04	2.62E-05
NEX33	4.70E-07	2.94E-06	5.59E-05	1.50E-03
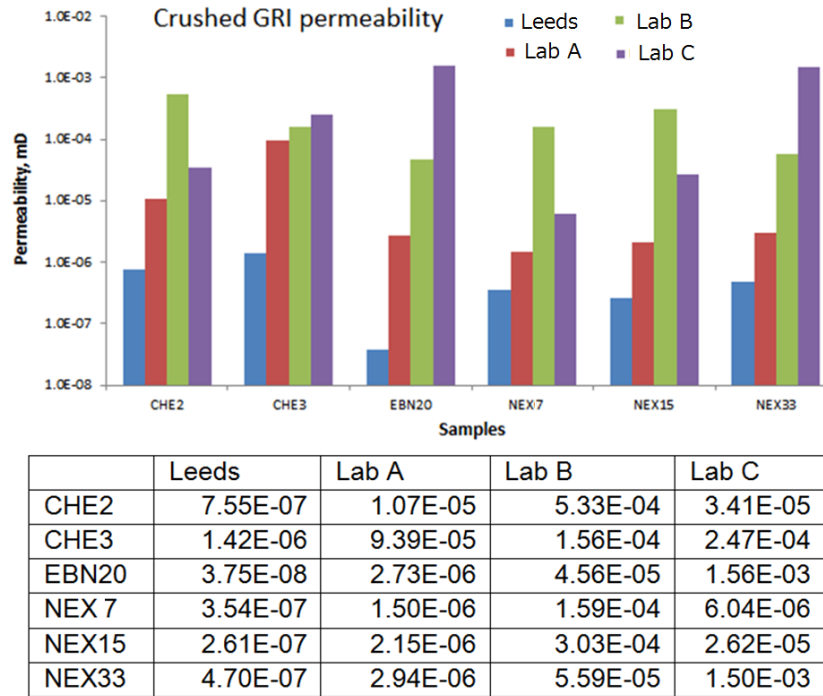
Figure 6.4. Permeability results provided by different laboratories for 6 samples analysed. All are dried except for Lab A, which measured samples in as received condition.

Crushed permeability showed huge variations in results between different laboratories. The differences reached up to 5 orders of magnitude for sample EBN20 between the values obtained in this research (Leeds) and Lab C. The closest match was shown by sample CHE3, where the three laboratories provided almost identical result, whereas difference between Leeds and other laboratories was two orders of magnitude. The smallest difference between Leeds and the control-test values was obtained for the sample NEX7 – Leeds permeability was about 4 times lower than Lab A. Permeability values obtained by Leeds are systematically lower for every sample compared to the other laboratories. Lab A provided the lowest permeability values compared to other Control-Test laboratories.

6.3.4.2 Control-Test core plug results

Linear pressure decay permeability (equivalent of MPD) was also one of the parameters obtained in the Control-Test experiment. Lab B provided only two results for this experiment. The results for remaining laboratories and Leeds are provided in Figure 6.5 and Figure 6.6. Permeability results of two core plug experiments obtained in this research (Leeds) were compared with Control-Test values.
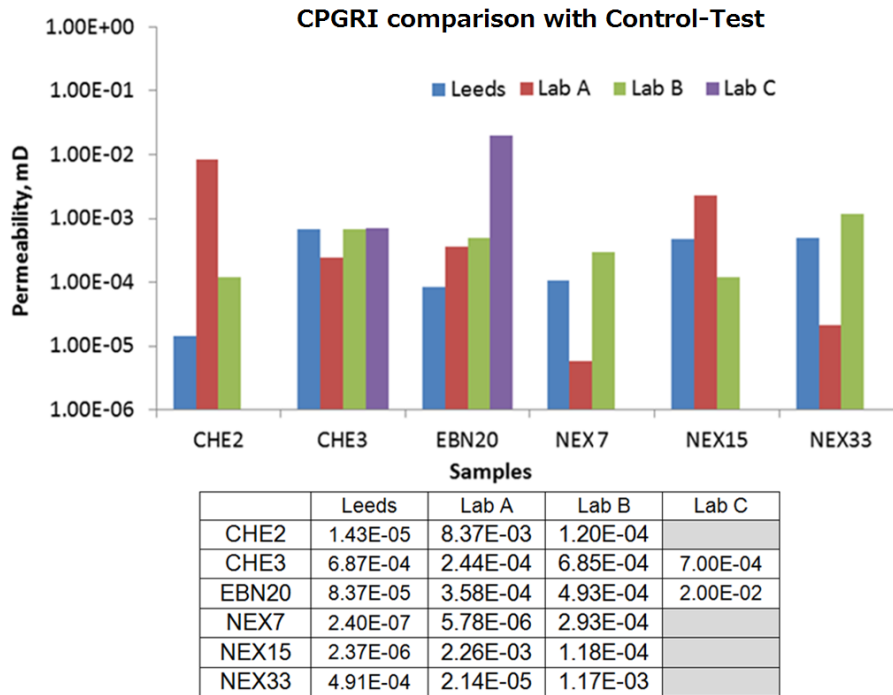
Figure 6.5. CPGRI permeability results comparison with control-test core plug permeability values. Lab C provided only 2 values for this test.

	Leeds	Lab A	Lab B	Lab C
CHE2	1.43E-05	8.37E-03	1.20E-04	
CHE3	6.87E-04	2.44E-04	6.85E-04	7.00E-04
EBN20	8.37E-05	3.58E-04	4.93E-04	2.00E-02
NEX7	2.40E-07	5.78E-06	2.93E-04	
NEX15	2.37E-06	2.26E-03	1.18E-04	
NEX33	4.91E-04	2.14E-05	1.17E-03	
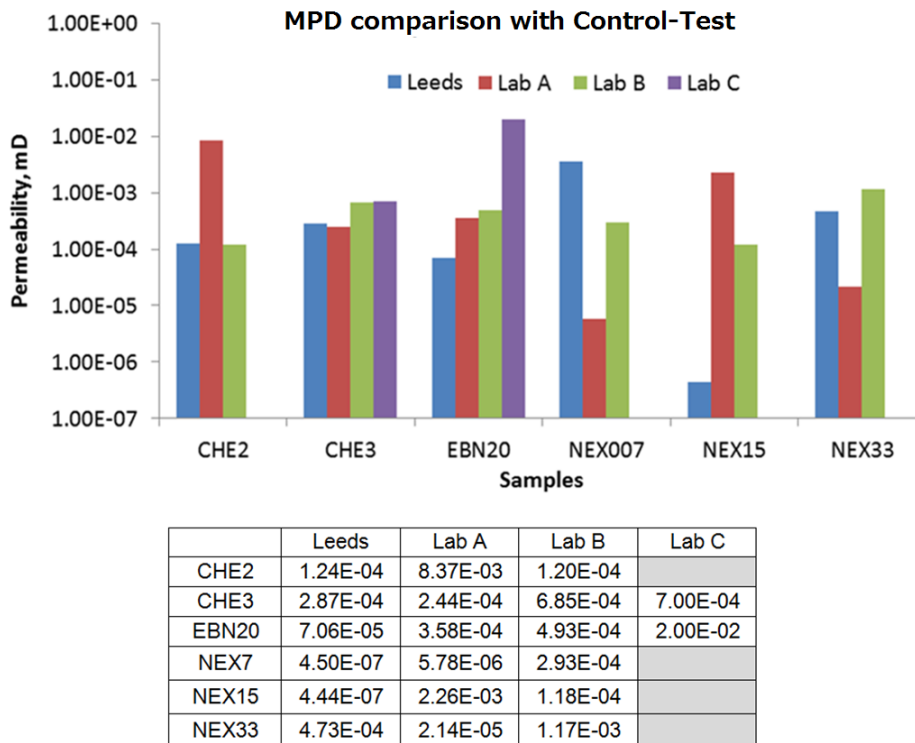
Figure 6.6. Leeds MPD permeability results and MPD-equivalent measurement by Control-Test companies comparison. Lab C provided only 2 values for this test.

	Leeds	Lab A	Lab B	Lab C
CHE2	1.24E-04	8.37E-03	1.20E-04	
CHE3	2.87E-04	2.44E-04	6.85E-04	7.00E-04
EBN20	7.06E-05	3.58E-04	4.93E-04	2.00E-02
NEX7	4.50E-07	5.78E-06	2.93E-04	
NEX15	4.44E-07	2.26E-03	1.18E-04	
NEX33	4.73E-04	2.14E-05	1.17E-03	

Unlike crushed permeability, the core plug pressure decay showed much better and more comparative results between different laboratories. There are no systematic outliers among the permeability values as it was in the case of crushed shale experiment. The

biggest mismatch between the Control-Test results was obtained for samples EBN20 (between Leeds and Lab C) and CHE2 (between Leeds and Lab A) – the difference between permeability values was about 2 orders of magnitude (Figure 6.5). MPD permeability results exhibit two notable outliers between Leeds and Control-Test experimental results – for the sample NEX7 and NEX15 (Figure 6.6). For the later sample the difference reaches up to 4 orders of magnitude (between Leeds and Lab A). For both experiments the most consistent data were obtained for sample CHE3 – all laboratories provided close results within 1 order of magnitude. It has to be noted that crushed permeability values were also the most comparative for the sample CHE3.

6.3.5 Comparison of results

6.3.5.1 Crushed shale correlations

To observe the trends and correlations between the presented results, the Control-Test and best-fit Leeds permeability values were cross-plotted with each other. The Control-Test crushed permeability results for each sample correlate neither with Leeds crushed values, nor between themselves (Figure 6.7).
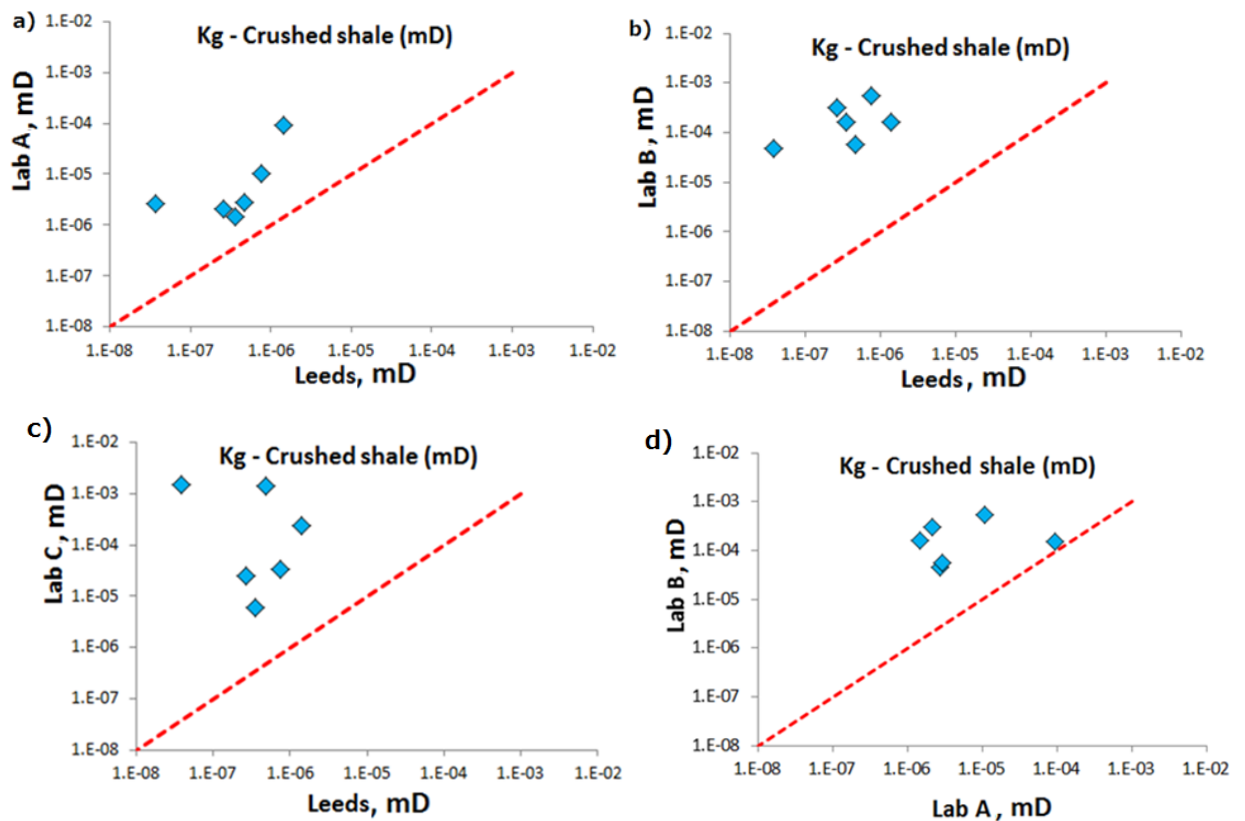
Figure 6.7. Correlation comparison between Leeds and Control-Test values. There is a systematic bias in Lab A compared to Lab B and Lab C.

e)

f)
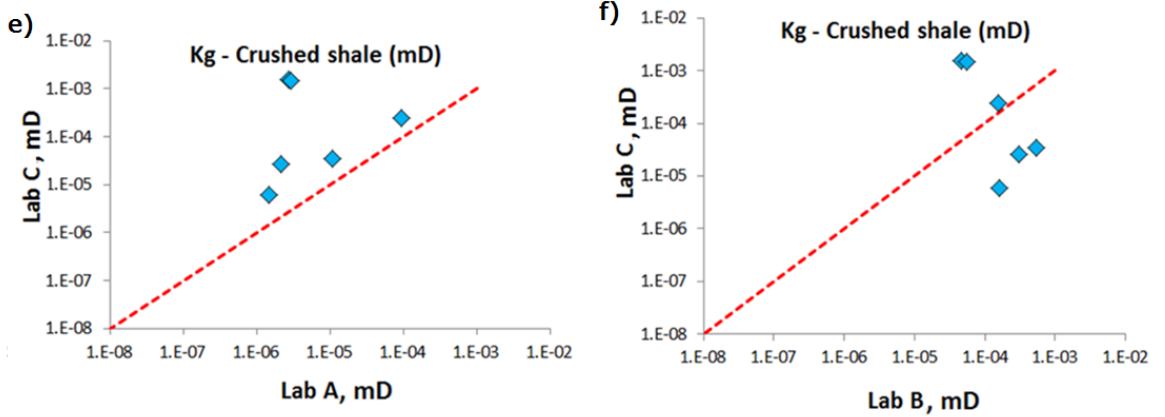
Figure 6.7 Continued. Correlation comparison between Leeds and Control-Test values.

6.3.5.2   Core plug correlations

In general, there is no good core plug correlation between the matrix permeability produced in this research and obtained by the Control-Test laboratories (Figure 6.8 for MPD and Figure 6.9 for CPGRI). The main tendency is for the Control-Test values to be higher than Leeds permeabilities. In contrast, when plotted against each other Lab A and Lab B permeabilities show no systematic correlation (Figure 6.9). Lab C provided only two permeability values so it is not included in this comparison.

a)

b)
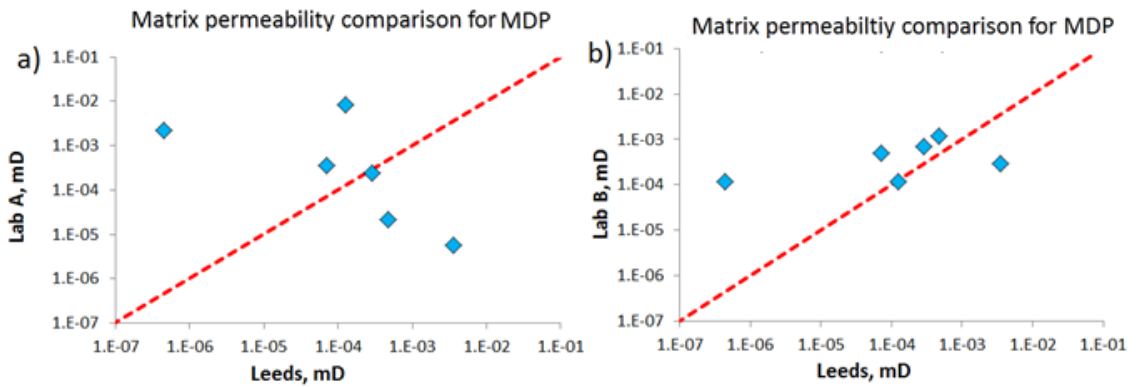
Figure 6.8. Correlations of control-test and Leeds core plug permeability results using MPD test.
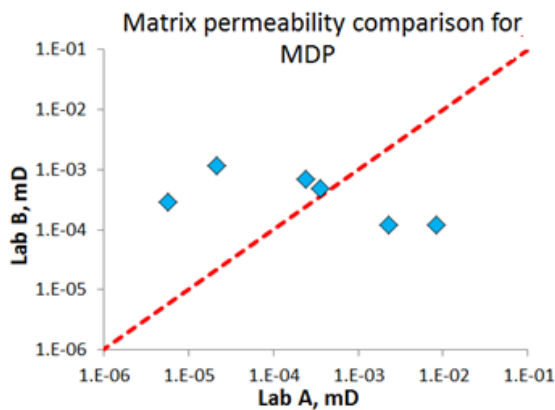
Figure 6.9. Comparison between Lab B and Lab A core plug permeability results.

6.3.5.3 Impact of gas pressure

The permeability – inverse of pressure plot is provided in Figure 6.10. Each plot is made out of the results of one pressure series experiment, where several pressures are applied (as described in the methodology Section 3.2). Almost all samples exhibited good correlations between the permeability and the inverse of pressure. EBN33 CPGRI methane, CHE3 CPGRI methane, EBN20 MPD helium and CHE2 MPD helium experiments produced perfect correlations of R^2 of 0.9 and higher (Figure 6.10a, f, j and l). Crushed GRI experiments resulted in poor - moderate correlations for 4 samples: NEX7, NEX15, NEX33 and CHE2 (Figure 6.10). CHE2 showed only general permeability – inverse of pressure trend. The NEX samples all correlated with the crushed core, whereas for the core plug tests only NEX15 correlated for MPD (Figure 6.10h) and NEX33 for CPGRI (Figure 6.10i). EBN20, EBN33, CHE2 and CHE2 showed better results for core plug experiments.
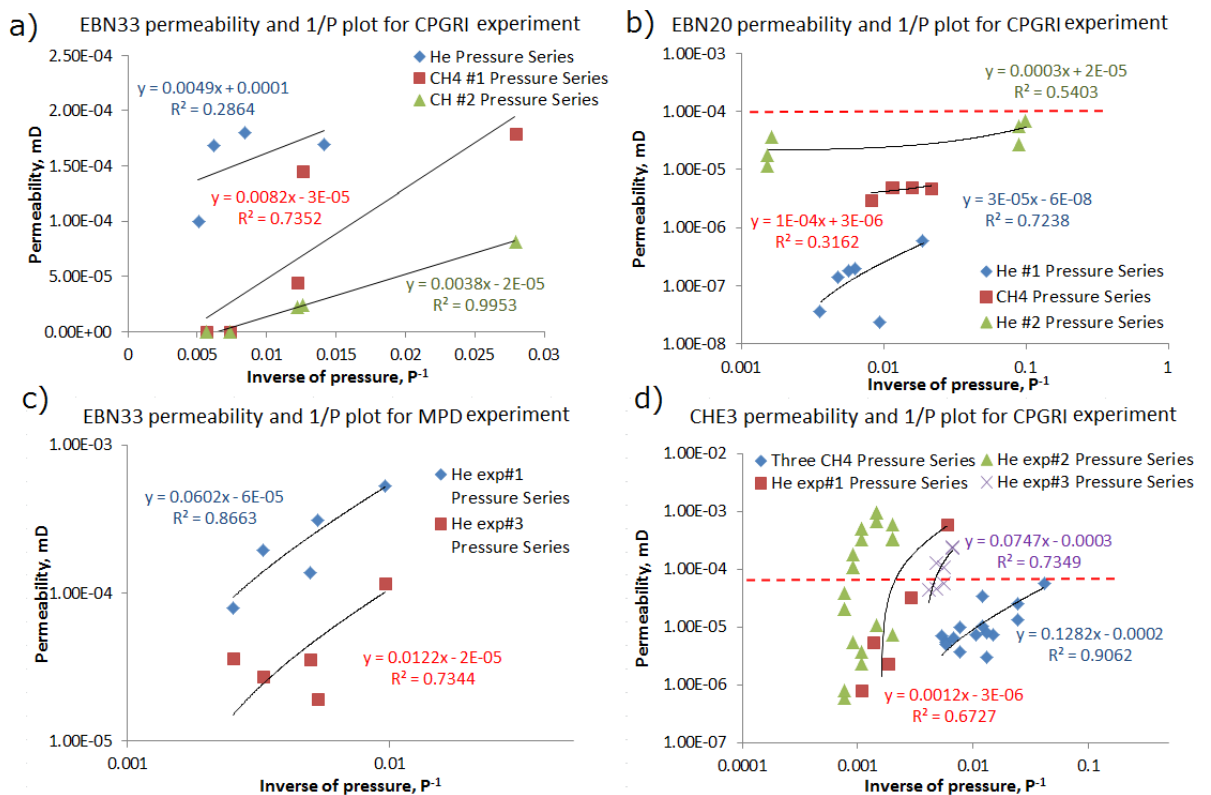
Figure 6.10. Obtained permeability versus inverse of pressure for Control-Test samples. Note that extrapolation to 1/p = 0 would give negative absolute permeability values for several samples.

183
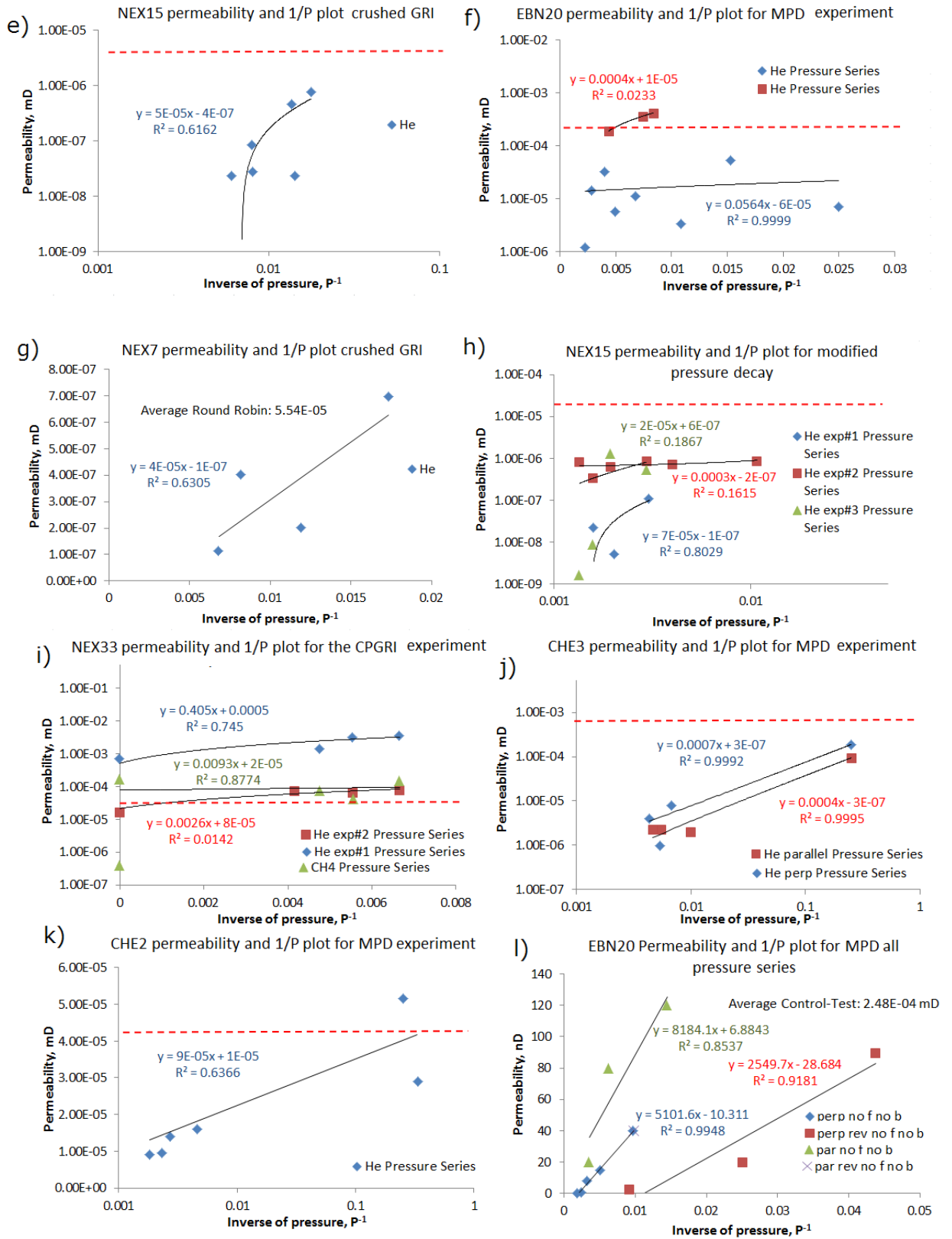
Figure 6.10. Continued. Obtained permeability versus inverse of pressure for Control-Test samples. Note that extrapolation to 1/p = 0 would give negative absolute permeability values for several samples.

6.3.5.4 Impact of confining pressure

Various confining pressures were tested for the MPD experiment. The objective was to measure the extent to which a change in confining pressure would impact the derived permeability values. The comparative plots of the confining pressure effects for the NEX15 sample are presented in Figure 6.11a) shows porosity-permeability plot; b) shows permeability-inverse of pressure plot; c) shows permeability-net stress ($P_{confining} - P_{pores}$) plot. Generally, a positive correlation can be observed between permeability and confining pressure in all figures.
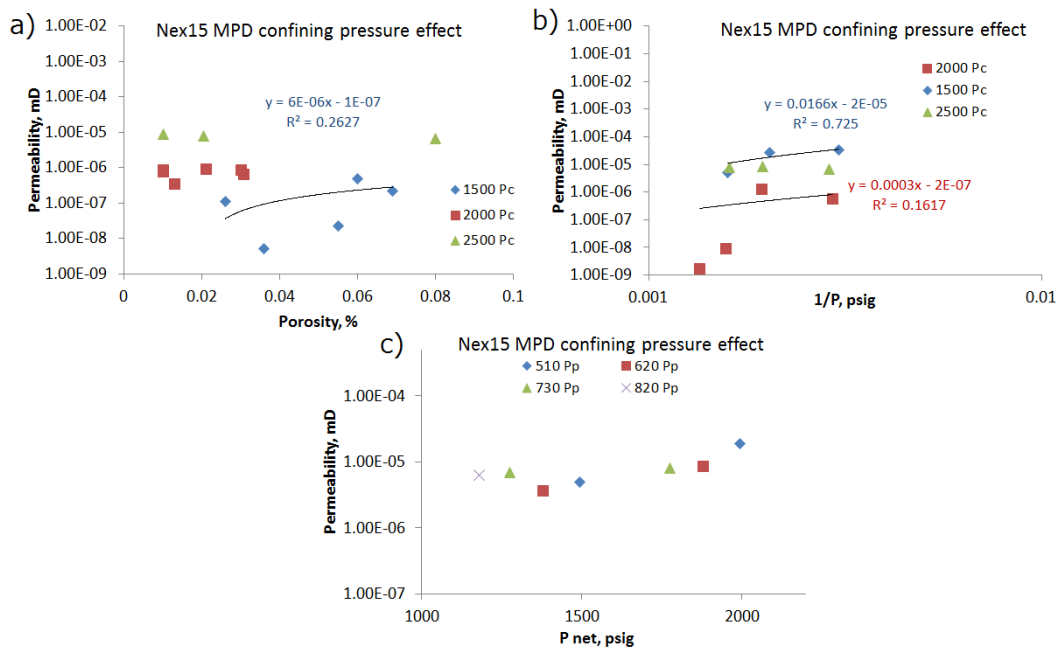
Figure 6.11. Comparison of confining pressure (Pc) effect on the results. Pore pressure is denoted by Pp. The permeability uncertainty might reach up to 50%.

6.4 Permeability Discussion

In this section, the differences between the experiments are discussed and arguments explaining the behaviour of gas flow in shale are presented. Firstly the crushed core results are discussed, followed by a discussion of the results from the core plugs. Finally, suggestions are made as to how the measurements might be improved.

6.4.1 Crushed results analysis

6.4.1.1 Permeability over-estimation

The crushed permeability results lack comparability between each other and overall there are no correlations between Control-Test laboratories (see Sections 6.3.1 to 6.3.5). In fact, crushed shale permeabilities obtained by the Control-Test laboratories showed unrealistically high values for shale rocks (Table 6.18). In particular Lab C with the permeability estimation for EBN20 of 1.56E-03 mD, which is comparable to the tight sandstone (TGS) permeability values, yet the TGS have clearly visible pores and microfractures (red arrows in Figure 6.12).

Table 6.18. Control-Test permeability summary - comparison.

Permeability	Lab A, mD	Lab B, mD	Lab C, mD	Leeds, mD
Minimum	1.50E-06	4.56E-05	6.04E-06	3.75E-08
Maximum	9.39E-05	5.33E-04	1.56E-03	1.42E-06
Average	1.90E-05	2.09E-04	5.62E-04	5.49E-07
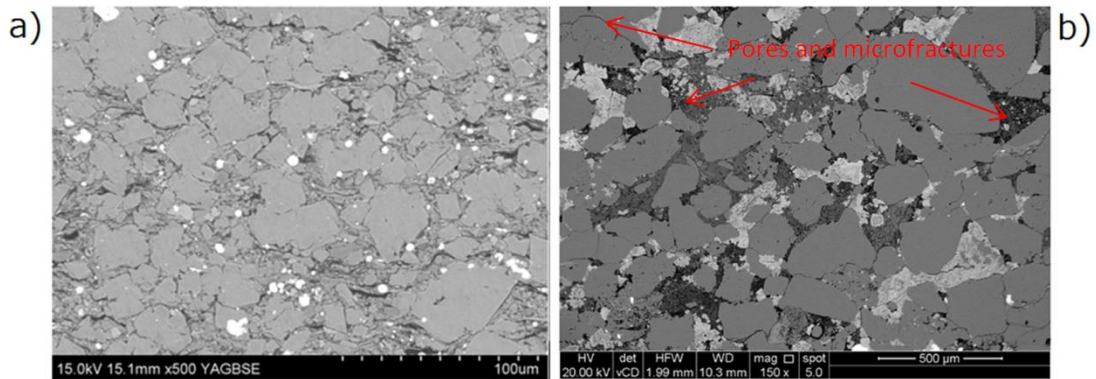
Figure 6.12. BSE Photomicrograph of sample EBN20 (a), which the crushed shale analysis indicates has a permeability of 1E-03 mD to 1E-04 mD. Whereas in the Figure b photomicrograph of a TGS sample is showed, which has a permeability of 8.5E-04 mD.

It was observed by simulation analysis that the shale chips of standard size (0.5 mm <d< 0.85 mm) with permeability higher than 10 nD equilibrate faster than 10 seconds (Figure 6.13). In comparison, the Control-Test values varied between 1.50 nD and 1.56E-03 mD (Table 6.18). The upper scale is considerably higher than 10 nD, which the simulation modelling suggests is an upper limit to what could be realistically measured using the crushed shale technique using a fragment size of 0.5 - 0.85 mm (Figure 6.13). Such high values would cause rapid pressure equilibration within milliseconds, which in turn would compromise permeability derivation.

Indeed, grain density analysis in Chapter 5 revealed that considerable amount of pressure decay was not being picked up by the transducers at the very start of the experiment (see Section 5.4.1.2 and Figure 5.25 in Section 5.4.2.4). In fact, the recorded pressure decay ranges from 37% down to only 8% of the actual pressure decay possibly taking place during the experiment (Table 6.19). Moreover, the pressure reading cannot be trusted during the very first second of the experiment as was shown with the glass reference plugs (see Figure 3.10 in Section 3.4.4.2). Such pressure behaviour was also observed by Profice et al. (2012) and Tinni et al. (2012). Overall, this means that high permeability layers cannot be detected using standard GRI test, because the gas enters the sample too quickly.
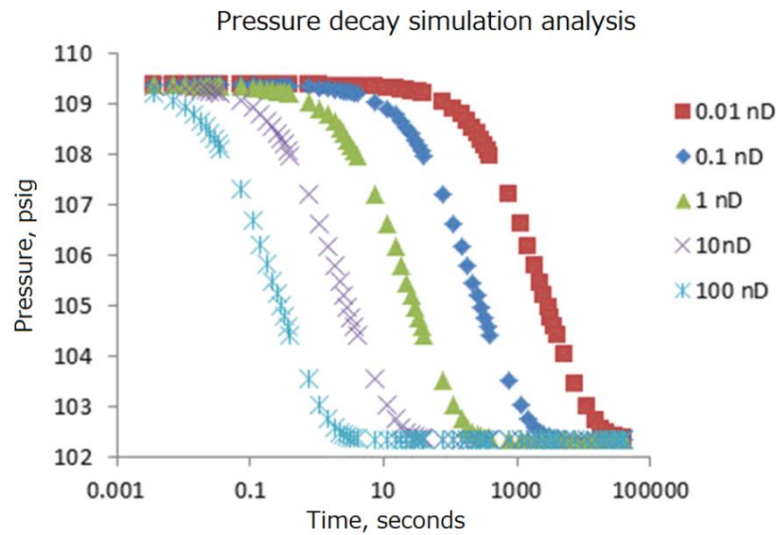
Figure 6.13. Simulated plots of the pressure decay vs time for crushed shale experiments. The shale is assumed to have a porosity of 10%, a particle size of 600 μm x 600 μm x 1800 μm and permeabilities between 0.01 nD and 100 nD. Note that the equilibration is reached extremely quickly (<10 seconds) for particles with a permeability of 100 and 10 nD.

Table 6.19. Differences between recorded and ideal initial pressures. Ideal case pressures were derived using Boyle's law and sample bulk volumes taken from Hg-immersion test. Not this comparison assumes Hg-immersion is not affected by high conductivity regions.

Pressures, psig	Samples					
	CHE2	CHE3	EBN20	NEX7	NEX15	NEX33
Recorded Initial	73.20	67.70	176.80	70.50	68.40	224.40
Ideal case Initial (Boyle's law)	74.99	69.47	177.85	71.77	71.04	225.92
Recorded Equilibrium	72.19	67.24	176.63	70.34	68.2	224.2
Recorded decay	1.01	0.46	0.175	0.16	0.2	0.2
Possible decay (Boyle's law)	2.80	2.23	1.22	1.43	2.84	1.72
Non-recorded ΔP	63.93%	79.40%	85.71%	88.78%	92.97%	88.37%

Peng and Loucks (2016) conducted similar Control-Test permeability experiment and reinterpreted crushed GRI pressure transient supplied by one of the service companies studied in this research. Their calculations on the same dataset produced permeabilities that were two orders of magnitude lower than the values provided by the service company (Peng and Loucks, 2016). These results resemble the permeability differences of around two-three order of magnitude (Table 6.18) on the same samples between Leeds and the corresponding Control-Test laboratory (Lab B). Therefore there is most likely a mathematical error in the proprietary derivation methodology of the given commercial laboratory.

6.4.1.2   Particle size effect on permeability

High permeability values produced by Lab C could be justified by the larger crushed particles used, as it was noted that Lab C returned back the samples with far larger and broader size fraction (d < 3.175 mm) than the standard size fraction used by Leeds, whereas Lab A and Lab B did not provide an indication of the particle size used during the analysis. Particles of different sizes were measured in this research and it was observed that bigger particles indeed produce higher permeabilities (Figure 6.14). Overall, the differences in permeability values reached up to one order of magnitude for the particles size of 0.85 mm to 7 mm. Tinni et al. (2012) in a similar study obtained a permeability change of two orders of magnitude with the variation of particle size from 0.7 mm to 7 mm. So the large differences in permeability values provided by different laboratories during the Control-Test could be explained by them using different grain sizes in their models. According to the trend obtained in Figure 6.14, the particle size for Lab A and Lab B should be over 7 mm. Results from Lab C also indicate ranges over 7 mm, however in reality the used fragment size by the company was d < 3.175 mm. Essentially, commercial laboratories should at least provide this significant information on measured particle size together with the permeability results.
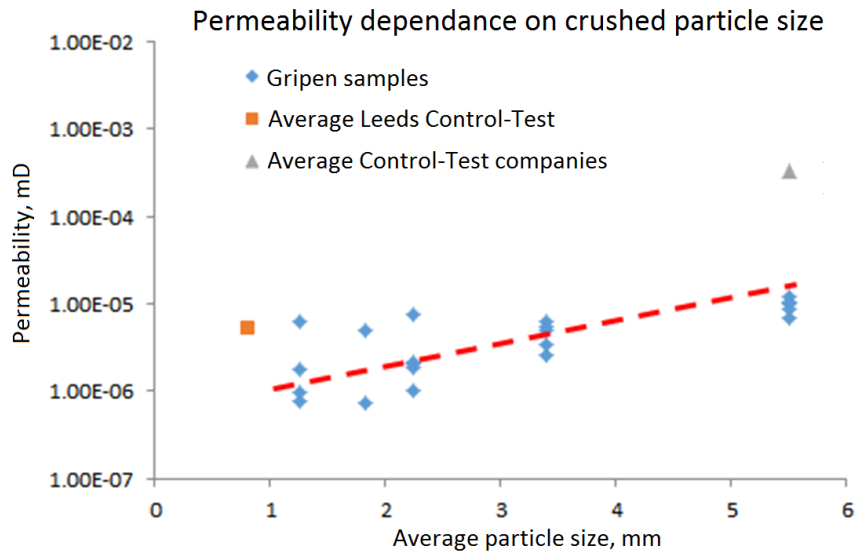
Figure 6.14. Relationship between permeability and particle size. For comparative purposes average values for Control-test samples obtained by Leeds and Control-Test companies is provided. Red line indicates increasing trend. The error range might reach 2 orders of magnitude.

It would, however, be difficult to judge what is the correct crushed particle size to use. Cui et al. (2009) argued that smaller particles have fewer cracks because the cracks and microfractures tend to develop among the main break points within the matrix of larger particles. Nevertheless, Cui et al. (2009) still recognized the need to account for the microfractures when deriving permeability. Handwerger et al. (2011) agrees that ultra-small fragments indeed contain less microfractures, whereas the pore structure still remains representative as pores in shale tend to be nano to micro scaled. Small shale fragments still should contain hundreds of thousands of micro-pores and, with some exceptions, can still be considered as representative of the overall matrix structure (Handwerger et al., 2011). However, Handwerger et al. (2011) did not provide any experimental data proving the applicability of the ultra-small shale particles to determine the permeability, apart from the SEM (Scanning Electron Microscope) images presenting the size of the pores.

In contrast, Profice et al. (2011) interpreted results of numerical models to argue that particles of 1 mm and less produce hardly any representative data for the pressure decay response. Profice et al. (2011) explained this to be due to less intact matrix remaining for the gas flow to properly develop within the crushed particles, which in turn might cause weak pressure response. Instead, Profice et al. (2012) suggested to determine an appropriate particle mean radius to be used for better pressure decay signal and in turn more accurate permeability inversion. Although Profice et al. (2012) included slip correction in their model, they did not address the heterogeneity still present within each

shale particle and used single permeability system similarly to Control-Test companies. So their presented permeability results may be biased towards the high permeability zone (especially microfractures) values, similarly to how Control-Test values were biased to higher values in this study.

In this work particle sizes of 0.5 mm <d< 0.85 mm produced decay curves that were successfully history matched. The permeability values obtained fit within the general trend shown in Figure 6.14. However smaller particles of 0.1 mm <d< 0.5 mm were found to produce almost no pressure response that could be used for the permeability derivation. This is because the pressure decay for such small particles happens in just several seconds where it might be compromised by the pressure fluctuations induced by the valve opening and temperature effects. Although bigger particles were successfully tested and modelled (Gripen samples), there are risks of increased amount of microfractures in these particles. Indeed SEM analysis of the crushed shale particles revealed the presence of microfractures (see Figure 4.27 in Section 4.4.2.2). These microfractures would create highly permeable pathways within the particle matrix and compromise the assumptions regarding the particle size used in the permeability inversion process. As a result, the effective particle size would be much smaller than the assumed during the inversion process, which in turn would increase the derived permeabilities as in the case of Control-Test results.

6.4.1.3 High permeability pathway model

There is no confirmation on whether high permeability region within the shale particles was considered by the Control-Test companies during the permeability inversion process. However, after the assessment of received information (single permeability value for each sample) and by personal communication, it was discovered that the shale was considered to be homogenous by each laboratory. Therefore the permeability value of the matrix was effectively averaged with any high-conductivity regions present, which in turn resulted in overestimation of the matrix permeability. This observation partly explains why all Control-Test permeability values are significantly higher than Leeds values, where separate high and low permeabilities were derived. In addition, the homogeneous matrix model is unable to produce a history match for the more complex pressure curves (Figure 6.15a), however the double porosity model produces nearly perfect match (Figure 6.15b).
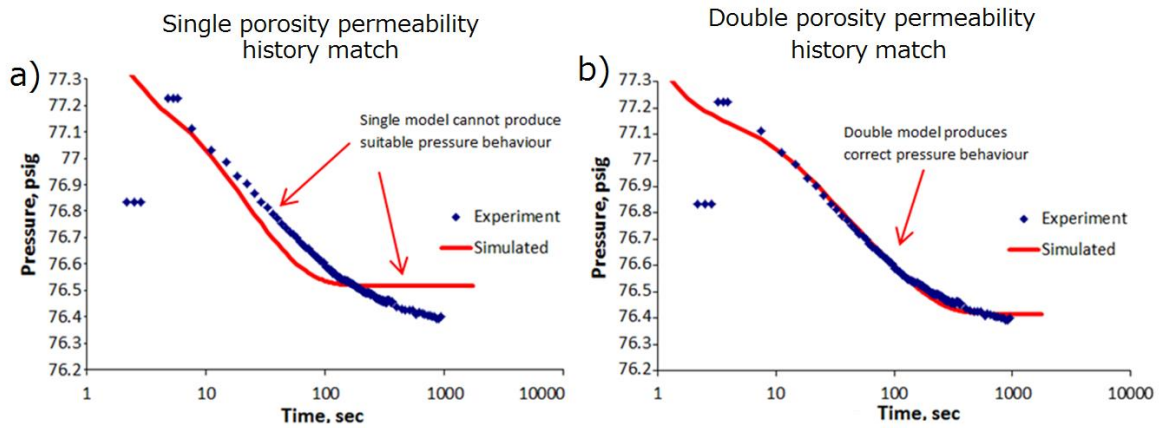
Figure 6.15. Comparison of (a) homogeneous (or single) and (b) heterogeneous (or double) crushed simulation history match.

Cui et al. (2009) in their crushed shale analysis agreed on the need to take into account heterogeneity. They compared it to the structure of coal, where the dual permeability system consists of microporous grains separated by macropores (Parkash and Chakrabartty, 1984). The permeability (k) relates to the particle size and would depend on micro (k_i) and macro (k_a) permeability values (Equation 6-1).

$$\frac{1}{k} = \frac{1}{k_a} + \frac{C_0 R_i^2}{R_a^2 k_i}$$
(Equation 6-1)

where C_0 is a constant (dimensionless) related to microporous particle size R_i (m), R_a is the radius of the crushed particles (m), k_a is the permeability of macropores (m²) and k_i is the permeability of micropores (m^2).

Cui et al. (2009) argued that the equation could be further expanded to include additional permeability parameters. According to his research, this was because different sized particles have microfractures with different permeabilities and the crushed sample might contain a hierarchy of different sized particles with their own parameters. The solution provided by Cui et al. (2009) was to improve the sieving process to narrow down the particle size and then to analyse it more extensively, by assigning various multipliers and looking at their effect. Cui et al. (2009) believed that eventually the crushed method can produce good matrix permeability values if either the particles would not contain microfractures, or the microfractures are understood and represented well.

In this research, a triple model, similar to the one described by Sinha et al. (2012), was also used to simulate crushed shale particles (see Section 3.6.3). Although the presence of 3 variable zones in this model produced almost perfect history matches, the issue is that

the decay curve gets subdivided into 3 zones which leave less of experimental pressure data to history match each permeability (Figure 6.16a & b). This is especially the case for the high permeability regions - in some cases merely 2-3 seconds were left to match the $1/3^{rd}$ of the high permeable zone area. This is an issue as high zone permeability values have large influences over the simulation outcome - from the simulated data (Appendix K) it should be noted that some of the high permeability values were in the range of hundreds of milliDarcies.
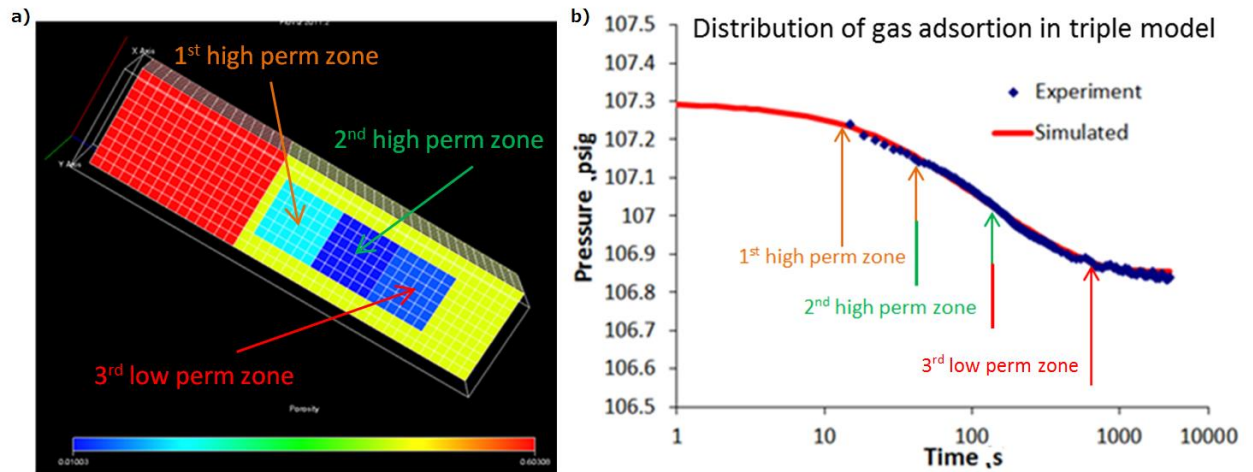
Figure 6.16. Triple model each zone due to its small size has limited gas absorption potential - Figure 6.16 b shows that each area corresponds to a small part of the overall pressure decay (in this case around 30 seconds or pressure decay) therefore overall the model is less representative of the shale particle than the double or even single model.

Nevertheless, correlations between low and high zone permeabilities were still obtained as shown in Figure 6.17a. There appears to be a positive correlation between low and high zone permeabilities. Another graph (Figure 6.17b) shows a negative correlation between low permeability and high porosity. This trend could be explained by the fact that the overall porosity is the sum of low and high porosities, hence if one decreases another increases. In this case as the high end porosity increases, it displaces the low end porosity which gets smaller – that in turn causes the low permeability zone to decreases.
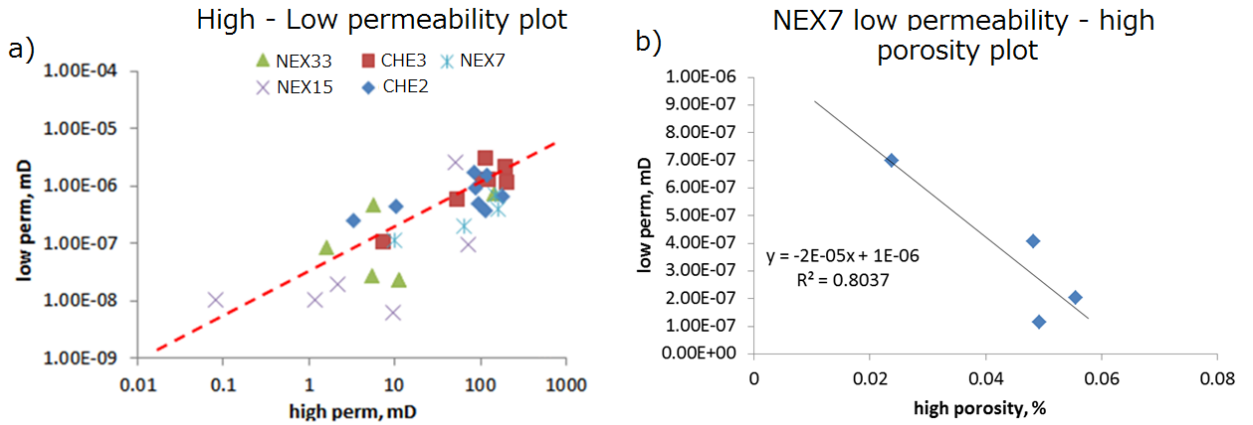
Figure 6.17 Correlations of low/high permeabilites (a) and low permeability/high porosity (b).

6.4.1.4 Microstructure effect on permeability

Crushed permeability correlation with porosity for sample NEX7 was the only among all the samples to construct a better correlation coefficient than core plugs (Figure 6.18). On the other hand, the permeability correlations for all the other samples (EBN20, EBN 33, CHE2 and CHE3) got worse when the crushed GRI experiment was used. The most logical reason for such results is that the NEX group of samples are much more heterogeneous than the other samples and their permeability results only improve once they are crushed. SEM images suggest that the matrix of the samples CHE2 and EBN33 is more uniform than for the NEX group of samples - the sorting is finer and there are no large fractures (Figure 6.19). Therefore when crushed the NEX group of samples must have broken along the major fractures therefore reducing heterogeneity. In contrast EBN and CHE group of samples must have broken in a way that increased heterogeneity of otherwise homogeneous samples. Overall, this might be a useful way of linking microstructural analysis of shale with the applicable experiment to obtain representative results.
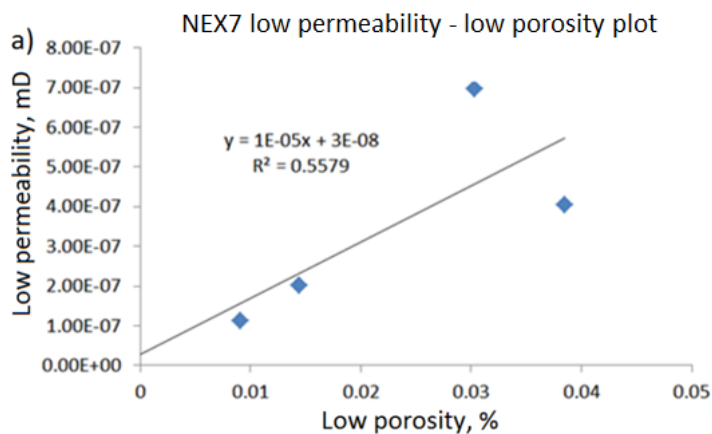
Figure 6.18. Correlation between fracture and matrix properties in crushed simulations.
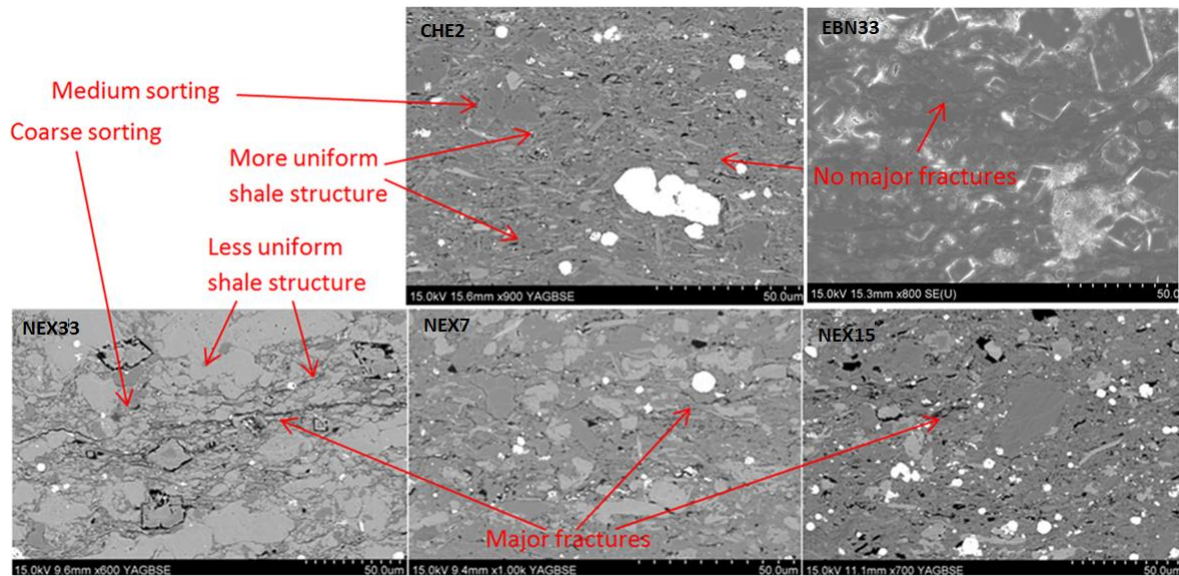
Figure 6.19. Comparison of the BSE microstructure of the control-test samples. NEX group of samples were taken from Carboniferous outcrop whereas other samples were cored from the Jurassic formation.

6.4.2   Core plug analysis

In general, core plug permeability values provided by the test companies are higher than those obtained by Leeds (see Figure 6.5 and Figure 6.6 in Section 6.3.4.2). In fact, high permeability results are a common issue among the laboratory measurement vendors (Ramirez et al., 2011; Moghadam and Chalaturnyk, 2015). To improve the gas flow measurements, it is important to understand what is biasing the values. The following section describes the reasons for the core plug permeability over-estimation and proposes both modelling and experimental solutions to improve the measurements.

6.4.2.1   Impact of Fracture on Pressure Tranients

Original pressure transient tests developed for the permeability derivation of low-permeable core samples assumed that the samples are homogeneous (Brace et al., 1968; Kamath et al., 1992). However, Kamath et al. (1992) recognised the drawbacks of such assumption and developed an analytical method interpreting heterogeneous samples using pressure transient test. The method makes use of the early time solution of the governing flow equation for the pulse decay problem (Kamath et al., 1992) and ratios of the core storage to the upstream (F_{cu}) and downstream (F_{du}) volumes to identify and quantify any deviations from the homogeneity.

According to Kamath et al. (1992), heterogeneous and homogeneous cores result in similar pressure response for small F_{cu} values (large upstream vessel volume compared to the sample storage). However with an increase in F_{cu} (decrease in upstream vessel volumes) the pressure response of the heterogeneous sample becomes different to that of the homogeneous sample. Figure 6.20 provides a comparison of the pressure responses for both homogeneous and heterogeneous cores depending on the F_{cu} values (upstream vessel size). Therefore Kamath et al. (1992) suggested to use a large vessel (small F_{cu}) to calculate an average permeability value of heterogeneous core sample, followed by the small vessel to accentuate heterogeneity.
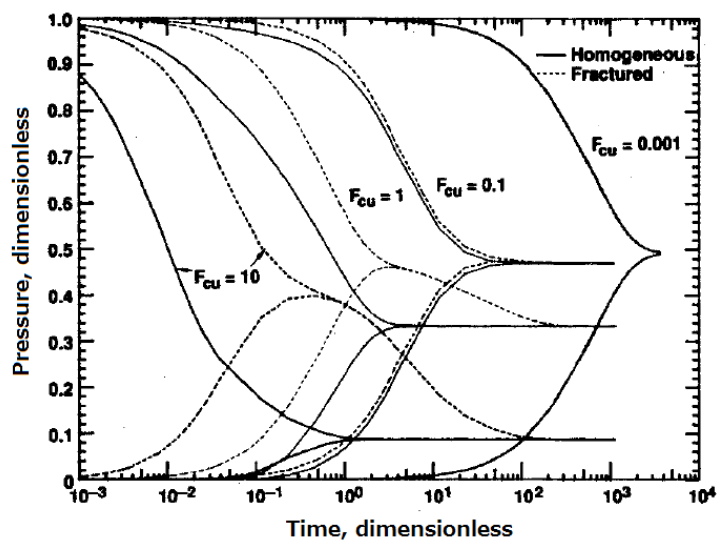
Figure 6.20. Comparison of homogeneous and heterogeneours core behaviour at different Fcu values (Kamath et al., 1992).

Kamath et al. (1992) used core samples of microDarcy range, whereas in this study samples with the nanoDarcy permaebilities were investigated. The use of large upstream cylinders on such low permeability samples is impractical due to long experimental times, leakage and errors when applying late-time solutions (Kamath et al., 1992; Cui et al., 2009). Therefore the aim was to use small vessels (large F_{cu}) to interpret heterogeneous samples.

The samples investigated in this study showed clear heterogeneity in pressure behaviour that was demonstrated by the xenon test - during MPD experiments there is a clear tendency for the gas to pass the matrix through a fracture-type of structure (see Figure 4.29 in Chapter 4.4.3.1). Analogue behaviour was achieved with the simulation model with fracture included as seen in Figure 6.21. It can be seen that the gas flowing through the highly conductive region of the matrix and as a result pressurizing the downstream

volume before equilibrating within the shale matrix itself is the best explanation for the recorded xenon flow through the sample (Figure 6.21).

Experimental pressure curves of the MPD experiment (Figure 6.22) agree with the heterogeneous sample behaviour described by Kamath et al. (1992) (Figure 6.20). Essentially the early time pressure decay (up to upstream/downstream curve intersection point) can be attributed to the fracture-dominated flow, whereas the late time pressure decay can be attributed to the homogeneous matrix flow. Therefore at least two permeability parameters are required to characterise such type of flow.
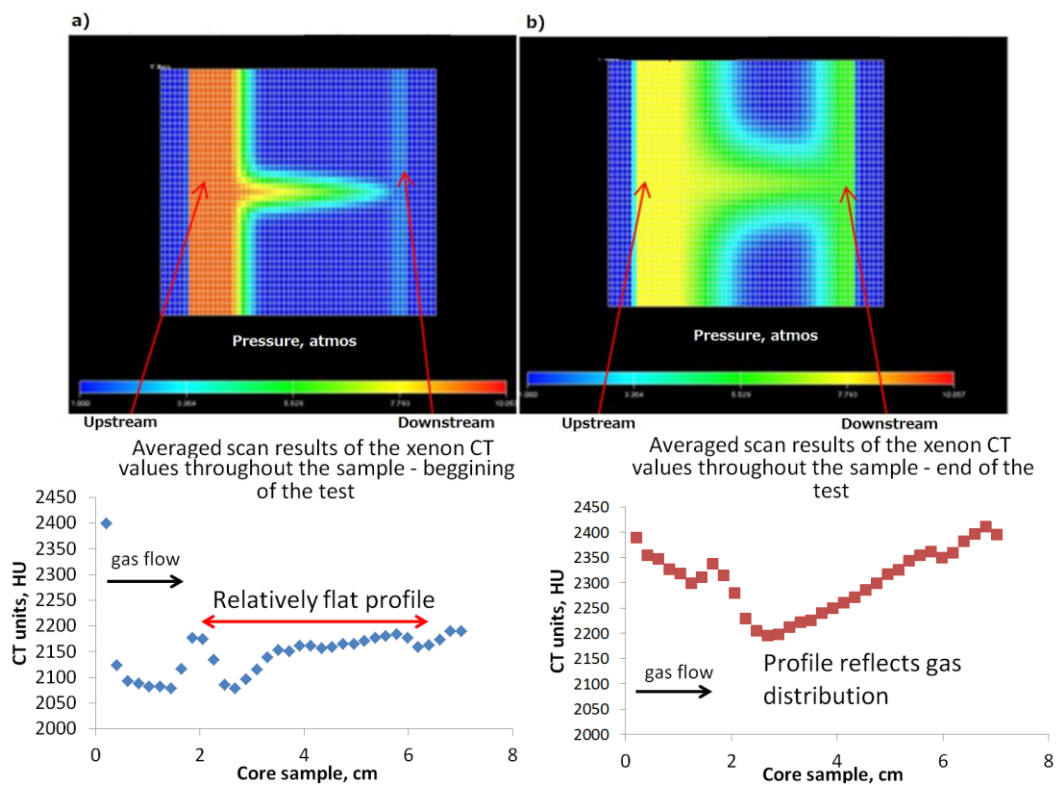
Figure 6.21. Simulation model attempting to reproduce the gas flow development throughout the matrix with a fracture present. The amount of gas at the end parts of the sample, with little or almost no gas in the middle, shows typical behaviour of the core with a fracture. Note the similarity with experimental data.
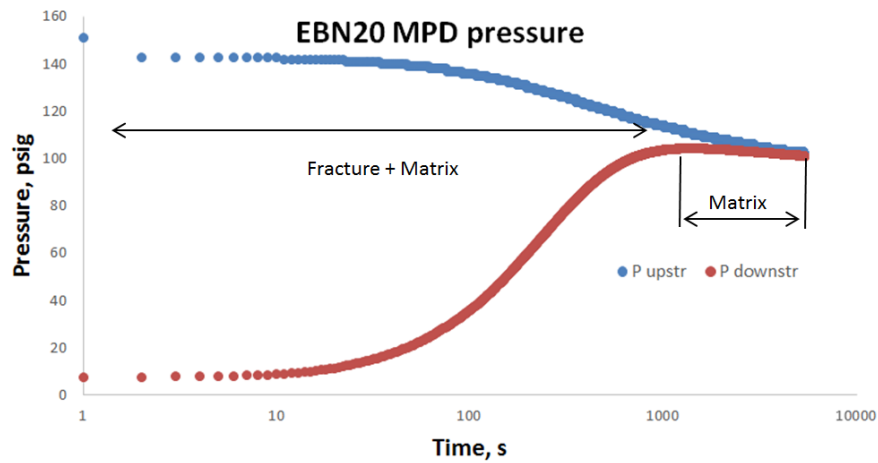
Figure 6.22. Pressure decay of MPD type of experiment. Pressure decay initially might be controlled by the fractures within the matrix.

Chesnakov et al. (2010) demonstrated the inversion of heterogeneous features within nanoDarcy range shale matrix using Effective Medium Theory (EMT). In this method, they assumed the core sample as a medium of patches, assigning separate patches to the matrix and fractures (Chesnakov et al., 2010). Significant improvement in the permeability results was noted. Similar principle of separating matrix from fractures was used in this research (see Section 3.6.2). For the core plugs the use of fracture (high permeability streak) in simulation models resulted in a better history match between the experimental and simulated data. A poor match (Figure 6.23b) was turned into a good match (Figure 6.23) after a fracture was included in the model.

Unfortunately, service companies did not provide the information on their gas flow assumptions, but it is most likely that single permeability model was being used to match the pressure curves such as the one in Figure 6.22. Effectively, this means that the higher permeability heterogeneous region (or in the core plug case a fracture) and low permeability matrix are both merged into one parameter. The permeability values provided by the test companies might be therefore dominated by this early time fracture dominated flow, which would explain the consistently higher results compared to Leeds.
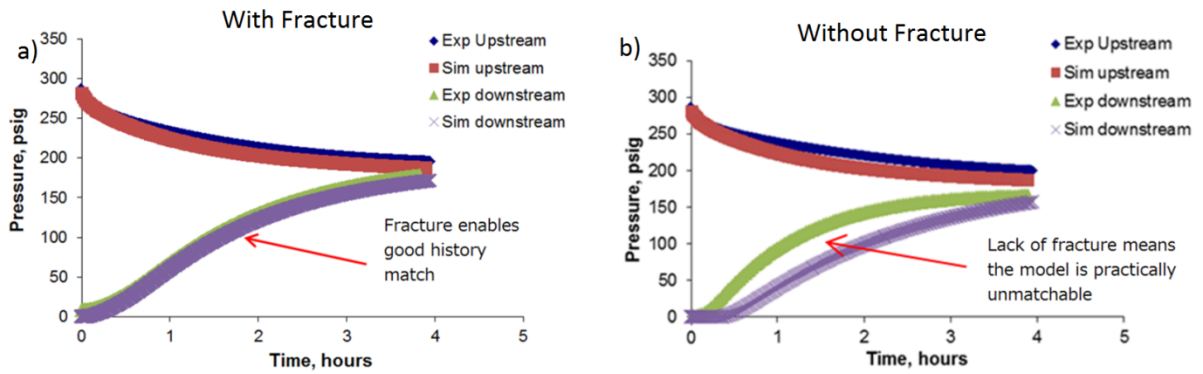
Figure 6.23. Impact of fracture for the history match. Some models cannot be history matched if fracture is not included in the model, suggesting there must be fracture or high conductivity region within the matrix.

In contrary to MPD results, the pressure curves of the CPGRI experiment do not allow to distinguish between fracture and matrix dominated flows that well. The reason for this is the geometry of the flow - in CPGRI the gas surrounds the core sample from all sides and then flows into the matrix. In contrast, during MPD the gas flows through the core from upstream towards downstream volume (Figure 5.24a & b). This enables high conductivity pathways to control the flow between the upstream and downstream volumes (Figure 6.23) and be identified as shown by Kamath et al. (1992).
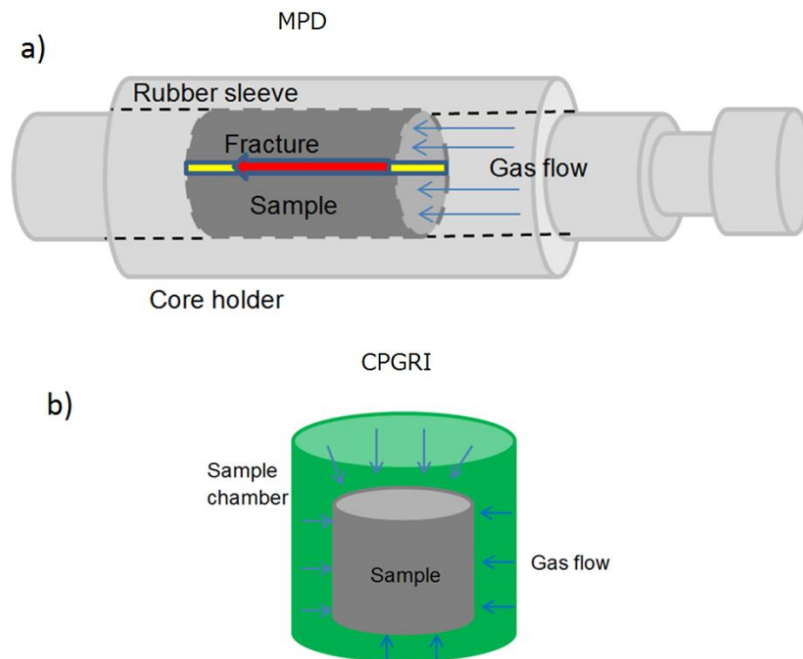
Figure 6.24. Gas flow geometrics of the tests.

Unlike in MPD, the CPGRI measurements are not made at the confining stress conditions. (Figure 6.24). Nevertheless, results from the CPGRI produce a good correlation with the data obtained from the MPD test (Figure 6.25). In fact, CPGRI results imply that it might

be less sensitive to fractures than the pulse-decay type experiments, such as MPD - obtained permeability results show that the CPGRI values are slightly lower than those obtained by the MPD. Nevertheless both CPGRI and MPD methods have a large advantage over the crushed method in terms of the matrix permeability representation. Gas flows rapidly into the crushed particles, making it practically impossible to distinguish between heterogeneous structures. In contrast, gas flow into the core plugs is much slower, which enables the tests to distinguish between the initial fracture dominated flow and slow matrix flow.
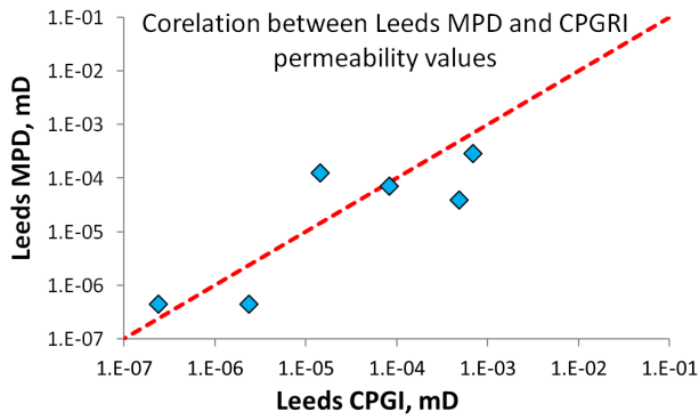
Figure 6.25. Comparison of core plug gas invasion and MPD results.

6.4.2.2 Improvement of permeability results using RPD technique

To further test the reliability of the core plug measurements different flow geometries were used to introduce additional factors in the experiments. The RPD experiment (or hole test), where a hole is drilled in the middle of the core plug so as to create an experiment similar to a well test was conducted. The resulting flow geometry into the sample in RPD test is completely different to that in both MPD and CPGRI (see Figure 3.1 in Section 3.2.3). Nevertheless, the test produced correlations with both MPD and CPGRI tests (Figure 6.26).
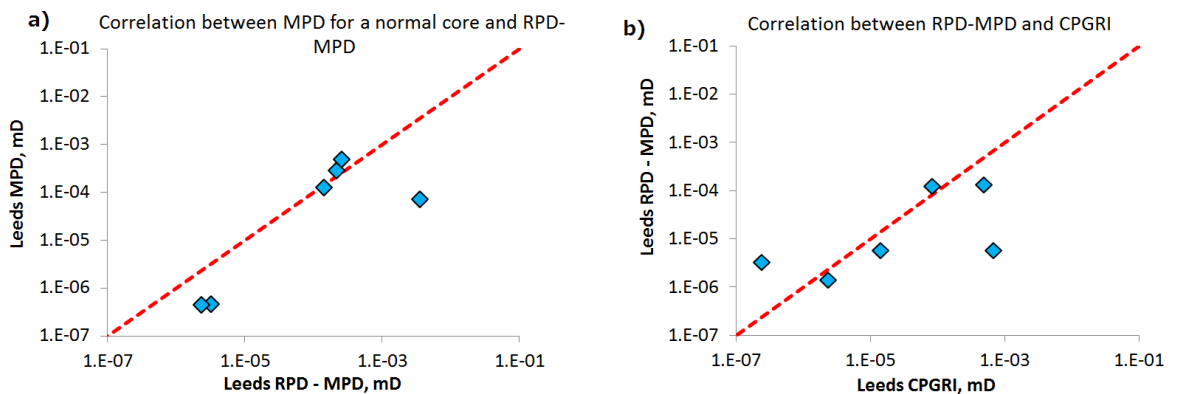
Figure 6.26. Comparison of permeability results obtained using CPGRI and MPD-RPD.

Compared to Control-Test results the permeability obtained from the RPD is lower than the values supplied by Lab A and Lab B (Figure 6.27). It is likely that this is because the samples are damaged (fractures are present in the core plugs due to coring and handling) and the service companies are not accounting for this damage. Once again interpretation of the results is suggesting that many of the measurements provided by the service companies are dominated by these fractures. In contrast, the permeability measurements conducted in Leeds had fracture effect minimized by using double permeability simulations.
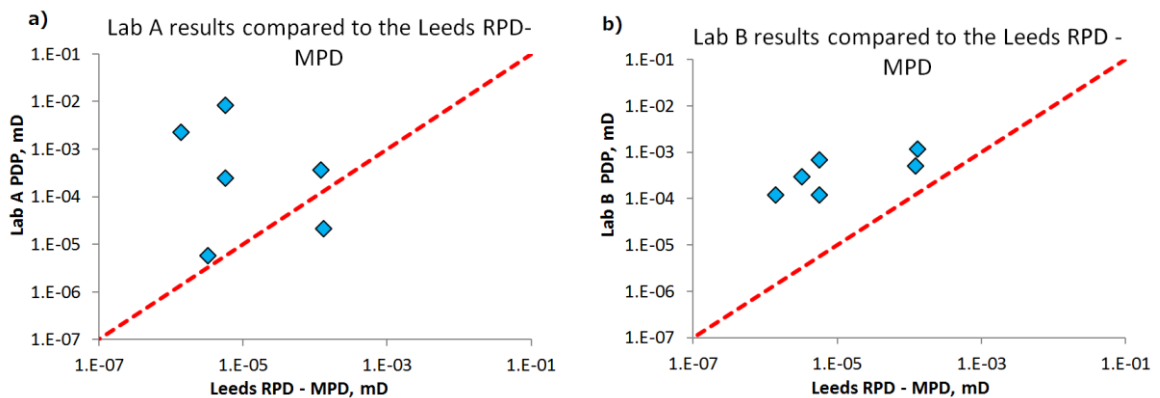
Figure 6.27. Control-Test PDP permeabilities compared to the MPD results of the samples with hole. Control-Test companies systematically over-predict permeability values.

Sample EBN5 had a hole drilled only half-way along the length of the core, hence one side had a hole whereas another side was intact. This adds another independent experimental variation and enables the sample to be tested with the hole facing both ways: upstream and downstream to the gas flow. Geometrically it results in a different gas flow development throughout the sample (Figure 6.28), which in turn requires a separate simulation model for permeability derivation. A plot of permeability versus 1/P for the downstream and upstream case for such sample is presented in Figure 6.29.

There are significant differences in permeability values between the two experimental set-ups for the same sample (Figure 6.29). First of all, the downstream sample configuration produced two orders of magnitude lower permeability than the analogue experiment with upstream sample configuration. Secondly, the upstream case produced a better trend between the permeability and the inverse of pressure than the downstream test. Another important observation is that all permeability values in plots Figure 6.29a & b are well within one order of magnitude, which is very precise compared to other core plug results. This is despite the permeability values for the sample EBN5 being so low – all derived values are in the range of nanoDarcies.

200

Schematic representation of the as flow in sample EBN5
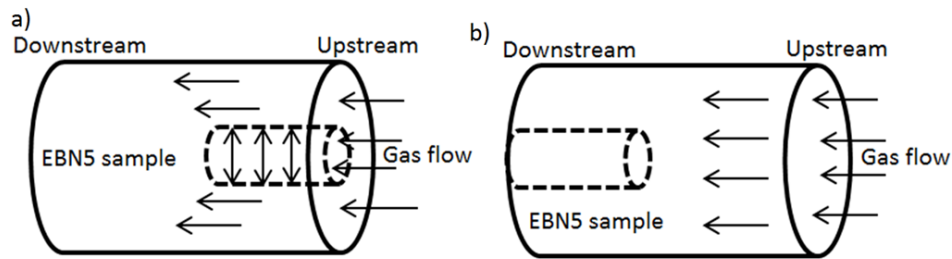
Figure 6.28. Gas flow development in the sample EBN5. The sample has a hole cut only partly through the centre, therefore it can be tested by applying gas from different sides.
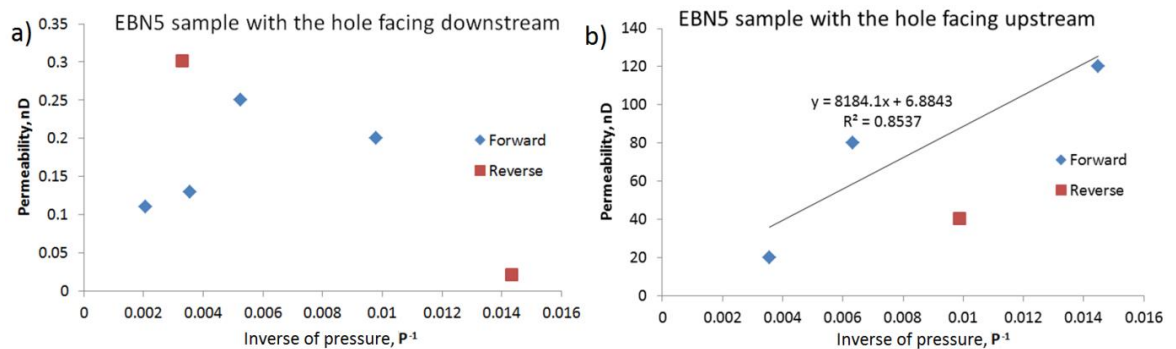
Figure 6.29. Correlations between permeability and 1/P for the sample with hole drilled half-way of the sample. The direction of the hole affects the results significantly.

There might be several reasons for these differences between the tests: the area around the drilled part of the sample might have been damaged during the drilling process, thus it may contain more microfractures than the non-drilled part of the sample (higher permeability values support this theory). The hole might have provided a better matrix coverage at the upstream part of the sample resulting in more representative permeability values than the downstream case (which is supported by the good trend obtained). Also both experiments produced only a partial permeability curve for each end of the sample and not for the entire plug (which is supported by neither of the experiments reaching equilibrium even after prolonged test time as shown in Figure 6.30).
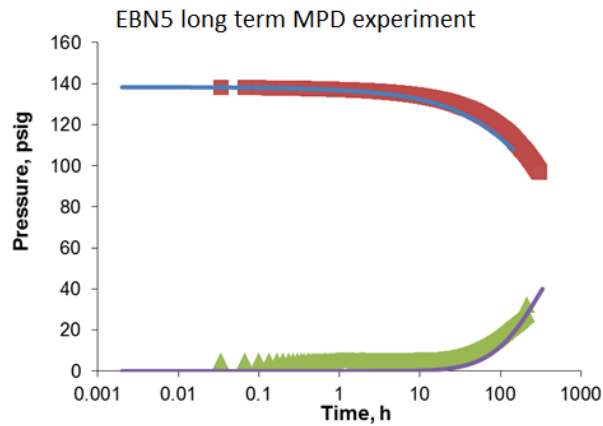
Figure 6.30. EBN5 MPD test showing that no equilibration was reached even after long experimental time. The direction of the hole during the test was downstream.

The latter theory yields further considerations on the lateral heterogeneity variations within each core plug. Although CT scans were done on each core plug to ensure the structural homogeneity, the images lack resolution to identify subtle changes in rock structure that might dominate the gas flow. Shorter core plugs would reduce the chances of samples containing heterogeneous features, however in this case the representation of the matrix would also decrease. This research did not focus on lateral variations within the core plugs, however further studies could be done on the statistical likelihood of these features, optimum core plug length and sensitivity of permeability on it.

Overall it was found that drilling the hole half-way into the sample was a good way of producing more permeability values at different conditions and therefore improving the sample characterisation. In addition the method outlined some of the issues with the core plugs, which would not be seen during standard measurements. The main problem with the measurements was the lack of sample material for EBN5 so no other configurations were measured (without hole, hole all the way, crushed).

6.4.2.3 Impact of confining pressure on permeability

The SEM images showed NEX group of samples to contain a large amount of fractures (see Figures 4.21; 4.22 and 4.33 in Section 4.4.1.1) therefore the permeability results should be affected by confining stress. Many authors have identified the relationship between confining pressure and presence of microfractures (Joel, 1982; Lorenz, 1999). Therefore sample NEX15 was tested under three different confining pressures using MPD test (see Section 6.3.5.4) to analyze the behavior of the identified fractures. As a result, a slight permeability - stress dependence was observed (see Figure 6.11 in Section 6.3.5.4

and Figure 6.31). Matrix permeability increases with the increase in pressure due to the Klinkenberg effect (see Section 2.3). Important observation is that the high-zone (fracture) permeability values appeared to show expected negative correlation with the net pressure values as shown in Figure 6.31. This means that the fractures close with an increase in pressure.
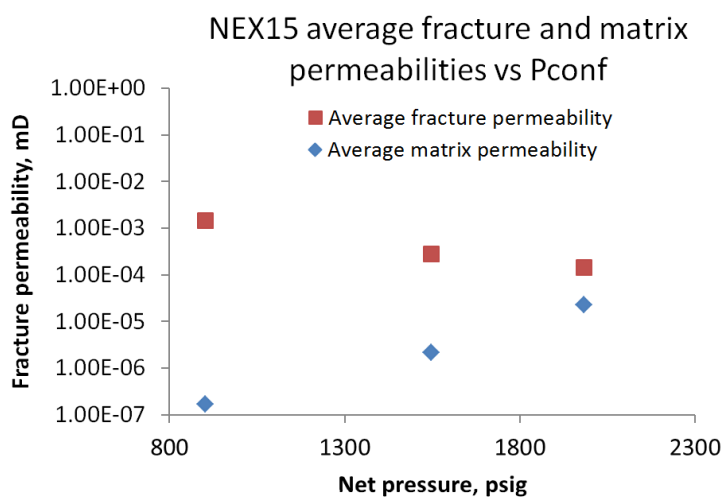
Figure 6.31. Relationship between average matrix/fracture permeabilities and net stress.

This fracture-pressure relationship is important as if the analysed fractures were natural and would be present in the subsurface conditions, they could be exploited for better production purposes. In particular, appropriate technological solutions such as restricted rate practice could be applied, where the well bottom-hole pressure is kept high to reduce the net-stress and keep the fractures open. However it is unknown if these fractures are natural and how many are present in the subsurface conditions, therefore this could be topic for the further research.

6.4.2.4 The impact of shale lamination on permeability results

The direction in which a core plug is taken relative to bedding could dominate the permeability results. The reason for that is characteristic shale anisotropy described by many authors, which results in the heterogeneous nature of the gas flow (Dokhani et al., 2013). In addition beddings of inter-bedded layers of different lithology (usually coarser inter-bedding or damage induced microfractures) were observed in the CT analysis (see Figures 4.12 and 4.13 in Section 4.3.4). It is important as even slight variations in these layers may dominate the flow leaving the rest of the matrix less involved in the gas flow process. This can be observed in the MPD experimental results

(see Figure 6.22 in Section 6.4.2.1), where only a fraction of pressure decay can be associated with the matrix.

For this reason, homogeneous MPD models (models without fracture) might result in an over estimation of the results for parallel laminated samples, and contrarily - under prediction for perpendicular laminated samples (damage induced microfractures usually form parallel to the bedding, hence in the perpendicular sample orientation case they would not aid the flow that much). The comparison of permeability-porosity plots for models with and without heterogeneity representation (models with and without fracture) is provided in the Figure 6.32a & b. Unlike MPD, CPGRI should not be as sensitive to the bedding direction of the sample. The main reason for that is geometrically different flow development of CPGRI compared to linear experiments such as MPD. Indeed, CPGRI pressure results representation is provided in the Figure 6.32c and d.
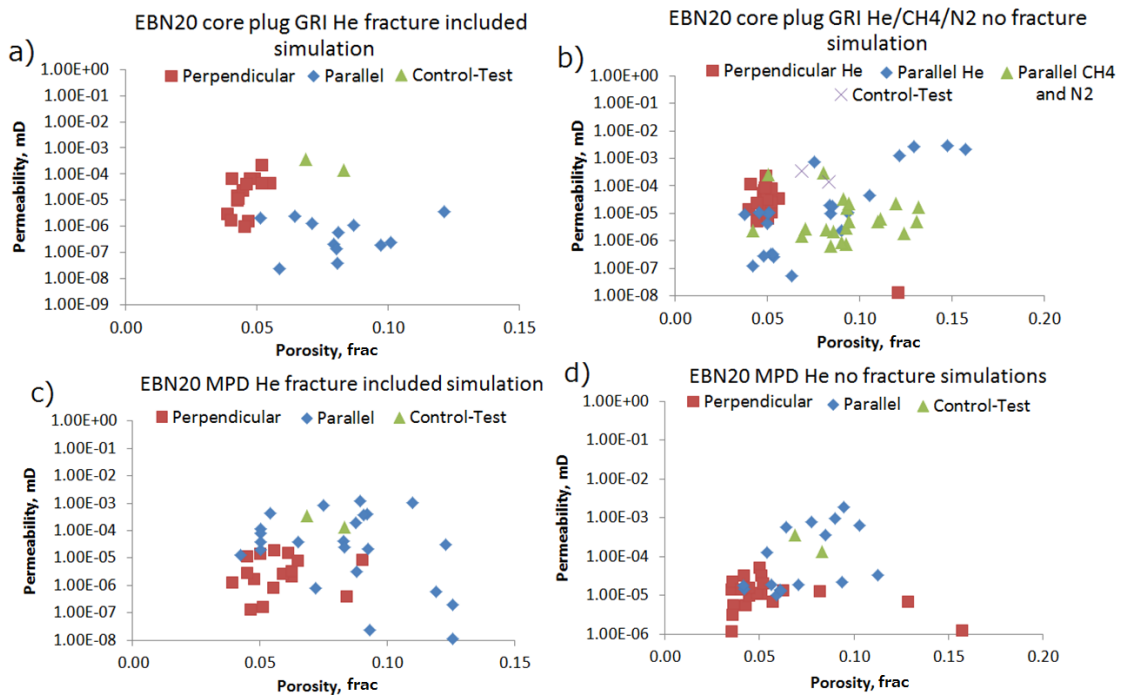
Figure 6.32. Comparison of permeability results depending on the bedding direction. Control-test results are provided for comparison.

For the MPD experiment, parallel laminated samples resulted in higher permeability values than for analogue perpendicular samples. In fact, MPD still remained biased towards the over prediction of parallel samples even in the fracture-included simulations. The reason for that is that heterogeneity was represented just by a simple high-permeability streak, whereas in reality it is composed of a complex network of microfractures and inter-bedded layers. Other authors have also noted similar over

prediction issue for parallel samples and the challenges of interpreting the measured data (Dokhani et al., 2013).

The CPGRI test exhibited a slight bias towards the permeability values of perpendicular samples. It might be the case that geometrically perpendicular fractures create better surface-to-matrix contact area than equivalent parallel fractures during the CPGRI experiment, and that is the reason for this permeability over prediction. On the other hand, CPGRI remained largely unaffected by the heterogeneity (fracture) inclusion in the model.

6.4.3 Improvement of the results using pressure series technique

Sinha et al. (2013) noted that measurements conducted at low pressures create the widest uncertainty. It was pointed out that the permeability measurement at around 150 psig is most likely to occur outside slip flow regime of Kn > 0.1 (Sinha et al., 2013). The reason for this is that Klinkenberg correction is unable to correctly describe the deviation from the Darcy flow. It was recommended by Sinha et al. (2013) to conduct measurements under a range of pressures. Therefore it is more useful to conduct experiments as a part of the pressure series test (see Section 3.4.2), rather than single pressure test. Pressure series test is the experiment where a series of pressures are applied after the end of the previous experiment (Figure 6.33). This experiment makes a series of experiments more comparable with each other, as the conditions of the sample, such as confining pressure (for MPD) or sample weight (for crushed GRI) remain the same throughout the test. The comparative graph of pressure series and single experiments is shown in Figure 6.33.

a) Multiple Modified Pressure Decay Experiemement

(Annotations on figure a):
- Pressure is applied on the sample
- 2nd pressure is applied on the sample after the end of first pressure decay
- End of first pressure decay
- End of 2nd pressure decay
- 3rd pressure
- End of 3rd
- 4th pressure
- End of 4th
- 5th pressure and possibly nth pressure application
- End of 5th or nth pressure decay
- End of 1st pressure build-up
- Pressure is allowed to be released from the sample and is monitored
- End of 2nd pressure build-up
- Start of 2nd and 3rd build-ups
- End of experiment

(Axes: Pressure, psig vs Time, hours)

b) EBN20 MPD sinlge step test

(Axes: Pressure, bars vs Time, s)

Figure 6.33. Comparison of the pressure series test (a) and single pressure experiment (b).

Pressure series experiment produces much better correlations between the inverted and experimental parameters, such as permeability versus inverse of pressure (see Figure 6.10 in Section 6.3.5.3) than single experiments. The obtained permeability values are easily comparable between themselves, and differences between them can be analysed as a result of the pore pressure change, rather than change in sample conditions (confining pressure, weight etc.). Furthermore, pressure series test helps to solve the non-uniqueness problem in the permeability derivation process, as discussed in Section 6.4.3.2. Ultimately, pressure series test provided crucial information on how to better conduct the crushed and core plug shale tests.

6.4.3.1 Klinkenberg correction and its correlation with permeability

A considerable part of the project was the assessment of the importance of gas flow mechanisms such as slippage, transitional; flow and Knudsen diffusion. This was

attempted by measuring and analyzing permeabilities and corresponding Klinkenberg factor (*b*) at different gas pressures. Measurements of apparent gas permeability made using the crushed shale method suggest that there is a clear evidence of gas slippage within the experiments. This is revealed by the general trend for derived permeabilities to increase with decreasing pressure (Figure 6.34). However, none of the experiments produced data that would meet the API criteria to obtain a Klinkenberg correction (i.e. straight line on k_{ap} vs 1/p with $r^2 < 0.95$ for nine points or $R^2 < 0.99$ for 4 points).
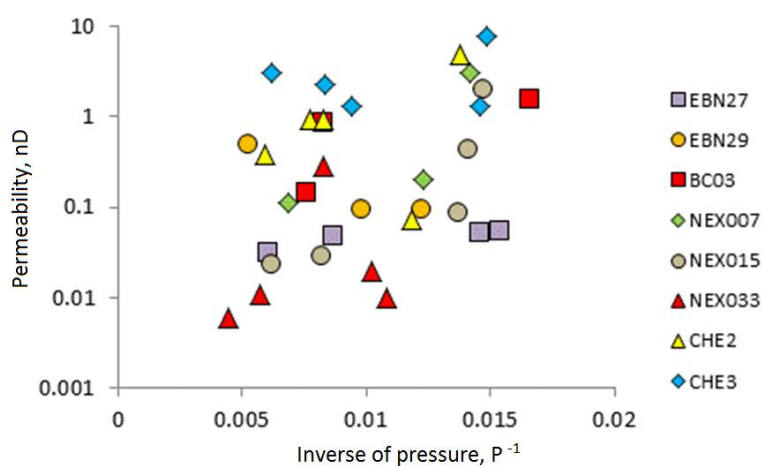
Figure 6.34. Plot of inverse pressure vs permeability for crushed shale experiments using helium gas.

Experiments on core plugs generally produced better positive correlations between apparent gas permeability and 1/pressure, which in turn allowed *b*-factors to be calculated (e.g. Figure 6.10a and l in Section 6.3.5.3). Usually in the case of the tight sandstones the extrapolation of this correlation yields intrinsic permeability value. However in this research some of the samples produced negative extrapolated values despite good general correlation (see Figure 6.10a, d, j, l in Section 6.3.5.3). This compromises the ability to obtain intrinsic permeability using the extrapolation method.

The issue of negative intrinsic permeability values, obtained by extrapolating apparent permeabilities was solved using Klinkenberg correction. The results of corrected permeability values for the samples EBN9 and CHE3 are compared in Figure 6.35. Klinkenberg correction equalized the permeability values at each pressure removing the slip effect.
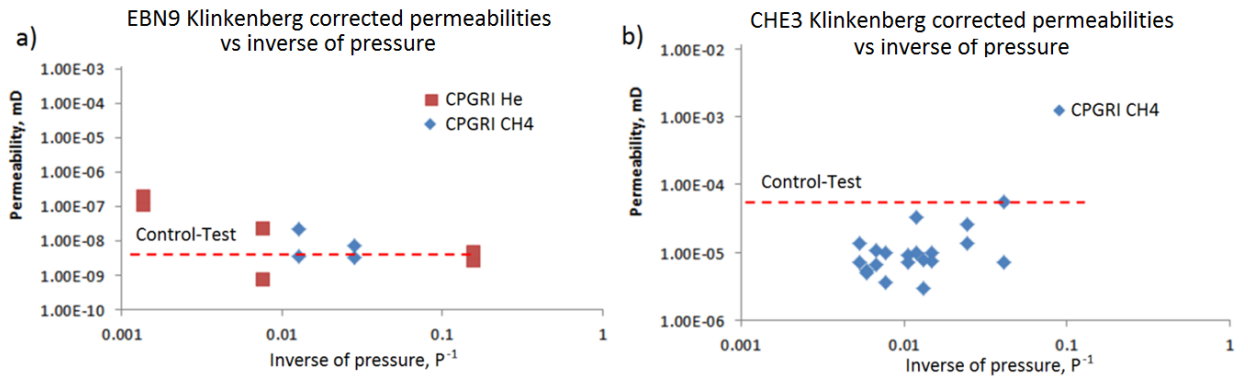
Figure 6.35. Klinkenberg corrected permeability values plotted vs inverse of pressure. It is seen that introduction of Klinkenberg correction removes the gradient from the permeability vs inverse of pressure curve.

The derived *b*-factor values used for the correction are scattered and vary from 1 to 10,000 psig^{-1}. Despite this the shale samples with relatively high permeabilities (200 nD) produced Klinkenberg *b*-factor values that fall on the same trend as results from tight gas sandstone reservoirs in published correlations (Figure 6.36). Usually high *b*-factor corresponds to samples with low permeabilities and small *b*-factor corresponds to samples with high permeability. In turn, extremely high *b*-values obtained in this research would suggest very low shale permeability.
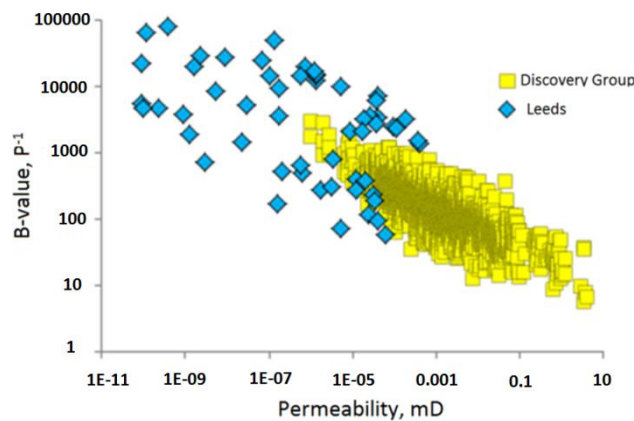
Figure 6.36. Plot of permeabilities vs *b*-factors. Results obtained in this research are compared with results from the other research from the Discovery Group (Discovery-Group, 2016).

Klinkenberg *b*-factor affects the average velocity component of the gas molecules moving through a narrow pore throat at the direction of the general flow, similarly like the permeability affects the flow according to Darcy's equation (see Equation 2.4 in Section 2.2). Permeability and b-factor show a reasonable correlation (Figure 6.37). The derived *b*-factor values from the high permeability samples are consistent with relationships in literature between *b* and k_g (Figure 6.38). The scatter in the results is to be expected given

the close correlation between b-value and permeability (Profice et al., 2011). Overall, until better data becomes available it is recommend to apply slippage corrections to permeability, based on good correlations between the *b*-value and permeability (Figure 6.38). In the longer term, the experimental methods require further improvement to remove the mentioned uncertainties in the measurement of gas flow in shale.
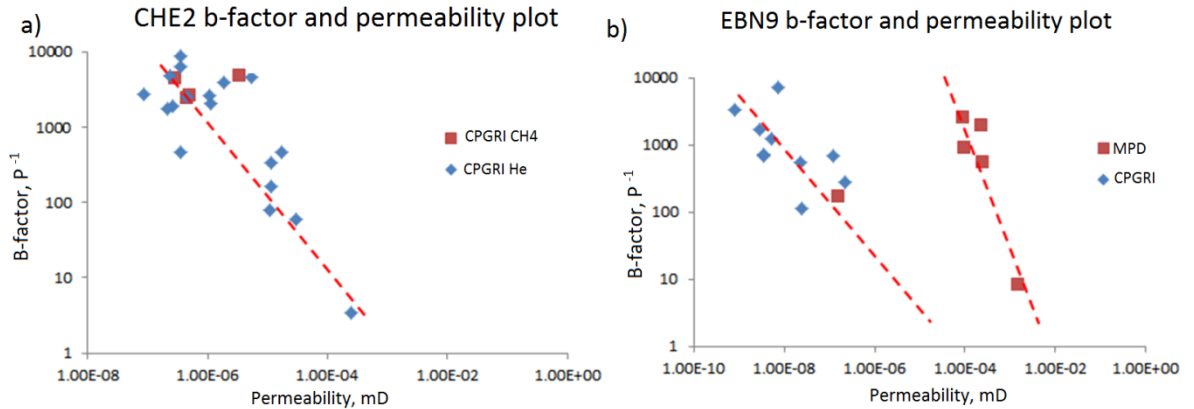
Figure 6.37. Relationship between *b*-factor and permeability values.
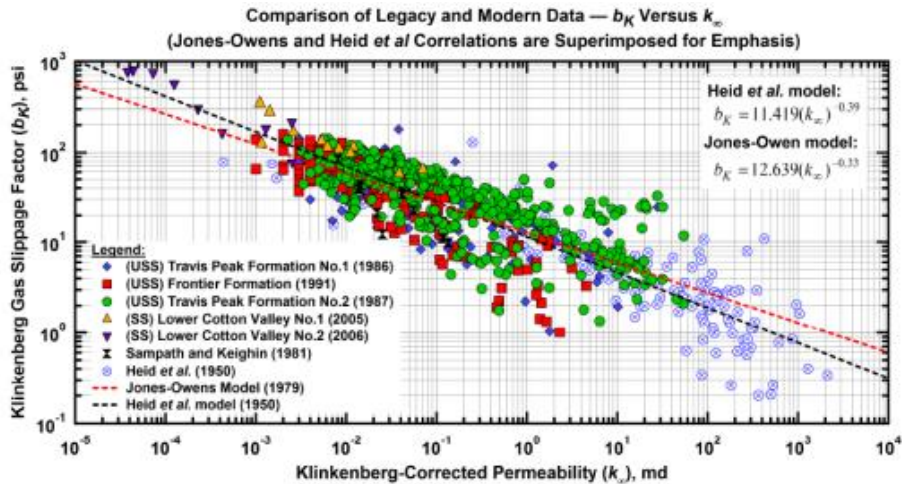
Figure 6.38. Plot of absolute gas permeability vs Klinkenberg b-value (Florence et al., 2007). The *b*-factor value of 300 was obtained from the 200 nD sample is consistent with these data.

6.4.3.2   Non-uniqueness of permeability inversions

The *b*-factor was made a variable parameter in some of the history matches, which often leads to non-uniqueness in the history match process, manifested when two different permeability values produce a match with experimental data. An example of this non-uniqueness is provided in Figure 6.39. To reduce the uncertainty and remove unwanted non-uniqueness in derived results, additional conditions have to be imposed to create a system of separate flow equations. The solution to this is a pressure series experiment

(Figure 6.33a) that creates new flow system without disturbing experimental conditions or adding more errors (Figure 6.40).
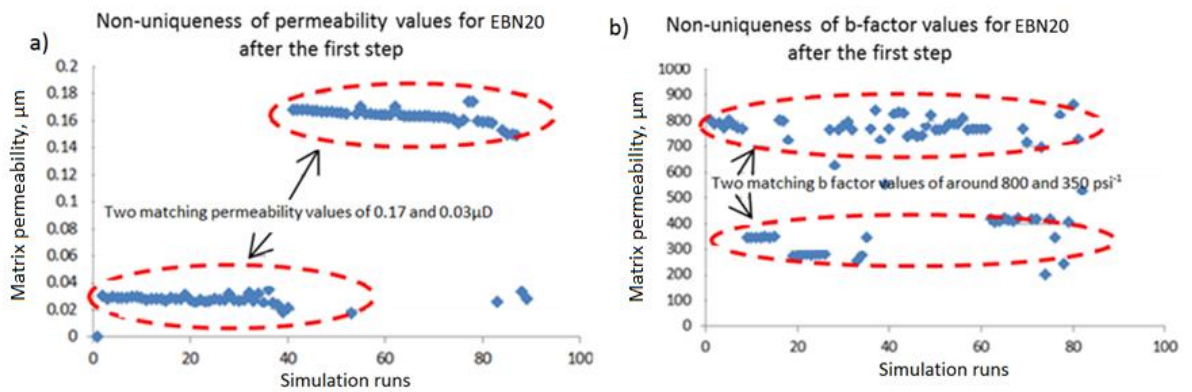
Figure 6.39. Non-uniquenes of the derived properties. Two distinct fitting permeability and *b*-factor values are obtained.
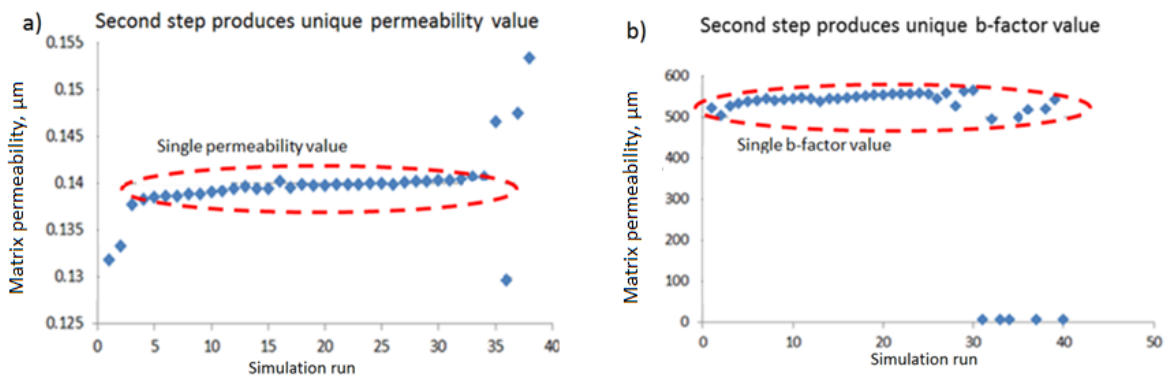
Figure 6.40. Unique results derived from the second step of the simulation. The non-uniqueness seen in Figure 6.39 disappears.

Pressure series experiment enables correct combination of permeability and *b*-factor to be found. Even if non-uniqueness of permeability/*b*-factor combination appears in the second or third step in derivation process, it eventually disappears in further steps - the correct permeability/*b*-factor combination will always result in the correct flow and distribution of gas within the sample, whereas the wrong combination will produce a condition impossible to history match (Figure 6.41).
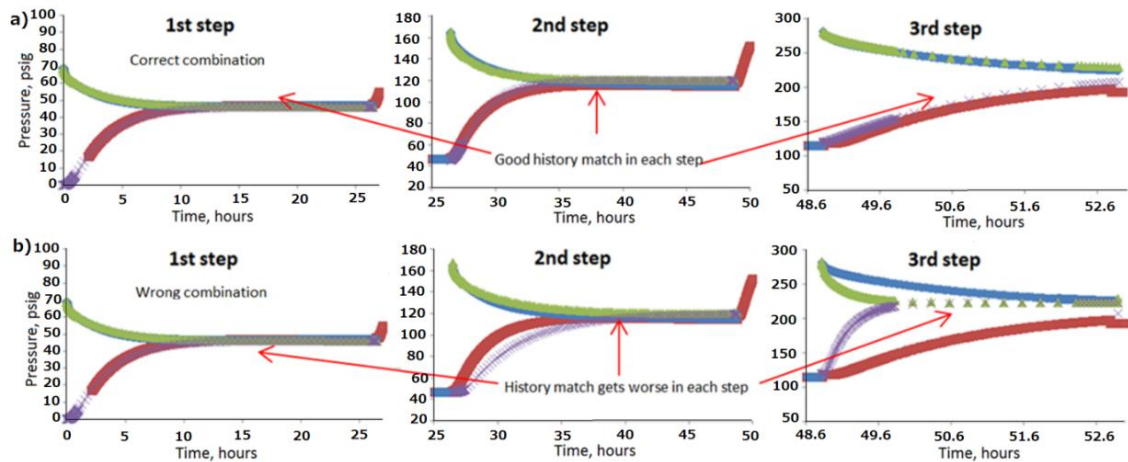
Figure 6.41. System for removal of non-uniquenes in the derived parameters – correct parameters create good history match in further steps, wheras wrong parameters create inconsistensies that get bigger in each successive step.

The history match of each step gets worse until no match can be obtained when the wrong combination of permeability and *b*-factor is used (Figure 6.41b). On the other hand, true permeability and *b*-factor values will result in correct representation of gas distribution within the sample at each successive step. This enables the correct permeability and *b*-factor combination to be discovered among incorrect values (Figure 6.41a).

This pressure series solution helps to identify correlated parameters and exclude them. This solution is easy, practical and could be potentially applied to other highly coupled parameters. In contrast state-of-the-art published models for gas flow in shales contain too many unknowns and parameters that are too correlated to make them practically useful for interpreting gas flow experiments (Lorinczi et al., 2014).

Overall the results provide a strong indication that non-Darcy flow is important. Indeed, *b*-factor values obtained from the experiments are consistent with those obtained from tight gas sandstones when plotted against absolute permeability. Unfortunately, too much uncertainty exists in the interpretation of the results to assess the dominant gas flow mechanisms. Until more conclusive experimental data becomes available, it is recommended that slippage corrections are made to experimental data based on established correlations between permeability and the Klinkenberg *b*-factor.

6.4.3.3 Impact of Adsorption on Permeability

Some authors argue that methane should to be used in the shale permeability measurements instead of helium or nitrogen, because it better represents shale

reservoirs (Fisher, 2015). Cui et al. (2009) argues that after applying adsorption isotherm corrections, shale permeability can easily be determined from pulse-decay, crushed or from on-site canister desorption experiments. However, it was showed by Fisher (2015) that crushed shale measurements do not provide accurate permeability results regardless of the gas used. Therefore the pulse-decay measurement is arguably the only experiment able to provide reasonable shale permeability results (Fisher, 2015).

Sorption experimental results (see Figure 5.13 in Section 5.3.6) provide additional information on the gas movement in and out of the shale samples during the GRI experiment. However in the literature no clear correlations between permeability and adsorption values are presented, apart from general trends and experiments using gasses with different sorptive properties. Figure 6.42 shows the permeability values of crushed Control-Test samples using three different gasses. The permeability values were taken from Appendix K and Appendix L after averaging.

Apart from sample NEX33, nitrogen and methane permeability values are very similar (Figure 6.42). For the sample NEX33 nitrogen permeability gets closer to the helium value, while methane permeability drops. This behaviour correlates with adsorption, where NEX33 was found to produce the lowest absolute adsorption values together with NEX15 (Table 5.11 in Section 5.3.6). On the other hand, the clear outlier Figure 6.42 – EBN20 sample was also a clear outlier in the adsorption graph. Therefore, the adsorption potential has a positive impact on methane permeability values.
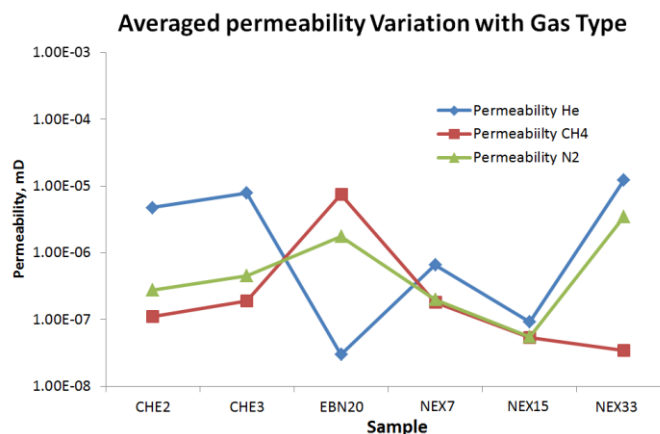
Figure 6.42. Permeability plot for each Control-Test sample depending on the gas type.

6.5 Conclusion

Crushed experiment results revealed that a considerable amount of gas enters into the sample at the rate that is too fast to be recorded and therefore cannot be modelled. This

results in wrong effective particle size assumptions when deriving permeability values. In addition, it is likely that proprietary inversion methods used by some of the commercial laboratories contain errors. Overall, no evidence was found to suggest that the crushed shale method is currently offering any valuable information regarding the permeability of samples from shale gas resource plays. Essentially, shale gas companies are supplied with non-representative permeability values. Commercial service laboratories should disclose their proprietary inversion algorithms for the scientific review and conduct more research when using crushed shale derivation methods. Alternatively, the recommendation is to use core plug methods for the permeability determination.

The core plug experiments showed more comparative and consistent permeability results between different laboratories than the crushed shale method. The results produced correlations that are to be expected from the literature, and followed the dataset trends published by other research groups. Among core plug tests, the best permeability results were achieved by the MPD experiment using high conductivity pathway (fracture) in the model and pressure series tests. The pressure series test was one of the improvements proposed in this study – it enables samples to be examined over a wide pressure range while assuring the core conditions are kept constant.

Essentially, it is always worth bearing in mind the end use of laboratory experiments. In the case of shale gas resource plays, the permeability values are often simply used during appraisal to compare the rock properties in new areas with properties in producing areas. Simulation modelling is not routinely conducted on shale gas plays. So to a certain extent, accurate permeability values are not required. Instead, the results could simply be viewed as index properties. In this case, it is essential that the vendor company provides all additional experimental data to for the permeability values to be comparable. Otherwise, it is difficult to put the provided permeability value into context when comparing with other values as differences between permeabilities may reach several orders of magnitude.

7 Chapter
Field study and reservoir scale gas behaviour

7.1 Introduction

The field study was undertaken in this research as part of collaboration effort between The University of Leeds and a small exploration company Gripen Oil & Gas. The objective was to collect shale cores and other field data. A reservoir model incorporating a large amount of both field and laboratory data was constructed to derive the GIP and simulate production. The impact of each parameter on the GIP values was evaluated using sensitivity analysis and Monte Carlo charts. Gas production and pressure build-up curves were analysed and the theory for reservoir behaviour was presented. This chapter presents the research done on this shale play development project.

7.2 Geological overview

The formation of interest, i.e. Cambro-Ordovician in Östergötland is found in a shallow north and east dipping half-graben. The local section of the Alum shale is termed the Tornby Member (Nielsen and Schovsbo, 2007) and is located on the southern margin of the Cambro-Ordovician graben. The simplified log of the Southern Sweden is shown in the Figure 7.1. The wells encountered an overall Tornby thickness of about 26 m separated by an intercalation of grey shale. The Alum Shale net thickness is about 17 m at this location. In Central Sweden, the Alum Shale is locally overlying the Kvarntorp Member and underlying Bjørkåsholmen limestone Formation (Nielsen and Schovsbo, 2007). Overal Alum Shale formation occurs in every Scandinavian country, with lower Ordovician underlying the Baltic Sea and extending towards Estonia and Russia.

The Alum Shale Formation is characterized by a series of black shales occasionally interbedded with thin (0.1-3 cm) fine grained calcareous sandstones. These sandstones vary in thickness and frequency throughout the cores and between the wells. Near the top of the Alum Shale a thicker (0.3-1.5 m) medium to fine grained calcareous sandstone occurs, with occasional graded bedding and traces of pyrite. This sandstone is continuous across the region and is correlated to the Skäningstorp Sandstone Bed (Nielsen and Schovsbo, 2007). Beds were upscaled to 1 m thickness for the reservoir model construction.
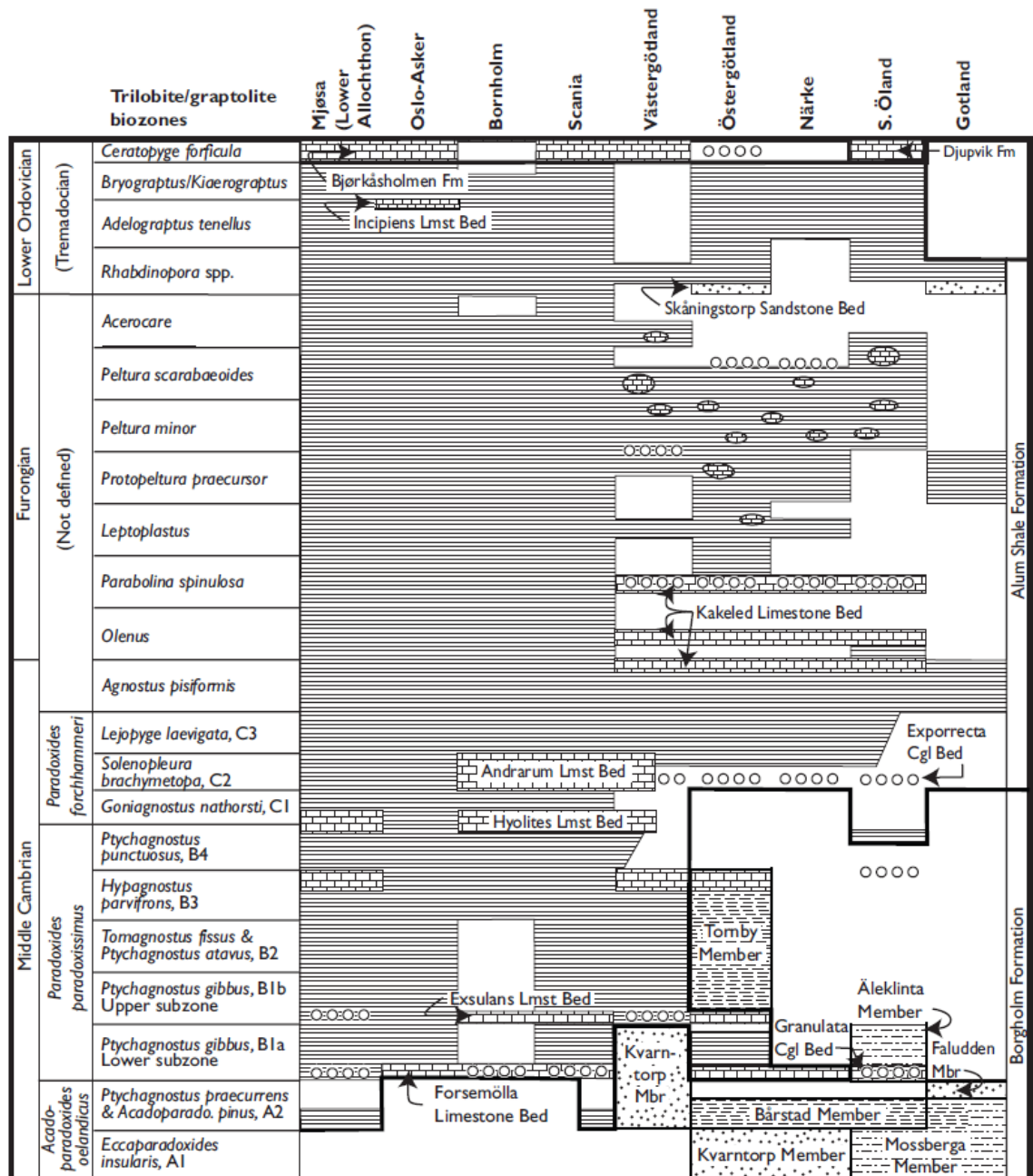
Figure 7.1. Southern Scandinavian lithostratigraphic scheme. The formation of interest, i.e. Alum Shale is part of the Tornny Member and occurs essentially in all districts of Scandinacia (Nielsen and Schovsbo, 2007).

Extensive study of the Cambro-Ordovician Alum shale formation was conducted by the research group in Aachen University as a part of the GASH (Gas Shale in Europe) project (Ghanizadeh et al., 2013). The flow properties of Gripen group of samples mostly agree with the findings of the GASH research conducted, in particular geological properties, helium versus methane behaviour and dependence on parallel and perpendicular bedding of the samples. The group also confirmed large dependence of the gas permeability on the moisture of the samples and effective stress. Ghanizadeh et al. (2014) reported matrix permeabilities of the Alum shale to be withing the 0.6 and 80 nanoDarcies. Previous study

by Pool et a. (2012) measured matrix permeabilities of around 40 nanoDarcies (Ghanizadeh et al., 2013).

7.3 Methods

A field study incorporating a wide range of research activities was undertaken to reach the objectives. These activities can be grouped into three categories: field work, laboratory tests and simulation modelling. This section provides an overview of the field and laboratory tests together with more detailed description of the simulation model construction.

7.3.1 Field work

7.3.1.1 Canister desorption

Canister desorption was performed on 5 wells (Table 7.1). In total, 103 cores were tested over the depth range of 85 m. Full methodology description is provided in Section 3.7.1.

Table 7.1. Overview of the cored range and canister desorption tests.

Well	Depth range cored, m	Number of cores tested
KN-1	84.9-103.4	16
FA-2	72.4-87.2	17
OA-1	19.2-37.5	17
NA-2	86.4-104.3	24
NA-3	71.2-94.1	29

7.3.1.2 Well pressure build-up

Well pressure build-up was done on 9 wells (Table 7.2). In total, 35 measurements were done. The wells that were hydraulically stimulated were also measured for pressure build-up after the stimulation. Although well FA-2A was hydraulically stimulated, well pressure build-up after the stimulation could not be conducted on this well due to field conditions.

Table 7.2. Overview of the wells tested for well pressure build-up.

Well	Number of pressure build-up tests	Pressure build-up test after fracturing		Well	Number of pressure build-up tests	Pressure build-up test after fracturing
KN-1	2			NA-2	3	
KN-1A	16	✓		NA-3	3	
FA-2	1			GH-2A	4	
FA-2A	1			GH-2B	4	✓
OA-1	1					

7.3.1.3   Well flow measurement

Gas flow rate measurement was conducted on 5 wells (Table 7.3). Both short- and long-term tests were done. The description of the equipment is provided in Section 3.7.3.

Table 7.3. Outline of the well flow measurement tests performed on the wells.

Well	Well flow measurement	
	Short-term (1-5 hours)	Long-term (1-100 days)
KN-1	✓	
KN-1A	✓	✓
FA-2	✓	
FA-2A	✓	✓
GH-2B	✓	✓

7.3.1.4   Well stimulation

Three different well stimulation techniques were tested on the wells to improve the gas production: nitrogen fracturing; acid treatment; and hydraulic fracturing. Overall 9 wells were stimulated using either of the methods (Table 7.4). Detailed specifications of each method are provided in Section 3.7.4.

Table 7.4. Outline of the well stimulation performed on the wells.

Well	Stimulation type		
	Nitrogen	Acid	Hydraulic fracturing
KN-1	✓		
KN-1A	✓		✓
FA-2	✓		
GH-2	✓		
GH-2A	✓		
GH-2B	✓		✓
NA-2	✓		
NA-3	✓	✓	
OA-1	✓		

7.3.1.5   Laboratory

Laboratory measurements were conducted to obtain basic petrophysical data on the samples, including porosity, permeability, density, SEM, CT, QXRD, BET, TOC and adsorption parameters (Table 7.5). The results were discussed in Chapters 4, 5 and 6.

Table 7.5. Outline of the petro-physical experiments performed on the samples.

Sample	Porosity	Permeability	QXRD	SEM	CT	TOC	BET	Adsorption	Density
GRPN7	✓	✓	✓	✓	✓	✓	✓		✓
F3	✓	✓	✓	✓		✓	✓		✓
E9	✓	✓	✓	✓		✓	✓		✓
OA1	✓	✓			✓				✓
E1	✓	✓						✓	✓
F1	✓	✓						✓	✓
E16	✓	✓						✓	✓
N2	✓	✓							✓
NG2	✓	✓							✓
NG3	✓	✓							✓
NG4	✓	✓							✓
NG8	✓	✓							✓
NG10	✓	✓							✓
NG12	✓	✓							✓

7.3.2 Simulation modelling

7.3.2.1 Model construction

A reservoir model was constructed to estimate GIP and also simulate gas production. The 3D reservoir simulations were undertaken for this purpose using the black-oil simulator "Tempest". Multiphase flow pressure/volume/temperature-models were created. These models were used to create a Monte-Carlo type statistical breakdown to produce a range of possible GIP outcomes. "Tempest Enable" statistical software was used for this purpose. "Tempest Enable" works with the "Tempest" simulation software interface and is used to aid the reservoir simulation process.

The area for the reservoir model was chosen to be constrained by the Alum shale outcrop as shown in Figure 7.2. The extent of the area to the west was discussed with the company and agreed based on the depth of the shale, which should not exceed 150 m (drilling equipment limitations). The obtained area of 20 km x 6 km (Figure 7.2) was divided into 100 x 100 blocks; an average depth of 100 m was considered which was divided into 10 blocks. A uniform gas/water contact at 100 m depth (true vertical depth) is the base of the reservoir, and the limestone layer at 70 m - 90 m depth is the cap rock. The average thickness of shale layer is about 10 m.

The model was populated with drilled wells using their coordinates. The sweet spot area between the wells KN-1 and FA-2, shown in Figure 7.3, was further divided into a refined grid of 30 x 16 x 40 blocks. This sweet spot area was identified from the analysis of well pressure build-up data, core desorption tests and well flow rate data presented further in the chapter. Therefore, from this point onwards, the area including the wells KN-1, KN-1A, FA-2, FA-2A, GH-2, GH-2A and GH-2B is called sweet spot.

The reservoir model was built as a dual system of matrix and fractures, so each grid-block was assigned separate matrix and fracture porosities and permeabilities. Wells KN-1 and FA-2 have additional high permeability fractures consisting of 60 x 20 x 40 blocks each to improve the simulation of pressure build-ups and gas production. The number of cells chosen was based on the optimisation of computational power, as hundreds of simulations had to be run as part of the sensitivity analysis. Therefore the maximum number of cells was selected considering the available computational resources.

Shale, tight sandstone and limestone layers were distinguished by the assigned porosity and permeability values. The porosity and permeability values were taken from the conducted laboratory measurements (see Chapters 5 and 6). The reservoir exhibits strong permeability contrasts between the shale, tight-sandstone and limestone rocks. The example of the code used to construct the layers is shown in Appendix B.
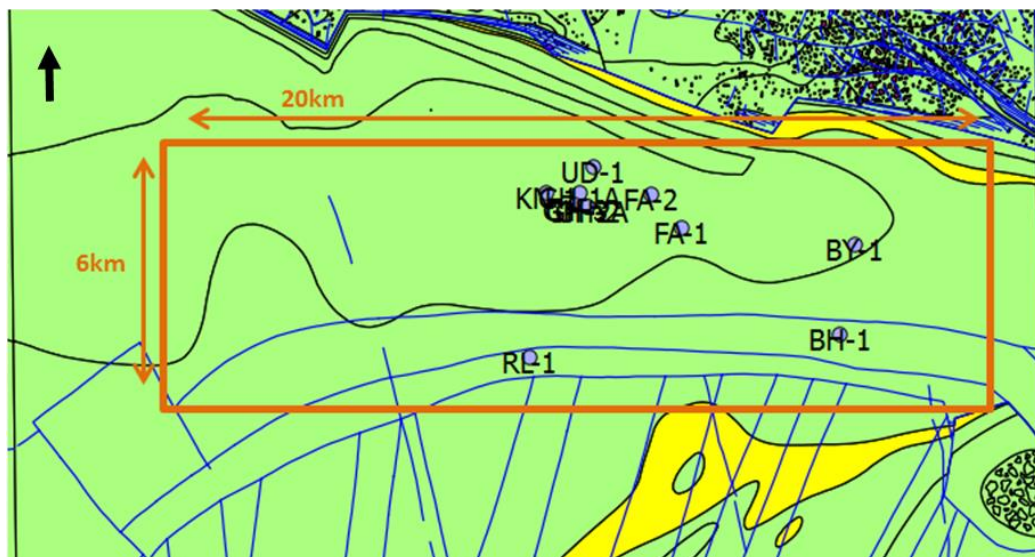
Figure 7.2. The area representing the model. Yellow colour denotes the Alum shale outcrop.
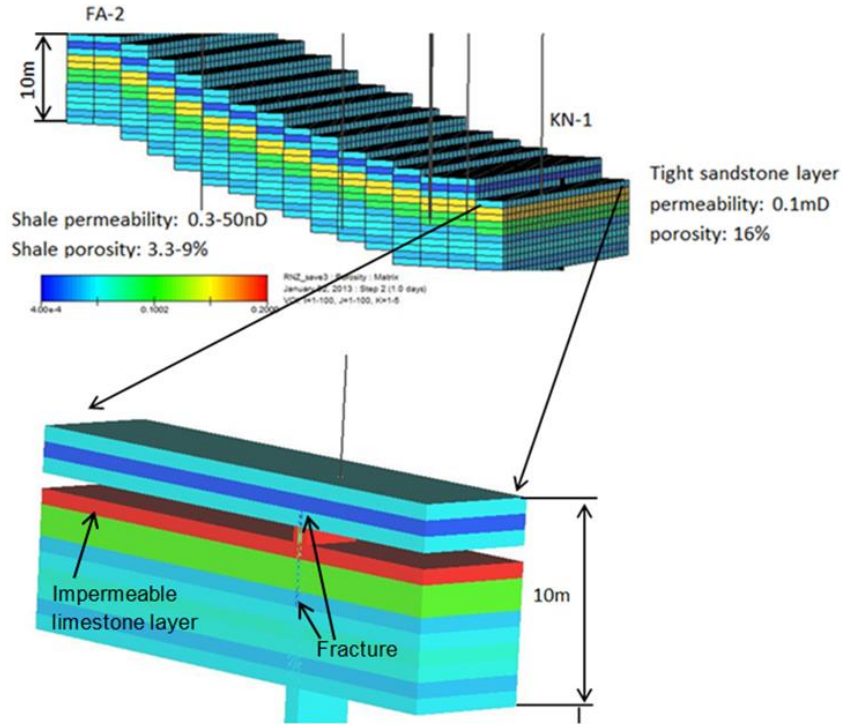
Figure 7.3. Area including wells KN-1, FA-2 and UD-1. Zoomed is KN-1 well area. The colours of the model represent matrix porosity.

7.3.2.2 GIP estimation methodology

GIP calculations were done using Equation 7-1. This equation is based on the multiplication of parameters impacting hydrocarbon volume, including area (A, ft^2), thickness (h, ft), water saturation (Swc, fractional), porosity (Φ, fractional), gas formation volume factor (Bg, rft^3/sft^3) and recovery factor (Rf, fractional). For simplification, adsorption volume was not considered as a stand-alone parameter in these variations, but rather as part of the porosity.

$$GIP = \frac{Ah\Phi(1 - S_{wc})}{B_G} \times Rf \qquad \text{(Equation 7-1)}$$

Monte-Carlo type of analysis was done to construct GIP probability curve by creating a number of possible GIP values based on all possible combination of parameters in Equation 7-1. A number of random values for the each parameter were generated within the specified range and according to specified distribution type. The range for the parameters to vary was determined from the laboratory measurements. The distribution type was chosen as uniform for each parameter.

After that the simulations were run with various combinations of these parameters, producing statistical breakdown of all possible GIP outcomes, which were then plotted versus the corresponding probability. Several combination classes were investigated for variation: porosity-only, saturation-only, area multiplied by thickness-only, and finally variation of all these properties altogether. Additional calculations were made applying a recovery factor to the GIP values.

7.3.2.3 Gas production estimation methodology

Gas production simulation was conducted in the form of a history match, as the data obtained in the field was attempted to be matched with the produced reservoir model. Similar approach to GIP estimation was taken: parameters affecting the production were varied until the best fit between field data and the simulated data was found. The history matched parameters included: matrix permeability, fracture permeability and fracture volume (in the form of fracture porosity). Each layer within the 10 m shale interval (Appendix C) was assigned its own value and modelled as a different variable. Tempest Enable software was used for this purpose.

7.4 Results

7.4.1 Core canister results

Overall, core desorption testing indicated gas presence along the entire depth of the shale formation, with the areas around the sandstone having the highest gas concentrations. The results for all five wells tested are shown in Tables 7.6 to 7.10. The data presented include the depth of the core retrieved and recorded pressure of the accumulated gas.

KN-1 well core desorption results indicate the presence of a highly gas saturated layer located at a depth between of 90 m - 100 m. The highest pressure of 70 psig was reached by the core recovered from the depth of 93.60 m - 94.07 m, whereas the lowest pressures were exhibited by the cores from the depths of 88 m, 97 m, 102 m and 104 m. Although low pressures were shown by sandstone cores, it is likely they have lost the majority of their gas during the core recovery procedure due to their high permeability.

The pressure profile from well FA-2 shows a high pressure region concentrated around the sandstone (Table 7.7). This region is higher in well FA-2 (73 – 84 m) than the analogue in KN-1 (90 m - 100 m), because the beds are dipping. The maximum pressure achieved was by the core from the depth of 73.12 m - 73.58 m, reaching 48 psig. Other cores

outside the most productive region accumulated very little gas, reaching a maximum pressure of only 1.6 psig as shown by the limestone core from a depth of 72.37 psig.

The pressure distribution of the well NA-2 (Table 7.8) looks much more uniform than in wells KN-1 and FA-2. So the actual boundary between gas saturated region and non-productive region is difficult to identify. The maximum pressure in the whole well reaches 28.1 psig and is much smaller than the pressure in wells KN-1 and FA-2. However, after leaving the core to accumulate gas overnight, it achieved a pressure of 43.6 psig.

The sandstone layer at the depth 91.15 m - 92.78 m showed no gas accumulation, possibly because it all leaked before the core was placed into the cylinder. The minimum pressure exhibited by this well is 3.9 psig shown by the core at 95.7 m depth and is larger than the smallest pressures in the previous wells. The uniformity of the pressure distribution could indicate that there is no single concentrated area able to produce gas at large volumes.

The pressure distribution in NA-3 (Table 7.9) is less uniform than in NA-2. The region between 71.2 m – 81 m shows the highest gas saturation within the well, with a maximum pressure of 25.4 psig achieved by the core sample from the depth of 72.3 m - 72.74 m. However, outside this region the cores fail to accumulate more than 10 psig with the smallest pressure of 2.9 psig showed at 89.2 m. Nevertheless, the cores retrieved from a depth of 92.4 m - 92.9 m and 93.6 m - 94.05 m and taken from the very bottom of the well showed an overnight accumulation of gas up to pressures of 8.1 psig and 12.2 psig respectively. That is 1.65 times higher than the ones accumulated within the first couple of hours, namely 4.91 psig and 7.5 psig respectively, as can be seen from Table 7.9.

The NA-3 (Table 7.9) core retrieved from a depth of 72.3 m - 72.74 m produced a gas pressure of 17 psig within the first couple of hours. This core was left accumulating the gas over two days and achieved a pressure of 30 psig, which is 1.76 times higher than the pressure achieved when the core was left for a couple of hours. Another three NA-3 cores, namely: 81.95 m - 82.43 m, 82.48 m - 82.75 m and 83.35 m - 83.87 m were also left accumulating pressure over two days and they achieved pressures of 47.3 psig, 49 psig and 54.5 psig respectively; they accumulated 5 and 11 times higher pressures than during initial build-ups in Table 7.9.

Well OA-1 (Table 7.10) shows relatively low pressures, with the highest value of 14 psig at the depth 24.45 m – 25.05 m. All other regions show pressures well below 10 psig. It has to be noted, however, that the well OA-1 is the shallowest of all drilled wells.

Although the cores from OA-1 produced very little gas in the field, a large amount of gas was produced during long-term tests on the cores. The core samples from the depths of 26.5 m - 27 m and 27.2 m - 27.75 m accumulated pressures of 4 psig and 5.5 psig respectively in the field, however overnight the core accumulated pressures of 15 psig and 18 psig respectively, resulting in an increase of gas by a factor of 3.75 and 3.27 respectively.

The core from the depth of 34.12 m - 34.6 m was left in the cylinder for several months and overall accumulated a pressure of over 330 psig (see Figure 5.15 in Section 5.3.7). The core was sealed in the cylinder in the field without taking any measurements on site. The earliest pressure measurements were taken after three days once the core was delivered to the laboratory and connected to the electronic pressure transducer. The results are provided in Figure 7.7.

Table 7.6. Well KN-1 data. Water saturations were obtained from the bulk volume of the core, field pressure accumulated during the field test, and the porosity was obtained in the laboratory.

Depth, m	Pressure, psig	Amount of gas surface conditions, cm^3	Water Saturation,%
84.90 - 85.40	5.0		
85.95 - 86.43			
88.54 - 89.09	1.0		
90.30 - 90.50	5.0	12.76	39.39
90.70 - 91.20	2.5	0.76	
91.80 - 92.33	31.7	8.26	7.76
93.60 - 94.07	70.0		
93.96 - 94.58	2.6	0.76	
94.47 - 94.92	7.7	1.26	
95.46 - 95.94	22.6	6.26	
97.01 - 97.50	1.4	4.26	83.91
97.97 - 98.52	13.4	1.76	
98.62- 99.10	6.1	4.26	
100.65 - 101.14	15.0	8.26	
102.91 - 103.40	2.0	0.76	
104.00 -104.45	2.5	0.76	

Table 7.7. Well FA-2 data.

Depth, m	Pressure, psig	Amount of gas surface conditions, cm^3	Water Saturation,%
72.37 - 72.82	1.6	1.26	

Depth	Pressure	Amount of gas	Overnight
73.12 - 73.58	48.0	24.26	
74.60 - 75.08		7.26	
75.06 - 75.42	14.2	7.26	77.93
76.99 - 77.45	11.4		
77.38 - 77.92	0.6	0.00	
79.73 - 80.20		0.26	
80.36 - 80.83	25.0	4.76	
81.10 - 81.51	0.3	0.00	
82.39 - 82.71	19.1	12.76	
83.48 - 83.90	3.2	1.76	
84.50 - 84.97		3.26	89.60
84.64 - 85.04	13.1	4.26	
85.42 - 85.92	2.5	0.76	
86.08 - 86.37	0.1	0.00	
86.03 - 86.56	1.0	0.51	
86.77 - 87.22	0.7	0.00	

Table 7.8. Well NA-2 data.

Depth, m	Pressure, psig	Amount of gas surface conditions, cm^3	Water Saturation,%	Overnight pressure, psi
86.45 - 86.85	13.3	5.26		
87.39 - 87.97	12.8	4.26	89.5	
88.45 - 88.95	6.7	0.76		
89.15 - 89.67	20.9	7.26		
89.95 - 90.40	28.1	9.26		43.6
90.60 - 91.13	13.0	3.26		
91.15 - 91.50		leak – sandstone		
91.50 - 92.08		leak – sandstone		
92.08 - 92.78		leak – sandstone		
93.72 - 94.20	10.2	7.26		
94.80 - 95.20	13.9	6.26		
95.20 - 95.64	10.9	6.26		
95.70 - 96.10	3.9	0.51		
96.10 - 96.80	5.0	3.26		
98.00 - 98.50	20.0	12.26		
98.50 - 98.75	14.2	6.26		
98.90 - 99.33	15.0	13.26		
99.64 - 100.15	14.4	10.26		
100.55 – 101.00	14.3	14.26		

101.00 - 101.50	11.5	14.26		
101.95 - 102.52	7.1	6.26		
102.52 - 102.95	6.0	3.26		
103.50 - 103.90	7.0	0.51		
103.90 - 104.25	4.5	2.26		

Table 7.9. Well NA-3 data.

Depth, m	Pressure, psig	Amount of gas surface conditions, cm^3	Water Saturation,%	Overnight pressure, psi	3days pressure, psi
71.20 - 71.6	25.4	8.26			
71.60 - 72.3	10.5	2.26			
72.30 - 72.74	17.0	16.26	46.8		30.0
72.74 - 73.2	12.7	12.26	60.6		
74.10 - 74.6	8.3	3.26			
74.60 – 75	18.3	7.26			
75.10 - 75.6	14.6	3.26			
76.00 - 76.6	10.8	5.26			
77.30 - 77.75	8.6	4.26			
77.85 - 78.2	8.2	4.26			
78.66 - 79.06	3.0	2.26			
80.37 - 80.95	14.1	5.26			
81.95 - 82.43	9.5	48.26			47.3
82.48 - 82.75	9.8	44.26			49.0
82.8 - 83.35	4.0	1.765			
83.35 - 83.87	4.8	54.26			54.5
84.15 - 84.6	9.0	10.26			
85.35 - 85.85	4.8	3.26			
86.3 - 86.8	3.5	0.51			
86.9 - 87.35	6.6	1.26			
87.35 - 87.8	4.0	2.26			
87.8 - 88.35	3.0	4.26			
88.35 - 88.7	2.9	1.26			
88.7 - 89.2	6.0	3.26			
89.2 - 89.7	10.0	8.26			
90.45 - 90.95	4.5	3.26			
91.61 - 92.2	3.7	1.26			
92.4 - 92.9	4.9	5.26		8.1	
93.6 - 94.05	7.5	8.26	91.6	12.2	

225

Table 7.10. Well OA-1 data.

Depth, m	Pressure, psig	Amount of gas surface conditions, cm³	Water Saturation,%	Overnight pressure, psig	6 months, psig
19.20 - 19.50	6.8	2.26			
19.50 – 20.00	3.0	1.26			
21.05 - 21.40	4.4	0.76			
21.55 - 22.05	7.1	1.26			
22.67 - 23.20	8.4	11.26			
23.2 - 23.70	50	2.26			
24.45 - 25.05	14.0	6.26			
26.50 – 27.00	4.0	10.26		15.0	
27.20 - 27.75	5.5	12.26		18.0	
32.10 - 32.55	1.0	0.76			330.0
32.70 - 33.24	0.8	0.26			
33.70 - 34.30	1.1	0.76			
34.30 - 34.80	6.1	0.28			
34.90 - 35.40	1.7	1.26			
35.40 – 36.00	5.0	12.26			
36.50 - 37.14	0.1	0.26			
37.14 - 37.50	0.3	0.46			

Long-term desorption revealed how the gas accumulation rate changes throughout the experiment (see Figure 5.15 in Section 5.3.7). The biggest rise can be seen after approximately 20 - 30 days, when the pressure gradually increases from around 50 psig to values above 300 psig. This final pressure is much higher than any of the short-term desorption experiments, meaning that a huge part of the overall gas is possibly stored in an adsorbed state. After the first desorption experiment reached equilibrium, the gas inside the cylinder was released and the core was set up for another gas desorption experiment shown in Figure 5.16 (see Section 5.3.7). The pressure reaches values of 20 psig - 30 psig much faster than during the primary desorption experiment, however there is little increase in pressure afterwards.

After the second desorption experiment, the pressure inside the cylinder was released and left open for several days for the core to degas. A gas adsorption experiment was then carried out by introducing methane into the sealed canister (see Figure 5.17 in Section 5.3.7). The decay of pressure into the core indicates a single porosity system with one initial large pressure decay followed by relative equilibration. It is difficult to distinguish matrix porosity from the adsorbed volume in this case. Mass balance of these

experiments was performed as a part of the gas volumetric study described in Chapter 5 (see Table 5.24 in Section 5.4.3.2).

7.4.1.1 Pore blockage on the core sample

A comparison was made to determine whether the drilling mud affected the ability of the matrix to release the gas. Two simultaneously retrieved cores from the NA-2 were selected: one was placed into the desorption canister in as-received condition, whereas mud was cleaned from the other core with a piece of cloth and water. Although the cleaned core started from the lower pressure because of the time spent during cleaning, the gas rate from the matrix was almost twice as high (Figure 7.4). It could indicate that the drilling mud covering the shale during the operations blocks the pores and partially prevents the gas from flowing.
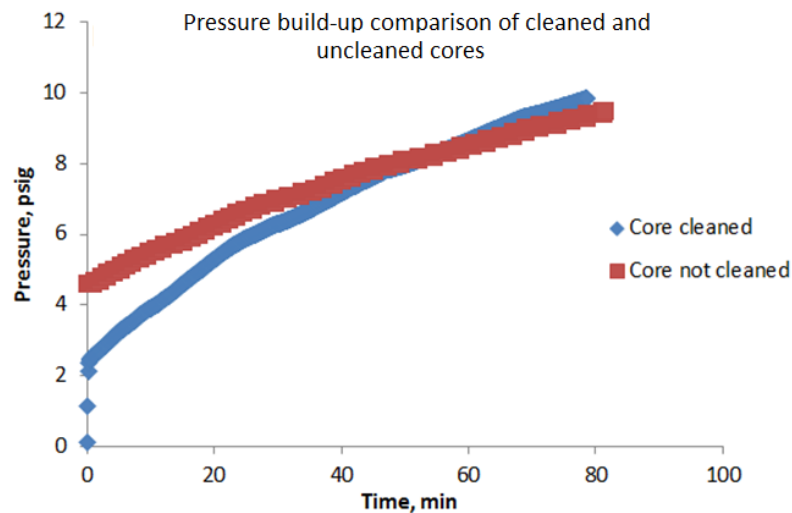
Figure 7.4. Comparison of pore blockage for cleaned and un-cleaned cores. Higher pressure build-up rates were shown by the cleaned core compared to the not cleaned core.

7.4.2 Well pressure build-up results

7.4.2.1 Well KN-1

Well KN-1 was first completed and started to be pressure tested on the 20th June 2013. Relatively high pressures of nearly 30 psig were recorded for two repeated measurements (Figure 7.5). In addition, a good consistency between the pressure build-ups can be observed, indicating good capacity of the formation to supply gas at a constant rate.
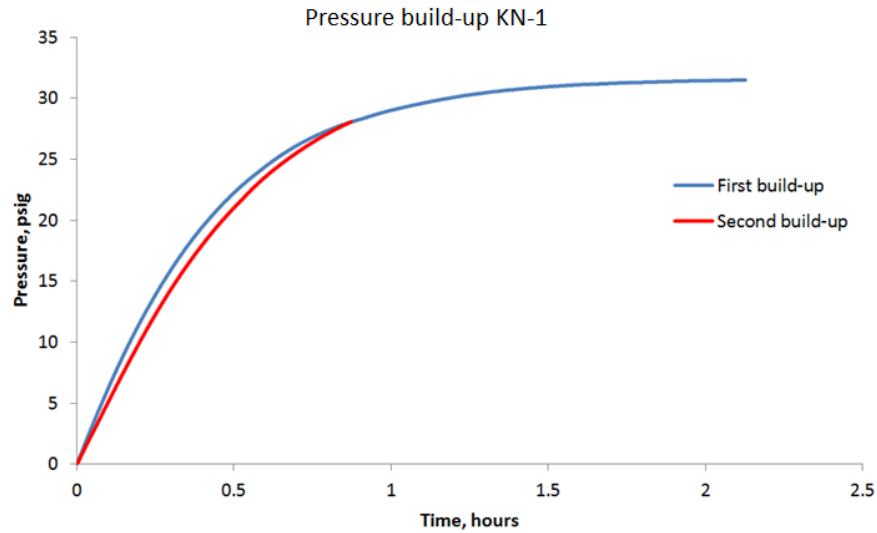
Figure 7.5. Well KN-1 pressure build-up results from two pressure build-up tests. Good agreement between the curves indicates good potential of the formation to provide constant gas flow rate.

A more comprehensive testing programme was carried out on the twin well KN-1A (neighbour well near KN-1) on the 15th July 2014. Several pressure build-up tests were performed (Figure 7.6). The subsequent pressure build-ups were lower either due to the nitrogen effect (see Section 3.7.2) or due to the depletion fractures and gas-saturated sandstone at the depth of 93 m – 94 m (Table 7.6). The well was also left shut overnight – the pressure readings are shown in Figure 7.7. The pressure build up tests conducted on 16th of July 2014 are presented in Figure 7.8. Similar behaviour was noted with the pressure build-ups lowering with each successive test.
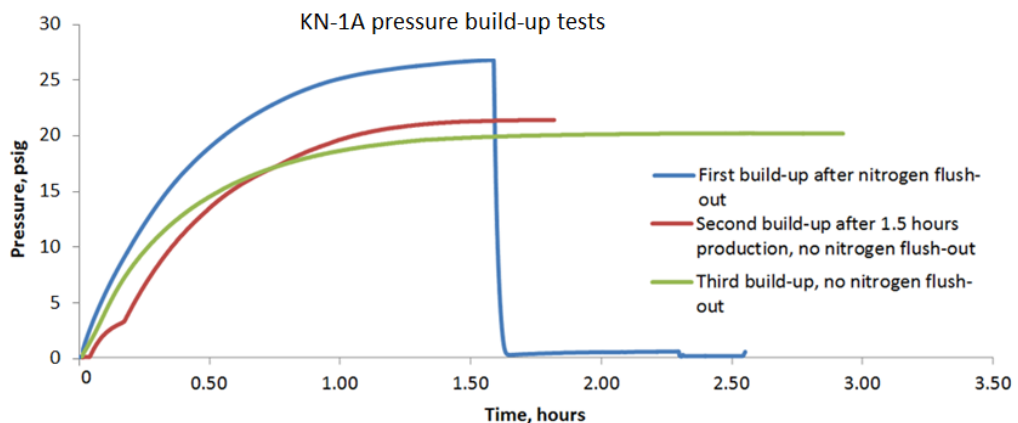
Figure 7.6. KN-1A pressure build-up results from three pressure build-up tests of the well. Tests showed different gas flow rate gradients indicating the formation might be depleting.
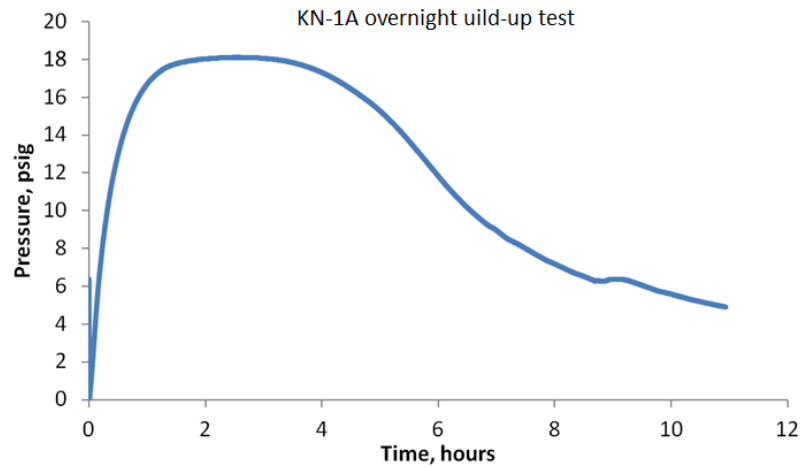
Figure 7.7. Well KN-1A overnight pressure build-up data. Sharp decline happened throughout the night, which was hypothesised to be caused by the temperature drop.
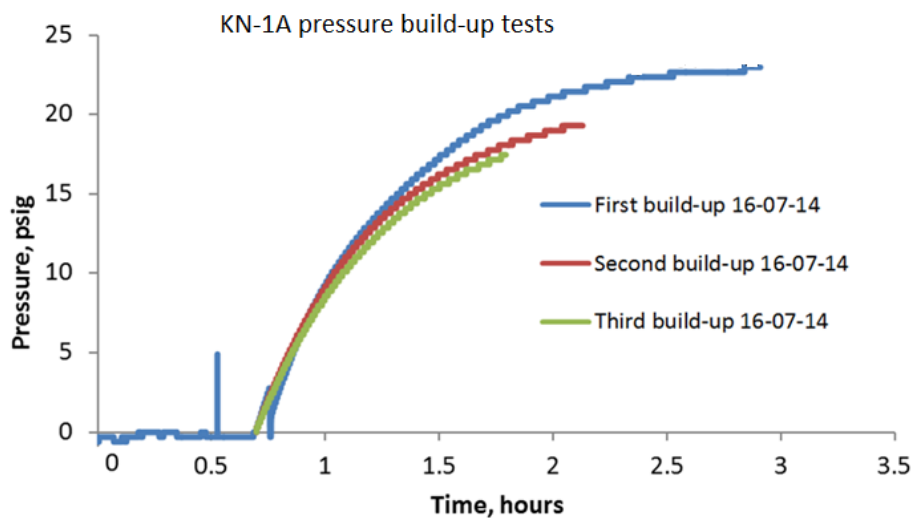
Figure 7.8. KN-1A pressure build-up results comparison. Results from three pressure build-up tests of the well are presented.

The well was left producing overnight with an intention of depleting fractures and highly conductive layers. The objective was to record gas pressure build-up of the shale layer. The first two pressure build-up tests undertaken after that on 17th of July 2014 indeed show signs of depletion (Figure 7.9). However, the following build-ups indicate stable gas accumulation rate. Also tests on 18th of July 2014 show stable pressure accumulation rates (Figure 7.10). However the maximum pressures achieved by the curves are much lower compared to the tests performed on 15th and 16th of July, 2014, reaching only up to 7 psig.
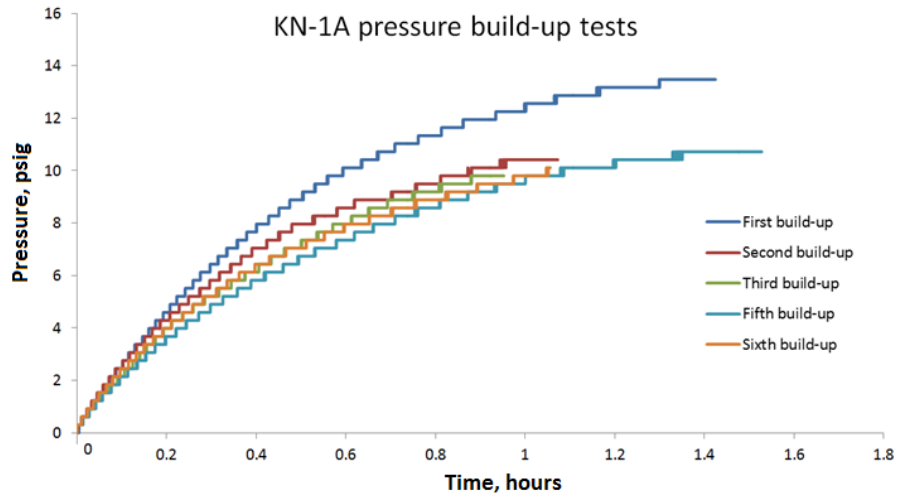
Figure 7.9. Well KN-1A 17th July pressure build-up comparison. Results from six pressure build-up tests of the well are presented.
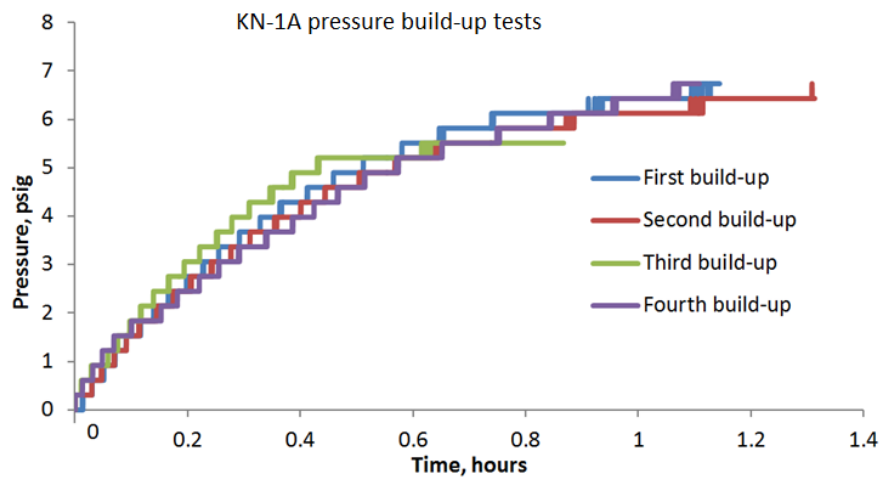
Figure 7.10. Well KN-1A 18th July pressure build-up comparison. Results from four pressure build-up tests of the well are presented. Build-up rates became the same meaning the constant matrix flow was achieved.

7.4.2.2 Water injection stimulation on well KN-1A

Hydraulic fracturing was performed on well KN-1A. The pressures were recorded both for the stimulated well (KN-1A) and for the twin well (KN-1S). Figure 7.11 shows the pressure of the well KN-1A during the injection and the pressure response of the well KN-1, which is located 24 meters away from well KN-1A. Overall 2.5 m^3 of water was used for the re-circulation of the well and 3.5 m^3 was used for the fracturing operation itself (see Section 3.7). Pure water without sand was used in this test. The obtained data (water volume used, pressure drop, hydraulic lag time between the wells and local stress information) can be used for further geomechanical analysis on the fracture properties (bedding opening, fracture length, fracture area etc.), but this was beyond the objectives of this particular study.
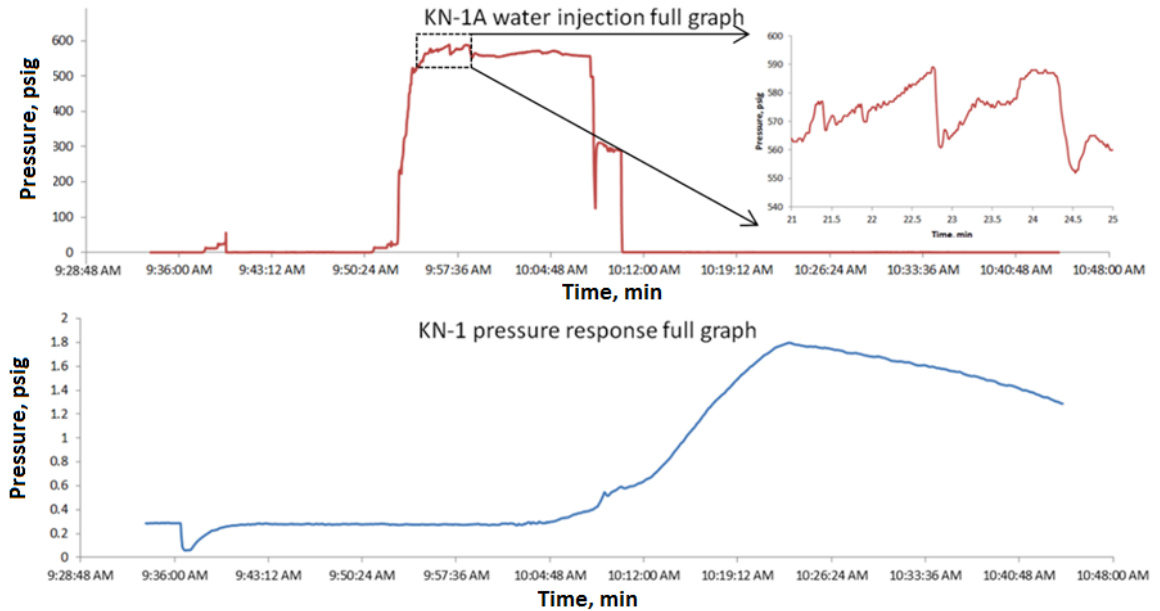
Figure 7.11. Well KN-1A pressure build-up and flow rate. The measurements were performed at the same time. It can be seen in the zoomed-in area that two formation break-ups occur.

Pressure build-up test followed the water injection procedure to test the effectiveness of the stimulation. The comparison of before/after stimulation for pressure build-up is provided in Figure 7.12. It is clear that the pressure failed to reach values shown before the water injection, probably because the water occupied the pore space near the well suppressing gas production. However, pressure build-up after 2 weeks showed significantly recovered pressure to the levels of the initial values on 15th June 2014 (Figure 7.13).
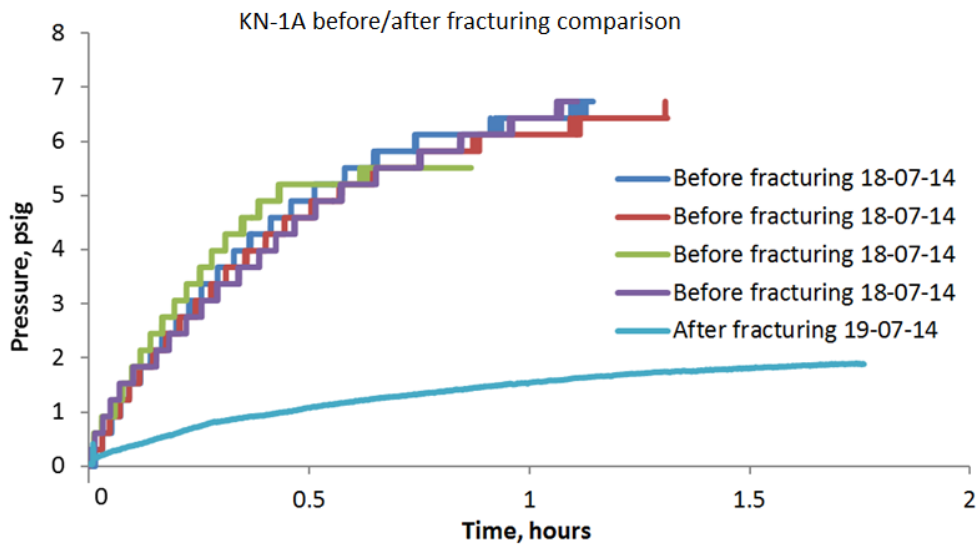
Figure 7.12. Well KN-1A pressure build-up results comparison. Several successive build-up tests before fracturing show stable matrix flow. The build-up pressure just after fracturing can be seen to be much lower.
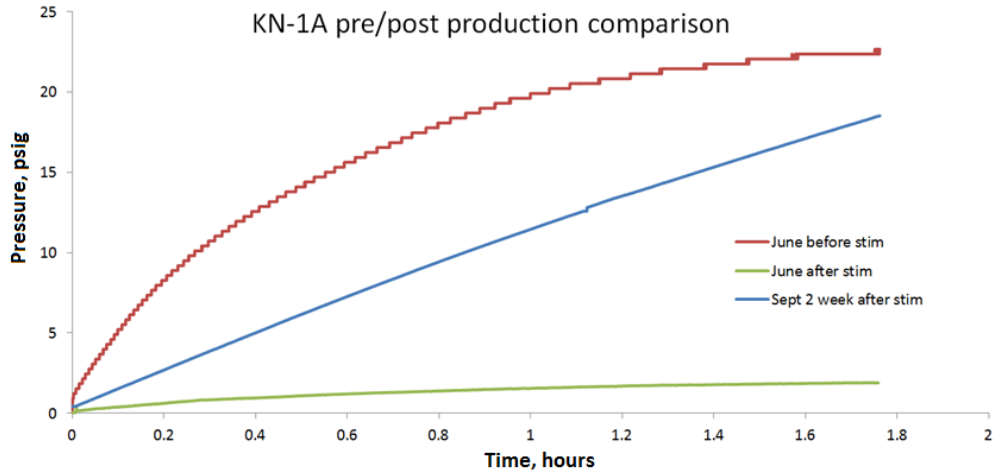
Figure 7.13. KN-1A pressure build-up comparison. The build-ups performed before and after fracturing operation and also 2 weeks after continuous production.

7.4.2.3 Well FA-2

Well FA-2 was first completed and started to be pressure tested on the 26th June 2013. Obvious fracture-type behaviour was observed (Figure 7.14), as most of the gas accumulating within the first 5 minutes, after which the curve remained flat. Twin well FA-2A was completed in September 2014 and a production test was carried out on this. Figure 7.15 shows pressure build-up after the 2 week production test.
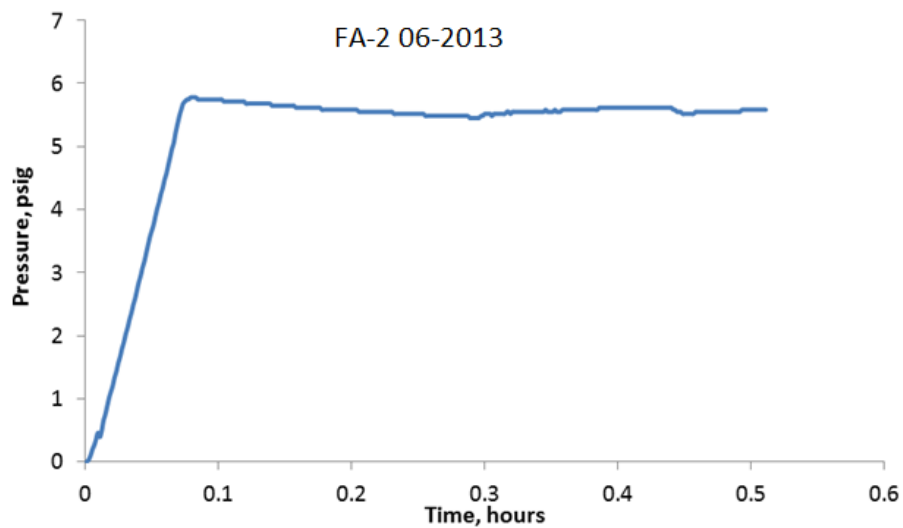
Figure 7.14. Well FA-2 pressure build-up results. The pressure build-up is dominated by the fracture as most of the gas accumulated within first 5 minutes after which the curve remained flat.
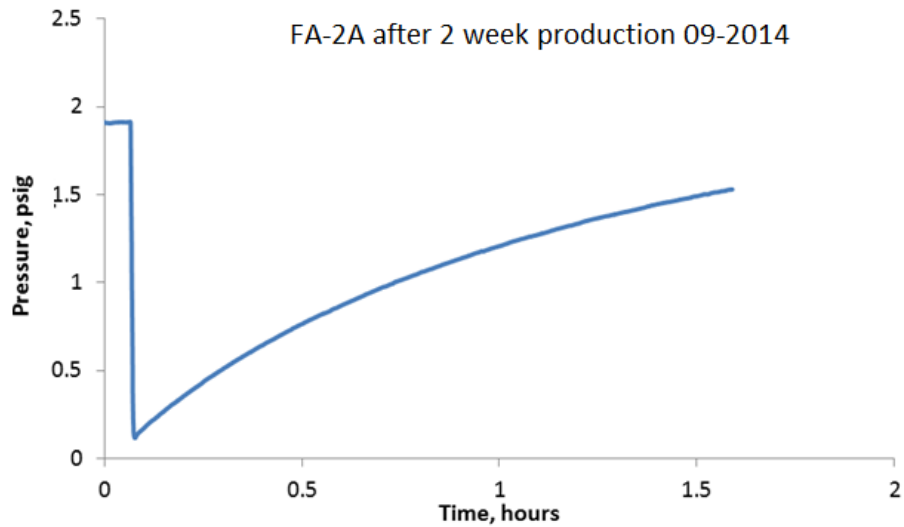
Figure 7.15. Well FA-2 pressure build-up test results. The pressure accumulates to around 1.6 psig in around 1.5 hours.

7.4.2.4 Well GH-2B

Well GH-2B was completed and pressure tested on the 18th of June 2014. Pressure build-up graphs are presented in Figure 7.16. Nitrogen was used on the well to flush-out the water; consequently the first build-up of the first graph might have been affected by nitrogen intruding the formation. A pressure response test was carried out overnight by leaving the well GH-2B open and recording pressures of the twin wells GH-2A and GH-2 (Figure 7.17a). A map showing relative locations distances of the wells is shown in Figure 7.17b. Well GH-2A was affected slightly by the open production at the GH-2B, indicating that the wells are connected by the high conductive layer. However, the further well, GH-2, showed no disturbances in pressure due to the overnight production at GH-2B.
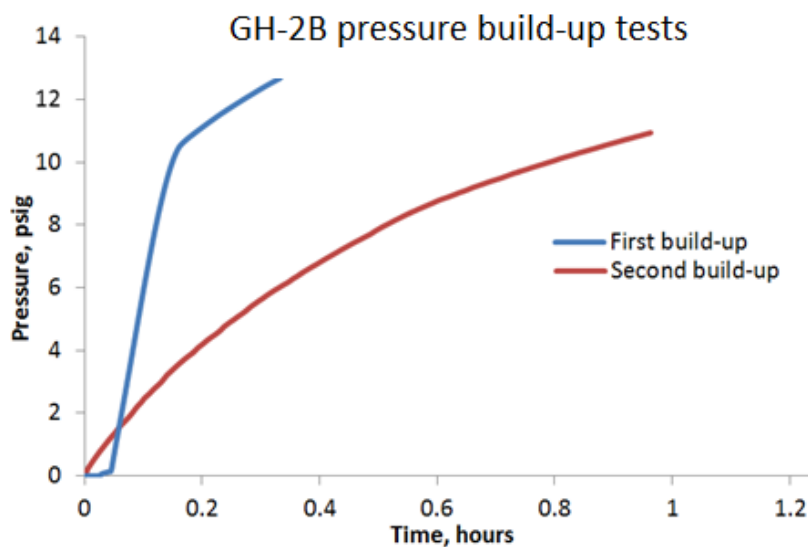
Figure 7.16. Well GH-2B pressure build-up. The build-up rates vary considerably meaning constant matrix flow was not achieved.

Pressure response test
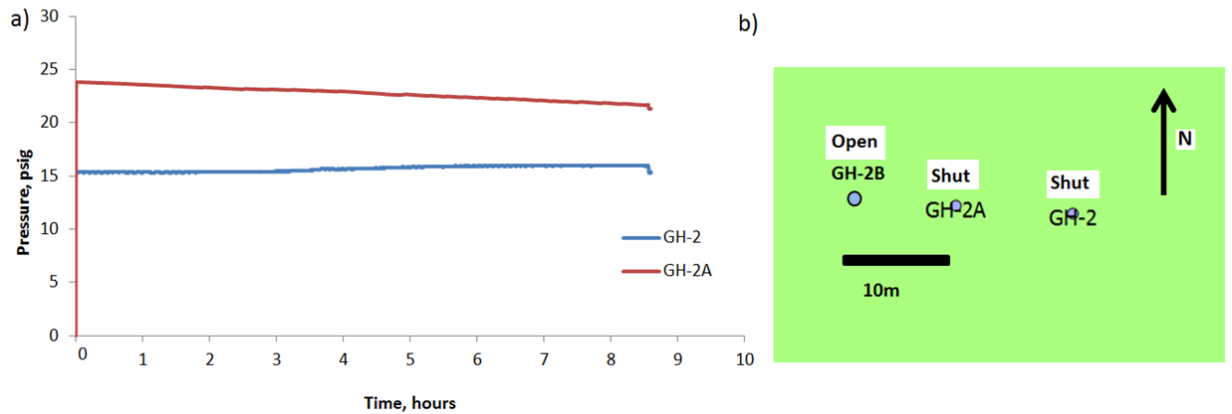
Figure 7.17. Pressure curves of wells GH-2 and GH-2A, recorded during production of well GH-2B (a), and the mini map with relative well locations (b). A slight decrease in the pressure of the well GH-2A is seen, meaning there must be gas communication between GH-2B and GH-2A. Well GH-2 remained unresponsive.

7.4.2.5   Well GH-2B water injection testing

Similarly to KN-1A, well GH-2B had undergone water injection stimulation (hydraulic fracturing). Water injection data for the well GH-2B and pressure responses of the twin wells GH-2A and GH-2 are shown in Figure 7.18. Unlike well KN-1A, the well GH-2B showed only one pressure drop followed by a steady plateau and then a decline phase. The reason for this might be that there are more natural fractures in the well KN-1A than in GH-2B – this could also explain higher production and pressure build-up values shown by well KN-1A. Similarly to KN-1A and KN-1, the twin well of GH-2B - GH-2A also took around 10 minutes to fully respond to the process, whereas the well GH-2, which is located 20 meters away from GH-2B, showed a pressure response only at the end of the injection process, after about 20 min.
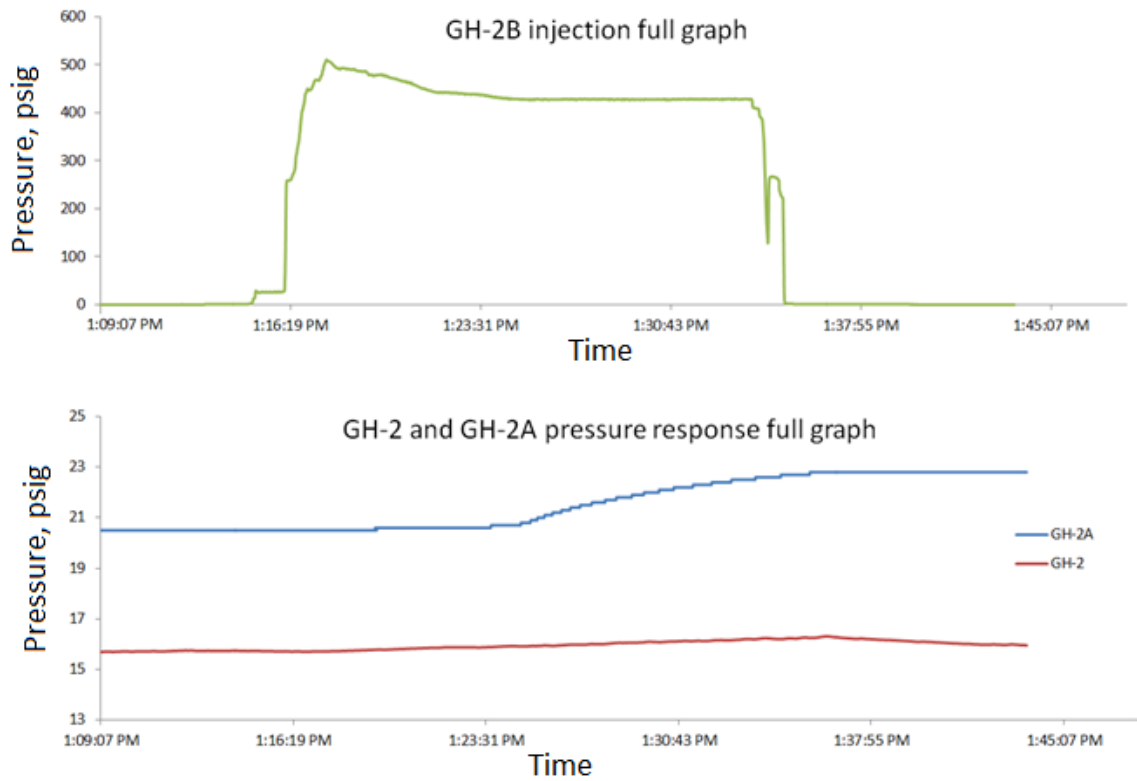
Figure 7.18. Water injection pressure measurement and pressure response in the twin wells. Measurements were done and recorded at the same time. Clear response in the well GH-2A is seen. Well GH-2 responded only slightly.

Pressure build-up testing was conducted on the wells GH-2B after its stimulation and also GH-2A for comparison. Unlike for well KN-1A, water stimulation seemed to have not initially reduced the well GH-2B pressure build-up rate as shown in Figure 7.19. Well GH-2A showed behaviour similar to well KN-1, indicating that the pressure peaked due to the water pushing gas towards it, followed by the decline due to the dispersion of the water into the formation (Figure 7.20). Fractured well GH-2B was tested again after 2 weeks of production, and similarly to well KN-1A, showed good results and sustainable shale flow (Figure 7.21).
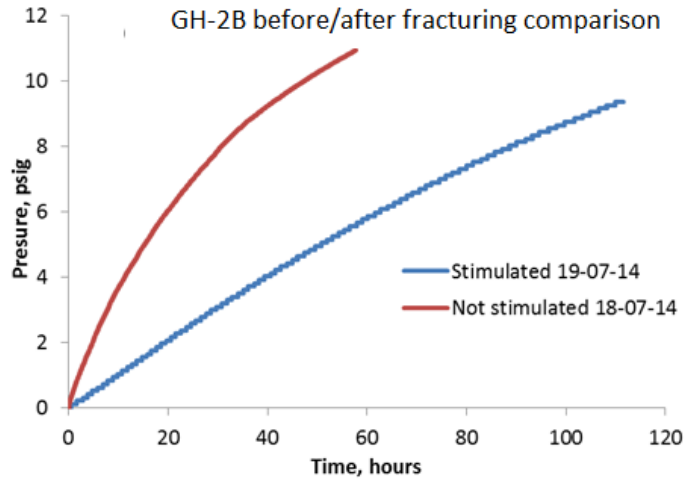
Figure 7.19. Well GH-2B before and after fracturing pressure build-up comparison. Stimulated well showed considerably lower pressure build-up after the injection.
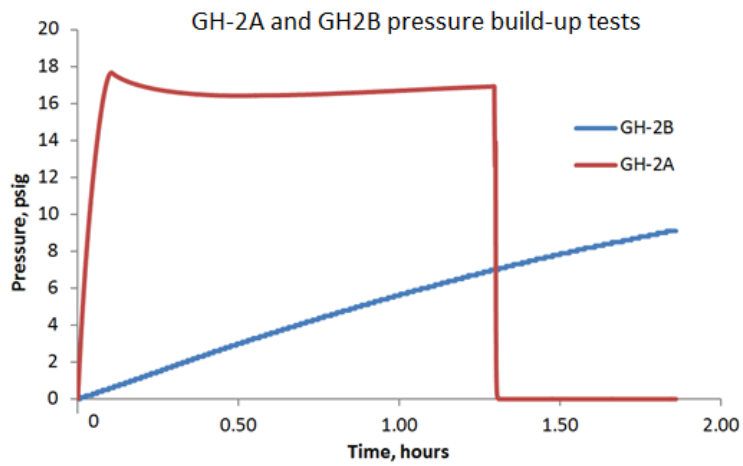
Figure 7.20. Wells GH-2A and GH-2B pressure build-up comparison. Different pressure response for two neighbouring wells can be observed.
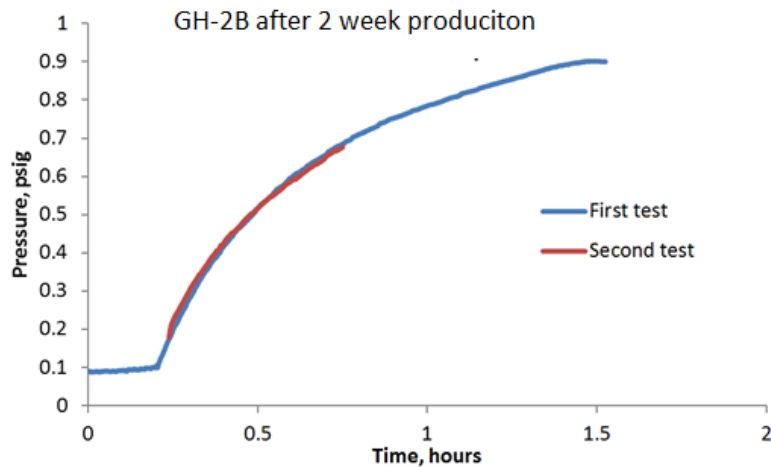
Figure 7.21. GH-2B pressure build-up comparison. The results indicate almost identical pressure build-up rate after two weeks of production of the well.

Well GH-2A was not produced, however it showed a decline compared to its previous build-up (Figure 7.22). This is most likely due to the depletion of connecting layer between GH-2B (which was produced) and GH-2A, as the connection between the two wells was proved by the injection tests (Figure 7.18). In October 2014, hydraulic fracturing operations including sand were performed on the wells GH-2A, KN-1A and FA-2A. The pressure data are not provided, however there was an increase in production rates of about 60% and 30% in the wells (Gripen, 2014). It was noticed that better results were achieved when using more sand.
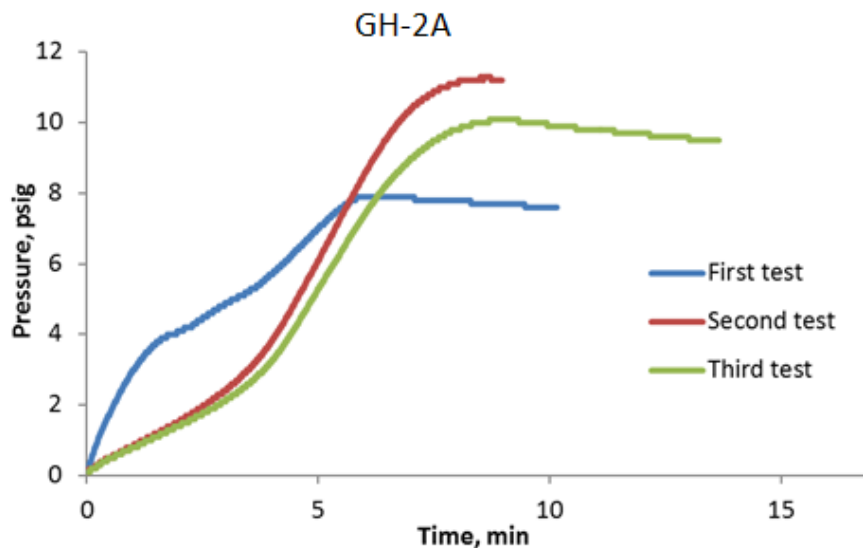
Figure 7.22. Well GH-2A pressure build-up comparison. The pressure build-up rate is fundamentally different between the first and subsequent tests, which might be explain by the release of the accumulated gas in the fractures.

7.4.2.6   Well NA-2

Well NA-2 was tested for pressure build-up on 11th of June 2014 (Figure 7.23). The first water flush-out showed considerable levels of mud being flushed out. The first pressure build-up produced small pressures of just 10 psig. However, after the well was flushed-out again, the pressure showed a significant increase during the second and third build ups.
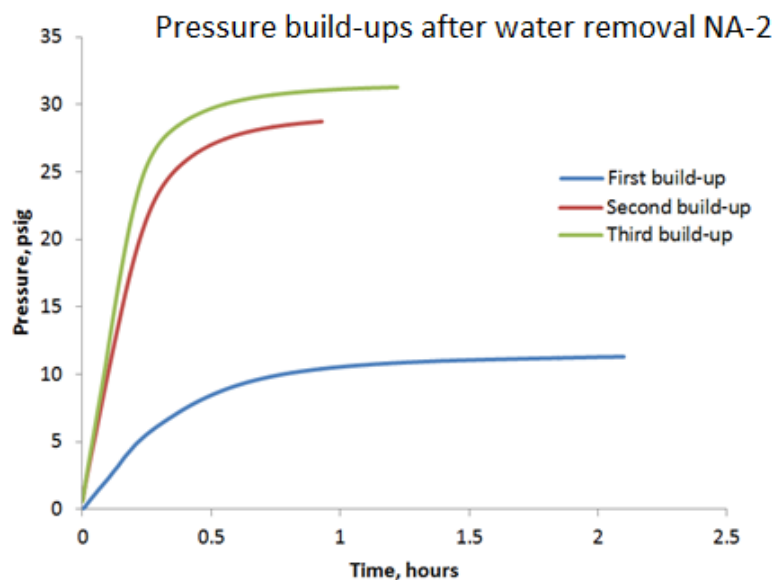
Figure 7.23. Well NA-2 pressure build-up comparison. Results from two typical pressure build-up tests of the well are presented, as well as results without water flushing.

7.4.2.7 Well NA-3

Well NA-3 was completed and pressure tested on 25th of June 2014. The well has undergone an acid stimulation (see Section 3.7.4.2). The results of the pressure build-ups before/after the stimulation are provided in the Figure 7.24. Overall, low and inconsistent pressure build-ups were observed.

Acid treatment improved the initial gas flow for the first half an hour of the test (Figure 7.24). As showed by the pore blockage results (see Figure 7.4 in Section 7.4.1.1), improved gas release rate could be seen in the core desorption tests of the cleaned cores but not in the cores which had not been cleaned. However, in the well case, acid stimulation did not provide significant improvement in terms of pressure accumulation, apart from the slightly improved gas rate at the initial 15 min. Therefore pore blockage cleaning has only short-term improvement on the gas flow.
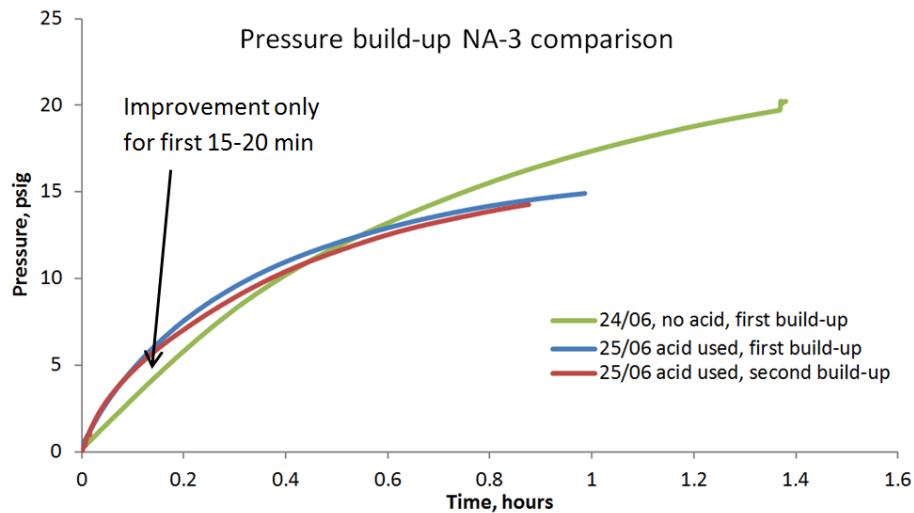
Figure 7.24. Well NA-3 pressure build-up comparison. Stimulation by acid can be seen to improve only initial pressure build-up.

7.4.2.8   Well OA-1

Well OA-1 was tested for the pressure build-up, however did not show any gas accumulation. This is despite core desorption indicating gas present within the shale, and the long-term desorption experiment accumulating pressures of around 350 psig over 6 months period. Failure of the formation to accumulate gas on the wellbore scale could be due to the unusually shallow depth of the Alum shale at this location, reaching only about 30 meters.

7.4.3   Well production data

7.4.3.1   Short-term gas flow results

The short-term production results for 5 wells tested for gas flow rate are provided in Table 7.11. The pressure of the well KN-1A was additionally monitored while the well was choked at the rate of around 100 scf/h (Figure 7.25). The graph shows that while the well was producing gas at a constant flow rate, the pressure of the well was continuously increasing. Furthermore, twin well KN-1, just 20 m away from KN-1A, also showed good production with the gas rate readings of around 130 scf/h before the test was stopped. This indicates the ability of the shale formation around these wells to sustain gas flow.

Well FA-2 produced a massive 1400 scf/hour during the first 40 minutes before gradually ceasing to flow (Table 7.11). The well did not flow again until the next day. This gas behaviour might indicate a large fracture connected to the well – initially the fracture was providing good gas flow, however after the fracture depleted the flow finished until the next day once the fracture was saturated again. This behaviour is also supported by the

well pressure build up – pressure accumulated quickly within minutes with no accumulation afterwards (see Figure 7.14 in Section 7.4.2.3). This fracture has to be connected to the shale formation to be able to be saturated with gas.

Twin well FA-2A, which is 100 m away from FA-2, did not show this fracture behaviour. The gas flow was at an average of 43 scf/h and lasted for around half an hour (Table 7.11). This is fundamentally different behaviour from the well FA-2. This implies that the fracture does not extend towards well FA-2A or is striking parallel to this well.

Well GH-2B showed relatively good gas production averaging 80 scf/hour for around 50 minutes (Table 7.11). Well pressure build-up also showed well GH-2B able to accumulate high pressures of gas comparable to wells KN-1 and KN-1A. The formation also seemed to be able to recover and provide similar amount of gas after some time (Figure 7.21), which is more consistent than for wells FA-2 and FA-2A.

Well NA-2 showed recordable gas production for only 5-10 minutes (Table 7.11), despite accumulating relatively high pressures during the build-up tests (Figure 7.23). Well NA-3 showed even lower gas production which lasted for just 2-3 minutes (Table 7.11). Even acid stimulation did not improve gas flow rate for the well NA-3 (Figure 7.24), therefore further well testing for these wells was stopped.

Table 7.11. Short-term production test. The gas rate readings for each well tested, the time the well was flowing, and the overall produced gas during the time the well was flowing is presented.

Well	Pre-stimulation prod rate, scf/hour	Flow time, hour	Produced gas, scf
KN-1	130	0.66	85.8
KN-1A	101	0.83	84.0
FA-2	1400	0.57	800.0
FA-2A	43	0.5	21.5
GH-2B	80	0.83	66.4
NA-2	30	0.16	4.8
NA-3	20	0.05	1.0
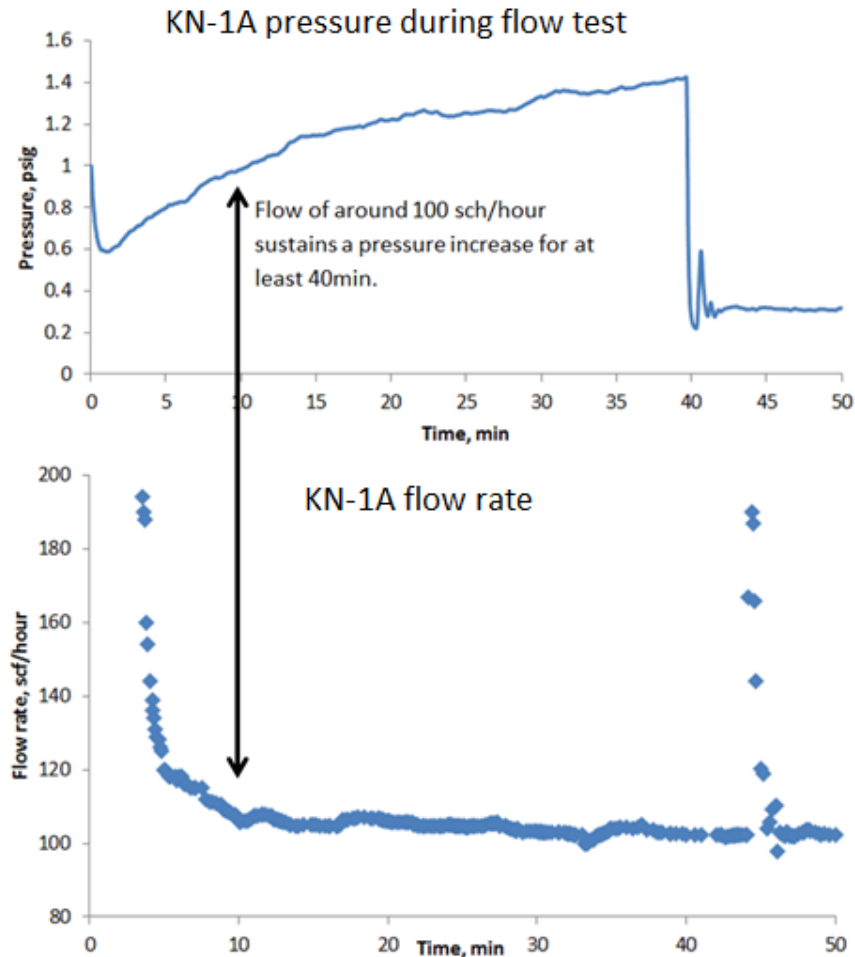
Figure 7.25. Well KN-1A pressure build-up and flow rate data. The measurements were performed at the same time and similar responses can be observed between the two curves.

7.4.3.2 Long-term gas flow results

This short-term production might be significantly affected by the fractures and high conductivity regions as seen in the case of wells KN-1A and FA-2 (see Sections 7.4.2.1 and 7.4.2.3). Long-term well flow tests allowed to evaluate the potential gas production of the shale formation. Wells were equipped with the long-term production rate measuring equipment (see Figure 3.28 in Section 3.7.3). The average production results are shown in Table 7.12. The wells were tested both before and after the stimulation. Unfortunately, well FA-2A could not be tested after the stimulation, whereas FA-2 could not be long-term tested at all due to unforeseen conditions at the well site.

The wells exhibit a sharp drop in production rates compared to the short-term results - well KN-1A showed the rates of 101 scf/hour during the short-term testing (Table 7.12), whereas the long-term average was just 140 scf/day. Similarly, the other wells GH-2B and FA-2A showed lower than expected daily rates when compared to the short-term hourly

production rates. This indicates the inaccuracy of the short-term tests (possibly caused by gas stored in fractures as in the FA-2 case), and the necessity to perform long-term tests for the more accurate results.

Water stimulation significantly improved the production results as shown in Table 7.12. The average flow rates for well KN-1A improved by more than 3 times to around 455 scf/day, while well GH-2B saw even higher improvement up to 680 scf/day. The production history of the well KN-1A is shown in Figure 7.26: the production was high at the start of the test, however the well was shut and reopened only after a month for technical reasons (Figure 7.26). The production was considerably smaller after the opening of the well, however water stimulation has significantly improved the gas rates.

Table 7.12. Long-term production results. The presented results show average long-term gas production readings before and after stimulation.

Well	Pre-stimulation prod rate, scf/day	Test time, days	Post-stimulation prod rate, scf/day	Test time, days	Total produced, Mscf
KN-1A	140	74	455	46	31.3 + 10.3*
FA-2A	31	40	N/A	60	20.5
GH-2B	127	20	680	80	56.9

*Note well KN-1A produced 10.3 Mscf during initial short term production period.
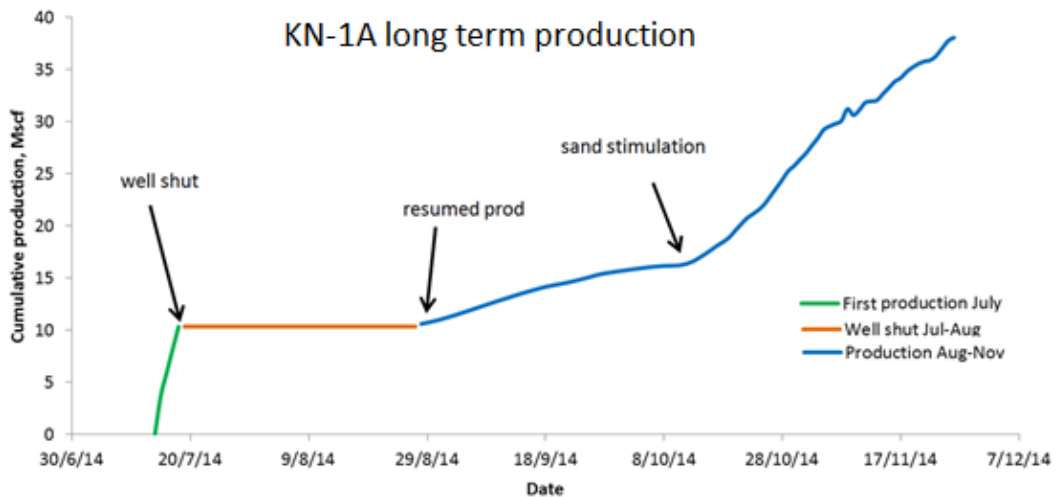
Figure 7.26. Cumulative gas production for a long-term gas production test. The well was shut the same day and opened for production only after a month.

7.5 Discussion

7.5.1 Reservoir model

The reservoir model constructed using combined field and a laboratory result is shown in Figure 7.27. The 10 m thick sandstone layer is the most distinctive within the formation in

terms of porosity and permeability (Figure 7.27). The layer is encountered at different depths in the wells, because the beds are dipping in the area (Nielsen and Schovsbo, 2007). KN-1 core samples retrieved from this depth are shown in Figure 7.28.
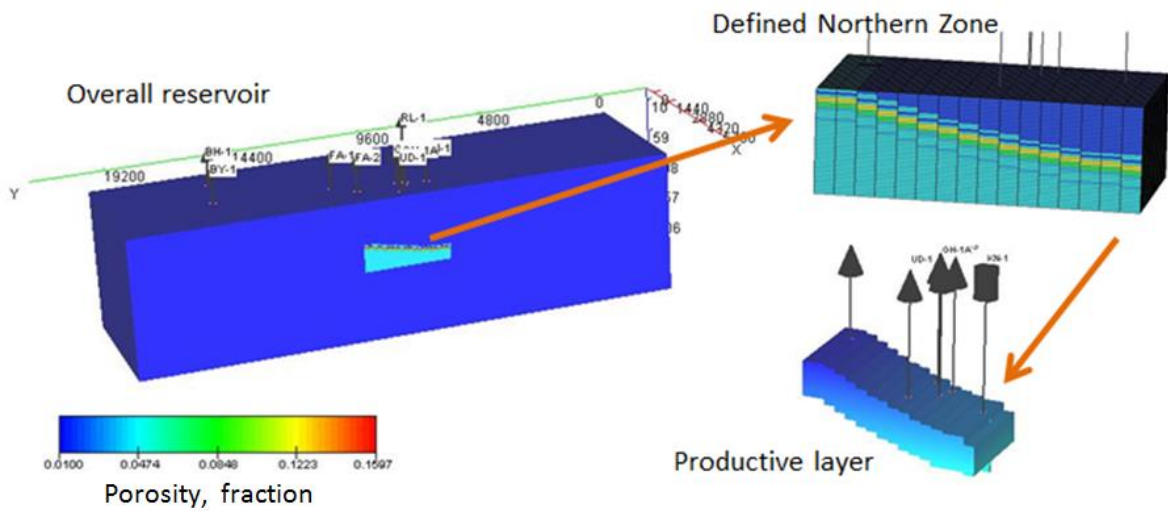
Figure 7.27 Reservoir model covering the 20 x 6 km sweet spot area.

Figure 7.28. KN-1 cores retrieved from the field.

This layer of tight sandstone was observed to produce the most amount of gas during the initial time, according to the core desorption results (see Table 7.6 in Section 7.4.1). It is likely that once this layer depletes around the wellbore, the production drops considerably, as was seen with the well pressure build-up graphs (see Figures 7.4 – 7.9 in Section 7.4.2.1). At well KN-1 this productive tight-sandstone layer starts at about 93m,

whereas at well FA-2 this layer starts at about 71 m. A wide range of permeability values were tested on the reservoir model described in this research, but none of these produced fitting history match value for either long or short-term reservoir behaviour.

Adsorption was shown to have the major impact for the gas production over the long term, as was shown by the long term core desorption results (see Figure 5.15 in Section 5.3.7). Therefore to correctly history match the long-term reservoir curves, a different type of model should be used, involving gas adsorption. The current model, described in this research is able to model the GIP but lacks capacity to accommodate certain types of flow mechanisms such as sorption processes in shale formations – it was unable to reproduce permeabilities as discussed in Section 6.4.3.3. Instead, a double porosity model accounted for additional volume created by adsorption. This way of representation of the additional porous volume due to adsorption is the easiest and mathematically correct when calculating the gas filled volume, however it cannot represent the dynamic behaviour of the gas properly when the pressure changes during production.

The saturation values were derived from canister desorption and porosity results (Table 7.6; Table 7.7; Table 7.8 and Table 7.9 in Section 7.4.1). The water was assumed to be bound to the clays within the shale, therefore water does not participate in the production process. Practically this is wrong as it was known that water participates in the flow and wells produce significant amount of water, however this assumption was still applied to keep the model simple. Essentially, derivation of the gas volume was of higher priority than simulating production.

The water which is produced, however, is supplied into the wellbore by the fractures from the aquifer underneath the shale. During production, this water is uplifted by the gas in the sludge/slurry flow regime. This in turn exerts the hydraulic pressure on the gas producing formation, decreasing the pressure gas drive potential. The solution to the water problem was the assembled water pump system, shown in Figure 7.29. The system continuously removes the water accumulating in the wellbore thus reducing the hydraulic pressure and increasing the gas production.

Figure 7.29 water pumping system

7.5.2   GIP Sensitivity analysis

7.5.2.1   Porosity

A range of porosity multipliers were chosen to alter the base model and evaluate the effect on the GIP. The minimal multiplier was chosen according to the experimental uncertainty of 0.7, whereas the maximum was taken as 3.1 according to the increase in the gas storage by adsorption effect of Alum shale (see Table 5.24 in Section 5.4.3.3). Two main scenarios were assumed: change of porosity in all layers and change of porosity only in the shale layers, while tight-sandstone areas were kept constant. The resulting distribution of GIP values depending on the porosity is shown in Figure 7.30a and b. Figure 7.30a represents the varying porosity only in the shale layers while keeping the porosity of the sandstone layer constant. Figure 7.30b represents the variation in porosities in both layers.

The graph displaying GIP variation depending only on shale porosities shows wide possible GIP range between 70,000 MMscf and 180,000 MMscf (Figure 7.30a) within the chosen 20 x 6 km^2 area (see Figure 7.2 in Section 7.3.2.1). The gradient of the curve is fairly uniform meaning the possibility for large GIP values decrease steadily without any significant GIP cut-offs. The introduction of varying tight-sandstone layers considerably alters the graph: the range of probably GIP values sharply drops from 70,000 MMscf - 180,000 MMscf for the shale-only case to 40,000 MMscf – 150,000 MMscf shale + tight sandstone case (Figure 7.30b). Gradient of the curve also changes with the midpoint of

100,000 MMscf becoming an inflection point – the probability for GIP values sharply drops from 40,000 MMscf to 100,000 MMscf, then the gradient changes and the probabilities drop more steadily up to 150,000 MMscf.
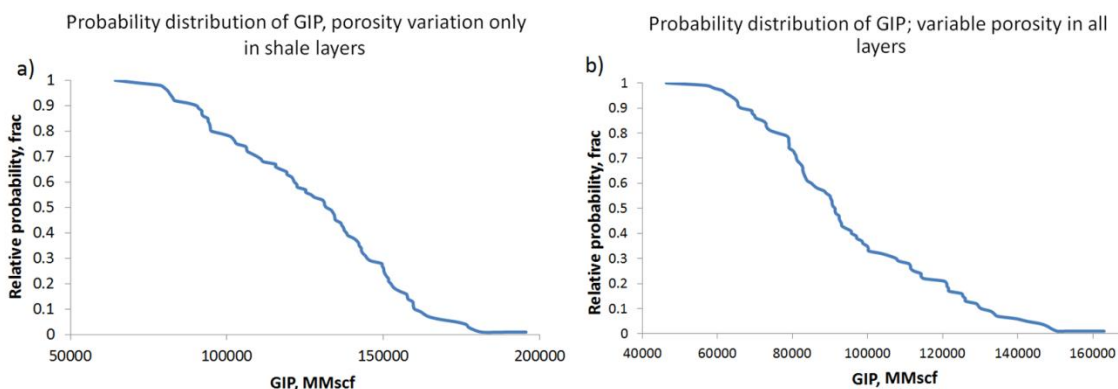
Figure 7.30 Gas in place (GIP) estimates based on possible range of porosity values: (a) porosity was changed only in shale layers and was left constant for the tight sandstone layer; (b) both shale and sandstone layer porosities were varied. The variations include possible effects of secondary porosity and adsorption. Base model scenario was assumed for all remaining parameters.

7.5.2.2 Water saturation

Water saturations were derived at three depth points in the well KN-1, that is 39.4% at 90.3 m - 90.5 m depth; 7.75% at 91.8 m - 92.33 m and 83.9% at 97.01 m - 97.5 m respectively. In the simulation model runs these values were fixed and the unknown saturations between these depths were varied. Two water saturation values are known from well FA-2, that is 77.9% at 75.06 m - 75.4 m and 89.6% at 84.5 m - 84.97 m depth. Figure 7.31 a represents the distribution of the GIP values according to the variation in the saturations only. Figure 7.31 b shows combined porosity and saturation simulation runs.

Gradient of the curve also changes with the midpoint of 100,000 MMscf becoming an inflection point – the probability for GIP values sharply drops from 40,000 MMscf to 100,000 MMscf, then the gradient changes and the probabilities drop more steadily up to 150,000 MMscf. The GIP probabilities on the water saturations produce a range between 70,000 MMscf to 100,000 MMscf (Figure 7.31 a). The probabilities for the GIP values remain similar between 70,000 MMScf to 80,000 MMscf, however after that the GIP drops sharply following fairly uniform gradient. When combined with porosity variation in all layers (Figure 7.30b), the GIP range drops to 40,000 MMscf – 100,000 MMscf (Figure 7.31b). The gradient of the curve smoothens and becomes less steep.
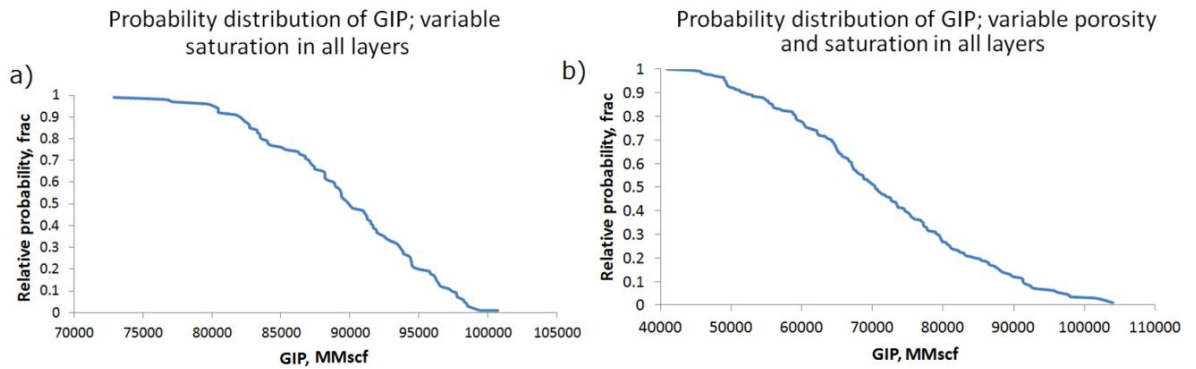
Figure 7.31 GIP estimates based on possible range of saturation values (a) and combined porosity-saturation uncertainty effect (b). Probability of original estimate is considerably lower compared to separate porosity and saturation cases.

7.5.2.3 Thickness and effective reservoir area

The medium thickness of the productive formation is 10 meters. It was approximated from the field core pressure test values for wells KN-1 and FA-2 and core geology. An additional error range of 5 meters (thickness varying hence between 5 and 15 meters) was chosen for the simulation runs. The effective reservoir area was chosen to vary linearly between 2,500 m^2 and 348,000 m^2. This value was discussed with the company and is the least known parameter which is why such a wide range was chosen. Figure 7.32a shows the GIP distribution when only the effective area is varied, whereas Figure 7.32b shows the combined effect on the GIP distribution of the porosity, saturation, and effective area and thickness variation.

Thickness and areal variation drastically reduces the GIP estimations from around 1,000 MMscf to 90,000 MMscf (Figure 7.32a). The GIP probabilities drop sharply to around 10,000 Mscf with the remaining probabilities showing a more steady drop. When combined with all previous variables, GIP estimation range varies from around 1,000 MMscf to around 80,000 MMscf with the sharp drop up to 40,000 MMscf and more constant decline afterwards (Figure 7.32b).
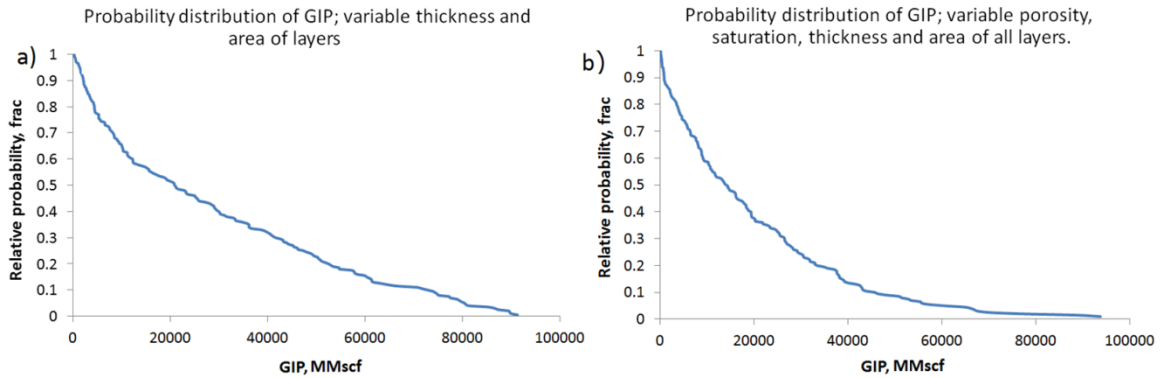
Figure 7.32 GIP estimates based on reservoir thickness and effective area only (a) and combined effect of porosity, saturation and thickness and effective area (b). It can be seen that effective area has a huge impact on the GIP estimates for this shale reservoir.

7.5.2.4 Recovery factor

Recovery factor (RF) was chosen to vary linearly between 0.15 and 0.35, which is typical for the shale plays in USA (USGS, 2011). It has to be noted that shallow depth and low pressures might considerably affect the RF of the studied shale resource play, however no other RF analogues were found. For this reason the standard RF of 0.15-0.35 was applied on the GIP value to obtain the amount of gas to be realistically recovered. After applying the RF, the probability distribution of reserves drops as shown in Figure 7.33.

The reserves are estimated to vary between around 100 MMscf and 25,000 MMscf (Figure 7.33). The probability curve gradient is relatively steep, meaning the chances for higher end reserve values are getting considerably lower. The values were classified into proved and unproved categories showed in Table 7.13. Furthermore, these values were compared to the Competent Person's study conducted by the Gripen Oil & Gas to independently obtain an estimation of the reserves. It can be seen that the estimations performed in this study compare well to the value obtained by a commercial evaluation.
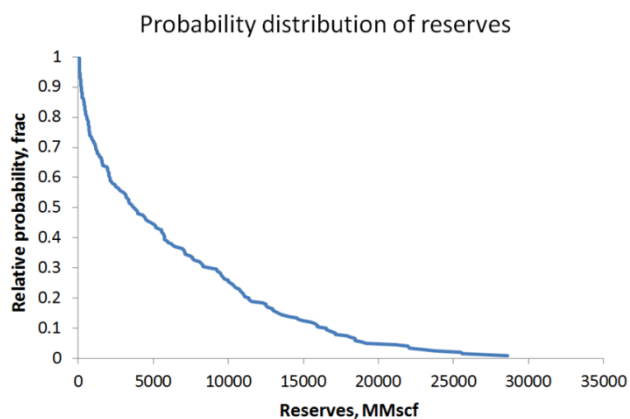
Figure 7.33. Addition of another parameter constructs probability distribution of reserves, which indicates the probability of amount of the gas that is likely to be actually extracted. Economical estimates of the shale play were based on this graph.

GIP and reserve values with their relative probabilities are summarised in Table 7.13. The provided volumes were categorised into the "proven" (>90% relative probability), "possible" (>50% relative probability) and "probable" (>10% relative probability) gas estimates, denoted as P90, P50 and P10 respectively. The company has also carried out a commercial competent person's volumetric evaluation and obtained a value of 52 bcf, shown in Table 7.13 (Oil&Gas, 2014). This value would correspond to the relative probability of 7.3% in Figure 7.32b and overall compares well with the P10 probable GIP value of 45.2 tcf derived in this study.

Table 7.13. Gas volume results. Provided are the P90, P50 and P10 cases for both GIP and Reserves. GIP value obtained by the competent person is provided for the comparison in the last column.

Parameter	P90, proven	P50, possible	P10, probable	Competent person
GIP, bcf	0.92	14.00	45.20	52
Reserves, bcf	0.19	3.70	16.20	

7.5.3 Flow simulation

Production estimation was a secondary objective of this study. It was performed using a Monte Carlo type of analysis by varying permeabilities of both matrix and fractures and fracture porosity to produce gas flow rates. The gas flow rates were then plotted versus the recorded well flow rate and are shown in Figure 7.34**.**

A sharp drop in production during the first days is clearly visible on the production graphs in Figure 7.34, however the gas production later stabilizes. Figure 7.34 presents the outcome of the history matching process. It was discussed that the initial decrease in production is most likely caused by the release of gas from the fractures and highly

permeable layers, such as tight sandstone. On the other hand, the stabilization in the flow rate is supported by the large amount of desorbed gas being released as was found in the long-term desorption experiments conducted.
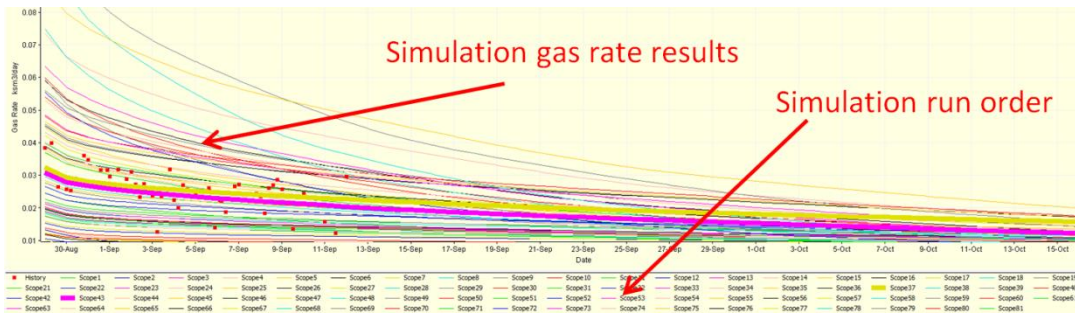
Figure 7.34 The actual well flow rate is shown by the scattered dots, whereas the best fit is represented by the bold pink line.

The presence of the desorption process means there has to be a different method of gas transport representation in the model, therefore the model would have to be significantly improved to properly reproduce the gas behaviour in the shale formation. Another issue with the current model is that a wide range of permeability values can produce a match with the field data, meaning the unique solution cannot be found (Figure 7.35). The values used to obtain a fit differ by several orders of magnitude:

- Simulation no. 244 was achieved using an average matrix permeability of 4.43E-2 nD and fracture permeability of 110,574 mD.
- Simulation no. 525 was achieved using an average matrix permeability of 9.87 nD and fracture permeability of 6,433 mD.
- Simulation no. 853 was achieved using an average matrix permeability of 6,311 nD and fracture permeability of 20 mD.
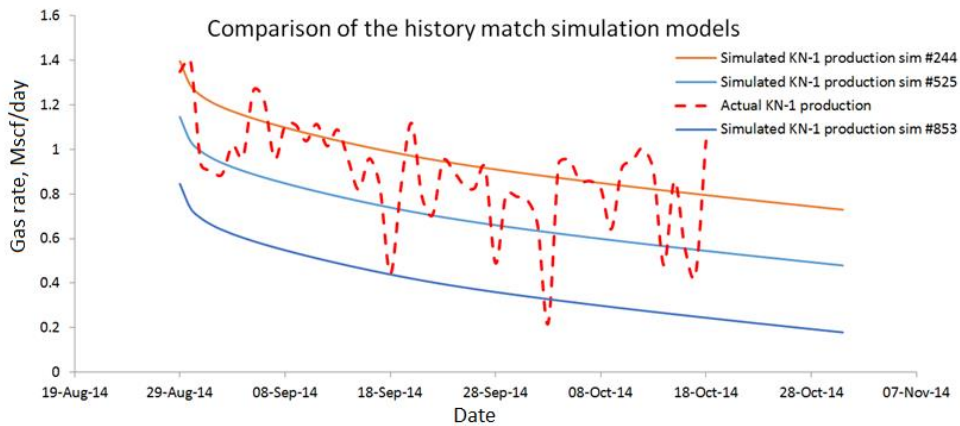
Figure 7.35. Well gas flow history matching examples. Different simulation models match the field data.

The comparison of the recorded well cumulative production versus simulated cumulative production is shown in Figure 7.36. Overall, the match of the curve is relatively good, however the varying gradient of the curve caused by the stimulation failed to be reproduced. There are several reasons why the well flow behaviour model is not representative enough:

- Permeabilities are several orders of magnitude different. Permeability determination itself using the GRI method might create huge inaccuracies (see Chapter 6).

- The simulation software lacks proper representation of adsorption system.

- Fracture network has to be better characterised, the computational resources used lacked the power for the multimillion-cell representation of the complex fracture network.
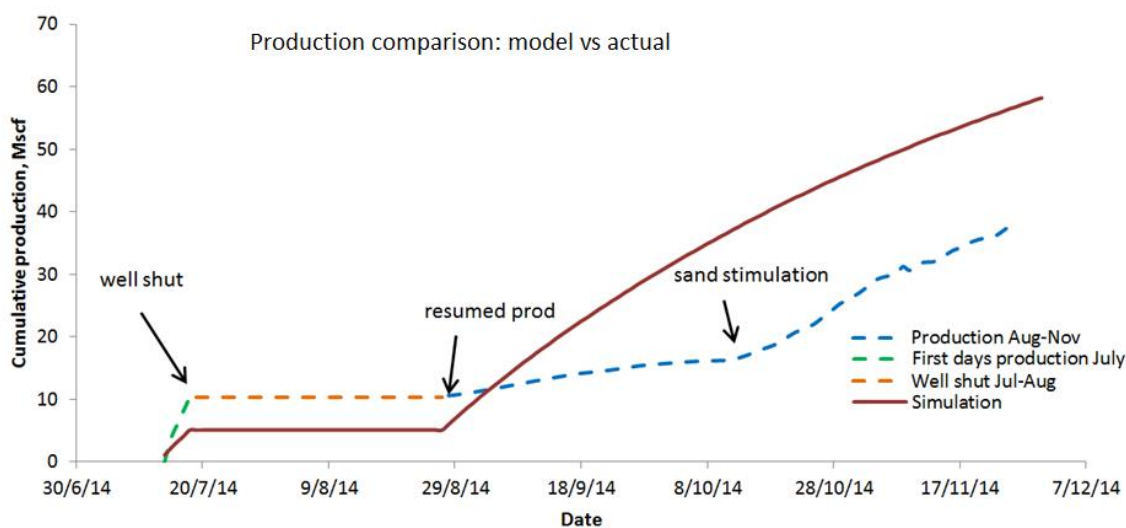
Figure 7.36. Recorded well gas flow rate. The match of production data was not achieved.

7.5.4 Drainage regions and boundaries

Diagnostic plot (or Bourdet's plot) was constructed for the well KN-1A. This plot is essentially a pressure versus time graph (usually log-log or semi-log used to determine the type of flow (spherical or radial) and the flow regime (steady state, non-steady and transient) (Dake, 1978) (Lake and Holstein, 2007). Once the equilibration region is reached, the infinite acting radial flow (IARF) can be mapped. Depending on time, the plot can be divided into three regions: early, middle and late as shown in Figure 7.37. Skin effect of the formation can be determined from the shape of the plot as shown in Figure 7.38.
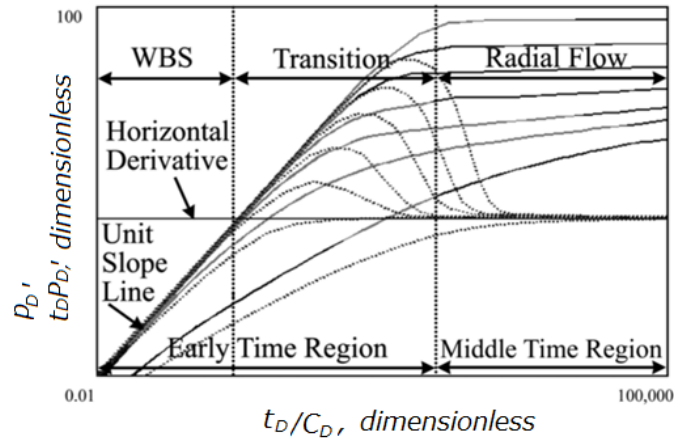
Figure 7.37. Diagnostic plot of the steady state flow reservoir. The early time curve is mostly influenced by the near wellbore effects such as wellbore storage, skin and fractures. The middle time represents the matrix flow while the reservoir is regarded as infinite acting. The late time shows the type of boundary that reservoir exhibits – sealing fault, fluid contacts or different formation (Lake and Holstein, 2007).
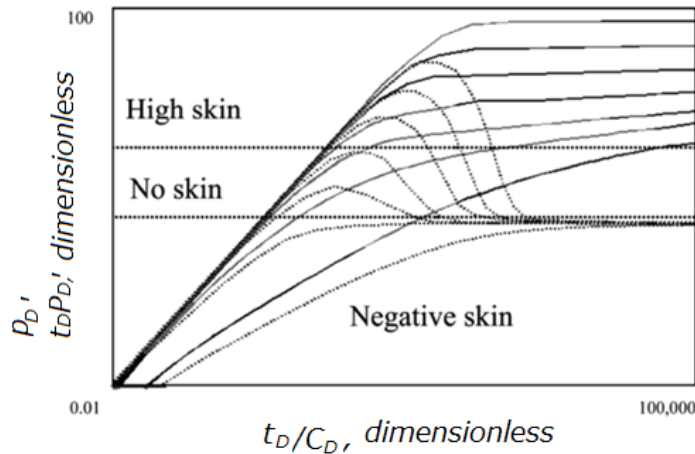
Figure 7.38. Skin effect (Lake and Holstein, 2007).

The long-term pressure build-up and flow tests of the well KN-1A are shown in Figure 7.39. Diagnostic plot can be used to identify the type and extend of the boundary by analysing the IAFR line: equilibration means stabilized matrix flow until the boundary is reached – in that case the pressure curve changes accordingly. No equilibration was achieved during the field experiment after about 10 hours of build-up (MBPU). It could be suggested that that the reservoir exhibits semi-steady state condition, possibly involving strong fracture and adsorption flows. It requires more parameters and computational resources to derive the solution and cannot be simulated using the current model.
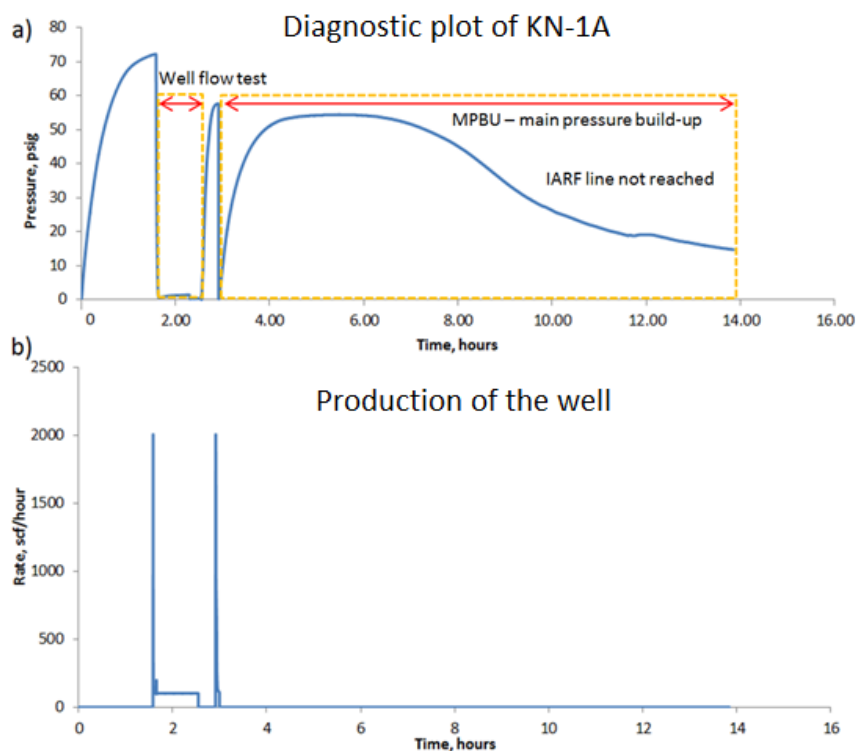
Figure 7.39 Well pressure build-up curve together with the gas flow rate measurements. Analysis of the pressure build-up reveals that the infinite acting radial flow (IARF) was not achieved.

7.6 Conclusion

The company developing the field was provided with the GIP estimates and also the theory behind the gas behaviour in the reservoir as an outcome of the Alum shale play study. The work was done by constructing a model which incorporated a large amount of both field and laboratory data. The impact of each parameter on the GIP values was evaluated using sensitivity analysis and Monte Carlo charts. The range of possible porosity types was well defined as various experimental methods were used to complement the porous volume, such as adsorption/desorption, SEM and mineralogy.

Overall, research was done over the 2 years of data collection and analysis of the given field. As a result, the development project received an approval for the next phase stage, during which the pilot production project consisting of clusters of several wells is to be undertaken in the area investigated. This will further identify the possibility for the industrial scale deliverability of gas in Östergötland county.

As an outcome of the field study, following "lessons learnt" key points could be made:

- Desorption canisters proved to be cheap and useful method for the determination of *in-situ* gas properties, pressure distribution within the well and long-term production potential of the shale.

- Application of laboratory pressure transducers in the field proved to be convenient multi-purpose tool for pressure recording – it was used for the well pressure build-up, hydraulic fracturing and desorption canisters.

- Long-term production rate measurement system feeding data live on the website through GPS proved to be an option for convenient remote monitoring of the well behaviour and flow rate data recording.

- It was found that significant methane gas concentration within the shale layers could accumulate relatively large pressures. Most importantly, the petroleum system was proven to work as gas production for a prolonged period of time was demonstrated.

- Conducted measurements showed significant gas quantities stored in the Alum shale.

- Water stimulation (hydraulic fracturing) resulted in only partial improvement of the gas flow rate.

- The production rate and behaviour of the gas could not be represented properly due to the lack of proper flow transport representation and computational power.

8   Chapter
Conclusion

An extensive study including experimental and modelling work was carried out on shale samples from various locations to characterise their porosity and permeability. A literature review provided a framework for the study and highlighted the main issues of high uncertainty among these two main parameters. The experimental techniques used in this study included industry-standard methods as well as new methods developed and modified throughout this research. The derived porosity and permeability results were cross-checked with the other laboratories in a Control-Test exercise. Finally, the results obtained were tested on a shale resource play currently being appraised to understand the gas flow behaviour and its commercial viability.

8.1   Sample characterisation

Multi-scale analysis on the samples demonstrated complexity on all analysed scales: mineralogical, SEM-scale and CT-scale. SEM analysis showed very heterogeneous shale matrix, with clays, organic matter and microfractrures being the most prominent features. Three main types of pores were identified: organic, matrix and fractures (both artificial and natural). Fractures were found to considerably influence pore volume identified within the SEM images, comprising over 70% of overall pore volume in some of the samples. This porosity will lead to an underestimation of bulk density and an overestimation of porosity at *in-situ* conditions unless a stress correction is applied.

CT images showed fairly homogeneous matrix for the given resolution of 1 mm without any noticeable fractures but with occasional inter-bedded layers observed. Nevertheless, injection of highly luminous xenon gas revealed within CT images the dominance of high conductive layers/fractures on the gas flow. Therefore such highly permeable features have to be considered when investing for the permeability results.

8.2   Density

Bulk and grain densities were measured using several different methods in this research. Each density measurement method was found to be prone to the specific bias. The crushed shale method proved to be the most precise method for grain density, producing the lowest average standard deviation of 0.02 g/cm^3 between Leeds and other laboratories. The samples have to be dried before the crushed shale measurement to

remove water blocking the pores and improve reproducibility. In contrast, fluid intrusion techniques for grain density measurement such as mercury injection capillary pressure (MICP) and water pycnometry were influenced by ineffective saturation and produced higher standard deviations between Leeds and other laboratories of 0.03 g/cm^3 and 0.08 g/cm^3 respectivelly. QXRD/TOC results can be used to calculate the grain density of the shale if the density of individual components is known; it is the only non-intrusive grain density measurement technique. It correlated well with crushed shale grain density measurements and produced standard deviation between Leeds and other laboratories of 0.03 g/cm^3. However the technique might produce errors due to uncertainties in the grain densities of the constituents of the shale. There is particular uncertainty in the densities of organic matter, and minerals with complex solid solution series (e.g. Fe carbonates and clays).

Lack of confining stress is the main issue for shale bulk density measurements. Microfractures present within the shale samples caused higher values of bulk volume, hence lower bulk density and higher porosity, when measured by Hg-immersion. Although average standard deviations were not too high (0.03 g/cm^3 between Leeds Hg-immersion and Control-Test and 0.06 g/cm^3 between Leeds GRI and Control-Test), the correlations between the methods were very poor, with some correlation coeficients between Leeds and Control-Test laboratories being below 0.1. Pressure extrapolation method was used to correct GRI-derived bulk density results to account for the lost gas due to microfractures, however it still did not provide the necessary precision.

MICP test might be a solution to artificial microfractures problem: mercury might be compressing the sample instead of intruding the shale pores thus closing the microfractures. The results can therefore be recast as sample volume change vs. pressure instead of injected volume vs pressure. If this proves correct MICP data may provide fracture-corrected bulk volumes (i.e. *in-situ* values). Although high average standard deviation was obtained for MICP bulk density results (0.21 g/cm^3) more research is needed regarding possible sample compressibility.

The Control-Test comparison indicated systematic difference in the grain density and hence porosity results produced by different laboratories. The key difference appears to be related to the method used to clean and dry the crushed shale. In particular, two laboratories simply oven dried the samples at 100-110°C for 7 days, one laboratory used Dean Stark extraction with a toluene solvent followed by oven drying for 7 days. The forth

laboratory used the retort method to remove water and oil from the samples and produced grain densities that were systematically lower by 0.03 g/cm^3. Previous studies have argued that this is due to removal of structural water from clay minerals. However, the results from this study show that this is an unlikely explanation as the difference is not related to the clay content of the samples. These results indicate that the retort method as it is currently used is an inappropriate way of cleaning shale samples.

8.3 Porosity

The crushed shale method for porosity estimation was found to produce better porosity results in terms of precision (average standard deviation 1.3%), practicality and comparability with other laboratories than core plug methods (average standard deviation 2.8%). Microfractures and gas leakages from the system might disrupt porosity measurements; however it was shown that the use of reverse pressure build-up tests allows to quality control the porosity results by verifying mass balance of gas. In fact, the most precise results were achieved using reverse pressure build-up test, with the average standard deviation of just 0.4%.

The average difference between the service companies was around 18% (average standard deviation 0.6%). The highest difference came from the laboratory using retort method to clean samples. In fact, preparation of the samples was identified to be the major factor affecting the porosity values: samples in as-received conditions contain water blocking the pores (especially micro-pores as was identified between the comparisons of dried-, non-dried- and SEM-derived porosity values), which in turn results in high scatter between the obtained results (average standard deviation for AR samples 1.9%). In contrast, porosity tests on dried particles provided much less scatter (average standard deviation 1.3%) and a better opportunity to compare different samples without the inaccuracies of unknown amount of water-blocked pores.

Finally, porosity values obtained from the measurements using gas with high adsorptive properties (methane) were higher than those obtained with non-adsorptive gas. However, when taking into consideration adsorption parameters of the samples, this mismatch may be explained and corrected. Nevertheless, it is recommended to use non-adsorptive gasses as adsorptive gasses take too long to equilibrate and correcting the porosity for gas adsorption could introduce errors as there is significant uncertainty regarding the amount that organic matter swells as gas is adsorbed.

8.4 Permeability

Permeability results obtained using the crushed shale method from both Leeds and service companies were found to vary by up to four orders of magnitude for a given sample and produced no correlations with other parameters (porosity, pressure etc.). Part of the problem was the lack of information sharing by the service companies on the experimental data, as it was noted that some inaccuracies might have been caused by chosen experimental specifications such as crushed particle size.

It was confirmed that small microfractures still remain within the crushed shale particles, resulting in fast pressure decay into the sample and thus wrong effective grain size assumptions. Moreover, possible presence of highly permeable lithology within shale matrix increases the overall effective permeability of the samples. Indeed, gas movement into shale particles with a permeability of >10 nD is so fast that it cannot be recorded. So the crushed shale method may not measure the permeability of highly permeable shale layers that would actually control flow in the subsurface. Dual models provided good history matches of the pressure transient data obtained using the crushed shale method. Nevertheless, so many problems were identified with the crushed shale method that it seems to provide little or no information relevant to the characterization of shale permeability in the subsurface.

All core plug methods provided more precise permeability results compared to crushed shale method: there were clear correlations against experimental pressure, porosity and the results between other core plug methods and service companies. It should, however, be noted that most experiments appear to show clear signs of a dual porosity-permeability system. It is likely that this is due to the presence of fractures formed during or following coring. Dual porosity-permeability model was employed in this research to overcome this issue. In contrast other laboratories used one effective permeability value, which was higher when compared to Leeds inverted values. It is therefore possible that the permeability values provided by service companies reflect damage and are not representative of subsurface values. The matrix permeability value obtained by Leeds is more likely to reflect subsurface permeabilities.

The scatter in the permeabilities obtain using the core plug based methods was also lower than obtained using the crushed method, in most cases within one order of magnitude. Among the core plug methods, the most consistent results were achieved by applying pressure series methodology – it helped to avoid non-uniqueness in the results when

simulating several possibly coupled parameters (permeability, high zone permeability, *b*-factor etc.). The correlation between *b*-factor and permeability obtained using this method was comparable to those for tight gas sandstones in the literature. Furthermore, the developed methodology is easily adaptable to industry standard software.

Finally, it is worth bearing in mind the end use of the permeability results. Regardless of the method used, there is still relatively wide uncertainty range for the shale permeability values. For this reason any economic calculations based on shale permeability values in nanoDarcy range would not be accurate. Instead, the permeability values could be used as an index to cross-compare different shale formations. There is, however, potential for the improvement for both core plug and crushed measurements. The main requirement for that is the transparency of the experimental and inversion methods.

8.5   Field results

Field testing techniques conducted by Gripen Oil & Gas and University of Leeds on the shallow shale gas play in the Swedish county of Östergötland were presented in this thesis. This unconventional gas development is one of the pioneer shale gas exploitation attempts in Europe. The company was provided with the GIP estimates of probable reseves ranging from 0.92 bcf up to 45.2 bcf and also the theory behind the gas behaviour in the reservoir as a result of this study. Consequently, the development project received an approval by the compant for the next phase stage, during which the pilot production wells will be drilled in the prospective area. Among the theoretical developments, field testing technique for laboratory purposes was developed:

- Desorption canisters proved to be cheap and useful method for the determination of *in-situ* gas properties, pressure distribution within the well and long-term production potential of the shale.

- Application of laboratory pressure transducers in the field proved to be convenient multi-purpose method of pressure recording – it was used for the well pressure build-up, hydraulic fracturing and desorption canisters.

- Long-term production rate measurement system feeding data live on the website through GPS proved to be an option for convenient remote monitoring of the well behaviour and flow rate data recording.

Results were obtained from the desorption experiment of the shale reservoir cores - large adsorption values were exhibited by the formation of interest. The resulting increase in

gas storage means that desorption dominates the GIP and gas transport mechanism, which resulted in simulation difficulties predicting the gas production rates. During the initial production around 30% of gas is produced from the adsorbed state while the rest is produced from the matrix porosity. The desorption begins to dominate the gas production at later stages in the process.

8.6 Future work and recommendations

The next step in this research would be further cooperation with Control-Test companies to expand on the analysis of the main petrophysical properties. The workflows and assumption used in their methods should be disclosed so more scientific analysis could be done. Moreover more simulations can be undertaken to determine the permeability dependence on adsorption, similarly like it was done with Klinkenberg correction. Finally further SEM analysis of large samples polished using a broad ion beam could be undertaken to establish whether organic porosity within bitumen filled microfractures could provide pathways for enhanced gas flow.

Regarding the experimental equipment, the design has to be improved to either reduce or monitor the rate of leakage to improve the accuracy of long-term experiments. Crushed GRI experimental set-up could be improved to allow for the greater pressures to be applied, whereas modified pressure decay experiment needs modifications for easier sample loading and removal, as it has the tendency to break the samples.

Further analysis on the use of methane gas could be done. Adsorption models could be improved to include Dubinin's model instead of the Langmuir model used at the moment. In addition to that large scale simulations could be improved to include various flow regimes similarly to the core scale flow simulations.

For the field work the use of desorption canisters could be further analysed – the obtained data can be used for the derivation of the permeability, porosity and gas saturation information on site. The canisters themselves could be developed with better sealing mechanism to reduce the leakage. Well pressure build-up measurements could be conducted with more autonomous pressure transducers that would not require to be constantly connected to the laptop to record the measurements. Similar system to the remote well flow monitoring could be installed so that well pressure measurements could be delivered online.

9 References

Aboujafar, S. M. (2009). The Use of High Pressure MICP Data in Reservoir Characterisation, Developing A New Model For Lybian Reservoirs. 2009 SPE/EAGE Reservoir Characterisation and Simulation Conference Abu Dhabi, UAE, SPE, 20. 10.2118/124425-MS.

Amann-Hildenbrand, A., Bertier, P., Busch, A. and Krooss, B. M. (2016). Transport and retention processes in low-permeable mudstones and shales - an experimental study. Institute of Geology and Geochemistry of Petroleum and Coal, RWTH Aachen University, Germany, 38.

Andersen, M., Duncan, B. and McLin, R. (2013). "Core Truth in Formation Evaluation." Oilfield Review 25(2), 10.

API (1998). Recommended Practices for Core Analysis.

Arri, L. E., Yee, D., Morgan, W. D. and Jeansonne, M. W. (1992). Modelling coalbed methane production with binary gas sorption. Proceedings of Society of Petroleum Engineers (SPE) Rocky Mountains Regional Meeting, Casper, Wyoming, SPE. 10.2118/24363-MS, 459-472

Aviles, I., Dardis, M. and Marya, M. (2013). "Degradable Frac Ball Hold Solution to Persistent Problem in Fracturing." Journal of Petroleum Technology, 32-33.

Bae, J. S., Bhatia, S. K. and Massarotto, P. (2009). "Pore accessibility of methane and carbon dioxide in coals." Energy & Fuels 20, 2599-2607.

Bernard, S., Brown, L., Wirth, R., Schreiber, A., Schulz, H., M. and Horsfield, B. (2013). FIB-SEM and TEM investigations of an Organic-rich Shale Maturation Series from the Lower Toarcian Posidonia Shale, Germany: Nanoscale Pore System and Fluid-rock Interactions., AAPG. 102, 53-66. doi.org/10.1306/13391705M1023583.

Bhowmik, S. (2012). Sorption properties of some Indian coals for coalbed methane recovery and carbon sequestration. Doctor of Philosophy, Bengal Engineering and Science University, 200

Blackbourn, G., A. (2012). Core and Core Logging. Dunbeath, Scotland, Whitles Publishing, 144.

Borysenko, A., Clennell, M., B., Sedev, R., Burgar, I., Ralston, J., Raven, M., Dewhurst, D. N. and Liu, K. (2009). "Experimental investigations of the wettability of clays and shales." Journal of Geophysical Research 114. 10.1029/2008JB005928.

Boulin, P. F., Angulo-Jaramillo, R., Talandier, J., Berne, P. and Daian, J. F. (2011). "Contribution of the Dusty Gas Model to Permeability/Diffusion Tests on Partially Saturated Clay Rocks." Transport in Porous Media 93, 609-634.

Brace, W. F. (1980). "Permeability of crystalline and argillaceous rocks: Internat." J. Rock Mech. Min. Scie & Geomech 17, 241-251.

Brace, W. F., Walsh, J. B. and Frangos, W. T. (1968). "Permeability of Granite Under High Pressure." Journal of Geophysical Research 73, 2225-2236.

Brace, W. F., Walsh, J. B. and Frangos, W. T. (1968). "Permeability of Granite under High Pressure " Journal of Geophysical Research 73(2225), 2225–2236.

Brighenti, G. (1989). Effect of confining pressure on gas permeability of tight sandstones. Instituto di Scienze Minerarie, Bologna, Italy, Maury & Fourmaintraux.

Britt, L., K., and Schoeffler, J. (2009). The Geomechaniscs of a Shale Play: What Makes a Shale Prospective. SPE Eastern Regional Meeting. Charleston, WVA, SPE, 9. 10.2118/125525-MS.

Brunauer, S., Emmet, P. H. and Teller, E. (1938). "Adsorption of gasses in multi-molecular layers." Journal of the American Chemical Society. 60, 309-319.

Brunton, C., H., C.,, Besterman, T., P., and Cooper, J., A. (1985). "Guidelines for the curation of geological materials." Geological Society Miscelllaneous Paper no. 17, 50.

Camp, W. K. and Wawak, B. (2013). "Enhancing SEM Grayscale Images through Pseudocolor Conversion: Examples from Eagle Ford, Haynesville and Marcellus Shales." Electron microscopy of shale hydrocarbon reservoirs: AAPG Memoir **102**, 15-26.

Carman, P., C. (1956). Flow of Gases Through Porous Media. London, Butterworth, 182.

Casse, F., J. (1974). The effect of tempterature and confining pressure on fluid flow properties of consolidated rocks. Doctor of Philosophy, Stanford University. PB-262732; SGP-TR-3, 196

Chenevert, M. E. and Sharma, A. K. (1993). Permeability and Effective Pore Pressure of Shales. University of Texas, SPE, 7. 10.2118/21918-PA.

Chesnakov, E. M., Bayuk, I. O. and Metwally, Y. (2010). Inversion of shale microstructure parameters from permeability emasurements. SEG Anual Meeting. SEG. Denver, SEG, 5. 2634.

CIA (2011) "Country Comparison: Natural Gas - Production."

Cipolla, C. L., Lolon, E. P., Mayhofer, M. J. and Warpinski, N. R. (2009). Fracture Design Considerations in Horizontal Wells Drilled in Unconventional Gas Reservoirs. Hydraulic Fracturing Technology Conference. The Woodlands, Texas, SPE, 10. 10.2118/119366-MS.

Civan, F. and Devegowda, D. (2014). Rigorous Modelling for Data Analysis towards Accurate Determination of Shale Gas-Permeability by Multiple-Repeated Pressure-Pulse Transmission Tests on Crushed Sampels. Annual Technical Conference and Exhibition. SPE. Amsterdam, The Netherlands, SPE, 28. doi:10.2118/170659-MS.

Civan, F., Devegowda, D. and Sigal, R. (2013). Improved Data Analysis and Interpretation Method for Laboratory Determination of Crushed-Sample Shale Gas Permeability. Unconventional Resources Technology Conference. Denver, Colorado, SPE, 11.

Civan, F., Devegowda, R. and Sigal, R. (2013). Improved Data Analysis and Interpretation Method for Laboratory Determination of Crushed-Sample Shale Gas Permeability. Unconventional Resources Technology Conference. Denver, USA, SPE, 11. SPE 168840.

Civan, F., Rai, C. S. and Sondergeld, C. H. (2011). "Shale-Gas Permeability and Diffusivity Inferred by Improved Formulation of Relevant Retention and Transport Mechanisms." Transport in Porous Media **86**(3), 925-944.

Clarkson, C. R. and Bustin, R. M. (2000). "Binary gas adsorption/desorption isotherms: effect of moisture and coal composition upon carbon dioxide selectivity over methane." International Journal of Coal Geology **42**, 241-271.

Clarkson, C. R., Bustin, R. M. and Levy, J. F. (1997). "Application of the mono/multilayer and adsorption potential theories to coal methane adsorption isotherms at elevated temperature and pressures." Carbon **35**(12), 1689-1705.

Clavier, C., Heim, A. and Scala, C. (1976). Effect of pyrite on resistivity and other logging measurements. SPWLA 17th Annual Logging Symposium. SPWLA, SPWLA, 34.

Clennell, M., B. (1997). "Tortuosity: a guide through the maze." Geological Society London Special Publications **122**, 299-344.

Comisky, J. T., Newsham, K. E., Rushig, J. A. and Blasingame, T. A. (2007). A Comprehensive Study of Capillary-Pressure-Based Empirical Models for Estimating Absolute Permeability in Tight Gas Sands. SPE Annual Technical Conference. Anaheim, California, SPE, 18. SPE 110050.

Coyner, K., Katsube, T. J., Best, M. E. and Williamsone, M. (1993). Gas and water permeability of tight shales from the venture gas field, offshore Nova Scotia. Current research, Part D. G. S. o. Canada, 129-136.

Crook, T. (2012). Implementation and Validation of a Model for Gas flow in Low Porosity Shale. Swansea, Three Cliffs Geomechanical Analysis, 34.

Cui, X., Bustin, A. M. M. and Bustin, R. M. (2009). "Measurements of gas permeability and diffusivity of tight reservoir rocks: different approaches and their applications." Geofluids **9**, 208-223.

Cuthiell, D., Sedgwick, G., Kissel, G. and Woolley, J. (1993). "Steam corefloods with concurrent X-ray CT imaging." Journal of Canadian Petroleum Technoogy **32**(3).

Dake, L. P. (1978). Fundamentals of Reservoir Engineering, 462.

Dastidar, R., Chandra, R. and Sondergeld, C. H. (2004). Integrating NMR With Other Petrophysical Information to Characterize a Turbidite. SPE Annual Technical Conference and Exhibition. Houston, Texas, Society of Petroleum Engineers, 15. doi:10.2118/89948-MS.

Davies, K. D., Bryant, W. R., Vessel, R. K. and Burkett, P. J. (1991). Porosity, permeabilities and microfabrics of Devonian shales. . Microstructure of fine-grained sediments. New York, Springer, 109-119.

Dewhurst, D. N., Aplin, A. C., Sarda, J. P. and Yang, Y. (1998). "Compaction-driven evolution of porosity and permeability in natural mudstone: An experimental study." Journal of Geophysical Research **103**, 651-661.

Diffen. (2015). "CT scan vs MRI." Retrieved 17-08-15, 2015, from http://www.diffen.com/difference/CT_Scan_vs_MRI.

Discovery-Group (2016). Discovery-Group.

Dokhani, V., Yu, M. and Miska, S. Z. (2013). The Effect of Bedding Plane Orientation on Pore Pressure in Shale Formations; Laboratory Test and Mathematical Modeling. 47th US Rock Mechanic/Geomechanic Symposium. San Fransisco, USA, ARMA, 9. ARMA 13-121.

Drake, S. (2007). Unconventional Gas Plays. Southwest Land Institute, AAPL.

Driskill, B., Walls, J. D., DeVito, J. and Sinclair, S. W. (2013). Applications of SEM Imaging to Reservoir Characterisation in the Eagle Ford Shale. South Texas, AAPG. **102**, 115-136.

Dubinin, M. M. (1975). Physical adsorption of gases and vapors in micropores. New York, Academic press. **9**, 1-70.

Dubinin, M. M. and Astakhov, V. A. (1971). Advances in Chemistry Series: No. 102, American Chemical Society, 69-85.

Dzyaloshinskii, I. E., Lifshitz, E. M. and Pitaevskii, L. P. (1961). "General Theory of Van der Waals' Forces." Soviet Physics Uspekhi **4** (2), 153. 10.1070/PU1961v004n02ABEH003330.

East, B. (2011). Porosity - Core Plug Measurements Perspective. Conference presentation FESM

EIA (2012). "What is U.S. electricity generation by energy source?".

EIA (2015). Assumptions to the Annual Energy Outlook 2015, U.S. Energy Information Administration.

EIA (2016). Annual Energy Outlook 2016 with projections to 2040, EIA. DOE/EIA-0383 (2016).

Eurostat (2014). "Production of primary energy, EU-28, 2014."

Fagerlund, G. (1973). "Determination of specific surface by the BET method." Materiaux et Constructions **6**(33), 239-245.

Fick, A. (1995). "On liquid diffusion." Juornal of Membrane Science(100), 33-38.

Fisher, Q. J., Grattoni, C., Rybalcenko, K., Lorinczi, P. and Leeftink, T. N. (2016). Laboratory Measurements of Porosity and Permeability of Shale. Fith EAGE Shale Workshop. Catania, Sicily, EAGE, 5. doi: 10.2118/167750-MS.

Florence, F. A., Rushing, J., Newsham, K. E. and Blasingame, T. A. (2007). Improved Permeability Prediction Relations for Low Permeability Sands. Rocky Mountains Oil & Gas Technology Symposium. Denver, Colorado USA, Society of Petroleum Engineers, 18. 10.2118/107954-MS.

Fogden, A., Latham, S., McKay, T., Marathe, R., Turner, M., Kingston, A. and Senden, T. (2014). Micro-CT Analysis of Pores and Organics in Unconventionals Using Novel Contrast Strategies. Unconventional Resources Technology Conference, 10. 10.15530/URTEC-2014-1922195.

Freeman, C. M., Moridis, G. J. and Blasingame, T. A. (2011). "A Numerical Study of Microscale Flow Behaviour in Tight Gas and Shale Gas Reservoir Systems." Transport in Porous Media **90**, 253-268. doi:10.2118/141125-STU.

Ghanizadeh, A., Gasparik, M., Amann-Hildenbrand, A. and Gensterblum, Y. (2013). "Experimental study of fluid transport processes in the matrix system of the European organic-rich shales: I.Scandinavian Alum Shale." Marine and Petroleum Geology **51**, 79-99.

Gilicz, A. (1991). Application of the Pulse Decay Technique. 66th Anual Technical Conference and Exhibition of the Society of Petroleum Engineers. H. H. Institute. Dallas, Texas, SPE, 13. doi:10.2118/22688-MS.

Golin, Y., L.,, Karyarin, V., E., and Pospelov, B., S. (1992). "Pore tortuosity estimates in porous media." Soviet Electrochemistry **28**, 87-91.

Halliburton. (2015). "Stimulation Planning, Optimization and Placement." Retrieved 5 November, 2015, from http://www.halliburton.com/en-US/ps/solutions/unconventional-resources/tight-gas-complex-gas/challenges-solutions/high-temperature-zonal-isolation-during-horizontal-well-stimulation.page?node-id=hgjyd46u.

Handwerger, D. A., Suarez-Rivera, R., Vaughn, K. I. and Keller, J. F. (2011). Improved Petrophysical Core Measurements on Tight Shale Reservoirs Using Retort and Crushed Samples. Annual Technical Conference and Exhibition. Denver, USA, SPE, 21. doi:10.2118/147456-MS.

Harikesavanallur, A., Deimbacher, F., Crick, M., Zhang, X. and Forster, P. (2010). Volumetric Fracture Modelling Approach (VFMA)L Incorporating Microseismic Data in the Simulation of Shale Gas Reservoirs. SPE Annual Technical Conference and Exhibition SPE. Florence, Italy, SPE. **1**, 9. 978-1-61738-964-1.

Haskett, S. E., Nahara, G. M. and Holditch, S. A. (1986). A Method for the Simultaneous Determination of Permeability and Porosity in Low-Permeability and Porosity in Low-Permeability Cores. SPE Annual Technical Conference and Exhibition. New Orleans, SPE, 8. SPE 15379.

Healthcare, G. E. (2015). "Revolution HD ct scanner." Retrieved 17-08-15, 2015, from http://www3.gehealthcare.com/en/products/categories/computed_tomography/revolution_hd#tabs/tab061CFB42D74442878CE9C6A241423460.

Heller, R., Vermylen, J. and Zoback, M. (2014). Experimental investigation of matrix permeabiltiy of gas shales. AAPG Bulletin. AAPG, AAPG. **98**, 975-995. 10.1306/092313130253.

Huet, C. C. (2005). Semi-Analytical Estimates of Permeability Obtained from Capillary Pressure. Master of Science, Texas A&M University, 120

Huet, C. C., Rushig, J. A. and Blasingame, T. A. (2005). A Modified Purcell/Burdine Model for Estimating Absolute Permeabilityfrom Mercury Injection Capillary Pressure Data. International Technology Conference. Doha, Qatar, IPTC.

Javadpour, F. (2009). "Nanopores and Apparent Permeability of Gas Flow in Mudrocks (Shales and Siltsone)." Journal of Canadian Petroleum Technoogy **48**(8), 6. 10.2118/09-08-16-DA.

Jianchao, L., Zhang, L. H. and Chen, Y. (2015). Adsorption Behaviour Study of Shale Gas: Models and New Combination Approach. SPE Asia Pasific Unconventional Resources Conference and Exhibition. Brisbane, Australia, SPE, 18. 10.2118/176880-MS.

Joel, D. W. (1982). "Tight Gas Sands - Permeability, Pore Structure and Clay." Journal of Petroleum Technology 11, 2708-2714.

Jones, J., R. and Britt, L., K. (2009). Design and Appraisal of Hydraulic Fractures. Richardson, Society of Petroleum Engineers, 150.

Jones, S. C. (1997). A Technique for Faster Pulse-Decay Permeability Measurements in Tigh Rocks. SPE Anual Technical Conference and Exhibition. New Orleans, USA, SPE, 7. 10.2118/28450-PA.

Kalantari-Dahaghi, A. and Mohaghegh, S., D. (2011). Numerical Simulation and Mulitple Realizations for Sensitivity Study of Shale Gas Reservoir. SPE Production and Operations Symposium SPE. Oklahoma, USA, SPE, 11. 10.2118/141058-MS.

Kamath, J., Boyer, R. E. and Nakagawa, F. M. (1992). "Characterization of Core-Scale Heterogeneities Using Laboratory Pressure Transients." SPE Formation Evaluation(9), 219-227. 10.2118/20575-PA.

Kang, S. M., Fathi, E., Ambrose, R. J., Akkutlu, I. Y. and Sigal, R. F. (2010). Carbon Dioxide Storage Capacity of Organic-Rich Shales. Annual Technical Conference and Exhibition. Florence, Italy, SPE. 7, 9. 10.2118/20575-PA.

Karastathis, A. (2007). Petrophysical measurements on Tight Gas Shale. MS, University of Oklahoma, 50

Katsube, T. J. (2000). Shale permeability and pore-structure evolution characteristics. Current Research 2000-E-15. G. s. o. Canada. 9, 19. 211622.

Kaye, G. W. C. and Laby, T. H. (1986). Tables of Physical and Chemical Constants. New York, Longman.

King, E., George (2010). Thirty Years of Gas Shale Fracturing: What Have We Learned? SPE Anual Technical Conference and Exhibition. Italy, SPE, 50. doi:10.2118/133456-MS.

Klinkenberg, L. J. (1941). "The Permeability of Porous Media to Liquids and Gases." Production Practice, 200-213.

Kuila, U. (2013). Measurement and Interpretation of Porosity in and Pore-Size Distributionin MudRocks: The Hole Story of Shales. PhD, Colorado School of Mines, 290

Kulander, B. R., L., D. S. and Ward, B. J. J. (1990). Fractured Core Analysis: Interpretation, Logging, and Use of Natural and Induced Fractures in Core. Oklahoma, USA, AAPG, 88.

Kumar, S., Prasad, M. and Pini, R. (2015). Selective Adsorptives to Study Pore Structure and Wetting Behaviour of Self-resourcing Shales. 56th Annual Logging Symposium SPWLA. Long Beach, California, USA, SPWLA, 8.

Lake, L., W., and Holstein, E., D. (2007). Petroleum Engineering Handbook. Texas, Society of Petroleum Engineers. 7, 170.

Lancaster, D. E., Holditch, S. A. and Hill, D. G. (1993). A Multi-laboratory comparison of isotherm measurements on anthrim shale samples. SCA Conference. Otsego County, SCA, 1. 9303.

Lane, H. S., Lancaster, D. E., Holditch, S. A. and Watson, A. T. (1990). Estimating Gas Desorption Parameters From Devonian Shale Well Test Data. SPE Eastern Regional Meeting. Columbus, Ohio, SPE, 12. doi:10.2118/21272-MS.

Langmuir, I. (1918). "The Adsorption of Gases on Plane Surface of Glass, Mica and Platinum." The Research Laboratory of The Geneal Electric Company, 1361-1402. doi:10.1021/ja02242a004.

Langmuir, I. (1918). "The adsorption of gases on plane surfaces of glass, mica and platinum. ." The Journal of American Chemical Society **40:9**, 1361-1403.

Lemmens, H. and Richards, D. (2013). "Multiscale Imaging of Shale Sample in the Scanning Electron Microscope." Electron microscopy of shale hydrocarbon reservoirs: AAPG Memoir **102**, 27-35.

Lewis, R., Singer, P., Jiang, T., Rylander, E., Sinclair, S. and Mclin, R. H. (2013). NMR T2 Distributions in the Eagle Ford Shale: Reflections on Pore Size. SPE Unconventional Resources Conference. The Woodlands, USA, SPE, 15. SPE-164554-MS.

Li, S., Dong, M., Dai, L., Li, Z. and Pan, X. (2004). Determination of Gas Permeability of Tight Reservoir Cores without Using Klinkenberg Correlation. Asia Pacific Oil and Gas Conference and Exhibition. Perth, Australia, SPE, 11. doi:10.2118/88472-MS.

London, M., Cameron, S., Donald, J., Wassmuth, F. and Innovates, A. (2014). Waterflooding Experiments with X-ray CT Imaging. SPE Heavy Oil Conference Alberta, Canada, SPE, 15. doi:10.2118/170147-MS.

Lorenz, J. C. (1999). "Stress-Sensitive Reservoirs." JPT **1**, 61-63.

Lorinczi, P., Burns, A. D., Lesnic, D., Fisher, Q. J., Crook, A. J., Grattoni, C. and Rybalcenko, K. (2014). Direct and Inverse Methods for Determining Gas Flow Properties of Shale European Unconventional Conference and Ehxibition. Vienna, Austria, SPE, 26. 10.2118/167750-MS.

Loucks, R. G., Reed, R. M., Ruppek, S. C. and Hammes, U. (2010). "Primary classification of matrix pores in mudrocks: Gulf Coast Association of Geological Societies Transactions." **60**, 7.

Lu, X. C., Li, F. C. and Watson, A. T. (1995). "Adsorption Studies of Natural Gas Storage in Devonian Shales." SPE Formation Evaluation(June), 5. 10.2118/26632-PA.

Luffel, D. L., Hopkins, C. W., Holditch, S. A. and Shettler, P. D. (1993). "Matrix Permeability Measurement of Gas Productive Shales." SPE 26633, 261-270.

Mason, E. A. and Malinauskas, A. P. (1983). Gas Transport in Porous Media: The Dusty-Gas Model. Amsterdam, The Netherlands, Elsevier Science Publishers B.V., 194.

Mensor. (2015). "Precision pressure sensor." Retrieved 17 July, 2015, from http://www.mensor.com/cpt6100_cpt6180_en_co.WIKA?ProductGroup=62005.

Moghadam, A., A. and Chalaturnyk, R. (2015). Laboratory Investigation of Shale Permeability. SPE/CSUR Unconventional Resources Conference Calgary, Alberta, Canada, SPE, 27. 10.2118/175919-MS.

Nielsen, A., T. and Schovsbo, N., H. (2007). "Cambrian to basal Ordovician lithostragitaphy in southern Scandinavia." Bulletin of the Geological Society of Denmark **53**, 47-92.

NIH (2016). ImageJ (IJ 1.45m), U.S. National Institute of Health. **2016**.

Nordeng, S. H. (2012). "Basic Geochemical Evaluation of Unconventional Resource Plays." Geo News(12), 5.

Nunez-Betelu, L. and Baceta, J. L. (1994). "Basics and Applications of Rock-Eval/TOC Pyrolysis: an example from the uppermost Paleocene/lowermost Eocene In the Basque Basin, Western Pyrenees." San Sebastian **46**, 46-62.

Oil&Gas, G. (2014). Competent person's report, personal communication.

Omega. (2015). "USB Output Pressure Transducer " Retrieved 17 July, 2015, from http://www.omega.co.uk/pressure/.

Osborne, M. J. and Swarbrick, R. E. (1997). Mechanisms for generating overpressure in sedimentary basins: A revaluation. Bulletin 81, 1023-1041

Parkash, S. and Chakrabartty, S. K. (1984). "Microporosity in Alberta Plains coals." International Journal of Coal Geology **6**(1), 55-70.

Peng, S. and Loucks, B. (2016). "Permeability measurements in mudrocks using gas-expansion methods in plug and crushed-rock samples." Marine and Petroleum Geology **73**, 299-310.

Perry, R. H. (2007). Perry's Chemical Engineers' Handbook. Kansas, McGraw-Hill.

Polayni, M. (1932). "Section III - Theories of the adsorption of gases. A general survey and some additional remarks. Introductory paper to section III." Transactions of the Faraday Society **28**, 316-333.

Prince, C. M., Steele, D. D. and Devier, C. A. (2010). Permeability Estimation in Tight Gas Sands and Shales using NMR - A New Interpretive Methodology. AAPG International Conference and Exhibition. Rio de Janeiro, Brazil, 9. 40522.

Profice, S., Lasseux, D., Jannot, Y., Jebara, N. and Hamon, G. (2011). Permeability. Porosity and Klinkenberg Coefficient Determination on Crushed Porous Media. International Symposium of the Society of Core Analysts. Austin, Texas, SPE, 9. SPWLA-2012-v53n6a5.

Purcell, W. R. (1947). Capillary Pressures - their Measurement using Mercury and the Calculation of Permeability Thereform. Branch Fall Meeting. Dallas, Texas., Branch, 10. 10.2118/949039-G.

Ramirez, T. R., Klein, J. D., Bonnie, J. M. and Howard, J. J. (2011). Comparative Study of Formation Evaluation Methods for Unconventional Shale-Gas Reservoirs: Application to the Haynesville Shale (Texas). SPE North American Unconventional Gas Conference and Exhibition Texas, USA, SPE, 31. 10.2118/144062-MS.

Ramos, G. G. and Rathmell, J. J. (1989). Effects of Mechanical Anisotropy on Core Strain Measurements for In-Situ Stress Determination. 64th Anual Technical Conference and Exhibition. San Antonio, USA, SPE, 13. 10.2118/19593-MS.

Rather, J. B. (1917). "An accurate loss on ignition method for determination of organic matter in soils." Arkansas Agric.(140), 439-442. 10.1021/ie50102a016.

Rine, J. M., Smart, E., Dorsey, W., Hooghan, K. and Dixon, M. (2013). "Comparison of Porosity Distribution within Selected North American Shale Units by SEM Examination of Argon-ion-milled Samples." Electron microscopy of shale hydrocarbon rexervoirs: AAPG memoir **102**, 137-152.

Rodriguez, R., Crandall, D., Song, X., Verba, C. and Soeder, D. (2014). Imaging Techniques for Analysing Shale Pores and Minerals. National Energy Technology Laboratory: Morgantown, U.S. Department of Energy, 40.

Rune, M. H. and Cor, J. K. (1992). Laboratory simulation of core damage induced by stress release. Roch Mechanics. T. Wawersik. Rotterdam, Balkema, 10.

Rushig, J. A., Newsham, K. E., Lasswell, P. M., Cox, J. C. and Blasingame, T. A. (2004). Klinkenberg-Corrected Permeabiltiy Measurements in Tight Gas Sands: Steady-State Versus Unsteady-State Techniques. Annual Technical Conference and Exhibition. Houston, USA, SPE, 18. 10.2118/89867-MS.

Sakhaee-Pour, A. and Bryant, S. L. (2012). Gas Permeabiltiy of Shale. Annual Technical Conference and Exhibition. Denver, USA, SPE, 9.

Santarelli, F. J. and Dusseault, M. B. (1991). Core quality control in petroleum engineering. Rock Mechanics as a Multidisciplinary Science Roegiers, 10.

Saraji, S. and Piri, M. (2014). High-resolution three-dimensional characterisation of pore networks in shale reservoir rocks. Unconventional Resources Technology Conference 2879. 1870621.

Schettler, J. P. D., Parmely, C. R. and Juniata, C. (1991). Contributions to Total Storage Capacity in Devonian Shales. SPE Eastern Regional Meeting. Lexington, Kentucky, Society of Petroleum Engineers 12. 10.2118/23422-MS.

Schieber, J. (2013). "SEM Observations on Ion-milled Samples of Devonian Black Shales from Indiana and New York: The Petrographic Context of Multiple Pore Types."

Electron microscopy of shale hydrocarbon reservoirs: AAPG memoirs **102**, 153-171.

Schlumberger (2011). "Eclipse Reservoir Simulation Software Technical Description."

Segawa, H., Susumu, W., Tamura, A., Yoshimasu, N., Nakamura, O. and Ohta, M. (1983). "Computed Tomographic Measurement of Local Cerebral lood Flow by Xenon Enhancement." Stroke **14**(3), 356-362.

Sinha, S., Braun, E. M., Determan, M. D., Passey, S. A., Leonardi, J. A., Wood III, A. C., Zirkle, T. and Kudva, R. A. (2013). Steady-State Permeability Measurements on Intact Shale Samples at Reservoir Conditions - Effect of Stress, Temperature, Pressure, and Type of Gas. Middle East Oil and Gas Show and Conference Manama, Bahrain, SPE, 15. 10.2118/164263-MS.

Sondergeld, C. H., Ambrose, J., Rai, C. S. and Moncrieff, J. (2010). Micro-Structural Studies of Gas Shales. SPE Unconventional Gas Conference Pittsburgh, SPE, 17. doi:10.2118/131771-MS.

Stevens, P. (2012). "The 'Shale Gas Revolution': Development and Changes." Energy, Environment and Resources(04), 12.

Sutera, S. P. and Skalak, R. (1993). "The history of Poiseuille's law." Annual Review of Fluid Mechanics **25**, 1-19. 10.1146/annurev.fl.25.010193.000245.

Swanson, B. F. (1981). "A Simple Correlation between Permeability and Mercury Capillary Pressures." JPT **Dec**, 2488-2504.

Tinni, A., Fathi, E., Agarwal, R. and Sondergeld, C. H. (2012). Shale Permeability Measurements on Plugs and Crushed Samples. SPE Canadian Uncinventional Resources Conference. Calgary, Alberta, SPE, 14. 10.2118/162235-MS.

USGS (2011). U.S. Geological Survey Information Relevant to the U.S. Gegological Survey Assesment of the Middle Devonian Marcellus Shale of the Appalachian Basin Province. U.S. Department of the Interior,

U.S. Geological Survey.

Verba, C., Crandall, D. and Moore, J. (2016). Multiscale Shale Pore Characterisation. Unconventional Resources Technology Conference San Antonio, SPE, AAPG, SEG, 11. URTeC: 2448192.

Virnovsky, G. A., Skjaeveland, S. M., Surdal, J. and Ingsoy, P. (1995). Steady-State Relative Permeability Measurements Corrected for Capillary Effects. Annual Technical Conference & Exhibition Dallas, USA, SPE, 11. 10.2118/30541-MS.

Walls, J. D., Nur, A. M. and Bourbie, T. (1982). "Effects of Pressure and Partial Water Saturation on Gas Permeability in Tight Sands: Experimental Results." JPT **April**, 930-936. 10.2118/9378-PA.

Warpinski, N. R., Mayhofer, M. J., Vincent, M. C., Cipolla, C. L. and Lolon, E. P. (2008). Stimulating Unconventional Reservoirs: Maximising Network Growth While Optimizing Fracture Conductivity. Unvonventional Reservoirs Conference. Keystone, Colorado, SPE, 19. 10.2118/114173-MS.

Washburn, E., W. (1921). "The Dynamics of Capillary Flow " Physical Review **17**(3), 273.

Washburn, E., W. (1921). "The Dynamics of Capillary Flow." Physical Review **17**, 273-283.

Webb, S. W. and Pruess, K. (2002). "The Use of Fick's Law for Modeling Trace Gas Diffusion in Porous Media." Transport in Porous Media **51**, 327-341.

Wells, J. D. and Amaefule, J. O. (1985). Capillary Pressureand Permeability Relationship in Tight Gas Sands. Low Permeabiltiy Gas Reservoir. Denver, USA, SPE, 10. 10.2118/13879-MS.

Witkowsky, J., Galford, J., Quirein, J. and Truax, J. (2012). Predicting Pyrite and Total Organic Carbon from Well Logs for Enhancing Shale Reservoir Interpretation. SPE Eastern Regional Meeting SPE. Lexington, Kentucky, USA, SPE, 14. 10.2118/161097-MS.

Yang, Y. and Aplin, A. C. (2007). "Permeability and petrophysical properties of 30 natural mudstones." Journal of Geophysical Research **112**, 1-14.

Yortsos, Y. C. and Chang, J. (1990). "Capillary Effects in Steady-State flow in Heterogeneous Cores." Transport in Porous Media **5**, 399-420.

Zhang, T., Ellis, G. S., Stephen, C., Milliken, K., Lewan, M. and Sun, X. (2013). Effect of Organic Matter Properties, Clay Mineral Type and Thermal Maturity on Gas Adsorption in Organi-Rich Shale Systems. Unconventional Resources Technology Conference. SPE. Denver, Colorado, USA, SPE, 6. 10.1190/urtec2013-205.

Zhengwen, Z., Grigg, R. and Ganda, S. (2003). Experimental Study of Overburden and Stress Influence on Non-Darcy Gas Flow in Dakota Sandstone. SPE Annual Technical Conference and Exhibition. Denver, Colorado, USA, SPE, 10. 10.2118/84069-MS.

Appendix A

Table A.1 General description and material resources of the shale samples in this research.

Sample name	Well	Location	Formation	Geological Period	SCAL	Crushed GRI	Full core
Karoo	Outcrop	Karoo, South Africa	Whitehill	Permian	Yes	Yes	Yes
E-1	E	Östergötland, Sweden			No	No	Yes
E-2	E	Östergötland, Sweden			No	No	Yes
E-3	E	Östergötland, Sweden			No	No	Yes
E-6	E	Östergötland, Sweden			No	No	Yes
E-7	E	Östergötland, Sweden			No	No	Yes
E-8	E	Östergötland, Sweden			No	No	Yes
E-9	E	Östergötland, Sweden			No	No	Yes
E-10	E	Östergötland, Sweden			No	No	Yes
E-16	E	Östergötland, Sweden			No	No	Yes
F-1	F	Östergötland, Sweden			No	No	Yes
F-2	F	Östergötland, Sweden			No	No	Yes
F-3	F	Östergötland, Sweden			No	No	Yes
F-6	F	Östergötland, Sweden	Alum Shale	Cambro-Ordovician	No	No	Yes
D-1	D	Östergötland, Sweden			No	No	Yes
D-2	D	Östergötland, Sweden			No	No	Yes
D-3	D	Östergötland, Sweden			No	No	Yes
D-4	D	Östergötland, Sweden			No	No	Yes
D-6	D	Östergötland, Sweden			No	No	Yes
D-7	D	Östergötland, Sweden			No	No	Yes
Gripen-7	E	Östergötland, Sweden			Yes	Yes	Yes
Gripen-5	E	Östergötland, Sweden			No	No	Yes
Gripen-1	E	Östergötland, Sweden			No	No	Yes
N-1	N	Östergötland, Sweden			No	Yes	No
N-2	N	Östergötland, Sweden			No	Yes	No
N-3	N	Östergötland, Sweden			No	Yes	No
N-4	N	Östergötland, Sweden			No	Yes	No
N-5	N	Östergötland, Sweden			No	Yes	No
N-6	N	Östergötland, Sweden			No	Yes	No
N-7	N	Östergötland, Sweden			No	Yes	No
NG-1	NG	Östergötland, Sweden			No	Yes	No
NG-2	NG	Östergötland, Sweden			No	Yes	No
NG-3	NG	Östergötland, Sweden			No	Yes	No
NG-4	NG	Östergötland, Sweden			No	Yes	No

NG-5	NG	Östergötland, Sweden			No	Yes	No
NG-6	NG	Östergötland, Sweden			No	Yes	No
NG-7	NG	Östergötland, Sweden			No	Yes	No
NG-8	NG	Östergötland, Sweden			No	Yes	No
NG-9	NG	Östergötland, Sweden			No	Yes	No
NG-10	NG	Östergötland, Sweden			No	Yes	No
NG-11	NG	Östergötland, Sweden			No	Yes	No
NG-12	NG	Östergötland, Sweden			No	Yes	No
EBN1	EBN1	Netherlands	N/A	Carboniferous	Yes	Yes	Yes
EBN3	EBN1	Netherlands	N/A	Carboniferous	Yes	Yes	Yes
EBN4	EBN1	Netherlands	N/A	Carboniferous	Yes	Yes	Yes
EBN5	EBN1	Netherlands	Geverik	Carboniferous	Yes	No	Yes
EBN7	EBN1	Netherlands	N/A	Carboniferous	Yes	Yes	Yes
EBN9	EBN1	Netherlands	Geverik	Carboniferous	Yes	No	Yes
EBN13	EBN4	Netherlands	N/A	Jurassic	Yes	Yes	Yes
EBN14	EBN4	Netherlands	N/A	Jurassic	Yes	Yes	Yes
EBN16		Netherlands	N/A	N/A	Yes	Yes	Yes
EBN18	EBN5	Netherlands	N/A	Jurassic	Yes	Yes	Yes
EBN19	EBN5	Netherlands	N/A	Jurassic	Yes	Yes	Yes
EBN20	**EBN6**	**Netherlands**	**Posidonia**	**Jurassic**	**Yes**	**Yes**	**Yes**
CASP	Outcrop	UK	N/A	Carboniferous	Yes	Yes	Yes
ABE	Outcrop	UK	N/A	Carboniferous	Yes	Yes	Yes
EBN21	EBN7	Netherlands	N/A	Jurassic	Yes	Yes	Yes
EBN22	EBN4	Netherlands	N/A	Jurassic	Yes	Yes	Yes
EBN23	EBN4	Netherlands	N/A	Jurassic	Yes	Yes	Yes
EBN24	EBN4	Netherlands	N/A	Jurassic	Yes	Yes	Yes
EBN25	EBN8	Netherlands	N/A	Jurassic	Yes	Yes	Yes
EBN26	EBN8	Netherlands	N/A	Jurassic	Yes	Yes	Yes
EBN27	EBN9	Netherlands	N/A	Jurassic	Yes	Yes	Yes
EBN28	EBN10	Netherlands	N/A	Jurassic	Yes	Yes	Yes
EBN29	EBN10	Netherlands	N/A	Jurassic	Yes	Yes	Yes
EBN30	EBN10	Netherlands	N/A	Jurassic	Yes	Yes	Yes
EBN31	EBN11	Netherlands	N/A	Jurassic	Yes	Yes	Yes
EBN32	EBN11	Netherlands	N/A	Jurassic	Yes	Yes	Yes
EBN33	EBN11	Netherlands	Aalburg	Jurassic	Yes	Yes	Yes
EBN34	EBN11	Netherlands	N/A	Jurassic	Yes	Yes	Yes
EBN35	EBN11	Netherlands	N/A	Jurassic	Yes	Yes	Yes
EBN36	EBN12	Netherlands	N/A	Jurassic	Yes	Yes	Yes
CHE1	CHE1	Romania	N/A	Carboniferous	Yes	Yes	Yes

CHE2	CHE2	USA	N/A	Carboniferous	Yes	Yes	Yes
CHE3	CHE3	USA	N/A	Carboniferous	Yes	Yes	Yes
BC1	NEX1	British Columbia, Canada	N/A	Devonian	Yes	Yes	Yes
BC2	NEX1	British Columbia, Canada	N/A	Devonian	Yes	Yes	Yes
BC3	NEX1	British Columbia, Canada	N/A	Devonian	Yes	Yes	Yes
BC4	NEX1	British Columbia, Canada	N/A	Devonian	Yes	Yes	Yes
BC5	NEX1	British Columbia, Canada	N/A	Devonian	Yes	Yes	Yes
BC6	NEX1	British Columbia, Canada	N/A	Devonian	Yes	Yes	Yes
BC7	NEX1	British Columbia, Canada	N/A	Devonian	Yes	Yes	Yes
BC8	NEX1	British Columbia, Canada	N/A	Devonian	Yes	Yes	Yes
BC9	NEX1	British Columbia, Canada	N/A	Devonian	Yes	Yes	Yes
BC10	NEX1	British Columbia, Canada	N/A	Devonian	Yes	Yes	Yes
BC11	NEX1	British Columbia, Canada	N/A	Devonian	Yes	Yes	Yes
NEX7	Field	Europe	N/A	Carboniferous	Yes	Yes	Yes
NEX15	Field	Europe	N/A	Carboniferous	Yes	Yes	Yes
NEX33	Field	N/A	N/A	Carboniferous	Yes	Yes	Yes
NEX205	Field	N/A	N/A	Carboniferous	Yes	Yes	Yes

Appendix B - Preparation of the input file

Samples have different dimensions (length/diameter for the full core and weight for the crushed samples), so each simulation model has to be created uniquely for the particular sample.

The sections of each of the main three simulations are explained.

Crushed model preparation is shown below:

```
RUNSPEC
TITLE
GAS-PULSE DECAY
-- Maximum well/connection/group values
--     #wells  #cons /w  #grps  #wells /grp
--     ------  -------   -----  ----------
WELLDIMS
          1         3        1       1 /
--          Number of cells
--        NX       NY       NZ
--        --       --       --
DIMENS
         10        10       41   /
REGDIMS
     2 /
-- Phases
GAS
-- Units
LAB
-- Unified output files
UNIFOUT
-- Simulation start date
START
1 JAN 2000 /
NSTACK
100 /
NUPCOL
100 /
```

Figure B.1. Runspec code section.

The main keywords in this section are: WELLDIMS, where the number of wells for the leakage representation is specified; DIMENS, where the number of cells in each dimension is defined

and LAB, which specifies the units used in the simulation. The keyword REGDIMS was used to tune up the Eclipse simulation with Enable – it creates two necessary regions one of which accommodates the well and can be cancelled later in the simulation. This function is used solely for the purpose of higher accuracy which is vital in the crushed sample simulations.

The lines beginning with double slash (--) are ignored by the simulator, therefore enabling user comments to be written for the easier understanding of the model.

```
GRID
--GRIDFILE
-- 2 /
-- Size of each cell in X, Y and Z directions
DX
4100*0.01 /
DY
4100*0.01  /
DZ
4100*0.01  /
--TVDSS of top layer only
--         X1  X2      Y1  Y2      Z1  Z2
--         --  --      --  --      --  --
BOX
           1   10      1   10      1   41  /
TOPS
100*0       /
ENDBOX
ACTNUM
100*0
4000*1
/
--RPTGRID
-- 'DX' 'DY' 'DZ' 'TOPS' 'PORV' 'DEPTH' 'COORD=
-- 'PERMZ' 'PORO' /
-- Permeability in X, Y and Z directions for ea
PERMX
4100*5000 /
PERMY
4100*5000 /
PERMZ
4100*5000 /
-- Phi void
PORO
4100*0.4348  /

-- Phi void
PORO
4100*0.4348  /
EQUALS
-- k high
PERMX 0.0067468218 3 8 3 8 18 26 /
-- k low
PERMX 1.077441E-8 3 8 3 8 27 35 /
-- phi high
PORO 0.14897151 3 8 3 8 18 26  /
-- phi low
PORO 0.010034168 3 8 3 8 27 35  /
-- Phi exp
PORO 0.6030754 1 10 1 10 1 16 /
/
COPY
PERMX PERMY /
PERMY PERMZ /
/
MINPV
0.000000000001 /
MINPVV
4100*0.000000000001 /
INIT
```

Figure B.2. Grid code section.

The main objectives in the GRID section are: to define the size of the cells according to the size of the sample using keywords DX, DY and DZ; to input the permeabilities and porosities of the sample and the system (the volume surrounding the sample named "Phi void", which is defined by very high permeability value). As can be seen from the code, the sample can be divided into low and high permeability regions for the better representation of the geology of the shale.

As stated before, best results are achieved when specifying porosity values as an input rather as variables. The Permeability of the shale is defined as variable in the Enable and is adjusted to match the experimental results.

As written previously about the REGDIMS keyword creating two groups, the keyword ACTNUM in the GRID section defines the groups and their activity status (0 for inactive and 1 for the active cells).Gas properties and matrix compressibility are the main parameters to be defined in the PROPS section. Keyword PVDG is used to define the gas PVT data. The tables for Helium, Methane and Nitrogen are showed in the Figure B3.

```
PROPS
-- Densities in g /cc
--         Oil      Wat      Gas
--         ---      ---      ---
DENSITY
         0.7849   1.009    0.000165 /
-- PVT data for gas
PVDG
1          1         0.019846
2          0.500237118  0.019849
3          0.333649491  0.019853
4          0.2503475    0.019856
5          0.200372848  0.01986
6          0.167061863  0.019864
7          0.143256856  0.019867
8          0.125407598  0.019871
9          0.111525568  0.019874
10         0.100420271  0.019878
15         0.067102746  0.019896
20         0.050443983  0.019913
30         0.03378522   0.019948
40         0.025455021  0.019983
50         0.020457556  0.020017
60         0.017126457  0.02005
70         0.014747428  0.020084
80         0.012962666  0.020117
90         0.01157479   0.020149
100        0.010464424  0.020181    /
/
EXTRAPMS
1 /
-- Rock compressibility
--       P          Cr
--       ----       -----
ROCK
         1          2.7E-05 /
```

CH4 ↓

He ↙

```
PVDG
0.689655172    1.500649553   0.0112
1.379310345    0.749311346   0.0112
2.068965517    0.498865689   0.0112
3.448275862    0.298509994   0.0112
6.896551724    0.148245834   0.0113
10.34482759    0.098160644   0.0113
13.79310345    0.073119312   0.0113
20.68965517    0.048083876   0.0114
27.5862069     0.035572418   0.0115
34.48275862    0.028071685   0.0117
51.72413793    0.018094533   0.012
68.96551724    0.013141638   0.0125
137.9310345    0.006031399   0.0154
/
PVDG
1          1            0.01772
5.995      0.166637762  0.0178
15.985     0.062391775  0.017969
20.98      0.047507211  0.018057
25.975     0.038351517  0.018148
30.97      0.032152817  0.018241
35.965     0.027679086  0.018337
40.96      0.024300287  0.018436
45.955     0.021658683  0.018538
50.95      0.019537406  0.018642
55.945     0.017797055  0.018749
60.94      0.016344409  0.018859
65.935     0.015113581  0.018972
70.93      0.014058233  0.019088
75.925     0.013143196  0.019206
80.92      0.012342904  0.019328
85.915     0.011637178  0.019452
90.91      0.011010313  0.019579
95.905     0.010450467  0.01971
100.9      0.009946515  0.019843
/
```

N2 ↘

Figure B.3. Props code section together with the tables for different gasses.

```
REGIONS
FIPNUM
1600*1
2500*2
/
RPTREGS
/
```

Figure B.4. Regions code section.

Following PROPS is the REGIONS section, which further specifies the regions of the model. Several Keywords can be used, in this simulation FIPNUM was used to specify fluid-in-place region to distinguish between the expansion and sample volumes.

```
SOLUTION
-- Output to Restart file for t=0 (.UNRST)
--      Restart file        Graphics
--      for init cond       only
--      ------------        --------        SUMMARY
RPTRST                                      --ALL
        BASIC=2             NORST=1 /       BPR
PRESSURE                                    1 1 2 /
-- P input P0                               /
4100*14.0333 /                              RPR
EQUALS                                      /
-- P input P2                               --TCPU
PRESSURE 1 1 10 1 10 17 41  /               EXCEL
/
```

Figure B.5. Solution and Summary code section.

The SOLUTION section mainly specifies the pressure of the system using the keyword PRESSURE. Keyword EQUALS is used to specifically define the expansion and sample vessel volumes.

The initial gas pressure was estimated by extrapolating the experimental pressure data in the sample chamber to t = 0. In theory, the initial pressure and the final pressure should give an accurate indication of porosity.

Following section in SUMMARY and is used to specify the location where the simulation data has to be recorded. Keyword EXCEL specifies that the output data is produced in the Excel form.

```
SCHEDULE
--RPTSCHED
--30*1    /
TUNING
/
/
20 5 200 10 200 10 0.0001 0.0001 /
-- Output to Restart file for t>0 (.UNRST)
--      Restart file       Graphics
--        every step          only
--      ------------      --------
RPTRST
        BASIC=2              NORST=1 /
-- Location of wellhead and pressure gauge.
--      Well   Well   Location    BHP    Pref.
--      name   group   I   J     datum   phase
--      -----  ----    -   -     -----   -----
WELSPECS
        PROD1   G1     1   1   1    GAS  /
/
-- Completion interval|
--      Well   Location  Interval  Status        Well
--      name    I   J    K1  K2    O or S         ID
--      ----    -   -    --  --    ------       --??----
COMPDAT
        PROD1   1   1   1   1     OPEN        2* 0.00198 /
/
-- Production control
--  Well  Status  Control   Oil   Wat   Gas   Liq  Resv  BHP
--  name           mode    rate  rate  rate  rate  rate  limit
--  ----  ------  ------   ----  ----  ----  ----  ----  -----
WCONPROD
    PROD1  OPEN    GRAT    2*     0   2*  1 /
/
-- Number and size (days) of timesteps
TSTEP
10*0.0001
10*0.0002
10*0.001
10*0.01 /
END
```

Figure B.6. Schedule code section.

The last section SCHEDULE provides additional information about the wells in the keyword WELSPECS, COMPDAT and WCONPROD. The length of the simulation is then defined by the keyword TSTEP. Finally keyword END is used to show the end of the simulation.

Key input parameters for the model are the initial pressure, P_i, porosity of cells representing the void around the shale samples in the sample cell, $\emptyset_{vs}$, and reference cell, $\emptyset_{vr}$, and porosity of the shale $\emptyset_{sh}$. P_i is estimated by plotting pressure vs $t^{0.5}$ and then extrapolating to t = 0. $\emptyset_{vs}$ and $\emptyset_{vr}$ are calculated using Equation - 1 and Equation - 2.

$$\emptyset_{vs} = \frac{N_{sh} V_{vs}}{N_{vs} V_{sh}}$$ (Equation - 1)

$$\emptyset_{vr} = \frac{\emptyset_{vs} N_{vs} V_{vr}}{N_{vr} V_{vs}}$$ (Equation - 2)

where N_{sh}, N_{vs} and N_{vr} are the number of cells representing the shale, void in the sample cell and void in the reference cell respectively; V_{sh}, V_{vs}, and V_{vr} are the real volumes of shale (cm^3), void in the sample cell and the reference cell volume respectively . As mentioned above, V_{sh} can be estimated based on the weight of the crushed shale and its bulk density measured using Hg immersion (Equation - 3).

$$V_s = V_s - V_{sh} \qquad \text{(Equation - 3)}$$

Where V_s is the volume of the sample chamber (cm^3).

The porosity of the chips can be calculated using Equation - 4.

$$\emptyset_c = \frac{P_{eq}(V_{vr} - P_{vs}) + P_i V_{vp} - P_a V_{vs}}{V_{sh}(P_a - P_{eq})} \qquad \text{(Equation - 4)}$$

where P_{eq} is the equilibration pressure (psig).

Core plug model preparation is shown below:

```
RUNSPEC
TITLE
                 Full core GRI
METRIC
-- Maximum well/connection/group values
--      #wells  #cons/w  #grps  #wells/grp
--      ------  -------  -----  ----------
WELLDIMS
           1        3       1       1 /
RADIAL
GAS
DIMENS
23 2 140 /
--WELLDIMS
--1 2 1 10 /
START
 1 'JAN' 2011 /                          ROCKCOMP
ROCKCOMP                                 REVERS 1 /
REVERS 1 /                               UNIFOUT
UNIFOUT                                  UNIFIN
GRID
```

Figure B.7. Runspec code section.

The first section of the simulation model for the full core experiment is mostly the same as for crushed core, except for the keyword RADIAL, which converts the simulation geometry from the Cartesian to the radial. Another important feature of is the keyword UNIFIN, which is only used in RESTART type of simulations. This keyword has to be used on the step 2,3,4 etc. simulations following the first one. Keyword UNIFIN indicates that the output files are unified – this is for the purpose of better organisation and clarity in the folders, as without this keyword, the simulator creates output files for every time step, hence filling the folders with files. Keyword NORST, used later in the following sections, has to be deleted in RESTART type of simulations.

```
GRID
--=================================================================
-------- IN THIS SECTION , THE GEOMETRY OF THE SIMULATION GRID AND THE
-------- ROCK PERMEABILITIES AND POROSITIES ARE DEFINED.
-------------------------------------------------------------------
--  SPECIFY INNER RADIUS OF 1ST GRID BLOCK IN THE RADIAL DIRECTION
INRAD
  0.05 /
--  SPECIFY GRID BLOCK DIMENSIONS IN THE R DIRECTION
DRV
    1*0.05 22*0.091  /
-- SPECIFY CELL THICKNESSES ( DZ ), RADIAL PERMEABILITIES ( PERMR )
-- AND POROSITIES ( PORO ) FOR EACH LAYER OF THE GRID. ALSO CELL TOP
-- DEPTHS ( TOPS ) FOR LAYER 1. DTHETA IS SET TO 360 DEGREES FOR EVERY
-- GRID BLOCK IN THE RESERVOIR.
--    ARRAY    VALUE  ------ BOX ------
DTHETA
6440*180   / BOX DEFAULTS TO THE WHOLE GRID
EQUALS
DZ 0.2  1 23  1  2  1  39 /
DZ 0.0425  1 23  1  2  40  140 /
/
Box
1 23  1  2  1  1  /
TOPS
46*0  /
ENDBOX
PERMR
6440*1000000  /
PERMZ
6440*1000000  /
PERMTHT
6440*1000000 /
-- sample chamber poro
PORO
6440*0.964755 /
EQUALS
      PERMR   0.25  1  21  1  2  40 139  /
      PERMZ   0.25  /
      PERMTHT 0.25 /
      PORO 0.05/
/
-- expansion vol poro
EQUALS
      PORO   0.94561  1  21  1  2  1  17  /
/
COORDSYS
2* COMP /
INIT
```

Figure B.8. Grid code section.

The GRID section of the full core GRI simulation is similar to the crushed core. The major difference arises from the radial geometry which has to be defined. It is done using keywords INRAD and DRV, to define the size of the cells, and also keyword DTHETA, which splits the radial direction of the model into the required number of cells. The permeabilities and porosities of the void volumes and the sample are defined according to the necessary volumetric dimensions.

```
PROPS
-- Densities in g/cm3
--          Oil      Wat      Gas
--          ---      ---      ---        EXTRAPMS
DENSITY                                  1 /
          0.7849   1.009   0.000165 / ROCKTAB
-- PVT data for gas                     1 1 55.6668265306122
PVDG                                    2 1 28.3334132653061
1            1          0.019846        3 1 19.2222755102041
2      0.500237118      0.019849        4 1 14.6667066326531
3      0.333649491      0.019853        5 1 11.9333653061224
4      0.2503475        0.019856        6 1 10.111137755102
5      0.200372848      0.01986         7 1 8.80954664723032
6      0.167061863      0.019864        8 1 7.83335331632653
7      0.143256856      0.019867        9 1 7.0740918367347
8      0.125407598      0.019871        10 1 6.46668265306122
9      0.111525568      0.019874        11 1 5.96971150278293
10     0.100420271      0.019878        12 1 5.55556887755102
15     0.067102746      0.019896        13 1 5.20514050235479
20     0.050443983      0.019913        14 1 4.90477332361516
30     0.03378522       0.019948        15 1 4.64445510204082
40     0.025455021      0.019983        16 1 4.41667665816327
50     0.020457556      0.020017        17 1 4.21569567827131
60     0.017126457      0.02005         18 1 4.03704591836735
70     0.014747428      0.020084        19 1 3.87720139634801
80     0.012962666      0.020117        20 1 3.73334132653061
90     0.01157479       0.020149        /
100    0.010464424      0.020181
/
```

Figure B.9. Props code section.

The PROPS section is defined in the same way as in the crushed simulation. The keyword ROCTAB includes the permeability multiplier depending on the pressure. This keyword was applied in this research to derive the *b*-factor. Note: when ROCKTAB keyword is used, keyword ROCK must be taken out.

```
SOLUTION                                          SOLUTION
-- Initial equilibration conditions               -- Initial equilibration conditions
--      Datum   Pi@datum    WOC     Pc@WOC         --      Datum   Pi@datum    WOC     Pc@WOC
--      -----   --------    -----   ------         --      -----   --------    -----   ------
--EQUIL                                            --EQUIL
--          1       1       700       0 /          --          1       1       700       0 /
-- Output to Restart file for t=0 (.UNRST)        -- Output to Restart file for t=0 (.UNRST)
--     Restart file         Graphics              --     Restart file         Graphics
--     for init cond          only                --     for init cond          only
--     ------------         --------              --     ------------         --------
                                                  RPTRST
RPTRST                                                   BASIC=2              /
        BASIC=2             /                     /
PRESSURE                                          RESTART
6440*1.01379 /                                    CHE2_FOR-1MREFINE40 160 /
EQUALS                                            /
PRESSURE   34.82  1  23  1  2  1  17  /           EQUALS
/                                                 PRESSURE   48.82  1  23  1  2  1  17  /
                                                  /
```

Figure B. 10. Solution code section.

The SOLUTION section is the same as in crushed core model. The main difference is the absence of the NORST keyword - as was mentioned earlier this keyword is not used in RESTART type of simulations. Figure b shows the SOLUTION section for the 2, 3, 4 etc. run step of the simulation. RESTART keyword is used in this case followed by the name of the simulation file to be restarted and the time-step it to be restarted from. The initial pressure distribution in the restarted simulation is taken exactly as the defined time-step of the first one.

```
SCHEDULE
-- Output to Restart file for t>0 (.UNRST)
--      Restart file         Graphics
--      every step             only
--      ------------         --------
RPTRST
        BASIC=2                 /
/
-- Location of wellhead and pressure gauge
--      Well   Well   Location   BHP     Pref.
--      name   group   I    J    datum   phase
--      -----  ----    -    -    -----   -----
WELSPECS
        PROD   G1      1    1    1       GAS  /
/
-- Completion interval
--      Well    Location   Interval  Status        Well
--      name     I    J     K1  K2   O or S         ID
--      ----     -    -     --  --   ------       --??----
COMPDAT
        PROD     1    1     1   1    OPEN         2* 0.025 /
/
-- Production control
--  Well  Status  Control   Oil   Wat   Gas   Liq   Resv   BHP
--  name           mode     rate  rate  rate  rate  rate   limit
--  ----  ------  ------    ----  ----  ----  ----  ----   -----
WCONPROD
    PROD  OPEN    GRAT      2*      0    2*   1 /
/
SUMMARY       -- Number and size (HOURS) of timesteps
BPR           TSTEP
1 1 3 /
--10 1 4/ 10*0.0000041667
--23 1 1/ 100*0.000099584
/        50*0.0008334 /
EXCEL    END
```

Figure B.11. Schedule and Summary code section.

The SUMMARY and SCHEDULE sections are the same as for the previous simulation. The NORST keyword is absent due to the RESTART type of simulations.

Preparation of the Modified pressure decay model is shown below:

```
RUNSPEC
TITLE
KTP linear plus fracture
LAB
GAS
DIMENS
58 40 41 /
--WELLDIMS                      ROCKCOMP
--1 2 1 10 /                    REVERS 1 /
START                           UNIFOUT
 1 'JAN' 2011 /                 UNIFIN
UNIFOUT
```

Figure B.12. Runspec code section.

The simulation for the modified pulse decay is of Cartesian geometry, so it is defined similarly like the crushed core model. However the RESTART function is used in the modified pressure decay model as the pressure is not getting to equilibrium.

```
GRID
--=======================================
-------- IN THIS SECTION , THE GEOMETRY OF
-------- ROCK PERMEABILITIES AND POROSITIES
-------------------------------------------
--  SPECIFY GRID BLOCK DIMENSIONS
DX
95120*0.065588 /
DY
95120*0.082796 /                   --PORO upstream
DZ                                 PORO
95120*0.082796 /                   95120*0.99/
-- SPECIFY CELL PERMEABILITIES ( PERM )    --matrix
-- AND POROSITIES ( PORO ). ALSO CELL TOP  EQUALS
-- DEPTHS ( TOPS ) FOR LAYER 1.              PERMX   0.00004  16  49  1  40  1  41  /
--      ARRAY    VALUE  ------ BOX ------    PERMZ   0.00004  16  49  1  40  1  41  /
Box                                          PERMY   0.00004 16  49  1  40  1   41 /
1 58  1  40  1  1  /                         PORO    0.05 16  49  1  40  1  41 /
TOPS                               --fracture
2320*0  /                            PERMX   0.004  16  49  1  40  21  21  /
ENDBOX                               PERMZ   0.004  16  49  1  40  21  21 /
PERMX                                PERMY   0.004  16  49  1  40  21  21 /
95120*100  /                         PORO    0.05 16  49  1  40  21  21 /
PERMY                              --PORO downstream
95120*100  /                         PORO    0.827264 50 52 1 40 1 41 /
PERMZ                              /
95120*100  /                       INIT
```

Figure B.14. Grid code section.

The GRID section defines the size and the permeabilities/porosities of the cells. As can be seen additional feature of the fracture is represented in this model.

```
PROPS
-- Densities in g/cm3
--        Oil      Wat     Gas
--        ---      ---     ---
DENSITY
        0.7849   1.009   0.000165 /
-- PVT data for gas
PVDG
1           1        0.019846
2     0.500237118    0.019849
3     0.333649491    0.019853
4     0.2503475      0.019856          ROCKTAB
5     0.200372848    0.01986           1 1 12.0262299319728
6     0.167061863    0.019864          2 1 6.51311496598639
7     0.143256856    0.019867          3 1 4.67540997732426
8     0.125407598    0.019871          4 1 3.7565574829932
9     0.111525568    0.019874          5 1 3.20524598639456
10    0.100420271    0.019878          6 1 2.83770498866213
15    0.067102746    0.019896          7 1 2.57517570456754
20    0.050443983    0.019913          8 1 2.3782787414966
30    0.03378522     0.019948          9 1 2.22513665910809
40    0.025455021    0.019983          10 1 2.10262299319728
50    0.020457556    0.020017          11 1 2.00238453927025
60    0.017126457    0.02005           12 1 1.91885249433107
70    0.014747428    0.020084          13 1 1.84817153322868
80    0.012962666    0.020117          14 1 1.78758785228377
90    0.01157479     0.020149          15 1 1.73508199546485
100   0.010464424    0.020181          16 1 1.6891393707483
/                                      17 1 1.64860176070428
EXTRAPMS                               18 1 1.61256832955404
1 /                                    19 1 1.58032789115646
-- Rock compressibility                20 1 1.55131149659864
--       P           Cr               /
--       ----        -----
ROCK
        1       1.12E-06 /
```

Figure B.15. Props code section.

The PROPS section and SOLUTION sections are the same as explained in previous simulation models.

```
SOLUTION                                        SOLUTION
-- Initial equilibration conditions             -- Output to Restart file for t=0 (.UNRST)
--       Datum   Pi@datum    WOC      Pc@WOC     --       Restart file       Graphics
--       -----   --------    -----    ------     --       for init cond       only
--EQUIL                                          --       -------------       --------
--       1    1      700      0 /                RPTRST
-- Output to Restart file for t=0 (.UNRST)                BASIC=2                /
--       Restart file       Graphics             /
--       for init cond       only                RESTART
--       -------------       --------            EBN20#1_KTP_He_101p9psig1 220 /
RPTRST                                           /                                          SUMMARY
         BASIC=2                /                EQUALS                                     BPR
PRESSURE                                         Pressure 1 1 6 1 40 1 41 /                 10 1 1
95120*7.9378 /                                   Pressure 1 53 58 1 40 1 41 /               51 1 1 /
EQUALS                                           Pressure 14.193 7 15 1 40 1 41 /           /
PRESSURE  1  16 58  1  40  1  41  /              /                                          EXCEL
Pressure 1 1 6 1 40 1 41 /
/
```

Figure B.16. Solution code section.

The SOLUTION and SUMMARY sections (Figure B.) are the same as described in the previous sections.

```
SCHEDULE
-- Output to Restart file for t>0 (.UNRST)
--       Restart file       Graphics
--       every step          only
--       -------------       --------
RPTRST
         BASIC=2                /
/
- Location of wellhead and pressure gauge
--       Well  Well    Location   BHP    Pref.
--       name  group   I    J     datum  phase
--       ----  ----    -    -     -----  -----
WELSPECS
         PROD1  G1      10   20  1    GAS  /
         PROD2  G1      51   20  1    GAS  /
/
-- Completion interval
--       Well   Location  Interval  Status      Well
--       name   I    J    K1  K2    O or S       ID
--       ----   -    -    --  --    ------      --??----
COMPDAT
         PROD1   10   20   1   1    OPEN        2* 0.005 /
         PROD2   51   20   1   1    OPEN        2* 0.005 /
/
-- Production control
-- Well   Status  Control   Oil   Wat   Gas   Liq  Resv   BHP
-- name           mode      rate  rate  rate  rate rate   limit
-- ----   ------  ------    ----  ----  ----  ---- ----   -----
WCONPROD
   PROD1  OPEN    GRAT    2*     0    2*  0.1 /
   PROD2  OPEN    GRAT    2*     0    2*  0.1 /
/
-- Number and size (HOURS) of timesteps
TSTEP
100*0.00000833
100*0.000015391
100*0.000291667 /
END
```

Figure B.17. Schedule code section.

The SCHEDULE section is different in the modified pressure decay simulation model, as it has two wells – one for both upstream and downstream.

History matching procedure

The procedure of the history matching using Enable is as follows:

1. Simulation file is uploaded into the software as shown in Figure B 18. Parameters to be varied are selected and the option "Insert New User Modifier" is chosen for each of them (Figure B.19.). This option defines the range and type of distribution for the parameter to be varied (Figure B 20).
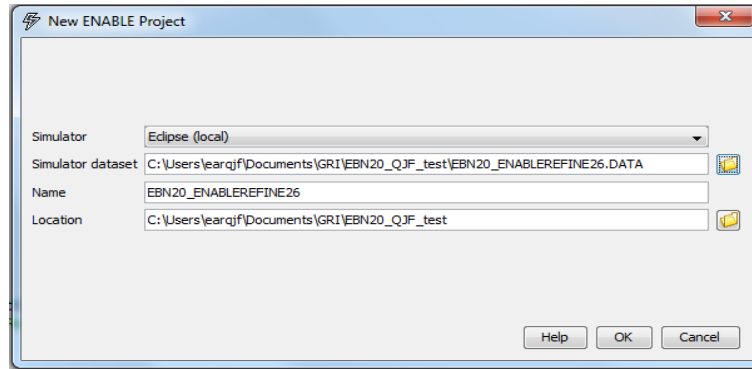
Figure B.18. New simulation upload window.
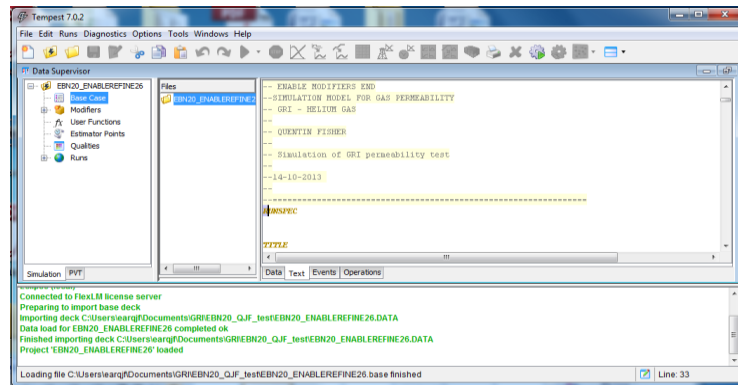
Figure B.19. Enable simulation text editor.
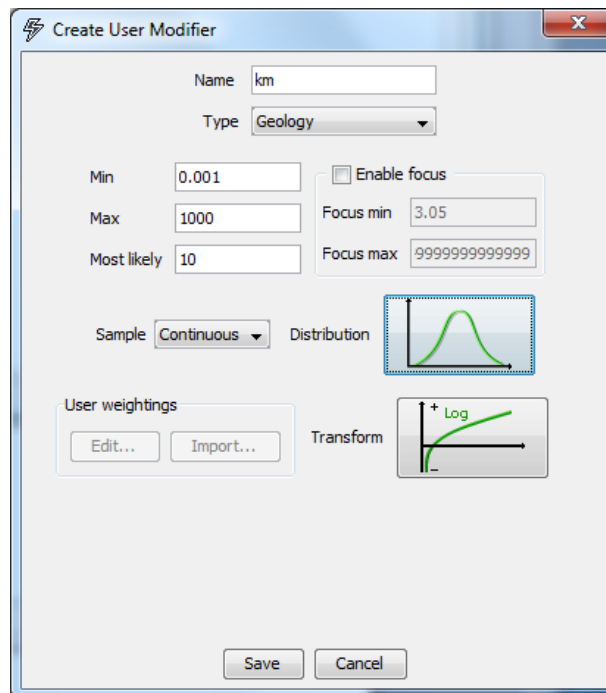
Figure B.20. Property window of the variables. The type of variable distribution is the trial and error process, good results were found to be obtained using Log type of variable transform.

2. Once the parameters to be inverted are defined, the "scoping Runs" option is selected. This option allows number of scoping simulations to be selected and ran – Enable generates a number of input parameters selected from the pre-defined range using the pre-defined distribution and uses this data as an input for the simulations. A number of 25 to 50 scoping runs are usually made.

3. After scoping simulations are completed, the results are plotted against experimental data as shown in Figure B 21a. History estimator ranges are then selected across the curves specifying the acceptable uncertainty range (Figure B 21b).
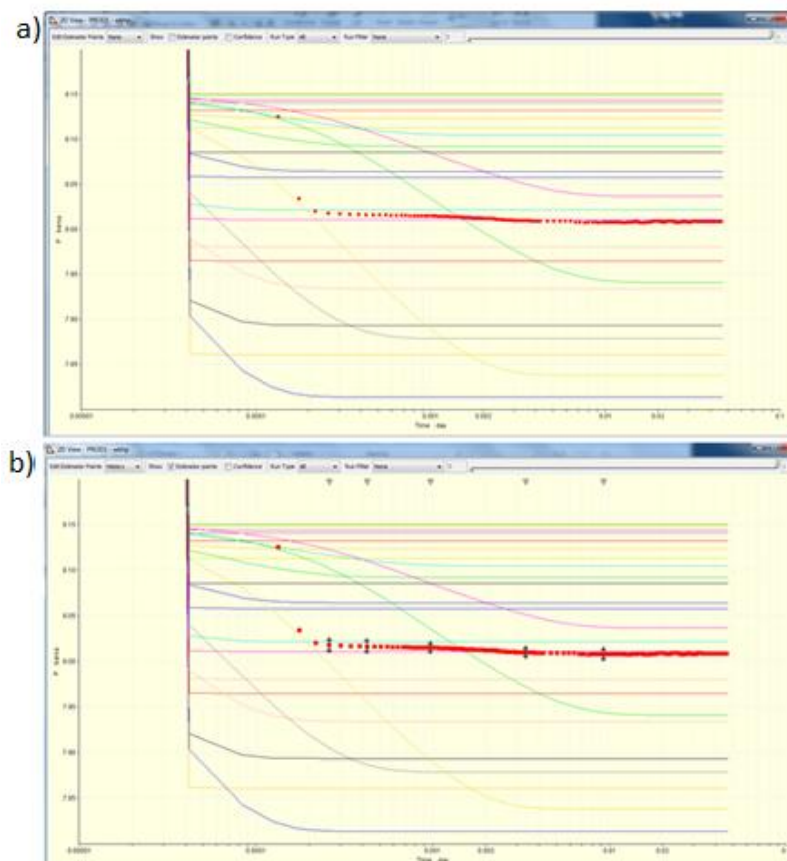
Figure B.21.Experimental and simulation pressure curves

4. After selecting the range, "Refinement Runs" option is selected. This option defines the number of refinement simulations to be run – Enable selects the matches from the scoping simulation that fit within the selected range in step 3 and tries to narrow down the error range by calculating new parameters that produce a better fit.

5. After the refinement simulations are finished, the results are exported using the "Export Modifiers and Qualities" option. By using this option, Enable creates an Excel file with all derived results together with their qualities. Enable can also create a graph showing all the variables and their qualities of all runs (Figure B 22).
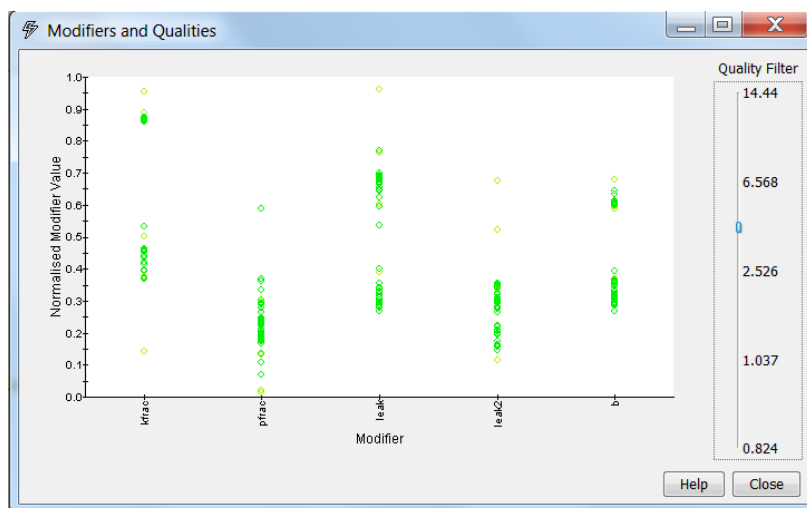
Figure B.22. Enable window showing the qualities and dependencies of all variables. Quality values below 1 usually represents a good result.

User Defined Functions and Inclusion of the Klinkenberg Correction:

Essentially Klinkenberg correction (59) modifies the apparent permeability value according to the *b*-factor during the simulation run. To do this modification, rock compaction table keyword ROCKTAB is used in PROPS section:

<div align="center">

PROPS

ROCKTAB

1 1		*1.0*
5 1		*1.0*
15	*1*	*1.0*
20	*1*	*1.0*

</div>

Numbers in the first column represent pressure, second column is pore volume multiplier and the third column is permeability multiplier. Shown values ignore all effects. To include *b*-factor into the run, permeability multiplier (numbers in third column) have to be changed according to the equation:

$$k_a = k_i \times (1 + b/P) \qquad\qquad \text{(Equation - 5)}$$

Where k_a is apparent permeability for which the correction is made, k_i is intrinsic permeability which will show up as the inverted result, *b* is the b factor, and *P* is the pressure. The pressure values have to be specified up to 20atmos, the simulator uses this data for extrapolation.

The example below shows the ROCKTAB section modified by the *b*-factor of 13.75264:

ROCKTAB

1	1	1.9355537414966
2	1	1.4677768707483
3	1	1.31185124716553
4	1	1.23388843537415
5	1	1.18711074829932
6	1	1.15592562358277
7	1	1.13365053449951
8	1	1.11694421768707
9	1	1.10395041572184
10	1	1.09355537414966
11	1	1.08505034013605
12	1	1.07796281179138
13	1	1.07196567242282
14	1	1.06682526724976
15	1	1.06237024943311
16	1	1.05847210884354
17	1	1.05503257302921
18	1	1.05197520786092
19	1	1.04923967060508
20	1	1.04677768707483

Figure B.23. The keyword and column modifying permeability according to the *b*-factor. The numbers are divided into three columns, where column 1 represents the pressure, column 2 is the pore volume multiplier and column 3 is the permeability multiplier. In this case the Tempest Enable produced values are presented obtained using scoping run *b*-factor of 13.75264.

As a result of the b-factor, permeabilities will be changed according to the third column (permeability multiplier) during the run. To include this equation in Enable simulations, user defined function has to be included. Enable has an option called "User Functions", which allows incorporating *b*-factors, relative permeability and capillary curves etc.

To invert the *b*-factor function, following steps have to be taken:

1. The simulation file is uploaded into the Enable software. Note – when using keyword ROCKTAB, keywords ROCKCOMP AND REVERS 1 have to be included into the RUNSPEC section, as was mentioned in Section 3.1.5.3. Also ROCK keyword in PROPS section should not be used.

2. Choose "User Functions" option in the right hand panel and paste the code provided in the Appendix F.
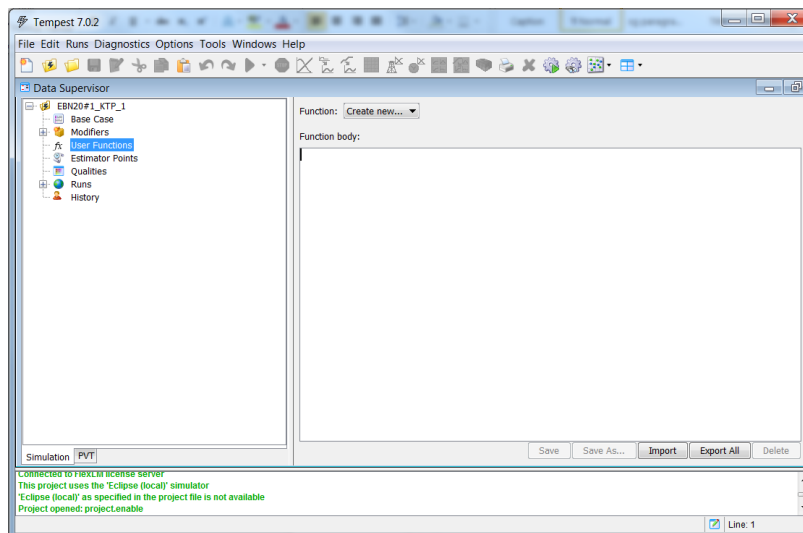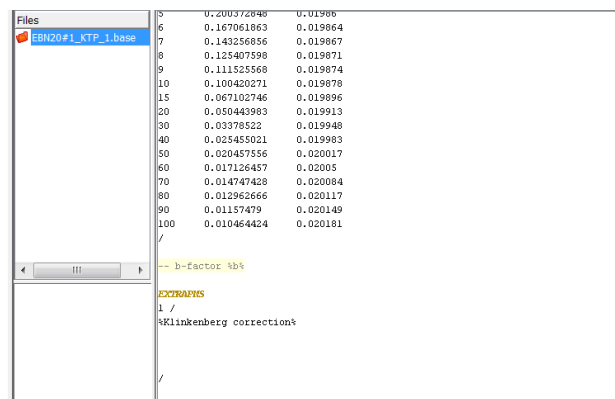
Figure B.24.User functions window.

The code modifies permeability according to Equation - 6:

$$k_a = k_i \times (1 + b/P)$$

(Equation - 6)

3. Click "Save As" option (in the bottom right) and name the function (e.g. Klinkenberg_correction). The name of the function does not have any impact on the simulation – it is only for user reference (note – function name has to contain no spaces).

4. Go back to the "Base case" option in the hand panel and write letter b in comment section – it represents the *b*-factor used in code and will be used for the user define a new modifier.
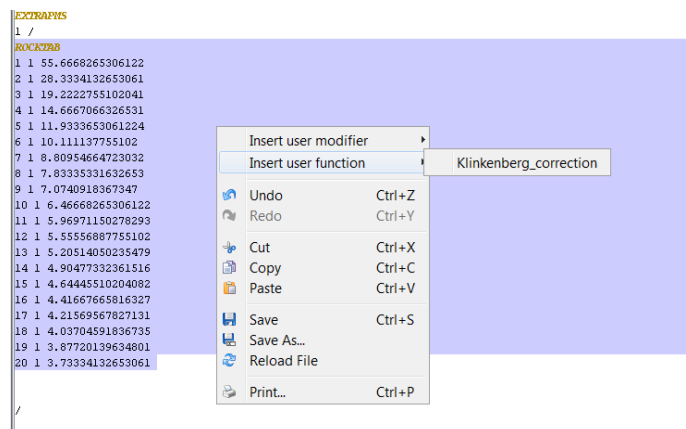
Figure B.25. Part of the code for the *b*-factor function.

5. Highlight the symbol b with the mouse and then click right button and select "Insert New User Modifier". The following procedure is the same as with other history matched parameters: choosing a name for the variable, estimating a maximum, minimum and most likely result. Select the type of transform and click "ok".

6. With the mouse highlight the keyword ROCKTAB together with the whole column and slash at the end, then click right mouse button and choose option "Insert user function". Select the function saved before (e.g. Klinkenberg_correction).

Figure B.26. Insertion of the function for the b factor.

The further steps are generating scoping and refinement simulation as already described.

Simulation model

```
-- DEFINED LAYERS

LGRD 30 16 40 71 100 43 58 4 5 unite /
REFI unite
PORO Vari
--REFI FOR WELLS KN-1 UD-1 AND FA-2
--<<<<<<<<<<<<<<<<<<<<<<<<<<<<<<<<<<
--LAYER 1 :: 71.9(m)
420*0 -- LIMESTONE
60*0 -- SHALE
--<<<<<<<<<<<<<<<<<<<<<<<<<<<<<<<<<<
--LAYER 2 :: 72.9(m)
390*0 -- LIMESTONE
30*0 -- SHALE
60*0 -- LIMESTONE
--<<<<<<<<<<<<<<<<<<<<<<<<<<<<<<<<<<
--LAYER 3 :: 74(m)
390*0 -- LIMESTONE
30*0 -- SHALE
60*0 -- SHALE
--<<<<<<<<<<<<<<<<<<<<<<<<<<<<<<<<<<
--LAYER 4 :: 75(m)
360*0 -- LIMESTONE
30*0 -- SHALE
30*0 -- LIMESTONE
60*0 -- SANDSTONE
--<<<<<<<<<<<<<<<<<<<<<<<<<<<<<<<<<<
--LAYER 5 :: 76(m)
360*0 -- LIMESTONE
30*0 -- SHALE
30*0 -- SHALE
60*0 -- SANDSTONE
--<<<<<<<<<<<<<<<<<<<<<<<<<<<<<<<<<<
--LAYER 6 :: 77(m)
330*0 -- LIMESTONE
30*0 -- SHALE
30*0 -- LIMESTONE
30*0 -- SANDSTONE
60*0 -- SHALE
--<<<<<<<<<<<<<<<<<<<<<<<<<<<<<<<<<<
--LAYER 7 :: 78(m)
330*0 -- LIMESTONE
30*0-- SHALE
30*0 -- SHALE
30*0 -- SANDSTONE
60*0-- SHALE
--<<<<<<<<<<<<<<<<<<<<<<<<<<<<<<<<<<
--LAYER 8 :: 79.1(m)
300*0 -- LIMESTONE
30*0 -- SHALE
30*0 -- LIMESTONE
30*0 -- SANDSTONE
30*0 -- SHALE
60*0 -- SHALE
--<<<<<<<<<<<<<<<<<<<<<<<<<<<<<<<<<<
--LAYER 9 :: 80.1(m)
300*0 -- LIMESTONE
30*0 -- SHALE
30*0 -- SHALE
30*0 -- SANDSTONE
30*0 -- SHALE
60*0 -- SHALE
--<<<<<<<<<<<<<<<<<<<<<<<<<<<<<<<<<<
--LAYER 10 :: 81.1(m)
270*0 -- LIMESTONE
30*0 -- SHALE
30*0 -- SHALE
30*0 -- SANDSTONE
30*0 -- SHALE
30*0 -- SHALE
60*0 -- SHALE
--<<<<<<<<<<<<<<<<<<<<<<<<<<<<<<<<<<
--LAYER 11 :: 82.2(m)
240*0 -- LIMESTONE
30*0 -- SHALE
30*0 -- SHALE
30*0 -- SHALE
30*0 -- SANDSTONE
30*0 -- SHALE
30*0 -- SHALE
60*0 -- SHALE
```

Appendix C

Table C.1. Representation of different layers in the model.

empty vessel			56.671 cm3 plug					54.135 cm3 plug					37.627 cm3 plug				
Initial Pressure P1, psig	Initial Pressure P1, psig	Ratio	Initial Pressure P1, psig	Initial Pressure P1, psig	Ratio	V2, cm3	V1, cm3	Initial Pressure P1, psig	Initial Pressure P1, psig	Ratio	V2, cm3	V1, cm3	Initial Pressure P1, psig	Initial Pressure P1, psig	Ratio	V2, cm3	V1, cm3
60.403	21.909	1.757	60.265	42.817	0.408	73.78	41.99	60.105	40.899	0.470	73.88	42.05	59.997	31.840	0.884	75.75	43.11
69.882	24.425	1.861	70.877	50.936	0.392	71.77	38.56	70.005	47.771	0.465	72.19	38.79	70.055	36.821	0.903	73.06	39.26
81.012	28.700	1.823	79.130	56.375	0.404	72.79	39.93	80.431	54.598	0.473	73.11	40.11	79.879	42.178	0.894	73.84	40.51
90.386	32.200	1.807	90.221	63.959	0.411	73.33	40.58	89.991	61.142	0.472	73.27	40.54	90.164	47.678	0.891	74.23	41.08
100.142	35.500	1.821	99.760	70.728	0.410	73.16	40.18	99.678	67.671	0.473	73.13	40.16	100.512	53.111	0.893	73.80	40.53
110.000	38.700	1.842	110.031	77.708	0.416	73.20	39.73	110.679	75.171	0.472	72.80	39.51	109.790	58.011	0.893	72.99	39.61
119.987	42.357	1.833	120.201	85.218	0.411	73.03	39.85	120.119	81.548	0.473	72.97	39.81	120.331	63.515	0.895	73.50	40.10
129.652	45.939	1.822	129.969	91.847	0.415	73.39	40.27	130.058	88.187	0.475	73.21	40.17	127.667	67.415	0.894	73.84	40.52
140.113	49.450	1.833	140.121	98.744	0.419	73.46	40.07	140.705	95.483	0.474	72.99	39.81	140.402	74.053	0.896	73.59	40.14
149.993	52.807	1.840	150.059	105.865	0.417	73.30	39.83	150.55	101.998	0.476	73.02	39.68	149.971	79.032	0.898	73.45	39.91
159.748	56.369	1.834	159.899	112.971	0.415	73.27	39.95	163.334	110.979	0.472	72.88	39.74	160.031	84.358	0.897	73.65	40.16
169.879	59.914	1.835	170.606	120.385	0.417	73.34	39.96	170.001	115.368	0.474	72.96	39.75	170.022	89.603	0.897	73.63	40.12
180.186	63.564	1.835	180.315	127.210	0.417	73.36	39.99	179.954	122.032	0.473	73.03	39.80	179.992	94.766	0.899	73.80	40.23
190.505	67.131	1.838	189.997	133.952	0.418	73.38	39.93	190.301	129.051	0.475	72.98	39.71	189.333	99.742	0.898	73.60	40.05
202.486	71.445	1.834	200.113	140.884	0.420	73.52	40.09	199.059	134.854	0.476	73.11	39.86	202.168	106.606	0.896	73.60	40.12
210.245	73.770	1.850	210.032	147.950	0.420	73.30	39.62	210.029	142.318	0.476	72.88	39.39	210.006	110.461	0.901	73.36	39.66
220.396	77.590	1.841	220.225	155.245	0.419	73.35	39.85	220.025	149.385	0.473	72.85	39.58	220.255	115.976	0.899	73.57	39.97
229.967	80.939	1.841	230.105	162.152	0.419	73.37	39.85	229.162	155.343	0.475	72.97	39.63	230.364	121.283	0.899	73.56	39.95
238.735	84.137	1.837	240.345	169.335	0.419	73.43	39.96	241.626	163.734	0.476	73.05	39.75	240.944	126.871	0.899	73.68	40.10

Table C.2. Vessel G1 calibration data.

empty vessel			56.671 cm3 plug					54.135 cm3 plug					37.627 cm3 plug				
Initial Pressure P1, psig	Initial Pressure P1, psig	Ratio	Initial Pressure P1, psig	Initial Pressure P1, psig	Ratio	V2, cm3	V1, cm3	Initial Pressure P1, psig	Initial Pressure P1, psig	Ratio	V2, cm3	V1, cm3	Initial Pressure P1, psig	Initial Pressure P1, psig	Ratio	V2, cm3	V1, cm3
60.13	21.31	1.82	60.35	42.11	0.43	74.36	40.82	59.78	39.65	0.51	75.05	41.20	60.44	33.23	0.82	68.35	37.52
70.08	24.75	1.83	70.62	49.27	0.43	74.23	40.53	69.88	46.12	0.52	75.32	41.13	70.61	37.46	0.88	72.80	39.75
80.44	28.62	1.81	80.01	55.82	0.43	74.50	41.15	80.21	53.44	0.50	74.84	41.33	80.35	42.38	0.90	74.48	41.14
90.13	31.99	1.82	90.36	63.04	0.43	74.41	40.94	90.22	60.33	0.50	74.42	40.95	90.42	47.98	0.88	73.30	40.33
100.06	35.55	1.81	99.86	69.67	0.43	74.45	41.03	100.36	67.25	0.49	74.29	40.94	100.52	53.48	0.88	73.02	40.24
110.22	39.12	1.82	110.51	77.10	0.43	74.41	40.94	110.66	73.88	0.50	74.56	41.02	109.85	58.12	0.89	73.74	40.57
120.41	42.79	1.81	120.31	83.94	0.43	74.46	41.05	120.53	80.66	0.49	74.41	41.02	120.24	63.17	0.90	74.96	41.32
130.02	46.17	1.82	129.68	90.48	0.43	74.43	40.98	129.67	86.88	0.49	74.28	40.90	130.32	68.37	0.91	75.09	41.35
139.96	49.68	1.82	140.21	97.82	0.43	74.41	40.95	140.65	94.26	0.49	74.24	40.85	140.88	73.89	0.91	75.09	41.32
150.07	53.31	1.82	150.12	104.74	0.43	74.44	41.01	150.55	100.53	0.50	74.58	41.09	150.23	79.24	0.90	74.30	40.94
160.25	56.87	1.82	160.05	111.67	0.43	74.41	40.93	160.35	107.34	0.49	74.33	40.89	160.21	84.32	0.90	74.52	41.00
170.29	60.46	1.82	169.78	118.46	0.43	74.42	40.97	170.42	113.87	0.50	74.50	41.01	170.41	89.96	0.89	74.11	40.80
180.06	63.91	1.82	179.96	125.56	0.43	74.41	40.94	180.44	120.86	0.49	74.28	40.87	179.69	94.28	0.91	75.02	41.28
190.07	67.41	1.82	190.07	132.61	0.43	74.38	40.88	190.73	127.34	0.50	74.52	40.96	190.24	99.73	0.91	75.07	41.25
199.88	70.95	1.82	200.12	139.62	0.43	74.41	40.95	200.36	134.05	0.49	74.38	40.93	201.34	106.43	0.89	73.88	40.66
210.51	74.74	1.82	210.13	146.61	0.43	74.42	40.97	210.12	140.51	0.50	74.43	40.98	210.24	111.73	0.88	73.11	40.25
220.24	78.23	1.82	220.55	153.88	0.43	74.44	41.01	219.68	146.8	0.50	74.51	41.05	220.32	116.34	0.89	74.12	40.83
230.29	81.75	1.82	230.32	160.69	0.43	74.42	40.96	230.32	153.87	0.50	74.51	41.01	229.88	121.67	0.89	73.70	40.56
240.14	85.3	1.82	239.68	167.22	0.43	74.44	41.01	240.55	160.76	0.50	74.51	41.05	240.36	126.32	0.90	74.86	41.24
249.97	88.81	1.81	250.32	174.65	0.43	74.45	41.02	250.64	167.6	0.50	74.47	41.04	250.66	132.43	0.89	74.07	40.82
260.04	92.33	1.82	260.33	181.63	0.43	74.42	40.97	260.23	174.36	0.49	74.27	40.89	260.42	137.31	0.90	74.30	40.91
270.12	95.89	1.82	270.62	188.81	0.43	74.42	40.96	270.66	181.35	0.49	74.26	40.87	270.31	142.28	0.90	74.54	41.03

Table C.3. Vessel G2 calibration data.

empty vessel			56.671 cm3 plug					54.135 cm3 plug					37.627 cm3 plug				
Initial Pressure P1, psig	Initial Pressure P1, psig	Ratio	Initial Pressure P1, psig	Initial Pressure P1, psig	Ratio	V2, cm3	V1, cm3	Initial Pressure P1, psig	Initial Pressure P1, psig	Ratio	V2, cm3	V1, cm3	Initial Pressure P1, psig	Initial Pressure P1, psig	Ratio	V2, cm3	V1, cm3
59.97	19.62	2.06	60.06	40.70	0.48	73.72	35.85	60.28	39.20	0.54	73.30	35.65	60.13	29.74	1.02	74.80	36.37
70.10	22.86	2.07	70.38	48.22	0.46	72.88	35.26	70.62	46.15	0.53	72.82	35.23	70.23	35.11	1.00	72.91	35.27
80.44	25.97	2.10	79.98	54.53	0.47	72.89	34.76	80.10	52.21	0.53	72.64	34.64	79.15	39.53	1.00	72.07	34.37
90.02	29.23	2.08	89.65	61.33	0.46	72.84	35.03	90.32	58.82	0.54	72.91	35.06	89.92	44.91	1.00	72.62	34.92
99.96	32.36	2.09	100.11	68.37	0.46	72.87	34.88	99.69	64.81	0.54	72.92	34.91	100.63	50.15	1.01	72.62	34.76
110.12	35.79	2.08	110.26	75.44	0.46	72.86	35.08	110.19	71.78	0.54	72.92	35.11	109.75	54.82	1.00	72.71	35.01
120.30	39.09	2.08	119.63	81.83	0.46	72.88	35.08	120.25	78.36	0.53	72.89	35.09	120.10	59.91	1.00	72.86	35.07
129.93	42.10	2.09	129.67	88.57	0.46	72.89	34.94	130.10	84.71	0.54	72.85	34.92	130.18	64.83	1.01	72.81	34.90
139.87	45.36	2.08	140.00	95.68	0.46	72.87	34.98	140.55	91.55	0.54	72.85	34.96	139.65	69.55	1.01	72.88	34.98
149.97	48.61	2.09	150.03	102.65	0.46	72.78	34.90	149.99	97.65	0.54	72.86	34.94	150.24	74.81	1.01	72.85	34.94
160.15	51.82	2.09	159.70	109.10	0.46	72.83	34.84	160.32	104.32	0.54	72.84	34.84	159.78	79.44	1.01	72.89	34.87
170.17	55.11	2.09	170.00	116.21	0.46	72.81	34.88	170.23	110.81	0.54	72.85	34.89	170.30	84.74	1.01	72.86	34.90
179.95	58.29	2.09	180.08	123.20	0.46	72.77	34.86	179.69	116.88	0.54	72.91	34.93	180.11	89.58	1.01	72.95	34.95
189.69	61.35	2.09	190.40	130.21	0.46	72.75	34.77	190.06	123.59	0.54	72.87	34.83	189.77	94.45	1.01	72.70	34.75
199.75	64.59	2.09	200.11	136.66	0.46	72.83	34.80	200.37	130.31	0.54	72.85	34.81	200.30	99.61	1.01	72.79	34.78
210.39	68.15	2.09	210.11	143.65	0.46	72.81	34.89	210.24	136.75	0.54	72.91	34.93	210.29	104.64	1.01	72.88	34.92
220.11	71.30	2.09	220.26	150.56	0.46	72.82	34.89	219.86	143.05	0.54	72.89	34.92	220.12	109.54	1.01	72.88	34.92
230.16	74.41	2.09	230.47	157.35	0.46	72.84	34.80	230.24	149.67	0.54	72.88	34.82	230.27	114.53	1.01	72.75	34.76
240.03	77.80	2.09	240.20	164.05	0.46	72.90	34.96	240.31	156.39	0.54	72.89	34.96	240.09	119.53	1.01	72.88	34.95
249.86	80.95	2.09	250.06	170.75	0.46	72.90	34.94	250.06	162.65	0.54	72.91	34.94	249.86	124.35	1.01	72.88	34.93
259.95	84.03	2.09	260.01	177.53	0.46	72.84	34.79	259.97	169.11	0.54	72.82	34.78	260.38	129.47	1.01	72.77	34.76
270.02	87.36	2.09	270.57	184.71	0.46	72.87	34.85	270.13	175.67	0.54	72.88	34.85	269.47	133.99	1.01	72.86	34.85

Appendix D

Table D.4. Calibration experiment.

Initial Pressure P1, psig	Pressure P2, psig	Ratio	Known plug volume, cm³	Obtained plug volume	Error, frac	Error,%
60.16	32.40	0.86	35.18	34.29	0.026	2.591
80.07	43.11	0.86	35.18	34.27	0.026	2.649
89.95	48.42	0.86	35.18	34.26	0.027	2.686
100.17	53.89	0.86	35.18	34.22	0.028	2.800
110.18	59.28	0.86	35.18	34.23	0.028	2.784
121.01	65.11	0.86	35.18	34.23	0.028	2.775
130.52	70.23	0.86	35.18	34.23	0.028	2.766
140.36	75.52	0.86	35.18	34.23	0.028	2.778
150.04	80.73	0.86	35.18	34.23	0.028	2.774
160.28	86.22	0.86	35.18	34.22	0.028	2.819
169.98	91.44	0.86	35.18	34.22	0.028	2.815
179.95	96.77	0.86	35.18	34.19	0.029	2.882
189.99	102.07	0.86	35.18	34.13	0.031	3.072
200.41	107.73	0.86	35.18	34.17	0.030	2.959
209.84	112.82	0.86	35.18	34.18	0.029	2.923
219.90	118.24	0.86	35.18	34.19	0.029	2.904
229.78	123.48	0.86	35.18	34.15	0.030	3.019
249.82	134.19	0.86	35.18	34.12	0.031	3.106
259.68	139.42	0.86	35.18	34.09	0.032	3.199
269.99	144.96	0.86	35.18	34.09	0.032	3.193

Appendix E

Table E.1. Calibration error analysis.

Pressure error margin, psig		Pressure, psig									
		60.16	80.07	89.95	100.17	110.18	121.01	130.52	140.36	150.04	160.28
	0.1	0.269	0.202	0.180	0.162	0.148	0.134	0.125	0.116	0.108	0.102
	0.5	1.327	1.003	0.894	0.806	0.733	0.668	0.620	0.577	0.540	0.506
	1	2.615	1.982	1.771	1.598	1.455	1.326	1.231	1.146	1.073	1.006
	2	5.078	3.877	3.471	3.139	2.862	2.613	2.427	2.262	2.119	1.989
	5	11.676	9.088	8.191	7.448	6.821	6.252	5.826	5.444	5.113	4.810
	0.1	169.98	179.95	189.99	200.41	209.84	219.90	229.78	249.82	259.68	269.99
	0.5	0.096	0.091	0.086	0.082	0.078	0.074	0.071	0.066	0.063	0.061
	1	0.477	0.452	0.430	0.407	0.388	0.370	0.355	0.328	0.316	0.304
	2	0.949	0.899	0.856	0.809	0.773	0.737	0.708	0.653	0.630	0.606
	5	1.878	1.779	1.695	1.604	1.532	1.462	1.404	1.296	1.251	1.204
		4.549	4.317	4.119	3.903	3.732	3.566	3.429	3.171	3.062	2.949

Table E.2. Calibration error analysis.

Pressure error margin, psig	V1 error,%	Pressure, psig							
		60.13	69.89	80.22	90.34	99.67	110.43	119.57	130.41
	0.1	0.380	0.331	0.291	0.255	0.229	0.208	0.189	0.176
	0.5	1.901	1.657	1.454	1.277	1.144	1.040	0.945	0.879
	1	3.808	3.317	2.911	2.557	2.289	2.082	1.892	1.760
	2	7.636	6.650	5.834	5.123	4.585	4.171	3.788	3.524
	5	19.228	16.730	14.672	12.873	11.513	10.471	9.504	8.842
		140.16	150.04	160.35	169.69	180.35	190.19	200.42	
	0.1	0.164	0.154	0.143	0.134	0.128	0.121	0.115	
	0.5	0.822	0.769	0.716	0.672	0.639	0.604	0.573	
	1	1.645	1.539	1.433	1.344	1.279	1.209	1.147	
	2	3.293	3.082	2.869	2.691	2.561	2.421	2.296	
	5	8.260	7.729	7.194	6.747	6.420	6.067	5.754	

Table E.3. Calibration error analysis.

Pressure error margin, psig	V2 error,%	Pressure, psig							
		60.13	69.89	80.22	90.34	99.67	110.43	119.57	130.41
	0.1	0.137	0.125	0.111	0.096	0.085	0.077	0.069	0.065
	0.5	0.681	0.621	0.551	0.478	0.421	0.383	0.346	0.325
	1	1.350	1.232	1.096	0.951	0.838	0.762	0.689	0.647
	2	2.656	2.430	2.166	1.882	1.659	1.511	1.367	1.284
	5	6.333	5.830	5.228	4.556	4.027	3.680	3.335	3.140
		140.16	150.04	160.35	169.69	180.35	190.19	200.42	

0.1	0.062	0.058	0.053	0.050	0.048	0.045	0.043	
0.5	0.308	0.289	0.266	0.249	0.240	0.225	0.215	
1	0.614	0.577	0.531	0.496	0.479	0.450	0.428	
2	1.220	1.146	1.056	0.986	0.952	0.895	0.852	
5	2.987	2.809	2.592	2.422	2.341	2.202	2.100	

Table E.4. Calibration error analysis.

	V3 error,%	Pressure, psig						
		60.13	**69.89**	**80.22**	**90.34**	**99.67**	**110.43**	**119.57**	**130.41**
Pressure error margin, psig	**0.1**	1.503	1.868	1.627	1.370	1.232	1.143	1.063	1.032
	0.5	7.409	9.232	8.051	6.790	6.108	5.674	5.278	5.127
	1	14.567	18.207	15.902	13.430	12.096	11.245	10.468	10.176
	2	28.178	35.425	31.031	26.284	23.722	22.089	20.596	20.047
	5	64.127	81.895	72.309	61.737	56.041	52.424	49.096	47.956
		140.16	**150.04**	**160.35**	**169.69**	**180.35**	**190.19**	**200.42**	
	0.1	0.955	0.870	0.822	0.752	0.698	0.616	0.622	
	0.5	4.746	4.325	4.092	3.740	3.475	3.066	3.099	
	1	9.426	8.593	8.133	7.437	6.911	6.099	6.166	
	2	18.589	16.961	16.066	14.701	13.670	12.070	12.210	
	5	44.606	40.802	38.740	35.520	33.078	29.253	29.645	

Appendix F

Sequence no. 1	Sequence no. 2	Sequence no. 3
#intrinsic permeability	$ka4=$ki*(1+%b% / $pp4);	"$p15 $pv $km15 \n" .
$ki=1;	$ka5=$ki*(1+%b% / $pp5);	"$p16 $pv $km16 \n" .
#pressure values in atmos	$ka6=$ki*(1+%b% / $pp6);	"$p17 $pv $km17 \n" .
$p1=1;	$ka7=$ki*(1+%b% / $pp7);	"$p18 $pv $km18 \n" .
$p2=2;	$ka8=$ki*(1+%b% / $pp8);	"$p19 $pv $km19 \n" .
$p3=3;	$ka9=$ki*(1+%b% / $pp9);	"$p100 $pv $km100 \n" .
$p4=4;	$ka10=$ki*(1+%b% / $pp10);	"/\n" ;
$p5=5;	$ka11=$ki*(1+%b% / $pp11);	return $rocktab_table;
$p6=6;	$ka12=$ki*(1+%b% / $pp12);	
$p7=7;	$ka13=$ki*(1+%b% / $pp13);	
$p8=8;	$ka14=$ki*(1+%b% / $pp14);	
$p9=9;	$ka15=$ki*(1+%b% / $pp15);	
$p10=10;	$ka16=$ki*(1+%b% / $pp16);	
$p11=11;	$ka17=$ki*(1+%b% / $pp17);	
$p12=12;	$ka18=$ki*(1+%b% / $pp18);	
$p13=13;	$ka19=$ki*(1+%b% / $pp19);	
$p14=14;	$ka100=$ki*(1+%b% / $pp100);	
	#permeability multiplier kmult	

$p15=15;
$p16=16;
$p17=17;
$p18=18;
$p19=19;
$p100=100;
#pvmult
$pv=1;
#pressure values in psi
$pp1=$p1*14.7;
$pp2=$p2*14.7;
$pp3=$p3*14.7;
$pp4=$p4*14.7;
$pp5=$p5*14.7;
$pp6=$p6*14.7;
$pp7=$p7*14.7;
$pp8=$p8*14.7;
$pp9=$p9*14.7;
$pp10=$p10*14.7;
$pp11=$p11*14.7;
$pp12=$p12*14.7;
$pp13=$p13*14.7;
$pp14=$p14*14.7;
$pp15=$p15*14.7;
$pp16=$p16*14.7;
$pp17=$p17*14.7;
$pp18=$p18*14.7;
$pp19=$p19*14.7;
$pp100=$p100*14.7;
#apparent permeability
ka = ki*(1+b/pp)
$ka1=$ki*(1+%b%/ $pp1);
$ka2=$ki*(1+%b% / $pp2);
$ka3=$ki*(1+%b% / $pp3);
	$km1=$ka1 / $ki;
	$km2=$ka2 / $ki;
	$km3=$ka3 / $ki;
	$km4=$ka4 / $ki;
	$km5=$ka5 / $ki;
	$km6=$ka6 / $ki;
	$km7=$ka7 / $ki;
	$km8=$ka8 / $ki;
	$km9=$ka9 / $ki;
	$km10=$ka10 / $ki;
	$km11=$ka11 / $ki;
	$km12=$ka12 / $ki;
	$km13=$ka13 / $ki;
	$km14=$ka14 / $ki;
	$km15=$ka15 / $ki;
	$km16=$ka16 / $ki;
	$km17=$ka17 / $ki;
	$km18=$ka18 / $ki;
	$km19=$ka19 / $ki;
	$km100=$ka100 / $ki;
	#constructing the table
	$rocktab_table = "ROCKTAB\n"
	.
	"$p1 $pv $km1 \n" .
	"$p2 $pv $km2 \n" .
	"$p3 $pv $km3 \n" .
	"$p4 $pv $km4 \n" .
	"$p5 $pv $km5 \n" .
	"$p6 $pv $km6 \n" .
	"$p7 $pv $km7 \n" .
	"$p8 $pv $km8 \n" .
	"$p9 $pv $km9 \n" .
	"$p10 $pv $km10 \n" .
	"$p11 $pv $km11 \n" .
	"$p12 $pv $km12 \n" .
	"$p13 $pv $km13 \n" .
	"$p14 $pv $km14 \n" .	

Appendix G

Table G.1. Main SCAL results of the shale samples used in the research.

Sample	BET, m^2g^{-1}	Bulk density (Hg), g/cm^3	Grain density (Hg), g/cm^3	Grain density (WP), g/cm^3	TOC, wt%	Clay + organic, wt%	Clay + organics / (carbonate + quartz +organics), wt%	Weight organics, wt%
EBN1	0.53			2.78	0.78			0.82
EBN3	6.43	2.42	2.6	2.69	2.24	24.5	0.3	2.66
EBN4	6.41	2.75		2.64	0.24	10.0	0.1	0.26
EBN5	2.33	2.66		2.67	1.71	11.4	0.1	2.10
EBN7	6.80	2.58		2.66	2.33	16.8	0.2	2.91
EBN9	12.11	2.52		2.49	4.33	28.5	0.3	4.97
EBN13	1.31	2.40	2.41	2.43	7.93	41.9	0.5	9.47
EBN14	1.72	2.45	2.48		6.81	50.5	0.5	8.43
EBN16	3.82				5.45			
EBN18	8.80	2.37		2.86	7.76	16.9	0.2	9.62
EBN19	9.30	2.18	2.49	2.56	5.12	31.5	0.4	6.96
EBN20	6.03	2.45	6.18	2.61	5.67	25.4	0.3	7.02
CASP	25.70	2.44	2.68	2.72	1.76	57.6	0.6	2.22
ABE	5.10	2.64	2.70	2.75	0.67	46.1	0.5	0.87
EBN21	8.87	1.95	1.31	2.32	10.53	40.9	0.5	14.02
EBN22	1.27	2.42	1.33	2.42	6.51	52.6	0.6	7.82
EBN23	1.28	2.51	11.75	2.55	5.15	43.7	0.5	6.14

EBN24	1.30	2.37	9.21	2.46	7.96	25.4	0.3	9.49
EBN25	11.45	2.58	3.14	2.72	1.18	36.5	0.4	2.22
EBN26	8.97	2.62	5.90	2.77	1.23	41.7	0.5	1.97
EBN27	3.14			2.75	4.46	7.9	0.1	5.59
EBN28	5.76	2.30	13.52	2.61	7.20	43.6	0.5	9.31
EBN29	11.50	2.09	8.78	2.48	5.81	52.7	0.6	7.60
EBN30	13.20	2.40	7.96	2.62	4.17	54.8	0.6	5.52
EBN31	8.60	2.06	2.39	2.58	9.13	25.6	0.3	11.98
EBN32	7.80	2.00	2.39	2.62	6.10	25.0	0.3	8.48
EBN33	6.13	2.08	7.98	2.59	9.23	23.9	0.3	12.12
EBN34	7.91	2.10	8.59	2.34	11.07	30.1	0.4	14.45
EBN35	7.82	1.96	2.28	2.21	13.24	28.7	0.4	16.87
EBN36	8.40	2.22	12.09	2.64	4.66	19.8	0.2	6.51
CHE1	11.61	2.65	2.68	2.58	2.26	35.8	0.4	2.74
CHE2	11.78	2.53	2.62		2.54	52.7	0.5	3.07
CHE3	5.18	2.40	2.56		4.43	48.9	0.5	5.03
BC1	9.68	2.51	2.56	2.86	2.63	17.0	0.2	2.95
BC2	14.09	2.51	2.56	2.87	2.20	22.2	0.2	2.53
BC3	10.40	2.37	2.52	2.90	2.62	22.7	0.2	2.96
BC4	16.19	2.43	2.61	2.90	2.71	33.3	0.4	3.05
BC5	18.47	2.53	2.58	2.87	2.87	37.7	0.4	3.21
BC6	6.03	2.63	2.69	3.07	0.48	26.4	0.3	0.63
BC7	12.08	2.64	2.67	2.99	1.92	18.1	0.2	2.23

BC8	16.40	2.41	2.5	3.10	3.22	23.0	0.2	3.61
BC9	24.03	2.39	2.49	2.83	5.28	28.1	0.3	5.83
BC10	17.62			3.40	4.35	24.9	0.3	4.86
BC11	16.66	2.53	2.59	2.97	2.12	37.8	0.4	2.39
NEX7	4.79	2.52	7.95	2.94	3.27	38.8	0.4	3.80
NEX15	5.77	2.44	0.00	2.81	3.21	33.9	0.4	3.71
NEX33	7.17	2.46	0.00	3.04	2.01	23.4	0.2	2.42
NEX205	7.77	2.20	0.00	2.68	9.27	38.2	0.4	11.10

Appendix H

Table H.1. Main SCAL results of the shale samples used in the research.

	A	B	BC	BD	BE	BF	BG	BH	BI	BJ	BK	BL	BM	BN	BS	BT	BU
1																	
2		Sample	Quartz, %	Albite, %	Microcline, %	Calcite, %	Dolomite, %	Mica, %	Illite-smectite, %	Kaolinite, %	Chlorite, %	Pyrite, %	Siderite, %	Total, %	Weight organics, g	Grain fraction	DensityXR D+C, g/cm³
3			2.65	2.63	2.63	2.71	2.87	2.82	2.55	2.44	2.84	4.84	3.74		1.15		
14	11	EBN20	10.10	1.88	0.00	8.40	46.21	16.42	5.14	5.01	0.00	4.36	0.00	97.53	7.02	0.95	2.56
36	33	CHE2	26.20	8.90	0.00	12.00	0.00	38.00	4.80	0.00	13.10	0.00	0.00	103.00	2.26	0.95	2.65
37	34	CHE3	32.00	6.20	0.00	3.10	2.10	33.30	14.10	0.00	4.20	5.40	0.00	100.40	2.26	0.97	2.68
52	47	NEX7	44.50	1.70	1.90	7.60	1.60	3.10	32.50	3.90	0.80	2.20	0.20	100.00	3.80	0.96	2.52
53	48	NEX15	44.80	1.80	0.00	9.90	3.20	2.70	26.70	4.90	0.80	4.90	0.20	99.90	3.71	0.96	2.56
54	49	NEX33	7.80	2.90	0.60	59.40	3.10	2.60	20.20	0.00	1.20	2.20	0.00	100.00	2.42	0.98	2.62

	B	BV	BW	BX	BY	BZ	CA	CB	CC	CD	CE	CF	CG	CH	CI	CJ
1							Rock Eval									
2	Sample	S1	S2	S3	T max	Tmax (S2)	HI	OI	PI	S2/S3	Weight loss on acidification (%)	C (wt%)	S (wt%)	TOC (corrected), %	atomic C/H ratio	atomic C/O
3		mg/g	mg/g	mg/g	deg C											
14	EBN20	2.77	36.47	0.69	433	477	643.57	12.18	0.07	52.86	63.22	15.41	6.36	5.67	1.47	0.09
36	CHE2	0.33	0.61	0.46	413	457	26.95	20.32	0.35	1.33	29.20	3.20	0.98	2.26		
37	CHE3	0.33	0.61	0.46	413	457	26.95	20.32	0.35	1.33	29.20	3.20	0.98	2.26		
52	NEX7	1.29	6.4	0.26	438	481	195.95	7.96	0.17	24.62	18.97	4.03	1.13	3.27	0.84	0.07
53	NEX15	0.85	5.47	0.24	441	484	170.44	7.48	0.13	22.79	12.92	3.69	2.10	3.21	0.81	0.07
54	NEX33	0.43	4.7	0.29	441	484	233.44	14.40	0.08	16.21	66.14	5.95	1.46	2.01	0.89	0.10

	B	BC	BD	BE	BF	BG	BH	BI	BJ	BK	BL	BM	BN	BS	BT
1															
2	Sample	Quartz, %	Albite, %	Microcline, %	Calcite, %	Dolomite, %	Mica, %	Illite-smectite, %	Kaolinite, %	Chlorite, %	Pyrite, %	Siderite, %	Total, %	Weight organics, g	Grain fraction
3		2.65	2.63	2.63	2.71	2.87	2.82	2.546	2.439	2.838	4.84	3.74		1.15	
14	EBN20	10.1	1.88	0	8.4	46.21	16.42	5.14	5.013	0	4.36	0	97.52	=CH14*(1+CI14/12+	=((100-BS14)/BN14
36	CHE2	26.2	8.9	0	12	0	38	4.8	0	13.1	0	0	=SUM(BC36:BM36)	=CH36*(1+CI36/12+	=((100-BS36)/BN36
37	CHE3	32	6.2	0	3.1	2.1	33.3	14.1	0	4.2	5.4	0	=SUM(BC37:BM37)	=CH37*(1+CI37/12+	=((100-BS37)/BN37
52	NEX7	44.5	1.7	1.9	7.6	1.6	3.1	32.5	3.9	0.8	2.2	0.2	100	=CH52*(1+CI52/12+	=((100-BS52)/BN52
53	NEX15	44.8	1.8	0	9.9	3.2	2.7	26.7	4.9	0.8	4.9	0.2	99.9	=CH53*(1+CI53/12+	=((100-BS53)/BN53
54	NEX33	7.8	2.9	0.6	59.4	3.1	2.6	20.2	0	1.2	2.2	0	100	=CH54*(1+CI54/12+	=((100-BS54)/BN54

BU
DensityXRD+C, g/cm³

```
=100/((BT14*(BC14/$BC$3+BD14/$BD$3+BE14/$BE$3+BF14/$BF$3+BG14/$BG$3+BH14/$BH$3+BI14/$BI$3+BJ14/$BJ$3+BK14/$BK$3+BL14/$BL$3+BM14/$BM$3))+BS14/$BS$3)
=100/((BT36*(BC36/$BC$3+BD36/$BD$3+BE36/$BE$3+BF36/$BF$3+BG36/$BG$3+BH36/$BH$3+BI36/$BI$3+BJ36/$BJ$3+BK36/$BK$3+BL36/$BL$3+BM36/$BM$3))+BS36/$BS$3)
=100/((BT37*(BC37/$BC$3+BD37/$BD$3+BE37/$BE$3+BF37/$BF$3+BG37/$BG$3+BH37/$BH$3+BI37/$BI$3+BJ37/$BJ$3+BK37/$BK$3+BL37/$BL$3+BM37/$BM$3))+BS37/$BS$3)
=100/((BT52*(BC52/$BC$3+BD52/$BD$3+BE52/$BE$3+BF52/$BF$3+BG52/$BG$3+BH52/$BH$3+BI52/$BI$3+BJ52/$BJ$3+BK52/$BK$3+BL52/$BL$3+BM52/$BM$3))+BS52/$BS$3)
=100/((BT53*(BC53/$BC$3+BD53/$BD$3+BE53/$BE$3+BF53/$BF$3+BG53/$BG$3+BH53/$BH$3+BI53/$BI$3+BJ53/$BJ$3+BK53/$BK$3+BL53/$BL$3+BM53/$BM$3))+BS53/$BS$3)
=100/((BT54*(BC54/$BC$3+BD54/$BD$3+BE54/$BE$3+BF54/$BF$3+BG54/$BG$3+BH54/$BH$3+BI54/$BI$3+BJ54/$BJ$3+BK54/$BK$3+BL54/$BL$3+BM54/$BM$3))+BS54/$BS$3)
```

	B	BV	BW	BX	BY	BZ	CA	CB	CC	CD	CE	CF	CG	CH	CI	CJ
1							Rock Eval									
2	Sample	S1	S2	S3	T max	Tmax (S2)	HI	OI	PI	S2/S3	Weight loss on acidification (%)	C (wt%)	S (wt%)	TOC (corrected), %	atomic C/H ratio	atomic C/O
3		mg/g	mg/g	mg/g	deg C											
14	EBN20	2.77	36.47	0.69	433	477	=BW14/CH14*100	=BX14/CH14*100	=+BV14/(BV14+BW14)	=+BW14/BX14	63.22	15.41	6.36	=CF14*(100-CE14)/100	=0.0014*CA14+0.5665	=0.0041*CB14+0.0372
36	CHE2	0.33	0.61	0.46	413	457	=BW36/CH36*100	=BX36/CH36*100	=+BV36/(BV36+BW36)	=+BW36/BX36	29.2	3.1975	0.98	=CF36*(100-CE36)/100		
37	CHE3	0.33	0.61	0.46	413	457	=BW37/CH37*100	=BX37/CH37*100	=+BV37/(BV37+BW37)	=+BW37/BX37	29.203	3.1975	0.98	=CF37*(100-CE37)/100		
52	NEX7	1.29	6.4	0.26	438	481	=BW52/CH52*100	=BX52/CH52*100	0.17	24.62	18.97	4.031	1.13	=CF52*(100-CE52)/100	=0.0014*CA52+0.5665	=0.0041*CB52+0.0372
53	NEX15	0.85	5.47	0.24	441	484	=BW53/CH53*100	=BX53/CH53*100	0.13	22.79	12.92	3.6855	2.1	=CF53*(100-CE53)/100	=0.0014*CA53+0.5665	=0.0041*CB53+0.0372
54	NEX33	0.43	4.7	0.29	441	484	=BW54/CH54*100	=BX54/CH54*100	0.08	16.21	66.14	5.946	1.46	=CF54*(100-CE54)/100	=0.0014*CA54+0.5665	=0.0041*CB54+0.0372

Appendix I

Table I.1. Pressure expansion experiment results.

Sample	Setup	Gas	AR or Dry	Weight chips, g	Bulk density, Hg injection, cm^3/g	Bulk density, GRI pressures, cm^3/g	Volume chips density ,weight/bulk density Hg	Volume chips (pressures), cm^3	Po, psig	P1 (V1), psig	P2 (V2), psig	P3 (extrapolated), psig	P4 (final), psig	V1, cm^3	V2, cm^3	Vg, cm^3	Grain density (Bulk volume), cm^3/g
BC01	X	He	AR	78.86	2.51	2.61	31.42	30.26	131.14	239.05	0.00	129.50	129.50	50.31	72.82	30.26	2.61
BC01	G3	He	Dry	69.70	2.51	2.48	27.77	28.16	120.46	246.20	0.00	121.12	117.23	34.94	64.24	25.80	2.70
BC01	G3	He	Dry	69.70	2.51	2.60	27.77	26.85	59.77	-0.21	117.23	60.50	60.75	34.94	64.24	26.53	2.63
BC02	X	He	AR	87.33	2.55	2.58	34.25	33.85	133.02	235.00	0.00	132.43	131.30	50.31	72.82	33.08	2.64
BC02	G2	He	Dry	69.89	2.50	2.53	27.96	27.65	127.86	246.24	0.00	127.37	124.00	41.07	65.98	25.49	2.74
BC02	G2	He	Dry	69.89	2.50	2.60	27.96	26.90	59.40	-0.25	123.83	60.25	60.68	41.07	65.98	26.36	2.65
BC03	X	He	AR	80.56	2.37	2.56	33.99	31.48	137.27	243.20	0.00	133.50	132.30	50.31	72.82	30.65	2.63
BC03	G2	He	Dry	66.12	2.37	2.69	27.90	24.62	127.96	246.60	0.00	122.88	121.95	41.07	65.98	24.00	2.76
BC03	G2	He	Dry	66.12	2.37	2.57	27.90	25.77	58.54	-0.19	121.88	60.20	60.84	41.07	65.98	24.91	2.65
BC04	X	He	AR	80.07	2.57	2.56	31.16	31.33	133.77	244.55	0.00	134.02	132.75	50.31	72.82	30.45	2.63
BC04	G3	He	Dry	69.00	2.57	2.68	26.85	25.75	118.77	245.87	0.00	116.99	115.65	34.94	64.24	24.90	2.77

BC04	G3	He	Dry	69.00	2.57	2.58	26.85	26.71	59.63	-0.21	115.56	59.74	60.53	34.94	64.24	25.67	2.69
BC05	X	He	AR	87.33	2.53	2.52	34.52	34.72	133.94	235.90	0.00	134.25	133.00	50.31	72.82	33.89	2.58
BC05	G3	He	Dry	73.90	2.53	2.63	29.21	28.15	123.03	246.38	0.00	121.19	120.11	34.94	64.24	27.51	2.69
BC05	G3	He	Dry	73.90	2.53	2.59	29.21	28.55		-0.17	120.13	60.61	61.60	34.94	64.24	27.36	2.70
BC06	X	He	AR	85.95	2.68	2.67	32.07	32.18	135.03	244.40	0.00	135.20	134.85	50.31	72.82	31.95	2.69
BC06	G2	He	Dry	74.26	2.66	2.74	27.92	27.11	79.19	152.58	0.00	78.39	78.07	41.07	65.98	26.77	2.77
BC06	G2	He	Dry	74.26	2.66	2.73	27.92	27.18	131.21	180.47	78.07	130.72	130.52	41.07	65.98	26.87	2.76
BC06	G2	He	Dry	74.26	2.66	2.69	27.92	27.56	62.52	-0.49	130.52	62.83	63.09	41.07	65.98	27.25	2.73
BC07	X	He	AR	79.36	2.63	2.63	30.17	30.20	134.07	247.70	0.00	134.10	133.45	50.31	72.82	29.75	2.67
BC07	G2	He	Dry	73.35	2.61	2.69	28.10	27.23	79.15	152.13	0.00	78.29	77.73	41.07	65.98	26.66	2.75
BC07	G2	He	Dry	73.35	2.61	2.71	28.10	27.06	132.32	182.66	77.73	131.61	131.22	41.07	65.98	26.49	2.77
BC07	G2	He	Dry	73.35	2.61	2.66	28.10	27.54	62.70	-0.49	131.22	63.19	63.78	41.07	65.98	26.83	2.73
BC08	X	He	AR	75.21	2.41	2.51	31.21	29.96	132.78	242.60	0.00	131.00	129.20	50.31	72.82	28.66	2.62
BC08	G2	He	Dry	69.98	2.41	2.58	29.04	27.10	128.94	244.91	0.00	125.81	123.53	41.07	65.98	25.62	2.73
BC08	G2	He	Dry	69.98	2.41	2.52	29.04	27.73	58.38	-0.21	123.53	59.46	60.49	41.07	65.98	26.44	2.65
BC09	X	He	AR		2.39				0.00					50.31	72.82		
BC09	G3	He	Dry	70.02	2.39	2.47	29.30	28.36	122.53	245.07	0.00	120.91	119.45	34.94	64.24	27.49	2.55
BC09	G3	He	Dry	70.02	2.39	2.47	29.30	28.32	59.69	-0.17	119.53	60.51	61.59	34.94	64.24	27.00	2.59
BC09		He		76.21	2.39		31.89		123.52								
BC10	G2	He	Dry	79.39	2.91	3.06	27.27	25.91	126.46	245.62	0.00	124.33	123.43	41.07	65.98	25.32	3.14
BC10	G2	He	Dry	79.39	2.91	3.06	27.27	25.91	59.82	-0.21	123.52	60.89	61.49	41.07	65.98	25.12	3.16
BC11	X	He	AR	82.95	2.53	2.60	32.79	31.87	134.55	241.60	0.00	133.20	132.50	50.31	72.82	31.39	2.64
BC11	G2	He	Dry	68.54	2.51	2.65	27.31	25.88	78.64	152.69	0.00	77.26	76.40	41.07	65.98	24.96	2.75
BC11	G2	He	Dry	68.54	2.51	2.65	27.31	25.88	129.19	178.89	76.40	128.26	127.70	41.07	65.98	25.01	2.74
BC11	G2	He	Dry	68.54	2.51	2.64	27.31	25.94	172.50	214.68	127.70	171.75	171.31	41.07	65.98	25.13	2.73
BC11	G2	He	Dry	68.54	2.51	2.60	27.31	26.38	82.83	-0.49	171.31	83.84	84.53	41.07	65.98	25.75	2.66

CHE2	X	He	AR	79.72	2.53	2.60	31.51	30.64	130.53	237.70	0.00	129.30	128.20	50.31	72.82	29.85	2.67
CHE2	G3	He	AR	67.21	2.53	2.67	26.57	25.14	72.13	149.90	0.00	70.74	69.75	34.94	64.24	24.09	2.79
CHE2	G3	He	AR	67.21	2.53	2.65	26.57	25.36	123.12	180.67	69.76	122.25	121.77	34.94	64.24	24.67	2.72
CHE2	G3	He	AR	67.21	2.53	2.65	26.57	25.39	163.93	209.35	121.81	163.26	162.79	34.94	64.24	24.54	2.74
CHE2	G3	He	AR	67.21	2.53	2.60	26.57	25.87	84.26	-0.37	162.75	85.00	86.23	34.94	64.24	24.69	2.72
CHE2	G2	He	Dry	64.81	2.52	2.67	25.72	24.29	122.97	243.51	0.00	120.85	119.55	41.07	65.98	23.39	2.77
CHE2	G2	He	Dry	64.94	2.52	2.64	25.77	24.59	78.09	154.54	0.00	76.97	76.00	41.07	65.98	23.53	2.76
CHE2	G2	He	Dry	64.94	2.52	2.64	25.77	24.60	129.70	182.22	76.06	128.94	128.39	41.07	65.98	23.73	2.74
CHE2	G2	He	Dry	64.94	2.52	2.66	25.77	24.44	170.28	211.30	128.38	169.61	169.20	41.07	65.98	23.61	2.75
CHE2	G2	He	Dry	64.94	2.52	2.60	25.77	24.96	83.45	-0.48	169.18	84.30	85.23	41.07	65.98	24.05	2.70
CHE3	G3	N2	AR	63.75	2.40	2.66	26.56	23.98	72.25	150.16	0.00	69.77	68.91	34.94	64.24	23.04	2.77
CHE3	G3	N2	AR	63.75	2.40	2.66	26.56	23.98	122.71	180.73	68.91	120.87	120.03	34.94	64.24	22.75	2.80
CHE3	G3	N2	AR	63.75	2.40	2.67	26.56	23.90	163.54	210.45	120.03	162.00	161.48	34.94	64.24	22.96	2.78
CHE3	G3	N2	AR	63.75	2.40	2.69	26.56	23.74	199.44	240.38	161.48	198.02	197.62	34.94	64.24	22.90	2.78
CHE3	G3	He	AR	63.73	2.40	2.62	26.56	24.33	72.21	150.10	0.00	70.07	69.56	34.94	64.24	23.79	2.68
CHE3	G3	He	AR	63.73	2.40	2.62	26.56	24.35	122.49	179.57	69.56	120.93	120.37	34.94	64.24	23.53	2.71
CHE3	G3	He	AR	63.73	2.40	2.60	26.56	24.50	163.57	210.16	120.37	162.38	162.21	34.94	64.24	24.20	2.63
CHE3	G3	He	AR	63.73	2.40	2.63	26.56	24.21	199.77	240.29	162.21	198.60	197.91	34.94	64.24	22.77	2.80
CHE3	G3	He	Dry	63.35	2.38	2.67	26.62	23.75	71.84	149.20	0.00	69.11	68.54	34.94	64.24	23.13	2.74
CHE3	G3	He	Dry	63.35	2.38	2.64	26.62	23.99	122.10	179.77	68.54	120.23	119.87	34.94	64.24	23.46	2.70
CHE3	G3	He	Dry	63.35	2.38	2.66	26.62	23.84	163.10	209.66	119.87	161.51	161.39	34.94	64.24	23.62	2.68
CHE3	G3	He	Dry	63.35	2.38	2.66	26.62	23.80	199.42	240.37	161.39	198.00	197.80	34.94	64.24	23.39	2.71
CHE3	G3	He	Dry	63.35	2.38	2.62	26.62	24.19	102.48	-0.15	197.79	105.57	106.16	34.94	64.24	23.71	2.67
CHE3	G3	N2	Dry	63.52	2.37	2.65	26.80	23.93	72.66	150.52	0.00	69.89	68.44	34.94	64.24	22.34	2.84
CHE3	G3	N2	Dry	63.52	2.37	2.66	26.80	23.87	122.39	180.20	68.44	120.29	119.34	34.94	64.24	22.46	2.83
CHE3	G3	N2	Dry	63.52	2.37	2.67	26.80	23.78	163.07	209.93	119.34	161.32	160.65	34.94	64.24	22.56	2.82

CHE3	G3	N2	Dry	63.52	2.37	2.67	26.80	23.79	204.14	250.74	160.65	202.40	201.83	34.94	64.24	22.75	2.79
CHE3	G3	N2	AR	63.75	2.40	2.65	26.56	24.03	102.45	-0.19	197.62	105.65	106.83	34.94	64.24	23.05	2.77
CHE3	G3	He	AR	63.73	2.39	2.57	26.67	24.82	102.45	-0.21	197.91	104.82	105.45	34.94	64.24	24.31	2.62
CHE3	G3	N2	Dry	63.52	2.37	2.66	26.80	23.91	104.28	-0.25	201.83	108.02	109.32	34.94	64.24	22.85	2.78
EBN1	X	He	AR	73.17	2.67	2.74	27.37	26.74	126.94	241.60	0.00	126.10	126.10	50.31	72.82	26.74	2.74
EBN7	G2	He	Dry	72.44	2.56	2.64	28.30	27.43	81.32	155.93	0.00	80.44	80.15	41.07	65.98	27.15	2.67
EBN7	G2	He	Dry	72.44	2.56	2.65	28.30	27.30	134.26	183.93	80.12	133.58	133.40	41.07	65.98	27.03	2.68
EBN7	G2	He	Dry	72.44	2.56	2.61	28.30	27.72	63.56	-0.49	133.38	64.07	64.23	41.07	65.98	27.54	2.63
EBN16	G2	He	Dry	35.90	2.00	2.47	17.95	14.55	70.89	153.78	0.00	68.28	67.84	41.07	65.98	13.95	2.57
EBN16	G2	He	Dry	35.90	2.00	2.12	17.95	16.92	119.70	180.35	67.84	119.11	117.61	41.07	65.98	14.21	2.53
EBN16	G2	He	Dry	35.90	2.00	2.27	17.95	15.79	63.40	0.00	117.61	64.68	65.01	41.07	65.98	15.21	2.36
EBN19	X	He	AR	70.17	2.29	2.41	30.64	29.07	130.99	240.80	0.00	128.80	128.50	50.31	72.82	28.85	2.43
EBN19	G2	He	Dry	51.04	2.14	2.50	23.85	20.44	121.46	246.05	0.00	116.68	116.50	41.07	65.98	20.31	2.51
EBN19	G2	He	Dry	51.04	2.14	2.50	23.85	20.41	182.01	249.31	116.40	179.40	179.28	41.07	65.98	20.23	2.52
EBN19	G2	He	Dry	51.04	2.14	2.48	23.85	20.56	210.55	242.89	179.02	209.35	209.25	41.07	65.98	20.27	2.52
EBN20	G3	He	AR	60.03	2.50	2.52	24.01	23.82	113.32	243.79	0.00	113.04	111.84	34.94	64.24	23.02	2.61
EBN20	G3	He	AR	60.03	2.50	2.45	24.01	24.52	171.11	239.33	111.86	171.51	170.45	34.94	64.24	23.16	2.59
EBN20	G3	He	AR	60.03	2.50	2.52	24.01	23.81	203.03	240.97	170.07	202.94	202.53	34.94	64.24	22.85	2.63
EBN20	G2	He	Dry	57.32	2.45	2.62	23.40	21.90	177.96	243.68	114.58	176.85	176.63	41.07	65.98	21.60	2.65
EBN20	G2	He	Dry	57.32	2.45	2.41	23.40	23.77	117.28	238.87	0.00	117.80	114.73	41.07	65.98	21.54	2.66
EBN20	G2	He	Dry	57.32	2.45	2.62	23.40	21.92	211.20	247.10	176.57	210.60	210.48	41.07	65.98	21.60	2.65
EBN20	G2	He	AR	63.48	2.50	2.58	25.39	24.63	115.34	229.32	0.00	114.27	113.80	41.07	65.98	24.29	2.61
EBN20	G2	He	AR	63.48	2.50	2.59	25.39	24.46	181.04	247.51	113.79	180.29	180.21	41.07	65.98	24.36	2.61
EBN20	G2	He	AR	63.48	2.50	2.62	25.39	24.26	200.44	220.60	180.04	200.16	200.08	41.07	65.98	23.93	2.65
EBN20	X	He	AR	78.14	2.50	2.60	31.26	30.08	127.21	232.30	0.00	125.60	125.60	50.31	72.82	30.08	2.60
EBN20	G3	CH4	AR	67.42	2.47	2.70	27.33	24.98	75.65	155.57	0.00	73.25	72.67	34.94	64.24	24.38	2.76

EBN20	G3	CH4	AR	67.42	2.47	2.75	27.33	24.55	37.21	-0.25	72.67	38.53	38.61	34.94	64.24	24.37	2.77
EBN21	G2	He	Dry	34.92	1.95	2.20	17.91	15.88	112.33	243.80	0.00	109.83	108.70	41.07	65.98	14.93	2.34
EBN21	G2	He	Dry	34.92	1.95	2.20	17.91	15.86	172.45	247.19	108.60	171.02	170.23	41.07	65.98	14.69	2.38
EBN21	G2	He	Dry	34.92	1.95	2.19	17.91	15.95	203.88	243.33	170.18	203.16	202.78	41.07	65.98	14.88	2.35
EBN21	G2	He	AR	35.66	1.95	2.18	18.28	16.36	110.60	239.04	0.00	108.25	107.77	41.07	65.98	15.95	2.23
EBN21	G2	He	AR	35.66	1.95	2.22	18.28	16.03	168.07	238.07	107.80	166.58	166.08	41.07	65.98	15.25	2.34
EBN21	G2	He	AR	35.66	1.95	2.13	18.28	16.72	205.74	251.88	166.00	205.05	204.55	41.07	65.98	15.55	2.29
EBN22	G2	He	AR	55.85	2.42	2.46	23.08	22.71	107.79	220.38	0.00	107.32	107.03	41.07	65.98	22.48	2.48
EBN22	G2	He	AR	55.85	2.42	2.44	23.08	22.85	163.67	222.82	107.04	163.52	163.05	41.07	65.98	22.15	2.52
EBN22	G2	He	AR	55.85	2.42	2.47	23.08	22.65	205.68	250.19	163.08	205.47	205.23	41.07	65.98	22.16	2.52
EBN23	X	He	AR	71.22	2.51	2.48	28.38	28.70	125.47	236.30	0.00	125.90	125.60	50.31	72.82	28.48	2.50
EBN23	G3	He	AR	71.21	2.51	2.52	28.37	28.28	119.45	242.09	0.00	119.31	118.70	34.94	64.24	27.92	2.55
EBN23	G3	He	AR	71.21	2.51	2.51	28.37	28.33	164.17	210.91	118.64	164.14	163.85	34.94	64.24	27.87	2.55
EBN23	G3	He	AR	71.21	2.51	2.52	28.37	28.30	205.48	248.30	163.77	205.44	205.20	34.94	64.24	27.89	2.55
EBN23	G2	He	Dry	71.38	2.49	2.71	28.66	26.36	116.24	221.84	0.00	112.92	109.65	41.07	65.98	23.96	2.98
EBN23	G2	He	Dry	71.38	2.49	2.86	28.66	24.93	168.83	222.72	109.52	166.14	165.50	41.07	65.98	24.00	2.97
EBN23	G2	He	Dry	71.38	2.49	2.88	28.66	24.77	208.35	247.39	165.39	206.32	206.10	41.07	65.98	24.33	2.93
EBN23	G2	He	Dry	66.55	2.49	2.51	26.72	26.51	79.67	155.81	0.00	79.46	78.97	41.07	65.98	26.02	2.56
EBN23	G2	He	Dry	66.55	2.49	2.51	26.72	26.55	126.95	172.80	78.97	126.84	126.47	41.07	65.98	25.92	2.57
EBN23	G2	He	AR	66.55	2.49	2.44	26.72	27.24	61.81	0.00	126.47	61.39	61.86	41.07	65.98	26.66	2.50
EBN24	X	He	AR	72.77	2.37	2.45	30.73	29.67	131.09	240.75	0.00	129.60	129.35	50.31	72.82	29.49	2.47
EBN24	G3	He	AR	46.48	2.37	2.36	19.61	19.68	102.02	232.34	0.00	102.11	101.38	34.94	64.24	19.10	2.43
EBN24	G3	He	AR	46.48	2.37	2.31	19.61	20.11	157.17	228.50	101.34	157.53	156.95	34.94	64.24	19.29	2.41
EBN24	G3	He	AR	46.48	2.37	2.33	19.61	19.95	190.81	234.44	156.66	190.96	190.53	34.94	64.24	18.94	2.45
EBN24	G2	He	AR	63.21	2.37	2.37	26.67	26.70	122.52	239.78	0.00	122.56	121.95	41.07	65.98	26.30	2.40
EBN24	G2	He	AR	63.21	2.37	2.39	26.67	26.47	180.84	237.21	121.94	180.69	180.48	41.07	65.98	26.17	2.42

EBN24	G2	He	AR	63.21	2.37	2.39	26.67	26.45	212.53	243.20	180.48	212.44	212.30	41.07	65.98	26.09	2.42
EBN24	G3	He	Dry	58.54	2.37	2.24	24.70	26.08	115.01	245.17	0.00	117.18	113.50	34.94	64.24	23.71	2.47
EBN24	G3	He	Dry	58.54	2.37	2.39	24.70	24.53	173.61	241.86	113.30	173.47	173.10	34.94	64.24	24.06	2.43
EBN24	G3	He	Dry	58.54	2.37	2.38	24.70	24.58	208.07	247.77	173.00	208.02	207.78	34.94	64.24	24.07	2.43
EBN25	G3	He	AR	43.93	2.58	2.81	17.03	15.64	95.73	225.08	0.00	94.14	93.99	34.94	64.24	15.50	2.83
EBN25	G3	He	AR	43.93	2.58	2.78	17.03	15.81	157.79	244.01	93.99	156.86	156.67	34.94	64.24	15.55	2.82
EBN25	G3	He	AR	43.93	2.58	2.76	17.03	15.93	195.37	247.64	156.69	194.86	194.70	34.94	64.24	15.58	2.82
EBN25	G3	He	Dry	43.49	2.58	2.61	16.86	16.67	92.93	218.96	0.00	92.72	90.57	34.94	64.24	14.71	2.96
EBN25	G3	He	Dry	43.49	2.58	2.82	16.86	15.45	147.65	225.15	90.51	146.69	146.55	34.94	64.24	15.24	2.85
EBN25	G3	He	Dry	43.49	2.58	2.87	16.86	15.16	189.70	248.53	146.32	188.82	188.70	34.94	64.24	14.92	2.92
EBN26	S1	He	AR	38.44	2.60	2.60	14.79	14.77	160.77	441.25	0.00	160.76	159.40	44.60	92.60	13.73	2.80
EBN26	S1	He	AR	38.44	2.60	2.45	14.79	15.68	213.25	307.98	158.95	213.65	212.65	44.60	92.60	13.42	2.87
EBN26	G2	He	Dry	38.15	2.58	2.72	14.79	14.04	67.90	152.53	0.00	67.35	66.83	41.07	65.98	13.31	2.87
EBN26	G2	He	Dry	38.15	2.58	2.58	14.79	14.81	119.44	185.03	66.83	119.46	118.68	41.07	65.98	13.43	2.84
EBN26	G2	He	Dry	38.15	2.58	2.56	14.79	14.89	65.85	0.00	118.68	65.79	66.10	41.07	65.98	14.35	2.66
EBN27	G2	He	AR	51.67	2.68	2.68	19.28	19.27	116.77	249.53	0.00	116.75	116.47	41.07	65.98	19.06	2.71
EBN27	G2	He	AR	51.67	2.68	2.72	19.28	19.03	168.75	228.17	116.49	168.60	168.49	41.07	65.98	18.84	2.74
EBN27	G2	He	AR	51.67	2.68	2.70	19.28	19.16	197.72	231.09	168.37	197.68	197.58	41.07	65.98	18.84	2.74
EBN27	G2	He	Dry	51.29	2.55	2.75	20.11	18.68	70.18	148.55	0.00	69.04	68.89	41.07	65.98	18.48	2.78
EBN27	G2	He	Dry	51.29	2.55	2.71	20.11	18.94	124.01	185.58	68.88	123.28	123.05	41.07	65.98	18.57	2.76
EBN27	G2	He	Dry	51.29	2.55	2.62	20.11	19.60	64.89	0.00	123.00	65.23	65.39	41.07	65.98	19.37	2.65
EBN28	G3	He	AR	57.56	2.30	2.42	25.03	23.79	116.07	246.33	0.00	114.16	113.90	34.94	64.24	23.62	2.44
EBN28	G3	He	AR	57.56	2.30	2.40	25.03	23.93	171.74	236.66	113.89	170.90	170.79	34.94	64.24	23.79	2.42
EBN28	G3	He	AR	57.56	2.30	2.38	25.03	24.21	203.40	240.01	170.77	203.04	202.90	34.94	64.24	23.88	2.41
EBN29	G3	He	Dry	38.39	2.09	2.41	18.37	15.93	106.54	246.40	0.00	103.42	102.00	34.94	64.24	14.78	2.60
EBN29	G3	He	Dry	38.39	2.09	1.83	18.37	21.00	166.25	250.84	101.82	168.42	163.83	34.94	64.24	15.21	2.52

EBN29	G3	He	Dry	38.39	2.09	2.36	18.37	16.29	193.49	232.49	163.78	192.74	192.40	34.94	64.24	15.30	2.51
EBN29	S1	He	AR	39.41	2.09	2.23	18.85	17.63	83.22	220.81	0.00	82.37	82.10	44.60	92.60	17.24	2.29
EBN30	G2	He	AR	63.42	2.40	2.53	26.43	25.11	116.30	228.30	0.00	114.43	114.21	41.07	65.98	24.95	2.54
EBN30	G2	He	AR	63.42	2.40	2.51	26.43	25.28	175.98	236.05	113.61	175.11	174.97	41.07	65.98	25.10	2.53
EBN31	G2	He	Dry	53.33	2.06	2.30	25.89	23.21	121.35	239.81	0.00	117.48	116.40	41.07	65.98	22.43	2.38
EBN32	G2	He	Dry	54.92	2.00	2.52	27.46	21.75	76.63	148.49	0.00	71.50	71.38	41.07	65.98	21.61	2.54
EBN32	G2	He	Dry	54.92	2.00	2.52	27.46	21.80	128.21	181.53	71.35	124.43	124.33	41.07	65.98	21.63	2.54
EBN32	G2	He	Dry	54.92	2.00	2.44	27.46	22.48	60.17	0.00	124.32	63.94	64.05	41.07	65.98	22.33	2.46
EBN33	G3	HE	AR	50.92	2.08	2.36	24.48	21.56	110.98	237.26	0.00	106.80	106.56	34.94	64.24	21.38	2.38
EBN33	G3	HE	AR	50.92	2.08	2.35	24.48	21.70	167.28	236.39	106.55	165.10	164.97	34.94	64.24	21.52	2.37
EBN35	G3	He	Dry	50.55	1.96	2.18	25.79	23.19	111.09	233.35	0.00	107.29	106.83	34.94	64.24	22.86	2.21
EBN35	G3	He	Dry	50.55	1.96		25.79	23.13	163.31	225.47	106.82	161.33	161.26	34.94	64.24	23.03	2.19
EBN35	G3	He	Dry	50.55	1.96		25.79	23.19	195.64	233.50	161.23	194.46	194.30	34.94	64.24	22.82	2.21
EBN35	G2	He	AR	47.33	1.96	2.17	24.15	21.77	117.24	236.64	0.00	113.97	113.78	41.07	65.98	21.63	2.19
EBN35	G2	He	AR	47.33	1.96	2.18	24.15	21.67	173.72	234.76	113.78	171.98	171.51	41.07	65.98	20.98	2.26
EBN35	G2	He	AR	47.33	1.96	2.19	24.15	21.59	211.93	253.10	171.51	210.72	210.67	41.07	65.98	21.47	2.20
EBN35	S1	He	Wet	63.47	1.96	2.06	32.38	30.82	95.74	225.00	0.00	94.34	93.90	44.60	92.60	30.32	2.09
EBN36	S1	He	AR	41.81	2.22	2.35	18.83	17.81	92.12	244.47	0.00	91.33	90.92	44.60	92.60	17.27	2.42
EBN36	S1	He	AR	41.81	2.22	2.51	18.83	16.65	188.07	348.88	90.83	186.31	185.60	44.60	92.60	15.75	2.65
EBN36	S1	He	AR	41.81	2.22	2.36	18.83	17.68	210.34	251.64	185.37	210.10	209.75	44.60	92.60	15.96	2.62
EBN36	G2	He	Dry	41.26	2.20	2.61	18.75	15.79	71.14	152.94	0.00	68.83	68.70	41.07	65.98	15.62	2.64
EBN36	G2	He	Dry	41.26	2.20	2.58	18.75	16.00	123.28	186.04	68.70	121.63	121.43	41.07	65.98	15.64	2.64
EBN36	G2	He	Dry	41.26	2.20	2.47	18.75	16.74	64.94	0.00	121.41	66.20	66.33	41.07	65.98	16.52	2.50
EBN8	X	He	AR	69.17	2.67	2.58	25.88	26.84	125.25	242.10	0.00	126.50	126.10	50.31	72.82	26.54	2.61
NEX7	G3	He	Dry	70.71	2.43	2.52	29.10	28.06	106.43	-0.20	212.45	107.97	108.54	34.94	64.24	27.68	2.56
NEX7	G3	He	Dry	70.71	2.43	2.56	29.10	27.65	146.90	213.05	81.13	145.57	145.35	34.94	64.24	27.40	2.58

NEX7	G3	He	Dry	70.71	2.42	2.53	29.22	27.99	54.21	-0.22	108.52	55.15	55.59	34.94	64.24	27.40	2.58
NEX7	G3	He	Dry	70.71	2.42	2.57	29.22	27.52	92.16	184.53	0.00	89.98	89.74	34.94	64.24	27.33	2.59
NEX7	G3	He	Dry	70.71	2.42	2.56	29.22	27.59	214.20	274.93	153.60	212.82	212.59	34.94	64.24	27.32	2.59
NEX7	G3	He	Dry	70.71	2.42	2.56	29.22	27.64	155.53	221.46	89.76	154.08	153.79	34.94	64.24	27.31	2.59
NEX7	G3	He	Dry	70.71	2.42	2.56	29.22	27.57	83.60	167.40	0.00	81.68	81.23	34.94	64.24	27.18	2.60
NEX7	X	He	AR	80.83	2.48	2.51	32.59	32.25	135.42	243.70	0.00	134.91	134.40	50.31	72.82	31.90	2.53
NEX15	X	He	AR	80.19	2.47	2.52	32.46	31.88	125.30	225.80	0.00	124.50	123.60	50.31	72.82	31.22	2.57
NEX15	G3	He	Dry	65.13	2.45	2.65	26.58	24.55	70.41	146.30	0.00	68.50	68.24	34.94	64.24	24.27	2.68
NEX15	G3	He	Dry	65.13	2.45	2.63	26.58	24.74	112.93	161.10	68.23	111.82	111.73	34.94	64.24	24.59	2.65
NEX15	G3	He	Dry	65.13	2.45	2.63	26.58	24.73	147.86	186.82	111.71	146.96	146.92	34.94	64.24	24.64	2.64
NEX15	G3	He	Dry	65.13	2.45	2.63	26.58	24.79	175.64	206.61	146.91	174.95	174.90	34.94	64.24	24.66	2.64
NEX15	G3	He	Dry	65.13	2.45	2.63	26.58	24.77	199.87	226.80	174.88	199.26	199.17	34.94	64.24	24.49	2.66
NEX15	G3	He	Dry	65.13	2.45	2.63	26.58	24.76	219.62	241.69	199.15	219.12	219.08	34.94	64.24	24.60	2.65
NEX15	G3	He	Dry	65.13	2.45	2.63	26.58	24.80	241.32	265.30	219.08	240.79	240.74	34.94	64.24	24.62	2.65
NEX15	G3	He	Dry	65.13	2.45	2.65	26.58	24.62	84.29	175.14	0.00	82.07	81.92	34.94	64.24	24.49	2.66
NEX15	G3	He	Dry	65.13	2.45	2.63	26.58	24.76	141.91	206.58	81.92	140.44	140.30	34.94	64.24	24.57	2.65
NEX15	G3	He	Dry	65.13	2.45	2.63	26.58	24.80	182.19	227.34	140.29	181.18	181.07	34.94	64.24	24.60	2.65
NEX15	G3	He	Dry	65.13	2.45	2.65	26.58	24.58	73.29	152.28	0.00	71.33	71.20	34.94	64.24	24.45	2.66
NEX15	G3	He	Dry	65.13	2.45	2.63	26.58	24.76	123.90	180.70	71.21	122.61	122.51	34.94	64.24	24.61	2.65
NEX15	G3	He	Dry	65.13	2.45	2.63	26.58	24.77	165.43	211.70	122.50	164.39	164.30	34.94	64.24	24.62	2.65
NEX15	G3	He	Dry	65.13	2.45	2.63	26.58	24.76	201.04	240.65	164.30	200.14	200.08	34.94	64.24	24.62	2.65
NEX15	G3	He	Dry	65.13	2.45	2.63	26.58	24.78	124.86	0.00	240.71	127.67	127.33	34.94	64.24	25.00	2.60
NEX15	G3	He	Dry	65.13	2.45	2.58	26.58	25.20	66.02	0.00	127.28	67.17	67.44	34.94	64.24	24.87	2.62
NEX15	G3	He	Dry	65.13	2.45	2.59	26.58	25.14	93.86	-0.14	181.06	95.56	95.85	34.94	64.24	24.89	2.62
NEX15	G3	He	Dry	65.13	2.45	2.60	26.58	25.07	49.61	-0.23	95.85	50.55	50.75	34.94	64.24	24.74	2.63
NEX15	G3	He	Dry	65.13	2.45	2.59	26.58	25.14	103.72	-0.13	200.08	105.59	105.87	34.94	64.24	24.93	2.61

NEX15	G3	He	Dry	65.13	2.45	2.60	26.58	25.08	54.80	-0.24	105.87	55.83	56.04	34.94	64.24	24.78	2.63
NEX33	G2	He	Dry	72.66	2.49	2.67	29.18	27.24	95.04	180.19	0.00	92.73	92.59	41.07	65.98	27.12	2.68
NEX33	G2	He	Dry	72.66	2.49	2.67	29.18	27.17	101.29	192.04	0.00	98.75	98.67	41.07	65.98	27.11	2.68
NEX33	G2	He	Dry	72.66	2.49	2.67	29.18	27.21	173.23	240.11	98.59	171.39	171.24	41.07	65.98	27.04	2.69
NEX33	G2	He	Dry	72.66	2.49	2.68	29.18	27.15	225.78	274.72	171.15	224.39	224.22	41.07	65.98	26.89	2.70
NEX33	G2	He	Dry	72.66	2.49	2.66	29.18	27.30	100.69	190.90	0.00	98.31	98.09	41.07	65.98	27.12	2.68
NEX33	G2	He	Dry	72.66	2.49	2.67	29.18	27.26	177.09	247.91	98.05	175.19	174.99	41.07	65.98	27.05	2.69
NEX33	G2	He	Dry	72.66	2.49	2.67	29.18	27.22	225.69	271.19	174.90	224.44	224.23	41.07	65.98	26.88	2.70
NEX33	G2	He	Dry	72.66	2.49	2.62	29.18	27.75	105.78	-0.24	224.12	107.92	108.19	41.07	65.98	27.56	2.64
NEX33	X	He	AR?	84.02	2.47	2.61	34.01	32.19	132.56	234.80	0.00	129.90	129.90	50.31	72.82	32.19	2.61
NEX205	G2	He	Dry	58.67	2.18	2.52	26.91	23.24	77.08	150.39	0.00	73.70	73.55	41.07	65.98	23.07	2.54
NEX205	G2	He	Dry	58.67	2.18	2.52	26.91	23.25	127.27	178.36	73.55	124.92	124.81	41.07	65.98	23.07	2.54
NEX205	G2	He	Dry	58.67	2.18	2.44	26.91	24.00	60.84	0.00	124.81	63.09	63.37	41.07	65.98	23.61	2.48
NEX33	G2	He	Dry	69.00	2.47	2.58	27.93	26.75	121.00	233.08	0.00	119.22	116.48	41.07	65.98	24.86	2.78
NEX33	G2	He	Dry	69.00	2.47	2.64	27.93	26.18	55.81	-0.39	116.48	57.13	57.25	41.07	65.98	26.01	2.65
NEX15	G3	He	Dry	68.47	2.45	2.34	27.95	29.23	115.69	235.86	0.00	117.82	111.00	34.94	64.24	24.94	2.75
NEX15	G3	He	Dry	68.47	2.45	2.57	27.95	26.67	56.44	0.00	110.78	57.40	57.91	34.94	64.24	25.97	2.64
NEX7	G2	He	Dry	65.51	2.47	2.60	26.52	25.19	121.47	238.17	0.00	119.50	118.10	41.07	65.98	24.23	2.70
NEX7	G2	He	Dry	65.51	2.47	2.53	26.52	25.87	57.66	-0.39	118.10	58.15	58.72	41.07	65.98	25.09	2.61
CHE3	G3	He	Dry	69.08	2.39	2.60	28.91	26.53	118.79	238.93	0.00	114.91	112.83	34.94	64.24	25.19	2.74
CHE3	G3	He	Dry	69.08	2.39	2.56	28.91	27.01	56.60	-0.25	112.82	58.08	59.01	34.94	64.24	25.76	2.68
CHE2	G3	He	Dry	67.15	2.49	2.50	26.97	26.90	114.10	235.81	0.00	113.98	109.64	34.94	64.24	24.03	2.79
CHE2	G3	He	Dry	67.15	2.49	2.57	26.97	26.17	56.46	-0.27	109.64	57.04	58.15	34.94	64.24	24.60	2.73
NEX33	G1	He	Dry	75.37	2.47	2.66	30.52	28.33	122.46	179.04	69.39	121.10	121.08	40.14	73.31	28.30	2.66
CHE2	G1	He	Dry	81.01	2.49	2.61	32.53	31.01	74.75	150.68	0.00	73.36	72.19	40.14	73.31	29.67	2.73
CHE2	G1	He	Dry	81.01	2.49	2.62	32.53	30.92	125.33	179.30	72.20	124.29	123.60	40.14	73.31	29.81	2.72

EBN20	G1	He	Dry	73.11	2.45	2.63	29.84	27.79	123.59	178.90	72.53	122.37	122.32	40.14	73.31	27.70	2.64
NEX15	G1	He	Dry	81.86	2.45	2.61	33.41	31.34	75.48	150.50	0.00	73.57	73.35	40.14	73.31	31.09	2.63
NEX7	G1	He	Dry	79.52	2.47	2.60	32.19	30.55	71.76	145.26	0.00	70.59	70.34	40.14	73.31	30.55	2.60
CHE3	G1	He	Dry	63.47	2.39	2.68	26.56	23.67	69.47	150.39	0.00	67.88	67.24	40.14	73.31	23.67	2.68

Table I.2. Gripen dried helium.

Sample	Size	Setup	Weight chips, g	Bulk density (Hg injection), cm3/g	Bulk density (pressures) cm3/g	Volume chips density (weight/bulk density HgI)	Volume chips (pressures), cm3	Po	P1 (V1), psig	P2 (V2), psig	P3 (extrapolated), psig	P4 (final), psig	V1, cm3	V2, cm3	Vg, cm3	Grain density (Bulk volume) cm3/g
N-2	1.676<d<2.8	G2	50.26	2.13	2.20	23.57	22.87	73.66	149.72	0.00	73.05	72.34	41.07	65.98	22.04	2.28
N-2	1.676<d<2.8	G2	50.26	2.13	2.22	23.57	22.66	124.80	178.99	72.34	124.24	123.62	41.07	65.98	21.64	2.32
N-2	1.676<d<2.8	G2	50.26	2.13	2.13	23.57	23.56	62.58	-0.46	123.62	62.58	63.81	41.07	65.98	21.85	2.30
N-2	2.8<d<4	G3	53.61	2.13	2.20	25.14	24.37	71.91	152.38	0.00	71.17	70.20	34.94	64.24	23.34	2.30
N-2	2.8<d<4	G3	53.61	2.13	2.19	25.14	24.48	120.23	176.21	70.20	119.79	119.18	34.94	64.24	23.55	2.28
N-2	2.8<d<4	G3	53.61	2.13	2.16	25.14	24.84	62.78	-0.33	119.18	63.00	64.12	34.94	64.24	23.33	2.30
N-2	4<d<7	G3	51.27	2.13	2.19	24.04	23.40	69.70	149.88	0.00	69.11	68.40	34.94	64.24	22.62	2.27
N-2	4<d<7	G3	51.27	2.13	2.19	24.04	23.38	118.48	176.09	68.40	118.04	117.25	34.94	64.24	22.16	2.31
N-2	4<d<7	G3	51.27	2.13	2.14	24.04	23.98	62.58	-0.33	117.25	62.62	63.68	34.94	64.24	22.49	2.28

NG-2	0.85<d<2.8	G3	51.51	2.03	2.24	25.40	22.97	69.93	147.67	0.00	67.70	66.78	34.94	64.24	21.92	2.35
NG-2	0.85<d<2.8	G3	51.51	2.03	2.23	25.40	23.12	121.19	181.67	66.78	119.56	119.45	34.94	64.24	22.97	2.24
NG-2	0.85<d<2.8	G3	51.51	2.03	2.16	25.40	23.83	62.74	-0.30	119.45	63.93	64.82	34.94	64.24	22.60	2.28
NG-2	2.8<d<4	G3	51.50	2.03	2.22	25.39	23.21	71.32	150.62	0.00	69.28	68.09	34.94	64.24	21.89	2.35
NG-2	2.8<d<4	G3	51.50	2.03	2.20	25.39	23.41	121.11	180.06	68.09	119.72	119.01	34.94	64.24	22.36	2.30
NG-2	2.8<d<4	G3	51.50	2.03	2.17	25.39	23.77	62.51	-0.31	119.01	63.73	64.81	34.94	64.24	22.26	2.31
NG-2	4<d<7	G2	50.03	2.03	2.17	24.67	23.09	75.56	151.56	0.00	74.14	73.21	41.07	65.98	22.02	2.27
NG-2	4<d<7	G2	50.03	2.03	2.14	24.67	23.36	127.59	182.28	73.21	126.74	125.95	41.07	65.98	22.11	2.26
NG-2	4<d<7	G2	50.03	2.03	2.10	24.67	23.81	62.95	-0.41	125.95	63.60	64.60	41.07	65.98	22.46	2.23
NG-3	0.85<d<1.676	G2	47.98	2.03	2.20	23.66	21.78	73.49	149.21	0.00	71.87	71.01	41.07	65.98	20.75	2.31
NG-3	0.85<d<1.676	G2	47.98	2.03	2.17	23.66	22.08	125.99	182.64	71.01	124.97	124.45	41.07	65.98	21.26	2.26
NG-3	0.85<d<1.676	G2	47.98	2.03	2.12	23.66	22.59	62.96	-0.41	124.45	63.73	64.71	41.07	65.98	21.21	2.26
NG-3	1.676<d<2.8	G1	68.35	2.03	2.18	33.70	31.40	76.66	152.31	0.00	74.51	73.81	40.14	73.31	30.62	2.23
NG-3	1.676<d<2.8	G1	68.35	2.03	2.20	33.70	31.08	128.12	181.71	73.81	126.39	125.71	40.14	73.31	29.99	2.28
NG-3	1.676<d<2.8	G1	68.35	2.03	2.15	33.70	31.76	62.49	0.11	125.71	64.00	65.16	40.14	73.31	30.18	2.26
NG-3	2.8<d<4	G2	48.40	2.03	2.17	23.86	22.31	74.08	150.05	0.00	72.72	71.79	41.07	65.98	21.21	2.28
NG-3	2.8<d<4	G2	48.40	2.03	2.14	23.86	22.59	125.83	181.25	71.79	125.02	124.26	41.07	65.98	21.37	2.26
NG-3	4<d<7	G1	66.45	2.03	2.15	32.76	30.87	75.52	151.79	0.00	73.79	72.78	40.14	73.31	29.73	2.23
NG-3	4<d<7	G1	66.45	2.03	2.16	32.76	30.75	126.20	180.15	72.78	124.90	124.17	40.14	73.31	29.59	2.25
NG-3	4<d<7	G1	66.45	2.03	2.13	32.76	31.18	62.46	0.11	124.17	63.64	64.76	40.14	73.31	29.64	2.24
NG-4	0.85<d<2.8	G2	50.78	2.03	2.19	25.04	23.21	75.40	150.56	0.00	73.75	72.61	41.07	65.98	21.88	2.32
NG-4	0.85<d<2.8	G2	50.78	2.03	2.16	25.04	23.49	127.35	181.91	72.61	126.33	125.71	41.07	65.98	22.52	2.26
NG-4	0.85<d<2.8	G2	50.78	2.03	2.12	25.04	23.98	62.55	-0.41	125.71	63.35	64.55	41.07	65.98	22.36	2.27
NG-4	2.8<d<4	G2	47.91	2.03	2.15	23.62	22.26	74.08	150.48	0.00	72.89	72.02	41.07	65.98	21.24	2.26
NG-4	2.8<d<4	G2	47.91	2.03	2.13	23.62	22.55	127.06	183.83	72.02	126.36	125.92	41.07	65.98	21.85	2.19
NG-4	2.8<d<4	G2	47.91	2.03	2.06	23.62	23.28	63.72	-0.43	125.92	63.97	64.69	41.07	65.98	22.29	2.15

NG-4	4<d<7	G3	53.86	2.03	2.20	26.56	24.54	73.29	152.34	0.00	71.31	70.29	34.94	64.24	23.45	2.30
NG-4	4<d<7	G3	53.86	2.03	2.17	26.56	24.76	124.01	181.96	70.29	122.72	121.99	34.94	64.24	23.71	2.27
NG-4	4<d<7	G3	53.86	2.03	2.14	26.56	25.16	63.13	-0.35	121.99	64.23	65.21	34.94	64.24	23.89	2.25
NG-8	0.8<d<1.676	G2	40.75	1.91	2.17	21.31	18.76	73.50	153.44	0.00	71.38	70.77	41.07	65.98	18.00	2.26
NG-8	0.8<d<1.676	G2	40.75	1.91	2.13	21.31	19.18	122.81	179.42	70.77	121.55	121.03	41.07	65.98	18.26	2.23
NG-8	0.8<d<1.676	G2	40.75	1.91	2.59	21.31	15.72	62.84	-0.45	121.03	66.40	64.02	41.07	65.98	19.54	2.09
NG-8	1.676<d<2.8	G3	49.04	1.91	2.21	25.64	22.20	72.47	152.53	0.00	69.24	68.64	34.94	64.24	21.54	2.28
NG-8	1.676<d<2.8	G3	49.04	1.91	2.18	25.64	22.53	122.81	182.65	68.64	120.61	120.06	34.94	64.24	21.71	2.26
NG-8	1.676<d<2.8	G3	49.04	1.91	2.14	25.64	22.88	62.86	-0.35	120.06	64.92	65.43	34.94	64.24	22.17	2.21
NG-8	2.8-d-4	G1	49.07	1.91	2.15	25.66	22.81	69.25	151.47	0.00	67.08	66.35	40.14	73.31	21.81	2.25
NG-8	2.8-d-4	G1	49.07	1.91	2.17	25.66	22.61	118.72	180.90	66.35	116.96	116.43	40.14	73.31	21.64	2.27
NG-8	2.8-d-4	G1	49.07	1.91	2.11	25.66	23.25	63.27	0.15	116.43	64.69	65.22	40.14	73.31	22.31	2.20
NG-10	0.85<d<1.676	G2	47.31	1.91	2.04	24.74	23.18	75.08	150.48	0.00	73.69	72.99	41.07	65.98	22.38	2.11
NG-10	0.85<d<1.676	G2	47.31	1.91	2.04	24.74	23.21	127.14	181.52	72.99	126.16	125.50	41.07	65.98	22.15	2.14
NG-10	0.85<d<1.676	G2	47.31	1.91	2.00	24.74	23.68	62.62	-0.51	125.50	63.42	64.18	41.07	65.98	22.65	2.09
NG-10	1.676<d<2.8	G1	62.87	1.91	2.06	32.87	30.59	74.38	149.31	0.00	72.33	71.33	40.14	73.31	29.43	2.14
NG-10	1.676<d<2.8	G1	62.87	1.91	2.06	32.87	30.58	126.08	181.24	71.33	124.57	123.75	40.14	73.31	29.28	2.15
NG-10	1.676<d<2.8	G1	62.87	1.91	2.03	32.87	30.98	62.16	0.11	123.75	63.57	64.43	40.14	73.31	29.78	2.11
NG-12	0.85<d<1.676	G3	58.09	2.30	2.84	25.31	20.48	70.01	148.03	0.00	65.72	65.83	34.94	64.24	20.61	2.82
NG-12	0.85<d<1.676	G3	58.09	2.30	2.80	25.31	20.78	120.94	182.35	65.83	117.76	117.75	34.94	64.24	20.77	2.80
NG-12	0.85<d<1.676	G3	58.09	2.30	2.75	25.31	21.12	61.90	-0.34	117.75	64.90	65.02	34.94	64.24	20.94	2.77
Ng-12	1.676<d<2.8	G3	60.41	2.30	2.82	26.32	21.43	70.32	146.65	0.00	65.91	65.89	34.94	64.24	21.42	2.82
Ng-12	1.676<d<2.8	G3	60.41	2.30	2.80	26.32	21.57	120.12	178.97	65.89	116.80	116.75	34.94	64.24	21.48	2.81
Ng-12	1.676<d<2.8	G3	60.41	2.30	2.74	26.32	22.04	60.60	-0.33	116.75	63.72	63.97	34.94	64.24	21.67	2.79
NG12	4-d-7	G3	68.00	2.30	2.76	29.62	24.65	75.82	150.94	0.00	70.77	70.14	34.94	64.24	23.99	2.83
NG12	4-d-7	G3	68.00	2.30	2.73	29.62	24.93	126.56	182.45	70.14	122.99	122.49	34.94	64.24	24.22	2.81

NG12	4-d-7	G3	68.00	2.30	2.73	29.62	24.94	166.03	209.16	122.49	163.28	162.83	34.94	64.24	24.12	2.82
NG12	4-d-7	G3	68.00	2.30	2.65	29.62	25.64	81.01	-0.06	162.83	85.44	86.89	34.94	64.24	24.24	2.81

Table I.3. Gripen as received with helium.

Sample	Size	Setup	Weight chips, g	Bulk density (Hg injection) cm3/g	Bulk density (pressures) cm3/g	Volume chips density (weight/bulk density Hgl) cm3/g	Volume chips (pressures)	Po, psig	P1 (V1) , psig	P2 (V2) , psig	P3 (extrapolated) , psig	P4 (final) , psig	V1, cm3	V2, cm3	Vg, cm3	Grain density (Bulk volume) cm3/g
N-2	1.676<d<2.8	G3	57.53	2.13	2.19	26.97	26.22	77.45	160.05	0.00	76.65	76.10	34.94	64.24	25.70	2.24
N-2	1.676<d<2.8	G3	57.53	2.13	2.18	26.97	26.36	129.50	186.46	76.10	129.05	128.67	34.94	64.24	25.84	2.23
N-2	1.676<d<2.8	G3	57.53	2.13	2.18	26.97	26.36	167.71	209.34	128.67	167.38	167.03	34.94	64.24	25.69	2.24
N-2	1.676<d<2.8	G3	57.53	2.13	2.15	26.97	26.70	86.11	-0.18	167.03	86.43	87.18	34.94	64.24	26.01	2.21
N-2	1.676<d<2.8	G3	57.53	2.13	2.17	26.97	26.57	44.90	-0.21	87.18	45.13	45.60	34.94	64.24	25.75	2.23
N-2	2.8<d<4	G2	53.28	2.13	2.16	24.98	24.70	72.79	145.45	0.00	72.54	72.17	41.07	65.98	24.28	2.19
N-2	2.8<d<4	G2	53.28	2.13	2.17	24.98	24.55	124.01	175.76	72.17	123.74	123.41	41.07	65.98	24.01	2.22
N-2	2.8<d<4	G2	53.28	2.13	2.16	24.98	24.62	166.69	209.89	123.41	166.50	166.18	41.07	65.98	23.99	2.22
N-2	2.8<d<4	G2	53.28	2.13	2.12	24.98	25.12	82.83	-0.37	166.18	82.69	83.28	41.07	65.98	24.54	2.17
N-2	2.8<d<4	G2	53.28	2.13	2.13	24.98	25.04	41.41	-0.38	83.28	41.38	41.76	41.07	65.98	24.28	2.19
N-6	0.85<d<2.8	G2	58.39		2.28		25.57	58.39	152.19	0.00	76.71	76.24	41.07	65.98	25.06	2.33
N-6	0.85<d<2.8	G2	58.39		2.30		25.39	116.93	182.30	76.24	129.58	129.19	41.07	65.98	24.78	2.36

N-6	0.85<d<2.8	G2	58.39		2.29		25.48	159.73	208.79	129.19	169.27	168.97	41.07	65.98	24.86	2.35
N-6	0.85<d<2.8	G2	58.39		2.25		25.98	104.00	-0.37	168.97	83.18	84.01	41.07	65.98	25.19	2.32
N-6	0.85<d<2.8	G2	58.39		2.25		25.92	51.63	-0.38	84.01	41.29	41.73	41.07	65.98	25.06	2.33
N-6	2.8<d<4	G2	54.57	2.40	2.49	22.70	21.92	79.18	162.62	0.00	78.46	77.63	41.07	65.98	21.01	2.60
N-6	2.8<d<4	G2	54.57	2.40	2.47	22.70	22.06	128.51	182.14	77.63	128.13	127.64	41.07	65.98	21.22	2.57
N-6	2.8<d<4	G2	54.57	2.40	2.47	22.70	22.07	168.94	212.45	127.64	168.63	168.14	41.07	65.98	21.04	2.59
N-6	2.8<d<4	G2	54.57	2.40	2.43	22.70	22.49	86.21	-0.12	168.14	86.41	87.47	41.07	65.98	21.38	2.55
N-6	2.8<d<4	G2	54.57	2.40	2.44	22.70	22.35	44.78	-0.20	87.47	44.96	45.67	41.07	65.98	20.90	2.61
NG-2	0.85<d<2.8	G2	53.17	2.03	2.17	26.21	24.51	85.31	167.90	0.00	83.54	83.12	41.07	65.98	24.08	2.21
NG-2	0.85<d<2.8	G2	53.17	2.03	2.19	26.21	24.26	133.69	182.66	83.12	132.50	132.17	41.07	65.98	23.71	2.24
NG-2	0.85<d<2.8	G2	53.17	2.03	2.18	26.21	24.39	167.39	201.48	132.17	166.61	166.36	41.07	65.98	23.79	2.23
NG-2	0.85<d<2.8	G2	53.17	2.03	2.14	26.21	24.88	81.64	-0.38	166.36	83.02	83.71	41.07	65.98	24.19	2.20
NG-2	0.85<d<2.8	G2	53.17	2.03	2.15	26.21	24.79	40.98	-0.39	83.71	41.73	42.29	41.07	65.98	23.67	2.25
NG-2	2.8<d<4	G3	54.51	2.03	2.20	26.87	24.82	80.86	167.33	0.00	78.63	78.16	34.94	64.24	24.37	2.24
NG-2	2.8<d<4	G3	54.51	2.03	2.18	26.87	24.98	128.24	181.79	78.16	126.96	126.59	34.94	64.24	24.42	2.23
NG-2	2.8<d<4	G3	54.51	2.03	2.18	26.87	25.01	162.39	200.67	126.59	161.49	161.15	34.94	64.24	24.27	2.25
NG-2	2.8<d<4	G3	54.51	2.03	2.15	26.87	25.34	83.20	-0.16	161.15	84.81	85.43	34.94	64.24	24.74	2.20
NG-2	2.8<d<4	G3	54.51	2.03	2.16	26.87	25.21	44.05	-0.22	85.43	44.98	45.49	34.94	64.24	24.26	2.25
NG-2	4<d<7	G2	52.35	2.03	2.19	25.81	23.87	84.20	166.54	0.00	82.23	81.93	41.07	65.98	23.56	2.22
NG-2	4<d<7	G2	52.35	2.03	2.18	25.81	23.98	134.50	185.91	81.93	133.34	133.05	41.07	65.98	23.51	2.23
NG-2	4<d<7	G2	52.35	2.03	2.18	25.81	23.97	175.19	216.41	133.05	174.26	174.02	41.07	65.98	23.48	2.23
NG-2	4<d<7	G2	52.35	2.03	2.14	25.81	24.51	85.85	-0.38	174.02	87.24	87.85	41.07	65.98	23.92	2.19
NG-2	4<d<7	G2	52.35	2.03	2.14	25.81	24.43	43.24	-0.38	87.85	43.99	44.42	41.07	65.98	23.62	2.22
NG-3	0.85<d<1.676	G2	54.47	2.03	2.16	26.86	25.18	80.78	157.72	0.00	79.12	78.58	41.07	65.98	24.61	2.21
NG-3	0.85<d<1.676	G2	54.47	2.03	2.17	26.86	25.06	131.14	181.22	78.58	129.99	129.62	41.07	65.98	24.46	2.23
NG-3	0.85<d<1.676	G2	54.47	2.03	2.16	26.86	25.17	170.05	208.57	129.62	169.22	168.97	41.07	65.98	24.66	2.21

NG-3	0.85<d<1.676	G2	54.47	2.03	2.12	26.86	25.65	82.23	-0.39	168.97	83.52	84.35	41.07	65.98	24.85	2.19
NG-3	1.676<d<2.8	G2	56.78	2.03	2.20	28.00	25.83	83.52	160.76	0.00	81.29	80.86	41.07	65.98	25.40	2.24
NG-3	1.676<d<2.8	G2	56.78	2.03	2.22	28.00	25.63	136.65	188.25	80.86	135.03	134.66	41.07	65.98	25.07	2.27
NG-3	1.676<d<2.8	G2	56.78	2.03	2.21	28.00	25.74	174.41	211.18	134.66	173.31	173.05	41.07	65.98	25.18	2.25
NG-3	1.676<d<2.8	G2	56.78	2.03	2.16	28.00	26.24	82.94	-0.38	173.05	84.90	85.67	41.07	65.98	25.53	2.22
NG-3	1.676<d<2.8	G2	56.78	2.03	2.17	28.00	26.13	40.97	-0.37	85.67	42.00	42.42	41.07	65.98	25.34	2.24
NG-3	2.8<d<4	G2	53.94	2.03	2.14	26.59	25.24	85.13	166.75	0.00	83.72	83.26	41.07	65.98	24.79	2.18
NG-3	2.8<d<4	G2	53.94	2.03	2.16	26.59	24.94	134.63	183.89	83.26	133.59	133.21	41.07	65.98	24.31	2.22
NG-3	2.8<d<4	G2	53.94	2.03	2.15	26.59	25.05	169.15	203.61	133.21	168.47	168.17	41.07	65.98	24.34	2.22
NG-3	2.8<d<4	G2	53.94	2.03	2.11	26.59	25.57	82.13	-0.38	168.17	83.21	83.83	41.07	65.98	24.97	2.16
NG-3	4<d<7	G2	50.16	2.03	2.17	24.73	23.13	83.26	166.88	0.00	81.67	81.38	41.07	65.98	22.82	2.20
NG-3	4<d<7	G2	50.16	2.03	2.16	24.73	23.23	134.93	188.71	81.38	133.97	133.64	41.07	65.98	22.70	2.21
NG-3	4<d<7	G2	50.16	2.03	2.19	24.73	22.88	170.41	207.33	133.64	169.60	169.46	41.07	65.98	22.56	2.22
NG-3	4<d<7	G2	50.16	2.03	2.11	24.73	23.73	84.72	-0.38	169.46	85.74	86.20	41.07	65.98	23.27	2.16
NG-3	4<d<7	G2	50.16	2.03	2.12	24.73	23.63	43.00	-0.39	86.20	43.57	43.92	41.07	65.98	22.94	2.19
NG-4	0.85<d<2.8	G3	57.95	2.03	2.17	28.57	26.65	79.87	161.41	0.00	77.75	77.13	34.94	64.24	26.06	2.22
NG-4	0.85<d<2.8	G3	57.95	2.03	2.17	28.57	26.74	129.98	183.94	77.13	128.65	128.22	34.94	64.24	26.13	2.22
NG-4	0.85<d<2.8	G3	57.95	2.03	2.16	28.57	26.78	163.76	200.05	128.22	162.88	162.55	34.94	64.24	26.07	2.22
NG-4	0.85<d<2.8	G3	57.95	2.03	2.14	28.57	27.12	82.01	-0.20	162.55	83.64	84.48	34.94	64.24	26.34	2.20
NG-4	2.8<d<4	G3	57.31	2.03	2.17	28.26	26.43	80.16	162.73	0.00	78.16	77.67	34.94	64.24	25.98	2.21
NG-4	2.8<d<4	G3	57.31	2.03	2.16	28.26	26.53	129.35	182.59	77.67	128.13	127.73	34.94	64.24	25.95	2.21
NG-4	2.8<d<4	G3	57.31	2.03	2.16	28.26	26.57	164.56	202.50	127.73	163.71	163.36	34.94	64.24	25.85	2.22
NG-4	2.8<d<4	G3	57.31	2.03	2.13	28.26	26.89	82.81	-0.15	163.36	84.33	84.98	34.94	64.24	26.29	2.18
NG-4	4<d<7	G3	53.16	2.03	2.16	26.21	24.57	81.83	170.89	0.00	80.03	79.65	34.94	64.24	24.21	2.20
NG-4	4<d<7	G3	53.16	2.03	2.15	26.21	24.70	134.30	193.78	79.65	133.19	132.84	34.94	64.24	24.21	2.20
NG-4	4<d<7	G3	53.16	2.03	2.15	26.21	24.70	171.02	212.59	132.84	170.25	169.91	34.94	64.24	24.02	2.21

NG-4	4<d<7	G3	53.16	2.03	2.12	26.21	25.10	88.49	-0.14	169.91	89.71	90.20	34.94	64.24	24.64	2.16
NG-4	4<d<7	G3	53.16	2.03	2.13	26.21	24.97	46.90	-0.23	90.20	47.63	48.00	34.94	64.24	24.32	2.19
NG-8	0.85<d<1.676	G2	41.08	1.91	2.14	21.48	19.24	77.35	161.15	0.00	75.38	74.86	41.07	65.98	18.64	2.20
NG-8	0.85<d<1.676	G2	41.08	1.91	2.15	21.48	19.12	128.20	185.99	74.86	126.77	126.37	41.07	65.98	18.44	2.23
NG-8	0.85<d<1.676	G2	41.08	1.91	2.14	21.48	19.17	162.62	201.90	126.37	161.67	161.37	41.07	65.98	18.42	2.23
NG-8	0.85<d<1.676	G2	41.08	1.91	2.09	21.48	19.63	83.73	-0.39	161.37	85.38	86.00	41.07	65.98	18.90	2.17
NG-8	1.676<d<2.8	G3	49.93	1.91	2.22	26.11	22.49	78.28	163.71	0.00	74.58	74.02	34.94	64.24	21.91	2.28
NG-8	1.676<d<2.8	G3	49.93	1.91	2.20	26.11	22.73	126.73	184.25	74.02	124.40	123.95	34.94	64.24	22.04	2.27
NG-8	1.676<d<2.8	G3	49.93	1.91	2.19	26.11	22.79	167.21	214.42	123.95	165.33	165.00	34.94	64.24	22.17	2.25
NG-8	2.8<d<4	G3	58.29	1.91	2.17	30.48	26.83	76.79	151.00	0.00	72.93	72.37	34.94	64.24	26.28	2.22
NG-8	2.8<d<4	G3	58.29	1.91	2.16	30.48	26.95	127.88	181.51	72.37	125.17	124.99	34.94	64.24	26.71	2.18
NG-8	2.8<d<4	G3	58.29	1.91	2.19	30.48	26.63	167.09	207.78	124.99	164.86	164.45	34.94	64.24	25.86	2.25
NG-8	2.8<d<4	G3	58.29	1.91	2.13	30.48	27.31	80.75	-0.13	164.45	84.44	85.22	34.94	64.24	26.60	2.19
NG-8	2.8<d<4	G3	58.29	1.91	2.14	30.48	27.19	41.77	-0.22	85.22	43.75	44.25	34.94	64.24	26.31	2.22
NG-10	0.85<d<1.676	G3	55.66	1.91	1.95	29.10	28.50	82.18	164.83	0.00	81.49	80.96	34.94	64.24	28.04	1.99
NG-10	0.85<d<1.676	G3	55.66	1.91	1.96	29.10	28.39	132.24	183.81	80.96	131.72	131.68	34.94	64.24	28.33	1.96
NG-10	0.85<d<1.676	G3	55.66	1.91	0.87	29.10	64.22	172.34	213.24	131.68	213.18	171.43	34.94	64.24	27.49	2.02
NG-10	0.85<d<1.676	G3	55.66	1.91	1.91	29.10	29.08	85.77	-0.37	171.43	85.80	86.54	34.94	64.24	28.47	1.96
NG-10	0.85<d<1.676	G3	55.66	1.91	1.93	29.10	28.88	43.21	-0.36	86.54	43.35	43.83	34.94	64.24	28.10	1.98
NG-10	1.676<d<2.8	G3	55.20	1.91	2.07	28.86	26.69	79.22	159.45	0.00	76.85	76.20	34.94	64.24	26.07	2.12
NG-10	1.676<d<2.8	G3	55.20	1.91	2.07	28.86	26.71	129.77	184.02	76.20	128.18	127.52	34.94	64.24	25.78	2.14
NG-10	1.676<d<2.8	G3	55.20	1.91	2.06	28.86	26.83	165.31	203.58	127.52	164.25	163.93	34.94	64.24	26.19	2.11
NG-10	1.676<d<2.8	G3	55.20	1.91	2.03	28.86	27.17	82.39	-0.17	163.93	84.30	85.11	34.94	64.24	26.44	2.09
NG-12	d<0.8	G3	48.08	2.30	2.70	20.95	17.84	74.31	166.40	0.00	71.48	71.29	34.94	64.24	17.62	2.73
NG-12	d<0.8	G3	48.08	2.30	2.65	20.95	18.13	123.18	187.49	71.29	121.38	121.15	34.94	64.24	17.76	2.71
NG-12	d<0.8	G3	48.08	2.30	2.64	20.95	18.23	159.03	205.97	121.15	157.76	157.54	34.94	64.24	17.75	2.71

NG-12	d<0.8	G3	48.08	2.30	2.61	20.95	18.45	87.11	-0.17	157.54	89.28	89.51	34.94	64.24	18.18	2.64
NG-12	d<0.8	G3	48.08	2.30	2.62	20.95	18.37	49.42	-0.25	89.51	50.70	50.86	34.94	64.24	18.03	2.67
NG-12	0.85<d<1.676	G3	60.58	2.30	2.66	26.39	22.76	78.06	162.62	0.00	74.35	74.05	34.94	64.24	22.45	2.70
NG-12	0.85<d<1.676	G3	60.58	2.30	2.65	26.39	22.86	126.16	182.61	74.05	123.75	123.56	34.94	64.24	22.57	2.68
NG-12	0.85<d<1.676	G3	60.58	2.30	2.65	26.39	22.90	162.10	203.86	123.56	160.34	160.16	34.94	64.24	22.52	2.69
NG-12	0.85<d<1.676	G3	60.58	2.30	2.61	26.39	23.21	83.20	-0.16	160.16	86.43	86.75	34.94	64.24	22.88	2.65
NG-12	1.676<d<2.8	G3	68.74	2.30	2.66	29.95	25.89	78.60	155.74	0.00	74.25	73.85	34.94	64.24	25.49	2.70
NG-12	1.676<d<2.8	G3	68.74	2.30	2.63	29.95	26.10	127.34	179.84	73.85	124.52	124.22	34.94	64.24	25.66	2.68
NG-12	1.676<d<2.8	G3	68.74	2.30	2.63	29.95	26.12	166.07	207.16	124.22	163.88	163.58	34.94	64.24	25.56	2.69
NG-12	1.676<d<2.8	G3	68.74	2.30	2.60	29.95	26.48	80.94	-0.17	163.58	84.88	85.51	34.94	64.24	25.90	2.65
NG-12	2.8<d<4	G3	67.17	2.30	2.64	29.26	25.44	75.31	150.70	0.00	71.40	71.00	34.94	64.24	25.02	2.68
NG-12	2.8<d<4	G3	67.17	2.30	2.62	29.26	25.60	124.17	177.39	71.00	121.52	121.18	34.94	64.24	25.10	2.68
NG-12	2.8<d<4	G3	67.17	2.30	2.62	29.26	25.61	168.33	215.54	121.18	165.99	165.65	34.94	64.24	25.04	2.68
NG-12	2.8<d<4	G3	67.17	2.30	2.59	29.26	25.93	82.80	-0.14	165.65	86.56	87.02	34.94	64.24	25.51	2.63
NG-12	2.8<d<4	G3	67.17	2.30	2.60	29.26	25.84	43.42	-0.23	87.02	45.45	45.79	34.94	64.24	25.24	2.66
NG-12	4<d<7	G2	56.40	2.30	2.52	24.57	22.34	83.03	166.75	0.00	80.85	80.46	41.07	65.98	21.93	2.57
NG-12	4<d<7	G2	56.40	2.30	2.53	24.57	22.33	137.40	194.82	80.46	135.90	135.55	41.07	65.98	21.79	2.59
NG-12	4<d<7	G2	56.40	2.30	2.53	24.57	22.31	174.55	213.88	135.55	173.51	173.22	41.07	65.98	21.64	2.61
NG-12	4<d<7	G2	56.40	2.30	2.47	24.57	22.85	86.77	-0.38	173.22	88.54	89.05	41.07	65.98	22.34	2.52
NG-12	4<d<7	G2	56.40	2.30	2.48	24.57	22.72	44.53	-0.35	89.05	45.51	45.80	41.07	65.98	22.15	2.55
NA-2	0.85<d<1.676	G2	51.92	2.14	2.18	24.26	23.85	83.32	167.95	0.00	82.91	82.52	41.07	65.98	23.45	2.21
NA-2	0.85<d<1.676	G2	51.92	2.14	2.19	24.26	23.71	134.29	186.88	82.52	133.95	133.67	41.07	65.98	23.25	2.23
NA-2	0.85<d<1.676	G2	51.92	2.14	2.19	24.26	23.67	169.59	206.09	133.67	169.34	169.13	41.07	65.98	23.18	2.24
NA-2	0.85<d<1.676	G2	51.92	2.14	2.15	24.26	24.14	85.03	-0.38	169.13	85.16	85.73	41.07	65.98	23.57	2.20

Appendix J

Figure J.1. Experimental and history match data.

BC07 He 131 psi Dried Reverse
Porosity H (%): 8.2
Porosity L (%): 3.8
Total Porosity (%): 12.1
Permeability H (mD): 0.0060
Permeability L (nD): 0.13

BC08 He 244 psi Dried Forward
Porosity H (%): 6.4
Porosity L (%): 3.5
Total Porosity (%): 9.9
Permeability H (mD): 107
Permeability L (nD): 0.25

BC08 He 123 psi Dried Reverse
Porosity H (%): 6.1
Porosity L (%): 3.0
Total Porosity (%): 9.1
Permeability H (mD): 80
Permeability L (nD): 0.68

BC09 He 245 psi Dried Forward
Porosity H (%): 1.7
Porosity L (%): 3.5
Total Porosity (%): 5.2
Permeability H (mD): 87
Permeability L (nD): 1.5

BC09 He 245 psi Dried Forward
Porosity H (%): 1.7
Porosity L (%): 3.5
Total Porosity (%): 5.2
Permeability H (mD): 87
Permeability L (nD): 1.5

BC09 He 119 psi Dried Reverse
Porosity H (%): 3.2
Porosity L (%): 4.8
Total Porosity (%): 8.0
Permeability H (mD): 82
Permeability L (nD): 3.23

BC10 He 245 psi Dried Forward
Porosity H (%): 3.8
Porosity L (%): 2.1
Total Porosity (%): 5.9
Permeability H (mD): 120
Permeability L (nD): 0.8

BC10 He 123 psi Dried Reverse
Porosity H (%): 6.0
Porosity L (%): 2.2
Total Porosity (%): 8.2
Permeability H (mD): 110
Permeability L (nD): 0.56

BC11 He 152 psi Dried Forward
Porosity H (%): 4.7
Porosity L (%): 3.1
Total Porosity (%): 7.8
Permeability H (mD): 89
Permeability L (nD): 0.32

BC11 He 173 psi Dried Reverse
Porosity H (%): 4.4
Porosity L (%): 3.4
Total Porosity (%): 7.8
Permeability H (mD): 89
Permeability L (nD): 0.18

CHE2 He 151 psi Dried Forward
Porosity High - 4.5%
Porosity Low - 3.8%
Kg high - 12 nD
Kg low 4.8 nD

CHE2 He 211 psi Dried Forward
Porosity H (%): 5.1
Porosity L (%): 2.8
Total Porosity (%): 7.9
Permeability H (mD): 115
Permeability L (nD): 0.39

CHE2 He 169 psi Dried Reverse
Porosity H (%): 3.5
Porosity L (%): 3.9
Total Porosity (%): 7.4
Permeability H (mD): 180
Permeability L (nD): 0.074

CHE2 He 244 psi Dried Forward
Porosity H (%): 4.0
Porosity L (%): 3.2
Total Porosity (%): 7.2
Permeability H (mD): 95
Permeability L (nD): 0.5

CHE2 He 182 psi Dried Forward
Porosity H (%): 4.0
Porosity L (%): 2.9
Total Porosity (%): 6.9
Permeability H (mD): 87
Permeability L (nD): 0.92

CHE02 He 237 psi As received Forward
Porosity H (%): 1.2
Porosity L (%): 3.0
Total Porosity (%): 3.2
Permeability H (mD): 3.3
Permeability L (nD): 0.26

CHE2 He 180 psi As recieved Forward
Porosity H (%): 3.7
Porosity L (%): 3.1
Total Porosity (%): 6.8
Permeability H (mD): 85
Permeability L (nD): 1.7

CHE3 He 150 psi Dried Forward
Porosity - 9.9%
Kg - 7.9 nD

316

Figure J.1. Experimental and history match data.

Figure J.1. Experimental and history match data.

Appendix K

Table K.1. Pressure expansion experiment results.

Sample	Setup	Gas	AR or Dry	P1 (V1), psig	Porosity, frac	Double porosity PhiH, frac	PhL, frac	Impact of high phi,%	Impact of low phi,%	Dual permeability Kh, mD	Kl, nD
BC01	X	He	AR	239.05	0.04	0.037	0.000	100.00	0.00		
BC01	G3	He	Dry	246.20	0.07	-0.013	0.084	-18.11	118.11	120.512	1.11E-07
BC01	G3	He	Dry	-0.21	0.04	0.033	0.012	73.22	26.78	79.777	2.60E-07
BC02	X	He	AR	235.00	0.03	0.011	0.023	33.29	66.71	63.916	1.36E-07
BC02	G2	He	Dry	246.24	0.09	0.010	0.078	11.47	88.53	0.042	1.22E-07
BC02	G2	He	Dry	-0.25	0.06	0.037	0.020	64.85	35.15	65.100	1.19E-07
BC03	X	He	AR	243.20	0.10	0.072	0.026	73.17	26.83	264.196	1.47E-07
BC03	G2	He	Dry	246.60	0.14	0.114	0.026	81.75	18.25	138.774	8.79E-07
BC03	G2	He	Dry	-0.19	0.11	0.074	0.033	68.95	31.05	95.807	1.55E-06
BC04	X	He	AR	244.55	0.02	-0.005	0.028	-23.33	123.33		
BC04	G3	He	Dry	245.87	0.07	0.040	0.033	54.50	45.50	34.412	5.48E-07
BC04	G3	He	Dry	-0.21	0.04	0.005	0.039	11.35	88.65	180.261	3.77E-07
BC05	X	He	AR	235.90	0.02	-0.006	0.024	-32.05	132.05		
BC05	G3	He	Dry	246.38	0.06	0.035	0.023	60.98	39.02	25.958	1.13E-06
BC05	G3	He	Dry	-0.17	0.06	0.021	0.042	33.96	66.04	186.315	1.31E-06

BC06	X	He	AR	244.40	0.00	-0.003	0.007	-90.38	190.38		
BC06	G2	He	Dry	152.58	0.04	0.029	0.012	69.95	30.05	0	3.34E-08
BC06	G2	He	Dry	180.47	0.04	0.026	0.011	69.92	30.08		
BC06	G2	He	Dry	-0.49	0.02	0.013	0.011	52.58	47.42	0	2.73E-08
BC07	X	He	AR	247.70	0.01	-0.001	0.015	-5.55	105.55		
BC07	G2	He	Dry	152.13	0.05	0.030	0.021	59.17	40.83	14.400	2.36E-07
BC07	G2	He	Dry	182.66	0.06	0.036	0.021	62.94	37.06		
BC07	G2	He	Dry	-0.49	0.05	0.020	0.025	43.66	56.34	0.147	1.24E-07
BC08	X	He	AR	242.60	0.08	0.038	0.043	46.93	53.07		
BC08	G2	He	Dry	244.91	0.12	0.063	0.054	53.72	46.28	107.124	2.52E-07
BC08	G2	He	Dry	-0.21	0.09	0.043	0.046	48.10	51.90	79.961	6.78E-07
BC09	G3	He	Dry	245.07	0.06	0.031	0.031	50.39	49.61	87.855	1.50E-06
BC09	G3	He	Dry	-0.17	0.08	0.032	0.047	40.45	59.55	81.554	3.23E-06
BC10	G2	He	Dry	245.62	0.07	0.049	0.023	68.15	31.85	120.997	7.88E-07
BC10	G2	He	Dry	-0.21	0.08	0.048	0.030	61.55	38.45	109.346	5.58E-07
BC11	X	He	AR	241.60	0.04	0.027	0.015	64.47	35.53		
BC11	G2	He	Dry	152.69	0.09	0.050	0.035	58.78	41.22	88.625	3.23E-07
BC11	G2	He	Dry	178.89	0.08	0.050	0.034	59.70	40.30		
BC11	G2	He	Dry	214.68	0.08	0.048	0.031	60.74	39.26		
BC11	G2	He	Dry	-0.49	0.06	0.033	0.024	57.79	42.21	89.651	1.80E-07
CHE2	X	He	AR	237.70	0.05	0.027	0.026	50.89	49.11	3.299	2.57E-07
CHE2	G3	He	AR	149.90	0.09	0.051	0.042	55.16	44.84		
CHE2	G3	He	AR	180.67	0.07	0.044	0.027	62.25	37.75	85.276	1.75E-06
CHE2	G3	He	AR	209.35	0.08	0.043	0.033	56.12	43.88		
CHE2	G3	He	AR	-0.37	0.07	0.025	0.045	35.55	64.45		
CHE2	G2	He	Dry	243.51	0.09	0.053	0.037	59.01	40.99	95.476	5.02E-07
CHE2	G2	He	Dry	154.54	0.09	0.044	0.043	50.46	49.54		
CHE2	G2	He	Dry	182.22	0.08	0.044	0.035	55.44	44.56	87.526	9.24E-07
CHE2	G2	He	Dry	211.30	0.08	0.050	0.034	59.41	40.59	115.517	3.85E-07
CHE2	G2	He	Dry	-0.48	0.07	0.030	0.037	45.10	54.90	179.807	6.86E-07
Che3	G3	N2	AR	150.16	0.13	0.093	0.039	70.39	29.61		
Che3	G3	N2	AR	180.73	0.14	0.092	0.051	64.23	35.77		
Che3	G3	N2	AR	210.45	0.14	0.096	0.040	70.88	29.12		
Che3	G3	N2	AR	240.38	0.14	0.103	0.035	74.46	25.54		
Che3	G3	He	AR	150.10	0.10	0.082	0.022	78.60	21.40		
Che3	G3	He	AR	179.57	0.11	0.080	0.034	70.36	29.64		
Che3	G3	He	AR	210.16	0.09	0.076	0.012	86.13	13.87		
Che3	G3	He	AR	240.29	0.14	0.083	0.060	58.20	41.80		
Che3	G3	He	Dry	149.20	0.13	0.105	0.026	79.97	20.03	124.594	1.31E-06

Che3	G3	He	Dry	179.77	0.12	0.096	0.022	81.27	18.73	191.898	2.27E-06
Che3	G3	He	Dry	209.66	0.11	0.103	0.009	91.89	8.11	112.261	3.12E-06
Che3	G3	He	Dry	240.37	0.12	0.104	0.017	85.67	14.33	7.395	1.06E-07
Che3	G3	He	Dry	-0.15	0.11	0.090	0.020	81.82	18.18	104.691	1.34E-06
Che3	G3	N2	Dry	150.52	0.17	0.100	0.067	60.06	39.94		
Che3	G3	N2	Dry	180.20	0.16	0.103	0.059	63.56	36.44		
Che3	G3	N2	Dry	209.93	0.16	0.107	0.051	67.59	32.41		
Che3	G3	N2	Dry	250.74	0.15	0.108	0.044	71.06	28.94		
Che3	G3	N2	AR	-0.19	0.13	0.091	0.041	69.22	30.78		
Che3	G3	He	AR	-0.21	0.09	0.068	0.020	76.82	23.18		
Che3	G3	N2	Dry	-0.25	0.15	0.103	0.044	69.89	30.11		
EBN1	X	He	AR	241.60	0.02	0.023	0.000	100.00	0.00		
EBN7	G2	He	Dry	155.93	0.04	0.030	0.010	74.46	25.54	57.602	1.93E-08
EBN7	G2	He	Dry	183.93	0.04	0.035	0.010	77.98	22.02		
EBN7	G2	He	Dry	-0.49	0.03	0.020	0.007	75.16	24.84	410.102	3.39E-08
EBN16	G2	He	Dry	153.78	0.22	0.181	0.041	81.37	18.63		
EBN16	G2	He	Dry	180.35	0.21	0.048	0.160	23.02	76.98	18.451	1.58E-05
EBN16	G2	He	Dry	0.00	0.15	0.116	0.037	75.99	24.01	7.235	5.08E-07
EBN19	X	He	AR	240.80	0.06	0.051	0.008	87.09	12.91		
EBN19	G2	He	Dry	246.05	0.15	0.142	0.007	95.59	4.41		
EBN19	G2	He	Dry	249.31	0.15	0.143	0.008	94.43	5.57	30.749	1.22E-08
EBN19	G2	He	Dry	242.89	0.15	0.136	0.014	90.72	9.28		
EBN20	G3	He	AR	243.79	0.04	0.008	0.034	18.14	81.86		
EBN20	G3	He	AR	239.33	0.04	-0.020	0.055	-56.20	156.20		
EBN20	G3	He	AR	240.97	0.05	0.008	0.040	16.57	83.43		
EBN20	G2	He	Dry	243.68	0.08	0.063	0.014	81.70	18.30	72.145	2.36E-08
EBN20	G2	He	Dry	238.87	0.08	-0.014	0.094	-17.98	117.98		
EBN20	G2	He	Dry	247.10	0.08	0.062	0.014	81.30	18.70	59.144	5.13E-08
EBN20	G2	He	AR	229.32	0.04	0.030	0.014	68.23	31.77		
EBN20	G2	He	AR	247.51	0.04	0.036	0.004	89.94	10.06		
EBN20	G2	He	AR	220.60	0.06	0.044	0.014	76.33	23.67		
EBN20	X	He	AR	232.30	0.04	0.038	0.000	100.00	0.00		
EBN20	G3	CH$_4$	AR	155.57	0.11	0.084	0.024	77.98	22.02		
EBN20	G3	CH$_4$	AR	-0.25	0.11	0.101	0.007	93.07	6.93		
EBN21	G2	He	Dry	243.80	0.17	0.106	0.060	64.08	35.92	45.132	8.50E-08
EBN21	G2	He	Dry	247.19	0.18	0.106	0.074	58.97	41.03		
EBN21	G2	He	Dry	243.33	0.17	0.102	0.067	60.17	39.83		
EBN21	G2	He	AR	239.04	0.13	0.103	0.025	80.63	19.37	72.118	6.73E-09
EBN21	G2	He	AR	238.07	0.17	0.117	0.049	70.67	29.33		

EBN21	G2	He	AR	251.88	0.15	0.079	0.070	53.11	46.89		
EBN22	G2	He	AR	220.38	0.03	0.016	0.010	60.58	39.42	32.262	1.92E-08
EBN22	G2	He	AR	222.82	0.04	0.009	0.031	23.19	76.81		
EBN22	G2	He	AR	250.19	0.04	0.018	0.022	45.39	54.61		
EBN23	X	He	AR	236.30	0.00	-0.011	0.008	322.92	-222.92		
EBN23	G3	He	AR	242.09	0.02	0.003	0.013	18.62	81.38		
EBN23	G3	He	AR	210.91	0.02	0.001	0.016	8.07	91.93		
EBN23	G3	He	AR	248.30	0.02	0.002	0.015	13.86	86.14	39.398	2.76E-08
EBN23	G2	He	Dry	221.84	0.16	0.073	0.091	44.44	55.56	13.563	1.44E-07
EBN23	G2	He	Dry	222.72	0.16	0.125	0.038	76.89	23.11		
EBN23	G2	He	Dry	247.39	0.15	0.133	0.018	88.14	11.86		
EBN23	G2	He	Dry	155.81	0.03	0.008	0.019	29.17	70.83		
EBN23	G2	He	Dry	172.80	0.03	0.007	0.023	21.76	78.24		
EBN23	G2	He	AR	0.00	0.00	-0.019	0.021	-771.66	871.66		
EBN24	X	He	AR	240.75	0.04	0.034	0.006	84.95	15.05		
EBN24	G3	He	AR	232.34	0.03	-0.003	0.029	-12.98	112.98		
EBN24	G3	He	AR	228.50	0.02	-0.025	0.041	-151.75	251.75		
EBN24	G3	He	AR	234.44	0.03	-0.016	0.050	-48.27	148.27		
EBN24	G2	He	AR	239.78	0.01	-0.001	0.015	-6.92	106.92		
EBN24	G2	He	AR	237.21	0.02	0.008	0.011	40.52	59.48	66.905	3.05E-08
EBN24	G2	He	AR	243.20	0.02	0.008	0.013	38.40	61.60		
EBN24	G3	He	Dry	245.17	0.04	-0.051	0.091	-126.59	226.59		
EBN24	G3	He	Dry	241.86	0.03	0.007	0.019	26.62	73.38	90.328	4.40E-08
EBN24	G3	He	Dry	247.77	0.03	0.005	0.021	17.96	82.04	4.613	3.18E-08
EBN25	G3	He	AR	225.08	0.09	0.080	0.009	89.97	10.03		
EBN25	G3	He	AR	244.01	0.09	0.071	0.016	81.53	18.47	63.330	6.94E-08
EBN25	G3	He	AR	247.64	0.09	0.063	0.022	74.18	25.82		
EBN25	G3	He	Dry	218.96	0.13	0.010	0.117	7.76	92.24		
EBN25	G3	He	Dry	225.15	0.10	0.083	0.014	85.90	14.10		
EBN25	G3	He	Dry	248.53	0.12	0.099	0.016	86.35	13.65	163.789	8.80E-08
EBN26	S1	He	AR	441.25	0.07	0.001	0.071	0.90	99.10		
EBN26	S1	He	AR	307.98	0.09	-0.052	0.144	-55.91	155.91		
EBN26	G2	He	Dry	152.53	0.10	0.048	0.052	48.06	51.94		
EBN26	G2	He	Dry	185.03	0.09	-0.002	0.094	-1.76	101.76		
EBN26	G2	He	Dry	0.00	0.03	-0.007	0.036	-23.28	123.28		
EBN27	G2	He	AR	249.53	0.01	0.001	0.011	5.76	94.24	100.012	4.87E-08
EBN27	G2	He	AR	228.17	0.02	0.013	0.010	56.87	43.13	5.553	3.29E-08
EBN27	G2	He	AR	231.09	0.02	0.006	0.016	27.18	72.82	148.514	5.14E-08
EBN27	G2	He	Dry	148.55	0.08	0.071	0.010	87.13	12.87	0.593	5.44E-08

EBN27	G2	He	Dry	185.58	0.08	0.057	0.020	74.28	25.72		
EBN27	G2	He	Dry	0.00	0.04	0.025	0.012	67.86	32.14	17.293	1.17E-08
EBN28	G3	He	AR	246.33	0.06	0.049	0.007	87.21	12.79		
EBN28	G3	He	AR	236.66	0.05	0.043	0.006	87.71	12.29	22.315	1.39E-08
EBN28	G3	He	AR	240.01	0.05	0.032	0.013	70.47	29.53	54.239	3.80E-08
EBN29	G3	He	Dry	246.40	0.20	0.123	0.073	62.83	37.17	14.257	1.14E-07
EBN29	G3	He	Dry	250.84	0.17	-0.104	0.276	-60.40	160.40	105.406	5.73E-06
EBN29	G3	He	Dry	232.49	0.17	0.106	0.060	63.78	36.22	38.468	5.19E-07
EBN29	S1	He	AR	220.81	0.09	0.063	0.022	73.96	26.04	171.290	9.66E-08
EBN30	G2	He	AR	228.30	0.06	0.050	0.006	88.56	11.44	145.818	1.2E-08
EBN30	G2	He	AR	236.05	0.05	0.043	0.007	85.64	14.36		
EBN31	G2	He	Dry	239.81	0.13	0.100	0.034	74.79	25.21	61.769	3.16E-08
EBN32	G2	He	Dry	148.49	0.21	0.207	0.007	96.91	3.09		
EBN32	G2	He	Dry	181.53	0.21	0.205	0.007	96.52	3.48		
EBN32	G2	He	Dry	0.00	0.19	0.180	0.007	96.42	3.58		
EBN33	G3	HE	AR	237.26	0.13	0.118	0.008	93.59	6.41	26.551	2.20E-08
EBN33	G3	HE	AR	236.39	0.12	0.113	0.008	93.42	6.58	4.529	6.45E-09
EBN35	G3	He	Dry	233.35	0.11	0.099	0.014	87.58	12.42	181.752	1.98E-06
EBN35	G3	He	Dry	225.47	0.11	0.103	0.004	96.05	3.95		
EBN35	G3	He	Dry	233.50	0.12	0.099	0.016	86.22	13.78		
EBN35	G2	He	AR	236.64	0.10	0.098	0.007	93.73	6.27	2.766	1.22E-08
EBN35	G2	He	AR	234.76	0.13	0.099	0.032	75.58	24.42	123.125	9.24E-05
EBN35	G2	He	AR	253.10	0.11	0.105	0.005	95.25	4.75		
EBN35	S1	He	Wet	225.00	0.06	0.047	0.016	74.55	25.45		
EBN36	S1	He	AR	244.47	0.08	0.053	0.030	63.47	36.53	64.318	3.15E-08
EBN36	S1	He	AR	348.88	0.16	0.109	0.054	66.86	33.14		
EBN36	S1	He	AR	251.64	0.15	0.055	0.097	36.30	63.70		
EBN36	G2	He	Dry	152.94	0.17	0.156	0.011	93.46	6.54	14.976	3.39E-08
EBN36	G2	He	Dry	186.04	0.17	0.144	0.022	86.66	13.34		
EBN36	G2	He	Dry	0.00	0.12	0.106	0.013	89.06	10.94	37.896	1.38E-07
EBN8	X	He	AR	242.10	-0.03	-0.037	0.011	144.67	-44.67		
NEX7	G3	He	Dry	-0.20	0.05	0.035	0.014	71.79	28.21		
NEX7	G3	He	Dry	213.05	0.06	0.049	0.009	84.46	15.54	10.065	1.13E-07
NEX7	G3	He	Dry	-0.22	0.06	0.041	0.021	66.14	33.86		
NEX7	G3	He	Dry	184.53	0.06	0.058	0.007	89.35	10.65		
NEX7	G3	He	Dry	274.93	0.07	0.055	0.010	84.48	15.52		
NEX7	G3	He	Dry	221.46	0.07	0.053	0.012	81.75	18.25		
NEX7	G3	He	Dry	167.40	0.07	0.056	0.014	79.38	20.62	63.930	2.02E-07
NEX7	X	He	AR	243.70	0.02	0.010	0.011	49.42	50.58		

NEX15	X	He	AR	225.80	0.04	0.018	0.021	45.71	54.29	1.572	8.66E-08
NEX15	G3	He	Dry	146.30	0.09	0.076	0.011	86.90	13.10	10.965	2.35E-08
NEX15	G3	He	Dry	161.10	0.08	0.069	0.006	91.89	8.11		
NEX15	G3	He	Dry	186.82	0.07	0.070	0.003	95.31	4.69		
NEX15	G3	He	Dry	206.61	0.07	0.067	0.005	92.60	7.40		
NEX15	G3	He	Dry	226.80	0.08	0.067	0.011	85.55	14.45		
NEX15	G3	He	Dry	241.69	0.07	0.068	0.006	91.31	8.69		
NEX15	G3	He	Dry	265.30	0.07	0.067	0.007	90.42	9.58		
NEX15	G3	He	Dry	175.14	0.08	0.073	0.005	93.20	6.80		
NEX15	G3	He	Dry	206.58	0.08	0.068	0.007	90.20	9.80		
NEX15	G3	He	Dry	227.34	0.07	0.067	0.008	89.26	10.74		
NEX15	G3	He	Dry	152.28	0.08	0.075	0.005	93.20	6.80	5.624	4.67E-07
NEX15	G3	He	Dry	180.70	0.07	0.068	0.006	91.80	8.20	5.426	2.78E-08
NEX15	G3	He	Dry	211.70	0.07	0.068	0.006	91.63	8.37	10.965	2.35E-08
NEX15	G3	He	Dry	240.65	0.07	0.068	0.005	92.71	7.29		
NEX15	G3	He	Dry	0	0.06	0.068	-0.009	115.39	-15.39		
NEX15	G3	He	Dry	0	0.06	0.051	0.013	79.69	20.31		
NEX15	G3	He	Dry	-0.14	0.06	0.054	0.010	84.28	15.72		
NEX15	G3	He	Dry	-0.23	0.07	0.056	0.013	81.04	18.96		
NEX15	G3	He	Dry	-0.13	0.06	0.054	0.009	86.25	13.75		
NEX15	G3	He	Dry	-0.24	0.07	0.056	0.012	82.18	17.82		
NEX33	G2	He	Dry	180.19	0.07	0.066	0.004	93.91	6.09	0.081	1.04E-08
NEX33	G2	He	Dry	192.04	0.07	0.069	0.002	96.73	3.27		
NEX33	G2	He	Dry	240.11	0.07	0.067	0.006	91.47	8.53		
NEX33	G2	He	Dry	274.72	0.08	0.069	0.010	87.65	12.35		
NEX33	G2	He	Dry	190.90	0.07	0.064	0.007	90.45	9.55	2.165	1.97E-08
NEX33	G2	He	Dry	247.91	0.07	0.065	0.008	89.57	10.43	1.153	1.07E-08
NEX33	G2	He	Dry	271.19	0.08	0.066	0.013	83.97	16.03	9.596	6.43E-09
NEX33	G2	He	Dry	-0.24	0.06	0.049	0.007	87.80	12.20		
NEX33	X	He	AR?	234.80	0.05	0.054	0.000	100.00	0.00		
NEX05	G2	He	Dry	150.39	0.14	0.135	0.007	94.75	5.25	6.520	1.51E-07
NEX205	G2	He	Dry	178.36	0.14	0.135	0.008	94.58	5.42		
NEX205	G2	He	Dry	0.00	0.12	0.106	0.016	86.89	13.11		
NEX33	G2	He	Dry	233.08	0.11	0.039	0.071	35.74	64.26	72.722	9.47E-08
NEX33	G2	He	Dry	-0.39	0.07	0.062	0.006	90.76	9.24	50.840	2.68E-06
NEX15	G3	He	Dry	235.86	0.11	-0.039	0.147	-36.45	136.45		
NEX15	G3	He	Dry	0.00	0.07	0.044	0.026	62.72	37.28	142.998	7.61E-07
NEX7	G2	He	Dry	238.17	0.09	0.048	0.038	55.62	44.38	157.995	4.04E-07
NEX7	G2	He	Dry	-0.39	0.05	0.024	0.030	44.00	56.00	148.734	6.97E-07

CHE3	G3	He	Dry	238.93	0.13	0.078	0.051	60.68	39.32	197.738	1.19E-06
CHE3	G3	He	Dry	-0.25	0.11	0.063	0.046	57.43	42.57	53.689	5.93E-07
CHE2	G3	He	Dry	235.81	0.11	0.002	0.106	2.26	97.74	10.483	4.41E-07
CHE2	G3	He	Dry	-0.27	0.09	0.028	0.060	31.76	68.24	118.373	1.59E-06
NEX33	G1E	He	Dry	179.04	0.07	0.071	0.001	98.40	1.60		
CHE2	G1E	He	Dry	150.68	0.09	0.045	0.043	50.92	49.08	0.000	4.76E-06
CHE2	G1E	He	Dry	179.30	0.08	0.048	0.036	57.23	42.77		
EBN20	G1E	He	Dry	178.90	0.07	0.069	0.003	95.68	4.32		
NEX15	G1E	He	Dry	150.50	0.07	0.062	0.008	88.58	11.42		
NEX7	G1E	He	Dry	145.26	0.05	0.051	0.000	100.00	0.00		
CHE3	G1E	He	Dry	150.39	0.11	0.109	0.000	100.00	0.00		

Appendix L

Table L.1. Control-Test dry methane porosity results.

Sample	Size, µm	Setup	Gas	AR or Dry	P1 (V1), psig	Porosity, frac	PhiH, frac	PhL, frac
CHE2	500-d-850	G2	CH$_4$	Dry	149.93	0.24	0.064	0.178
CHE2	500-d-850	G2	CH$_4$	Dry	181.40	0.17	0.059	0.108
CHE2	500-d-850	G2	CH$_4$	Dry	196.87	0.17	0.066	0.101
CHE2	500-d-850	G2	CH$_4$	Dry	-0.23	0.18	0.086	0.093
NEX15	500-d-850	G2	CH$_4$	Dry	150.16	0.17	0.096	0.076
NEX15	500-d-850	G2	CH$_4$	Dry	168.94	0.13	0.083	0.052
NEX15	500-d-850	G2	CH$_4$	Dry	-0.37	0.16	0.112	0.044
NEX33	500-d-850	G3	CH$_4$	Dry	150.25	0.15	0.123	0.026
NEX33	500-d-850	G3	CH$_4$	Dry	167.76	0.13	0.105	0.023
NEX33	500-d-850	G3	CH$_4$	Dry	-0.01	0.15	0.139	0.014
NEX7	250-d-500	G1	CH$_4$	Dry	151.64	0.12	0.027	0.095
NEX7	250-d-500	G1	CH$_4$	Dry	167.65	0.11	0.026	0.083
NEX7	250-d-500	G1	CH$_4$	Dry	0.18	0.18	0.023	0.160
NEX7	500-d-850	G1	CH$_4$	Dry	150.93	0.19	0.083	0.103
NEX7	500-d-850	G1	CH$_4$	Dry	180.79	0.15	0.087	0.062
NEX7	500-d-850	G1	CH$_4$	Dry	195.07	0.14	0.093	0.047
NEX7	500-d-850	G1	CH$_4$	Dry	0.17	0.18	0.120	0.057
EBN20	1-2mm	G1	CH$_4$	Dry	148.56	0.13	0.102	0.025
EBN20	1-2mm	G1	CH$_4$	Dry	178.35	0.10	0.088	0.014

EBN20	1-2mm	G1	CH_4	Dry	0.19	0.14	0.132	0.008
EBN20	250-d-500	G2	CH_4	Dry	150.98	0.23	0.195	0.033
EBN20	250-d-500	G2	CH_4	Dry	179.61	0.20	0.177	0.024
EBN20	250-d-500	G2	CH_4	Dry	-0.37	0.24	0.232	0.009
CHE3	500-d-850	G3	CH_4	Dry	151.33	0.24	0.107	0.137
CHE3	500-d-850	G3	CH_4	Dry	181.66	0.19	0.111	0.084
CHE3	500-d-850	G3	CH_4	Dry	195.96	0.20	0.115	0.084
CHE3	500-d-850	G3	CH_4	Dry	-0.22	0.20	0.132	0.071

Table L.2. Control-Test samples dry N2 porosity results.

Sample	Size	Setup	Gas	AR or Dry	P1 (V1), psig	Porosity, frac	PhiH, frac	PhL, frac
NEX7	500-d-850	G2	N2	Dry	148.49	0.10	0.071	0.028
NEX7	500-d-850	G2	N2	Dry	179.04	0.10	0.070	0.027
NEX7	500-d-850	G2	N2	Dry	210.93	0.10	0.072	0.025
NEX7	500-d-850	G2	N2	Dry	-0.33	0.10	0.065	0.031
NEX33	500-d-850	G3	N2	Dry	150.69	0.09	0.035	0.055
NEX33	500-d-850	G3	N2	Dry	180.53	0.09	0.007	0.085
NEX33	500-d-850	G3	N2	Dry	208.52	0.10	-0.032	0.135
NEX33	500-d-850	G3	N2	Dry	0.01	0.07	-0.080	0.149
NEX33#2	500-d-850	G2	N2	Dry	148.10	0.09	0.084	0.008
NEX33#2	500-d-850	G2	N2	Dry	181.22	0.08	0.071	0.009
NEX33#2	500-d-850	G2	N2	Dry	211.15	0.08	0.069	0.012
NEX33#2	500-d-850	G2	N2	Dry	-0.37	0.08	0.075	0.001
CHE3	500-d-850	G3	N2	Dry	146.93	0.16	0.099	0.056
CHE3	500-d-850	G3	N2	Dry	181.29	0.14	0.102	0.042
CHE3	500-d-850	G3	N2	Dry	210.53	0.14	0.105	0.038
CHE3	500-d-850	G3	N2	Dry	0.00	0.14	0.093	0.045
EBN20	500-d-850	G1	N2	Dry	148.45	0.08	0.073	0.005
EBN20	500-d-850	G1	N2	Dry	181.06	0.08	0.075	0.004
EBN20	500-d-850	G1	N2	Dry	210.56	0.08	0.074	0.005
EBN20	500-d-850	G1	N2	Dry	0.15	0.08	0.076	0.003
NEX15	500-d-850	G1	N2	Dry	150.34	0.10	0.073	0.028
NEX15	500-d-850	G1	N2	Dry	177.51	0.10	0.081	0.021
NEX15	500-d-850	G1	N2	Dry	211.67	0.09	0.082	0.006
NEX15	500-d-850	G1	N2	Dry	0.15	0.10	0.079	0.023

CHE2	500-d-850	G1	N2	Dry	151.02	0.10	0.008	0.092
CHE2	500-d-850	G1	N2	Dry	180.57	0.08	0.014	0.070
CHE2	500-d-850	G1	N2	Dry	210.66	0.09	0.017	0.070
CHE2	500-d-850	G1	N2	Dry	0.19	0.08	0.004	0.078

Table L.3. Control-Test samples dry N2.

Sample	Size	Setup	Weight chips, g	Bulk density (Hg injection), cm3/g	Bulk density (pressures) cm3/g	Volume chips density (weight/bulk density HgI) cm3/g	Volume chips (pressures)	Po, psig	P1 (V1) , psig	P2 (V2) , psig	P3 (extrapolated) , psig	P4 (final) , psig	V1, cm3	V2, cm3	Vg, cm3	Grain density (Bulk volume) cm3/g
NEX7	500-d-850	G2	59.27	2.42	2.61	24.49	22.71	73.87	148.49	0.00	72.31	71.77	41.07	65.98	22.08	2.68
NEX7	500-d-850	G2	59.27	2.42	2.61	24.49	22.72	125.14	179.04	71.77	124.02	123.64	41.07	65.98	22.11	2.68
NEX7	500-d-850	G2	59.27	2.42	2.61	24.49	22.70	167.07	210.93	123.64	166.14	165.85	41.07	65.98	22.12	2.68
NEX7	500-d-850	G2	59.27	2.42	2.59	24.49	22.85	83.18	-0.33	165.85	84.79	85.47	41.07	65.98	22.15	2.68
NEX33	500-d-850	G3	31.69	2.49	2.58	12.73	12.26	60.90	150.69	0.00	60.57	60.11	34.94	64.24	11.58	2.74
NEX33	500-d-850	G3	31.69	2.49	2.51	12.73	12.63	108.77	180.53	60.11	108.72	108.13	34.94	64.24	11.56	2.74
NEX33	500-d-850	G3	31.69	2.49	2.40	12.73	13.20	148.70	208.52	108.13	148.92	148.09	34.94	64.24	11.42	2.78
NEX33	500-d-850	G3	31.69	2.49	2.28	12.73	13.92	88.25	0.01	148.09	87.41	88.85	34.94	64.24	11.85	2.67
NEX33#2	500-d-850	G2	63.18	2.49	2.72	25.38	23.23	74.47	148.10	0.00	72.56	72.40	41.07	65.98	23.03	2.74
NEX33#2	500-d-850	G2	63.18	2.49	2.68	25.38	23.55	127.12	181.22	72.40	125.92	125.78	41.07	65.98	23.33	2.71
NEX33#2	500-d-850	G2	63.18	2.49	2.68	25.38	23.61	168.71	211.15	125.78	167.80	167.66	41.07	65.98	23.33	2.71
NEX33#2	500-d-850	G2	63.18	2.49	2.69	25.38	23.47	83.16	-0.37	167.66	85.09	85.11	41.07	65.98	23.45	2.69
CHE3	500-d-850	G3	63.21	2.40	2.68	26.34	23.57	70.48	146.93	0.00	67.90	66.73	34.94	64.24	22.24	2.84
CHE3	500-d-850	G3	63.21	2.40	2.68	26.34	23.55	121.68	181.29	66.73	119.65	118.96	34.94	64.24	22.55	2.80
CHE3	500-d-850	G3	63.21	2.40	2.69	26.34	23.46	162.89	210.53	118.96	161.22	160.72	34.94	64.24	22.56	2.80

Sample	Size, μm	Setup	Weight chips, g	Bulk density (Hg injection), cm3/g	Bulk density (pressures), cm3/g	Volume chips density (weight/bulk density HgI), cm3/g	Volume chips (pressures), cm3	Po, psig	P1 (V1), psig	P2 (V2), psig	P3 (extrapolated), psig	P4 (final), psig	V1, cm3	V2, cm3	Vg, cm3	Grain density (Bulk volume), cm3/g
CHE3	500-d-850	G3	63.21	2.40	2.66	26.34	23.77	83.63	0.00	160.72	86.26	87.30	34.94	64.24	22.70	2.79
EBN20	500-d-850	G1	78.52	2.47	2.66	31.83	29.48	73.01	148.45	0.00	70.97	70.84	40.14	73.31	29.33	2.68
EBN20	500-d-850	G1	78.52	2.47	2.67	31.83	29.42	125.04	181.06	70.84	123.49	123.42	40.14	73.31	29.31	2.68
EBN20	500-d-850	G1	78.52	2.47	2.66	31.83	29.47	166.27	210.56	123.42	165.07	165.00	40.14	73.31	29.34	2.68
EBN20	500-d-850	G1	78.52	2.47	2.67	31.83	29.39	83.93	0.15	165.00	86.28	86.37	40.14	73.31	29.30	2.68
NEX15	500-d-850	G1	72.53	2.45	2.65	29.61	27.37	71.97	150.34	0.00	70.11	69.49	40.14	73.31	26.61	2.73
NEX15	500-d-850	G1	72.53	2.45	2.67	29.61	27.14	121.20	177.51	69.49	119.73	119.40	40.14	73.31	26.58	2.73
NEX15	500-d-850	G1	72.53	2.45	2.67	29.61	27.15	163.58	211.67	119.40	162.32	162.24	40.14	73.31	27.00	2.69
NEX15	500-d-850	G1	72.53	2.45	2.67	29.61	27.20	84.64	0.15	162.24	86.81	87.35	40.14	73.31	26.57	2.73
CHE2	500-d-850	G1	79.27	2.49	2.51	31.83	31.56	74.28	151.02	0.00	74.03	71.49	40.14	73.31	28.66	2.77
CHE2	500-d-850	G1	79.27	2.49	2.53	31.83	31.35	125.14	180.57	71.49	124.82	123.43	40.14	73.31	29.15	2.72
CHE2	500-d-850	G1	79.27	2.49	2.54	31.83	31.24	166.33	210.66	123.43	166.02	164.92	40.14	73.31	29.06	2.73
CHE2	500-d-850	G1	79.27	2.49	2.50	31.83	31.69	83.90	0.19	164.92	84.04	86.42	40.14	73.31	29.22	2.71

Table L.4. Dry methane on Control-Test samples.

Sample	Size, μm	Setup	Weight chips, g	Bulk density (Hg injection), cm3/g	Bulk density (pressures), cm3/g	Volume chips density (weight/bulk density HgI), cm3/g	Volume chips (pressures), cm3	Po, psig	P1 (V1), psig	P2 (V2), psig	P3 (extrapolated), psig	P4 (final), psig	V1, cm3	V2, cm3	Vg, cm3	Grain density (Bulk volume), cm3/g
CHE2	500-d-850	G2	61.23	2.49	2.70	24.59	22.67	74.68	149.93	0.00	72.98	69.65	41.07	65.98	18.64	3.29
CHE2	500-d-850	G2	61.23	2.49	2.67	24.59	22.97	125.31	181.40	69.65	124.24	122.67	41.07	65.98	20.48	2.99

CHE2	500-d-850	G2	61.23	2.49	2.69	24.59	22.80	159.63	196.87	122.67	158.84	157.88	41.07	65.98	20.50	2.99
CHE2	500-d-850	G2	61.23	2.49	2.75	24.59	22.26	79.13	-0.23	157.88	81.29	83.12	41.07	65.98	20.19	3.03
NEX15	500-d-850	G2	56.74	2.45	2.73	23.16	20.76	73.51	150.16	0.00	71.47	70.19	41.07	65.98	19.18	2.96
NEX15	500-d-850	G2	56.74	2.45	2.69	23.16	21.13	118.54	168.94	70.19	117.39	116.80	41.07	65.98	20.04	2.83
NEX15	500-d-850	G2	56.74	2.45	2.78	23.16	20.44	59.44	-0.37	116.80	61.24	61.81	41.07	65.98	19.54	2.90
NEX33	500-d-850	G3	65.70	2.49	2.85	26.38	23.05	72.12	150.25	0.00	68.96	68.42	34.94	64.24	22.45	2.93
NEX33	500-d-850	G3	65.70	2.49	2.79	26.38	23.54	116.10	167.76	68.42	114.31	113.99	34.94	64.24	23.01	2.86
NEX33	500-d-850	G3	65.70	2.49	2.90	26.38	22.67	59.27	-0.01	113.99	61.93	62.14	34.94	64.24	22.35	2.94
NEX7	250-d-500	G1	41.40	2.42	2.49	17.11	16.60	63.18	151.64	0.00	62.85	61.85	40.14	73.31	15.03	2.75
NEX7	250-d-500	G1	41.40	2.42	2.49	17.11	16.63	105.93	167.65	61.85	105.71	105.09	40.14	73.31	15.25	2.71
NEX7	250-d-500	G1	41.40	2.42	2.49	17.11	16.65	61.38	0.18	105.09	61.59	62.76	40.14	73.31	13.98	2.96
NEX7	500-d-850	G1	68.41	2.42	2.67	28.27	25.65	71.12	150.93	0.00	69.00	66.99	40.14	73.31	23.01	2.97
NEX7	500-d-850	G1	68.41	2.42	2.67	28.27	25.64	120.62	180.79	66.99	119.01	118.09	40.14	73.31	24.05	2.84
NEX7	500-d-850	G1	68.41	2.42	2.68	28.27	25.51	154.37	195.07	118.09	153.23	152.76	40.14	73.31	24.31	2.81
NEX7	500-d-850	G1	68.41	2.42	2.77	28.27	24.66	80.86	0.17	152.76	83.78	84.86	40.14	73.31	23.24	2.94
EBN20	1-2mm	G1	71.62	2.47	2.76	29.03	25.99	70.64	148.56	0.00	68.18	67.68	40.14	73.31	25.34	2.83
EBN20	1-2mm	G1	71.62	2.47	2.71	29.03	26.44	120.30	178.35	67.68	118.73	118.51	40.14	73.31	26.06	2.75
EBN20	1-2mm	G1	71.62	2.47	2.85	29.03	25.17	62.25	0.19	118.51	64.71	64.84	40.14	73.31	24.96	2.87
EBN20	250-d-500	G2	59.03	2.47	3.09	23.93	19.11	74.60	150.98	0.00	70.51	70.01	41.07	65.98	18.48	3.20
EBN20	250-d-500	G2	59.03	2.47	3.01	23.93	19.60	124.16	179.61	70.01	121.48	121.21	41.07	65.98	19.13	3.09
EBN20	250-d-500	G2	59.03	2.47	3.22	23.93	18.34	61.13	-0.37	121.21	64.92	65.02	41.07	65.98	18.17	3.25
CHE3	500-d-850	G3	62.83	2.40	2.74	26.18	22.93	72.43	151.33	0.00	69.34	66.59	34.94	64.24	19.78	3.18
CHE3	500-d-850	G3	62.83	2.40	2.73	26.18	23.00	121.66	181.66	66.59	119.37	118.07	34.94	64.24	21.08	2.98
CHE3	500-d-850	G3	62.83	2.40	2.75	26.18	22.88	155.35	195.96	118.07	153.74	152.86	34.94	64.24	20.96	3.00
CHE3	500-d-850	G3	62.83	2.40	2.80	26.18	22.46	79.59	-0.22	152.86	83.15	84.56	34.94	64.24	20.87	3.01

Table L.5. Gripen porosity results.

Sample	Size, μm	Setup	Gas	AR or Dry	P1 (V1), psig	Porosity, frac	PhiH, frac	PhL, frac
N-2	1.676<d<2.8	G2	He	Dry	149.72	0.06	0.029	0.036
N-2	1.676<d<2.8	G2	He	Dry	178.99	0.08	0.037	0.045
N-2	1.676<d<2.8	G2	He	Dry	-0.46	0.07	0.000	0.073
N-2	2.8<d<4	G3	He	Dry	152.38	0.07	0.029	0.042
N-2	2.8<d<4	G3	He	Dry	176.21	0.06	0.025	0.038
N-2	2.8<d<4	G3	He	Dry	-0.33	0.07	0.011	0.061
N-2	4<d<7	G3	He	Dry	149.88	0.06	0.026	0.033
N-2	4<d<7	G3	He	Dry	176.09	0.08	0.026	0.052
N-2	4<d<7	G3	He	Dry	-0.33	0.06	0.002	0.062
NG-2	0.85<d<2.8	G3	He	Dry	147.67	0.14	0.091	0.046
NG-2	0.85<d<2.8	G3	He	Dry	181.67	0.10	0.089	0.007
NG-2	0.85<d<2.8	G3	He	Dry	-0.30	0.11	0.059	0.052
NG-2	2.8<d<4	G3	He	Dry	150.62	0.14	0.081	0.057
NG-2	2.8<d<4	G3	He	Dry	180.06	0.12	0.075	0.045
NG-2	2.8<d<4	G3	He	Dry	-0.31	0.12	0.060	0.064
NG-2	4<d<7	G2	He	Dry	151.56	0.11	0.061	0.046
NG-2	4<d<7	G2	He	Dry	182.28	0.10	0.050	0.054
NG-2	4<d<7	G2	He	Dry	-0.41	0.09	0.033	0.057
NG-3	0.85<d<1.676	G2	He	Dry	149.21	0.12	0.076	0.047
NG-3	0.85<d<1.676	G2	He	Dry	182.64	0.10	0.064	0.038
NG-3	0.85<d<1.676	G2	He	Dry	-0.41	0.10	0.042	0.061
NG-3	1.676<d<2.8	G1	He	Dry	152.31	0.09	0.066	0.025
NG-3	1.676<d<2.8	G1	He	Dry	181.71	0.11	0.075	0.035
NG-3	1.676<d<2.8	G1	He	Dry	0.11	0.10	0.055	0.050
NG-3	2.8<d<4	G2	He	Dry	150.05	0.11	0.062	0.049
NG-3	2.8<d<4	G2	He	Dry	181.25	0.10	0.050	0.054
NG-3	4<d<7	G1	He	Dry	151.79	0.09	0.056	0.037
NG-3	4<d<7	G1	He	Dry	180.15	0.10	0.059	0.038
NG-3	4<d<7	G1	He	Dry	0.11	0.10	0.046	0.049
NG-4	0.85<d<2.8	G2	He	Dry	150.56	0.13	0.069	0.057
NG-4	0.85<d<2.8	G2	He	Dry	181.91	0.10	0.060	0.041
NG-4	0.85<d<2.8	G2	He	Dry	-0.41	0.11	0.039	0.068
NG-4	2.8<d<4	G2	He	Dry	150.48	0.10	0.055	0.046
NG-4	2.8<d<4	G2	He	Dry	183.83	0.07	0.044	0.031
NG-4	2.8<d<4	G2	He	Dry	-0.43		-0.042	0.042
NG-4	4<d<7	G3	He	Dry	152.34	0.12	0.073	0.044

NG-4	4<d<7	G3	He	Dry	181.96	0.11	0.065	0.043
NG-4	4<d<7	G3	He	Dry	-0.35	0.10	0.050	0.051
NG-8	0.8<d<1.676	G2	He	Dry	153.44	0.16	0.115	0.041
NG-8	0.8<d<1.676	G2	He	Dry	179.42	0.14	0.095	0.048
NG-8	0.8<d<1.676	G2	He	Dry	-0.45	0.08	0.326	-0.243
NG-8	1.676<d<2.8	G3	He	Dry	152.53	0.16	0.130	0.030
NG-8	1.676<d<2.8	G3	He	Dry	182.65	0.15	0.117	0.036
NG-8	1.676<d<2.8	G3	He	Dry	-0.35	0.14	0.104	0.031
NG-8	2.8-d-4	G1	He	Dry	151.47	0.15	0.106	0.044
NG-8	2.8-d-4	G1	He	Dry	180.90	0.16	0.114	0.043
NG-8	2.8-d-4	G1	He	Dry	0.15		-0.040	0.040
NG-10	0.85<d<1.676	G2	He	Dry	150.48	0.10	0.061	0.035
NG-10	0.85<d<1.676	G2	He	Dry	181.52	0.10	0.059	0.046
NG-10	0.85<d<1.676	G2	He	Dry	-0.51	0.08	0.041	0.044
NG-10	1.676<d<2.8	G1	He	Dry	149.31		0.037854	0.037854
NG-10	1.676<d<2.8	G1	He	Dry	181.24	0.11	0.066741	0.042638
NG-10	1.676<d<2.8	G1	He	Dry	0.11	0.09	0.055255	0.038878
NG-12	0.85<d<1.676	G3	He	Dry	148.03	0.19	0.192	-0.006
NG-12	0.85<d<1.676	G3	He	Dry	182.35	0.18	0.179	0.001
NG-12	0.85<d<1.676	G3	He	Dry	-0.34	0.17	0.164	0.008
Ng-12	1.676<d<2.8	G3	He	Dry	146.65	0.19	0.185	0.001
Ng-12	1.676<d<2.8	G3	He	Dry	178.97	0.18	0.180	0.004
Ng-12	1.676<d<2.8	G3	He	Dry	-0.33	0.18	0.160	0.017
NG12	4-d-7	G3	He	Dry	150.94	0.19	0.163	0.027
NG12	4-d-7	G3	He	Dry	182.45	0.18	0.154	0.029
NG12	4-d-7	G3	He	Dry	209.16	0.19	0.153	0.033
NG12	4-d-7	G3	He	Dry	-0.06	0.18	0.127	0.055

Table M.0.1. Pressure expansion experiment results.

Sample	Size, µm	Setup	Gas	AR or Dry	P1 (V1), psig	Porosity, frac	PhiH, frac	PhL, frac
N-2	1.676<d<2.8	G3	He	AR	160.05	0.05	0.027	0.020
N-2	1.676<d<2.8	G3	He	AR	186.46	0.04	0.022	0.020
N-2	1.676<d<2.8	G3	He	AR	209.34	0.05	0.022	0.025
N-2	1.676<d<2.8	G3	He	AR	-0.18	0.04	0.010	0.026
N-2	1.676<d<2.8	G3	He	AR	-0.21	0.05	0.015	0.031
N-2	2.8<d<4	G2	He	AR	145.45	0.03	0.011	0.017
N-2	2.8<d<4	G2	He	AR	175.76	0.04	0.017	0.022
N-2	2.8<d<4	G2	He	AR	209.89	0.04	0.014	0.025

N-2	2.8<d<4	G2	He	AR	-0.37	0.02	-0.005	0.023
N-2	2.8<d<4	G2	He	AR	-0.38	0.03	-0.002	0.030
N-6	0.85<d<2.8	G2	He	AR	152.19	1.00	0.980	0.020
N-6	0.85<d<2.8	G2	He	AR	182.30	1.00	0.976	0.024
N-6	0.85<d<2.8	G2	He	AR	208.79	1.00	0.976	0.024
N-6	0.85<d<2.8	G2	He	AR	-0.37	1.00	0.970	0.030
N-6	0.85<d<2.8	G2	He	AR	-0.38	1.00	0.967	0.033
N-6	2.8<d<4	G2	He	AR	162.62	0.07	0.033	0.042
N-6	2.8<d<4	G2	He	AR	182.14	0.06	0.027	0.038
N-6	2.8<d<4	G2	He	AR	212.45	0.07	0.026	0.047
N-6	2.8<d<4	G2	He	AR	-0.12	0.06	0.009	0.049
N-6	2.8<d<4	G2	He	AR	-0.20	0.08	0.015	0.065
NG-2	0.85<d<2.8	G2	He	AR	167.90	0.08	0.064	0.017
NG-2	0.85<d<2.8	G2	He	AR	182.66	0.10	0.073	0.023
NG-2	0.85<d<2.8	G2	He	AR	201.48	0.09	0.068	0.024
NG-2	0.85<d<2.8	G2	He	AR	-0.38	0.08	0.049	0.028
NG-2	0.85<d<2.8	G2	He	AR	-0.39	0.10	0.052	0.045
NG-2	2.8<d<4	G3	He	AR	167.33	0.09	0.075	0.018
NG-2	2.8<d<4	G3	He	AR	181.79	0.09	0.069	0.023
NG-2	2.8<d<4	G3	He	AR	200.67	0.10	0.067	0.030
NG-2	2.8<d<4	G3	He	AR	-0.16	0.08	0.056	0.024
NG-2	2.8<d<4	G3	He	AR	-0.22	0.10	0.060	0.038
NG-2	4<d<7	G2	He	AR	166.54	0.09	0.074	0.013
NG-2	4<d<7	G2	He	AR	185.91	0.09	0.070	0.020
NG-2	4<d<7	G2	He	AR	216.41	0.09	0.070	0.021
NG-2	4<d<7	G2	He	AR	-0.38	0.07	0.049	0.024
NG-2	4<d<7	G2	He	AR	-0.38	0.09	0.052	0.033
NG-3	0.85<d<1.676	G2	He	AR	157.72	0.08	0.061	0.023
NG-3	0.85<d<1.676	G2	He	AR	181.22	0.09	0.065	0.024
NG-3	0.85<d<1.676	G2	He	AR	208.57	0.08	0.061	0.020
NG-3	0.85<d<1.676	G2	He	AR	-0.39	0.07	0.044	0.031
NG-3	1.676<d<2.8	G2	He	AR	160.76	0.09	0.076	0.017
NG-3	1.676<d<2.8	G2	He	AR	188.25	0.10	0.083	0.022
NG-3	1.676<d<2.8	G2	He	AR	211.18	0.10	0.079	0.022
NG-3	1.676<d<2.8	G2	He	AR	-0.38	0.09	0.061	0.027
NG-3	1.676<d<2.8	G2	He	AR	-0.37	0.09	0.065	0.030
NG-3	2.8<d<4	G2	He	AR	166.75	0.07	0.050	0.018
NG-3	2.8<d<4	G2	He	AR	183.89	0.09	0.061	0.025
NG-3	2.8<d<4	G2	He	AR	203.61	0.08	0.056	0.028

NG-3	2.8<d<4	G2	He	AR	-0.38	0.06	0.038	0.024
NG-3	4<d<7	G2	He	AR	166.88	0.08	0.064	0.013
NG-3	4<d<7	G2	He	AR	188.71	0.08	0.059	0.023
NG-3	4<d<7	G2	He	AR	207.33	0.09	0.074	0.014
NG-3	4<d<7	G2	He	AR	-0.38		-0.020	0.020
NG-3	4<d<7	G2	He	AR	-0.39		-0.029	0.029
NG-4	0.85<d<2.8	G3	He	AR	161.41	0.09	0.066	0.022
NG-4	0.85<d<2.8	G3	He	AR	183.94	0.09	0.062	0.023
NG-4	0.85<d<2.8	G3	He	AR	200.05	0.09	0.061	0.026
NG-4	0.85<d<2.8	G3	He	AR	-0.20	0.08	0.049	0.029
NG-4	2.8<d<4	G3	He	AR	162.73	0.08	0.063	0.017
NG-4	2.8<d<4	G3	He	AR	182.59	0.08	0.060	0.022
NG-4	2.8<d<4	G3	He	AR	202.50	0.09	0.058	0.027
NG-4	2.8<d<4	G3	He	AR	-0.15	0.07	0.047	0.022
NG-4	4<d<7	G3	He	AR	170.89	0.08	0.062	0.015
NG-4	4<d<7	G3	He	AR	193.78	0.08	0.056	0.020
NG-4	4<d<7	G3	He	AR	212.59	0.08	0.056	0.028
NG-4	4<d<7	G3	He	AR	-0.14	0.06	0.042	0.018
NG-4	4<d<7	G3	He	AR	-0.23	0.07	0.046	0.026
NG-8	0.85<d<1.676	G2	He	AR	161.15	0.13	0.101	0.031
NG-8	0.85<d<1.676	G2	He	AR	185.99	0.14	0.106	0.036
NG-8	0.85<d<1.676	G2	He	AR	201.90	0.14	0.103	0.039
NG-8	0.85<d<1.676	G2	He	AR	-0.39	0.12	0.083	0.037
NG-8	1.676<d<2.8	G3	He	AR	163.71	0.16	0.135	0.026
NG-8	1.676<d<2.8	G3	He	AR	184.25	0.16	0.125	0.030
NG-8	1.676<d<2.8	G3	He	AR	214.42	0.15	0.124	0.027
NG-8	2.8<d<4	G3	He	AR	151.00	0.14	0.117	0.021
NG-8	2.8<d<4	G3	He	AR	181.51	0.12	0.114	0.009
NG-8	2.8<d<4	G3	He	AR	207.78	0.15	0.123	0.029
NG-8	2.8<d<4	G3	He	AR	-0.13	0.13	0.101	0.026
NG-8	2.8<d<4	G3	He	AR	-0.22	0.14	0.104	0.032
NG-10	0.85<d<1.676	G3	He	AR	164.83	0.04	0.020	0.016
NG-10	0.85<d<1.676	G3	He	AR	183.81	0.03	0.024	0.002
NG-10	0.85<d<1.676	G3	He	AR	213.24	0.06	-0.517	0.572
NG-10	0.85<d<1.676	G3	He	AR	-0.37	0.02	0.001	0.021
NG-10	0.85<d<1.676	G3	He	AR	-0.36	0.03	0.007	0.027
NG-10	1.676<d<2.8	G3	He	AR	159.45	0.10	0.074	0.023
NG-10	1.676<d<2.8	G3	He	AR	184.02	0.11	0.072	0.035
NG-10	1.676<d<2.8	G3	He	AR	203.58	0.09	0.068	0.024

NG-10	1.676<d<2.8	G3	He	AR	-0.17	0.08	0.057	0.027
NG-12	d<0.8	G3	He	AR	166.40	0.16	0.147	0.012
NG-12	d<0.8	G3	He	AR	187.49	0.15	0.132	0.020
NG-12	d<0.8	G3	He	AR	205.97	0.15	0.126	0.026
NG-12	d<0.8	G3	He	AR	-0.17	0.13	0.117	0.015
NG-12	d<0.8	G3	He	AR	-0.25	0.14	0.121	0.018
NG-12	0.85<d<1.676	G3	He	AR	162.62	0.15	0.136	0.014
NG-12	0.85<d<1.676	G3	He	AR	182.61	0.14	0.132	0.013
NG-12	0.85<d<1.676	G3	He	AR	203.86	0.15	0.130	0.017
NG-12	0.85<d<1.676	G3	He	AR	-0.16	0.13	0.119	0.014
NG-12	1.676<d<2.8	G3	He	AR	155.74	0.15	0.133	0.015
NG-12	1.676<d<2.8	G3	He	AR	179.84	0.14	0.126	0.017
NG-12	1.676<d<2.8	G3	He	AR	207.16	0.15	0.125	0.021
NG-12	1.676<d<2.8	G3	He	AR	-0.17	0.14	0.113	0.022
NG-12	2.8<d<4	G3	He	AR	150.70	0.14	0.129	0.016
NG-12	2.8<d<4	G3	He	AR	177.39	0.14	0.123	0.020
NG-12	2.8<d<4	G3	He	AR	215.54	0.14	0.122	0.022
NG-12	2.8<d<4	G3	He	AR	-0.14	0.13	0.112	0.017
NG-12	2.8<d<4	G3	He	AR	-0.23	0.14	0.114	0.023
NG-12	4<d<7	G2	He	AR	166.75	0.11	0.089	0.018
NG-12	4<d<7	G2	He	AR	194.82	0.11	0.089	0.024
NG-12	4<d<7	G2	He	AR	213.88	0.12	0.089	0.030
NG-12	4<d<7	G2	He	AR	-0.38	0.09	0.068	0.022
NG-12	4<d<7	G2	He	AR	-0.35	0.10	0.073	0.025
NA-2	0.85<d<1.676	G2	He	AR	167.95	0.03	0.017	0.017
NA-2	0.85<d<1.676	G2	He	AR	186.88	0.04	0.022	0.020
NA-2	0.85<d<1.676	G2	He	AR	206.09	0.04	0.024	0.021
NA-2	0.85<d<1.676	G2	He	AR	-0.38	0.03	0.005	0.024

Appendix M

Table M.1. Pressure expansion experiment results for core plug GRI.

Sample	gas	P, psig	Pclass, psig	1/P, psig^{-1}	Peq, psig	1/Peq psig^{-1}	lamination	hole	fracture	b-val	Kmatrix, md	Phimatrix, frac	Kfrac, mD	Phifrac, frac	b_val psig^{-1}	REV
EBN20	He	144.19	150	0.007	52.820	0.019	par	no	yes	yes	5.91E-07	0.08	1.84E-05	0.06	4260.96	no
EBN20	He	196.71	210	0.005	104.960	0.010	par	no	yes	yes	2.35E-08	0.06	1.88E-03	0.09	506.11	no
EBN20	He	246.74	240	0.004	156.290	0.006	par	no	yes	yes	1.99E-07	0.08	8.20E-06	0.09	18327.13	no
EBN20	He	297.51	high	0.003	207.170	0.005	par	no	yes	yes	1.38E-07	0.08	8.10E-06	0.09	15852.51	no
EBN20	He	401.04	high	0.002	277.140	0.004	par	no	yes	yes	3.67E-08	0.08	1.40E-04	0.09	19008.20	no
EBN20	He	1.05	REV	0.952	175.460	0.006	par	no	yes	yes	1.82E-07	0.10	6.84E-05	0.09	21708.64	yes
EBN20	He	144.19	150	0.007	52.820	0.019	par	no	no	no	2.42E-06	0.09				no
EBN20	He	196.71	210	0.005	104.960	0.010	par	no	no	no	4.33E-06	0.05				no
EBN20	He	246.74	240	0.004	156.290	0.006	par	no	no	no	9.00E-06	0.04				no
EBN20	He	297.51	high	0.003	207.170	0.005	par	no	no	no	1.10E-05	0.05				no
EBN20	He	401.04	high	0.002	277.140	0.004	par	no	no	no	9.81E-06	0.05				no
EBN20	He	1.05	REV	0.952	175.460	0.006	par	no	no	no	1.04E-05	0.05				yes
EBN20	He	144.19	150	0.007	52.820	0.019	par	no	no	yes	5.37E-08	0.06			79283.46	no
EBN20	He	196.71	210	0.005	104.960	0.010	par	no	no	yes	1.23E-07	0.04			70680.86	no
EBN20	He	246.74	240	0.004	156.290	0.006	par	no	no	yes	2.52E-07	0.05			27556.74	no
EBN20	He	297.51	high	0.003	207.170	0.005	par	no	no	yes	3.30E-07	0.05			27170.93	no
EBN20	He	401.04	high	0.002	277.140	0.004	par	no	no	yes	3.33E-07	0.05			23206.98	no

EBN20	He	1.05	REV	0.952	175.460	0.006	par	no	no	yes	2.71E-07	0.05			30679.76	yes
EBN20	He	144.19	150	0.007	52.820	0.019	par	no	yes	no	2.37E-07	0.10	9.93E-02	0.09		no
EBN20	He	196.71	210	0.005	104.960	0.010	par	no	yes	no	1.05E-06	0.09	1.69E-04	0.09		no
EBN20	He	246.74	240	0.004	156.290	0.006	par	no	yes	no	1.29E-06	0.07	2.13E-05	0.09		no
EBN20	He	297.51	high	0.003	207.170	0.005	par	no	yes	no	2.04E-06	0.05	5.90E-06	0.06		no
EBN20	He	401.04	high	0.002	277.140	0.004	par	no	yes	no	2.34E-06	0.06	5.49E-06	0.08		no
EBN20	He	1.05	REV	0.952	175.460	0.006	par	no	yes	no	3.51E-06	0.12	1.80E-03	0.09		yes
EBN20	CH4	165.86	180	0.006	59.780	0.017	par	no	no	no	6.18E-06	0.11				no
EBN20	CH4	185.89	180	0.005	103.830	0.010	par	no	no	no	1.92E-06	0.12				no
EBN20	CH4	208.10	210	0.005	139.950	0.007	par	no	no	no	2.81E-06	0.07				no
EBN20	CH4	0.94	REV	1.064	88.650	0.011	par	no	no	no	2.22E-06	0.09				yes
EBN20	CH4	0.77	REV	1.299	57.310	0.017	par	no	no	no	2.55E-06	0.08				yes
EBN20	CH4	165.86	180	0.006	59.780	0.017	par	no	no	yes	7.69E-07	0.09			3409.49	no
EBN20	CH4	185.89	180	0.005	103.830	0.010	par	no	no	yes	9.05E-07	0.09			3696.43	no
EBN20	CH4	208.10	210	0.005	139.950	0.007	par	no	no	yes	1.51E-06	0.07			2599.16	no
EBN20	CH4	0.94	REV	1.064	88.650	0.011	par	no	no	yes	2.27E-06	0.04			2429.75	yes
EBN20	CH4	0.77	REV	1.299	57.310	0.017	par	no	no	yes	6.46E-07	0.08			2336.24	yes
EBN20	CH4	165.86	180	0.006	59.780	0.017	par	no	yes	no	4.06E-06	0.09	4.10E-04	0.11		no
EBN20	CH4	185.89	180	0.005	103.830	0.010	par	no	yes	no	1.90E-06	0.13	3.47E-05	0.12		no
EBN20	CH4	208.10	210	0.005	139.950	0.007	par	no	yes	no	4.31E-07	0.12	2.72E-03	0.13		no
EBN20	CH4	0.94	REV	1.064	88.650	0.011	par	no	yes	no	8.16E-07	0.15	1.28E-04	0.08		yes
EBN20	CH4	0.77	REV	1.299	57.310	0.017	par	no	yes	no	1.17E-06	0.11	1.75E-04	0.09		yes
EBN20	CH4	165.86	180	0.006	59.780	0.017	par	no	yes	yes	1.97E-07	0.10	2.69E-05	0.10	5722.88	no
EBN20	CH4	185.89	180	0.005	103.830	0.010	par	no	yes	yes	4.41E-07	0.11	1.94E-04	0.10	2063.69	no
EBN20	CH4	208.10	210	0.005	139.950	0.007	par	no	yes	yes	1.22E-06	0.12	5.80E-06	0.09	973.65	no
EBN20	CH4	0.94	REV	1.064	88.650	0.011	par	no	yes	yes	1.56E-05	0.08	1.29E-03	0.08	4038.47	yes

EBN20	CH4	0.77	REV	1.299	57.310	0.017	par	no	yes	yes	1.03E-07	0.11	9.95E-04	0.11	4675.74	yes
EBN20	He	153.42	150	0.007	68.589	0.015	par	yes	no	no	7.22E-04	0.08				no
EBN20	He	181.53	180	0.006	119.273	0.008	par	yes	no	no	1.30E-03	0.12				no
EBN20	He	211.27	210	0.005	160.472	0.006	par	yes	no	no	2.93E-03	0.15				no
EBN20	He	246.33	240	0.004	198.915	0.005	par	yes	no	no	2.09E-03	0.16				no
EBN20	He	-0.14	REV	-7.143	109.248	0.009	par	yes	no	no	2.76E-03	0.13				yes
EBN20	He	153.42	150	0.007	68.589	0.015	par	yes	no	yes	1.05E-05	0.09			29920.16	no
EBN20	He	181.53	180	0.006	119.273	0.008	par	yes	no	yes	9.69E-06	0.08			27047.95	no
EBN20	He	211.27	210	0.005	160.472	0.006	par	yes	no	yes	2.01E-05	0.08			18663.15	no
EBN20	He	246.33	240	0.004	198.915	0.005	par	yes	no	yes	4.43E-05	0.10			12208.95	no
EBN20	He	-0.14	REV	-7.143	109.248	0.009	par	yes	no	yes	1.84E-05	0.09			20897.41	yes
EBN20	He	68.00	150	0.015	66.600	0.015	perp	no	yes	yes	1.57E-06	0.05	4.95E-05	0.08	609.20	no
EBN20	He	0.00	REV	3600.017	1.018	0.983	perp	no	yes	yes	1.46E-09	0.12	3.60E-03	0.13	4442.84	no
EBN20	He	132.20	150	0.008	130.900	0.008	perp	no	yes	yes	9.95E-06	0.04	4.00E-01	0.06	1022.41	no
EBN20	He	623.00	high	0.002	608.000	0.002	perp	no	yes	yes	1.47E-05	0.04	4.70E+01	0.04	60.22	no
EBN20	He	1.00	REV	1.000	10.000	0.100	perp	no	yes	yes	3.00E-06	0.04	1.06E+00	0.06	3107.49	no
EBN20	He	665.00	high	0.002	650.000	0.002	perp	no	yes	yes	4.61E-05	0.05	7.59E-01	0.05	43.66	no
EBN20	He	1.00	REV	1.000	11.000	0.091	perp	no	yes	yes	6.75E-05	0.05	2.75E+00	0.06	3.74	no
EBN20	He	668.00	high	0.001	653.000	0.002	perp	no	yes	yes	1.02E-06	0.04	1.80E+00	0.09	2547.32	no
EBN20	He	1.00	REV	1.000	11.000	0.091	perp	no	yes	yes	1.74E-06	0.04	1.07E+01	0.09	3282.71	no
EBN20	He	68.00	150	0.015	66.600	0.015	perp	no	yes	no	2.29E-04	0.05	6.73E-03	0.12		no
EBN20	He	0.00	REV	3600.017	1.018	0.983	perp	no	yes	no	2.79E-06	0.10	3.30E-02	0.12		no
EBN20	He	132.20	150	0.008	130.900	0.008	perp	no	yes	no	6.86E-05	0.04	1.34E-04	0.11		no
EBN20	He	623.00	high	0.002	608.000	0.002	perp	no	yes	no	4.63E-05	0.05	1.29E-04	0.11		no
EBN20	He	1.00	REV	1.000	10.000	0.100	perp	no	yes	no	6.81E-05	0.05	3.40E-03	0.08		no
EBN20	He	665.00	high	0.002	650.000	0.002	perp	no	yes	no	2.43E-05	0.04	1.88E-04	0.06		no

EBN20	He	668.00	high	0.001	653.000	0.002	perp	no	yes	no	1.16E-05	0.04	8.72E-02	0.12		no
EBN20	He	1.00	REV	1.000	11.000	0.091	perp	no	yes	no	4.43E-05	0.05	1.35E-02	0.05		no
EBN20	He	68.00	150	0.015	66.600	0.015	perp	no	no	yes	5.32E-06	0.04			2001.71	no
EBN20	He	0.00	REV	3600.017	1.018	0.983	perp	no	no	yes	1.33E-08	0.12			8416.54	no
EBN20	He	132.20	150	0.008	130.900	0.008	perp	no	no	yes	1.42E-05	0.04			655.16	no
EBN20	He	623.00	high	0.002	608.000	0.002	perp	no	no	yes	3.64E-05	0.06			40.50	no
EBN20	He	1.00	REV	1.000	10.000	0.100	perp	no	no	yes	6.79E-05	0.05			7.68	no
EBN20	He	665.00	high	0.002	650.000	0.002	perp	no	no	yes	1.13E-05	0.05			134.57	no
EBN20	He	1.00	REV	1.000	11.000	0.091	perp	no	no	yes	5.59E-05	0.05			4.18	no
EBN20	He	668.00	high	0.001	653.000	0.002	perp	no	no	yes	1.77E-05	0.05			86.92	no
EBN20	He	1.00	REV	1.000	11.000	0.091	perp	no	no	yes	2.72E-05	0.05			256.96	no
EBN20	He	68.00	150	0.015	66.600	0.015	perp	no	no	no	2.33E-04	0.05				no
EBN20	He	0.00	REV	3600.017	1.018	0.983	perp	no	no	no	6.51E-06	0.05				no
EBN20	He	132.20	150	0.008	130.900	0.008	perp	no	no	no	1.20E-04	0.04				no
EBN20	He	623.00	high	0.002	608.000	0.002	perp	no	no	no	3.50E-05	0.05				no
EBN20	He	1.00	REV	1.000	10.000	0.100	perp	no	no	no	8.36E-05	0.05				no
EBN20	He	665.00	high	0.002	650.000	0.002	perp	no	no	no	3.36E-05	0.05				no
EBN20	He	1.00	REV	1.000	11.000	0.091	perp	no	no	no	8.52E-05	0.05				no
EBN20	He	668.00	high	0.001	653.000	0.002	perp	no	no	no	2.52E-05	0.04				no
EBN20	He	1.00	REV	1.000	11.000	0.091	perp	no	no	no	8.79E-05	0.05				no
CHE3	He	150.30	150	0.007	100.979	0.010	par	no	no	no	2.41E-04	0.08				no
CHE3	He	180.43	180	0.006	154.294	0.006	par	no	no	no	1.08E-04	0.08				no
CHE3	He	210.39	210	0.005	191.836	0.005	par	no	no	no	1.29E-04	0.08				no
CHE3	He	240.83	240	0.004	224.645	0.004	par	no	no	no	9.47E-05	0.07				no
CHE3	He	150.30	150	0.007	100.979	0.010	par	no	no	yes	2.47E-06	0.09			38635.88	no
CHE3	He	180.43	180	0.006	154.294	0.006	par	no	no	yes	5.01E-06	0.08			17889.21	no

CHE3	He	210.39	210	0.005	191.836	0.005	par	no	no	yes	1.70E-05	0.09			7902.88	no
CHE3	He	240.83	240	0.004	224.645	0.004	par	no	no	yes	3.15E-06	0.07			22171.00	no
CHE3	He	-0.42	REV	-2.392	73.326	0.014	par	no	no	yes	4.41E-06	0.08			22317.41	yes
CHE3	He	150.30	150	0.007	100.979	0.010	par	no	yes	yes	6.44E-07	0.09	1.19E-03	0.11	62348.84	no
CHE3	He	180.43	180	0.006	154.294	0.006	par	no	yes	yes	2.70E-05	0.08	3.76E-05	0.06	2791.52	no
CHE3	He	210.39	210	0.005	191.836	0.005	par	no	yes	yes	6.40E-06	0.07	2.94E-05	0.11	13026.63	no
CHE3	He	240.83	240	0.004	224.645	0.004	par	no	yes	yes	1.17E-05	0.08	2.93E-01	0.12	11534.16	no
CHE3	He	-0.42	REV	-2.392	73.326	0.014	par	no	yes	yes	1.59E-06	0.09	1.47E-03	0.06	42845.26	yes
CHE3	He	150.30	150	0.007	100.979	0.010	par	no	yes	no	2.30E-04	0.08	2.91E-03	0.11		no
CHE3	He	180.43	180	0.006	154.294	0.006	par	no	yes	no	5.69E-05	0.07	1.81E-02	0.11		no
CHE3	He	210.39	210	0.005	191.836	0.005	par	no	yes	no	4.57E-05	0.07	6.92E-02	0.09		no
CHE3	He	240.83	240	0.004	224.645	0.004	par	no	yes	no	4.38E-05	0.08	1.73E-01	0.08		no
CHE3	He	-0.42	REV	-2.392	73.326	0.014	par	no	yes	no	7.92E-05	0.09	3.87E-01	0.09		yes
Karoo	He	150.13	150	0.007	76.226	0.013	perp	no	no	no	1.13E-03	0.18				no
Karoo	He	180.36	180	0.006	129.260	0.008	perp	no	no	no	2.10E-03	0.22				no
Karoo	He	209.87	210	0.005	170.422	0.006	perp	no	no	no	3.30E-03	0.22				no
Karoo	He	239.91	240	0.004	205.833	0.005	perp	no	no	no	3.35E-03	0.22				no
Karoo	He	-0.42	REV	-2.387	100.172	0.010	perp	no	no	no	4.22E-03	0.26				yes
Karoo	He	150.13	150	0.007	76.226	0.013	perp	no	no	yes	3.53E-03	0.14			33.99	no
Karoo	He	180.36	180	0.006	129.260	0.008	perp	no	no	yes	3.25E-03	0.16			186.58	no
Karoo	He	209.87	210	0.005	170.422	0.006	perp	no	no	yes	1.41E-03	0.17			1458.20	no
Karoo	He	239.91	240	0.004	205.833	0.005	perp	no	no	yes	6.80E-03	0.18			148.26	no
Karoo	He	-0.42	REV	-2.387	100.172	0.010	perp	no	no	yes	7.22E-04	0.20			3809.91	yes
Karoo	He	150.13	150	0.007	76.226	0.013	perp	no	yes	yes	7.79E-05	0.18	2.06E-04	0.16	9886.32	no
Karoo	He	180.36	180	0.006	129.260	0.008	perp	no	yes	yes	6.72E-05	0.17	7.85E-05	0.15	10000.00	no
Karoo	He	209.87	210	0.005	170.422	0.006	perp	no	yes	yes	1.72E-04	0.16	2.39E-03	0.22	9726.22	no

Karoo	He	239.91	240	0.004	205.833	0.005	perp	no	yes	yes	7.49E-05	0.07	6.41E-04	0.12	5183.61	no
Karoo	He	-0.42	REV	-2.387	100.172	0.010	perp	no	yes	yes	1.65E-05	0.05	2.08E-02	0.17	669.89	yes
Karoo	He	150.13	150	0.007	76.226	0.013	perp	no	yes	no	5.47E-04	0.12	1.26E-03	0.04		no
Karoo	He	180.36	180	0.006	129.260	0.008	perp	no	yes	no	1.20E-03	0.18	1.98E-02	0.04		no
Karoo	He	209.87	210	0.005	170.422	0.006	perp	no	yes	no	3.12E-03	0.20	3.26E-03	0.17		no
Karoo	He	239.91	240	0.004	205.833	0.005	perp	no	yes	no	2.57E-03	0.21	3.62E-03	0.17		no
Karoo	He	-0.42	REV	-2.387	100.172	0.010	perp	no	yes	no	1.16E-06	0.15	1.34E-01	0.15		yes
Karoo	CH4	150.12	150	0.007	59.836	0.017	perp	no	no	no	4.26E-03	0.17				no
Karoo	CH4	179.77	180	0.006	107.929	0.009	perp	no	no	no	3.27E-04	0.10				no
Karoo	CH4	210.02	210	0.005	149.026	0.007	perp	no	no	no	1.45E-04	0.05				no
Karoo	CH4	-0.16	REV	-6.135	90.085	0.011	perp	no	no	no	1.86E-03	0.17				yes
Karoo	CH4	-0.27	REV	-3.759	54.315	0.018	perp	no	no	no	2.84E-03	0.28				yes
Karoo	CH4	150.12	150	0.007	59.836	0.017	perp	no	no	yes	1.46E-04	0.11			2277.75	no
Karoo	CH4	179.77	180	0.006	107.929	0.009	perp	no	no	yes	4.14E-05	0.05			1102.26	no
Karoo	CH4	210.02	210	0.005	149.026	0.007	perp	no	no	yes	7.33E-05	0.04			973.58	no
Karoo	CH4	-0.16	REV	-6.135	90.085	0.011	perp	no	no	yes	1.65E-04	0.10			3108.75	yes
Karoo	CH4	-0.27	REV	-3.759	54.315	0.018	perp	no	no	yes	3.89E-07	0.11			1116.96	yes
Karoo	CH4	150.12	150	0.007	59.836	0.017	perp	no	yes	yes	7.79E-05	0.18	2.06E-04	0.16	9886.32	no
Karoo	CH4	179.77	180	0.006	107.929	0.009	perp	no	yes	yes	6.72E-05	0.17	7.85E-05	0.15	10000.00	no
Karoo	CH4	210.02	210	0.005	149.026	0.007	perp	no	yes	yes	1.72E-04	0.16	2.39E-03	0.22	9726.22	no
Karoo	CH4	-0.16	REV	-6.135	90.085	0.011	perp	no	yes	yes	7.49E-05	0.07	6.41E-04	0.12	5183.61	yes
Karoo	CH4	-0.27	REV	-3.759	54.315	0.018	perp	no	yes	yes	1.65E-05	0.05	2.08E-02	0.17	669.89	yes
Karoo	CH4	150.12	150	0.007	59.836	0.017	perp	no	yes	no	1.18E-04	0.08	6.61E-04	0.18		no
Karoo	CH4	179.77	180	0.006	107.929	0.009	perp	no	yes	no	6.72E-04	0.05	6.72E-04	0.15		no
Karoo	CH4	210.02	210	0.005	149.026	0.007	perp	no	yes	no	1.85E-04	0.06	2.55E-03	0.13		no
Karoo	CH4	-0.16	REV	-6.135	90.085	0.011	perp	no	yes	no	4.32E-04	0.08	1.87E-03	0.14		yes

Karoo	CH4	-0.27	REV	-3.759	54.315	0.018	perp	no	yes	no	5.87E-04	0.16	6.08E-02	0.11		yes
EBN33	He	146.40	150	0.007	84.780	0.012	par	no	no	no	1.16E-02	0.09				no
EBN33	He	239.83	240	0.004	138.809	0.007	par	no	no	no	4.40E-03	0.10				no
EBN33	He	512.36	high	0.002	294.222	0.003	par	no	no	no	8.05E-04	0.08				no
EBN33	He	240.97	240	0.004	197.506	0.005	par	no	no	no	4.92E-03	0.16				no
EBN33	He	-0.25	REV	-4.049	106.277	0.009	par	no	no	no	2.98E-03	0.11				yes
EBN33	He	155.07	150	0.006	70.688	0.014	par	no	no	yes	4.55E-09	0.05			143.61	no
EBN33	He	175.55	180	0.006	118.633	0.008	par	no	no	yes	2.41E-03	0.06			8032.68	no
EBN33	He	210.92	210	0.005	160.858	0.006	par	no	no	yes	1.84E-03	0.08			165.94	no
EBN33	He	240.97	240	0.004	197.506	0.005	par	no	no	yes	1.63E-03	0.17			1512.25	no
EBN33	He	-0.25	REV	-4.049	106.277	0.009	par	no	no	yes	1.23E-03	0.09			1062.02	yes
EBN33	He	155.07	150	0.006	70.688	0.014	par	no	yes	yes	1.70E-04	0.09	5.51E-04	0.15	6652.44	no
EBN33	He	175.55	180	0.006	118.633	0.008	par	no	yes	yes	1.80E-04	0.05	1.22E-02	0.13	4155.83	no
EBN33	He	210.92	210	0.005	160.858	0.006	par	no	yes	yes	1.69E-04	0.05	1.18E-02	0.14	4217.70	no
EBN33	He	240.97	240	0.004	197.506	0.005	par	no	yes	yes	9.99E-05	0.11	1.51E-03	0.07	6043.89	no
EBN33	He	-0.25	REV	-4.049	106.277	0.009	par	no	yes	yes	4.55E-04	0.16	1.10E-03	0.13	4790.39	yes
EBN33	He	155.07	150	0.006	70.688	0.014	par	no	yes	no	2.34E-03	0.04	6.39E-02	0.10		no
EBN33	He	175.55	180	0.006	118.633	0.008	par	no	yes	no	6.17E-04	0.07	1.58E-03	0.16		no
EBN33	He	210.92	210	0.005	160.858	0.006	par	no	yes	no	9.61E-04	0.07	1.29E-03	0.16		no
EBN33	He	240.97	240	0.004	197.506	0.005	par	no	yes	no	6.71E-04	0.06	8.62E-03	0.13		no
EBN33	He	-0.25	REV	-4.049	106.277	0.009	par	no	yes	no	4.34E-04	0.04	3.44E-03	0.14		yes
EBN33	CH4	149.27	150	0.007	81.836	0.012	par	no	no	no	1.66E-04	0.05				no
EBN33	CH4	180.51	180	0.006	136.219	0.007	par	no	no	no	3.70E-07	0.05				no
EBN33	CH4	208.78	210	0.005	176.353	0.006	par	no	no	no	3.84E-08	0.08				no
EBN33	CH4	-0.40	REV	-2.488	79.502	0.013	par	no	no	no	4.52E-04	0.16				yes
EBN33	CH4	-0.41	REV	-2.469	35.841	0.028	par	no	no	no	6.90E-04	0.09				yes

EBN33	CH4	149.27	150	0.007	81.836	0.012	par	no	no	yes	4.44E-05	0.05			1025.27	no
EBN33	CH4	180.51	180	0.006	136.219	0.007	par	no	no	yes	1.04E-07	0.05			1782.98	no
EBN33	CH4	208.78	210	0.005	176.353	0.006	par	no	no	yes	9.81E-09	0.10			3796.28	no
EBN33	CH4	-0.40	REV	-2.488	79.502	0.013	par	no	no	yes	1.46E-04	0.18			2335.97	yes
EBN33	CH4	-0.41	REV	-2.469	35.841	0.028	par	no	no	yes	1.79E-04	0.08			1775.72	yes
EBN33	CH4	149.27	150	0.007	81.836	0.012	par	no	yes	yes	2.27E-05	0.05	1.21E-02	0.09	1145.71	no
EBN33	CH4	180.51	180	0.006	136.219	0.007	par	no	yes	yes	8.34E-08	0.05	8.66E-06	0.05	2232.23	no
EBN33	CH4	208.78	210	0.005	176.353	0.006	par	no	yes	yes	2.63E-08	0.04	1.41E-05	0.07	281.35	no
EBN33	CH4	-0.40	REV	-2.488	79.502	0.013	par	no	yes	yes	2.43E-05	0.13	7.67E-04	0.19	3319.87	yes
EBN33	CH4	-0.41	REV	-2.469	35.841	0.028	par	no	yes	yes	8.17E-05	0.08	1.10E-03	0.20	3923.39	yes
EBN33	CH4	149.27	150	0.007	81.836	0.012	par	no	yes	no	8.27E-05	0.05	1.70E-03	0.10		no
EBN33	CH4	180.51	180	0.006	136.219	0.007	par	no	yes	no	3.02E-07	0.04	3.76E-06	0.13		no
EBN33	CH4	208.78	210	0.005	176.353	0.006	par	no	yes	no	1.13E-08	0.11	7.92E-04	0.11		no
EBN33	CH4	-0.40	REV	-2.488	79.502	0.013	par	no	yes	no	4.90E-04	0.16	1.48E-04	0.08		yes
EBN33	CH4	-0.41	REV	-2.469	35.841	0.028	par	no	yes	no	5.41E-05	0.08	2.42E-03	0.14		yes
CHE2	He	489.19	high	0.002	185.990	0.005	par	no	no	no	2.66E-06	0.06				no
CHE2	He	692.24	high	0.001	376.550	0.003	par	no	no	no	3.14E-06	0.05				no
CHE2	He	899.79	high	0.001	573.540	0.002	par	no	no	no	1.79E-06	0.06				no
CHE2	He	1196.03	high	0.001	805.230	0.001	par	no	no	no	1.86E-06	0.06				no
CHE2	He	1326.61	high	0.001	991.130	0.001	par	no	no	no	2.97E-06	0.18				no
CHE2	He	0.50	REV	0.667	18.800	0.051	par	no	no	no	9.82E-06	0.04				yes
CHE2	He	489.19	high	0.002	185.990	0.005	par	no	no	yes	1.14E-06	0.06			2104.56	no
CHE2	He	692.24	high	0.001	376.550	0.003	par	no	no	yes	1.07E-06	0.05			2663.77	no
CHE2	He	899.79	high	0.001	573.540	0.002	par	no	no	yes	5.30E-06	0.05			4589.74	no
CHE2	He	1196.03	high	0.001	805.230	0.001	par	no	no	yes	4.60E-07	0.05			2521.83	no
CHE2	He	1326.61	high	0.001	991.130	0.001	par	no	no	yes	3.50E-07	0.19			6350.95	no

CHE2	He	0.50	REV	0.667	18.800	0.051	par	no	no	yes	1.85E-06	0.04			3970.80	yes
CHE2	He	489.19	high	0.002	185.990	0.005	par	no	yes	yes	2.56E-07	0.10	1.35E-06	0.12	1935.63	no
CHE2	He	692.24	high	0.001	376.550	0.003	par	no	yes	yes	8.65E-08	0.09	1.32E-03	0.11	2765.80	no
CHE2	He	899.79	high	0.001	573.540	0.002	par	no	yes	yes	3.48E-07	0.06	5.73E-04	0.12	468.93	no
CHE2	He	1196.03	high	0.001	805.230	0.001	par	no	yes	yes	2.07E-07	0.05	7.02E-06	0.08	1744.38	no
CHE2	He	1326.61	high	0.001	991.130	0.001	par	no	yes	yes	2.31E-07	0.19	6.69E-06	0.16	4943.83	no
CHE2	He	0.50	REV	0.667	18.800	0.051	par	no	yes	yes	3.53E-07	0.04	2.70E-03	0.10	8997.27	yes
CHE2	He	489.19	high	0.002	185.990	0.005	par	no	yes	no	8.55E-07	0.09	9.12E-06	0.09		no
CHE2	He	692.24	high	0.001	376.550	0.003	par	no	yes	no	2.12E-07	0.09	5.86E-04	0.22		no
CHE2	He	899.79	high	0.001	573.540	0.002	par	no	yes	no	3.27E-07	0.09	5.54E-04	0.22		no
CHE2	He	1196.03	high	0.001	805.230	0.001	par	no	yes	no	2.27E-07	0.05	9.23E-03	0.21		no
CHE2	He	1326.61	high	0.001	991.130	0.001	par	no	yes	no	8.34E-07	0.14	5.63E-02	0.06		no
CHE2	He	0.50	REV	0.667	18.800	0.051	par	no	yes	no	4.89E-06	0.04	1.86E-02	0.09		yes
CHE3	CH4	151.16	150	0.007	94.189	0.011	par	no	no	no	7.70E-05	0.14				no
CHE3	CH4	180.45	180	0.006	148.191	0.007	par	no	no	no	3.27E-05	0.12				no
CHE3	CH4	211.37	210	0.005	187.712	0.005	par	no	no	no	3.44E-05	0.12				no
CHE3	CH4	-0.39	REV	-2.551	67.488	0.015	par	no	no	no	3.75E-05	0.10				yes
CHE3	CH4	-0.34	REV	-2.924	24.397	0.041	par	no	no	no	3.50E-05	0.12				yes
CHE3	CH4	151.16	150	0.007	94.189	0.011	par	no	yes	yes	9.29E-06	0.15	2.50E-04	0.15	1990.50	no
CHE3	CH4	180.45	180	0.006	148.191	0.007	par	no	yes	yes	1.07E-05	0.14	1.52E-05	0.15	2887.26	no
CHE3	CH4	211.37	210	0.005	187.712	0.005	par	no	yes	yes	1.36E-05	0.14	2.78E-05	0.15	2472.17	no
CHE3	CH4	-0.39	REV	-2.551	67.488	0.015	par	no	yes	yes	9.79E-06	0.12	1.40E-04	0.15	2472.01	yes
CHE3	CH4	-0.34	REV	-2.924	24.397	0.041	par	no	yes	yes	7.23E-06	0.14	1.24E-04	0.10	2451.23	yes
CHE3	CH4	151.16	150	0.007	94.189	0.011	par	no	yes	no	6.65E-05	0.13	5.57E-04	0.17		no
CHE3	CH4	180.45	180	0.006	148.191	0.007	par	no	yes	no	3.47E-05	0.12	6.29E-05	0.21		no
CHE3	CH4	211.37	210	0.005	187.712	0.005	par	no	yes	no	3.36E-05	0.11	6.85E-05	0.18		no

CHE3	CH4	-0.39	REV	-2.551	67.488	0.015	par	no	yes	no	2.15E-05	0.11	1.08E-02	0.24		yes
CHE3	CH4	-0.34	REV	-2.924	24.397	0.041	par	no	yes	no	3.58E-05	0.13	8.34E-05	0.11		yes
CHE3	CH4	151.16	150	0.007	94.189	0.011	par	no	no	yes	7.31E-06	0.15			3302.35	no
CHE3	CH4	180.45	180	0.006	148.191	0.007	par	no	no	yes	6.55E-06	0.12			3271.85	no
CHE3	CH4	211.37	210	0.005	187.712	0.005	par	no	no	yes	7.09E-06	0.11			2759.24	no
CHE3	CH4	-0.39	REV	-2.551	67.488	0.015	par	no	no	yes	7.38E-06	0.10			3679.87	yes
CHE3	CH4	-0.34	REV	-2.924	24.397	0.041	par	no	no	yes	5.73E-05	0.15			429.72	yes
EBN20	CH4	155.09	150	0.006	46.360	0.021	par	yes	yes	yes	1.15E-06	0.13	2.81E-04	0.15	2226.88	no
EBN20	CH4	182.04	180	0.005	85.710	0.012	par	yes	yes	yes	3.51E-06	0.12	1.21E-05	0.14	1781.97	no
EBN20	CH4	210.40	210	0.005	121.890	0.008	par	yes	yes	yes	1.96E-06	0.10	9.85E-06	0.14	2491.05	no
EBN20	CH4	1.92	REV	0.342	87.640	0.011	par	yes	yes	yes	3.30E-06	0.09	4.53E-06	0.12	2753.58	yes
EBN20	CH4	1.97	REV	0.337	63.060	0.016	par	yes	yes	yes	2.23E-06	0.11	2.70E-06	0.09	4286.09	yes
EBN20	CH4	155.09	150	0.006	46.360	0.021	par	yes	yes	no	1.64E-05	0.14	1.22E-04	0.14		no
EBN20	CH4	182.04	180	0.005	85.710	0.012	par	yes	yes	no	1.90E-05	0.12	7.54E-05	0.13		no
EBN20	CH4	210.40	210	0.005	121.890	0.008	par	yes	yes	no	1.67E-05	0.10	5.20E-05	0.14		no
EBN20	CH4	1.92	REV	0.342	87.640	0.011	par	yes	yes	no	2.70E-05	0.09	3.05E-05	0.15		yes
EBN20	CH4	1.97	REV	0.337	63.060	0.016	par	yes	yes	no	1.18E-05	0.10	7.26E-02	0.09		yes
EBN20	CH4	155.09	150	0.006	46.360	0.021	par	yes	no	yes	4.81E-06	0.13			816.04	no
EBN20	CH4	182.04	180	0.005	85.710	0.012	par	yes	no	yes	4.88E-06	0.11			1065.93	no
EBN20	CH4	210.40	210	0.005	121.890	0.008	par	yes	no	yes	2.93E-06	0.09			1919.95	no
EBN20	CH4	1.92	REV	0.342	87.640	0.011	par	yes	no	yes	4.95E-06	0.09			2175.97	yes
EBN20	CH4	1.97	REV	0.337	63.060	0.016	par	yes	no	yes	4.95E-06	0.09			2175.97	yes
EBN20	CH4	155.09	150	0.006	46.360	0.021	par	yes	no	no	1.68E-05	0.13				no
EBN20	CH4	182.04	180	0.005	85.710	0.012	par	yes	no	no	2.24E-05	0.12				no
EBN20	CH4	210.40	210	0.005	121.890	0.008	par	yes	no	no	1.55E-05	0.09				no
EBN20	CH4	1.92	REV	0.342	87.640	0.011	par	yes	no	no	3.36E-05	0.09				yes

EBN20	CH4	1.97	REV	0.337	63.060	0.016	par	yes	no	no	2.30E-05	0.09				yes
EBN9	CH4	144.31	150	0.007	79.667	0.013	par	no	yes	yes	3.58E-09	0.07	3.62E-04	0.06	711.38	no
EBN9	CH4	-0.35	REV	-2.874	35.852	0.028	par	no	yes	yes	3.50E-09	0.07	3.45E-04	0.06	701.59	no
EBN9	CH4	144.31	150	0.007	79.667	0.013	par	no	yes	no	5.99E-09	0.08	2.36E-04	0.09		no
EBN9	CH4	-0.35	REV	-2.874	35.852	0.028	par	no	yes	no	9.38E-09	0.11	5.96E-02	0.13		no
EBN9	CH4	144.31	150	0.007	79.667	0.013	par	no	no	yes	2.30E-08	0.04			552.29	no
EBN9	CH4	-0.35	REV	-2.874	35.852	0.028	par	no	no	yes	7.30E-09	0.06			7149.98	no
EBN9	CH4	144.31	150	0.007	79.667	0.013	par	no	no	no	2.79E-08	0.06				no
EBN9	CH4	-0.35	REV	-2.874	35.852	0.028	par	no	no	no	5.00E-08	0.06				no
EBN9	He	771.00	high	0.001	752.000	0.001	par	no	yes	yes	1.20E-07	0.09	2.97E-07	0.09	687.27	no
EBN9	He	1.00	REV	0.500	6.560	0.132	par	no	yes	yes	2.93E-09	0.06	2.13E-08	0.15	1719.53	no
EBN9	He	136.20	150	0.007	133.800	0.007	par	no	yes	yes	2.51E-08	0.03	3.02E-08	0.04	113.41	yes
EBN9	He	771.00	high	0.001	752.000	0.001	par	no	yes	no	3.47E-08	0.06	5.00E-05	0.04		no
EBN9	He	1.00	REV	0.500	6.560	0.132	par	no	yes	no	1.04E-08	0.05	1.17E-08	0.11		no
EBN9	He	136.20	150	0.007	133.800	0.007	par	no	yes	no	1.70E-09	0.05	3.39E-08	0.07		yes
EBN9	He	771.00	high	0.001	752.000	0.001	par	no	no	yes	2.20E-07	0.09			275.41	no
EBN9	He	1.00	REV	0.500	6.560	0.132	par	no	no	yes	5.29E-09	0.06			1225.04	no
EBN9	He	136.20	150	0.007	133.800	0.007	par	no	no	yes	7.94E-10	0.05			3307.82	yes
CHE3	CH4	149.47	150	0.007	76.503	0.013	perp	no	no	yes	7.91E-06	0.08			3024.48	no
CHE3	CH4	180.94	180	0.006	130.241	0.008	perp	no	no	yes	9.85E-06	0.06			2017.11	no
CHE3	CH4	209.03	210	0.005	170.904	0.006	perp	no	no	yes	5.51E-06	0.06			2703.04	no
CHE3	CH4	-0.09	REV	-11.765	83.540	0.012	perp	no	no	yes	1.02E-05	0.07			4884.43	yes
CHE3	CH4	-0.26	REV	-3.906	40.773	0.025	perp	no	no	yes	1.35E-05	0.07			2551.37	yes
CHE3	CH4	149.47	150	0.007	76.503	0.013	perp	no	no	no	3.20E-05	0.08				no
CHE3	CH4	180.94	180	0.006	130.241	0.008	perp	no	no	no	2.29E-05	0.06				no
CHE3	CH4	209.03	210	0.005	170.904	0.006	perp	no	no	no	1.04E-05	0.05				no

CHE3	CH4	-0.09	REV	-11.765	83.540	0.012	perp	no	no	no	1.16E-04	0.09				yes
CHE3	CH4	-0.26	REV	-3.906	40.773	0.025	perp	no	no	no	9.06E-05	0.10				yes
CHE3	CH4	149.47	150	0.007	76.503	0.013	perp	no	yes	no	2.76E-05	0.07	3.05E-05	0.11		no
CHE3	CH4	180.94	180	0.006	130.241	0.008	perp	no	yes	no	1.85E-05	0.06	1.19E-04	0.06		no
CHE3	CH4	209.03	210	0.005	170.904	0.006	perp	no	yes	no	1.51E-05	0.06	3.40E-05	0.13		no
CHE3	CH4	-0.09	REV	-11.765	83.540	0.012	perp	no	yes	no	7.14E-05	0.08	2.57E-04	0.19		yes
CHE3	CH4	-0.26	REV	-3.906	40.773	0.025	perp	no	yes	no	1.06E-04	0.11	1.84E-04	0.21		yes
CHE3	CH4	149.47	150	0.007	76.503	0.013	perp	no	yes	yes	2.95E-06	0.07	1.70E-05	0.15	6429.48	no
CHE3	CH4	180.94	180	0.006	130.241	0.008	perp	no	yes	yes	3.67E-06	0.06	4.08E-05	0.14	3754.21	no
CHE3	CH4	209.03	210	0.005	170.904	0.006	perp	no	yes	yes	4.99E-06	0.06	5.46E-05	0.15	2769.36	no
CHE3	CH4	-0.09	REV	-11.765	83.540	0.012	perp	no	yes	yes	3.34E-05	0.09	3.72E-05	0.12	2266.58	yes
CHE3	CH4	-0.26	REV	-3.906	40.773	0.025	perp	no	yes	yes	2.58E-05	0.09	4.52E-05	0.12	2242.05	yes
EBN20	N2	124.50	150	0.008	113.900	0.009	par	no	no	no	3.00E-04	0.08				no
EBN20	N2	0.00	REV	1.000	6.900	0.127	par	no	no	no	2.50E-04	0.05				yes
EBN9	He	771.00	high	0.001	752.000	0.001	par	no	no	no	5.00E-07	0.08				no
EBN9	He	1.00	REV	0.500	6.560	0.132	par	no	no	no	2.50E-07	0.02				yes
EBN9	He	136.20	150	0.007	133.800	0.007	par	no	no	no	5.00E-06	0.04				no
EBN9	N2	91.90	150	0.011	90.100	0.011	par	no	no	no	1.20E-05	0.05				no
EBN9	N2	129.80	150	0.008	127.800	0.008	par	no	no	no	1.20E-05	0.04				no
EBN9	N2	0.30	REV	0.769	2.000	0.333	par	no	no	no	1.20E-05	0.03				yes
EBN6	He	117.10	150	0.008	111.700	0.009	par	no	no	no	3.00E-07	0.07				no
CHE2	He	490.19	high	0.002	186.990	0.005	par	no	no	yes	1.12E-05	0.06			162.08	no
CHE2	He	693.24	high	0.001	377.550	0.003	par	no	no	yes	1.14E-05	0.08			341.78	no
CHE2	He	900.79	high	0.001	574.540	0.002	par	no	no	yes	1.10E-05	0.08			80.00	no
CHE2	He	1197.03	high	0.001	806.230	0.001	par	no	no	yes	1.73E-05	0.14			462.00	no
CHE2	He	1327.61	high	0.001	992.130	0.001	par	no	no	yes	3.00E-05	0.20			60.00	no

CHE2	He	1.50	REV	0.400	19.800	0.048	par	no	no	yes	2.50E-04	0.04			3.50	yes
CHE2	He	490.19	high	0.002	186.990	0.005	par	no	no	no	2.30E-06	0.07				no
CHE2	He	693.24	high	0.001	377.550	0.003	par	no	no	no	3.80E-06	0.06				no
CHE2	He	900.79	high	0.001	574.540	0.002	par	no	no	no	1.90E-06	0.07				no
CHE2	He	1197.03	high	0.001	806.230	0.001	par	no	no	no	2.80E-06	0.07				no
CHE2	He	1327.61	high	0.001	992.130	0.001	par	no	no	no	6.93E-06	0.15				no
CHE2	He	1.50	REV	0.400	19.800	0.048	par	no	no	no	6.90E-07	0.05				yes
CHE2	He	490.19	high	0.002	186.990	0.005	par	no	yes	no	2.04E-06	0.07	2.89E-04	0.03		no
CHE2	He	693.24	high	0.001	377.550	0.003	par	no	yes	no	2.04E-06	0.06	1.18E-02	0.04		no
CHE2	He	900.79	high	0.001	574.540	0.002	par	no	yes	no	3.52E-06	0.07	1.92E-02	0.05		no
CHE2	He	1197.03	high	0.001	806.230	0.001	par	no	yes	no	1.45E-06	0.07	1.14E-02	0.03		no
CHE2	He	1327.61	high	0.001	992.130	0.001	par	no	yes	no	3.56E-06	0.14	8.95E-04	0.03		no
CHE2	He	1.50	REV	0.400	19.800	0.048	par	no	yes	no	1.58E-07	0.04	1.73E-05	0.14		yes
CHE3	He	150.30	150	0.007	100.976	0.010	par	no	no	no	2.41E-04	0.08				no
CHE3	He	180.43	180	0.006	154.289	0.006	par	no	no	no	1.08E-04	0.09				no
CHE3	He	210.39	210	0.005	191.830	0.005	par	no	no	no	1.29E-04	0.08				no
CHE3	He	240.83	240	0.004	224.633	0.004	par	no	no	no	9.47E-05	0.07				no
CHE3	He	150.30	150	0.007	100.976	0.010	par	no	yes	no	2.30E-04	0.08	2.90E-03	0.11		no
CHE3	He	180.43	180	0.006	154.289	0.006	par	no	yes	no	5.69E-05	0.07	1.81E-02	0.11		no
CHE3	He	210.39	210	0.005	191.830	0.005	par	no	yes	no	4.57E-05	0.07	0.0692.3	0.09		no
CHE3	He	240.83	240	0.004	224.633	0.004	par	no	yes	no	4.37E-05	0.07	1.73E-01	0.08		no
CHE3	He	496.63	high	0.002	169.550	0.006	perp	no	no	yes	6.00E-04	0.12			220.00	no
CHE3	He	697.17	high	0.001	348.020	0.003	perp	no	no	yes	3.26E-05	0.11			27048.00	no
CHE3	He	930.74	high	0.001	544.040	0.002	perp	no	no	yes	2.30E-06	0.08			18498.00	no
CHE3	He	1106.83	high	0.001	733.010	0.001	perp	no	no	yes	5.40E-06	0.12			25338.57	no
CHE3	He	1323.92	high	0.001	929.780	0.001	perp	no	no	yes	7.90E-07	0.11			64803.00	no

CHE3	He	496.63	high	0.002	169.550	0.006	perp	no	no	no	3.38E-04	0.08				no
CHE3	He	697.17	high	0.001	348.020	0.003	perp	no	no	no	6.89E-04	0.07				no
CHE3	He	930.74	high	0.001	544.040	0.002	perp	no	no	no	3.27E-04	0.10				no
CHE3	He	1106.83	high	0.001	733.010	0.001	perp	no	no	no	1.79E-04	0.11				no
CHE3	He	1323.92	high	0.001	929.780	0.001	perp	no	no	no	3.90E-05	0.10				no
CHE3	He	496.63	high	0.002	169.550	0.006	perp	no	yes	no	3.27E-04	0.08	8.28E-03	0.03		no
CHE3	He	697.17	high	0.001	348.020	0.003	perp	no	yes	no	9.54E-04	0.09	6.20E-05	0.01		no
CHE3	He	930.74	high	0.001	544.040	0.002	perp	no	yes	no	5.00E-04	0.11	1.00E-05	0.09		no
CHE3	He	1106.83	high	0.001	733.010	0.001	perp	no	yes	no	1.09E-04	0.12	5.35E+01	0.09		no
CHE3	He	1323.92	high	0.001	929.780	0.001	perp	no	yes	no	2.05E-05	0.09	2.58E+00	0.01		no
CHE3	He	496.63	high	0.002	169.550	0.006	perp	no	yes	yes	7.46E-06	0.10	4.88E-05	0.06	27626.00	no
CHE3	He	697.17	high	0.001	348.020	0.003	perp	no	yes	yes	1.09E-05	0.10	6.00E-05	0.06	67063.76	no
CHE3	He	930.74	high	0.001	544.040	0.002	perp	no	yes	yes	3.74E-06	0.11	2.99E-04	0.00	39630.00	no
CHE3	He	1106.83	high	0.001	733.010	0.001	perp	no	yes	yes	8.99E-03	0.11	6.33E-03	0.05	64458.00	no
CHE3	He	1323.92	high	0.001	929.780	0.001	perp	no	yes	yes	5.90E-07	0.08	3.12E-04	0.05	22762.00	no
EBN9	He	771.00	high	0.001	752.000	0.001	par	no	no	no	5.00E-07	0.08				no
EBN9	He	1.00	REV	0.500	4.000	0.200	par	no	no	no	2.50E-07	0.02				yes
EBN9	He	136.20	150	0.007	133.900	0.007	par	no	no	no	5.00E-07	0.04				no
CHE2	CH4	149.29	150	0.007	80.000	0.013	perp	no	no	no	6.35E-07	0.20				no
CHE2	CH4	-0.25	REV	-3.937	34.558	0.029	perp	no	no	no	6.76E-07	0.14				yes
CHE2	CH4	149.29	150	0.007	80.000	0.013	perp	no	yes	no	8.70E-07	0.18	3.04E-05	0.16		no
CHE2	CH4	-0.25	REV	-3.937	34.558	0.029	perp	no	yes	no	7.61E-07	0.13	2.80E-04	0.09		yes
CHE2	CH4	149.29	150	0.007	80.000	0.013	perp	no	yes	yes	4.99E-07	0.11	4.613E-05	0.12	2655.71	no
CHE2	CH4	-0.25	REV	-3.937	34.558	0.029	perp	no	yes	yes	3.41E-06	0.07	1.88E-05	0.11	4882.29	yes
CHE2	CH4	149.29	150	0.007	80.000	0.013	perp	no	no	yes	4.44E-07	0.13			2476.12	no
CHE2	CH4	-0.25	REV	-3.937	34.558	0.029	perp	no	no	yes	2.93E-07	0.06			4525.73	yes

Appendix N

Table N.1. Pressure expansion experiment results for MPD experiment. All experiments were done using helium gas.

Sample	P, psig	Pclass, psig	1/P, psig^{-1}	Peq, psig	1/Peq	lamination	hole	fracture	b-val	Kmatrix, mD	Phimatrix, frac	Kfrac, mD	Phifrac, frac	b_val, psig^{-1}	Pconf, psig	REV
EBN20	68.05	150	0.014	45.90	0.021	par	no	yes	yes	3.32E-06	0.09	1.59E-05	0.07	821.06		no
EBN20	157.19	150	0.006	114.25	0.009	par	no	yes	yes	2.01E-07	0.13	3.00E-05	0.04	541.59		no
EBN20	280.45	high	0.004	224.89	0.004	par	no	yes	yes	3.91E-05	0.07	5.00E-06	0.04	3537.36		no
EBN20	100.16	150	0.010	135.69	0.007	par	no	yes	yes	6.08E-07	0.12	2.87E-05	0.04	512.08		yes
EBN20	68.05	150	0.014	45.90	0.021	par	no	yes	no	2.30E-08	0.09	1.34791E-05	0.07			no
EBN20	157.19	150	0.006	114.25	0.009	par	no	yes	no	1.15E-08	0.13	7.51796E-05	0.05			no
EBN20	280.45	high	0.004	224.89	0.004	par	no	yes	no	2.1145E-05	0.09	2.23737E-05	0.08			no
EBN20	100.16	150	0.010	135.69	0.007	par	no	yes	no	8.0481E-07	0.07	0.002329314	0.06			yes
EBN20	68.05	150	0.014	45.90	0.021	par	no	no	yes	1.38E-05	0.06			946.76		no
EBN20	157.19	150	0.006	114.25	0.009	par	no	no	yes	1.90E-05	0.07			838.14		no
EBN20	280.45	high	0.004	224.89	0.004	par	no	no	yes	1.05E-05	0.06			13440.45		no
EBN20	100.16	150	0.010	135.69	0.007	par	no	no	yes	1.48E-05	0.04			4330.67		yes
EBN20	68.05	150	0.014	45.90	0.021	par	no	no	no	1.31E-05	0.06					no
EBN20	157.19	150	0.006	114.25	0.009	par	no	no	no	1.86E-05	0.04					no
EBN20	280.45	high	0.004	224.89	0.004	par	no	no	no	1.89E-05	0.06					no
EBN20	100.16	150	0.010	135.69	0.007	par	no	no	no	1.28E-04	0.05					yes
EBN20	101.96	150	0.010	65.32	0.015	perp	no	yes	yes	1.76E-06	0.05	8.60E-04	0.09	278.76		no
EBN20	193.87	180	0.005	148.09	0.007	perp	no	yes	yes	3.01E-06	0.04	8.52E-04	0.08	303.05		no

EBN20	300.09	high	0.003	249.94	0.004	perp	no	yes	yes	1.19E-05	0.04	6.28E-04	0.11	395.75		no
EBN20	407.17	high	0.002	357.29	0.003	perp	no	yes	yes	2.03E-05	0.06	3.81E-05	0.10	383.46		no
EBN20	521.96	high	0.002	447.03	0.002	perp	no	yes	yes	1.68E-07	0.05	1.15E-04	0.08	3739.31		no
EBN20	108.77	150	0.009	201.39	0.005	perp	no	yes	yes	1.35E-06	0.04	5.73E-06	0.08	12697.01		yes
EBN20	39.90	150	0.025	92.21	0.011	perp	no	yes	yes	1.34E-07	0.05	4.38E-06	0.07	51481.49		yes
EBN20	22.83	150	0.044	40.05	0.025	perp	no	yes	yes	8.65E-06	0.09	9.29E-06	0.05	2120.17		yes
EBN20	101.96	150	0.010	65.32	0.015	perp	no	yes	no	4.10E-07	0.08	4.57E-04	0.08			no
EBN20	193.87	180	0.005	148.09	0.007	perp	no	yes	no	2.28E-06	0.06	4.61E-04	0.08			no
EBN20	300.09	high	0.003	249.94	0.004	perp	no	yes	no	1.52E-05	0.05	7.15E-05	0.09			no
EBN20	407.17	high	0.002	357.29	0.003	perp	no	yes	no	1.62E-05	0.06	3.99E-05	0.08			no
EBN20	521.96	high	0.002	447.03	0.002	perp	no	yes	no	2.74E-06	0.06	4.98E-04	0.10			no
EBN20	108.77	150	0.009	201.39	0.005	perp	no	yes	no	3.35E-06	0.06	7.56E-04	0.10			yes
EBN20	39.90	150	0.025	92.21	0.011	perp	no	yes	no	8.67E-07	0.05	5.77E-04	0.08			yes
EBN20	22.83	150	0.044	40.05	0.025	perp	no	yes	no	8.32E-06	0.06	3.96E-04	0.04			yes
EBN20	101.96	150	0.010	65.32	0.015	perp	no	no	yes	5.41E-05	0.05			77.90		no
EBN20	193.87	180	0.005	148.09	0.007	perp	no	no	yes	1.14E-05	0.05			608.20		no
EBN20	300.09	high	0.003	249.94	0.004	perp	no	no	yes	3.29E-05	0.05			147.37		no
EBN20	407.17	high	0.002	357.29	0.003	perp	no	no	yes	1.47E-05	0.04			578.06		no
EBN20	521.96	high	0.002	447.03	0.002	perp	no	no	yes	1.22E-06	0.03			9900.10		no
EBN20	108.77	150	0.009	201.39	0.005	perp	no	no	yes	5.74E-06	0.04			3852.33		yes
EBN20	39.90	150	0.025	92.21	0.011	perp	no	no	yes	3.37E-06	0.04			4006.60		yes
EBN20	22.83	150	0.044	40.05	0.025	perp	no	no	yes	7.19E-06	0.13			414.87		yes
EBN20	101.96	150	0.010	65.32	0.015	perp	no	no	no	1.002E-05	0.04					no
EBN20	193.87	180	0.005	148.09	0.007	perp	no	no	no	1.3023E-05	0.08					no
EBN20	300.09	high	0.003	249.94	0.004	perp	no	no	no	1.2288E-05	0.05					no
EBN20	407.17	high	0.002	357.29	0.003	perp	no	no	no	1.5978E-05	0.04					no

EBN20	521.96	high	0.002	447.03	0.002	perp	no	no	no	2.1041E-05	0.05					no
EBN20	108.77	150	0.009	201.39	0.005	perp	no	no	no	2.39E-05	0.04					yes
EBN20	39.90	150	0.025	92.21	0.011	perp	no	no	no	1.4757E-05	0.04					yes
EBN20	22.83	150	0.044	40.05	0.025	perp	no	no	no	1.3873E-05	0.06					yes
EBN20	69.05	150	0.014	45.96	0.022	par	yes	yes	yes	4.02E-05	0.08	3.91E-03	0.15	7240.18		no
EBN20	158.19	150	0.006	119.71	0.008	par	yes	yes	yes	4.14E-04	0.09	1.99E-03	0.12	1376.33		no
EBN20	281.45	high	0.004	230.50	0.004	par	yes	yes	yes	1.88E-04	0.09	2.92E-04	0.14	3351.55		no
EBN20	101.16	150	0.010	134.60	0.007	par	yes	yes	yes	3.64E-04	0.09	2.57E-03	0.20	1551.76		yes
EBN20	69.05	150	0.014	45.96	0.022	par	yes	yes	no	4.46E-04	0.05	5.60E-04	0.22			no
EBN20	158.19	150	0.006	119.71	0.008	par	yes	yes	no	1.09E-03	0.11	6.07E-02	0.21			no
EBN20	281.45	high	0.004	230.50	0.004	par	yes	yes	no	8.14E-04	0.07	1.05E-03	0.14			no
EBN20	101.16	150	0.010	134.60	0.007	par	yes	yes	no	1.19E-03	0.09	1.33E-03	0.15			yes
EBN20	69.05	150	0.014	45.96	0.022	par	yes	no	no	1.93E-03	0.09					no
EBN20	158.19	150	0.006	119.71	0.008	par	yes	no	no	9.84E-04	0.09					no
EBN20	281.45	high	0.004	230.50	0.004	par	yes	no	no	8.05E-04	0.08					no
EBN20	101.16	150	0.010	134.60	0.007	par	yes	no	no	5.77E-04	0.06					yes
EBN20	69.05	150	0.014	45.96	0.022	par	yes	no	yes	2.27E-05	0.09			34987.91		no
EBN20	158.19	150	0.006	119.71	0.008	par	yes	no	yes	3.37E-05	0.11			32440.35		no
EBN20	281.45	high	0.004	230.50	0.004	par	yes	no	yes	3.57E-04	0.08			1902.41		no
EBN20	101.16	150	0.010	134.60	0.007	par	yes	no	yes	6.51E-04	0.10			1171.28		yes
EBN20	71.55	150	0.014	66.04	0.015	perp	yes	no	yes	7.31E-06	0.06			3364.91		no
EBN20	23.16	150	0.043	26.31	0.038	perp	yes	no	yes	5.77E-06	0.04			6855.12		yes
EBN20	71.55	150	0.014	66.04	0.015	perp	yes	no	no	3.31E-05	0.04					no
EBN20	23.16	150	0.043	26.31	0.038	perp	yes	no	no	1.31E-06	0.16					yes
EBN9	146.40	150	0.007	84.78	0.012	par	no	no	no	9.41E-05	0.04					no
EBN9	239.83	240	0.004	138.81	0.007	par	no	no	no	2.05E-03	0.04					no

EBN9	512.36	high	0.002	294.22	0.003	par	no	no	no	1.48E-04	0.04					no
EBN9	146.40	150	0.007	84.78	0.012	par	no	no	yes	9.96E-05	0.04			894.80		no
EBN9	239.83	240	0.004	138.81	0.007	par	no	no	yes	2.56E-04	0.04			541.99		no
EBN9	512.36	high	0.002	294.22	0.003	par	no	no	yes	2.25E-04	0.04			1931.82		no
EBN9	146.40	150	0.007	84.78	0.012	par	no	yes	no	4.16E-09	0.18	4.96E-03	0.11			no
EBN9	239.83	240	0.004	138.81	0.007	par	no	yes	no	2.83E-09	0.13	5.56E-02	0.07			no
EBN9	512.36	high	0.002	294.22	0.003	par	no	yes	no	1.56E-09	0.13	4.32E-03	0.12			no
EBN33	206.00	210	0.005	104.00	0.010	par	no	no	no	8.14E-04	0.11					no
EBN33	298.00	high	0.003	201.00	0.005	par	no	no	no	6.87E-04	0.06					no
EBN33	409.00	high	0.002	305.00	0.003	par	no	no	no	7.03E-04	0.08					no
EBN33	491.00	high	0.002	397.00	0.003	par	no	no	no	7.79E-04	0.13					no
EBN33	3.00	REV	0.333	189.00	0.005	par	no	no	no	7.98E-04	0.09					yes
EBN33	206.00	210	0.005	104.00	0.010	par	no	no	yes	5.30E-04	0.13			289.61		no
EBN33	298.00	high	0.003	201.00	0.005	par	no	no	yes	1.37E-04	0.10			1852.36		no
EBN33	409.00	high	0.002	305.00	0.003	par	no	no	yes	1.96E-04	0.09			1345.59		no
EBN33	491.00	high	0.002	397.00	0.003	par	no	no	yes	7.87E-05	0.13			3871.23		no
EBN33	3.00	REV	0.333	189.00	0.005	par	no	no	yes	3.12E-04	0.08			752.56		yes
EBN33	206.00	210	0.005	104.00	0.010	par	no	yes	yes	1.16E-04	0.09	1.48E-04	0.12	2333.68		no
EBN33	298.00	high	0.003	201.00	0.005	par	no	yes	yes	3.59E-05	0.13	3.81E-04	0.05	6330.59		no
EBN33	409.00	high	0.002	305.00	0.003	par	no	yes	yes	2.73E-05	0.07	2.21E-03	0.07	3660.55		no
EBN33	491.00	high	0.002	397.00	0.003	par	no	yes	yes	3.64E-05	0.08	2.49E-03	0.08	2759.56		no
EBN33	3.00	REV	0.333	189.00	0.005	par	no	yes	yes	1.92E-05	0.08	2.57E-03	0.07	3212.69		yes
EBN33	206.00	210	0.005	104.00	0.010	par	no	yes	no	6.33E-04	0.11	1.21E-03	0.10			no
EBN33	298.00	high	0.003	201.00	0.005	par	no	yes	no	5.92E-04	0.10	9.89E-03	0.12			no
EBN33	409.00	high	0.002	305.00	0.003	par	no	yes	no	6.27E-04	0.08	5.62E-03	0.10			no
EBN33	491.00	high	0.002	397.00	0.003	par	no	yes	no	6.22E-04	0.07	8.10E-03	0.10			no

EBN33	3.00	REV	0.333	189.00	0.005	par	no	yes	no	2.74E-04	0.07	1.89E-02	0.10			yes
EBN20	69.05	150	0.014	46.90	0.021	par	no	yes	no	1.20E-04	0.05	4.00E-09	0.05			no
EBN20	158.19	150	0.006	115.25	0.009	par	no	yes	no	8.00E-05	0.05	4.00E-09	0.05			no
EBN20	281.45	high	0.004	225.89	0.004	par	no	yes	no	2.00E-05	0.05	4.00E-09	0.05			no
EBN20	101.16	150	0.010	136.69	0.007	par	no	yes	no	4.00E-05	0.05	4.00E-09	0.05			yes
EBN20	69.05	150	0.014	46.90	0.021	par	no	yes	yes	1.26E-05	0.04	5.70E-05	0.02	272.00		no
EBN20	158.19	150	0.006	115.25	0.009	par	no	yes	yes	3.11E-05	0.12	8.88E-03	0.01	231.38		no
EBN20	281.45	high	0.004	225.89	0.004	par	no	yes	yes	2.52E-05	0.08	7.40E-06	0.01	116.56		no
EBN9	147.40	150	0.007	85.78	0.012	par	no	yes	yes	1.59E-07	0.05	2.17E-02	0.01	166.75		no
EBN9	240.83	240	0.004	139.81	0.007	par	no	yes	yes	1.53E-03	0.01	1.45E-06	0.03	8.20		no
EBN9	513.36	high	0.002	295.22	0.003	par	no	yes	no	9.15E-05	0.01	1.83E-03	0.01	2523.83		no
NEX7	524.00	high	0.002	321.00	0.003	perp	no	yes	no	1.00E-09	0.06	7.21E-03	0.08			no
NEX7	641.00	high	0.002	513.30	0.002	perp	no	yes	no	2.66E-09	0.05	1.08E-01	0.05			no
NEX7	748.00	high	0.001	652.00	0.002	perp	no	yes	no	2.67E-07	0.10	1.62E-03	0.10			no
NEX7	850.00	high	0.001	769.00	0.001	perp	no	yes	no	3.00E-08	0.05	2.95E-03	0.10			no
NEX7	524.00	high	0.002	321.00	0.003	perp	no	yes	yes	1.16E-10	0.08	3.82E-03	0.09	67516.00		no
NEX7	641.00	high	0.002	513.30	0.002	perp	no	yes	yes	8.64E-11	0.06	6.51E-03	0.02	5612.36		no
NEX7	748.00	high	0.001	652.00	0.002	perp	no	yes	yes	8.52E-11	0.09	3.13E-04	0.10	22977.01		no
NEX7	850.00	high	0.001	769.00	0.001	perp	no	yes	yes	3.87E-10	0.10	4.20E-07	0.06	81718.55		no
NEX7	524.00	high	0.002	321.00	0.003	perp	no	no	no	2.22E-03	0.01					no
NEX7	641.00	high	0.002	513.30	0.002	perp	no	no	no	3.18E-03	0.01					no
NEX7	748.00	high	0.001	652.00	0.002	perp	no	no	no	3.54E-03	0.02					no
NEX7	524.00	high	0.002	321.00	0.003	perp	no	no	yes	2.60E-05	0.02			27849.82		no
NEX7	641.00	high	0.002	513.30	0.002	perp	no	no	yes	1.13E-04	0.02			12655.00		no
NEX7	748.00	high	0.001	652.00	0.002	perp	no	no	yes	1.03E-05	0.02			87006.50		no
NEX15	509.00	high	0.002	327.00	0.003	perp	no	no	no	3.25E-05	0.02				1500	no

NEX15	620.00	high	0.002	491.00	0.002	perp	no	no	no	2.69E-05	0.03				1500	no
NEX15	727.00	high	0.001	629.00	0.002	perp	no	no	no	4.90E-06	0.04				1500	no
NEX15	509.00	high	0.002	327.00	0.003	perp	no	no	yes	5.70E-08	0.03				1500	no
NEX15	620.00	high	0.002	491.00	0.002	perp	no	no	yes	1.23E-05	0.02			2476.26	1500	no
NEX15	727.00	high	0.001	629.00	0.002	perp	no	no	yes	5.69E-04	0.06			41520.38	1500	no
NEX15	509.00	high	0.002	327.00	0.003	perp	no	yes	no	2.20E-07	0.07	3.60E-03	0.09		1500	no
NEX15	620.00	high	0.002	491.00	0.002	perp	no	yes	no	4.89E-07	0.06	3.60E-03	0.09		1500	no
NEX15	509.00	high	0.002	327.00	0.003	perp	no	yes	yes	1.08E-07	0.03	6.36E-05	0.07	14781.70	1500	no
NEX15	620.00	high	0.002	491.00	0.002	perp	no	yes	yes	5.22E-09	0.04	1.47E-04	0.02	8580.29	1500	no
NEX15	727.00	high	0.001	629.00	0.002	perp	no	yes	yes	2.26E-08	0.06	4.00E-05	0.01	1450.16	1500	no
NEX15	532.00	high	0.002	339.00	0.003	perp	no	no	no	1.84E-05	0.02				2000	no
NEX15	626.00	high	0.002	516.00	0.002	perp	no	no	no	1.26E-05	0.04				2000	no
NEX15	735.00	high	0.001	636.00	0.002	perp	no	no	no	1.58E-05	0.02				2000	no
NEX15	821.00	high	0.001	742.00	0.001	perp	no	no	no	1.26E-05	0.06				2000	no
NEX15	4.00	REV	0.200	250.00	0.004	perp	no	no	no	1.30E-05	0.02				2000	yes
NEX15	3.00	REV	0.250	93.00	0.011	perp	no	no	no	1.09E-05	0.01				2000	yes
NEX15	532.00	high	0.002	339.00	0.003	perp	no	no	yes	8.90E-07	0.02			18709.01	2000	no
NEX15	626.00	high	0.002	516.00	0.002	perp	no	no	yes	6.56E-07	0.03			21521.99	2000	no
NEX15	735.00	high	0.001	636.00	0.002	perp	no	no	yes	3.40E-07	0.01			55260.00	2000	no
NEX15	821.00	high	0.001	742.00	0.001	perp	no	no	yes	8.30E-07	0.03			21741.00	2000	no
NEX15	4.00	REV	0.200	250.00	0.004	perp	no	no	yes	7.50E-07	0.01			18307.94	2000	yes
NEX15	3.00	REV	0.250	93.00	0.011	perp	no	no	yes	8.68E-07	0.01			13569.00	2000	yes
NEX15	532.00	high	0.002	339.00	0.003	perp	no	yes	no	9.00E-08	0.07	6.12E-04	0.02		2000	no
NEX15	626.00	high	0.002	516.00	0.002	perp	no	yes	no	2.56E-09	0.04	7.39E-04	0.02		2000	no
NEX15	735.00	high	0.001	636.00	0.002	perp	no	yes	no	1.18E-05	0.02	1.14E-04	0.04		2000	no
NEX15	821.00	high	0.001	742.00	0.001	perp	no	yes	no	1.25E-05	0.06	7.32E-05	0.03		2000	no

|																
NEX15	4.00	REV	0.200	250.00	0.004	perp	no	yes	no	1.69E-08	0.04	5.00E-04	0.05		2000	yes
NEX15	3.00	REV	0.250	93.00	0.011	perp	no	yes	no	2.00E-08	0.03	4.63E-04	0.06		2000	yes
NEX15	532.00	high	0.002	339.00	0.003	perp	no	yes	yes	5.47E-07	0.03	4.98E-04	0.07	649.53	2000	no
NEX15	626.00	high	0.002	516.00	0.002	perp	no	yes	yes	1.30E-06	0.03	2.20E-06	0.03	14951.00	2000	no
NEX15	735.00	high	0.001	636.00	0.002	perp	no	yes	yes	9.00E-09	0.03	2.40E-05	0.06	28427.00	2000	no
NEX15	821.00	high	0.001	742.00	0.001	perp	no	yes	yes	1.64E-09	0.06	4.00E-05	0.04	20859.00	2000	no
NEX15	4.00	REV	0.200	250.00	0.004	perp	no	yes	yes	1.00E-10	0.02	1.22E-04	0.05	4682.57	2000	yes
NEX15	3.00	REV	0.250	93.00	0.011	perp	no	yes	yes	1.27E-09	0.02	1.89E-04	0.04	1897.00	2000	yes
NEX15	516.00	high	0.002	346.00	0.003	perp	no	no	no	6.70E-06	0.08				2500	no
NEX15	619.00	high	0.002	513.00	0.002	perp	no	no	no	8.54E-06	0.01				2500	no
NEX15	715.00	high	0.001	623.00	0.002	perp	no	no	no	8.00E-06	0.02				2500	no
NEX15	516.00	high	0.002	346.00	0.003	perp	no	yes	no	6.80E-05	0.03	2.49E-04	0.04		2500	no
NEX15	516.00	high	0.002	346.00	0.003	perp	no	no	yes	4.28E-07	0.03			22018.00	2500	no
NEX15	516.00	high	0.002	346.00	0.003	perp	no	yes	yes	2.80E-08	0.07	4.13E-05	0.07	5403.00	2500	no

Appendix O
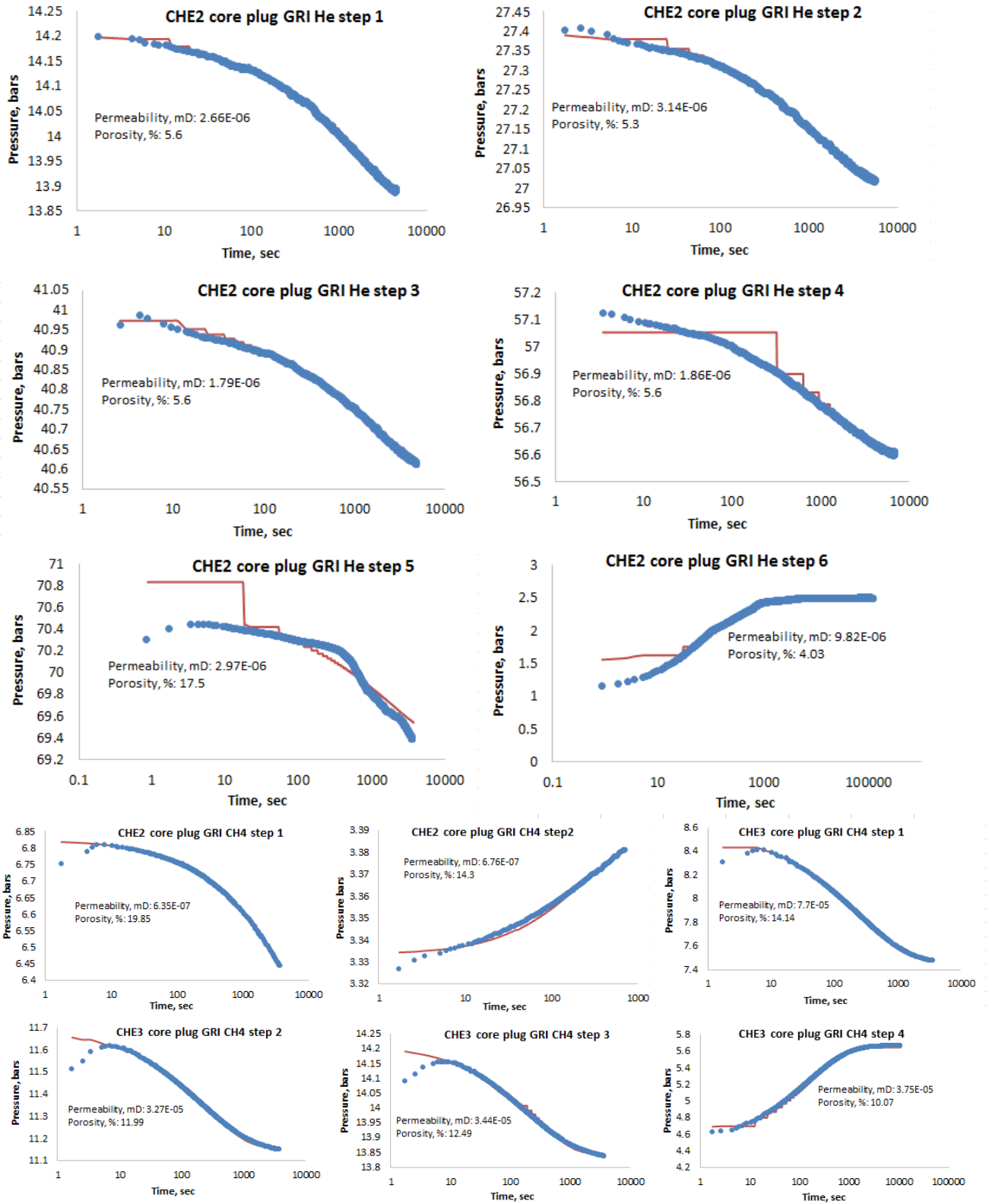
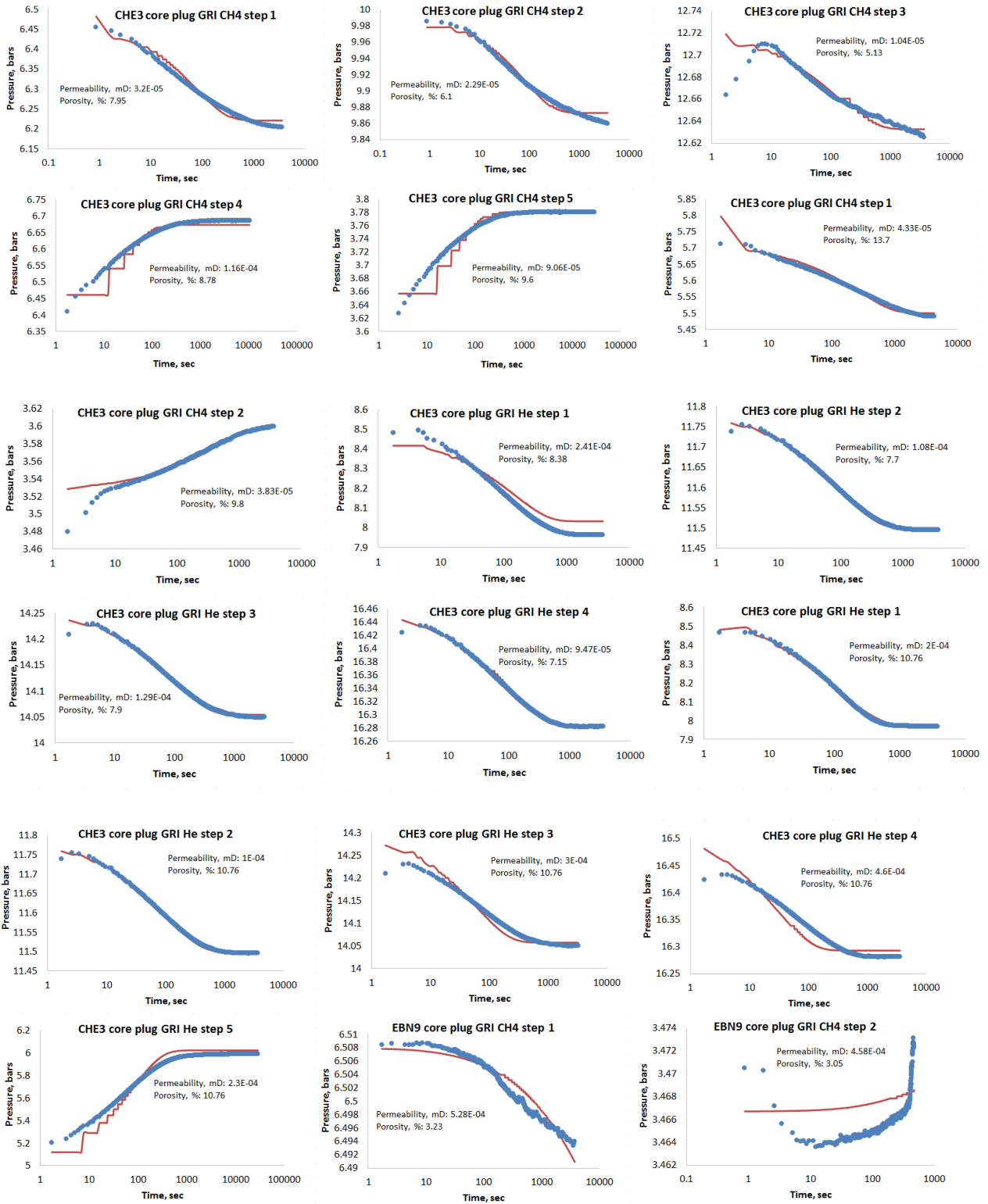**Figure O.1. History matches of the core plug GRI experiment.**

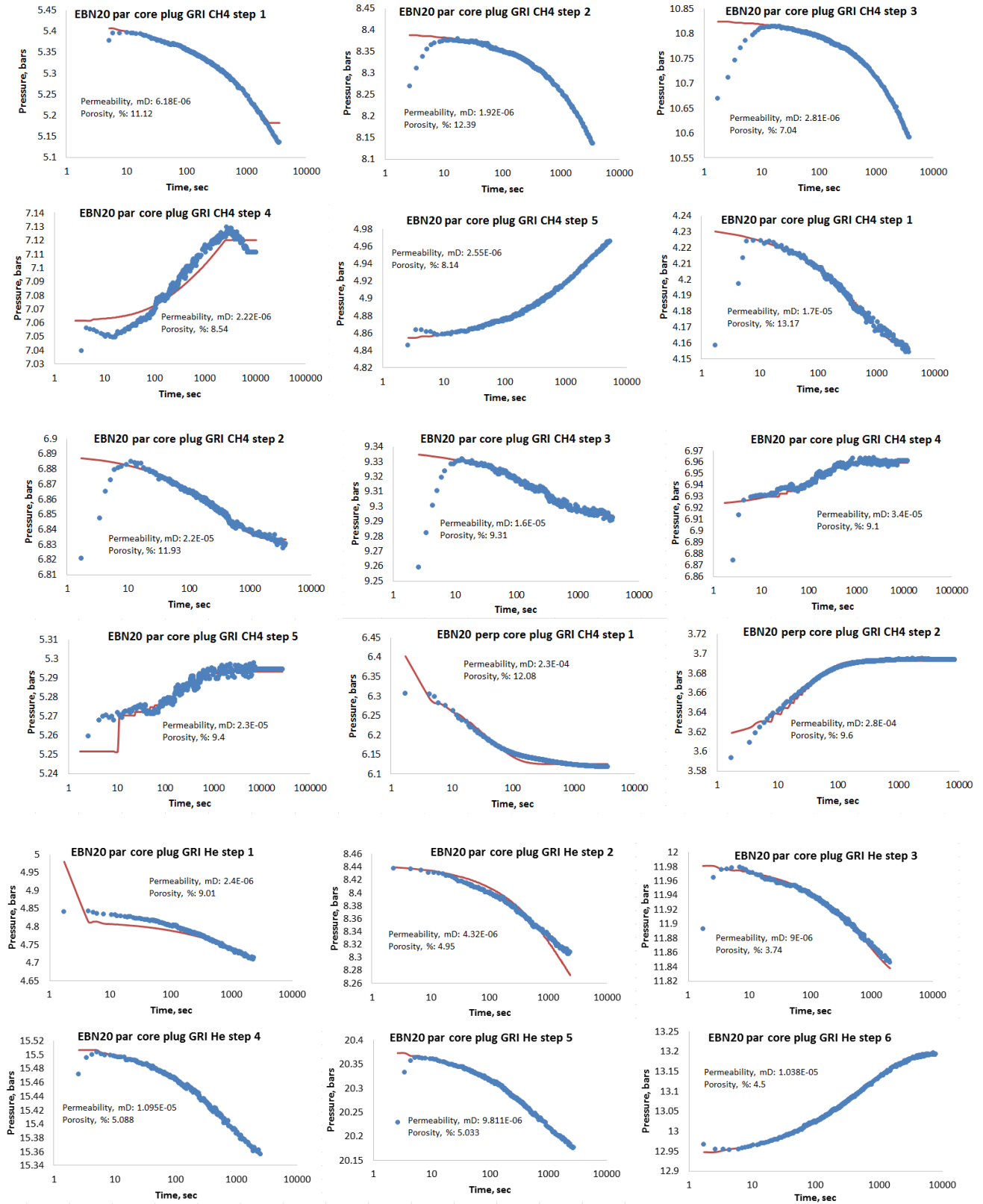**Figure O.2. History matches of the core plug GRI experiment.**

Figure O.3. History matches of the core plug GRI experiment.
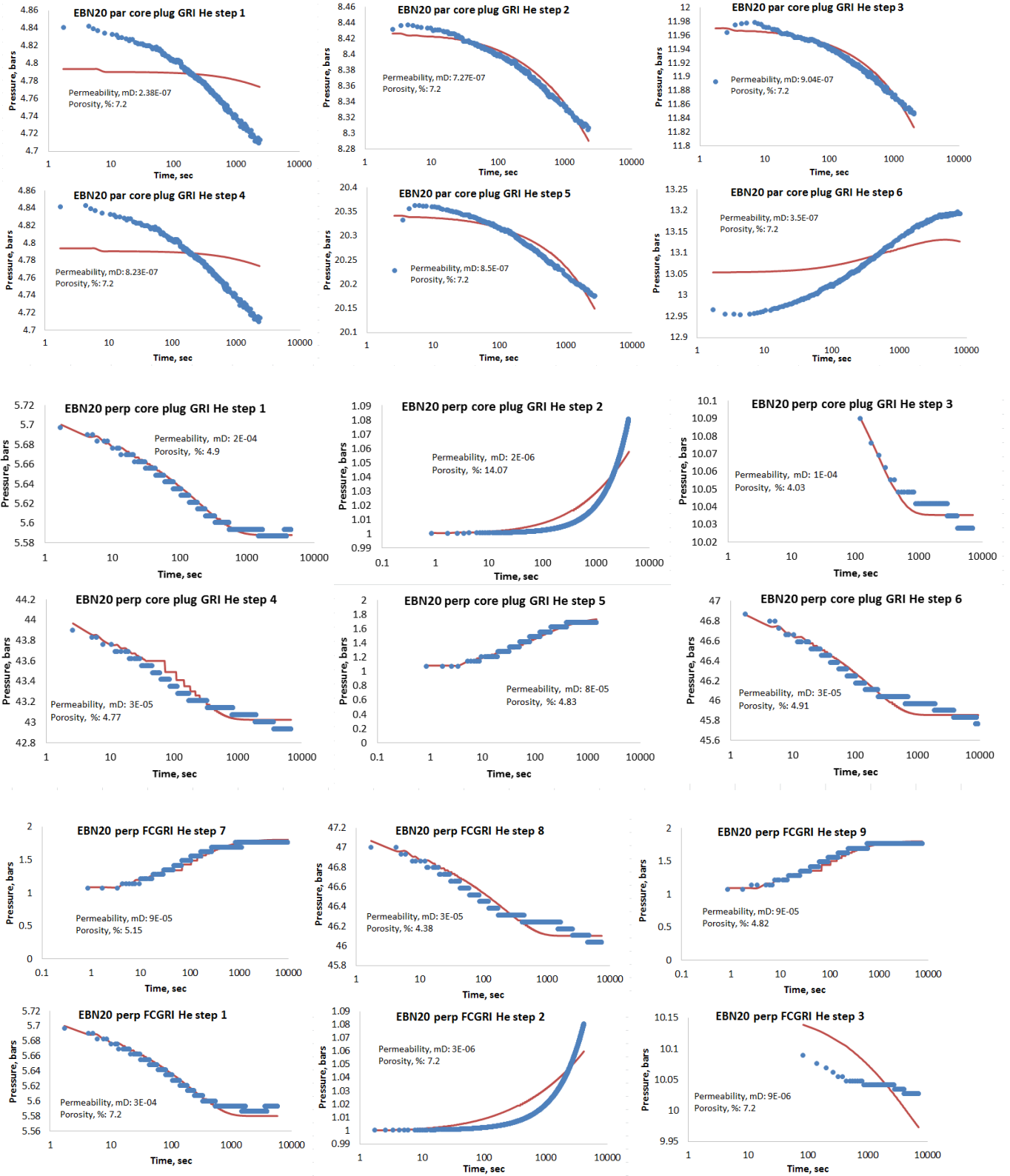
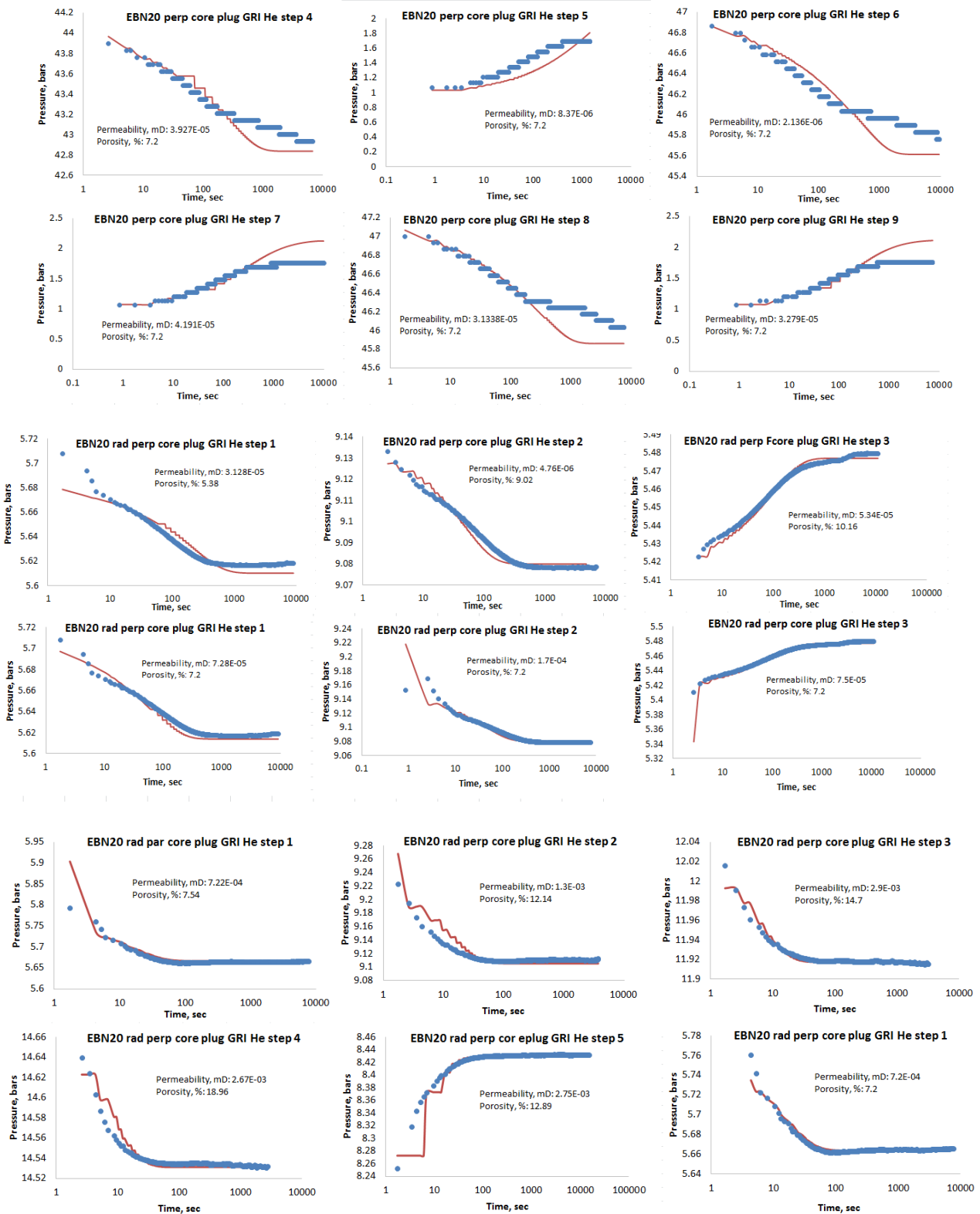**Figure O.4. History matches of the core plug GRI experiment.**

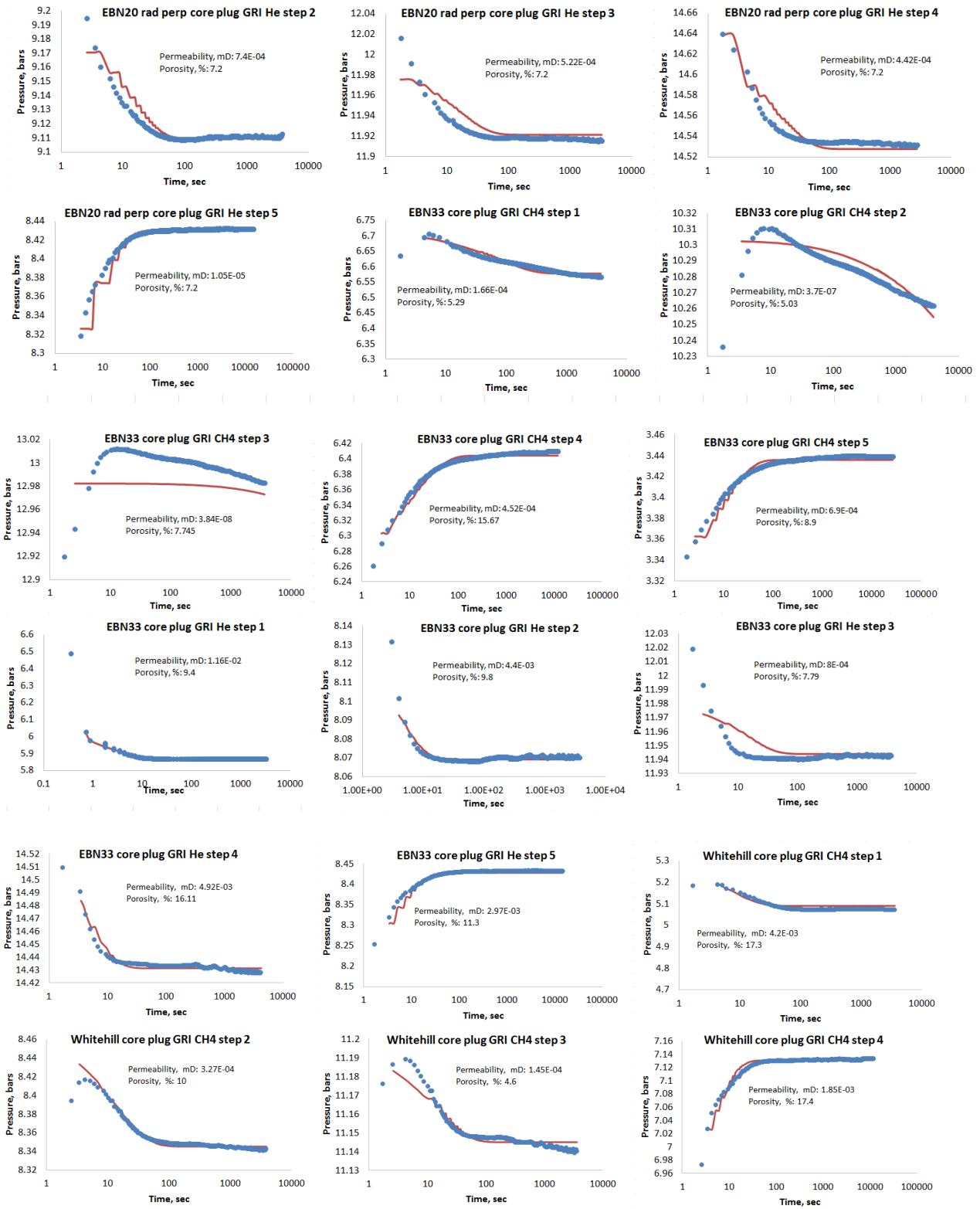**Figure O.5. History matches of the core plug GRI experiment.**

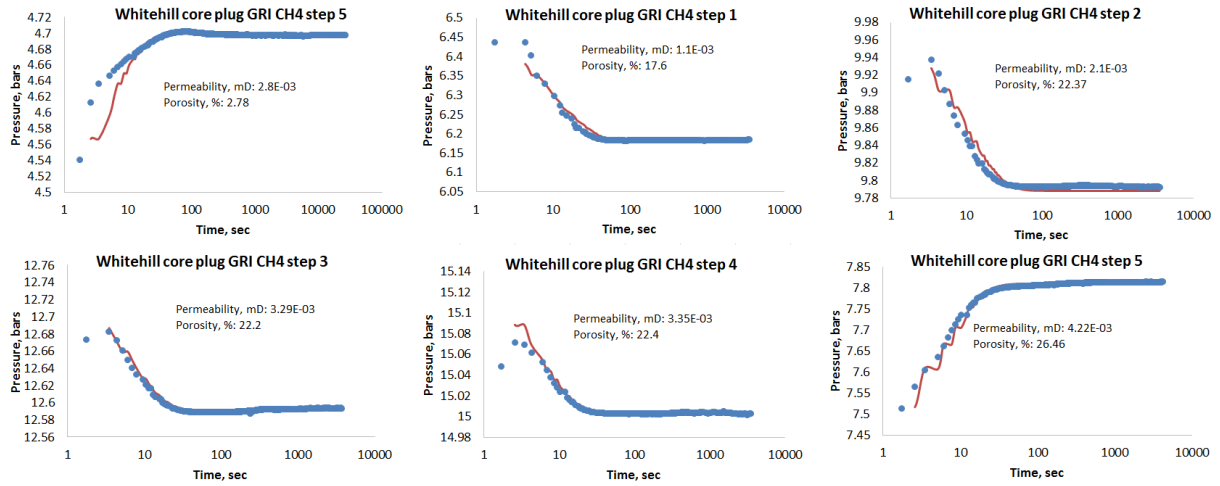**Figure O.6. History matches of the core plug GRI experiment.**

Figure P.7. History matches of the core plug GRI experiment.

Appendix P
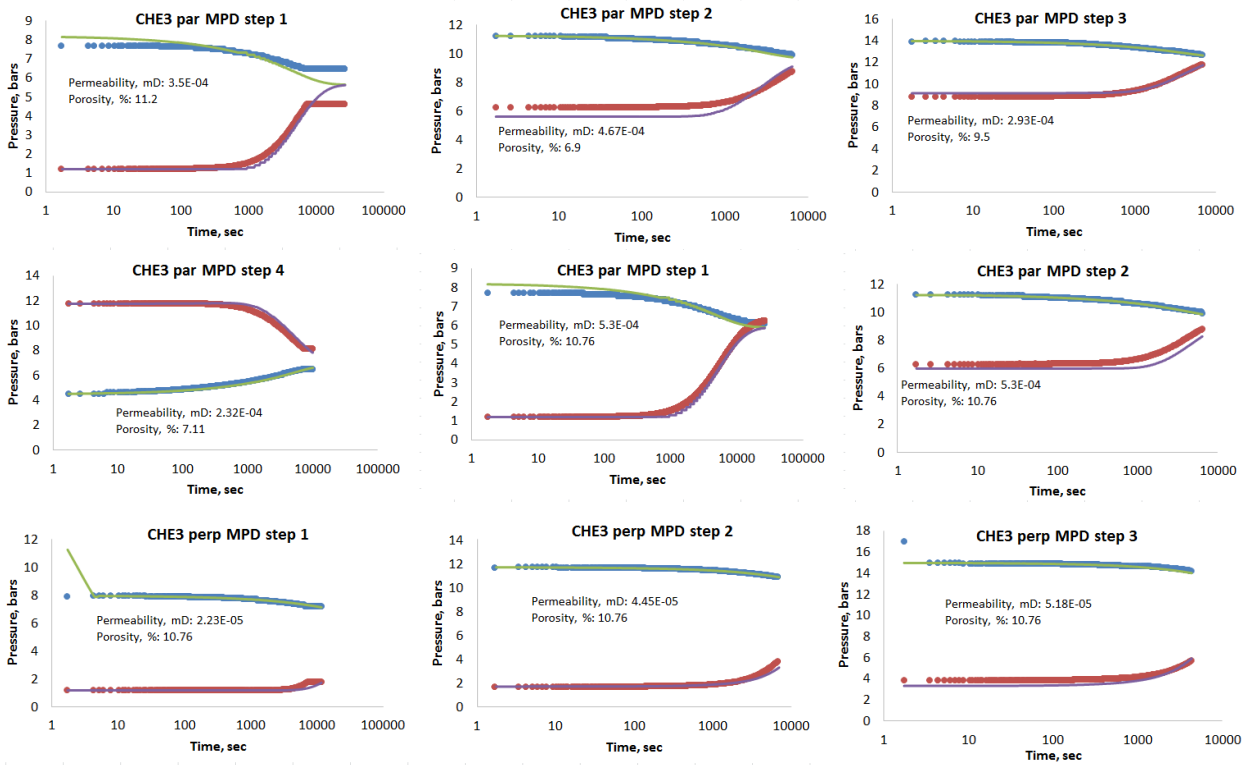
Figure P.1. History matches of the modified pressure decay experiment.
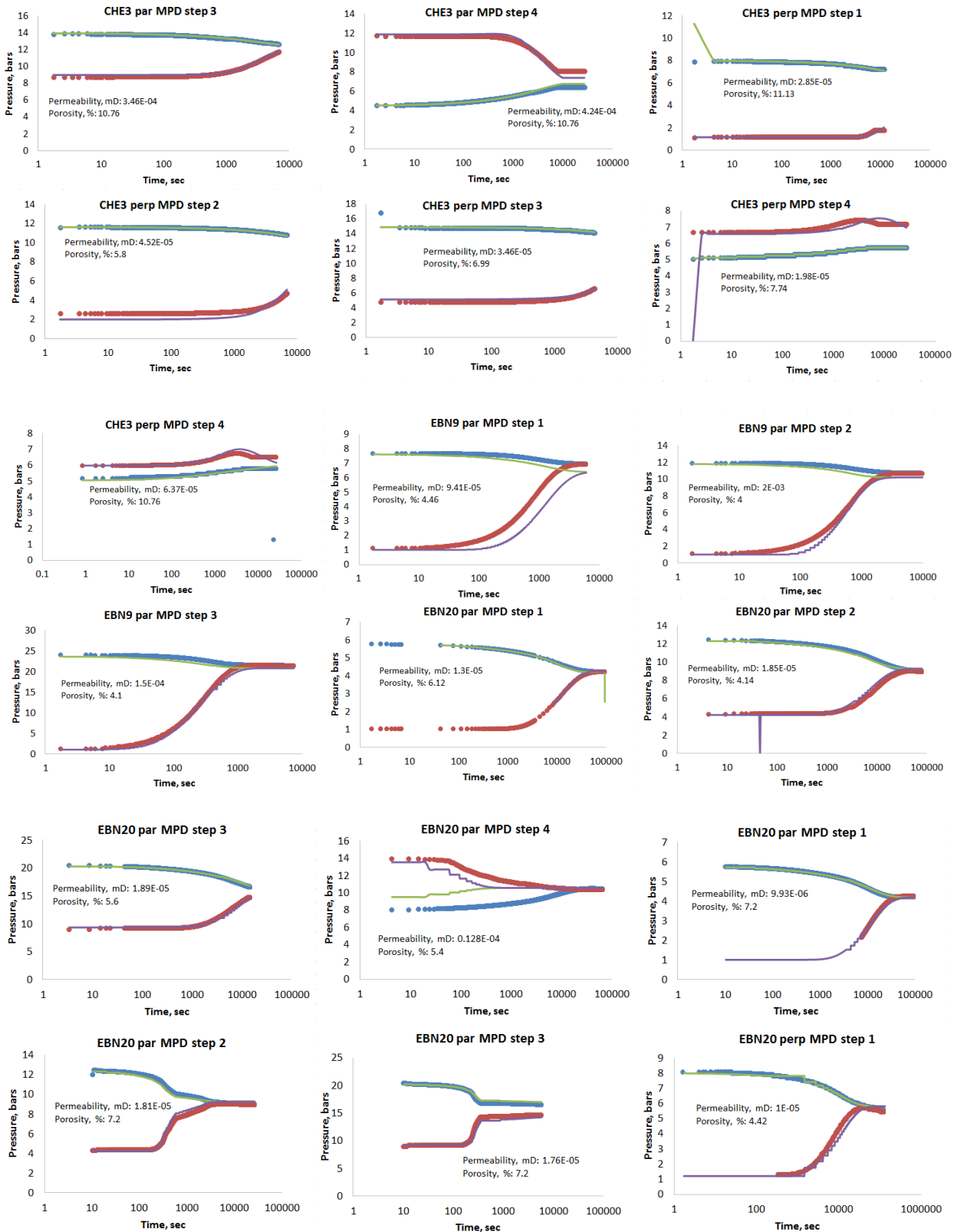
Figure P.2. History matches of the modified pressure decay experiment.
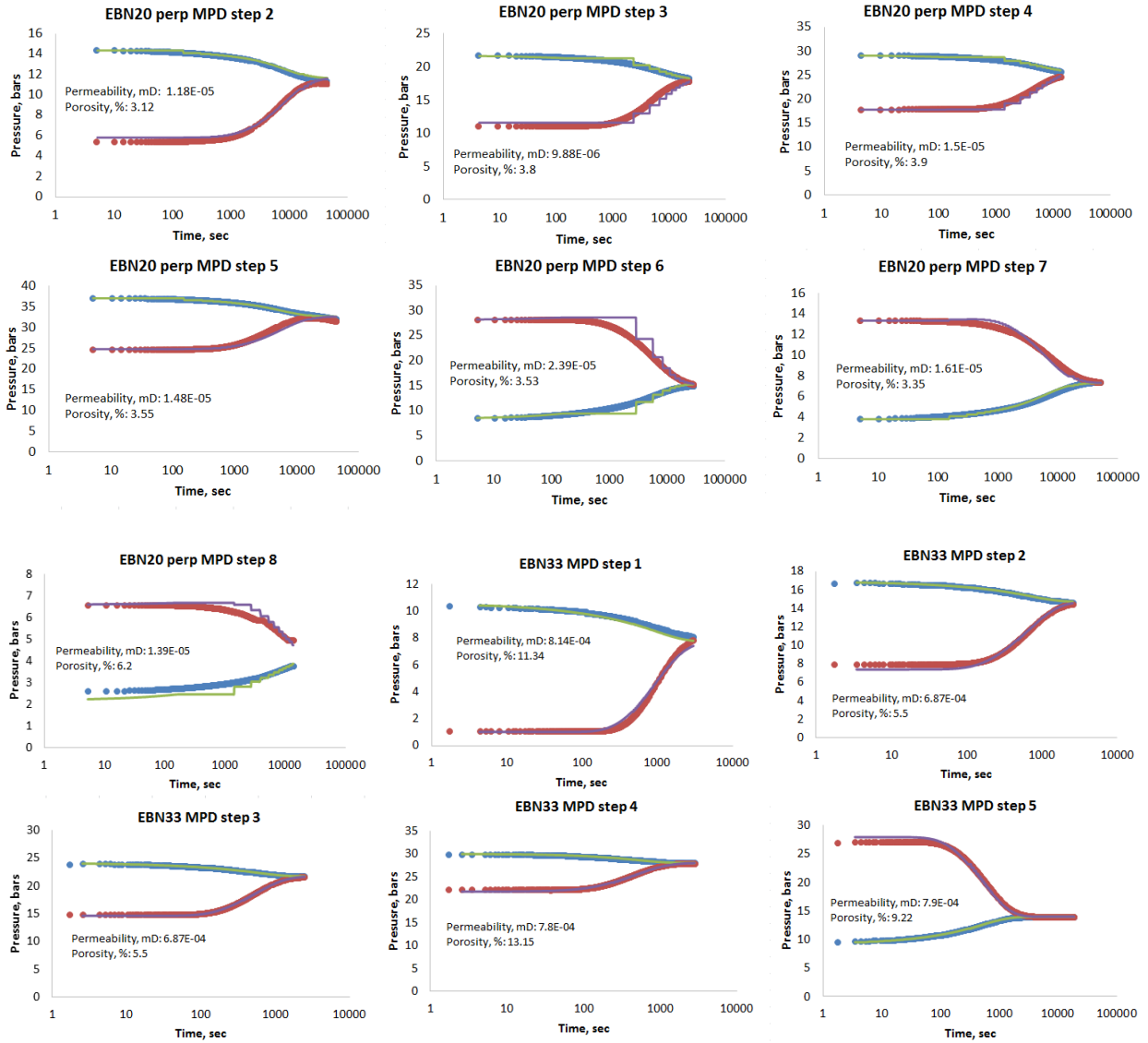
Figure P.3. History matches of the modified pressure decay experiment.

Appendix Q

Table Q. 1. Well KN-1 data.

Depth, m	Pressure, psig	Amount of gas surface conditions, cm^3	Water Saturation,%
84.90 - 85.40	5.0		
85.95 - 86.43			
88.54 - 89.09	1.0		
90.30 - 90.50	5.0	12.76	**39.39**
90.70 - 91.20	2.5	0.76	
91.80 - 92.33	31.7	8.26	**7.76**
93.60 - 94.07	70.0		
93.96 - 94.58	2.6	0.76	

94.47 - 94.92	7.7	1.26	
95.46 - 95.94	22.6	6.26	
97.01 - 97.50	1.4	4.26	**83.91**
97.97 - 98.52	13.4	1.76	
98.62- 99.10	6.1	4.26	
100.65 - 101.14	15.0	8.26	
102.91 - 103.40	2.0	0.76	
104.00 -104.45	2.5	0.76	

Table Q.2. Well FA-2 data.

Depth, m	Pressure, psig	Amount of gas surface conditions, cm^3	Water Saturation,%
72.37 - 72.82	1.6	1.26	
73.12 - 73.58	48.0	24.26	
74.60 - 75.08		7.26	
75.06 - 75.42	14.2	7.26	**77.93**
76.99 - 77.45	11.4		
77.38 - 77.92	0.6	0.00	
79.73 - 80.20		0.26	
80.36 - 80.83	25.0	4.76	
81.10 - 81.51	0.3	0.00	
82.39 - 82.71	19.1	12.76	
83.48 - 83.90	3.2	1.76	
84.50 - 84.97		3.26	**89.60**
84.64 - 85.04	13.1	4.26	
85.42 - 85.92	2.5	0.76	
86.08 - 86.37	0.1	0.00	
86.03 - 86.56	1.0	0.51	
86.77 - 87.22	0.7	0.00	

Table Q.3. Well NA-2 data.

Depth, m	Pressure, psig	Amount of gas surface conditions, cm^3	Water Saturation,%	Overnight pressure, psi
86.45 - 86.85	13.3	5.26	*No data*	
87.39 - 87.97	12.8	4.26	**89.5**	
88.45 - 88.95	6.7	0.76		
89.15 - 89.67	20.9	7.26		
89.95 - 90.40	28.1	9.26		43.6
90.60 - 91.13	13.0	3.26		

91.15 - 91.50	leak – sandstone				
91.50 - 92.08	leak – sandstone				
92.08 - 92.78	leak – sandstone				
93.72 - 94.20	10.2	7.26			
94.80 - 95.20	13.9	6.26			
95.20 - 95.64	10.9	6.26			
95.70 - 96.10	3.9	0.51			
96.10 - 96.80	5.0	3.26			
98.00 - 98.50	20.0	12.26			
98.50 - 98.75	14.2	6.26			
98.90 - 99.33	15.0	13.26			
99.64 - 100.15	14.4	10.26			
100.55 – 101.00	14.3	14.26			
101.00 - 101.50	11.5	14.26			
101.95 - 102.52	7.1	6.26			
102.52 - 102.95	6.0	3.26			
103.50 - 103.90	7.0	0.51			
103.90 - 104.25	4.5	2.26			

Table Q.4.Well NA-3 data.

Depth, m	Pressure, psig	Amount of gas surface conditions, cm^3	Water Saturation,%	Overnight pressure, psi	3days pressure, psi
71.20 - 71.6	25.4	8.26			
71.60 - 72.3	10.5	2.26			
72.30 - 72.74	17.0	16.26	**46.8**		30.0
72.74 - 73.2	12.7	12.26	**60.6**		
74.10 - 74.6	8.3	3.26			
74.60 - 75	18.3	7.26			
75.10 - 75.6	14.6	3.26			
76.00 - 76.6	10.8	5.26			
77.30 - 77.75	8.6	4.26			
77.85 - 78.2	8.2	4.26			
78.66 - 79.06	3.0	2.26			
80.37 - 80.95	14.1	5.26			
81.95 - 82.43	9.5	48.26			47.3
82.48 - 82.75	9.8	44.26			49.0
82.8 - 83.35	4.0	1.76			
83.35 - 83.87	4.8	54.26			54.5

Depth, m	Pressure, psig	Amount of gas surface conditions, cm³	Water Saturation,%	Overnight pressure, psig	6 months, psig
84.15 - 84.6	9.0	10.26			
85.35 - 85.85	4.8	3.26			
86.3 - 86.8	3.5	0.51			
86.9 - 87.35	6.6	1.26			
87.35 - 87.8	4.0	2.26			
87.8 - 88.35	3.0	4.26			
88.35 - 88.7	2.9	1.26			
88.7 - 89.2	6.0	3.26			
89.2 - 89.7	10.0	8.26			
90.45 - 90.95	4.5	3.26			
91.61 - 92.2	3.7	1.26			
92.4 - 92.9	4.9	5.26		8.1	
93.6 - 94.05	7.5	8.26	**91.6**	12.2	

Table Q. 5. Well OA-1 data.

Depth, m	Pressure, psig	Amount of gas surface conditions, cm³	Water Saturation,%	Overnight pressure, psig	6 months, psig
19.20 - 19.50	6.8	2.26			
19.50 – 20.00	3.0	1.26			
21.05 - 21.40	4.4	0.76			
21.55 - 22.05	7.1	1.26			
22.67 - 23.20	8.4	11.26			
23.2 - 23.70	50.0	2.26			
24.45 - 25.05	14.0	6.26			
26.50 – 27.00	4.0	10.26		15.0	
27.20 - 27.75	5.5	12.26		18.0	
32.10 - 32.55	1.0	0.76			330.0
32.70 - 33.24	0.8	0.26			
33.70 - 34.30	1.1	0.76			
34.30 - 34.80	6.1	0.287			
34.90 - 35.40	1.7	1.26			
35.40 – 36.00	5.0	12.26			
36.50 - 37.14	0.1	0.26			
37.14 - 37.50	0.3	0.46			